ROCK FABRIC STUDY OF KAROO DOLERITE SILLS ALONG THE KWAZULU-NATAL NORTH COAST, SOUTH AFRICA: IMPLICATIONS FOR THE MAGMA SOURCE.

by

LAUREN HOYER

A thesis submitted in fulfilment of the academic
requirements for the degree of Doctor of Philosophy in the

Discipline of Geological Sciences

in the School of Agricultural, Earth and Environmental Sciences,
University of KwaZulu-Natal,
Durban, South Africa

2015

- Acknowledgements -

This work has spanned more than five years of my life and there are a lot of people that have helped me complete massive undertaking. At the beginning of this year, I got engaged and we decided to plan our wedding for the week I hand in this work. It has been a whirlwind year where so much has been accomplished with the help of so many amazing people.

Firstly I would like to thank my supervisor and mentor, Mike Watkeys. With your guidance and supervision I am able to submit a body of work that I can be proud of and start of my academic career with enthusiasm and a multitude of ideas. I would also like to thank Steve McCourt and Simon Kattenhorn for their help and kind words of encouragement when they were needed.

The financial assistance of the National Research Foundation (NRF) towards this research, in the form of a Scarce Skills Scholarship, is hereby acknowledged. I would not have been able to complete this project without this generous financial support. Opinions expressed and conclusions arrived at, are those of the author and not necessarily to be attributed to the NRF.

I was awarded a Visiting Research Fellowship from the Institute of Rock Magnetism (IRM) at the University of Minnesota, for which I am extremely grateful. All of the magnetic analyses described in this thesis were undertaken at the IRM in a whirlwind twelve days (and nights). Without this fellowship, I fear this thesis would never have been completed. Thanks must go in particular to Mike Jackson and Dario Bilardello for all of their help and guidance whilst I was at the IRM. Also thank you to the staff and students at the IRM and in the Geology Department, for friendly and informative conversations during the Friday afternoon “tea” sessions.

Thanks must go to Patrick Launeau, who early on in this thesis helped me to understand the necessary processes to undertake in acquiring an adequate fabric using the SPO-2003 and Ellipsoid-2003 programmes. Without his help I would not have been able to produce the copious amounts of petrofabrics in this thesis and at such a high standard.

Thank you to everyone at UKZN who has helped me with all of my sample collection and preparation. Thanks must first go to Mukesh Seyambu and Charishma Ramchurram for making the ridiculous amount of thin sections that were needed for this project (upwards of 400). I think there were making thin sections for me for about 3 years, so thank you for all your hard work. Thank you to Pat Suthan for the geochemical analyses. And a big thank you must go to the

following students; Shannon Aberdeen, Alfie Krebs, Keegan Benallack, David Cousins, Kyle Ridgeway, Leslie Salzmann, Jannie Weitz, Errol Wiles and Warwick Hastie, for basically being my slaves when I needed to go sampling. They endured many hot and windy days on the beaches of the north coast. I could never have managed to finish all this work without your heavy lifting and seemingly endless enthusiasm to drill cores and smell like two stroke oil.

Special thanks must go to the friends that I have made in my time as a postgrad in the Geology Department. The tea time breaks and hour long lunches got me through the tiresome number-crunching days. The days spent at the pool or the beach (or at the pub for that matter) helped keep my head clear. Warwick Hastie is such an awesome friend, he helped me so much when I was just starting out on this project and I own him many thanks for all the questions he's fielded over the years. He was even kind enough to proof read a couple of the chapters in this thesis. To Errol Wiles, my gentle giant and resident mother hen, you hold us all together when we're about to fall apart, thank you so much for your help, especially over the very frustrating past year. To Lauren Pretorius, my namesake and running buddy, you have helped keep me sane and grounded this last year, thank you so much. To all my other friends at varsity who have made my days there some of my happiest; Nkule Dladla and Palesa Leuta for your sweet smiles and words of encouragement; Shannon Dixon with your ridiculous laugh and kind heart, Jannie Weitz for your never-ending smile and sense of humour, Talicia Pillay for your enduring kindness and free spirit, Clarice Romer for your patience and Keegan Benallack for your awfully rude jokes. I will cherish your friendships forever. Thanks also to my friends in Chemistry, Letitia Pillay and Marc Humphries, even though you don't have rocks on the brain, you are still awesome friends that have supported me throughout this crazy process.

Let it just be said that I have the most amazing family in the world! My mom and dad have always supported my thirst for knowledge and my desire to do a PhD, both emotionally and financially. I am so grateful for all the opportunities you have afforded me in my life and I strive to be as kind and patience with my future (you'll have to wait a while) offspring as you have been to me. To my sisters, Joanne and Nicole, you have been such an enormous help, especially these last few months. I would never have been able to juggle so many things in my life if you two weren't always watching out for me and my sanity. And to your husbands, Nigel and Digby, thanks so much for being there when I needed a brother to talk to. Thank you all for such amazing support over the last five plus years, I love you all so much!

Lastly, I am so fortunate to have had my partner in crime by my side the whole way through my PhD, thank you Andy. And I am even luckier because he has been down this road before, finishing his PhD when we had just started dating. Andy, your incredible love for me and unwavering support has enabled me to come out of this process smiling. Your patience and kindness has never faltered and I know that this would have been an uphill scramble if I didn't have you to rely on. You calmed me down when I was worried about the silly things and the big things. You have held my hand through paper rejections, late night sleep-walking episodes and many a random crying fit. Thank you so much for always being there for me and for even reading through this project to make sure it all looks and sounds the way it should. I love you with all my heart and I am so excited to spend the rest of my life with you.

PREFACE

The experimental work described in this thesis was carried out in the Discipline of Geological Sciences, University of KwaZulu-Natal, Westville campus, from August 2012 to November 2015, under the supervision of Professor Mike K. Watkeys.

These studies represent original work by the author and have not otherwise been submitted, in any form, for any degree or diploma to any tertiary institution. Where use has been made of the work of others, it is duly acknowledged in the text.

- Plagiarism Declaration -

I, _____ declare that

1. The research reported in this thesis, except where otherwise indicated, is my original research.

2. This thesis has not been submitted for any degree or examination at any other university.

3. This thesis does not contain other persons' data, pictures, graphs or other information, unless specifically acknowledged as being sourced from other persons.

4. This thesis does not contain other persons' writing, unless specifically acknowledged as being sourced from other researchers. Where other written sources have been quoted, then:
    - Their words have been re-written but the general information attributed to them has been referenced

5. This thesis does not contain text, graphics or tables copied and pasted from the Internet, unless specifically acknowledged, and the source being detailed in the thesis and in the References sections.

Signed: _____

- Contents -

- page –

- Abstract –

This study focuses on magma flow dynamics and directions in Jurassic Karoo dolerite sills along the KwaZulu-Natal (KZN) North Coast, South Africa. The aim of this study is to constrain the magma provenance of these sills and to investigate their relationship with a previously proposed mantle plume at Mwenezi (formerly Nuanetsi), associated with the Karoo triple junction. Magma flow directions within the sills are determined by comparing the results from three methods. Field observations of magma flow indicators are used to infer magma flow directions. These directions are compared to the Shape Preferred Orientation (SPO) of plagioclase grains from 126 samples (378 photomicrographs), and the Anisotropic Magnetic Susceptibility (AMS) of magnetite grains in 238 samples, the fabrics of which are used as a proxy for magma flow.

The SPO programme used to determine the plagioclase fabrics (SPO-2003) is scrutinised, and the process of how the fabric ellipsoids are determined is constrained, using a long axis plagioclase crystal length threshold of 2mm. It is also important to not segment the images upon analyses as this decreases the accuracy of the fit of the ellipses into an ellipsoid. These advancements in the process of a fabric ellipsoid procurement allows for the most accurate fabric to be determined. This fabric may then be used as a proxy for magma flow if the fabric is a reflection of the magma flow sense.

Certain intrusions exhibit fluid-assisted deformation, such as the presence of sedimentary dykes and breccias, which have formed as a result of high volatile components in the sills or adjacent country rocks. A dolerite-hosted breccia is studied in detail so that the nature of the brecciation process may be constrained. The mechanism of fragmentation is defined as being triggered by a high-volatile component confined between two sill segments. The significance of a high volatile component is that the melts that produced these sills intruded at a high crustal level. The volatile component may have been associated with the original melt, which is not typical of Karoo mafic magmas.

The SPO and AMS fabrics are used as a proxy for magma flow within the sills. The fabric results are locally parallel to the directions of magma flow implied by the structures observed in the field with the upper contact AMS fabrics are most commonly coaxial with those directions. Late stage magma flow merged sill segments is indicated by the magmatic and magnetic fabrics where the flow is perpendicular to the long axis orientation of the magma flow indicators

obtained from the field. These fabrics are reflective of a process that occurred after the initial intrusion when magma subsequently flowed between the adjacent sill segments. Fabrics must therefore be carefully interpreted when using these techniques to obtain magma flow in sills. The magma flow indicators showing the initial magma intrusion direction should be used to imply a magma flow direction indicative of a magma source.

Based on the magma flow directions obtained using the above processes, two sill magma flow orientations exist: sills with NE-SW intrusion directions and sills with predominantly NW-SE intrusion directions. The NE-SW magma flow direction may be linked to NW-SE striking dykes in the field area that are associated with the Underberg dyke swarm further inland. The second category of sills formed in a high-level setting through sill linkage, due to crustal thinning in the initial stages of Gondwana breakup.

All the evidence indicates that the Karoo sills along the KZN North Coast were not derived by magma flow from the Karoo triple junction and the proposed related plume head. The melts that formed these sills were derived from global mantle warming beneath Gondwana, prior to breakup, with the magmatic centre located in the Weddell Sea.

"The world we live in presents an endless variety of fascinating problems which excite our wonder and curiosity. The scientific worker, like a detective, attempts to formulate these problems in accurate terms and, so far as is humanly possible, to solve them in the light of all the relevant facts that can be collected by observation and experiment."

- *Arthur Holmes (Principals of Physical Geology, 1964)*

- CHAPTER 1 -

INTRODUCTION

1.1. Research Aims and Objectives

The principal aim of this study is to analyse and determine the original magma flow directions within a series of Karoo dolerite sills exposed along the KwaZulu-Natal (KZN) North Coast, South Africa. These sills are most likely a component of Karoo magmatism that occurred between 184 – 181 Ma (Jourdan et al., 2008), although they could be linked to ~176 Ma dolerites (e.g. Riley et al., 2006). Magma flow information is critical in understanding the evolution of the Karoo Igneous Province (KIP), in particular the magma source of the KIP.

The main centre of sub-volcanic activity in the KIP is the Karoo triple junction where a plume is theorised to have impacted the lithosphere beneath Mwenezi (formerly Nuanetsi) in southern Zimbabwe (Fig. 1.1). The Karoo triple junction consists of three main branches, namely the Okavango Dyke Swarm (ODS), the Sabe-Limpopo Dyke Swarm (SLDS) and both the proximal Lebombo Dyke Swarm (LDS) and the distal Rooi Rand Dyke Swarm (RRDS) (Fig. 1.1). The ODS comprises laterally emplaced Karoo-aged dykes with a strong component of inheritance of Proterozoic dyke orientations (~10% WNW) (Le Gall et al., 2005; Jourdan et al., 2006). The SLDS extends to the NE, but has not been researched in any significant detail (Fig. 1.1). The LDS and the RRDS have been analysed for flow-related fabrics, with the dominant flow direction in the dykes being proximally vertical and distally lateral from the Karoo triple junction (Fig. 1.1) Hastie et al., 2013, 2014).

Although it seems that the main source for the magmatism surrounding the Karoo triple junction could be plume-based, the overlapping of Karoo magmatism may be an inherited feature along a weakened portion of the Kaapvaal Craton (Le Gall et al., 2002; Watkeys, 2002; Jourdan et al., 2004). If the magma source for the majority of Karoo magmatism is from the Karoo triple junction (whether the magma formed due to a plume impinging on the lithosphere or not) the magma flow direction for the intrusion along the KZN North Coast should be predictable based on the regional flow pattern inherited from the main dyke swarms. Thus, if the sills analysed here were fed by the same feeder system that produced the LDS and RRDS, the flow within dykes would be towards the south and flow within the sills injected above the dykes would be

toward the west and the east. The flow directions within the sills could thus constrain the nature of the magma source linked to the Karoo triple junction. This forms the crux of this thesis. This is of particular interest as the east coast of South Africa coincides with a continental margin developed during Gondwana break-up, shortly after the cessation of Karoo magmatism.

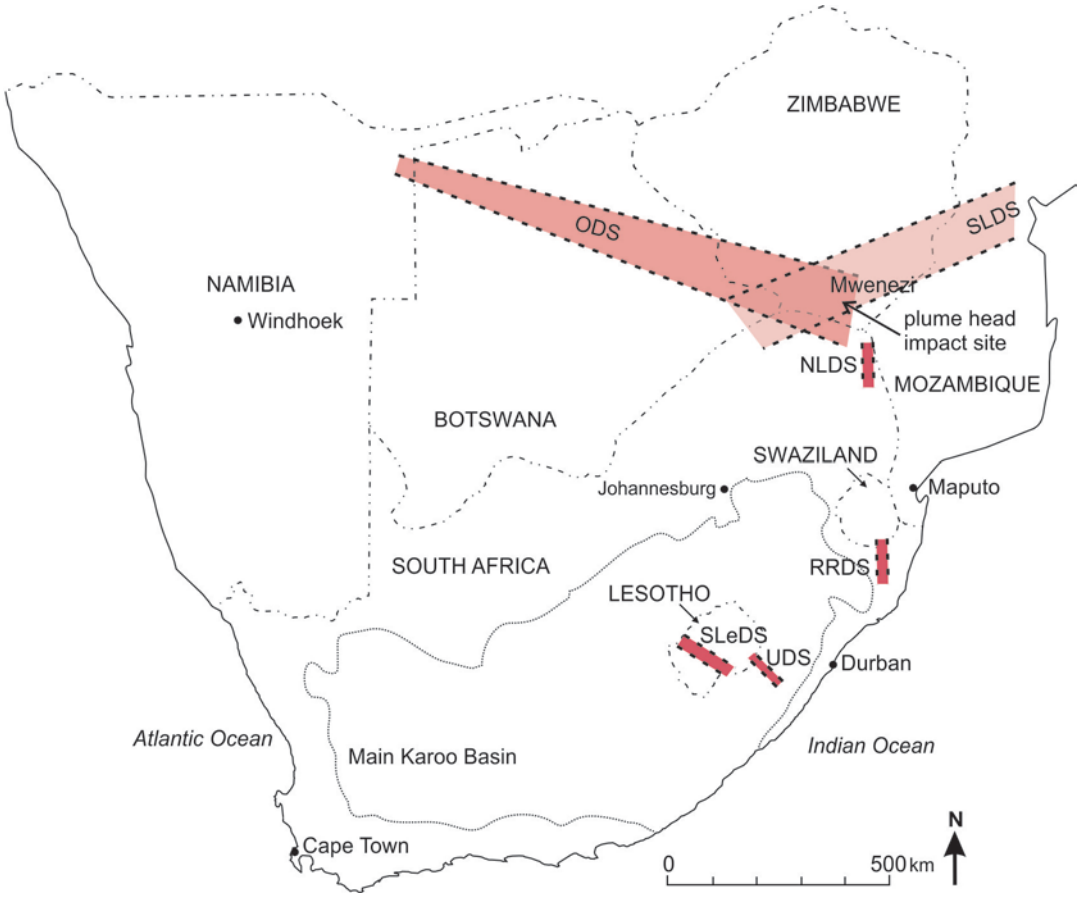

Fig. 1.1. Outline map of Southern Africa showing the location of the major dyke swarms associated with the KIP. At Mwenezi in southern Zimbabwe, a plume is proposed to have impacted the lithosphere, which Burke and Dewey (1973) initially proposed was the source of the KIP rocks. RRDS = Rooi Rand Dyke Swarm, NLDS = Northern Lebombo Dyke Swarm, ODS = Okavango Dyke Swarm. After Duncan and Marsh (2006); Jourdan et al. (2009).

This thesis examines the field evidence of emplacement and flow-related fabrics of sills from the KZN North Coast using combinations of field data, shape-preferred orientation (SPO) analyses of mineral grains, and anisotropy of magnetic susceptibility (AMS) analyses. The following objectives are proposed in order to best answer the main research questions.

1. What is the most successful method used to petrographically determine the magmatic fabric within the samples?

2. What are the mechanisms of emplacement associated with the intrusion of the sills and how has this deformed the adjacent country rocks?

3. To what extent do the determined petrofabrics agree with the field evidence?

4. How successfully do the field magma flow indicators predict magma flow within the sills?

5. How do the fabrics determined relate to the mantle plume model that predicts lateral flow in dykes away from the magma source?

6. Where was the magma source(s) for these sills?

1.2. Thesis Structure and Layout

This thesis comprises a series of manuscripts that have been either published in peer review journals, or are in preparation. These are as follows.

Chapter 4: Hoyer, L., Watkeys, M.K., 2015. Assessing APO techniques to constrain magma flow: Examples from sills of the Karoo Igneous Province, South Africa. Tectonophysics, 656, 61-73.

Chapter 5: Hoyer, L., Watkeys, M.K., *accepted.* Breccia formation during intrusion of a dolerite sill: an example from Sheffield Beach, KwaZulu-Natal North Coast, South Africa. South African Journal of Geology

Chapter 6: Hoyer, L., Watkeys, M.K., *in preparation*. An integrated field, SPO and AMS study on magma flow indicators in Karoo dolerite sills, KwaZulu-Natal North Coast, South Africa.

Chapter 7: Hoyer, L., Watkeys, M.K., *in preparation.* Magma flow directions in Karoo sills, KwaZulu-Natal, South Africa: implications for different intrusive mechanisms.

The first author, L. Hoyer, was responsible for the following:

- Sample collection in the field and the preparation of the samples for thin section production and AMS analyses.
- Undertaking all of the analyses.
- Collection and interpretation of all data.

- Writing, editing and preparation of all the manuscripts and figures.
- All submission, editorial, peer-review and revision processes resulting in the publication of the manuscripts.

The second author aided in a supervisory and editorial role and thus warranted authorship from that perspective.

In this thesis, there is no specific "Results" section. All of the results from this work are contained as stand-alone studies (*Chapters 4 – 7*), but with common themes throughout. Each paper has been edited in order to maintain a consistent style. Due to the format of this thesis, there is an element of overlap in the introductions of each chapter. This repetition has been kept to a minimum; however the reader is made aware that it occurs in order to clarify the topics to be discussed in each chapter. *Chapter 4* comprises the edited published manuscript; this paper in its original format is located in *Appendix A.* All data in their native format, either as field maps, sample locality maps or tables, together with any additional data that are of peripheral overlap to this study are provided in *Appendix B.*

1.3. Chapters Overview

The introductory chapter, *Chapter 1*, outlines the aims and objectives of this thesis and how the objectives will be met by the analyses conducted. *Chapter 2* describes the theoretical background to the thesis and *Chapter 3* examines the geological setting and the potential magma source of the rocks comprising the KIP. The references for *Chapter 1 – 3* are found after *Chapter 3*. For the subsequent chapters, the references appear after each discussion. *Chapter 4* scrutinises and improves upon the technique used to obtain mineral preferred orientation which is applied to the results presented throughout this thesis. *Chapter 5* describes the occurrence and formational environment of a breccia found confined between two sill segments. The properties of the breccia are described in detail and the process of formation is discussed. *Chapter 6* examines the relationship between magma flow indicators and petrofabrics and illustrates their efficacy when implying a sense of magma flow. *Chapter 7* studies the magma flow directions in the sills, their linkages with possible magma sources and their intrusive mechanisms. *Chapter 8* concludes the thesis.

- CHAPTER 2 –

BACKGROUND RESEARCH AND METHODOLOGIES

2.1. Context of Study

Sills are tabular igneous intrusions that are typically horizontal to slightly-inclined in form with large length to thickness ratios (Corry, 1988; Liss, 2004). Sills form in dilated fractures that are ideally perpendicular to the minimum compressive stress direction (Anderson, 1951) and largely originate from vertically intruding magmatic bodies known as dykes. The process of a dyke deflecting into a sill requires a significant change in the nature of the intrusion (Gretener, 1969). Together sills and dykes form the sub-surface plumbing system that is frequently linked to surface volcanism. The migration of magma in dykes and particularly sills is thus responsible for a large portion of magma movement in the upper reaches of the crust (Callot et al., 2001; Cartwright and Hansen, 2006; Muirhead et al., 2014).

Dykes have traditionally been assumed as the primary structure that transports magma to upper crustal levels (Fig. 2.1) (e.g. Pollard, 1987; Gudmundsson, 2003). However, recent studies have shown how sills act as magma conduits where magma is transported to higher crustal levels and eruptive complexes (e.g. Cartwright and Hansen, 2006; Thomson, 2007; Muirhead et al., 2012, 2014). The implication of magma being transported by sills is that the magma source in the lower crust may not necessarily underlie the high-level intrusive complexes and eruptive centres where the magmatism culminates in eruption (e.g. Cartwright and Hansen, 2006; Leat, 2008; Stevenson et al., 2007).

Through the intrusion of magma into the brittle crust, macroscopic features form in and adjacent to sills and dykes. These features may be used to infer the direction of magma flow in dykes where the magma flow may be vertical or laterally propagating (e.g. Pollard, 1987; Philpotts and Philpotts, 2007). In sills, magma flow may be directionally inferred using these magma flow indicators (e.g. Schofield et al., 2012 a, b; Magee et al., 2012). In order to increase the accuracy of the magma flow direction determined, microscopic and sub-microscopic techniques are typically employed. These techniques have also been used to determine magma flow in sills and dykes where no other magma flow indicators are present.

During the intrusion of magma to form a sill (or dyke) the magma adjacent to the country rock is sheared and creates a preferred orientation of the phenocrysts in the magma. These phenocrysts become imbricated along the intrusive contacts and can be used to provide the sense of magma flow (e.g. Gay, 1966, 1967; Geoffroy et al., 2002; Gil-Imaz et al., 2006).

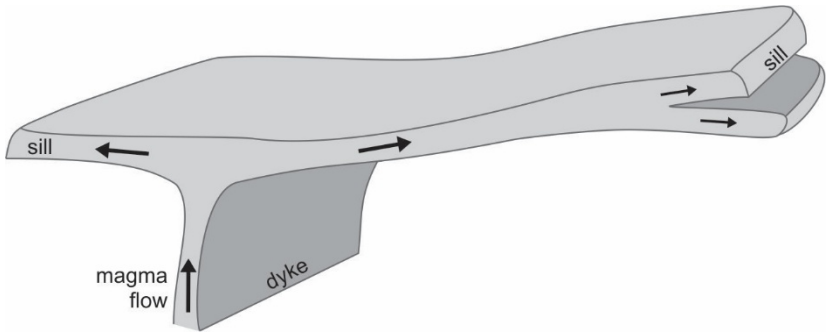

Fig. 2.1. A simplified model for the formation of sills through dyke injection illustrating how separate sill segments may form through the intrusion of one sill.

By using macroscopic magma flow indicators and microscopic mineral preferred orientations, a magma flow direction may thus be determined for an igneous intrusion. Magma flow directions within intrusions may then be used to infer the region from where the magma has flowed (i.e. directionally for sills or vertically/laterally for dykes) and therefore the magma source location. Directions of magma flow may also indicate the rate of magma influx (e.g. Cruden, 1990), lava flow dynamics and internal structures (e.g. Cañón-Tapia et al., 1995, 1997; Loock et al., 2008), as well as the relationship between magma flow indicators and microscopic petrofabrics (e.g. Liss et al., 2002; Horsman et al., 2005; Philpotts and Philpotts, 2007).

This study analyses the significance of magma flow-related petrofabrics and the relationships between the fabrics and the macroscopic magma flow indicators. The focus of this study is framed by the implications for understanding the sill intrusive mechanism and the magma origin of the numerous sills along the KZN North Coast.

2.2. Dyke and Sill Formation

Sill and dykes may form through direct magma injection from a deep reservoir or they may originate from a shallow small chamber where magma has accumulated (Gudmundsson, 2000; Barnett and Gudmundsson, 2014). The conditions for sill emplacement discussed below pertain to the most relevant scenarios with respect to this study. Numerous processes and features can be related to sill emplacement and the examples provided here form the background to the study are necessary for the process of sill formation. The historical and extensive explanations of the

various processes of sill emplacement and formation are set out in: Anderson (1951), Mudge (1968), Gretener (1969), Pollard (1973), Pollard and Johnson (1973), Francis (1982), Kavanagh et al. (2006) and Schofield (2009).

2.2.1. Dyke emplacement through fracture propagation

The majority of sills form in the lithosphere due to the formation of dykes that subsequently form sills. Therefore in order to understand the process of sill formation, the dyke emplacement process must be understood. Dykes are vertical to sub-vertical planar intrusions where the process of magma injection may dilate fractures within the material into which they are intrusive or may form new fractures. The stress regime in the crust present at the time of the propagation of the initial fracture, the crustal stress regime thus, controls dyke formation.

According to the Griffith Theory of crack propagation, a large amount of tiny cracks/fractures occur in natural rock (Griffith, 1924). When rock experiences additional stresses, the fractures (Griffith cracks) that are appropriately oriented will propagate towards the maximum compressive stress (σ_1) and dilate in the direction of the minimum compressive stress (σ_3) (Griffith, 1924; Spera, 1980). With an increase in the volatile component, or fluid phase the strength of the material under stress is greatly reduced which significantly increases the probability of forming a new fracture and subsequent propagation (Spera, 1980).

Magma that migrates through the crust may take advantage of previously existing fractures or may be constrained by tensile fractures or an inherent foliation of the original rock fabric (Delaney et al., 1986). Where an intruding magmatic body creates new fractures the dilation of the fractures by the magma occurs when the magma pressure exceeds the lithostatic pressure of the country rocks (Spera, 1980). The propagation of the intrusion is largely undertaken through the advancement of the process zone which occurs ahead of an intruding magmatic body.

2.2.2. Process Zone

The process zone is a circular region at the propagating tip of the intrusion causing fracturing of the country rocks ahead of and adjacent to the intrusion. This deformation allows for the continuation of fracture dilation and magma injection. The size of the zone depends on the structure of the rock (Peck et al., 1985). Pollard (1987) defined the radius (R) of the process zone from the central point of propagating dyke tip using Equation 2.1:

$$R \approx \frac{a}{2}\left(\frac{P-S}{T_U+S}\right)^2 \quad (2.1)$$

Where P is the internal magma pressure, S is the regional compressive stress perpendicular to the intrusion, T_U is the tensile strength of the rock and a is the half length of the intrusion (Pollard et al., 1987). Thus the longer the intrusive sheet, the wider the process zone will be (Kattenhorn, 1994). Even though this was calculated for dykes, the same parameters can be attributed to sill formation (Fig. 2.2).

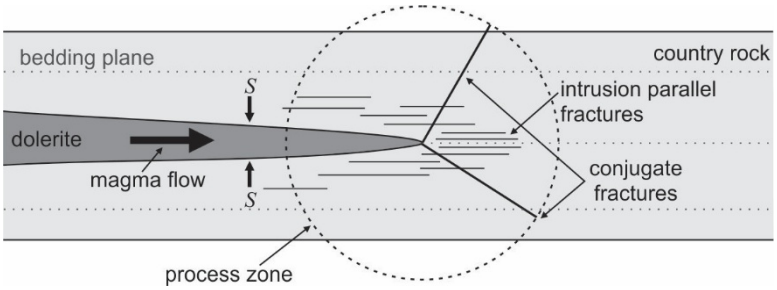

Fig. 2.2. Simplified diagram of the process zone ahead of a sill where conjugate fractures form at the propagating sill tip. Intrusion parallel fractures would also typically form with opening occurring along discontinuities or bedding planes. After Pollard (1987).

Within the process zone, joints form parallel to the plane of the intrusion and conjugate fractures develop at 30° to the minimum compressive stress, σ_3. Fractures are at the greatest concentration closest to the centre of the process zone with fracture formation decreasing in number and increasing in separation as the distance away from the process zone increases (Delaney et al., 1986; Pollard, 1987; Kattenhorn, 1994).

2.2.3. Dyke Morphologies

Dykes are defined as vertically oriented planar intrusions, although the form of a dyke depends on the type of fracture that becomes dilated by the intruding magma. The shape of the dilating fracture will depend on the relative movement between the two separating fracture margins. Therefore, as the fractures dilate, different fracture modes result in morphologically different intrusions, as shown in Fig. 2.3 (Pollard, 1987).

These fracture types can be separated by the mode of formation, namely Mode I, Mode II and Mode III cracks. Mode I cracks open perpendicularly relative to the margins. Mode II cracks host a shear displacement perpendicular to the margins and Mode III cracks have a shear

displacement parallel to the fracture margins. The combination of any of the crack modes results in different dyke and/or sill morphologies.

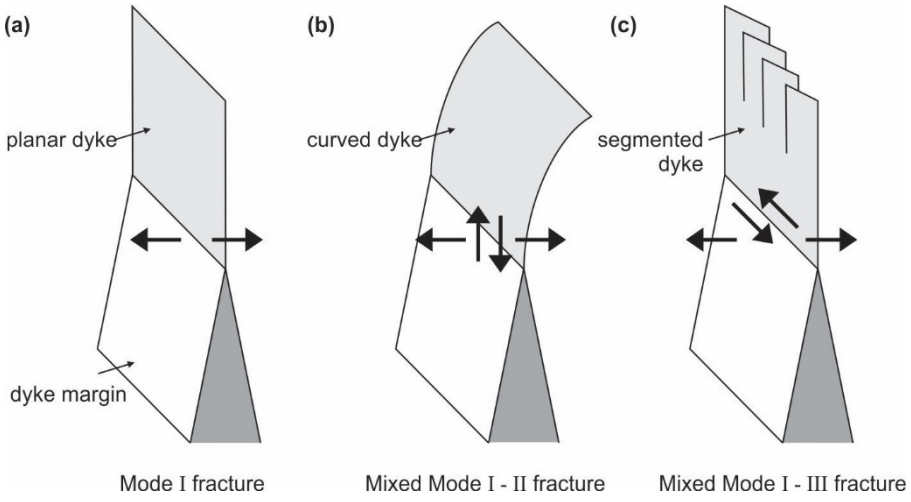

Fig. 2.3. Dyke propagation paths for (a) Mode I fractures where σ_3 (bold black arrows) is perpendicular to the dyke margins forming a planar dyke. (b) Mixed Mode I – II fracture where σ_3 is rotated to perpendicular with the dyke margins resulting in a curved dyke. (c) Mixed Mode I – III fracture where σ_3 is rotated parallel to the dyke margins producing a segmented dyke. (Modified after Pollard, 1987).

2.2.4. From Dykes to Sills

The presence of dykes does not automatically imply the presence of sills as not all dykes experience the necessary conditions to form sills. However, as magma ascends through the crust in the form of dykes, or from shallow magma chambers, magma may become trapped due to significant changes in the properties of the surrounding rock across a discontinuity that is not favourable to continued dyke propagation.

One of the most common scenarios for a dyke changing into a sill is when an intruding dyke intersects a discontinuity (Menand, 2011). Through field evidence and numerical modelling (e.g. Barnett and Gudmundsson, 2014; Kavanagh et al., 2015) it has been shown that one of four situations may occur when an intrusion encounters a discontinuity which, in this case is a lithological contact (Fig. 2.4) (Gudmundsson, 2011):

(1) The intruding dyke may become arrested at the contact and become a blunt-ended dyke (Fig. 2.4a)

(2) The dyke may penetrate through the discontinuity between the two layers (Fig. 2.4b)

(3) The dyke may become deflected along the contact between the two layers and propagate laterally in one direction (Fig. 2.4c) or

(4) The dyke may become deflected along two directions creating a T-shaped sill (Fig. 2.4d).

Although lithological contacts are one of the most common situations where sills form, dykes may deflect into sills due to an inherent fabric in fracture pattern in a host rock or due to the stress regime present (Menand, 2011). Because the majority of sills along the KZN north coast occur near lithological contacts, this example has been used to best describe dyke arrest and sill propagation in this study.

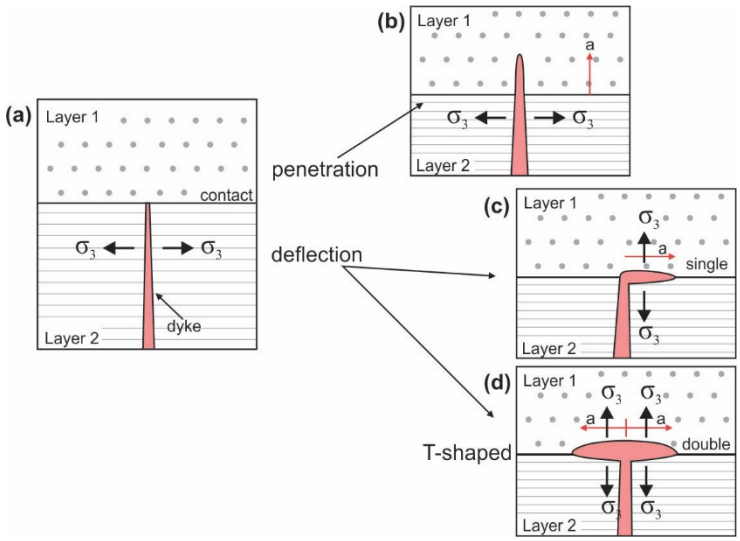

Fig. 2.4. A magma-filled crack propagating upwards in Layer 2 may be (a) arrested at the discontinuity, here the contact, between Layer 1 and Layer 2. (b) The crack may propagate through the contact or (c) be singly deflected or (d) doubly deflected along the contact (modified after Hutchinson, 1996; Barnett and Gudmundsson, 2014).

Although it has been widely accepted that sills formed from dykes when “neutral buoyancy” is attained (magmatic pressure = lithostatic pressure), a magma reaching neutral buoyancy is not solely adequate to trigger sill propagation (Menand, 2011). Other parameters must come into play for sills to form.

There are three parameters critical to the arrest of dyke or sill formation along discontinuities or lithological contacts (Gudmundsson, 2011) providing the mechanisms by which dykes deflect into sills:

(a) The Cook-Gordon mechanism refers to when the induced tensile stress in the process zone allows for the opening and propagation of the tensile fracture that will become the

dyke. A weak contact will be debonded where the tensile strength of the contact is less than 20% of the tensile strength of the rock layers perpendicular to the dyke. This creates a pathway for a sill to deflect along (Cook et al., 1964; Gudmundsson, 2011). A sill may only deflect along this pathway if the conditions for lateral propagation are met.

(b) The change of the principal stress direction at the contact may create a stress barrier as the principal stress directions change (Gretener, 1969). A tension fracture will propagate in the direction of σ_1, and perpendicular to σ_3 (Anderson, 1951). If the σ_1 direction becomes horizontal at a discontinuity/contact, this rotates the σ_3 direction into the vertical plane allowing for opening in the horizontal direction as the stress barrier prevents further ascent (Gretener, 1969). If the fracture continues to propagate, it will do so in the direction of σ_1, thus a vertical dyke will deflect into a horizontal sill (Gretener, 1969; Gudmundsson, 2006; Gudmundsson and Philipp, 2006). The layer where σ_1 becomes horizontal would therefore be favourable for sill growth (Menand, 2011). If magma overpressure in the dyke is not sufficient, the dyke will become arrested (Gudmundsson, 2011). The orientation of the intrusion cannot be solely attributed to stress controls, as some larger intrusion may need to lose magmatic pressure before the intrusion becomes perpendicular to the σ_3 direction (Mériaux and Lister, 2002).

(c) The material toughness of a rock or discontinuity is the measure of how much energy is needed for a fracture to propagate though the material or discontinuity/contact and is measured in energy per unit area (Hull and Clyne, 1996; Chawla, 1998). If there is a difference between the material toughness of the contact and the adjacent rock layers, dykes will become deflected into sills when the strain energy release rate reaches the material toughness of the contact (Gudmundsson, 2011). The stiffness of the units on either side of the contact must also be taken into consideration. If the two unit stiffness' are equal, the dyke will only be deflected along the contact if the material toughness of the contact is less than a quarter of that of the overlying unit (He and Hutchinson, 1989; He et al., 1994; Gudmundsson, 2011; Menand, 2011). With an increase in the stiffness of the overlying unit, the likelihood of a dyke deflecting along the contact increases, whereas a dyke will most likely propagate through the rock pile if the overlying unit has a lower stiffness than the underlying unit (Kavanagh et al., 2006; Menand, 2008; Gudmundsson, 2011). For a single or double deflection to form (Fig. 2.4c, d) the difference in the elastic strain release rate needs to be minimal (He et al., 1994).

According to the above parameters, sills commonly form along discontinuities in rocks which can occur along contacts between different or similar lithological layers (Anderson, 1951; Gretener, 1969). However, sills are more likely to deflect along contacts when the overlying layer is stiffer than the underlying layer (Gudmundsson, 2011). Fractures that extend along contacts where dykes deflect into sills will typically be mixed mode fractures due to loading and the nature of the fracture (Hutchinson, 1996; Xu et al., 2003). Kavanagh et al. (2015) used analogue experiments to show that at the point of dyke deflection/ sill inception, where the magma flux is constant, the magma pressure drops by up to ~60% resulting in a rapid contraction across the dyke from where the sill deflected.

The amalgamation of sills may lead to the formation of a laccolith with successive stacking of individual sheets (Menand, 2011), often resulting in host rock slivers trapped between the individual sills (Quick et al., 1994; Westerman et al., 2004). The primary difference between the formation of a sill and a laccolith is that sills propagate laterally away from the magma source whilst laccoliths extend vertically before propagating laterally (Menand, 2011).

In terms of what level sills are most likely to form at in the crust, the crustal heterogeneities, physical properties, rheological controls and the regional tectonic stresses need to be understood (Menand et al., 2010). The depth at which sills form is controlled by the balance between the maximum horizontal principal stresses, the deviatoric compressive stress responsible for sill formation and the magma neutral buoyancy which drives the magma vertically.

2.2.5. Mechanisms of Sill Emplacement

As mentioned above, sills are now believed to be significant magma conduits providing magma to high-level systems and eruptive centres (e.g. Cartwright and Hansen, 2006; Thomson, 2007; Muirhead et al., 2014). This type of system is typically dominated by sills which become linked by intrusive steps, thin dykes and inclined sheets and termed the ‘crack lid’ model (Fig. 2.5.a) (Muirhead et al., 2014). In such a high-level sill-fed system long transport distances of magma can be accommodated within the sills thus the magma source and the resultant intrusions may not be proximal to each other (e.g. Cartwright and Hansen, 2006; Muirhead et al., 2014). These interconnected sill complexes are able to transport magma great horizontal and vertical distances, and can ultimately erupt as lava flows (Cartwright and Hansen, 2006; Muirhead et al., 2012).

Because there is no significant volume of dykes in the crack lid model, it is difficult to determine a minimum compressive stress direction, along which dykes would typically intrude. For example, establishing the σ_3 direction (responsible for the direction of dyke emplacement) would allow for a magma source to be inferred. In such a sill-fed system; however, the magma flow within the sills may be uni-directional from a distal source or multi-directional from a proximal source.

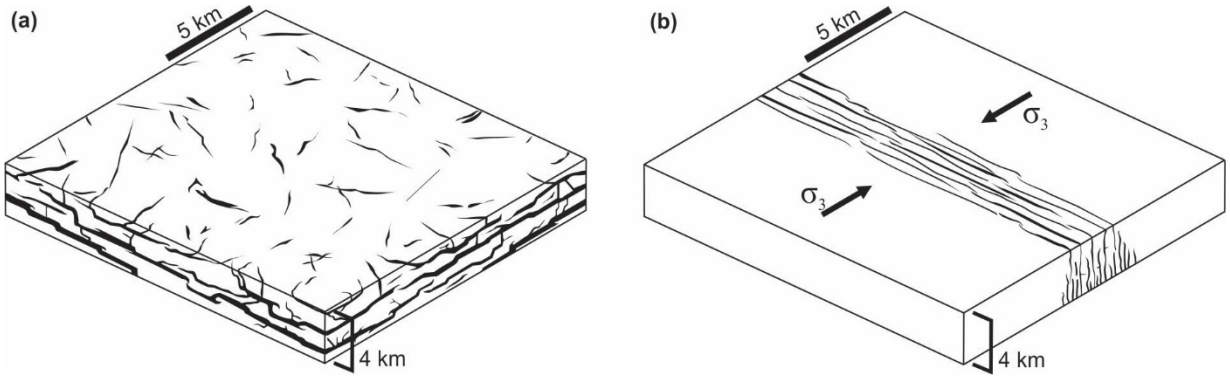

Fig. 2.5. Illustrations of shallow (< 4 km depth) feeder system typical in flood basalt provinces. (a) The crack lid model where sills are the primary magma conduits in system. Small narrow dykes may occur in this environment in no particular orientation. (b) Long, parallel aligned dykes in a large craton, oriented perpendicular to the regional minimum compressive stress direction. Redrawn from Muirhead et al., 2014.

Where dykes are the primary source for magmatism in the crust, the magma flow direction within the dykes indicates whether it is vertical or horizontal and therefore hint at a location of the magma source (Fig. 2.5b) (e.g. Aubourg et al., 2008; Hastie et al., 2011a). If planar dykes intrude vertically and once the necessary criteria are met (see *Section 2.2.4* above), a sill may form. A sill that forms from such a vertically-fed planar dyke will be fed by parallel flow within the sill (Fig. 2.6) in either a single deflection or double deflection (Fig. 2.4c, d) (Ferré et al., 2002). If a sill forms from a feeder dyke that has a pipe or 'finger-like' form, magma flow within the sill will be radial away from the dyke (Ferré et al., 2002). Finger-like feeders have been related to the formation of saucer-shaped sills (Burger et al., 1981; Thomson and Hutton, 2004) as found in the main Karoo Basin in South Africa (Chevallier and Woodford, 1999).

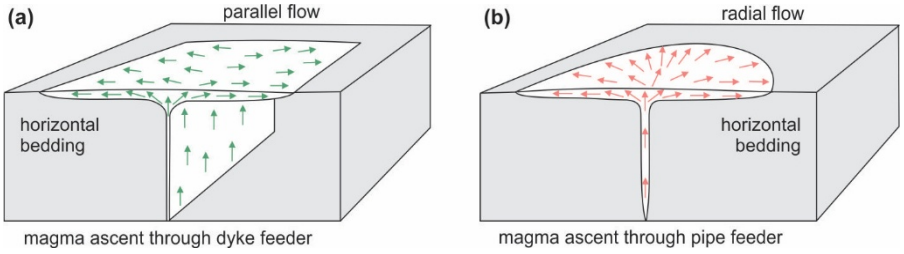

Fig. 2.6. Illustration showing (a) parallel flow originated from vertical flow in a dyke where the magma flow in the sill is perpendicular to the trend of the dyke and (b) radial magma flow produced from a pipe feeder. After Ferré et al. (2002).

With a dyke-fed sill system, the magma flow within the sills should be laterally or bi-laterally perpendicular to the dyke orientation, provided the sills were fed by planar flow as described above (Fig. 2.7). If the magma flow direction/orientation within the sills is known, the orientation of the feeder dykes may be inferred – and the orientation of the dykes may then be linked to known dyking events within an area and a magma source determined.

2.3. Deformation of Country Rocks by Magma Intrusion

2.3.1. Brittle Propagation-related Features

When magma segments intrude into rocks, and the fractures into which they are injected become dilated, the manner in which the country rock fractures can produce remnant structures. Examples of these are bridge structures and intrusive steps that form when separate, propagating magmatic segments, that have exploited different stratigraphic horizons during emplacement, become merged (Nicholson and Pollard, 1985; Nicholson and Ejiofor, 1987; Hutton, 2009; Schofield et al., 2012 a, b). When the intruding magma segments are overlapping, bridge structures are produced (Fig. 2.7). When the magma segments are adjacent but not overlapping, intrusive steps form (Fig. 2.8).

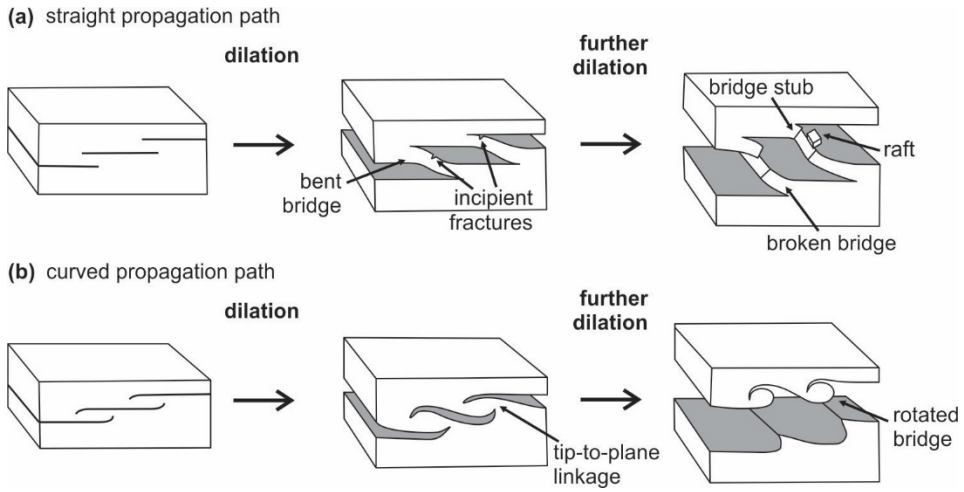

Fig. 2.7. The formation processes of bridge structures. (a) Fracture propagation paths of straight and (b) curved fractures (after Nicholson and Pollard (1985) and Kattenhorn and Watkeys (1995). As the fractures are filled with the injecting magma, the magma tubes expand to form bent bridges of country rock which, when broken, form coalesced magma pods with remnant broken or rotated bridges and floating rafts.

To form bridge structures the country rock between two overlapping fractures, which may have straight or curved propagation paths, is deformed as the magma is injected and dilates the fractures, creating an intervening bridge structure (Fig. 2.7a). Once the fracture becomes dilated with magma, the excessive magma pressure cross-fractures the country rock at inflection points

to form a broken bridge with little deformation within the bridge beyond the zones of folding (Nicholson and Ejiofor, 1987; Morris et al., 2008). The morphologies of these broken bridges may be either bent or rotated in shape, depending on whether the shape of the propagating fractures was straight (Fig. 2.7a) or curved (Fig. 2.7b) (Nicholson and Pollard, 1985). Where the bridge material breaks away from the country rock, the separated host rock segment, or "raft", is entrained into the intruding magma and the resultant host rock structure is termed a "bridge stub".

Intruding magma segments that merge without lateral overlap join by producing an intrusive step between the magma segments (Pollard et al., 1975; Rickwood, 1990; Schofield et al., 2012a). Intrusive steps link sills at varying stratigraphic levels with the vertical difference between the magma segments increasing with distance from the magma source (Fig. 2.8) (Rickwood, 1990; Schofield et al., 2012a). These intrusive steps are typically steeply inclined compared to the sills with which they become linked. As a result of fracture linkage and magma flow, the long axes of bridge structures and intrusive steps may be used to imply the orientation of primary flow within an intrusion.

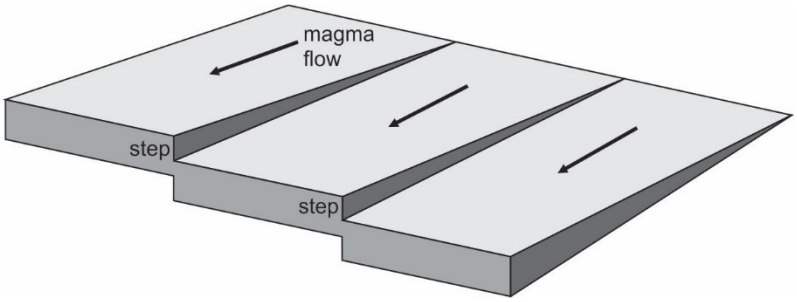

Fig. 2.8. Steps are formed through the linkage of magma-filled fractures that are adjacent but do not overlap. Modified after Pollard et al. (1975) and Rickwood (1990).

2.3.2. Non-brittle Propagation-related Features

Magma lobes (Fig. 2.9a) and fingers (Fig. 2.9b) form in separate fractures as magma initially intrudes into the host rock where host rock fluidisation, or disaggregation, may occur. These lobes later coalesce to form a continuous sheet-like intrusion (Pollard et al., 1975; Schofield et al., 2010, 2012a). Magma lobe geometry allows for the magma flow direction to be inferred; that is flow is towards the bulbous termination of the lobes, away from the lobe opening direction (Stevenson et al., 2007; Magee et al., 2012). Magma fingers that have been preserved on the outskirts of sills allow for the magma flow to be inferred as being towards the direction

in which the fingers diverge into separate intrusions (Fig. 2.9b) (Pollard et al., 1975; Baer and Reches, 1987; Rickwood, 1990; Horsman et al., 2005; Schofield et al., 2012b).

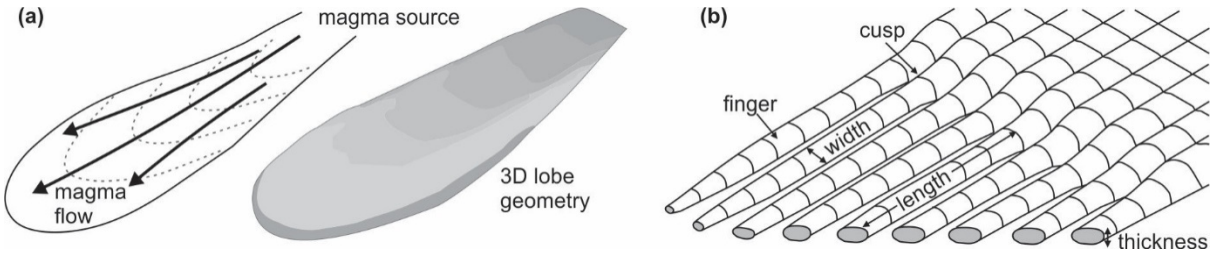

Fig. 2.9. (a) An example of the shape of a magma lobe formed through dispersive magma flow away from the magma source. Redrawn after Stevenson et al., (2007). (b) The progressive formation of fingers showing how the finger thickness is related to the length of the finger. Redrawn after Pollard et al. (1975).

2.3.3. Internal Magma Flow-related Features

Magmas that have a relatively high volatile content may be subject to devolatilisation, with the exsolved vapours forming vesicles (micro- to macroscopic) as the magma/lava cools. Larger vesicles (>1 cm diameter) are the product of vesicle coalescence, which can rise vertically and create large, flattened vesicles near the upper contacts of an intrusion (Manga and Stone, 1994; Varga et al., 1998; Liss et al., 2002). Such vesicles may be deformed within the intrusion through continuous shearing as the magma flow moves, causing the vesicles to become elongated parallel to magma flow typically occurring in vesicles with long axis lengths of >6 cm (Fig. 2.10a). The long axes of elongated and flattened vesicles are therefore parallel to the direction of magma movement (Rickwood, 1990). The effect of magma movement in intrusions that contain large vesicles is more pronounced and may form ropy-flow structures (e.g. Liss et al., 2002). These features form when a rind of chilled magma on the outside of a large vesicle is plastically deformed, particularly when the underside of the vesicle is dragged into folds or "ripples" by the underlying flowing magma. The direction of flow is thus parallel to the plunge direction of the fold axis (Fig. 2.10b) (Fink and Fletcher, 1978; Liss et al., 2002).

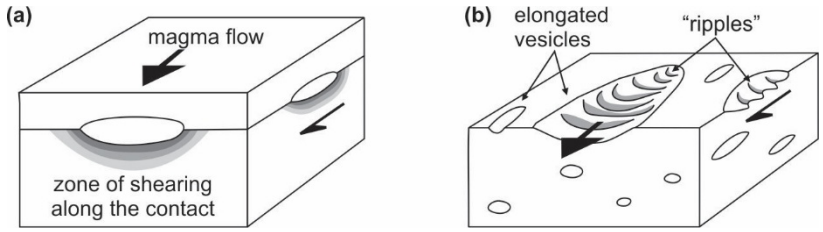

Fig. 2.10. Deformation of vesicles near the upper surface of the sill. (a) A skin of chilled magma forms around the vesicle, as the magma continues to flow this skin becomes sheared resulting in (b) elongation of the vesicles and the formation of ropy-flow structures. Magma flow is implied by the preserved "ripples".

2.4. The Influence of Volatiles on a Magmatic System

The origin of volatile phases, other than from the original melt, could be attributed to pore-fluids present in the country rocks or the production of volatiles through the metamorphism of the carbonate-rich country rocks (e.g. Svensen et al., 2007; Aarnes et al., 2011). The presence of volatiles in or surrounding an intruding magmatic body not only assists in the propagation of the initial fracturing (Spera, 1980) but may also have an effect on the intrusion structure and morphology. A volatile phase within magma may exsolve and form vesicles in the sill, which typically migrate to the upper portions of the intrusion. Vesicles are generally spherical when formed and grow through vesicle coalescence. Importantly, vesicles may exhibit ellipsoidal shapes if deformed during magma flow (Manga and Stone, 1994; Smith, 2002).

Another result of volatile-rich melts or magma interaction with volatiles is the formation of rheomorphic sedimentary dykes. This occurs when fluids are introduced into the magmatic system through sill formation and the volatile-rich country rocks experience excessive pressurisation, resulting in fluidisation of the country rock (Schofield et al., 2010, 2012b). The subsequent mobilisation of the fluidised material leads to its injection, typically as an intrusion into the adjacent country rocks as a sedimentary dyke (Svensen et al., 2010; Schofield et al., 2012b). The presence of sedimentary dykes is an indicator of relatively high volatile content in the system.

Low viscosity, volatile-enriched magmas are able to erode the surrounding rocks which may result in the formation and entrainment of xenoliths into the migrating magma (Spera, 1980; Lensky et al., 2006). The higher the volatile component of the magma, the larger the percentage of xenoliths the magma is able to entrain and transport, which is typical of kimberlite magmas for example (Lensky et al., 2006).

Magmas with a significant volatile component, or that encounter volatile-rich sediments or sedimentary units during ascent, may cause fragmentation of the adjacent country rocks. These rocks may be inelastically deformed through brecciation due to drastic pressure changes or the forceful intrusion of magma such that magma pressure exceeds the lithostatic pressure (Delaney, 1982). For example, when magma encounters wet sediments, peperites may form (White et al., 2000). Peperites are a form of breccia where the magma disaggregates upon interaction with the sediments resulting in an igneous-clast sedimentary-matrix breccia (e.g. Pichler, 1965; Honnorez and Kirst, 1975; Kokelaar, 1982; McClintock and White, 2002). Fragmentation of country rocks adjacent to the magma conduit is often triggered by the

injection of volatile-rich melts into the system. These breccias have a large xenolith component that has been entrained into the magma and is typically associated with the formation of kimberlite pipes (e.g. Sparks et al., 2006; Lorenz and Kurszlaukis, 2007). Igneous breccia may also form by the intrusion of a dry magma into volatile-rich sedimentary rocks. The sudden and dramatic increase in the pore-fluid pressure in the country rocks triggers fragmentation around the intrusion. The most common example of this is the formation of hydrothermal vent complexes through the intrusion of large dolerite sills (e.g. Jamtveit et al., 2004; Svensen et al., 2006).

2.5. Sampling

The samples (rock drill cores) in this study were obtained using a hand-held petroleum powered drill fitted with a hollow 25 mm diameter diamond-tipped drill bit (Fig. 2.11). Samples were obtained from along the upper and/or lower contacts of each sill. Where the upper (or lower) contact was obstructed by sand or high sea level, this contact was not sampled. Where both the upper and lower contacts were able to be sampled, a minimum of four cores were obtained from each contact. In the field, each sample was oriented (plunge and plunge direction) prior to removal from the sill contact using a magnetic compass with the magnetic declination (24°) manually added at a later stage. The cores were taken along the lengths of the contacts with the number of cores constrained by the extent of the outcrop. Thus, the larger the outcrop, the more samples that could be obtained but the degree of fracturing along the contacts of numerous sills prohibited the procurement of the desired number of cores.

For dykes it has been found that the most successful AMS results (i.e. those compatible with magma flow direction) are found in samples obtained from intrusions with widths greater than 1 m (Rochette et al., 1999). This is because, if a dyke (or indeed a sill) intrudes and crystallises extremely rapidly – which would occur for such a thin intrusion and directly against the chilled margin – it is unlikely that a flow-related fabric would form and, similarly, if the magma flow is too slow or too turbulent, the crystals may not become imbricated along the contacts and would not yield a “good” SPO or AMS result. In a preserved intrusion it is seldom possible to identify whether flow was slow and/or turbulent, but the magmatic fabric and magnetic fabric should be well grouped in intrusions thicker than 1 m.

However as there is no such estimation for the sampling of sills, no minimum sill thickness was adhered to whilst sampling (the thinnest sill sampled was 0.5 m thick) although the distance from the chilled margin was considered a factor, and so samples were obtained from 10–20 cm

from the sill contacts with the country rock. In this study, the samples were obtained from the intrusions that were easily accessible, apparently undisturbed by any significant deformation and, for purpose of comparison, had some form of magma flow indicator present along the sill contacts, such as those discussed in *Section 2.4*.

The samples obtained were used for SPO and AMS analysis. A total of 232 core samples, ranging from 25 mm to 150 mm in length, were obtained from the 16 sills analysed in this study. This resulted in 126 samples (378 thin sections) for SPO analyses and 283 samples for AMS analyses. Tabulated data for each SPO and AMS sample is presented in *Chapter 5*. For detailed maps on the sampling localities, the reader is referred to *Section 3* in *Appendix B.*

Fig. 2.11. Equipment required to obtain cores here from the upper sill contact, including (a) petroleum powered hand held drill, (b) water and water pump cooling system and (c) magnetic compass core orientator.

2.6. Plagioclase Shape-preferred Orientation

2.6.1. Overview and Application

Defining the SPO is a process where the three-dimensional (3-D) shape ellipsoid of a mineral phase, preferably with a well-defined habit, is determined. The process combines three two-dimensional (2-D) ellipses into a 3-D ellipsoid. The analysis of mineral SPO has been widely used in a number of studies to define a shape ellipsoid of the minerals under analysis, particularly in reference to stress and strain analysis, as opposed to igneous flow fabrics. Early studies that determined the mineral SPO in sub-magmatic conditions include Gay (1966, 1967),

Blumenfeld and Bouchez (1988), Kattenhorn (1994) and Baer (1995). However, with the introduction of the SPO-2003 and Ellipsoid-2003 software packages (Robin, 2002; Launeau, 2004; Launeau and Robin, 2005) the process of using mineral SPO to infer magma flow became more widely used (Launeau and Robin, 1996, 2005; Launeau and Cruden, 1998; Launeau, 2004) and the technique has since been used to determine magma flow within dykes (Archanjo and Launeau, 2004; Hastie et al., 2011a, b, 2013; Launeau and Robin, 2005) and sills (Horsman et al., 2005).

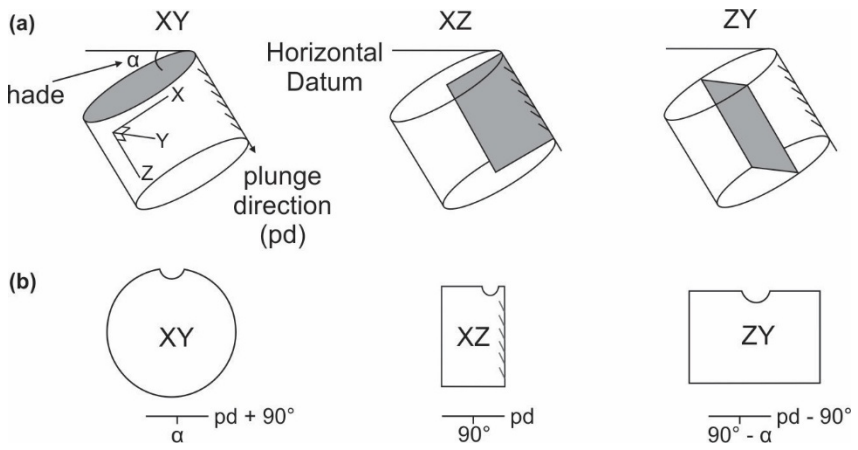

Fig. 2.12. (a) The orientations of the thin section XY, XZ and ZY as they are cut from the core (grey shapes) where the hade (α) and plunge direction (pd) are used to (b) define the orientations of the thin sections. (After Hastie et al., 2011b).

In order to successfully analyse the magma flow within an intrusion, it is necessary to analyse the fabric within the sill and determine whether the fabric(s), provided they are not isotropic, imply magma flow mechanisms and directions. If the SPO ellipsoids of one or more selected minerals are determined to be representative of one or more magmatic fabric across the intrusion, the fabric(s) may be used to infer a magma flow direction. The technique of fabric acquisition using SPO-2003 is scrutinised in detail in *Chapter 4*.

2.6.2. Determining the Shape-preferred Orientation

The procurement of the SPO fabric of plagioclase grains is undertaken by producing and analysing three orthogonal thin sections for each of the samples. The thin sections are cut from different portions of the core based on an XYZ system. The three thin sections are labelled XY, XZ and ZY where XY is the top of the core and perpendicular to the core axis, XZ is perpendicular to XY and parallel to the plunge direction of the core and ZY is perpendicular to XY and XZ (Fig. 2.12). Photomicrographs of each thin section are then obtained at varying magnifications. The plunge and plunge direction of the core (corrected for a magnetic

declination of 24°) is used to define the orientation of the thin sections using a dip and strike (right-hand rule) (Table 2.1). The angle (α) measured by the magnetic compass is technically the hade, the angle from the vertical and not the plunge angle, which is 90° - α.

Table 2.1. *Example of thin section orientations*

XY	252°	17°
XZ	162°	90°
ZY	072°	73°

Original hade/plunge direction of core: 17°/138°
Plunge direction with magnetic declination: 162°

The dip of XY is that of the hade of the core, the strike is the plunge direction of the core + 90°. For the XZ section, the dip is always 90° (because it is cut in the plane of the hade) and the strike is the plunge direction of the core. The dip of the ZY section is the plunge (i.e. 90° – hade) and the strike is the plunge direction of the core – 90°.

The images obtained from each thin section are converted into negative black and white images and filtered using a threshold level of 128 in the image editing software Photostudio (ArcSoft®) (Fig. 2.13a). As the software analyses each individual grain, the plagioclase grains from each section are extracted and any grains that are truncated by the image boundary are removed (Fig. 2.13b). Where twinning of the plagioclase occurs, the twin in or close to extinction may not be preserved through the thresholding technique. If the entire grain is not preserved, this may affect subsequent results such as the average shape and anisotropy of the grains. Once the threshold has been applied, any intersecting grains are then manually separated, allowing each grain to be analysed individually in order to prevent intersecting grains being digitised or analysed as an

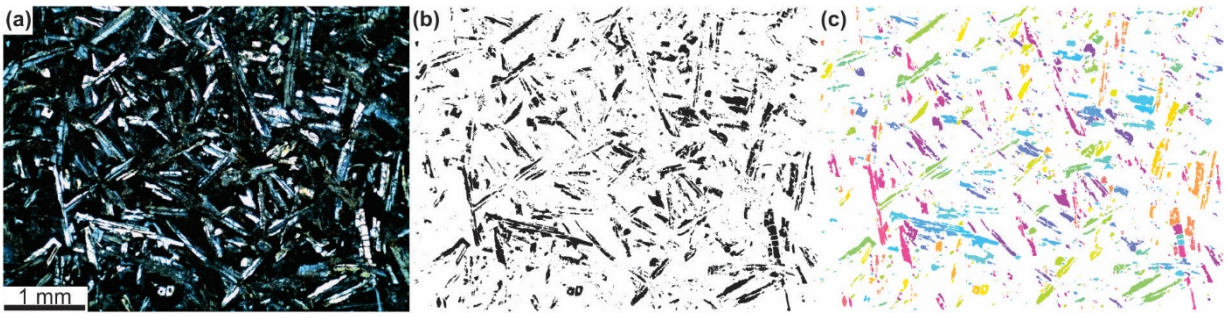

Fig. 2.13. Photomicrographs of sample SHF7 UZ XY (a) taken under cross-polarisers highlighting the plagioclase grains. (b) Manipulation of the image allows for only the plagioclase grains to be extracted. At this stage, any intersecting grains are manually separated. Grains that are truncated by the image boundary are removed. (c) In the SPO-2003 programme, each individual plagioclase crystal is highlighted in the orientation of the grain, these data are used to create the ellipse for this image. Modified after Archanjo and Launeau (2004).

individual grain with potentially spurious orientation. The final digitised images are then imported into SPO-2003 (Launeau, 2004; Launeau and Bouchez, 1992; Launeau and Robin, 2005) in which a 2-D inertia tensor is generated from all the grain directional data and an ellipse is defined (Fig. 2.13c) (Launeau and Robin, 1996; 2005).

The 2-D inertia tensor is formed by the stacking of every grain in the image into a column which determines the average shape within the image. The three mutually perpendicular 2-D tensors are then combined in the programme Ellipsoid-2003, in which each ellipse holds an equal weight in the 3-D calculation, regardless of the number of grains measured for each 2-D tensor. This allows a 3-D ellipsoid to be created, the parameters of which define the petrofabric. The shape of the ellipsoid (T) and the degree of anisotropy (P') are determined by the software and recorded for each ellipsoid (Jelinek, 1981). The parameter T, as defined in formula by Jelinek (1981), is the best descriptor used to define ellipsoidal shapes (see Equation 2.5. in *Section 2.8.2* below) (Tarling and Hrouda, 1993).

2.6.3. Important Shape Parameters

It has been suggested by Launeau and Robin (2005) that thin section images should be segmented before any grains are analysed in order to obtain the maximum number of combinations of the three 2-D ellipses in an ellipsoid. For the segmentation of each image, nine overlapping rectangles (each rectangle is one quarter of the size of the image) are used as separate images, therefore allowing for the formation of nine ellipses per thin section. Three perpendicular images are used in one sample, therefore nine segments from each image allow for 279 combinations of these ellipses. In unsegmented images, where one image is the equivalent of one segment, only three combinations are possible. The more combinations that are utilised in the analysis of each image, the more accurately the final ellipsoid is supposedly constrained.

When the ellipses are combined in Ellipsoid-2003 an error in the fit of the ellipsoid may occur and is measured by the Global Incompatibility Index ($\sqrt{F}$) (Launeau and Robin, 2005). A perfect fit of the three ellipses would result in a $\sqrt{F}$ value of 0. Results with $\sqrt{F}$ values < 10% are desirable (Launeau and Robin, 2005; Launeau et al., 2010) and are the generally accepted value below which the results may be trusted for accuracy.

The shape of the ellipsoid is also a critical factor when using the ellipsoid to define the fabric (Fig. 2.14). A spherical-shaped fabric will have three identical axes (Fig. 2.14a). Ellipsoid

shapes have three variable length axes and may be either prolate or oblate. Prolate ellipsoids are cigar-shaped where the long axis is longer than the intermediate axis which is longer than or equivalent to the short axis (Fig. 2.14b). Oblate ellipsoids are disc-shaped where the long axis is longer than or equivalent to the intermediate axis which is longer than the short axis (Fig. 2.14c). If an ellipsoid is prolate, the fabric will be best defined by the lineation, which for SPO is the linear fabric determined for the SPO. If the ellipsoid is oblate, the fabric will be best defined by the foliation, the plane that comprises the poles of the long and intermediate axes.

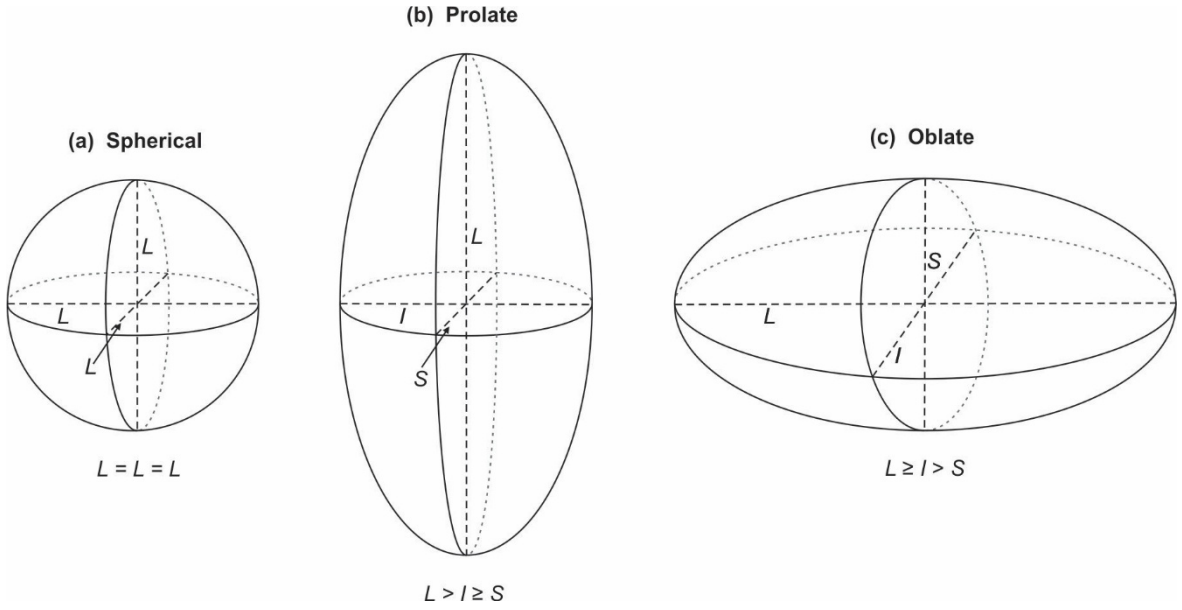

Fig. 2.14. Possible shapes that may be obtained for 3D fabrics. (a) Spherical shapes have equal length axes. (b) Prolate shapes have similar short (*S*) and intermediate (*I*) axes and a significantly longer long (*L*) axis. (c) Oblate shapes have similar long (*L*) and intermediate (*I*) axes and a significantly shorter short (*S*) axis.

2.6.4. Grain Size

As discussed in *Chapter 4*, the grain size of the crystals is an important parameter when determining the SPO of the minerals as the thin sections are imaged at varying magnifications based on the general size of the plagioclase crystals, which influences the number of grains that fit into one image. In order to standardise the magnifications at which photomicrographs were obtained, the long and short axes of the plagioclase grains were determined using 2-D ellipse data from each sample set. Using these data, the maximum grain sizes were obtained for each sample. The grain size is then used to determine the threshold grain sizes that should be adhered to when taking the photomicrographs.

2.7. Inferring Magma Flow Directions using a Mineral Shape-preferred Orientation

2.7.1. Typical Dolerite Textures

The texture of the dolerite in the sills on a microscopic scale is an important parameter when obtaining a mineral SPO. The fabrics obtained should, ideally, be from textures that have resulted from rigid-body rotation of the crystals present. If the texture of the sample has a large component of glass or a significant fraction of phenocrysts, the groundmass should be imaged in order to obtain the fabric that formed in the latest stages of crystallisation. Some of the textures common in this study are sub-ophitic, variolitic (spherulite-like radiating aggregates of plagioclase and pyroxene grains of crystals) (Cas and Wright, 1987) and glomeroporphyritic (a porphyritic texture in which the phenocrysts are glomerocrysts – clustered aggregates of larger crystals) (Hogan, 1993).

2.7.2. Use of Plagioclase to Determine the Rock Fabric

Plagioclase has been used in this study to elucidate the magmatic rock fabric, which is then used to infer the magma flow. Biotite and magnetite (in the form of opaque minerals) and often used to determine the rock fabrics (e.g. Hastie et al., 2011a; Schopa et al., 2015) but the study of the magmatic fabric is generally undertaken through the preferred orientation analysis of plagioclase, either with or without the analysis of secondary minerals, such as pyroxene or amphibole (e.g. Varga et al., 1998; Archanjo and Launeau, 2004; O'Driscoll et al., 2007; Archanjo et al., 2012; Horst et al., 2014; Payacán et al., 2014). In these examples, the plagioclase laths are undeformed and yield SPO fabrics that are generally parallel to the magnetic fabrics obtained through AMS analyses.

The common mineralogy of the samples is in the form of plagioclase, clinopyroxene crystals and opaque mineral phases. The main motivation to use plagioclase as the magmatic fabric indicator in this study was dominated by the ability to separate the well-defined elongate plagioclase laths from the mafic minerals in photomicrographs. The majority of the samples are sub-ophitic in texture thus the plagioclase grains are partially encapsulated in clinopyroxene grains. When attempting to threshold the images to extract the pyroxene or opaque grains, there were always plagioclase grains that could not be removed that would have obstructed the fabric acquisition of the darker minerals. As the opaque minerals are generally parallel to the plagioclase laths in this study, the plagioclase and opaque fabrics would most likely be coaxial. Secondly, plagioclase crystals form in early stages of magma crystallisation; this allows the plagioclase laths to be aligned parallel to the magma flow as they have already formed. Other minerals that crystallise at later stages, such as pyroxene and magnetite, do not have well

defined elongate habits or high anisotropy and therefore may not hold a rigid-body rotation, in response to magma flow, as well as plagioclase crystals can. The rigid-body rotation of the anisotropic plagioclase crystals preferentially aligns these crystals with the direction of magma flow, therefore the crystals act as good recorders of the magma flow direction. The plagioclase grains are abundant in the samples are generally well preserved with little to no alteration in most of the samples thus, the plagioclase grains were used to determine the magmatic fabric.

2.7.3. Timing of Fabric Formation

Melt viscosities play a crucial role in the formation and preservation of crystal fabrics in intrusive igneous rocks (Paterson et al., 1998). Mineral preferred orientations will not form in low-viscosity Newtonian liquids where the melt comprises less than 30% crystals. Once this limit is reached, the melt becomes a Binghamian liquid which begins to behave differently as the viscosity increases. In a Binghamian liquid, crystal fabrics will develop as a result of crystal movement in rigid-body rotation as a result of magma flow (Fernández and Gasquet, 1994; Hrouda et al., 1999). When the melt is crystal-dense, the lowered melt-to-crystal fraction present during crystallisation results in sub-magmatic flow suffering crystal interference and flow blockage (Passchier and Trouw, 1998; Arbaret et al., 2000). Thus, the rock fabric that will be most adequately used to define magma flow direction in an intrusion will be in the form of the preferred orientation of an appropriately shaped set of non-interfering grains, such as plagioclase laths.

In other words, the SPO fabric that can be used to infer magma flow within an intrusion must be attributed to a magmatic fabric and, in order to establish the origin of a fabric within an intrusion, certain criteria must be analysed such as the timing of fabric formation and the regional setting. If there has been no regional ductile deformation or metamorphism associated with or post-dating the intrusion, the fabrics observed can be considered to be the result of internal processes, and most likely a product of strain within the magma (Nicholas, 1992; Paterson et al., 1998). Such strain may be brought about by the original magma flow but may be affected by internal processes such as magma convection or surges/pulses of magma (Benn and Allard, 1989; Paterson et al., 1998).

A fabric forming during the last stages of magma intrusion preserves the final increment of strain before the magma nears solidification and crystallises (Paterson et al., 1998). If there has not been any reorganisation of the particles in the magma before it crystallises, such as

flattening due to overburden pressure, the preserved fabric may be used to obtain the direction of magma flow.

2.7.4. Using Fabrics to Infer Magma Flow

The dolerite sills analysed in this study are generally thin, at less than 2 m thick, and predominantly concordant with the stratigraphy. The field characteristics of the intrusions indicate that deformation associated with magma chambers, such as magma surges and/or convection, and post-emplacement processes are unlikely to have occurred. Consequently, it is likely that the preserved fabrics are related to the process of magma injection and flow.

In order to infer magma flow in an intrusion, plagioclase imbrications along the sill contacts are measured, here using SPO techniques. The shearing of plagioclase along the upper and lower sill contacts ideally creates an imbrication along the contacts, with the imbricated crystals dipping in opposite directions along opposing margins, creating symmetrical fabrics and therefore allowing a flow within the intrusion to be inferred (Fig. 2.15) (Geoffroy et al., 2002; Gil-Imaz et al., 2006). The dip of this crystal alignment is ideally between 15° and 20° from the wall of the intrusion with the direction of dip inferring the magma flow (Fig. 2.15) (Blanchard et al., 1979). The fabrics are generally inferred using the SPO foliation, the planar fabric, whereas some aspects of magma flow fabrics may be better represented using a lineation and not a foliation.

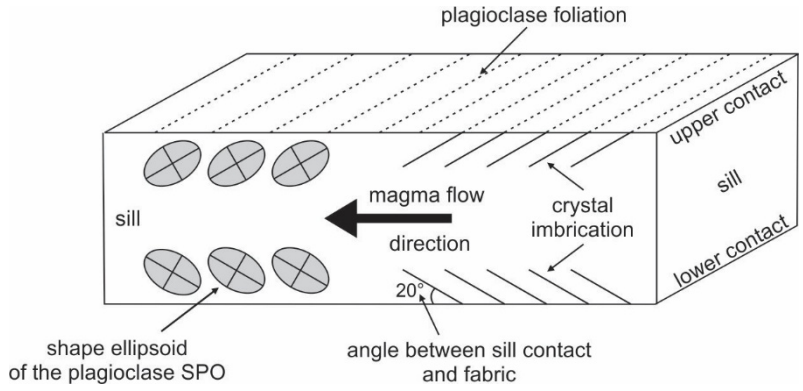

Fig. 2.15. Inferring the magma flow vector in an idealised situation where the plagioclase crystals are imbricated along the upper and lower contacts of the sill. The shape ellipsoids are used to infer the direction of magma flow, the upper contact ellipsoid dip towards the direction of magma flow, the lower contact ellipsoids dip symmetrically in the opposite direction. Modified after Gil-Imaz et al. (2006).

For each sill margin, several samples are analysed and the resultant ellipsoid for each sill contact/margin needs to be elucidated. The software programme GEOrient© 9.2 (HCOV Global) was used to determine the average principal axis for each of the three principal ellipsoid axes.

These three axes are then plotted along with all the SPO data from that margin as the average ellipsoid values for the sill margin.

It has been shown in previous studies that petrofabrics may preserve the primary magma flow patterns in igneous intrusions, allowing these petrofabrics to infer magma flow directions (Archanjo et al., 1995; Launeau and Cruden, 1998; Horsman et al., 2005; Hastie et al., 2011b). The SPO of the measured crystal phase determines the magmatic fabric but does not necessarily define the sense of magma flow. For this reason, SPO analyses are typically compared with other fabric data, such as AMS analyses of magnetic fabrics. If the grains, rotated into the plane of magma flow, are undeformed along the margins of the intrusions, the grains could provide an adequate fabric to indicate the sense of magma flow.
In the study area there has been no regional metamorphism or deformation that may have affected the crystal fabrics after the sills were intruded. Therefore the petrofabrics obtained from the margins of the sills analysed in this study have been used as a proxy for magma flow. The petrofabrics determined is this study, for the upper and lower contacts of the intrusions, are taken as a proxy for magma flow within the intrusions. The plunge and plunge directions of the fabrics for each sample site denote a petrofabric vector about which the magma flow can be inferred.

2.8. Rock Magnetism

In order to understand magnetic petrofabrics that are determined through AMS analysis, the magnetic minerals that are being studied (and their properties) must first be elucidated. This is undertaken through numerous magnetic mineralogy analyses including high temperature, low temperature and hysteresis analyses. These analyses described below were undertaken at the Institute for Rock Magnetism at The University of Minnesota.

High temperature analyses are undertaken in order to determine the Curie temperatures of the magnetic minerals present in the samples – the temperature at which all magnetic properties are lost from a material, including magnetic susceptibility. Magnetic susceptibility is the degree of magnetisation a material will have when exposed to an applied magnetic field, if the susceptibility is positive, the magnetic field strength of the material increases. This is determined per sample using rock powders that are analysed using a High-Temperature Susceptometer. The samples are heated in air to a temperature of 700°C and subsequently cooled to room temperature, with continuous susceptibility measurements during the heating-cooling cycles. A significant drop in the susceptibility of a sample indicates that the minerals'

Curie temperature has been exceeded. Minerals can be identified by their Curie temperatures on the heating cycle. For example, magnetite is evident at 575–585°C, pyrrhotite at 320°C and goethite (γ-FeOOH) at 120°C. Maghemite, the alteration product of stoichiometric magnetite breaks down at 645°C. Some samples may show an increase in susceptibility along the cooling curve relative to the heating curve. This is due to the production of magnetite from breakdown products of Fe-minerals that can form during the heating cycle.

Low temperature analyses are conducted using a Magnetic Properties Management System instrument (MPMS) where the magnetisation of minerals at low temperatures (20–300 K) is measured. Two different procedures can be used to analyse the low temperature transitions of the magnetic minerals; a basic cool-warm sweep and a more intricate (and time consuming) field-cooled, zero field-cooled, low temperature saturation isothermal remanent magnetisation (SIRM), room temperature SIRM (FC-ZFC-LTSIRM-RTSIRM) cycle (Bilardello and Jackson, 2013). For the cool-warm sweep, an SIRM is imparted at room temperature before the sample is cooled to 20 K. As the sample cools, the remanence is measured. A second SIRM is imparted to the sample at low temperature and the remanence subsequently measured as the sample is brought back to room temperature. For the FC-ZFC-LTSIRM-RTSIRM cycle the samples is initially cooled in an induced field to 20 K, the sample is then warmed and cooled again in the absence of an induced field. Whilst the sample is at 20 K for the second time, a low temperature SIRM is applied before the sample is brought back to 300 K. At room temperature an SIRM is applied to the sample and a final cool-warm sweep is conducted. Through all of these procedures, the remanence of the sample is measured to produce four different magnetisation/temperature (M/T) curves. The derivatives of these curves are used to determine the transition temperatures; the temperature at which the structure of the mineral changes.

The two most common minerals identified with low T transitions are magnetite and pyrrhotite. Stoichiometric magnetite (Fe_3O_4) has an unblocking (transition) temperature of between ~110 and 120 K called the Verwey Transition (T_v) where the grains transition from cubic to monoclinic in habit (Verwey, 1939; Zuo, 1990). Stoichiometric pyrrhotite (Fe_7S_8) transitions between 30 and 35 K exhibiting a distinct drop in remanence (Bensus and Meyer, 1964; Bensus, 1966; Rochette et al., 1990). This was recently named the Bensus Transition by Rochette et al. (2011).

Magnetic hysteresis is determined using a MicroMag Vibrating Sample Magnetometer at room temperature. Magnetic minerals may be in the state of single domain (SD), pseudo-single

domain (PSD) and multiple domain (MD) which can be inferred by the sample's hysteresis properties (Rochette et al., 1999). Hysteresis curves are determined using small rock chips where the samples are exposed to a 1 Tesla magnetic field with the magnetic moment determined at 5 milli-Tesla increments. First-order reversal (FORC) curves can be determined and plotted using FORCinel software (Harrison & Feinberg 2008) to visually predict the grain size of the magnetic minerals present, with different shapes of the graphs implying different mineral domain states. The coercivity, field strength and magnetisation of a sample is determined using DC Demagnetisation (DCD) analyses in order to plot the results in grain size/domain state graphs using the Day et al. (1977) and Dunlop (2002) parameters to determine the domain state of a given sample.

2.9. Anisotropy of Magnetic Susceptibility

The magnetic anisotropy of rocks was first used by Graham (1954) and later pioneered by Balsley and Buddington (1960) and Khan (1962) as a method to determine petrofabrics where the resultant fabrics were directly related to aspects of the rock fabrics. Since then it has become a widely-used method in determining the magnetic fabrics in rocks and is still considered a powerful tool in rock fabric studies (Cañón-Tapia and Chávez-Álvarez, 2004; O'Driscoll et al., 2015) and has significantly enhanced the processes and magma flow dynamics in lava flows, planar intrusions, plutons and layered intrusions (Ellwood, 1978; Ernst and Baragar, 1992; Tarling and Hrouda, 1993; Cañón-Tapia et al., 1996; Borradaile and Henry, 1997; Geoffroy et al., 2002; Martin-Hernandez et al., 2004; Hastie et al., 2013; O'Driscoll et al., 2015).

AMS is described using a second-rank tensor and represented graphically in the form of an ellipsoid where the shape and orientation are defined. AMS has been used frequently in determining the magma flow sense in dykes where the imbrication of ellipsoids of susceptibility along the dyke contacts infer a magma flow direction (Geoffroy et al., 2002; Gil-Imaz et al., 2006). In sills the imbrication of the AMS fabrics along the upper and lower contacts may be used to imply the sense of magma flow, provided the magnetic fabric is representative of the magma flow fabric.

2.9.1. Magnetic Susceptibility

When minerals are exposed to a magnetic field, the response of the minerals is termed induced magnetisation. All minerals can hold an induced magnetisation but the response is stronger is certain minerals, such as magnetite, as compared to silicates. Susceptibility is the measure of how magnetised a mineral may become when exposed to an induced magnetic field. As the

grains that contribute to the AMS in a sample are typically sub-microscopic in size, the number of grains may be in excess of millions, and therefore the same fabrics may not be petrographically obtainable.

The degree to which magnetisation occurs is described by different classes of magnetic ordering known as ferromagnetism, ferrimagnetism, antiferromagnetism, paramagnetism and diamagnetism. Ferri- and ferromagnetic grains are spontaneously magnetised and thus enhance the magnetic field when exposed to an induce field. Ferrimagnetic and ferromagnetic grains have a higher susceptibility than paramagnetic and diamagnetic grains that have the weakest bulk susceptibility (Butler, 1992). Susceptibility (κ) is a dimensionless ratio of magnetisation (M) to the magnetic field (H) represented in Equation 2.2.

$$\kappa = \frac{M}{H} \tag{2.2}$$

Where M is measured in magnetic moment per unit volume (A/m) and H is the strength of the applied field (A/m). The mass susceptibility (χ) of a sample is represented by the ratio of κ to the sample density (Equation 2.3.)

$$\chi = \frac{\kappa}{\text{density}} \tag{2.3}$$

Another measure of the magnetic field strength is *B* (Equation 2.4), called the Tesla which is a sum of the M and H multiplied by a dimensionless constant representing the permeability of free space (μ_0), that is equal to 4π x 10^{-7} (Henry/m):

$$B = \mu_0(H + M) \tag{2.4}$$

The different magnetic classes respond to induced magnetism differently. The magnetic minerals that are the focus of this study are magnetite (Mag – Fe_3O_4) and pyrrhotite (Po – Fe_7S_8) that are both ferrimagnetic minerals.

2.9.2. Principles of Magnetic Susceptibility

The orientation and distribution of the magnetic grains within a rock can be determined by exploiting their response to an induced magnetic field (their susceptibility); as the response of the grains is dependent on shape and orientation, the susceptibility is anisotropic. The anisotropy is determined by measuring the susceptibility of a sample along six or more assigned

directions. These six parameters are then used to evaluate the tensor and calculate the directions and magnitudes of the principal susceptibilities, and resolve these into an ellipsoid. A minimum of six measurements must be made to resolve the second-rank tensor, although six measurements are typically not sufficient for such. The standard 15 position procedure outlined by Jelinek (1978) is therefore most often used.

The AMS ellipsoid represents the 3-D proportions of the principal eigenvectors and is defined by the three principal susceptibility axes: κ_1 for the maximum axis, κ_2 for the intermediate axis and κ_3 for the minimum axis where $\kappa_1 > \kappa_2 > \kappa_3$ (Borradaile and Jackson, 2004). The ellipsoid is represented by lower hemisphere stereographic projections where the principal axes are defined as lineations (Fig. 2.16).

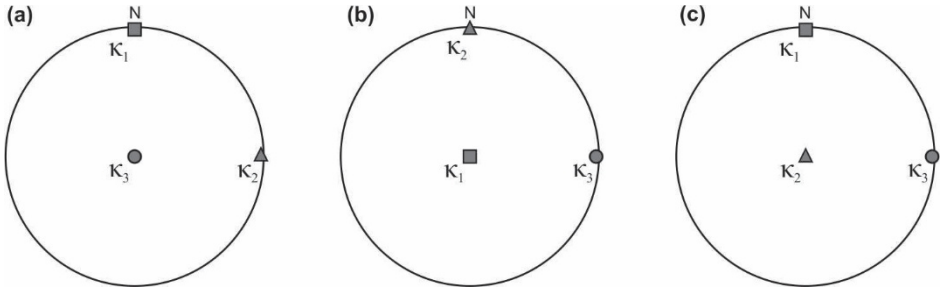

Fig. 2.16. Lower hemisphere equal area stereographic projections of the axes of an AMS ellipsoid where: (a) the lineation (κ_1) plunges horizontally towards north and the foliation striking north-south (plane to κ_3) is horizontal; (b) the lineation is vertical and the foliation is vertical striking north-south; (c) the lineation plunges horizontally towards the north and the foliation is vertical striking north-south. The symbols for κ_1, (■) κ_2 (▲) and κ_3 (●) shown here are used throughout this thesis. After Hastie, 2012.

A statistical confidence margin is used when defining the average ellipsoid for a sill margin. Jelinek Statistics (Jelinek, 1978) are used to determine the average ellipsoid, this is done by defining the average values for the principle axes using a minimum of five samples per margin. The mean orientation of the averaged data for each margin is then used to produce a density distribution of data, a 95 % confidence ellipse and the averaged margin ellipsoid (Jelinek, 1978).

The bulk susceptibility (κ_m) of a sample can also be obtained from AMS results, according to Equation 2.5.:

$$\kappa_m = \frac{\kappa_1 + \kappa_2 + \kappa_3}{3} \qquad (2.5)$$

The degree of anisotropy (anisotropy factor – P′) is a ratio representing a measure of how anisotropic the AMS ellipsoid is (Equation 2.6.) (Jelinek, 1981; Hrouda, 1982; Tarling and Hrouda, 1993). The shape parameter (T) is the measure of the shape of the ellipsoid and defined by Equation 2.7. (Jelinek, 1981; Hrouda, 1982; Tarling and Hrouda, 1993):

$$P' = exp\sqrt{2\left[\left(ln\frac{\kappa_{max}}{\kappa_{mean}}\right)^2 + \left(ln\frac{\kappa_{int}}{\kappa_{mean}}\right)^2 + \left(ln\frac{\kappa_{min}}{\kappa_{mean}}\right)^2\right]} \quad (2.6)$$

$$T = \frac{\ln\left(\frac{\kappa_{int}}{\kappa_{min}}\right) - \ln(\frac{\kappa_{max}}{\kappa_{int}})}{\ln\left(\frac{\kappa_{int}}{\kappa_{min}}\right) + (\frac{\kappa_{max}}{\kappa_{int}})} \quad (2.5)$$

2.9.3. Source of Magnetic Susceptibility

The source of the AMS may be from three sources as defined by Cañón-Tapia (2004). These are (1) "normal" fabrics where the κ_1 coincides with the long axis of the measured grain and κ_3 coincides with the short axis; (2) the SD effect, where the axes are inverted such that κ_1 coincides with the short axis of the grain and κ_3 with the long axis ("inverse" fabrics); (3) clustered magnetic grains where the AMS is a product of the cluster and not of the individual grains.

For normal fabrics obtained from extrusive or intrusive igneous rocks, the κ_1 is sub-parallel to the contacts and the κ_3 axes are perpendicular to the contacts hence, the κ_1 axis is relied upon to infer the magnetic flow vector as the long axes of the anisotropic magnetic grains will align with the direction of magma flow (Ellwood, 1978; Knight and Walker, 1988; Poland et al., 2004). κ_1 is not necessarily the best indicator for the magma flow vector and the shape of the AMS ellipsoid must be considered. Strongly prolate-shaped (elongate) ellipsoids are most adequately defined by the κ_1 axis as this is the lineation and hence, parallel to the long axis of the ellipsoid. However, in strongly oblate-shaped (flattened) ellipsoids, the κ_1 and κ_2 axes may become inverted due to the similarity in the susceptibilities (Rochette et al., 1999; Borradaile and Lagroix, 2001). For oblate ellipsoids the fabric is thus best described as being perpendicular to the pole of the foliation, which is defined by the κ_3 axis.

2.9.4. Magnetic Fabric Acquisition

AMS measurements were undertaken in the laboratories of the Institute for Rock Magnetism and the University of Minnesota, Minneapolis, United States of America. The rock samples were analysed using the AGICO Kappabridge MFK1-FA susceptibility bridge with the standard 15 position procedure outlined by Jelinek (1978). The results obtained were analysed and processed using Anisoft42 (vers. 1.0, AGICO) in which the principle susceptibility axes of the AMS ellipsoid are plotted in lower hemisphere equal area stereographic projections (stereonets). The final ellipsoids are determined by restoring the data about the paleohorizontal. The mean directions and related confidence ellipses are also displayed on the relevant stereonet plots.

2.9.5. Magnetic Mineralogical Control

Quantifying the mineralogy of the samples that is magnetically susceptible is crucial in understanding the fabrics that are determined; (O'Driscoll et al., 2015) hence rigorous magnetic mineralogy measurements were undertaken, as described in *Section 2.7*. As mentioned previously, ferromagnetic and ferromagnetic minerals have a magnetisation even in the absence of an applied field, thus knowing the mineralogy of the material being measured for AMS helps to further understand the resultant fabrics. These minerals may be in a SD state, PSD state and/or MD state (Rochette et al., 1999). Magnetic grains are composed of magnetic domains; each domain is magnetised differently and separated from adjacent domains by a domain wall (Dunlop and Özdemir, 1997). Typically, very small grains are in the SD state and thus only have a single domain which is uniformly magnetised. Larger grains are typically in the MD state and have numerous domains. Intermediate grain sizes may be in the PSD state as they share characteristics of both SD and MD grains. Such grains are the most commonly found in naturally occurring samples (Dunlop and Özdemir, 1997).

In terms of grain size or domain state of the minerals, MD minerals (e.g. magnetite, pyrrhotite) most commonly yield AMS ellipsoids that may be attributed to "normal" magnetic fabrics (Rochette et al., 1999). Whilst some minerals (e.g. fine-grained SD magnetite) may yield "inverse" fabrics as the AMS ellipsoid is not parallel to the elongation of the mineral (Stephenson, 1986; Potter and Stephenson, 1988; Rochette et al., 1999). PSD grains may yield "normal" fabrics through AMS processes and are not significant contributors to "inverse" fabrics.

Although the domain state of minerals may have an effect on the shape of the AMS ellipsoid, "inverse" fabrics may not be a direct result of an abundance of SD grains (Gaillot et al., 2006)

and abnormal fabrics may not be "inverse" in nature (Hastie et al., 2011b). Abnormal fabrics that create an "inverse" AMS ellipsoid may be attributed to not only the SD effect but also to other factors such as (Rochette et al., 1991; 1999): (1) The rolling of large elongate grains instead of rigid-body rotation; (2) Turbulent magma flow (3) The growth of the magnetic minerals perpendicular to the intrusion contacts, particularly at late stages of magnetic mineral crystallisation (Ferré et al., 2002;). The magnetic fabric determined through AMS analyses is, therefore, the result of the magnetic signal of orderly distributed anisotropic grains (Hargraves et al., 1991; Tarling and Hrouda, 1993) where "inverse" fabrics have likely formed through a particular magmatic mechanism (Hastie et al., 2011b).

In basaltic composition rocks, the magnetic susceptibility is generally dominated by ferri- and ferromagnetic minerals (such as magnetite or low-Ti titanomagnetite) even though these minerals typically occur in low abundances (<0.1%) (O'Driscoll et al., 2015). A sample's susceptibility can however, be greatly affected by the presence of Fe-bearing silicate minerals if these minerals exhibit sub-ordinate paramagnetic behaviour and an abundance of these minerals may contribute significantly to a sample's AMS (O'Driscoll et al., 2015).

The shape of the magnetic grains will have an influence on the magnetic fabric as with plagioclase grains used to determine the SPO fabrics. Plagioclase grains in igneous rocks are typically elongate or lath-like; this leads to an intrinsically strong degree of shape anisotropy of the plagioclase fabric. Magnetite grains are typically granular in igneous rocks and therefore have much lower natural shape anisotropy when compared with plagioclase grains. This low shape anisotropy is evident in typical AMS fabrics of magnetite where the highest P′ values are typically low (<1.20) (e.g. Ferré et al., 2002). Grains that are strongly prolate will yield fabrics parallel to the magma flow and oblate grains are more likely to result in "inverse" fabrics (Cañón-Tapia and Chávez-Álvarez, 2004). This effect is due to the inherent shape of the grains thus, the shape of the grains must be considered when applying magnetic fabrics to magmatic fabrics.

Alteration of the rocks that are sampled may change the fundamental properties of the magnetic mineralogy. The hydrothermal alteration of magnetite can result in the intergrowth of titanomagnetite, titanomaghemite and hematite, which can be identified through the magnetic analyses described in *Section 2.7*. Alteration of magnetite can affect the shape anisotropy of the ellipsoid and the samples bulk susceptibility, but the orientation of the principal axes of the ellipsoid are not affected (Krása and Herrero-Bervera, 2005). The presence of small amounts of

titanomagnetite, if any, will be overprinted by the susceptibility of the magnetite fraction as the magnetite grains have a significantly higher susceptibility.

Another process that can have an effect on the magnetic mineralogy and magnetisation of a sample is maghemitisation. Maghemitisation is the process of low temperature (<200°C) oxidation of magnetite where the crystal surface and small crystal fissures are altered to maghemite, a process accelerated by large amounts of adsorbed water (Dunlop and Özdemir, 1997). It is seldom that an entire crystal will become maghemitised; although, the presence of maghemite may be distinct in the magnetic mineralogy analyses. As the shape of the ellipsoid is the most important factor in this study, the effect of alteration is negligible, especially because the minerals formed by magnetite alteration will tend to mimic the original fabric.

2.9.6. Magnetic Fabric and Magma Flow

Anisotropy of magnetic susceptibility (AMS) analyses have fast become the standard technique used for determining rock fabrics and since the 1990's, a well-established tool in analysing

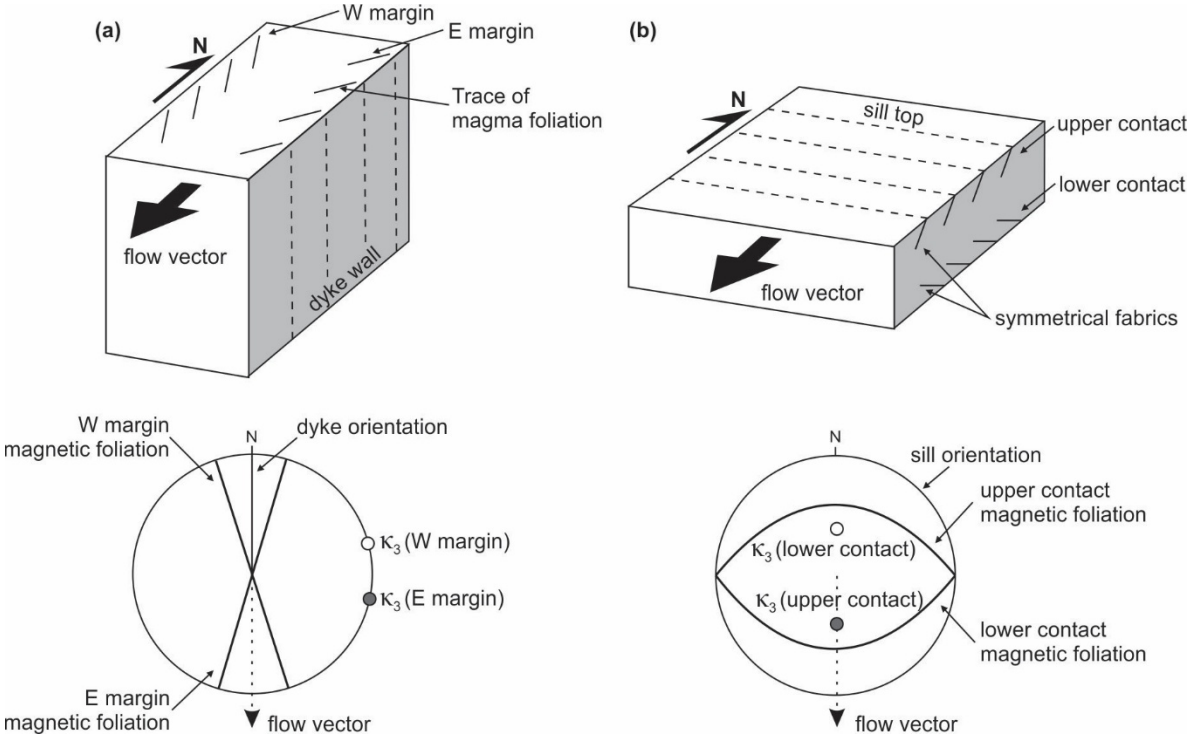

Fig. 2.17. Using AMS fabrics to infer the magma flow vector in idealised situations for planar intrusions. (a) The magma flow vector in a dyke is inferred by the magnetic fabrics adjacent to the E and W margins. Stereographically the dyke is vertical and the magnetic fabrics from the two margins are oriented so that the magma flow propagates towards the south. (b) For sills the situation is similar however the magma flow will always be sill parallel. The direction of magma flow is inferred by the magnetic fabrics obtained from the upper and lower sill contacts. Stereographically the sill is horizontal and the magnetic fabric from the contacts imply that magma flow is towards the south. Modified after Gil-Imaz et al. (2006).

fabrics of intrusive rocks (O'Driscoll et al., 2015). AMS analyses are most commonly used in characterising flow-related fabrics in volcanic, intrusive and metamorphic rocks (Khan, 1962; Ellwood, 1978; Knight and Walker, 1988; Tarling and Hrouda, 1993).
The relationship between the magnetic fabric and the magma flow in sills and dykes is typically defined by the magnetic lineation (κ_1) as being parallel to the magma flow direction (Knight and Walker, 1988; Rochette et al., 1991; Herrero-Bervera et al., 2001) however the magma flow has also been inferred by the foliation; the plane perpendicular to κ_3 (Geoffroy et al., 2002; Callot and Guichet, 2003).

As with the plagioclase fabrics used to infer magma flow using the SPO method, the imbrication of magnetic minerals along the margins of an intrusion may be used to infer magma flow direction (Fig. 2.17). The magnetite minerals that produce the AMS fabrics are typically granular in habit and have a low degree of anisotropy, therefore the imbrication of the magnetite crystals along the sill/dyke margins may not be as well defined as the SPO of elongate minerals (i.e. plagioclase). In dykes, the magma flow vector inferred by the AMS ellipsoid can be vertical or horizontal with respect to a vertical dyke plane. Horizontal magma flow would be inferred if the magnetic fabric foliation along the dyke walls dips vertically with a strike at an angle to the dyke wall (Fig. 2.17a). Vertical magma flow in dykes will be inferred if the strike of the foliation is parallel to the dyke walls with the dip at an angle to the dyke wall. For sills, in particular thin sills where no magma chamber processes apply, the magma flow will be lateral as it is confined between the upper and lower sill contacts.

The direction of the magma flow within sills can be determined using AMS fabrics; the imbrication of the magnetic fabrics along the upper contact should plunge/dip towards the propagation direction of magma flow (Fig. 2.17b). Given the symmetry of the fabric imbrications, it follows that the lower contact AMS data plunges/dips away from the direction of magma flow.

As with the formation of crystal fabrics that are determined by the rock-forming crystal phases (i.e. plagioclase) described in *Section 2.6.6*, the AMS fabrics will be preserved if the viscosity of the magma allows for a preferred mineral orientation to be preserved. For the magnetic phases in the magma, the timing of the crystallisation of the magnetic minerals is just as important.

If the magnetic phases crystallise early during magmatic crystallisation the AMS fabrics will represent the passive nature of the melt. If the magnetic phases crystallise later, i.e. contemporaneous with magma flow, then the AMS fabrics will likely be more representative of flow-related fabrics (Gil-Imaz et al., 2006). If the magmatic fabric forms contemporaneously to the formation of the magnetic phases in the rocks, it follows that the magmatic fabric will have the same fabric orientation as the magnetic fabrics, which is the common assumption when elucidating flow-fabrics using AMS. The magnetic fabric can, thus, be used as a proxy for the magmatic fabric which, if adhering to the above criteria, may be used to infer the magma flow direction. However, if magnetic grains form in the late stages of crystallisation, as is often the case with very fine SD magnetite grains, and therefore have no relationship with the magmatic fabric, the AMS results may not accurately infer a magma flow.

- CHAPTER 3 –

GEOLOGICAL SETTING AND THE KAROO IGNEOUS PROVINCE

3.1. Introduction to the Karoo Igneous Province

The study area is located along the North Coast of KwaZulu-Natal on the east coast of South Africa (Fig. 3.1.). On a regional scale, the basement rocks comprise granitoids and gneisses of the Mzumbe Terrane of the Natal Metamorphic Province (Thomas, 1989) which are overlain by arkosic and quartz arenites of the Natal Group (Marshall, 2002). Unconformably overlying the Natal Group is the Karoo Supergroup. The Karoo Supergroup was deposited in the Upper Carboniferous to Jurassic and comprises sedimentary rocks that are divided into six groups from stratigraphically lowest to highest; the Dwyka, Ecca, Beaufort, Stormberg Groups with the sedimentary rocks capped by the volcanics of the Drakensberg and Lebombo Groups. In the main Karoo Basin, the sedimentary pile attained a cumulative thickness of up to 12 km with the maximum preserved thickness of 5.5 km (Tankard et al., 2009). This covered an area of 630 000 km^2 (Svensen et al., 2015). The depositional environments of the Karoo Supergroup rocks ranged from marine to glacial to deltaic for the Dwyka and Ecca Groups, grading into a predominantly fluvial environment for the Beaufort Group and variable environments for the Stormberg Group. The Stormberg Group is separated into the Molteno and Elliot Formations (deposited in fluvial environments) and the Clarens Formations which was deposited in an aeolian environment (Catuneanu et al., 1998). The Vryheid Formation rocks (Ecca Group) that crop out in the study area range from thinly laminated siltstones to shales and gritstones which were largely deposited in fluvially dominated deltaic environments (Tavener-Smith et al., 1988).

Post-dating the final deposition of the Karoo sedimentary rocks are the rocks of the Karoo igneous event. This involved a crustal scale mantle melting event that produced voluminous mafic magmas of the Karoo, Ferrar and Tasman igneous provinces of southern Africa, Antarctica and Australia (Eales et al., 1984; Elliot, 1975; Fleming et al., 1995). In the following sections the KIP and related magmatic events are discussed including the ages, extent and source of the rocks belonging to and associated with the KIP.

3.2. Rocks of the Karoo Igneous Province

The KIP can be separated into volcanic and intrusive components, with the volcanics representing a continental flood basalt (CFB) province and the intrusions representing the sub-volcanic plumbing system. Due to continental configuration within Gondwana, at the time of formation of the KIP, Antarctica and Australia were attached to southern Africa. The resultant large scale magmatic event related to the break-up of Gondwana produced the voluminous magmas preserved today as the Karoo (southern Africa), Ferrar (Antarctica) and Tasman (SE Australia) large igneous provinces each of which comprise abnormal volume of mafic lava and associated dolerite intrusions (Elliot, 1975; Kyle et al., 1981; Courtillot, 1999; Fleming et al., 1995; Encarnación et al., 1996; Watkeys, 2002). Together the Karoo and Ferrar complexes cover an area of southern Africa and Antarctica of 6×10^6 km^2 (Le Gall et al., 2002). The Ferrar LIP is exposed in Antarctica and predominantly takes the form of massive dolerite sills, layered mafic intrusions and covering basalt sequences that are laterally extensive (Curtis et al., 2008).

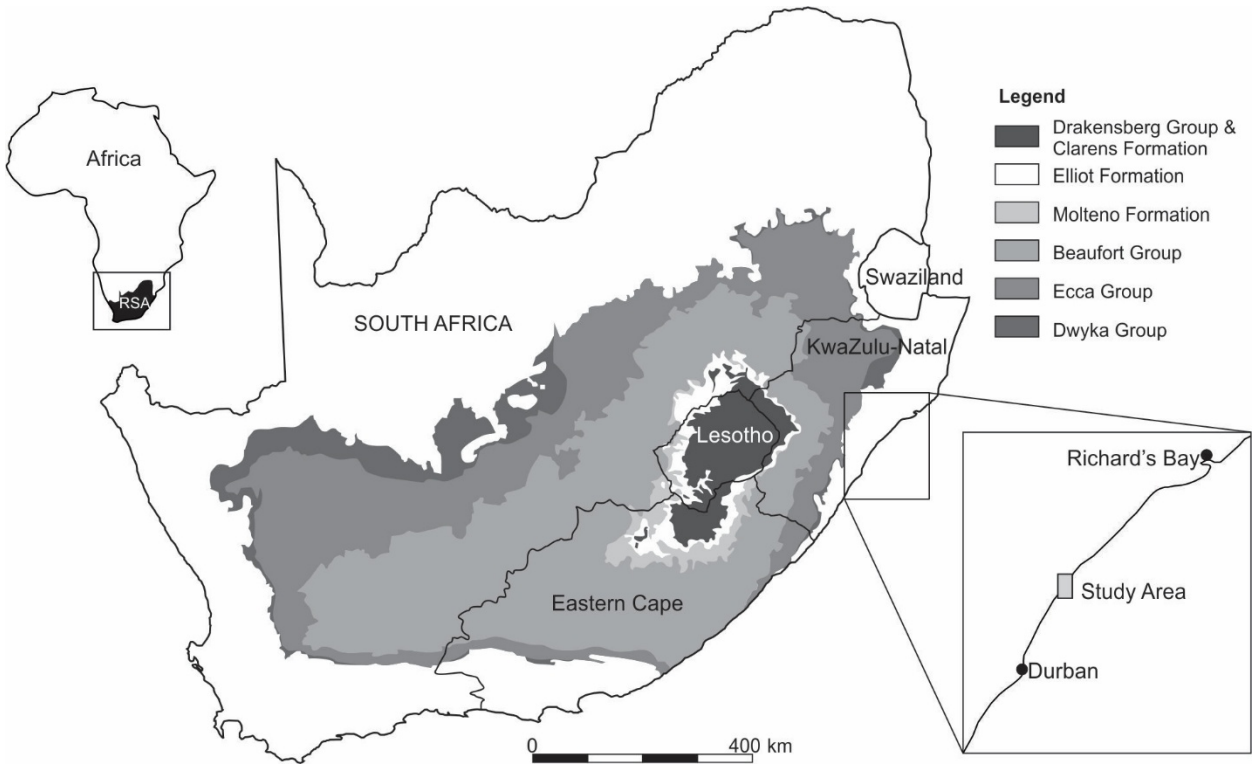

Fig. 3.1. The location of South Africa in Africa and the extent of the rocks of the various Groups of the Karoo Supergroup in South Africa, however not all the outcrop has been represented here. The locality of the study area on the east coast of KwaZulu-Natal is also shown. Modified after Catuneanu et al. (1998).

The rocks of the KIP have been the focus of studies for several decades with investigations into the extent, composition, age and origin of the KIP (e.g. Du Toit, 1929; Cox et al., 1967; Duncan

et al., 1984; Ellam et al., 1992; Jourdan et al., 2008, 2009; Hastie et al., 2014). A series of papers by Erlank (1984) provides an overview of the KIP, with more recent studies being undertaken on the source of the magma and the overlap of the different igneous provinces of Gondwana (e.g. Jourdan et al., 2004; 2006; 2009; Riley et al., 2006; Moulin et al., 2011; Hastie et al., 2014).

3.2.1. KIP volcanic rocks

When the KIP formed it was primarily a CFB province and formed one of the largest CFBs globally (White, 1997). The KIP comprises not only lavas and volcanic successions but intrusions that cover an extensive portion of southern Africa. The volcanic extent of the KIP used to cover a significantly larger area than the erosional remnants that are currently preserved in the southern African stratigraphy. It is estimated that the volcanics of the KIP originally covered an area of ~3 x 10^6 km^2 and blanketed the majority of South Africa, as inferred through the presence of Karoo lava xenoliths present in kimberlite pipes country-wide (Eales et al., 1984).

The lavas that formed the CFB province were erupted through successive fissure eruptions in the form of horizontal (to sub-horizontal) lava flows that become stacked into a lava pile (Duncan and Marsh, 2006). Over the southern African continent, the remnant lavas are separated into two main areas and stratigraphic units termed the Drakensberg Group and Lebombo Group.

The Lebombo Group incorporates the volcanism in the Mwenezi-Save area of the KIP and rift-related volcanic sequences of the Lebombo monocline (Fig. 3.2) (Duncan and Marsh, 2006). In the northern outcrops of the KIP, the rocks that were erupted in the Mwenezi-Save area form a supposed concentric pattern from nephelinites in the centre to tholeiitic picrites to tholeiitic basalts, separated into high-Ti and low-Ti varieties, on the outskirts (Fig. 3.2) (Cox et al., 1967; Klausen, 2009; Hastie, 2012). The volcanics are also associated with intrusive ring complexes of granite, gabbro, syenite, nepheline syenite and carbonatite of similar ages (Cox et al., 1965).

The Lebombo Group is separated into five formations; the Mashikiri, Letaba, Sabie River, Jozini and Mbuluzi Formations (Cleverly and Bristow, 1979). The Mashikiri Formation is spatially limited; it comprises nephelinites that are centred at Mwenezi overlying the Clarens Formation and the Precambrian basement in the northern Lebombo area. These nephelinites are enriched in incompatible trace elements and most likely formed through the melting of old metasomatically-enriched sub-continental lithospheric mantle (SCLM) (Ellam and Cox, 1989;

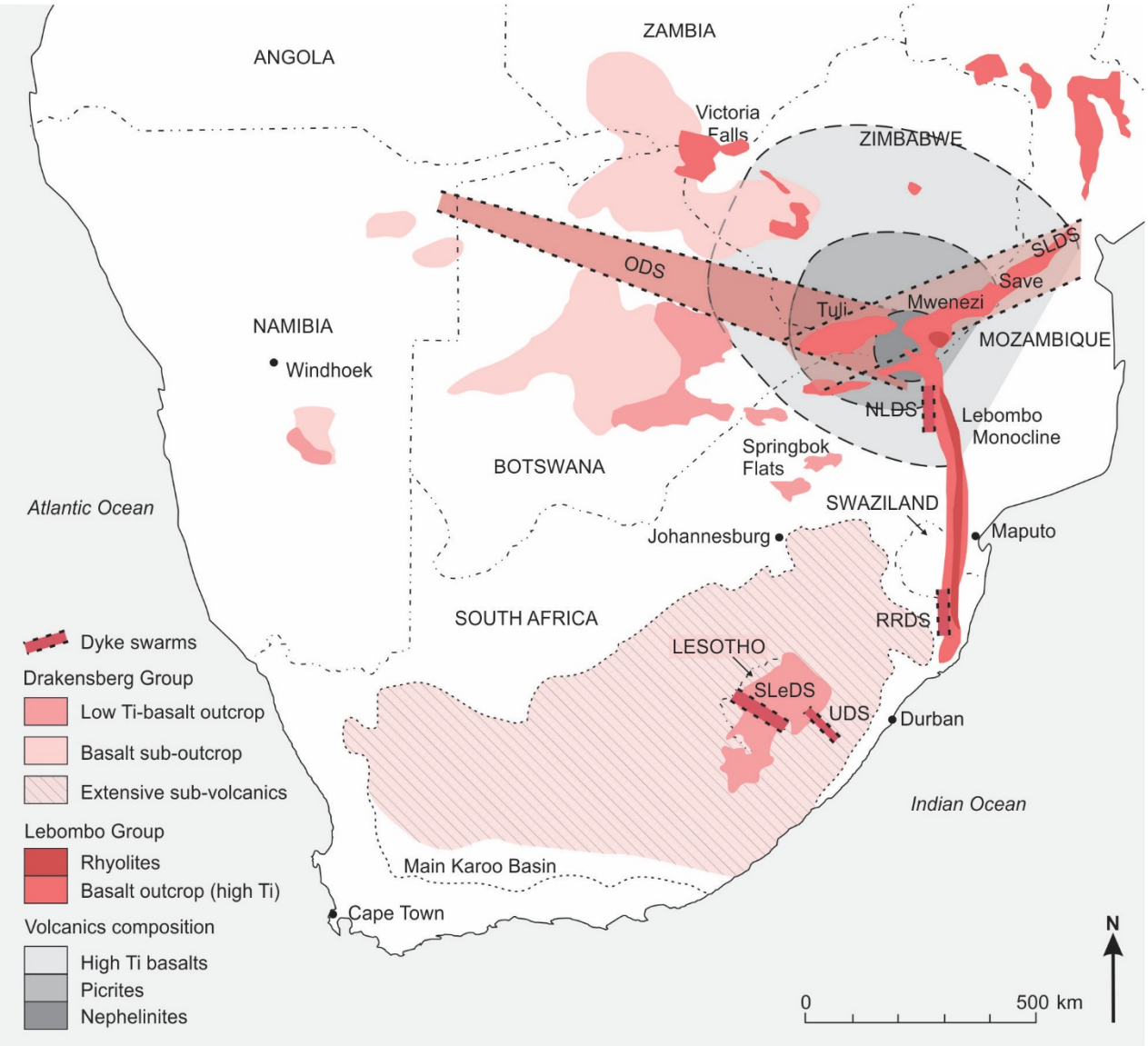

Fig. 3.2. Outcrop map of the rocks belonging to the Drakensberg and Lebombo Groups, these rocks comprise the volcanics of the KIP, illustrating the extent of the KIP rocks in southern Africa. The concentric distribution of the different rock compositions are highlighted in grey and range from nephelinites to picrites to high-Ti basalts. Further south and west of the outermost concentric circle, the rocks are predominantly low-Ti basalts. The occurrence of dolerite intrusions of sub-volcanic complex of the KIP is extensive in the main Karoo Basin but is not limited to this area. A few of the significant dyke swarms are highlighted, RRDS = Rooi Rand Dyke Swarm, NLDS = Northern Lebombo Dyke Swarm, ODS = Okavango Dyke Swarm. After Duncan and Marsh (2006); Jourdan et al. (2009); Klausen (2009).

Hawkesworth et al., 1999; Jourdan et al., 2007a). Overlying the Mashikiri nephelinites are the picrites of the Letaba Formation; these picrites have MgO weight% (wt%) of 10% – 24% and are voluminous in comparison to the nephelinites they overlie. There is no consensus on how these magmas may have formed. They could have resulted through the melting of the SCLM (Bristow, 1984; Ellam and Cox, 1989), the mixing of SCLM and asthenospheric mantle (Ellam and Cox, 1991; Sweeney et al., 1991) or they may have been derived directly from a heterogeneous source (Ellam, 2006). The Sabie River Formation comprises basalts that are interbedded with rhyolite flows and sills called the Olifants River Beds (Bristow, 1982; Riley et al., 2004).

The majority of the rocks of the KIP are made up of tholeiitic basalts grouped into low-Ti and high-Ti varieties, all with lower MgO wt% (2% - 9%) when compared to the nephelinites and picrites. A geographical distinction is evident between the high-Ti and low-Ti varieties (Fig. 3.2); in the northern Lebombo (and further north) the Ti wt% is greater than 2% whereas south (Lesotho and southern Lebombo) and west of this area (central Botswana and Namibia) the Ti wt% is lower (Cox et al., 1967; Duncan et al., 1984; Jourdan et al., 2007a). The large difference in the Ti wt% between the low-Ti and high-Ti basalts can be accounted for by slight differences in melt production as approximately a third of the incompatible elements in the high-Ti basalts are from lithospheric mantle material (Sweeney and Watkeys, 1990; Sweeney et al., 1994).

Along the Lebombo monocline the rhyodacites and rhyolites of the Jozini and Mbuluzi Formations dominate the stratigraphy (Fig. 3.2) (Cleverly et al., 1984; Bristow and Cox, 1984; Watkeys, 2002; Klausen, 2009). These formations are the youngest volcanics of the KIP and form the cap rock of the Lebombo monocline (Riley et al., 2004). The only magmatic event that occurred after the eruption of the Lebombo rhyolites was the intrusion of the RRDS in the southern Lebombo area (Armstrong et al., 1984).

The volcanic rocks of the Drakensberg Group are all similar in composition ranging from tholeiitic basalts to basaltic andesites that were erupted onto a relatively stable and dry cratonic environment (e.g. Bristow and Saggerson, 1983; Duncan et al., 1984; Marsh and Eales, 1984). Separation of the units within the Group is based on variations in the minor and trace element compositions of the lavas where the upper units of the Drakensberg Group have higher Ti/Zr ratios (and Ti wt%) when compared to the lower units (Marsh et al., 1997).

The Drakensberg Group is separated into the lower Barkly East Formation and the upper Lesotho Formation. The Barkly East Formation is separated into the following units although all are not laterally continuous; Moshesh's Ford, Golden Gate, Sani, Roma, Letele, Wonderkop, Kraai River and Vaalkop. Within certain units there are significant geochemical differences in rocks that are laterally adjacent between the northern Lesotho and northern Eastern Cape regions. This suggests that there may have been two different eruptive centres that formed the basalts of the Barkly East Formation (Duncan and Marsh, 2006).

The Lesotho Formation is separated into the following units from stratigraphically lowest to highest; Mafika Lisiu, Maloti, Senqu and Mothae. The preserved successions in the lava pile in Lesotho are in excess of 1.5 km thick, are laterally continuous and maintain a consistent thickness throughout Lesotho and the Eastern Cape Province of South Africa (Duncan and Marsh, 2006). It is thus assumed that the Lesotho Formation was formed through large successive fissure eruptions onto a planar surface (Duncan and Marsh, 2006). There has been some geochemical correlation between the basalts of the Drakensberg and Lebombo Groups and the stratigraphic units in the Lesotho area with the basalts in the Springbok Flats region, located ~400 km to the north (Fig. 3.2) (Duncan and Marsh, 2006).

3.2.2. KIP intrusive rocks

The sub-volcanic complex of the KIP predominantly comprises dolerite intrusions and is best developed in the main Karoo Basin, covering a large portion of South Africa (Fig. 3.2). In the main Karoo Basin, the dolerite outcrops bridge the erosional gaps between exposed lava remnants and are compositionally the same as the adjacent extrusive units (e.g. Marsh and Mndaweni, 1998). The dolerites represent a great volume of magmatic material and typically occur as dykes, sills and saucer-shaped sills of varying thicknesses that may be part of an interconnected system (Du Toit, 1920; Walker and Poldervaart, 1949; Marsh and Eales, 1984; Chevallier and Woodford, 1999).

3.2.3. Sills

The sills in the KIP are typically 2 – 10 m in thickness but may exceed 200 m in thickness in the main Karoo Basin. The sills within the main Karoo Basin have been extrapolated, using borehole data, to occupy a volume of 250 000 – 300 000 km^3 which is up to 32% of the basin volume (Svensen et al., 2015). Most of the sills in the KIP are tholeiitic in nature with small volumes of sills showing andesitic compositions and thus a more evolved geochemistry (Marsh and Eales, 1984). Thick sills can show evidence of minor magma chamber processes such as

internal differentiation and gravity settling (e.g. Le Roux and Reid, 1978; Richardson, 1979). Due to the interconnected nature of the sub-volcanic system of the KIP, it is very difficult to pinpoint a particular event of intrusion or deformation, thus making the relationships between the dykes and sills in the main Karoo Basin difficult to unravel (Chevallier and Woodford, 1999). The network of dykes and sills in the main Karoo Basin are so tightly connected that the intrusions take the form of a shallow "stock-work like reservoir" that most likely formed through intrusion of enormous volumes of magma that simultaneously infilled a series of fractures (Chevallier and Woodford, 1999). The majority of the sills were emplaced at ~182 Ma over a brief time period with ages ranging from 183.0 ± 0.5 to 182.3 ± 0.6 Ma (Svensen et al., 2012).

Planar (or non-saucer shaped) sills are common throughout the Karoo Supergroup rocks in southern Africa with the number, lateral extent and thickness of the sills increasing upward into the upper formations (Frankel, 1969). The sills that intruded into the Ecca Group rocks are typically thin (less than 10 m thick) and do not form a tight interconnected network. Du Toit (1920) observed that the Karoo sills intruded preferentially along lithological contacts in the sedimentary rocks, and along contacts between the different Groups in the Karoo Supergroup. The form of these planar sills is not always a flat horizontal sheet as the form of the sill depends on the fractures that are created (or opened) during magma intrusion and the directions of the surrounding principal compressive stresses.

Sills in the central Karoo were originally partially mapped by Rogers and Schwarz (1902), Rogers and Du Toit (1903) and Du Toit (1905). Walker and Poldevaart (1949) studied some of the intrusions in the Karoo Main Basin noting that the tholeiitic intrusions showed interesting intrusion-related structures such as rheomorphic sedimentary dykes. More recent studies of Le Roex and Reid (1978) and Marsh and Eales (1984) examined the geochemical and formative processes of the dolerites.

Some of the larger sills have been studied to determine the sill geochemistry, ages, morphological features and the magma flow dynamics within the intrusions. These sills include the Golden Valley saucer-shaped sill, the Insizwa sill and the New Amalfi Sheet (Encarnación et al., 1996; Ferré et al., 2002; Marsh et al., 2003; Maes et al., 2008; Schofield et al., 2010; Schofield et al., 2012a). The Insizwa sill occurs in the Mount Ayliff Complex in the Eastern Cape and is > 1 km thick and 25 km in diameter with mafic and ultramafic layers (Ferré et al., 2002; Marsh et al., 2003). Although more along the scale of a layered intrusion, the Insizwa sill

has been successfully analysed magnetically and has yielded petrofabric lineations that indicate uniform magma flow across the sill, plunging towards the NW (Ferré et al., 2002). It was therefore implied that a sub-vertical dyke SE of the sill was the single feeder to the Insizwa sill (Ferré et al., 2002; Marsh et al., 2003). The New Amalfi Sheet occurs NW of the Insizwa sill close to the Lesotho border with the Eastern Cape. This intrusion is a "bowl" shaped intrusion with a $^{206}Pb/^{238}U$ age of 183.7 ± 0.6 Ma representative of magmatism associated with some of the earliest Lesotho basalts (see *Section 3.3*) (Encarnación et al., 1996).

The intrusion mechanisms of the interconnected sills and dykes is often scrutinised regarding large-scale intrusions, however no detailed study has been conducted on the intrusion mechanisms of small scale separate intrusions away from the main Karoo Basin. Sills and dykes that show minimal overlap are a good indicator of the mechanism of intrusion as magma flow within them can be adequately elucidated. This is in contrast to the complex nature of a stock-work intrusive system, which may only indicate the general intrusive mechanism simply through the intrusions structures (Chevallier and Woodford, 1999).

A type of non-planar sill that has received attention in recent studies is the saucer-shaped sill. Saucer-shaped sills, or as they are sometimes referred to as ring-sills, are sub-circular basin like intrusive structures which may be stacked forming a series of intrusions (Chevallier and Woodford, 1999).The first examples of saucer-shaped sills were described by Du Toit (1905, 1920) in Queenstown in the Eastern Cape. These structures have been of interest to geologists ever since, with numerous authors attempting to unravel how they are formed (e.g. Lombaard, 1952; Burger et al., 1981; Chevallier and Woodford, 1999; Goulty and Schofield, 2008; Polteau et al., 2008; Schofield et al., 2010). Burger et al. (1981) presented a laccolith model for how the saucer-shaped sills formed where a pipe feeder created a laccolith where the thickness at the centre of the sill caused deformation in the overlying sedimentary layers resulting in faulting and dyking around the sill periphery. Based on evidence from ring-dyke complexes in the western Karoo Basin, Chevallier and Woodford (1999) proposed that saucer-shaped dykes formed through progressive magma propagation from a dyke to an outer sill, as the overburden is lifted the inner sill segment forms through downward magma flow. It has since been shown that saucer-shaped sills are unrelated to ring-dykes and that they are instead produced by a central feeder in the vicinity of the inner sill that subsequently propagates upwards into a rim structure and then into an outer sill (Thomson and Hutton, 2004; Hansen and Cartwright, 2006; Polteau et al., 2008; Schofield et al., 2010).

Large sills that are intrusive into high stratigraphic levels in the main Karoo Basin are commonly associated with hydrovolcanic pipes (hydrothermal vents) forming diatremes. As mentioned in *Section 2.3* above, these features form through explosive fragmentation by the interaction of groundwater and the intruding magma. This forms pipe-like structures comprising material ranging from lithified clastic sediments to volcaniclastic breccias. The volume change of the volatiles necessary to trigger country rock fragmentation is reliant on the depth of the critical point of water which is ~700 m (at 221 bars) below the palaeosurface (Duncan and Marsh, 2006) and are thus used as an indicator for the prediction of the maximum depth of an intrusion.

Recent studies regarding sills and sill complexes have been accomplished with the aid of 3D seismic data. These sections have been used to further understand the detailed morphologies of sills in 3D and the intricacies of the magma flow pathways (e.g. Bell and Butcher, 2002; Hansen et al., 2004; Thomson and Hutton, 2004; Cartwright and Hansen, 2006; Thomson, 2007; Thomson and Schofield, 2008; Hutton, 2009; Schofield et al., 2012a; Schofield et al., 2015). Although seismic data are very useful when elucidating the morphology and location of sills, the mechanism of intrusion is often difficult to determine (Schofield, 2009).

3.2.4. Dyke swarms

There are numerous dyke swarms up to 1500 km in length that make up a large portion of the KIP. The dyke swarms in the northern regions of the KIP have received the most attention in recent studies, with focus on the dyke swarms proximal to Mwenezi, i.e. the Okavango Dyke Swarm (ODS) (e.g. Reeves, 1978, 2000; Elburg and Goldberg, 2000; Le Gall et al., 2002, 2005; Jourdan et al., 2004; Aubourg et al., 2008).

The most extensive and volumetrically significant dyke swarm is the ODS which is ~1500 km in length and up to 300 km wide where it intersects the Save Limpopo Dyke Swarm (SLDS) in the northern Lebombo region (Fig. 3.2) (Jourdan et al., 2006). The dykes are intruded into rocks of Precambrian basement, where the ODS occurs in the Limpopo Belt, and intrudes the Karoo Supergroup rocks in the Tuli Basin (Smith, 1984; Elburg and Goldberg, 2000; Le Gall et al., 2005; Aubourg et al., 2008). The dyke swarm has a distinct ~110° trend and consists of a basaltic (doleritic) composition, with both high-Ti and low-Ti varieties present (Elburg and Goldberg, 2000; Aubourg et al., 2008). The orientation of the dykes in the ODS is not representative of the minimum compressive stress present when the dykes intruded as Le Gall et al. (2005) show that the dilation direction is actually NNW-SSE. Instead the dykes have taken

advantage of the pre-existing structural trend in the Zimbabwe Cratons and Limpopo Belt (Watkeys, 2002). This is also evident by the Proterozoic generation of dykes that comprise 13% of the WNW-ESE trending dykes and are parallel to the ODS further indicating that this orientation represents a significant zone of crustal weakness (Elburg and Goldberg, 2000; Le Gall et al., 2002, 2005; Jourdan et al., 2004). The Proterozoic dykes range from 1672 ± 7 Ma to 851 ± 6 Ma and the Jurassic dykes ages are well constrained between 179 ± 1.2 – 178.4 ± 1.1 Ma (Jourdan et al., 2004).

Geographically adjacent to the ODS is the SLDS; this dyke swarm is ~600 km in length and 50 – 100 km wide extending from SE Botswana to beyond the north-eastern limit of the Limpopo Belt. The dykes are doleritic in composition, trend ENE and dip vertically to sub-vertically (Hastie, 2012). The ages of the SLDS range from 180.4 ± 0.7 to 178.9 ± 0.8 Ma (Le Gall et al., 2005; Jourdan et al., 2005, 2006) and as with the ODS, there is an overlap between the Karoo-aged and older Proterozoic-aged dykes as evident from field relationships in the Mwenezi area (Watkeys, 2002).

The NLDS comprises north-south trending dykes intruded into Clarens Formation rocks and volcanics of the KIP (Fig. 3.2) (Hastie et al., 2011a). These dykes can be directly correlated to volcanic successions in the rocks of the Lebombo monocline including the Sabie River Formation basalts, Jozini Formation rhyolites. These span four different dyking events (Klausen, 2009). Jourdan et al. (2005) dated the dykes and obtained ages of 181.4 ± 0.7 – 182.3 ± 1.7 Ma, also recognising a lack of Proterozoic dykes in the same orientation. As the dyke orientation was not a product of an inherent lithospheric pattern, the distinct north-south orientation may have been derived from the east-west extension pattern that occurred in the Lebombo monocline in the Jurassic (Watkeys, 2002).

The Rooi Rand Dyke Swarm (RRDS) occurs in the southern regions of the Lebombo monocline. It comprises a dyke swarm 10 – 22 km in width that intruded the Karoo Supergroup sedimentary rocks and Sabie River Formation basalts (Saggerson et al., 1983; Hastie, 2012). The dykes of the RRDS generally trend north-south over ~180 km (Armstrong et al., 1984; Watkeys, 2002; Hastie et al., 2011b). The age of the dykes are 173 ± 0.7 Ma (Jourdan et al., 2007b, c) and are thought to have formed from asthenospheric melts during the early stages of continental break up of Gondwana (Armstrong et al., 1984; Meth, 1996; Saggerson et al., 1983).

In the Lesotho region, two significant dyke swarms are noted, the Underberg Dyke Swarm (UDS) and the Southern Lesotho Dyke Swarm (SLeDS); both swarms trend similarly in an approximate NW-SE orientation. The rocks of the SLeDS have not been investigated in terms of the magma flow directions or geochronology. The rocks of the UDS intruded into the Karoo Supergroup lithologies and the Lesotho basalts. Riley et al. (2006) studied the SE-oriented dykes and showed that they have a consistent strike direction (~130° – 140°) and an Ar^{40}/Ar^{39} age of ~176 Ma. These dykes are geochemically similar to the SLeDS and the Lesotho Group basalts but show some signs of crustal contamination, derived from sub-lithospheric melts (Riley et al., 2006).

Other dyke swarms that occur in southern Africa are the Gap dyke swarm, an east-west trending system in the Eastern Cape that extends for ~200 km (Jourdan et al., 2006), the ~ESE striking Southern Botswana dyke swarm (Jourdan et al., 2006) and the ~170 Ma NNE-striking SW-1 dyke swarm in southern Mozambique (Mekonnen, 2004). There are numerous dykes that occur collectively in areas across southern Africa that are not grouped as dyke swarms. These include the N to NW trending dykes in the western portion of the main Karoo Basin (Chevallier and Woodford, 1999) and the Fe-rich Oxbow dykes that intrude the entire Lesotho basalt pile and are likely related to eroded basaltic units (Duncan and Marsh, 2006).

3.2.5. Geochemistry

The geochemistry of the rocks of the KIP provide insight into the process of formation of the igneous province hence, many geochemical analyses have been undertaken on the KIP volcanics and intrusions (Cox et al., 1967; Duncan et al., 1984; Sweeney and Watkeys, 1990; Hergt et al., 1991; Ellam et al., 1992; Sweeney et al., 1994; Riley et al., 2006). CFB's typically comprise tholeiitic basalts which may also form in mid-ocean ridge (MOR) settings, oceanic plateaus and as ocean island basalts (OIB) (Winter, 2001).

Strictly the volcanic rocks of the KIP province are not basalts as they are generally more siliceous or "evolved" with SiO_2 weight percentages exceeding 52% thus, compositionally they are basaltic andesites (Le Maitre, 1989). Petrographically the low- and high-Ti-Zr basalts are sub-ophitic in texture comprising plagioclase, and clinopyroxene with titanomagnetite as a late crystallisation phase, whereas the picrites are typically porphyritic in texture with olivine and clinopyroxene phenocrysts (Duncan and Marsh, 2006). Petrographically and geochemically, the majority of the mafic rocks are tholeiitic in nature (Duncan and Marsh, 2006). As mentioned above, the volcanic rocks at Mwenezi-Save area became more evolved with successive

eruptions, beginning with nephelinites and concluding with low Ti-Zr basalts. These rocks make up the majority of the rocks in the southern Karoo area (Erlank, 1984). The dyke swarms prevalent in this area are dominated by high-Ti-Zr basalts.

The geochemistry of the Karoo basalts does not define a particular tectonic setting or basalt type; the radiogenic isotope ratios of the Karoo basalts differ from that of MOR basalts (MORBs) and are enriched in large-ion lithophile elements (e.g. K, RB) when compared to MORBs (Duncan and Marsh, 2006). Tectonomagmatic geochemical discrimination diagrams can help in determining the environment in which the magmas formed (Pearce and Cann, 1973; Pearce, 1976). This technique was applied by Duncan (1987) for the high-Ti-Zr basalts which were classified as "within-plate basalt". This is not always a good diagnostic tool however, as the low-Ti-Zr basalts in the Lebombo area were classified as arc-related tholeiites when there is no significant evidence for subduction occurring at the time (Duncan 1987).

To explain these inconsistencies it has been proposed that crustal contamination has overprinted the original magma chemistry (e.g. Arndt et al., 1993). Evidence for mixing of material in the melt source area includes: evidence from Sm-Nd systematics that the Karoo rocks yield a Proterozoic eruption "isochron" (Ellam and Cox, 1989); a generally MORB-like incompatible element signature and low levels of crustal contamination (Cox and Bristow, 1984; Hawkesworth et al., 1984); and an increase in their Sr^{87}/Sr^{86} ratios (Bristow et al., 1984).

3.3. Karoo Igneous Province Geochronology

Ages of the volcanics and intrusive rocks of the KIP preserved in southern Africa are represented in Fig. 3.3; the sources of the ages are referenced in the figure. A summary of the ages of the volcanic and intrusive rocks of the KIP was compiled by Jourdan et al. (2007b). In order to ensure the ages presented are reliable dates, only U-Pb and $^{40}Ar/^{39}Ar$ of single zircon and plagioclase grains (respectively) are shown, thus whole rock (including those obtained through K/Ar and Rb/Sr analyses), bulk sample and groundmass ages are not included as the meaning of these ages is debatable (Jourdan et al., 2005, 2007b; Hastie, 2012). Only Jurassic rock ages are included in the age summary in Fig. 3.3. Therefore it does not include pre-KIP igneous rocks that occur in southern Africa and Antarctica, like for example the Dokolwayo kimberlite in Swaziland which intruded at 200 ± 5 Ma during the deposition of the Karoo Supergroup sedimentary rocks (Allsopp and Roddick, 1984).

The ages displayed in Fig. 3.3 are the most statistically accurate ages extracted from the literature. The age of the Olifants Beds (silicic rocks interbedded with the Sabie River Formation basalts) was originally defined as 180.2 ± 2.7 Ma by Riley et al. (2004) but was recalculated by Jourdan et al. (2007b) and constrained as 178.4 ± 2.7 Ma, an age that is within error of the Jozini rhyolites at 177.8 ± 0.6 Ma (Jourdan et al., 2007b). The age of the Jozini rhyolites is derived from Jourdan et al. (2007b) as previous $^{40}Ar/^{39}Ar$ ages determined by Duncan et al. (1997) may be representative of cooling ages. The Ferrar dolerites in Antarctica have not been included in Fig. 3.3. The age of the eruption of the Ferrar basalts is however, significant in terms of the age relationship of eruption between the Karoo and Ferrar igneous provinces. The Ferrar basalts were originally dated by Heimann et al. (1994) and the data recalculated by Riley and Knight (2001) to yield an age range of 180.8 ± 0.7 – 180.0 ± 0.6 Ma. Recent age data of the Ferrar sills in Antarctica show that Ferrar magmatism may have begun earlier than previously shown, yielding an age of 182.8 ± 0.03 Ma (Burgess et al., 2015).

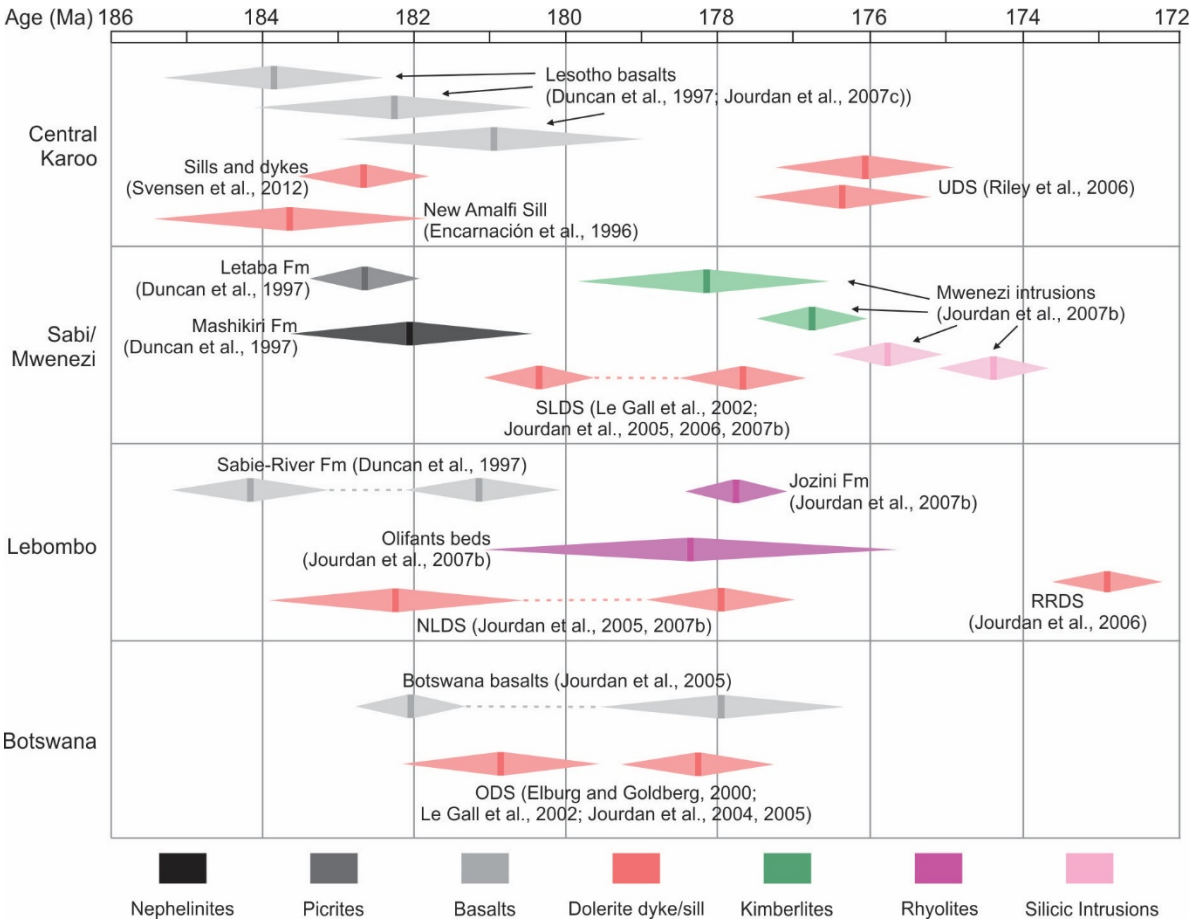

Fig. 3.3. Age data of the volcanic and intrusive rocks of the KIP, the ages are separated into areas of the Central Karoo, Sabi/Mwenezi region/ Lebombo and Botswana. The dark shaded area in the double triangle is the defined age with the triangles representing the error bar. Dashed lines represent age gaps between data sets. Modified after Hastie et al. (2014).

When contemplating the extent and volume of the rocks associated with the KIP, it was initially thought, on the basis of K-Ar dating, that the magmatic activity occurred in episodes over a 40 – 50 Ma period (Fitch and Miller, 1984). It has since been observed that this is inconsistent with geological evidence and other dating, thus the entire KIP event most likely occurred in a short period of time on the scale of a few million years (Hargraves et al., 1997). The age range of the KIP eruption became well constrained through Ar^{40}/Ar^{39} dating techniques (Duncan et al., 1997; Jourdan et al., 2009). The bulk of the magmatism occurred between ~183 Ma and ~178 Ma and finished with the last event, the intrusion of the RRDS in the southernmost Lebombo area at ~174 Ma (Duncan et al., 1997; Jourdan et al., 2005, 2007b, c).

The dating of the rocks of the KIP has yielded a large range in ages compared to other large igneous provinces of the volcanic and intrusive phases, with magmatism lasting for up to 8 Ma and the main magmatism occurring over a 6 Ma time period (Jourdan et al., 2005; 2007b). The zone of magmatism appears to have migrated from a southern Central Karoo centre to a northern Mwenezi located centre with scattered brief magma pulses in isolated areas of southern Africa (Jourdan et al., 2005). Typically CFB provinces are emplaced in a geologically brief time frame with the entire magmatism occurring in ~1 – 2 Ma (Courtillot and Renne, 2003). This time frame is clearly not reflected in the formation of the KIP. Although the ages of the KIP rocks are wide spread from ~184 - ~174 Ma, the magmatism was not consistent in any one region for the entire time period. Jourdan et al. (2007a, c) show that the bulk of the magmatism occurred within a 3 – 4.5 Ma time frame.

The onset of volcanism was heralded by the eruption of the Lesotho basalts and then the primitive lavas in the Mwenezi area at ~183 – 182 Ma. The sills and dykes that intruded the main Karoo Basin are similar in age to the basalts ranging between 183.0 ± 0.5 – 182.3 ± 0.6 Ma (Svensen et al., 2012) however some of the dyke swarms are younger (e.g. ~176 Ma for the UDS) (Riley et al., 2006). The NLDS has the longest period of intrusion between ~182 and 178 Ma, with dyke formation overlapping with the intrusion of the ODS and SLDS. The formation of the NLDS also coincides with the eruption of basalts in Botswana and the Sabie River Formation basalts, the latter being fed by second generation NLDS dykes (Klausen, 2009). At this time (~180 Ma) the Ferrar basalts were erupting in Antarctica, post-dating the bulk of the magmatism in southern Africa but similar in age (Elliot and Fleming, 2000). Whilst the Ferrar basalts were erupting, rhyolitic volcanism was occurring along the Lebombo monocline at ~178 Ma. Smaller dyke swarms then formed post-dating all volcanism in South Africa forming the UDS and RRDS at ~176 Ma and ~174 Ma respectively. Overlapping the intrusion of these dyke

swarms was the intrusion of the Mwenezi Igneous Complex between ~178 – 174 Ma (Marsh et al., 1997).

3.4. Magma flow

The magma flow directions within the major dyke swarms have been extensively investigated in recent decades. Understanding the magma flow dynamics in dyke swarms allows the location of a magma source to be constrained. Dykes that have been sampled belong to the ODS, NLDS, RRDS and UDS (Fig. 3.4). The magma flow direction in the ODS was determined using SPO and AMS techniques and yielded a sense of lateral flow propagating from SE to NW from a source at the Mwenezi (Fig. 3.4) (Aubourg et al., 2008). In the proximal areas (the Thune section) steep magma flow is recorded in the dykes with the flow becoming distinctly lateral in the distal regions towards the Shashe region (Aubourg et al., 2008). Ninety dykes of the NLDS were analysed using AMS and SPO fabrics that correlated and yielded a subtle lateral sense of magma flow from north to south (Fig. 3.4) implying that the Karoo triple junction could possibly be the magma source (Aubourg et al., 2008; Curtis et al., 2008; Hastie et al., 2011a, b; 2014).

The SLDS has not been sampled, thus magma flow directions in this dyke swarm are unknown. In the southern Lebombo region, the RRDS yielded AMS and SPO fabrics that were steeply inclined magma flow in the northern portion of the dyke swarm and lateral flow towards the southern portion (Fig. 3.4) (Hastie et al., 2011a). The petrofabric data were corroborated with field evidence from steeply dipping broken/rotated bridges along certain dyke margins (Hastie et al., 2014). Magma flow patterns in the RRDS imply that the magma source was not from the Karoo triple junction and Hastie et al. (2011a, b) postulate that the magma originated from a central magmatic source analogous to a mid-ocean ridge segment. Limited data have been acquired from the UDS with only three dykes yielding reliable AMS fabrics (Riley et al., 2006). The magma flow was interpreted as being sub-lateral towards the NW implying a possible magma source in the region of the Weddell Sea triple junction (Fig. 3.4) (Riley et al., 2006).

There have been few studies undertaken on the flow directions of sills in the KIP. Ferré et al. (2002) undertook a magma flow study on the Insizwa sill that yielded successful and consistent magnetic fabrics that were used as a proxy for magma flow. The results showed that the sill was fed through uniform flow from a feeder located towards the SE with magma flow in the sill propagating towards the NE (Ferré et al., 2002). A more recent study by Ferré et al. (2015) investigated the magma flow directions in 30 sills in the continental basin of South Africa. This

study used AMS fabrics as a reliable proxy for magma flow as the sill contacts provided sub-horizontal symmetrical fabrics implying magma flow in the sills from the NW to the SE (Ferré et al., 2015). The authors also stated that magma flow proxies obtained from AMS fabrics are reliable when samples mimic magmatic fabrics and are obtained from the upper margin chilled zone and not in the central portion of the intrusion. Ferré et al. (2015) ascribed the formation of the studied sills to a mantle plume but implied that the mantle plume may be located in Namibia and not below the Lesotho lava pile.

3.5. Origin of the Karoo Igneous Province

The structure of the Karoo triple junction is dominated by the three dyke swarms that converge at Mwenezi; the WNW trending ODS, the north-south trending NLDS and RRDS and the ENE trending SLDS (Jourdan et al., 2006). Due to the shape of the convergence of these three dyke swarms (and geochemical and geochemical data), it was believed that Mwenezi was the site of impact for a mantle plume that created the KIP (Burke and Dewey, 1973; White and McKenzie, 1989; Campbell and Griffiths, 1990; Cox, 1992; Ernst and Buchan, 1997; Storey and Kyle, 1997; White, 1997). Mwenezi is located in the Limpopo Belt; an Archaean orogen of poly-

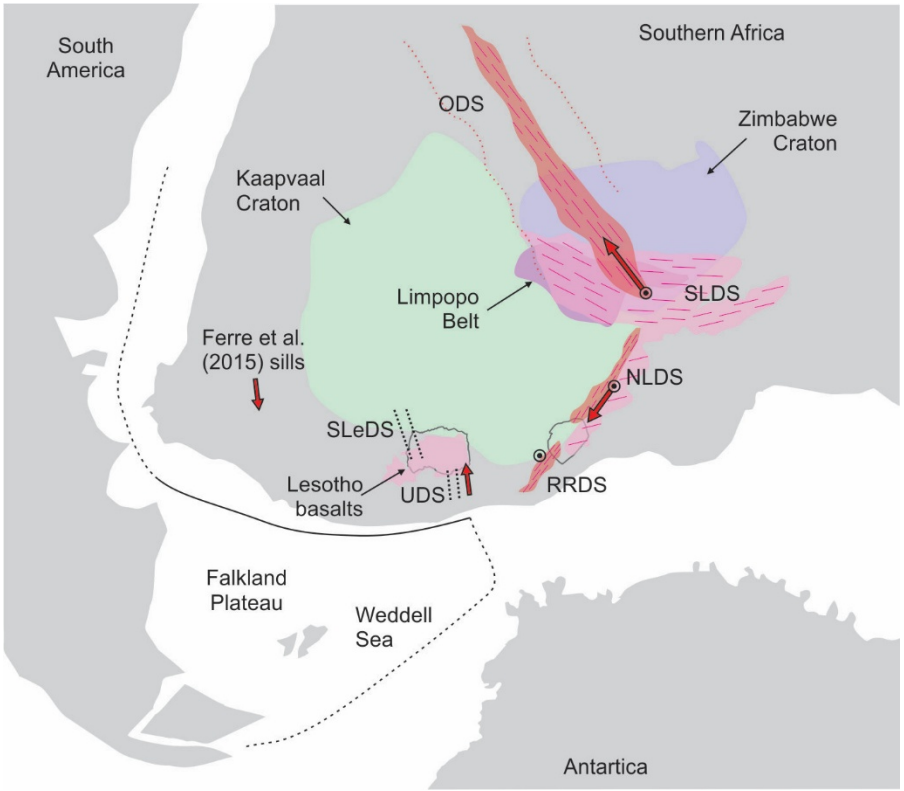

Fig. 3.4. A reconstructed portion of Gondwana corrected for the orientation at ~180 Ma. The Zimbabwe and Kaapvaal Cratons and the Limpopo Belt are highlighted as well as the Lesotho basalts. The magma flow of the dyke swarms for the ODS, SLDS, NLDS and UDS are shown with concentric circles indicating vertical flow and arrows indicating the direction of lateral flow. See in text for references. After Hastie et al. (2014).

metamorphosed rocks. Within the strongly deformed Limpopo belt, a dominant ENE-trending fabric occurs. Subsequent structural events have taken advantage of this fabric including faulting (Watkeys, 2002) and episodes of dyke intrusion (Uken and Watkeys, 1997, Jourdan et al., 2004). An enormous amount of magma was produced that resulted in the KIP; an unusual thermal regime would have had to have been active within the mantle in order to produce this volume in such a short time period (Duncan and Marsh, 2006). There is still no consensus in the scientific community about the petrogenesis of the KIP even though the topic has been widely debated. The most common argument was that the KIP originated through a mantle plume (White and McKenzie, 1989; Campbell and Griffiths, 1990; White, 1997).

A mantle plume is an upwelling jet of anomalously hot mantle that forms along a thermal boundary layer, travels through the mantle and impacts at the base of the lithospheric mantle. One known thermal boundary is the core-mantle interface (or the D″ layer) (Fig. 3.5). As the partially molten mantle rises, adjacent mantle is entrained into the rising plume and forms a mushroom-shaped head comprising hotter plume material and cooler mantle material (Griffiths and Campbell, 1990). Once the plume reaches a limiting thermal boundary layer (here the bas of the lithospheric mantle), the plume and entrained material spreads out laterally and ponds beneath the lithosphere (Campbell and Griffiths, 1990). Along with the volcanism resulting from the impact of a plume, the area directly above the plume head will be domed and uplifted, a process that typically results in the formation of a triple junction (Campbell and Griffiths, 1990).

Since the inception of the plume model, CFBs have been linked to plumes as the mechanism of melt production using the trails that are left behind by the plumes on oceanic crust called “hot-spot tracks” (Richards et al., 1989; White and McKenzie, 1989; Campbell and Griffiths, 1990). A good example of a plume forming a CFB province are the ~133 Ma Paraná-Etendeka flood basalts in Namibia and Brazil (Renne et al., 1992). The Tristan da Cunha plume created these magmas and the hot-spot track on the sea-floor recorded the movement of the diverging plates over the plume head (Richards et al., 1989; Milner et al., 1995; Ewart et al., 2004). Even though plumes may create CFB provinces, the production of CFBs does not automatically imply the presence of a plume.

3.5.1. Evidence for a mantle plume origin

Burke and Dewey (1973) were the first authors to link the shape of the Karoo triple junction to a mantle plume and ascribed this mantle plume to the origin of the KIP (Fig. 3.6 point a),

however they also suggested the KIP may have formed by a mantle plume situated to the NE of the Sabe/Limpopo arm of the Karoo triple junction (Fig. 3.6 point b). White and McKenzie (1989) then used a continental-scale (~2000 km in diameter) mantle plume positioned between the juncture of Antarctica and the Lebombo Mountains to explain the magmatism in the Karoo and Antarctica (Fig. 3.6 point c). Later studies positioned a mantle plume beneath the Karoo triple junction in agreement with Burke and Dewey (1973) as it adequately fitted the formation of the triple junction shape and the concentric eruption of primitive magmas from this area (Campbell and Griffiths, 1990; Storey, 1995). Storey and Kyle (1997) suggested the presence of a "superplume" (>2000 km in diameter) beneath the Falkland Plateau (Fig. 3.6 point d) in a pre-breakup Gondwana assembly as the best way to describe the enormity of the Karoo and Ferrar igneous provinces. Encarnación et al. (1996) linked the Karoo and Ferrar Provinces geochronologically and ascribed the magmatic event to subduction related processes based on the geochemistry and linear extent of the basalts in the provinces.

The magma source of the Ferrar Province has been ascribed to a (sedimentary) contaminated mantle source as a result of subduction (Hergt et al., 1991) and was not thought to be the product of a mantle plume by Cox (1992) due to the enormous linear extent of the igneous province. Elliot and Fleming (2000) subsequently suggested a mantle plume origin for the Ferrar Province placing the magma source below the Weddell Sea Triple Junction (Fig. 3.6 point e). Leat (2008) argued that the Ferrar magmas were emplaced laterally, transported for up to 4000 km from a source in the rift between Antarctica and SE Africa.

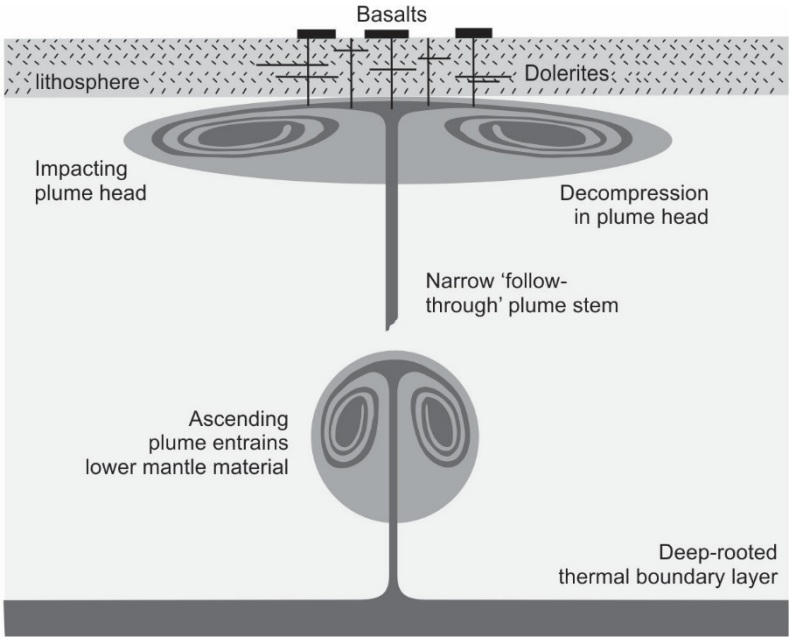

Fig. 3.5. Illustration showing the process of CFB formation through an impacting plume head at the base of the lithospheric mantle. After Richards et al. (1989); Campbell and Griffiths (1990); Griffiths and Campbell (1990).

Evidence for uplift associated with a mantle plume centred at Mwenezi was first noted by Cox (1989) who showed that the river drainage patterns in the northern Lebombo area broke along an arc that indicated the circumference of a mantle plume; the shape of the arc is consistent with the position proposed by White and McKenzie (1989). White (1997) also showed evidence of uplift but over a much larger area, up to 2000 km in diameter, implying the presence of a plume beneath. Even though a large area beneath Mwenezi may have experienced an upwelling of hot, low-density material, uplift in the area is difficult to ascribe only to the effects of a mantle plume as the area experienced a prolonged palaeo-high period in the Permo-Carboniferous (Watkeys, 2002).

Support for the plume model therefore includes (a) the pattern of faulted Karoo rocks in southern Zimbabwe and South Africa that led to Burke and Dewey's (1973) proposal that this region was a triple junction, (b) the volcanic palaeogeography and stratigraphy of the KIP with the older picrite basalts restricted to the Mwenezi district and adjacent regions, while the

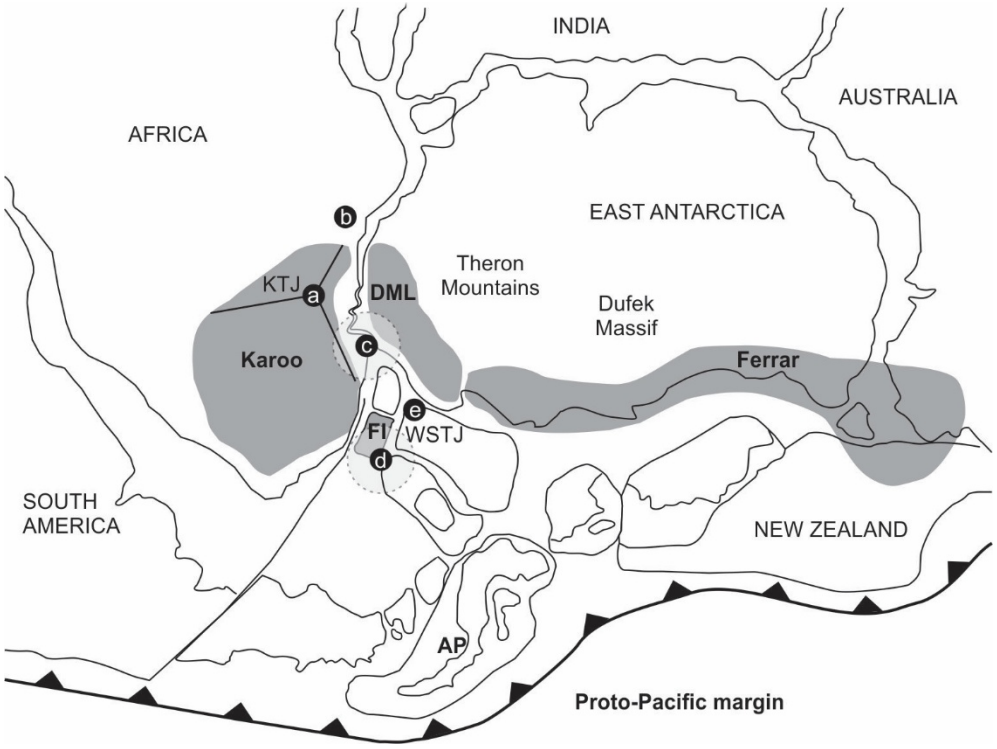

Fig. 3.6. A pre-Gondwana breakup model showing the relative positions of the continents and the extensive Karoo and Ferrar Igneous Provinces. FI: Falkland Island plate, DML: Drenning-Maud Land, AP: Antarctic Peninsula, KTJ: Karoo Triple Junction, WSTJ: Weddell Sea Triple Junction. After Riley et al. (2006) and Hastie (2012). (a) and (b) the possible positions of the Karoo plume suggested by Burke and Dewey (1973). (c) Karoo plume location hypothesized by White and McKenzie (1989). (d) Storey and Kyle (1997) postulated the presence of a "superplume" that produced the magmas of the Karoo and Ferrar Provinces. (e) A possible magma source for the laterally injected Ferrar magmas (Elliot and Fleming, 2000). The light grey circles with dashed outlines indicate the supposed presence of a "megaplume" with a diameter of > 2000 km.

overlying continental tholeiitic flood basalts are more widespread (Erlank, 1984), and (c) the dyke swarms radiating out from Mwenezi, forming the WNW-striking ODS (Reeves, 1978), N-S dykes along the Lebombo monocline (Kattenhorn and Watkeys, 1995; Hastie et al., 2011a) and ENE-dykes of the SLDS (Watkeys, 2002).

3.5.2. Evidence against a mantle plume origin

The position of the Limpopo Belt, between the Archaean Kaapvaal and Zimbabwe Cratons, represents a zone of weakness between areas of relatively undeformed rocks. The well-defined ENE-trending fabric and the structural weaknesses in the Limpopo Belt have been linked to the formation of the KIP and are considered to have controlled the eruption sites of the nephelinites and picrites (Le Gall et al., 2002, 2005; Watkeys, 2002; Jourdan et al., 2004). Magmatism produced by plumes progress from primitive to more evolved compositions through time, it is thus feasible that the low-Ti erupted towards the final stages of magmatism. However, it appears that the occurrence of the low-Ti and high-Ti basalts are controlled by the structure of the lithosphere where low-Ti basalts occur over mobile belts and high-Ti basalts occur over Archaean cratonic material (Cox et al., 1967) and the SCLM controls the melt compositions that are produced (Sweeney and Watkeys, 1990; Sweeney et al., 1994).

The two major types of basalts associated with CFBs produced through melting in the mantle are N-type (normal) MORBs and E-type (enriched) MORBs. N-type MORBs are typically derived through relatively shallow partial melting of the convecting asthenospheric mantle that is chemically depleted. E-type MORBs (and OIBs) are commonly generated by mantle plumes that originated in the deep mantle (Fig. 3.5).

In the KIP only a few OIB-like melts have been identified (Luttinen et al., 1998) and do not comprise the bulk of the magmatic component as would be expected with plume derived CFBs. Even though the primitive melts of the KIP (nephelinites and picrites) could have been derived from an uncontaminated plume-derived melt (White, 1997), the majority of the basalts are low-Ti tholeiites and do not have a typical MORB signature, particularly not an E-type plume-derived MORB (Sweeney et al., 1994). The process of melt production is therefore not as simplistic as the processes by which plume-derived MORBs are formed. The origin of the KIP melts is thus, not easily explained. There are two scenarios that could explain the origin of the KIP basalts by a mantle plume: either the mantle source where the melts were derived was different to the mantle that forms MORB (and OIB) melts or the mantle composition is the same

but undergoes significant alteration through the passage through and/or magma storage in the lithosphere (Duncan and Marsh, 2006).

The duration of the KIP magmatic event spans almost 10 Ma from ~184 – 174 Ma, even with a minimum duration of 6 Ma, the total volume of the KIP (2×10^6 km^3) would be produced at a rate of ~0.3 km^3 per year (Jourdan et al., 2005). Younger CFB provinces yielded production rates several times larger than that of the KIP, such as the Central Atlantic Magmatic Province with a rate of ~1 km^3 per year (Marzoli et al., 1999) and the Kerguelen Plateau at 2.3 km^3 per year (Nicolaysen et al., 2000). Although the magmatism lasted longer than is usual for CFBs, the centre of magma migration from south to north is too rapid to be the preservation of a hot-spot track (Jourdan et al., 2007b). The slow eruptive rates and long duration of the magmatism indicates long-term storage and overprinting of the primitive melt compositions.

Lastly, the dyke swarms of the KIP in the Mwenezi area are inextricably linked geographically with the Karoo Triple Junction, a configuration that is central to the Mwenezi plume hypothesis. Recent studies on these central dyke swarms have however, questioned a mantle plume origin for the KIP showing that the inherent lithospheric architecture of Karoo Triple Junction affected the position and orientation of the ODS and SLDS as evidenced by the presence of Proterozoic dykes in the same orientations (Uken and Watkeys, 1997; Watkeys, 2002; Le Gall et al., 2002, 2005; Jourdan et al., 2004). The Karoo Triple Junction is thus not considered by these authors as a feature of a Jurassic mantle plume event.

3.5.3. Supercontinent incubation model

The large range of compositions, ages and localities of the KIP igneous rocks make it problematic to reconcile the plume model with the formation of the KIP. Another mechanism of formation must therefore be considered; this comes in the form of the "supercontinent incubation model" proposed by Anderson (1994) and refined into the "global mantle warming model" by Coltice et al. (2007).

Anderson (1982) noted the geoid highs overlay areas that had previously experienced significantly volcanism. These zones coincide with areas of continental aggregation and insulation in the mantle, implying that the mantle below these geoid highs would be hotter than normal mantle (Anderson, 1982). Aggregated continents, or supercontinents, form through the continual accretion of smaller bodies onto shields or cratons that subsequently become welded together. The enormity of supercontinents allows the mantle beneath them to be isolated from

subduction, a process that cools the surrounding mantle. Supercontinent formation thus increases the temperature in the mantle directly below (Anderson, 1982). Continuing on in the supercontinent cycle, these large continental masses eventually break apart and the smaller continents move towards cold, down-welling mantle (Anderson, 1982). Anderson (1994) extrapolated this theory into the supercontinent incubation model in order to explain the formation of large igneous provinces without the need for mantle plumes. Anderson (1994) uses this model to argue that CFBs can result from the global reorganisation of tectonic plates where magmas are produced in the mantle beneath supercontinents and transported upwards through weakened portions of the lithosphere, such as extensional zones. In the upper mantle, large-scale reduced velocity regions are attributed to insulated mantle. It follows that this mantle provides magmas to large igneous provinces with production of melts occurring principally in relation to the initial stages of continental extension or breakup (Anderson, 1994).

The first authors to credit the formation of the KIP to mantle insulation were Hawkesworth et al. (1999) where the melts that produced the KIP were derived from mantle insulation (that lasted for ~300 Ma) beneath Gondwana. Upper mantle melts were produced because of this insulation and erupted at points of weakness in the lithosphere, such as along the Limpopo Belt and along the boundary of the Kaapvaal Craton (Hawkesworth et al., 1999). An increase in mantle temperature beneath the supercontinent would have weakened the lithosphere, making it more susceptible to regional tectonics which could have led to the breakup of Gondwana (Hawkesworth et al., 1999).

Coltice et al. (2007) modelled the convection in an internally heated mantle with regards to supercontinent incubation; the study showed that large-scale melting is promoted by continental aggregation without the necessity of a mantle plume. Through the assembly of a supercontinent, the flow wavelength in the underlying mantle increases, making the mantle less efficient at heat removal and in turn increasing the mantle temperature (Grigné et al., 2005). Coltice et al. (2007) show that an increase in mantle temperature of up to 100°C is possible due to thermal incubation. This temperature increase would be sufficient to partially melt the SCLM (Anderson, 1982), especially if assisted by the presence of volatiles (Gallagher and Hawkesworth, 1992) which is highly plausible as the supercontinent formed over the area where subduction occurred when the continents amalgamated (Lowman and Jarvis, 1999).

Coltice et al. (2007) proposed that CFB provinces originate from one of two scenarios: (1) Mantle plume scenarios; these systems are characterised by large melts volumes over short time

periods occurring in a restricted, typically radial, zone. (2) Global-warming scenario; this system forms over a supercontinent characterised by slower rates of eruptions than with the plume model, wide-spread magmatism that is not restricted to a radial zone and cessation of magmatism after the breakup of the supercontinent. Coltice et al. (2009) suggested that the KIP may have formed by melts produced through global mantle melting. Hastie et al. (2014) showed further evidence for a plate tectonic rather than plume origin for the KIP thus agreeing with Hawkesworth et al. (1999) that the Karoo triple junction should no longer be used as evidence for the existence of a mantle plume at Mwenezi.

References

Aarnes, I., Svensen, H., Polteau, S., Planke, S., 2011. Contact metamorphism devolitization of shales in the Karoo Basin, South Africa, and the effects of multiple sill intrusions. Chemical Geology, 281, 181-194.

Allsopp, H.L., Roddick, J.C., 1984. Rb-Sr and $^{40}Ar/^{39}Ar$ age determinations on phlogopite micas from the pre-Lebombo Group Dokolwayo kimberlite pipe. In: Erlank, A.J. (Eds.) Petrogenesis of the volcanic rocks of the Karoo province. Geological Society of South Africa Special Publication, 13, 267-272.

Anderson, D.L., 1982. Hotspots, polar wander, Mesozoic convection, and the geoid. Nature, 297, 391-393.

Anderson, D.L., 1994. Superplumes or supercontinents? Geology, 22, 39-42.

Anderson, E.M., 1951. The dynamics of faulting and dyke formation with applications to Britain. Edinburgh, Oliver and Boyd, 206 pp.

Arbaret, L., Fernández, A., Ježek, J., Ildefonse, B., Launeau, P., Diot, H., 2000. Analogue and numerical modelling of shape fabrics: application to strain and flow determination in magmas. Transactions of the Royal Society of Edinburgh: Earth Sciences, 90, 97-109.

Archanjo, C.J., Launeau, P., 2004. Magma flow inferred from preferred orientations of plagioclase of the Rio Ceará-Mirim dyke swarm (NE Brazil) and its AMS significance. In: Martín-Hernández, F., Luneberg, C.M., Aubourg, C. and Jackson, M. (Eds.) Magnetic Fabric: Methods and Applications. Geological Society of London, Special Publication, 238, 285-298.

Archanjo, C.J., Launeau, P., Bouchez, J.L., 1995. Magnetic fabric vs. magnetite and biotite shape fabrics of the magnetite-bearing granite pluton of Gameleiras (Northeast Brazil). Physics of the Earth and Planet Interiors, 89, 63-75.

Archanjo, C.J., Campanha, G.A.C., Salazar, C.A., Launeau, P., 2012. Using AMS combined with mineral shape preferred orientation to understand the emplacement fabrics of the Apiaí gabbro-norite (Ribeira Belt, SE Brazil). International Journal of Science, 101, 731-745.

Armstrong, R.A., Bristow, J.W., Cox, K.G., 1984. The Rooi Rand dyke swarm, southern Lebombo. In: Erlank, A.J. (Eds.) Petrogenesis of the volcanic rocks of the Karoo province. Geological Society of South Africa Special Publication, 13, 77-86.

Arndt, N.T., Czamanske, G.K., Wooden, J.L., Fedorenko, V.A., 1993. Mantle and crustal contributions to continental flood volcanism. In: Wortel, M.J.R., Hansen, U., Sabadini, R. (Eds.), Relationships between Mantle Processes and Geological Processes at or near the Earth's Surface. Tectonophysics, 223, 39–52.

Aubourg, C., Tshoso, G., Le Gall, B., Bertrand, H., Tiercelin, J.-J., Kampunzu, A.B., Dyment, J., Modisi, M., 2008. Magma flow revealed by magnetic fabric in the Okavango giant dyke swarm, Karoo igneous province, northern Botswana. Journal of Volcanology and Geothermal Research, 170, 247-261.

Baer, G., 1995. Fracture propagation and magma flow in segmented dykes: field evidence and fabric analysis, Makhtesh Ramon, Israel. In: Baer, G. and Heinmann, A.A. (Eds.) Physics and Chemistry of Dykes. Balkema, Rotterdam, 125-140.

Baer, G., Reches, Z., 1987. Flow patterns of magma in dikes, Makhtesh Ramon, Israel. Geology, 15, 569-572.

Barnett, Z.A., Gudmundsson, A., 2014. Numerical modelling of dykes deflected into sills to form a magma chamber, Journal of Volcanology and Geothermal Research, 281, 1-11.

Bell, B.R., Butcher, H., 2002. On the emplacement of sill complexes: evidence from the Faroe-Shetland Basin. In: Jolly, D.W., Bell, B., (Eds.) The North Atlantic Igneous Province: Stratigraphy, tectonic, volcanic and magmatic processes. Geological Society of London Special Publication, 197, 307-329.

Benn, K., Allard, B., 1989. Preferred mineral orientations related to magmatic flow in ophiolite layered gabbros. Journal of Petrology, 30, 925-946.

Bensus, M.J. 1966. Propriétés magnétiques de la pyrrhotine naturelle. Unpublished PhD Thesis, University of Strasbourg, 78 pp.

Bensus, M.J. & Meyer, A.J. 1964. Nouvelles données expérimentales sue le magnétisme de la pyrrhotine naturelle. Proceedings of the International Conference on Magnetism, Nottingham, 507-511.

Bilardello, D., Jackson, M., 2013. What do the Mumpsies do? The IRM Quarterly, 23.

Blanchard, J.-P., Boyer, P., Gagny, C., 1979. Un nouveau critere de sens de mise en place dans une caisse filonienne: Le “pincement” des mineraux aux epontes: Orientation des minéraux dans un magma en écoulement. Tectonohysics, 53, 1-25.

Blumenfeld, P., Bouchez, J.L., 1988. Shear criteria in granite and migmatite deformed in the magmatic and solid state. Journal of Structural Geology, 10, 361-372.

Borradaile, G.J., Henry, B., 1997. Tectonic applications of magnetic susceptibility and its anisotropy. Earth Science Reviews, 42, 49-93.

Borradaile, G.J., Jackson, M., 2004. Anisotropy of magnetic susceptibility (AMS): magnetic petrofabric of deformed rocks. In: Martín-Hernández, F., Luneberg, C.M., Aubourg, C. and Jackson, M. (Eds.), Magnetic Fabric: Methods and Applications. Geological Society of London, Special Publication, 238, 1-7.

Borradaile, G.J., Lagroix, F., 2001. Magnetic fabrics reveal upper mantle flow fabrics in the Troodos Ophiolite Complex. Cyprus Journal of Structural Geology, 23, 1299-1317.

Bristow, J.W., 1982. Geology and structure of Karoo volcanic and sedimentary rocks of the northern and central Lebombo. Transactions of the Geological Society of South Africa, 85, 167-178.

Bristow, J.W., 1984. Nephelinites of the north Lebombo and south-east Zimbabwe. In: Erlank, A.J. (Eds.) Petrogenesis of the volcanic rocks of the Karoo province. Geological Society of South Africa Special Publication, 13, 87-104.

Bristow, J. W., K. G. Cox, 1984. Volcanic rocks of the Lebombo-Nuanetsi-Sabi zone: classification and nomenclature. In: Erlank, A.J. (Eds.) Petrogenesis of the volcanic rocks of the Karoo province. Geological Society of South Africa Special Publication, 13, 69-75.

Bristow, J.W., Saggerson, E.P., 1983. A general account of Karoo vulcanicity in southern Africa. Geologische Rundschau, 72, 1015-1059.

Bristow, J.W., Allsopp, H.L., Erlank, A.J., Marsh, J.S., Armstrong, R.A, 1984. Strontium isotope characterization of Karoo volcanic rocks. In: Erlank, A.J. (Eds.) Petrogenesis of the volcanic rocks of the Karoo province. Geological Society of South Africa Special Publication, 13, 295-329.

Balsley, J.R., Buddington, A.F., 1960. Magnetic susceptibility anisotropy and fabric of some Adirondack granites and orthogneisses. American Journal of Science, 258, 6-20.

Burger, C.A.J., Hodgson, F.D.I., Van der Linde, P.J., 1981. Hidroliese eienskappe van akwifere in die Suid-Vrystaat. Die ontwikkeling en evaluering van tegnieke vir die bepaling van die ontginninspotensiaal van groundwaterbronne in die Suid-Vrystaat en in Noord-Kaapland. Institute for Groundwater Studies, University of the Orange Free State, Bloemfontein, South Africa, 2: 115.

Burgess, S.D., Bowring, S.A., Fleming, T.H., Elliot, D.H., 2015. High-precision geochronology links the Ferrar large igneous province with early-Jurassic ocean anoxia and biotic crisis. Earth and Planetary Science Letters, 415, 90-99.

Burke, K., Dewey, J.F. 1973. Plume-generated triple junctions: key indicators in applying plate tectonics to old rocks. Journal of Geology, 81, 406-433.

Bussel, M.A., 1989. A simple method for the determination of the dilation direction of intrusive sheets. Journal of Structural Geology, 81, 406-433.

Butler, R.F., 1992. Paleomagnetism: magnetic domains to geologic terranes. Blackwell Scientific Publications, Boston, 319 pp.

Callot, J.-P., Guichet, X., 2003. Rock texture and magnetic lineation in dykes: a simple analytical model. Tectonophysics, 366, 207-222.

Callot, J.-P., Geoffroy, L., Aubourg, C., Pozzi, J.P., Mege, D., 2001. Magma flow directions of shallow dykes from the East Greenland volcanic margin inferred from magnetic fabric studies. Tectonophysics, 335, 313-329.

Cañón-Tapia, E., 2004. Anisotropy of magnetic susceptibility of lava flows and dykes: a historical account. In: Martín-Hernández, F., Luneberg, C.M., Aubourg, C. and Jackson, M. (Eds.) Magnetic Fabric: Methods and Applications. Geological Society of London, Special Publication, 238, 1-7.

Cañón-Tapia, E., Chávez-Álvarez, M.J., 2004. Theoretical aspects of particle movement in flowing magma: implications for the anisotropy of magnetic susceptibility in dykes. In: Martín-Hernández, F., Luneberg, C.M., Aubourg, C. and Jackson, M. (Eds.) Magnetic Fabric: Methods and Applications. Geological Society of London, Special Publication, 238, 227-249.

Cañón-Tapia, E., Walker, G.P.L., Herrero-Bervera, E., 1995. Magnetic fabric and flow direction in basaltic Pahoehoe lava of Xitle Volcano, Mexico. Journal of Volcanology and Geothermal Research, 65, 249-263.

Cañón-Tapia, E., Walker, G.P.L., Herrero-Bervera, E., 1996. The internal structure of lavas: insights from AMS measurements I: near vent 'a'ā. Journal of Volcanology and Geothermal Research, 70, 254-264.

Cañón-Tapia, E., Walker, G.P.L., Herrero-Bervera, E., 1997. The internal structure of lava flows – insights from AMS measurements II: Hawaiian pahoehoe, toothpaste lava and 'a'ā. Journal of Volcanology and Geothermal Research, 76, 19-46.

Campbell, I.H., Griffiths, R.W. 1990. Implications of mantle plume structure for the evolution of flood basalts. Earth and Planetary Science Letters, 99, 79-93.

Cartwright, J., Hansen, D.M., 2006. Magma transport through the crust via interconnected sill complexes. Geology, 19, 929-932.

Cas, R.A.F., Wright, J.V., 1987. Volcanic Successions: Modern and Ancient. Allen and Unwin, London, 487 pp.

Catuneanu, O., Hancox, P.J., Rubidge, B.S., 1998. Reciprocal flexural behaviour and contrasting stratigraphies: a new basin development model for the Karoo retroarc foreland system, South Africa. Basin Research, 10, 417-439.

Chawla, K.K., 1998. Composite Materials: Science and Engineering, 2nd ed. Springer, Berlin. 483 pp.

Chevallier, L., Woodford, A., 1999. Morpho-tectonics and mechanism of emplacement of the dolerite rings and sills of the western Karoo, South Africa. South African Journal of Geology, 102, 48-54.

Cleverly, R.W., Bristow, J.W., 1979. Revised volcanic stratigraphy of the Lebombo monocline. Transactions of the Geological Society of South Africa, 82.27, 227-230.

Cleverly, R.W., Betton, P.J., Bristow, J.W., 1984. Geochemistry and petrogenesis of the Lebombo rhyolites. In: Erlank, A.J. (Eds.) Petrogenesis of the volcanic rocks of the Karoo province. Geological Society of South Africa Special Publication, 13, 171-195.

Coltice, N., Phillips, B.R., Bertrand, H., Ricard, Y., Rey, P., 2007. Global warming of the mantle at the origin of flood basalts over supercontinents. Geology, 35, 391-394.

Coltice, N., Bertrand, H., Rey, P., Jourdan, F., Phillips. B.R. and Ricard, Y. 2009. Global warming of the mantle beneath continents back to the Archaean. Gondwana Research, 15, 254-266.

Cook, J., Gordon, J.E., Evans, C.C., Marsh, D.M., 1964. A mechanism for the control of crack propagation in all-brittle systems. Proceedings of the Royal Society of London, A282, 508-520.

Corry, C.E., 1988. Laccoliths: Mechanics of Emplacement and Growth. Geological Society of America Special Paper, 220.

Courtillot, V.E., Renne, P.R., 2003. On the ages of flood basalt events. Comptes Rendus Geoscience, 113-140.

Courtillot, V., Jaupart, C., Manighetti, I., Tapponnier, P., Besse, J., 1999. On casual links between flood basalts and continental breakup. Earth and Planetary Science Letters, 166, 177-195.

Cox, K.G., 1989. The role of mantle plumes in the development of continental drainage patterns. Nature, 342, 873-877.

Cox, K.G. 1992. Karoo igneous activity, and the early stages of the break-up of Gondwanaland. In: Storey, B.C., Alabaster, T., and Pankhurst, R.J. (eds), Magmatism and the Causes of Continental Break-up. Geological Society of London Special Publication, 68, 37-148.

Cox, K.G., Bristow, J.W., 1984. The Sabie river basalt Formation of the Lebombo monocline and south-east Zimbabwe. In: Erlank, A.J. (Eds.) Petrogenesis of the volcanic rocks of the Karoo province. Geological Society of South Africa Special Publication, 13, 125-147.

Cox, K.G., Johnson, R.L., Monkman, L.J., Stillman, C., Vail, J., Wood, D.N., 1965. The geology of the Nuanetsi igneous province. Philosophical Transactions of the Royal Society, London, A257, 71-218.

Cox, K.G., MacDonald, R., Hornung, G., 1967. Geochemical and petrographic provinces in the Karroo basalts of southern Africa. American Mineralogist, 52, 1451-1474.

Cruden, A.R., 1990. Flow and fabric development during the diapiric rise of magma. Journal of Geology, 98, 681-698.

Curtis, M.L., Riley, T.R., Owens, W.H., Leat, P.T., Duncan, R.A., 2008. The form, distribution and anisotropy of magnetic susceptibility of Jurassic dykes in H.U. Sverdrupfjella, Drenning Maud Land, Antarctica. Implications for dyke swarm emplacement. Journal of Structural Geology, 30, 1429-1447.

Day, R.M., Fuller, M. & Schmidt, V.A. 1977. Hysteresis properties of titanomagnetites: grain size and composition dependence. Physics of the Earth and Planetary Interiors, 13, 260-267.

Delaney, P.T., 1982. Rapid intrusion of magma into wet rock: groundwater flow due to pore pressure increases. Journal of Geophysical Research, 87, 7739-7756.

Delaney, P.T., Pollard, D.D., Ziony, J.I., McKee, E.H., 1986. Field relations between dikes and joints: emplacement processes and paleostress analysis. Journal of Geophysical Research, 91, 4920-4938.

Du Toit, A.L., 1905. Geological Survey of Glen Gray and parts of Queenstown and Woodehouse, including the Indwe area. Annual Report of the Geological Commission of the Cape of Good Hope, 10, 95-140.

Du Toit, A.L., 1920. The Karoo dolerites of South Africa: a study of hypabyssal injection. Transactions of the Royal Society of South Africa, 18, 1-42.

Du Toit, A.L., 1929. The volcanic belt of the Lebombo: a region of tension. Transactions of the Royal Society of South Africa, 18, 189-218.

Duncan, A.R., 1987. The Karoo igneous province – a problem area for inferring tectonic setting from basalt geochemistry. Journal of Volcanology and Geothermal Research, 32, 13-34.

Duncan, A.R., Marsh, J.S., 2006. The Karoo Igneous Province. In: Johnson, M.R., Anhauesser, C.R., Thomas, R.J. (Eds) The Geology of South Africa. Geological Society of South Africa, 501-520.

Duncan, A.R., Erlank, A.J., Marsh, J.S., 1984. Regional geochemistry of Karoo igneous province. In: Erlank, A.J. (Eds.) Petrogenesis of the volcanic rocks of the Karoo province. Geological Society of South Africa Special Publication, 13, 355-388.

Duncan, R.A., Hooper, P.R., Rehacek, J., Marsh, J.S., Duncan, A.R., 1997. The timing and duration of the Karoo igneous event, southern Gondwanaland. Journal of Geophysical Research, 102, 18127-18138.

Dunlop, D.J., 2002. Theory and application of the Day plot (M_{rs}/M_s versus H_{cr}/H_c): 2. Application to data for rocks, sediments and soils. Journal of Geophysical Research, 107(B3), 2057, doi:10.1029/2001JB000487.

Dunlop, D.J., Özdemir, Ö., 1997. Rock Magnetism: Fundamentals and frontiers. Cambridge Univeristy Press, United Kingdom, 573 pp.

Eales, H.V., Marsh, J.S., Cox, K.G., 1984. The Karoo igneous province: An Introduction. In: Erlank, A.J. (Eds.) Petrogenesis of the volcanic rocks of the Karoo province. Geological Society of South Africa Special Publication, 13, 1-26.

Elburg, M., Goldberg, A., 2000. Age and geochemistry of Karoo dolerite dykes from northeast Botswana. Journal of African Earth Sciences, 31, 153-161.

Ellam, R.M., 2006. New constraints on the petrogenesis of the Nanetsi picrate basalts from Pb and Hf isotope data. Earth and Planetary Science Letters, 245, 153-161.

Ellam, R.M., Cox, K.G., 1989. A Proterozoic lithosphere source for Karoo magmatism: evidence from the Nuanetsi picrites. Earth and Planetary Science Letters, 92, 207-218.

Ellam, R.M., Cox, K.G., 1991. An interpretation of Karoo picrate basalts in terms of interaction between asthenospheric magmas and mantle lithosphere. Earth and Planetary Science Letters, 105, 330-342.

Ellam, R.M., Carlson, R.W., Shirley, S.B., 1992. Evidence from Re-Os isotopes for plume-lithosphere mixing in Karoo flood basalt genesis. Nature, 359, 718-721.

Elliot, D.H., 1975. Tectonics of Antarctica: a review. American Journal of Science, 275, 45-106.

Elliot, D.H., Fleming, 2000. Weddell triple junction: The principle focus of Ferrar and Karoo magmatism during initial breakup of Gondwana. Geology, 28, 539-542.

Ellwood, B.B., 1978. Flow and emplacement direction determined for selected basaltic bodies using magnetic susceptibility anisotropy measurements. Earth and Planetary Science Letters, 41, 1270-1273.

Encarnación, J., Fleming, T.H., Elliot, D.H., Eales, H.V., 1996. Synchronous emplacement of Ferrar and Karoo dolerites and the early breakup of Gondwana, 24, 535-538.

Erlank, A.J., 1984. Petrogenesis of the volcanic rocks of the Karoo province. Geological Society of South Africa Special Publication, 13, 395 pp.

Ernst, R.E., Baragar, W.R.A., 1992. Evidence from magnetic fabric for the flow pattern of magma in the Mackenzie giant radiating dyke swarm. Nature, 356, 511-513.

Ernst, R.E., Buchan, K.L., 1997. Giant Radiating Swarms: Their Use in Identifying Pre-Mesozoic Large Igneous Provinces and Mantle Plumes. Geophysical Monographs, 100, 297-333.

Ewart. A., Marsh, J.S., Milner, S.C., Duncan, A.R., Kamber, B.S., Armstrong, R.A., 2004. Petrology and Geochemistry of Early Cretaceous Bimodal Continental Flood Volcanism of the NW Etendeka, Namibia. Part 1: Introduction, Mafic Lavas and Re-evaluation of Mantle Source Components. Journal of Petrology, 45, 59-105.

Fernández, A.N., Gasquet, D.R., 1994. Relative reheological evolution of chemical contrasted coeval magmas: example of the Tichka plutonic complex (Morocco). Contribution in Mineralogy and Petrology, 116, 316-326.

Ferré, E.C., Bordarier, C., Marsh, J.S., 2002. Magma flow inferred from AMS fabrics in a layered mafic sill, Insizwa, South Africa. Tectonophysics, 354, 1-23.

Ferré, E., Geissman, J., Maes, S., Gillim, A., Marsh, J., 2015. Magma dynamics above the Karoo Plume, South Africa. Geophysical Research Abstracts, 17, EGU General Assembly, EGU2015-7077.

Fink, J.H., Fletcher, R.C., 1978. Ropy pahoehoe: Surface folding of a viscous fluid. Journal of Volcanology and Geothermal Research, 4, 151-170.

Fitch, F.J., Miller, J.A., 1984. Dating Karoo igneous rocks by the conventional K-Ar and $^{40}Ar/^{39}Ar$ age spectrum methods. In: Erlank, A.J. (Eds.) Petrogenesis of the volcanic rocks of the Karoo province. Geological Society of South Africa Special Publication, 13, 247-266.

Fleming, T.H., Poland, K.A., Elliot, D.H., 1995. Isotopic and chemical constraints on the crustal evolution and source signature of Ferrar magmas, north Victoria Land, Antarctica. Contributions to Mineralogy and Petrology, 121, 217-236.

Francis, E.H., 1982. Magma and sediments–I Emplacement mechanism of the late Carboniferous tholeiite sills in northern Britain. Journal of the Geological Society of London, 139, 1-20.

Frankel, J.J. 1969. The distribution and origin of the Effingham rock type, a dolerite derivative of intermediate composition, in Natal and Zululand, South Africa. Geological Society of America Memoir, 115, 149-173.

Gaillot, P., de Saint Blanquet, M., Bouchez, J.-L., 2006. Effects of magnetic interactions in anisotropy of magnetic susceptibility: Models, experiments and implications for igneous rock fabrics acquisition. Tectonophysics, 418, 3-19.

Gallagher, K., Hawkesworth, K., 1992. Dehydration melting and the generation of continental flood basalts. Nature, 358, 57-59.

Gay, N.C. 1966. Orientation of mineral lineation along the flow direction in rocks: A discussion. Tectonophysics, 3, 559-564.

Gay, N.C. 1967. Pure shear and simple shear deformation of inhomogeneous viscous fluids. 1. Theory. Tectonophysics, 5, 211-234.

Geoffroy, L., Callot, J.P., Aubourg, C., Moreira, M., 2002. Is the common use of AMS in mafic dykes scientifically correct? Terra Nova, 14, 183–190.

Gil-Imaz, A., Pocoví, A., Lago, M., Galé, C., Arranz, E., Rillo, C., Guerrero, E., 2006. Magma flow and thermal contraction fabric in tabular intrusions inferred from AMS analysis. A case study in a late-Variscan folded sill of the Albarracın Massif (southeastern Iberian Chain, Spain). Journal of Structural Geology, 28, 641–653.

Goulty, N., Schofield, 2008. Implications of simple flexure theory for the formation of saucer-shaped sills. Journal of Structural Geology, 30, 812-817.

Graham, J.W., 1954. Magnetic susceptibility anisotropy, an unexploited petrofabric element. Bulletin of the Geological Society of America, 65, 1257-1258.

Gretener, P.E., 1969. On the mechanics of the intrusion of sills. Canadian Journal of Earth Sciences, 6, 1415.

Griffith, A.A., 1924. The theory of rupture. In: Biezeno, C.B., Burgers, J.M., (Eds.), Proceedings of the First International Congress on Applied Mechanics. J. Waltman, Delft, 55-63.

Griffiths, R.W., Campbell, I.H., 1990. Stirring and structure in starting mantle plumes. Earth and Planetary Science Letters, 99, 66-78.

Grigné, C., Labrosse, S., Tacklay, P.J., 2005. Convective heat transfer as a function of wavelength: Implications for the cooling of the Earth. Journal of Geophysical Research, 110, B03409, doi:10.1029/2004JB003376.

Gudmundsson, A., 2000. Dynamics of volcanic systems in Iceland: example of tectonism and volcanism at juxtaposed hot spot and mid-ocean ridge system. Annual Review of Earth and Planetary Science, 28, 107-140.

Gudmundsson, A., 2003. Surface stresses associated with arrested dykes in rift zones. Bulletin of Volcanology, 65, 606-619.

Gugmundsson, A., 2006. How local stresses control magma-chamber ruptures, dyke injections, and eruptions in composite volcanoes. Earth Science Reviews, 79, 1-31.

Gudmundson, A., 2011. Deflection of dykes into sills at discontinuities and magma-chamber formation. Tectonophysics, 500, 50-64.

Gudmundsson, A., Philipp, S.L., 2006. How local stress fields prevent volcanic eruptions. Journal of Volcanology and Geothermal Research, 158, 257-268.

Hansen, D.M., Cartwright, J., 2006. Saucer-shaped sill and lobate morphology revealed by 3D seismic data: implications for resolving a shallow-level sill emplacement mechanism. Journal of the Geological Society, 163, 509-523.

Hansen, D.M., Cartwright, J.A., Thomas, D., 2004. 3D seismic analysis of the geometry of igneous sills and sill junction relationships. In: Davies, R.J., Cartwright, J.A., Stewart, S.A., Lappin, M., Underhill, J.R. (Eds.), 3D Seismic Technology: Application to the Exploration of Sedimentary Basins. Geological Society of London, Memoirs, 29, 199-208.

Hargraves, R.B., Johnson, D., Chan, C.Y., 1991. Distribution anisotropy: the cause of AMS in igneous rocks? Geophysical Research Letters, 18, 2193-2193.

Hargraves, R.B., Rehacek, J., Hooper, P.R., 1997. Palaeomagnetism of the Karoo igneous rocks in Southern Africa. South African Journal of Geology, 100, 195-212.

Harrison, R.J. & Feinberg, J.M., 2008. FORCinel: An improved algorithm for calculating first-order reversal curve distributions using locally weighted regression smoothing. Geochemistry, Geophysics, Geosystems, 9, Q05016, doi: 10/1029/2008GC001987.

Hastie, WW., 2012. Rock Farbic Study of the Northern Lebombo and Rooi Rand Dyke Swarms – Regional and Local Implications. Unpublished PhD thesis, University of KwaZulu-Natal, 370 pp.

Hastie, W.W., Aubourg, C., Watkeys, M.K., 2011a. Significance of magnetic and petrofabric in Karoo-feeder dykes, northern Lebombo. Tectonophysics, 513, 96-111.

Hastie, W.W., Aubourg, C., Watkeys, M.K., 2011b. When an inverse fabric is not inverse: an integrated AMS-SPO study in MORB-like dykes. Terra Nova, 23, 49-55.

Hastie, W.W., Watkeys, M.K., Aubourg, C., 2013. Characterisation of grain-size, shape and orientation of plagioclase in the Rooi Rand dyke swarm, South Africa. Tectonophysics, 583, 145-157.

Hastie, W.W., Watkeys, M.K., Aubourg, C., 2014. Magma flow in dyke swarms of the Karoo LIP: Implications for the mantle plume hypothesis. Gondwana Research, 25, 736-755.

Hawkesworth, C.J., Marsh, J.S., Duncan, A.R., Erlank, A.J., Norry, M.J., 1984. The role of continental lithosphere in the generation of the Karoo volcanic rocks: evidence from combined Nd- and Sr-isotope studies. In: Erlank, A.J. (Eds.) Petrogenesis of the volcanic rocks of the Karoo province. Geological Society of South Africa Special Publication, 13, 341-354.

Hawkesworth, C.J., Kelley, S., Turner, S., Le Roex, A., Storey B.C., 1999. Mantle processes during Gondwana break-up and dispersal. Journal of African Earth Sciences, 28, 239-261.

He, M.Y., Hutchinson, J.W., 1989. Crack deflection at an interface between dissimilar elastic materials. International Journal of Solids and Structures, 25, 1053-1067.

He, M.Y., Evans, A.G., Hutchinson, J.W., 1994. Crack deflection at an interface between dissimilar elastic materials: Roles of residual stresses. International Journal of Solids and Structures, 31, 3443-3455.

Heimann, A., Fleming, T.H., Elliot, D.H., Foland, K.A., 1994. A short interval of Jurassic continental flood basalt volcanism in Antarctica as demonstrated by $^{40}Ar/^{39}Ar$ geochronology. Earth and Planetary Science Letters, 121, 19-41.

Hergt, J.M., Peate, D.W., Hawkesworth, C.J., 1991. The petrogenesis of Mesozoic Gondwana low-Ti flood basalts. Earth and Planetary Science Letters, 105, 134-148.

Herrero-Bervera, E., Cañón-Tapia, E., Walker, G.P.L., Tanaka, H., 2001. Magnetic fabric study and inferred flow directions of lavas of the Old Pali Road, Oáhu, Hawaii. Journal of Volcanology and Geothermal Research, 118, 161-171.

Hogan, J.P., 1993. Monomineralic Glomerocrysts: Textural Evidence for Mineral Resorption during Crystallization of Igneous Rocks. The Journal of Geology, 101, 531-540.

Honnorez, J., Kirst, P., 1975. Submarine basaltic volcanism: morphometric parameters for discriminating hyaloclastites from hyalotuffs. Bulletin of Volcanology, 39, 1-25.

Horsman, E., Tikoff, B., Morgan S., 2005. Emplacement-related fabric and multiple sheets in the Maiden Creek sill, Henry Mountains, Utah, USA. Journal of Structural Geology, 27, 1426-1444.

Horst, A.J., Varga, R.J., Gee, J.S., Karson, J.A., 2014. Diverse magma flow directions during construction of sheeted dike complexes at fast- to superfast- spreading centres. Earth and Planetary Science Letters, 408, 119-131.

Hrouda, F., 1982. Magnetic anisotropy and its application in geology and geophysics. Geophysical Survey, 5, 37-82.

Hrouda, F., Táborská, S., Schulmann, K., Ježek, J., Dolejš, D., 1999. Magnetic fabric an rheology of co-mingled magmas in the Nasavrky Plutonic Complex (E. Bohemia): implications for intrusive strain regime and emplacement mechanism. Tectonophysics, 307, 93-111.

Hull, D., Clyne, T.W., 1996. An Introduction to Composite Material, 2nd ed. Cambridge University Press, Cambridge. 326 pp.

Hutchinson, J.W., 1996. Stresses and failure modes in thin films and multilayers. Notes for a DCamm Course. Technical University of Denmark, Lyngby, 45 pp.

Hutton, D.H.W., 2009. Insights into magmatism in volcanic margins: bridge structures and a new mechanism of basic sill emplacement – Theron Mountains, Antarctica. Petroleum Geoscience, 15, 269-278.

Jamtveit, B., Svensen, H., Podladchikov, Y.Y., Planke, S., 2004. Hydrothermal vent complexes associated with sill intrusions in sedimentary basins. In: Breitkreuz, C., Petford, N. (Eds.) Physical Geology of High-Level Magmatic Systems. Geological Society of London, Special Publication, 234, 233-241.

Jelinek, V., 1978. Statistical processing of anisotropy of magnetic susceptibility measured on a group of specimens and its applications. Studies in Geophysics and Geodynamics, 22, 50-62.

Jelinek, V. 1981. Characterisation of the magnetic fabric of rocks. Tectonophysics, 79, 63-67.

Jourdan, F., Féraud, G., Bertrand, H., Kampunzu, A.B., Tshoso, G., Le Gall, B., Tiercelin, J.-J., Capiez, P., 2004. The Karoo triple junction questioned: evidence from the Jurassic and Proterozoic $^{40}Ar/^{39}Ar$ ages and geochemistry of the giant Okavango dyke swarm (Botswana). Earth and Planetary Science Letters, 222, 989-1006.

Jourdan, F., Féraud, G., Bertrand, H., Kampunzu, A.B., Tshoso, G., Watkeys, M.K., Le Gall., B., 2005. Karoo large igneous province: Brevity, origin and relation to mass extinction question by new $^{40}Ar/^{39}Ar$ age data. Geology, 33, 745-748.

Jourdan, F., Féraud, G., Bertrand, H., Watkeys, M.K., Kampunzu, A.B., Le Gall, B. 2006. Basement control on dyke distribution in Large Igneous Provinces: Case study of the Karoo triple junction. Earth and Planetary Science Letters, 241, 307-322.

Jourdan, F., Bertrand, H., Sharer, U., Blichert-Toft, J., Féraud, G., Kampunzu, A.B., 2007a. Major and trace element and Sr, Nd, Hf, and Pb isotope compositions of the Karoo igneous province, Botswana-Zimbabwe: lithosphere vs. mantle plume contribution. Journal of Petrology, 48, 1043-1077.

Jourdan, F., Féraud, G., Bertrand, H., Watkeys, M.K., 2007b. From flood basalts to the inception of oceanization: Example from the $^{40}Ar/^{39}Ar$ high-resolution picture of the Karoo large igneous province. Geochemistry, Geophysics, Geosystems, 8, 989-1006.

Jourdan, F., Féraud, G., Bertrand, H., Watkeys, M.K., Renne, P.R. 2007c. Distinct brief major events in the Karoo large igneous province clarified by new $^{40}Ar/^{39}Ar$ ages on the Lesotho basalts. Lithos, 98, 195-209.

Jourdan, F., Féraud, G., Bertrand, H., Watkeys, M.K., Renne, P.R., 2008. $^{40}Ar/^{39}Ar$ ages of the sill complex of the Karoo large igneous province: implications for the Pliensbachian-Toarcian climate change. Geochem. Geophys. Geosys. 9, Q06009, doi:10.1029/2008GC001994.

Jourdan, F., Bertrand, H., Féraud, G., Le Gall, B., Watkeys, M.K. 2009. Lithospheric mantle evolution monitored by overlapping large igneous provinces: Case study in southern Africa. Lithos, 107, 257-268.

Kattenhorn, S.A. 1994. Mechanisms of sill and dyke intrusion. MSc thesis, University of Natal (Durban), South Africa.

Kattenhorn, S.A., Watkeys, M.K., 1995. Blunt-ended dyke segments. Journal of Structural Geology, 17, 1535-1542.

Kavanagh, J.L., Menand, T., Sparks, S.J., 2006. An experimental investigation of sill formation and propagation in layered elastic media. Earth and Planetary Science Letters, 245, 799-813.

Khan, M.A., 1962. Anisotropy of magnetic susceptibility of some igneous and metamorphic rocks. Journal of Geophysical Research, 67, 2873-2885.

Klausen, M.B. 2009. The Lebombo monocline and associated feeder dyke swarm: diagnostic of a successful and highly volcanic rifted margin? Tectonophysics, 468, 42-62.

Knight, M.D., Walker, G.P.L., 1988. Magma flow directions in dikes of the Koolau Complex, Oahu, determined from magnetic fabric studies. Journal of Geophysical Research, 93, 4301-4319.

Kokelaar, B.P., 1982. Fluidisation of wet sediments during the emplacement and cooling of various igneous bodies. Journal of the Geological Society of London, 139, 21-33.

Krása, D., Herrero-Bervera, E., 2005. Alteration induced changes of magnetic fabric as exemplified by dykes of the Koolau volcanic range. Earth and Planetary Science Letters, 240, 445-453.

Kyle, P.R., Elliot, D.H., Sutter, J.P., 1981. Jurassic Ferrar Supergroup tholeiites from the Transantarctic Mountains, Antarctica, and their relationship to the initial fragmentation of Gondwana. In: Creswell, MM., Vella, P. (Eds), Gondwana Five. Balkema, Rotterdam, 283-287.

Launeau, P., 2004. Mise en évidence des écoulements magmatiques par analyse d'images 2-D des distributions 3-D d'Orientations Préferentielles de Formes. Bulletin of the Geological Society of France, 175, 331–350.

Launeau, P., Bouchez, J.-L., 1992. Mode et orientation préférentielle de forme des granites par analyse d'images numériques, Bulletin of the Geological Society of France, 163, 721-732.

Launeau, P., Cruden, A.R., 1998. Magmatic fabric acquisition mechanisms in a syentire: Results of a combined anisotropy of magnetic susceptibility and image analysis study. Journal of Geophysical Research, 103, 5067-5089.

Launeau, P., Robin, P.-Y.F., 1996. Fabric analysis using the intercept method. Tectonophysics, 267, 91-119.

Launeau, P., Robin, P.-Y.F., 2005. Determination of fabric and strain ellipsoids from measured sectional ellipses—implementation and applications. Journal of Structural Geology, 27, 2223–2233.

Launeau, P., Archanjo, C.J., Picard, D., Arbaret, L., Robin, P.-Y.F., 2010. Two- and three-dimensional shape fabric analysis by the intercept methods in grey levels. Tectonophysics, 492, 230-239.

Leat, P.T., 2008. On the long-distance transport of the Ferrar Magmas. In: Thomson, K., Petford, N. (Eds.), Structure and Emplacement of High-Level Magmatic Systems. Geological Society of London, Special Publication, 302, 45-61.

Le Gall, B., Tshoso, G., Jourdan, F., Féraud, G., Bertrand, H., Tiercelin, J.-J., Kampunzu, A.B., Modisi, M., Dyment, J., Maia, M., 2002. $^{40}Ar–^{39}Ar$ geochronology and structural data from the giant Okavango and related mafic dyke swarms, Karoo igneous province, N Botswana. Earth and Planetary Science Letters, 202, 595-606.

Le Gall, B., Tshoso, G., Dyment, J., Kampunzu, A.B., Jourdan, F., Féraud, G., Bertrand, H., Aubourg, C., Vétel, W., 2005. The Okavango giant mafic dyke swarm (NE Botswana): its structural significance within the Karoo Large Igneous Province. Journal of Structural Geology. 27, 2234-2255.

Le Maitre, R.W. 1989. A Classification of Igneous Rocks and Glossary of Terms – Recommendations of the International Union of Geological Sciences Subcommission on the Systematics of Igneous Rocks. Blackwell Scientific Publishing, Oxford, 193 pp.

Le Roex, A.P., Reid, D.L., 1978. Geochemistry of Karroo dolerite sills in the Calvinia district, Western Cape Province, South Africa. Contributions to Mineralogy and Petrology, 66, 351-360.

Lensky, N.G., Niebo, R.W., Holloway, J.R., Lyakhovsy, V., Navon, O., 2006. Bubble nucleation as a trigger for xenolith entrapment in mantle melts. Earth and Planetary Science Letters, 245, 278-288.

Liss, D., 2004. Emplacement processes and magma flow geometries of the Whin Sill Complex. Unpublished PhD thesis, University of Burmingham, 236 pp.

Liss, D., Hutton, D.H.W., Owens, W.H., 2002. Ropy flow structures: A neglected indicator of magma-flow direction in sills and dikes. Geology, 30, 715-718.

Lombaard, B.V., 1952. Karroo dolerites and lavas. Transactions of the Geological Society of South Africa, 55, 175-198.

Loock S., Diot, H., Van Wyk de Vries, B., Launeau, P., Merle, O., Vedboin, F., Petronis, M.S., 2008. Lava flow internal structure found from AMS and textural data: An example in methodology form the Chaîne des Puys, France. Journal of Volcanology and Geothermal Research, 177, 1092-1104.

Lorenz, V., Kurszlaukis, S., 2007. Root zone in the phreatomagmatic pipe emplacement model and consequences for the evolution of maar-diatreme volcanoes. Journal of Volcanology and Geothermal Research, 159, 4-32.

Lowman, J.P., Jarvis, G.T., 1999. Effects of mantle heat source distribution on supercontinent stability. Journal of Geophysical Research, 104, 12733-12746.

Luttinen, A.V., Rämö, O.T., Huhma, H., 1998. Neodymium and strontium isotopic and trace element composition of a Mesozoic CFB suite from Dronning Maud Land, Antarctica. Journal of Volcanology and Geothermal Research, 198, 1-18.

Maes, S.M., Ferré, E.C., Tikoff, B, Brown, P.E., Marsh, J.S., 2008. Rock magnetic stratigraphy of a mafic layered sill: A key to the Karoo volcanics plumbing system. Journal of Volcanology and Geothermal Research, 172, 75-92.

Magee, C., Stevenson, C.T.E., O'Driscoll, B., Petronis, M.S. 2012. Local and regional controls on the lateral emplacement of the Ben Hiant Dolerite intrusion, Ardnamurchan (NW Scotland). Journal of Structural Geology, 39, 66-82.

Manga, M., Stone, H.A., 1994. Interactions between bubbles in magmas and laves: effects of bubble deformation. Journal of Volcanology and Geothermal Research, 63, 267-279.

Marsh, J.S., Eales, H.V., 1984. The chemistry and petrogenesis of igneous rocks of the Karoo central area, Southern Africa. In: Erlank, A.J. (Eds.) Petrogenesis of the volcanic rocks of the Karoo province. Geological Society of South Africa Special Publication, 13, 27-67.

Marsh, J.S, Mndaweni, M.J., 1998. Geochemical variations in a long Karoo dyke, Eastern Cape. South African Journal of Geology, 101, 119-122.

Marsh, J.S., Hooper, P.R., Rehacek, J., Duncan, R.A., Duncan, A.R., 1997. Stratigraphy and age of Karoo Basalts of Lesotho and implications for correlations within the Karoo Igneous Province, In: Mahoney, J.J., Coffin, M.F. (Eds.), Large igneous provinces: Continental, oceanic and planetary flood volcanism. American Geophysical Union Geophysical Monograph, 100, 247-272.

Marsh, J.S., Allen, P., Fenner, N., 2003. The geochemical structure of the Insizwa lobe of the Mount Ayliff complex with implications for the emplacement and evolution of the complex and its Ni-sulphide potential. South African Journal of Geology, 106, 409-428.

Marshall, C.G.A. 2002. The stratigraphy, sedimentology and basin evolution of the Natal Group. Council for Geoscience, Memoir 91. Pretoria, 179 pp.

Martín-Hernández, F., Luneberg, C.M., Aubourg, C., Jackson, M., 2004. Magnetic fabric: methods and applications – an introduction. In: Martín-Hernández, F., Luneberg, C.M., Aubourg, C., Jackson, M. (Eds.) Magnetic Fabric: Methods and Applications. Geological Society, London, Spec. Publ., 238, pp. 1-7.

Marzoli, A., Renne, P., Piccirillo, E., Ernesto, M., Bellieni, G., De Min, A., 1999. Extensive 200-million-year-old continental flood basalts of the Central Atlantic magmatic province. Science, 284, 616-618.

McClintock, M.K., White, J.D.L., 2002. Granulation of weak rock as a precursor to peperite formation: coal peperite: Coombs Hills, Antarctica. Journal of Volcanology and Geothermal Research, 114, 205-217.

Mekonnen, T.K., 2004. Interpretation and Geodatabase of Dykes Using Aeromagnetic Data of Zimbabwe and Mozambique (Unpublished MSc. Thesis), International Institute for Geoinformation Science and Earth Observation, Enschede, The Netherlands, 72 pp.

Menand, T., 2008. The mechanics and dynamics of sills in layered elastic rocks and their implications for the growth of laccoliths and other igneous complexes. Earth and Planetary Science Letters, 267, 93-99.

Menand, T., 2011. Physical controls and depth of emplacement of igneous bodies: A review. Tectonophysics, 500, 11-19.

Menand, T., Daniels, K., Benghiat, P., 2010. Dyke propagation and sill formation in a compressive tectonic environment. Journal of Geophysical Research, 115, doi: 10.1029/2009JB006791.

Mériaux, C., Lister, J.R., 2002. Calculation of dike trajectories from volcanic centres. Journal of Geophysical Research, 107, doi: 10.1027/2001JB000436.

Meth, D.L., 1996. The Geology and Geochemistry of the Rooi Rand Dyke Swarm (Unpublished MSc. thesis), University of Natal, Durban, South Africa, 189 pp.

Milner, S.C., Duncan, A.R., Whittingham, A.M., Ewart, A., 1995. Trans-Atlantic correlation of eruptive sequences and individual silicic units within the Paraná-Etendeka igneous province. Journal of Volcanology and Geothermal Research, 69, 137-157.

Morris, G.A., Kamada, M., Martinez, V., 2008. Emplacement of the Etive Dyke Swarm, Scotland: implacations of dyke morphology and AMS data. In: Thomson, K. and Petford, N. (Eds.) Structure and emplacement of High-Level Magmatic Systems. Geological Society of London, Special Publication, 302, 149-158.

Moulin, M., Fluteau, F., Courtillot, V., Marsh, J., Delpech, G., Quidelleur, X., Gérard, M., Jay, A.E., 2011. An attempt to constrain the age, duration, and eruptive history of the Karoo flood basalt: Naude's Nek section (South Africa). Journal of Geophysical Research, 116, B07403, doi: 10.1029/2011JB008210.

Mudge, M.R., 1968. Depth control on some concordant intrusions. Geological Society of America Bulletin, 79, 312-315.

Muirhead, J.D., Airlodi, G., Rowland, J.V., White, J.D.L., 2012. Interconnected sills and inclined sheet intrusions control shallow magma transport in the Ferrar large igneous province, Antarctica. Geological Society of America Bulletin, 124, 162-180.

Muirhead, J.D., Airlodi, G., White, J.D.L., Rowland, J.V., 2014. Cracking the lid: Sill-fed dikes are the likely feeders of flood basalt eruptions. Earth and Planetary Science Letters, 406, 187-197.

Nicholas, A., 1992. Kinematics in magmatic rocks with special reference to gabbros. Journal of Petrology, 33, 891-915.

Nicolaysen, K., Frey, F.A., Hodges, K.V., Weis, D., Giret, A., 2000. $^{40}Ar/^{39}Ar$ geochronology of flood basalts from the Kerguelen Archipelago, southern India Ocean: Impications for Cenozoic eruption rates of the Kerguelen plume. Earth and Planetary Science Letters, 174, 313-328.

Nicholson, R., Ejiofor, I.B., 1987. The three-dimensional morphology of arrays of echlon and sigmoidal, mineral-filled fractures: data from north Cornwall. Journal of the Geological Society of London, 144, 79-83.

Nicholson, R., Pollard, D.D., 1985. Dilation and linkage of echelon cracks. Journal of Structural Geology, 7, 583-590.

O'Driscoll, B., Hargraves, R.B., Emeleus, C.H., Troll, V.R., Donaldson, C.H., Reavy, R.J., 2007. Magmatic lineations inferred from anisotropy of magnetic susceptibility fabrics in Units 8, 9, and 10 of the Rum Eastern Layered Series, NW Scotland. Lithos, 98, 27-44.

O'Driscoll, B., Ferré, E.C., Stevenson, C., Magee, C., 2015. The significance of Magnetic Fabric in Layered Mafic-Ultramafic Intrusions. In: Charlier, B., Namur, O., Latypov, R.,Tegner, C. (Eds.) Layered Intrusions, Springer Geology, 295-329. doi: 10.1007/978-94-017_9652-1_7.

Passchier, C.W., Trouw, R.A.J., 1998. Micro-tectonics. Springer, Berlin, pp. 283.

Paterson, S.R., Fowler, T.K. Jr., Schmidt, K.L., Yoshinobu, A.S., Yuan, E.S., Miller, R.B., 1998. Interpreting magmatic fabric patterns in plutons. Lithos, 44, 53-82.

Payacán, I., Gutiérrez, F., Gelman, S.E., Bachmann, O., Parada, M.Á., 2014. Comparing magnetic and magmatic fabrics to constrain the magma flow record in La Gloria pluton, central Chile. Journal of Structural Geology, 32-46.

Pearce, J.A., 1976. Statistical analysis of Major Element Patterns in Basalts. Journal of Petrology, 1976, 15-43.

Pearce, J.A., Cann, J.R., 1973. Tectonic setting of basic volcanic rocks determined using trace element analyses. Earth and Planetary Science Letters, 19, 290-300.

Peck, L., Barton, C.C., Gordon, R.B., 1985. Microstructure and the resistance of rock to tensile failure. Journal of Geophysical Research, 90, DOI: 10.1029/JB090iB13p11533.

Philpotts, A.R., Philpotts, D.E. 2007. Upward and downward flow in a camptonite dike as recorded by deformed vesicles and the anisotropy of magnetic susceptibility (AMS). Journal of Volcanology and Geothermal Research, 161, 81-94.

Pichler, H., 1965. Acid hyaloclastites. Bulletin of Volcanology, 28, 293-310.

Poland, M.P., Fink, J.H., Tauxe, L. 2004. Patterns of magma flow in segmented silicic dikes at Summer Coon volcano, Colorado: AMS and thin sections analysis. Earth and Planetary Science Letters, 219, 155-169.

Pollard, D.D., 1973. Derivation and evaluation of a mechanical model for sheet intrusions. Tectonophysics, 19, 233-269.

Pollard, D.D., 1987. Elementary fracture mechanics applied to the structural interpretation of dykes. In: Halls, H.C. and Fahrig, W.F. (Eds.) Mafic Dyke Swarms. Geological Association of Canada Special Paper, 34, 5-24.

Pollard, D.D., Johnson, A.M., 1973. Mechanics of growth of some laccolithic intrusions in the Henry Mountains, Utah, II: Bending and failure of overburden layers and sill formation. Tectonophysics, 18, 311-354.

Pollard, D.D., Muller, O.H., Dockstader, D.R., 1975. The form and growth of fingered sheet intrusions. Geological Society of America Bulletin, 86, 351-363.

Polteau, S., Mazzini, A., Galland, O., Planke, S., Malthe-Sørenssen, A., 2008. Saucer-shaped intrusions: Occurrences, emplacement and implications. Earth and Planetary Science Letters, 266, 195-204.

Potter, D.K., Stephenson, A., 1988. Single-domain particles in rocks and magnetic fabric analysis. Geophysical Research Letters, 15, 1097-1100.

Quick, J.E., Sinigoi, S., Mayer, A., 1994. Emplacement dynamics of a large mafic intrusion in the lower crust, Ivrea-Verbano Zone, northern Italy. Journal of Geophysical Research, 99, 21559-21573.

Reeves, C.V., 1978. A failed Gondwana spreading axis in southern Africa. Nature, 273, 222-223.

Reeves, C.V., 2000. The geophysical mapping of Mesozoic dyke swarms in southern Africa and their origin in the disruption of Gondwana. Journal of African Earth Sciences, 30, 499-513.

Renne, P.R., Ernesto, M., Pacca, I.G., Coe, R.S., Glen, J.M., Prevot, M., Perrin, M., 1992. The Age of Parana Flood Volcanism, Rifting of Gondwanaland, and the Jurassic-Cretaceous Boundary. Science, 258, 975-979.

Richards, M.A., Duncan, R.A., Courtillot, V.E., 1989. Flood Basalts and Hot-Spot Tracks: Plume Heads and Tails. Science, 246, 103-107.

Richardson, S.H., 1979. Chemical variation induced by flow differentiation in an extensive Karoo dolerite sheet, southern Namibia. Geochimica et Cosmochimica Acta, 43, 1433-1441.

Rickwood, P.C., 1990. The anatomy of a dyke and the determination of propagation and magma-flow directions. In: Parker, A.J., Rickwood, P.C. and Tucker, D.H. (Eds.) Mafic dykes and Emplacement Mechanisms. Proceedings of the Second international dyke conference, Adelaide, South Australia, 2, 81-100.

Riley, T.R., Knight, K.B., 2001. Age of pre-break-up Gondwana magmatism: a review. Antarctic Science, 13, 99-110.

Riley, T.R., Millar, L.L., Watkeys, M.K., Curtis, M.L., Leat, P.T., Klausen, M.B., Fanning, C.M., 2004. U-Pb zircon (SHRIMP) ages for the Lebombo rhyolites, South Africa: refining the duration of Karoo volcanism. Journal of the Geological Society of London, 161, 547-550.

Riley, T.R., Curtis, M.L., Leat, P.T., Watkeys, M.K., Duncan, R.A., Millar, I.L., Owens, W.H. 2006. Overlap of Karoo and Ferrar Magma Types in KwaZulu-Natal, South Africa. Journal of Petrology, 47, 541-566.

Robin, P.-Y.F., 2002. Determination of fabric and strain ellipsoids from measured sectional ellipses – Theory. Journal of Structural Geology, 24, 531-544.

Rochette, P., Fillion, G., Mattéi, J.-L. & Dekkers, M.J. 1990. Magnetic transition at 30 – 34 K in pyrrhotite: insight into a widespread occurrence of this mineral in rocks. Earth and Planetary Science Letters, 98, 319-328.

Rochette, P., Jenatton, L., Dupuy, C., Boudier, F., Reuber, I., 1991. Diabase dikes emplacements in the Oman Ophiolite: a magnetic fabric study with reference to geochemistry. In: Peters, T., Nicolas, A., Coleman, R.G. (Eds.), Ophiolite Genesis and Evolution of the Oceanic Lithosphere. Kluwer, Dordrecht, 55-82.

Rochette, P., Aubourg, C., Perrin, M., 1999. Is this magnetic fabric normal? A review and case studies in volcanic formations. Tectonophysics, 307, 219-234.

Rochette, P., Fillion, G. & Dekkers., 2011. The Low-Temperature Magnetic Transition of Monoclinic Pyrrhotite. IRM Quarterly, 21 (1).

Rogers, A.W., Du Toit, A.L., 1903. Geological survey of parts of the division of Ceres, Sutherland and Calvinia. Annual Report of the Cape Geological Commission, 36-43.

Rogers, A.W., Schwarz, E.H.L., 1902. Report on parts of the divisions of Beaufort West, Prince Albert and Sutherland. Annual Report of the Cape Geological Commission, 97-128.

Saggerson, E.P., Bristow, J.W., Armstrong, R.A., 1983. The Rooi Rand dyke swarm. South African Journal of Science, 79, 365-369.

Schofield, N., 2009. Linking sill morphology to emplacement mechanisms. Unpublished PhD thesis, University of Burmingham, 210 pp.

Schofield, N., Stevenson, C., Reston, T. 2010. Magma fingers and host rock fluidisation in the emplacement of sills. Geology, 38, 63-66.

Schofield, N., Heaton, L., Holford, S.P., Archer, S.G., Jackson, C.A.-L., Jolley, D.W., 2012a. Seismic imaging of 'broken bridges': linking seismic to outcrop-scale investigations of intrusive magma lobes. Journal of the Geological Society of London, 169, 421-426.

Schofield, N., Brown, D.J., Magee, C., Stevenson, C.T., 2012b. Sill morphology and comparison of brittle and non-brittle emplacement mechanisms. Journal of the Geological Society of London, 169, 127-141.

Smith, J.V. 2002. Structural analysis of flow-related textures in lavas. Earth-Science Reviews, 57, 279-297.

Smith, R.A., 1984. The lithostratigraphy of the Karoo Supergroup in Botswana. Bulletin of the Geological Survey of Botswana, 26, 239.

Sparks, R.S.J., Baker, L., Brown, R.J., Field, M., Schumacher, J., Stripp, G., Walters, A., 2006. Dynamical constraints on kimberlite volcanism. Journal of Volcanology and Geothermal Research, 155, 18-48.

Spera, F.J., 1980. Aspects of magma transport. In: Hargraves, R.B. (Eds.), Physics of Magmatic Processes. Princeton University Press, Princeton, New Jersey, 265-323.

Stephenson, A., Sadikun, S., Potter, D.K., 1986. A theoretical and experimental comparison of the anisotropies of magnetic susceptibility and remanence in rocks and minerals, Geophysical Journal International, 84, 185-200.

Stevenson, C.T.E., Owens, W.H., Hutton, D.H.W., 2007. Flow lobes in granite: The determination of magma flow direction in the Trawenagh Bay Granite, northwestern Ireland, using anisotropy of magnetic susceptibility. Geological Society of America Bulletin, 119, 1368-1386.

Storey, B.C., Kyle, P.R., 1997. An active mantle mechanism for Gondwana break-up. South African Journal of Geology, 10, 283-290.

Svensen, H., Jamtveit, B., Planke, S., Chevallier, L., 2006. Structure and evolution of hydrothermal vent complexes in the Karoo Basin, South Africa. Journal of the Geological Society of London, 163, 671-682.

Svensen, H., Planke, S., Chevallier, L., Malthe-Sørenssen, A., Corfy, F., Jamtveit, B., 2007. Hydrothermal venting of greenhouse gases triggering Early Jurassic global warming. Earth and Planetary Science Letters, 256, 554-566.

Svensen, H., Aarnes, I., Podladchikov, Y.Y., Jettestuen, E., Harstad, C.H., Planke, S., 2010. Sandstone dikes in dolerite sills: Evidence for high-pressure gradients and sediment mobilization during solidification of magmatic sheet intrusions in sedimentary basins. Geosphere, 6, 211-224.

Svensen, H., Corfu, F., Polteau, S., Hammer, Ø., Planke, S., 2012. Rapid magma emplacement in the Karoo Large Igneous Province. Earth and Planetary Science Letters, 325-326, 1-9.

Svensen, H., Polteau, S., Cawthorn, G., Planke, S., 2015. Sub-volcanic Intrusions in the Karoo Basin, South Africa. In: Németh, K. (Eds.) Advances in Volcanology, Springer, Berlin, Heidelburg, 1-14. doi: 10.1007/11157_2014_7.

Sweeney, R.J., Watkeys, M.K., 1990. A possible link between Mesozoic lithosphere architecture and Gondwana flood basalts. Journal of African Earth Sciences, 10, 707-716.

Sweeney, R.J., Falloon, T.J., Green, D.H., Tatsumi, Y., 1991. The mantle origins of Karoo picrites. Earth and Planetary Science Letters, 107, 256-271.

Sweeney, R.J., Duncan, A.R., Erlank, A.J., 1994. Geochemistry and petrogenesis of central Lebombo basalts from the Karoo Igneous Province. Journal of Petrology, 35, 95-125.

Tankard, A., Welsink, H., Aukes, P., Newton, R., Stettler, E., 2009. Tectonic evolution of the Cape and Karoo basins of South Africa. Marine and Petroleum Geology, 26, 1379-1412.

Tarling, D.H., Hrouda, F. 1993. The Magnetic Anisotropy of Rocks. Chapman and Hall, London, 218 pp.

Tavener-Smith, R., Mason, T.R., Christie, A.D.M., Roberts, D.L., Smith, A.M., Van der Spy, A. 1988. Sedimentary models for coal formation in the Vryheid Formation, northern Natal. Bulletin for the Geological Survey of South Africa, 94, 46 pp.

Thomas, R.J. 1989. The tale of two tectonic terranes. South African Journal of Geology, 92, 306-321.

Thomson, K., 2007. Determining magma flow in sills, dykes and laccoliths and their implication for sill emplacement mechanisms. Bulletin of Volcanology, 70, 183-201.

Thomson, K., Hutton, D.H.W., 2004. Geometry and growth of sill complexes: insights using 3D seismic from the North Rockall Trough. Bulletin of Volcanology, 66, 364-375.

Thomson, K., Schofield, N., 2008. Lithological and structural controls on the emplacement and morphology of sills in sedimentary basins. In: Petford, N. (Eds.) Structure and emplacement of high-level systems. Geological Society of London, Special Publication, 302, 31-44.

Uken, R., Watkeys, M.K., 1997. An interpretation of mafic dyke swarms and their relationship with major mafic magmatic events on the Kaapvaal Craton and Limpopo Belt. South African Journal of Geology, 100, 341-349.

Varga, E.J., Gee, J.S., Staudigel, H., Tauxe, L., 1998. Dike surface lineations as magma flow indicators within the sheeted dike complex of the Troodos Ophiolite, Cyprus. Journal of Geophysical Research, 103, 5241-5256.

Verwey, E.J. 1939. Electron conduction of magnetite (Fe_3O_4) and its transition point at low temperature. Nature, 144, 327-328.

Walker, F., Poldervaart, A., 1949. Karroo Dolerites of the Union of South Africa. Geological Society of America Bulletin, 60, 591-706.

Watkeys, M.K. 2002. Development of the Lebombo rifted volcanic margin of southeast Africa. In: Menzies, M.A., Klemperer, S.L., Ebinger, C.J. & Baker, J. (Eds), Volcanic Rifted Margins. Geological Society of America Special Paper, 362, 27-46.

Westerman, D., Dini, A., Innocenti, F., Rocchi, S., 2004. Rise and fall of a nested Christmas-tree laccolith complex, Elba Island, Italy. In: Breitkreuz, C., Petford, N. (Eds.), Physical Geology of High-Level Magmatic Systems, Geological Society of London, Special Publication, 234, 195-213.

White, J.D.L., McPhie, J. and Skilling, I., 2000. Peperite: a useful genetic term. Bulletin of Volcanology, 62, 65-66.

White, R.S., 1997. Mantle Plume origin for the Karoo and Ventersdorp Flood Basalts, South Africa. South African Journal of Geology, 100, 271-283.

White, R.S., McKenzie, D., 1989. Magmatism at rift zones: The generation of volcanic continental margins and flood basalts. Journal of Geophysical Research, 94, 7685-7729.

Winter, J.D., 2001. An introduction to igneous and metamorphic petrology. Prentice-Hall Inc., New Jersey, 697 pp.

Xu, L.R., Huang, Y.Y., Rosakis, A.J., 2003. Dynamic crack deflection and penetration at interfaces in homogeneous materials: experimental studies and model predictions. Journal of Mechanics and Physics of Solids, 51, 461-486.

Zuo, J.M., 1990. Charge ordering in magnetite at low temperatures. Physical Review, 42, 8451-8464.

- CHAPTER 4 –

Tectonophysics 656 (2015) 61–73

Contents lists available at ScienceDirect

Tectonophysics

journal homepage: www.elsevier.com/locate/tecto

Assessing SPO techniques to constrain magma flow: Examples from sills of the Karoo Igneous Province, South Africa

Lauren Hoyer *, Michael K. Watkeys

Geological Sciences, School of Agricultural, Earth and Environmental Sciences, University of KwaZulu-Natal, Westville Campus, Private Bag X54001 Durban 4000, South Africa

4.1. Introduction

The Shape Preferred Orientations (SPO) analysis of minerals has been widely used in a number of studies in order to define a shape ellipsoid for the minerals under analysis. This is often done in order to determine the magma flow within dykes (Archanjo and Launeau, 2004; Hastie et al., 2011a; 2011b; 2013; Launeau and Robin, 2005) and sills (Kattenhorn, 1994; Horsman et al., 2005). With the introduction of the SPO-2003 and Ellipsoid-2003 software packages (Launeau, 2004; Launeau and Robin, 2005) the determination of the SPO of mineral phases has become a tool in describing the petrofabric associated with intrusions and intrusion mechanisms. Petrographic analyses are often integrated with Anisotropic Magnetic Susceptibility (AMS) analyses in order to determine not only the petrofabric but also the magnetic fabrics of the intrusions (e.g. Archanjo et al, 2006; 2012; Geoffroy, 2002; Horsman et al, 2005; Hastie et al, 2011b).

This study investigates dolerite sills that crop out along the KwaZulu-Natal North Coast (Fig. 4.1), South Africa, and which are part of the extensive ca. 181-184 Ma sills of the Karoo Igneous Province (Jourdan et al., 2008). They were sampled to obtain the petrofabric in order to infer the principal magma flow directions. Fabrics form from numerous flow-related and regional scale processes, but in order for a fabric to be preserved, the process of formation must occur at a particular point in the intrusion history. For plutonic rocks, a “crystal-mush zone” occurs at the margins of the intrusion whilst the magma is cooling and crystallising. As the

pluton cools, this zone migrates inwards (Marsh, 1989; Tait and Jaupart, 1990). Once the viscosity of the melt changes from a low viscosity Newtonian melt to a higher viscosity, crystal-dense Bingham melt, the magma is near solidi; it is at this point that the fabrics become preserved (Paterson et al., 1998; Yoshinobu et al., 1998).

In order to successfully analyse the magma flow within an intrusion, it is necessary to analyse the fabric within the sill and determine whether or not these fabrics imply magma flow mechanisms and directions. Whilst using the SPO programs it became evident that in order to obtain the most accurate petrofabric results, certain parameters needed to be analysed to elucidate which analytical technique should be used. The aim of this study is to ascertain the most accurate petrofabric data through the use of the SPO-2003 programme. The results need to be well-defined by using the correct analytical techniques so that the petrofabric data may be used to infer the magma flow direction in the sills sampled. In order to determine the most accurate results, the techniques used to acquire the petrofabric data must be constrained. The techniques that are scrutinised include (1) the error in the fit of the resultant ellipsoids as indicated by the Global Incompatibility Index ($\sqrt{F}$); (2) whether or not an image should be segmented upon analysis to improve the quality of the result and (3) in particular the variation in the grain size of the plagioclase crystals that are to be analysed.

Grain size has been previously discussed when defining how petrofabrics within intrusions may differ due to the presence of different crystal generations (e.g. Hastie et al., 2013). However prior to determining the shape ellipsoid for a sample, the grain size is generally not taken into consideration when selecting the magnification at which photomicrographs are taken. The issues of $\sqrt{F}$ are highlighted using the results from twelve sills sampled from the KwaZulu-Natal North Coast at Thompson's Bay (TB), Shaka's Rock (SR) and Sheffield Beach (SHF).

Due to tectonic activity related to the break-up of Gondwana, the rocks have been tilted and rotated so that there is no distinct link between the intrusions sampled here and the main Karoo Basin dolerites. This study should enable significant petrofabric results to be ascertained and possible magma flow directions to be inferred. This could greatly further the understanding of not only dolerite sill emplacement but also the extent and origin of the Karoo dolerites.

4.2. Geological Settings

The study area spans an 8 km stretch of coastline where numerous dolerite sills crop out. The beaches are narrow and only small portions of the intrusions may be observed at any one

locality. The dolerite suite is predominantly composed of sills with minor dykes that are poorly exposed. The sills are intruded into the Permian aged Vryheid Formation, of the Karoo Supergroup supracrustals. The country rocks comprise thinly laminated siltstones, shales and gritstones with minor interbedded coal seams and Iron-rich shales. The dolerites are Jurassic in age, ranging between 181 Ma – 184 Ma (Jourdan et al., 2008) and typically intrude into the laminated finer grained country rocks, although occasionally into the gritstones (e.g. SHF5).

Post-dating the intrusion of the dolerite suite were a series of brittle tectonic events related to the break-up of Gondwana. The faulting events that created the coastline have been preserved in both the country rocks and the dolerite intrusions, manifested as locally tilted and rotated stratigraphy.

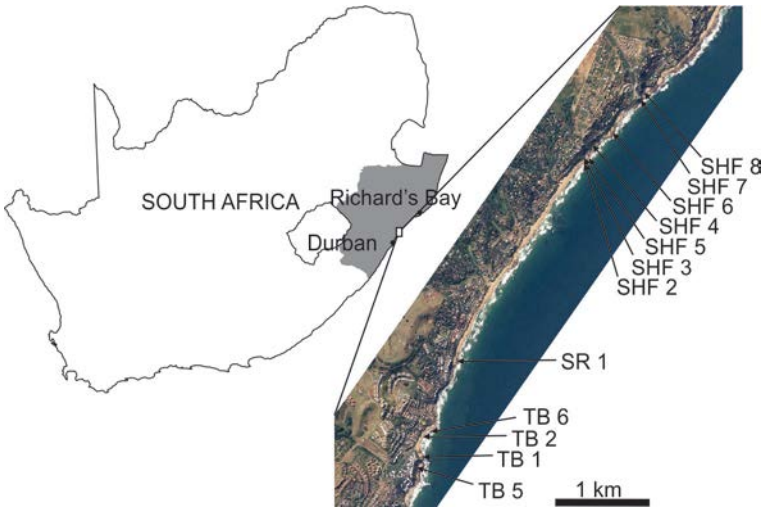

Fig. 4.1. The geographical position of the study area ~40 km north of Durban in KwaZulu-Natal, South Africa. The sills that were sampled and incorporated into this study are indicated and labelled on the aerial photograph.

4.2.1. Dolerite petrography and petrology

The sills investigated typically comprise ~50% plagioclase and ~45% augite, with the remaining fraction (5%) taken up by magnetite and minor pyrrhotite. Chlorite and biotite may also be present where alteration has taken place. For some of the sills, the original minerals are no longer discernible from alteration minerals and were therefore disregarded for this study.

Macroscopically the intrusions may contain one or all of the following features: amygdales, large and small vesicles, xenoliths of quartzofeldspathic material or local country rock and multiple layers indicating numerous magma pulses (Table 4.1). Microscopically, the grain size varies widely between the sills, and occasionally also between the upper and lower contacts (Fig. 4.2).

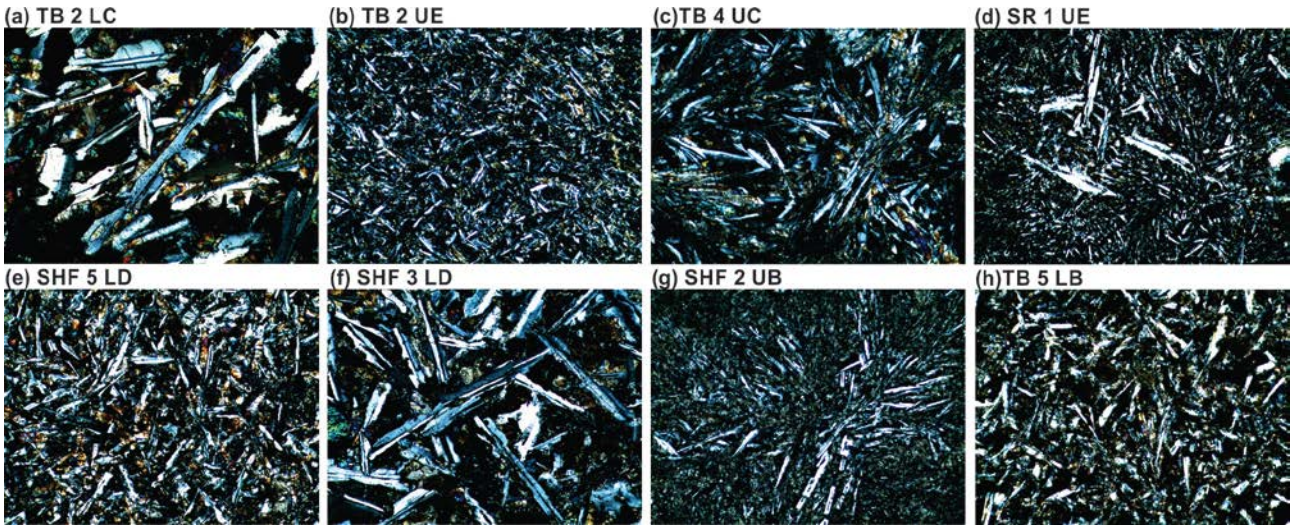

Fig. 4.2. Examples of photomicrographs with all images obtained at the same magnification (1.2 mm in width). (a) and (f) show a larger overall grain size than the finer grained sections of (b), (e), (g) and (h). (c) and (g) display textures between plumose augite crystals and variolitic to spherulitic plagioclase. (d) Elongate plagioclase phenocrysts within a finer grained matrix. (a), (c), and (f) show intergranular textures; (b), (d), (e), (g) and (h) are hemicrystalline.

The texture of the dolerites may also vary between and within the sills. This becomes an important consideration when the petrofabric is being analysed in terms of magma flow fabrics. The majority of the samples that were photomicrographed exhibited intergranular textures, although some samples show interesting plagioclase and/or pyroxene textures. A range of textures from acicular to spherulitic to variolitic plagioclase were observed with some sections showing fine grained plumose textured augite (Fig. 4.2). All of the textures appear to be magmatic in origin, although some samples have textural overprinting caused by alteration phases such as chlorite. Such samples were either disregarded or only photomicrographed at the fresh portions of the thin section.

Magma flow indicators occur within the sills and comprise magmatic features such as ropy-flow structures and magma lobes (Table 4.1). The morphological features such as broken bridges and steps along the contacts of the sills may have been obstacles that had a local effect on the magma flow (Wylie et al., 1999; Schofield et al., 2010).

Table 4.1. *Geographical position and characteristics of sills from Thompson's Bay and Sheffield Beach*

Sill	Geographical co-ordinates				Approximate	
Name	Latitude	Longitude	Dip	Strike	Thickness (m)	Characteristics
TB1	29° 31' 39.05"	31° 13' 41.17"	22°	172°	3.0	Xenolithic, minor amygdales
TB2	29° 31' 14.69"	31° 13' 42.05"	21°	167°	2.5	Elongated vesicle layer, amygdaloidal layer, xenolithic zone
TB4	29° 31' 13.87"	31° 13' 42.87"	25°	172°	1.0	Central vesicle stringer, spherulitic plagioclase and pyroxene
TB5	29° 31' 25.17"	31° 13' 39.03"	16°	160°	2.0	Massive, small broken bridge along upper contact
SR1	29° 30' 50.76"	31° 13' 54.48"	20°	206°	2.0	Xenolithic at upper contact, spherulitic grain size variation
SHF2	29° 29' 43.44"	31° 14' 46.68"	20°	000°	1.0	Fine grained with spherulitic plagioclase
SHF3	29° 29' 41.64"	31° 14' 46.93"	17°	340°	2.2	Broken bridge and associated sedimentary dyke, amygdaloidal layers
SHF4	29° 29' 37.32"	31° 14' 49.56"	12°	350°	1.5	Above average degree of alteration
SHF5	29° 29' 41.28"	31° 14.48.48"	10°	353°	1.2	High degree of alteration
SHF6	29° 29' 32.64"	31° 14' 57.48"	13°	013°	2.5	Occasional spherulitic pyroxene, large xenoliths
SHF7	29° 29' 23.64"	31° 15' 07.56"	10°	056°	>10	Phenocrystic plagioclase at the lower contact, xenolithic
SHF8	29° 29' 19.32"	31° 15' 10.44"	09°	088°	0.5	High degree of alteration, central vesicle stringer, xenolithic

4.3. Methods

4.3.1. Sampling and sample preparation

Twenty five millimetre diameter cores were collected using a petroleum-powered handheld drill and were typically sited within 10-15 cm of the sill contacts. All cores obtained were orientated in the field using a core-orientator and a magnetic compass. Ideally between 4 and 8 samples were collected from opposing sill margins (where available) within a single intrusion. The majority of the intrusions were thin (<2 m thick) and therefore cross-sectional sampling throughout such sills was not possible. However, for some of the thicker intrusions, certain layers or portions of the sill were sampled. The intrusion TB2 yielded samples not only from the margins but from a vesicular zone where ~4 cm long elongated vesicles were observed plunging towards the NW. The centre of the sills TB4 and SR1 were also sampled due to a distinct difference in grain size between the centre and the margins of the sills.

The cores were cut into mutually perpendicular sections based on a randomly assigned XYZ coordinate system (Fig. 4.3). The samples were prepared into thin sections for petrographic analyses and each thin section (3 per sample) was photographed under crossed polarisers. To account for the large variations in grain sizes within and between the intrusions, the thin sections were photographed at both lower and higher magnifications (2.5x and 10x magnification respectively) in order to image the greatest range of grain sizes. A total of 102 samples were photographed (306 thin sections); this resulted in 97 samples (291 thin sections) photographed at 10x magnification and 53 samples (159 thin sections) photographed at 2.5x magnification.

4.3.2. Shape Preferred Orientation (SPO) of plagioclase

The photomicrographs of orientated thin sections were digitised in order to measure the orientation and shape of the plagioclase crystals by means of measured ellipses. The images obtained were changed into negative black and white images and filtered using a threshold level of 128 in the image manipulation software ArcSoft Photostudio. This allowed only the plagioclase grains from each section to be extracted. Any grains that were truncated by the image boundary were removed. The thresholding process allows for only the lightest coloured portions of the image to remain. Where twinning of the plagioclase occurs, the twin in or close to extinction may not be preserved through the thresholding technique. If the entire grain is not preserved, this may affect subsequent results such as the average shape of the grains in the section and the degree of anisotropy of the grains. Once the threshold has been applied, any intersecting grains are manually separated. This allows each grain to be analysed individually in order to obtain an accurate fabric. The final digitised images were then imported into the programme SPO-2003 (Launeau, 2004; Launeau and Bouchez, 1992; Launeau and Robin, 2005) which creates a 2-D inertia tensor from all the grain data and defines an ellipse (Launeau and Robin, 1996; 2005). The 2-D inertia tensor is formed by the stacking of every grain in the image into a column which determines the average shape within the image. The three mutually perpendicular 2-D tensors are then combined in the programme Ellipsoid-2003, where each ellipse holds an equal weight regardless of the number of grains measured. This allows a 3-D ellipsoid to be created, the parameters of which define the petrofabric. The shape of the ellipsoid (T) and the degree of anisotropy (P') are determined by the software and recorded for each ellipsoid (Jelinek, 1981). T, as defined by Jelinek (1981), is the best descriptive formula used to define ellipsoidal shapes (Tarling and Hrouda, 1993).

According to Launeau and Robin (2005) the images should be segmented before the grains are analysed in order to obtain the maximum number of combinations of the three 2-D ellipses. For the segmentation of each image, nine overlapping rectangles (each rectangle is one quarter of the size of the image) are used as separate images, therefore allowing for the formation of 9 ellipses per thin section. Three perpendicular images are used in one sample, therefore nine segments from each image allow for 279 combinations of these ellipses. In unsegmented images, where one image is the equivalent of one segment, only three combinations are possible. Hence, the more combinations that are utilised in the analysis of each image, the more accurately the final ellipsoid is constrained. Once analyses had been undertaken on the samples in this study, it was clear that the segmentation process may not be statistically favourable in determining the petrofabric. Where each image was segmented into nine portions; many grains

were truncated at the segment to segment boundary and therefore misrepresented the fabrics each segment could produce. Therefore, for each sample the SPO results were obtained using segmented and unsegmented images.

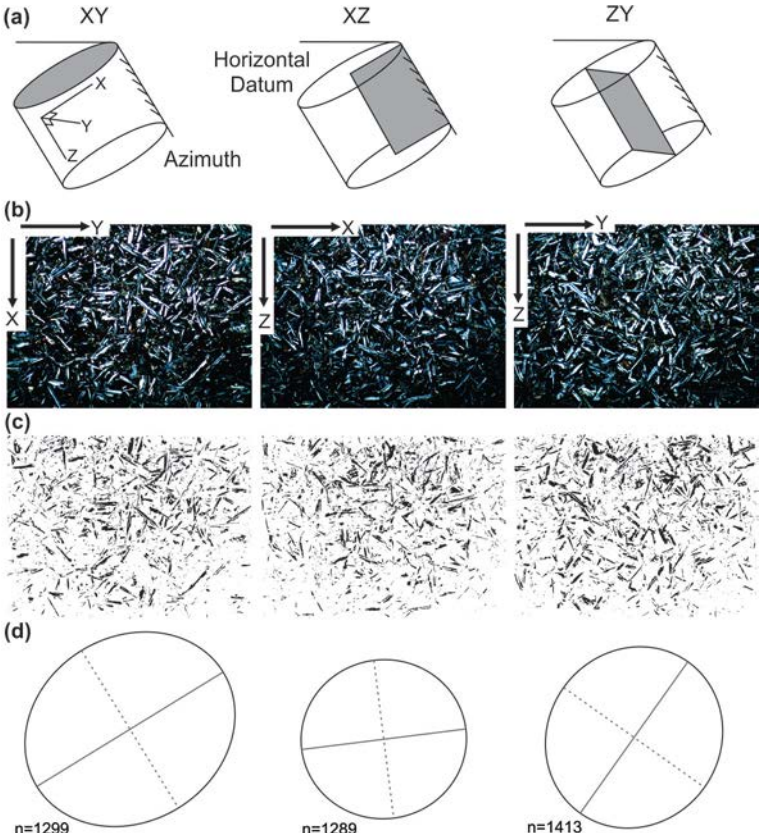

Fig. 4.3. (a) Diagram of the mutually perpendicular sections (grey) cut from a standard drill core sample. Each sample comprises three orthogonal sections as defined by an XYZ coordinate system after Hastie et al. (2011a). (b) Photomicrographs from sample SHF 6 LF taken under cross-polarisers (5 mm in width) with the coordinate directions shown down dip in black arrows. (c) Filtered images which are to be analysed in the SPO-2003 programme where the plagioclase grains have been extracted using a threshold grey scale value. (d) The resultant ellipse determined for each section.

When the ellipses are combined an error in the fit of the ellipsoid may occur and is measured by the Global Incompatibility Index ($\sqrt{F}$) (Launeau and Robin, 2005). A perfect fit of the three ellipses would result in a $\sqrt{F}$ value of 0. However the $\sqrt{F}$ value can be in excess of 26%, as in this study, where the compatibility of the ellipses in forming the final ellipsoid is low and therefore the ellipsoids may not be a reliable result. Results with $\sqrt{F}$ values < 10% are desirable (Launeau and Robin, 2005; Launeau et al., 2010) and are the generally accepted value below which the results may be trusted for accuracy.

4.3.3. Grain size

The long and short axes of the plagioclase grains were obtained using 2-D ellipse data from each sample set. For each image analysed, a table of data is acquired detailing the information obtained for every grain. The scale of the photomicrograph is used to change the scale of the images and therefore grains from pixels to millimetres. As the maximum size of the plagioclase grains in each thin section was the priority, an average long axis was determined for each sample. This was done by averaging the mean of the 10 largest grains from each section. This averaged maximum grain length is then used as a proxy for grain size for each sample. This does not accurately represent the mean grain size of each sample but is used as a tool for differentiating between samples at the same photomicrograph magnifications.

4.4. Results

Twelve dolerite sills were petrographically analysed to infer a magma flow regime. Here the processes and techniques used in order to determine the petrofabrics are described. The individual sample data for the sills from Thompson's Bay and Sheffield Beach are tabulated in Table 4.2 and Table 4.3 respectively. Examples of the petrofabric results are discussed in *Section 4.5* below, where these techniques have been applied to the fabric determination process.

4.4.1. Analyses errors

As the data were analysed, the results revealed that there were clear discrepancies in not only the final ellipsoid orientations but the $\sqrt{F}$ values for the same images at different magnifications (Fig. 4.4). For the samples photographed at 10x magnification there is a significant difference in the number of samples that have $\sqrt{F}$ values < 10% (Fig. 4.4). For the images obtained at the higher magnification (10x magnification) and segmented, there are no $\sqrt{F}$ values less than 4%. The mean $\sqrt{F}$ value is 12.7% and 27.8% of the data plot below 10% $\sqrt{F}$. For the unsegmented images at higher magnification the $\sqrt{F}$ values are much lower with a mean value of 6.8%; 76 results (78.4%) show $\sqrt{F}$ values lower than 10%. There is also a large fraction of data (21.3%) that show errors of between 0 – 2% $\sqrt{F}$, the closest fit that may be obtained for any ellipsoid.

This trend is mimicked in the lower magnification images; the mean $\sqrt{F}$ values for the segmented and unsegmented images are 8.3% and 4.7% respectively. At 2.5x magnification the $\sqrt{F}$ values that occur below the 10% $\sqrt{F}$ mark comprise 67.9% and 86.8% of the population of 53 samples for the segmented and unsegmented images respectively. No results have $\sqrt{F}$ values

Table 4.2. *SPO results from the Thompson's Bay sills including the petrofabric vecotr used to infer magma flow for each sample*

		Foliation			Maximum Axis		Minimum Axis					Grain size	Restored Foliation		Restored Lineation		Petrofabric Vector	
Sample	Mag.	Dip	Strike	Rake	Plunge	Trend	Plunge	Trend	[a]P'	[b]T	[c]vF(%)	proxy (mm)	Dip	Strike	Plunge	Trend	Plunge	Trend
TB-1 UA	10x	69.0°	265.0°	158.3°	20.2°	086.8°	21.0°	175.0°	1.158	*-0.551*	4.0	0.12	69.7°	256.5°	*41.5°*	*088.0°*	*41.5°*	*088.0°*
TB-1 UB	10x	61.4°	328.1°	037.2°	32.1°	348.1°	28.6°	238.1°	1.259	*-0.633*	6.0	0.14	41.8°	320.2°	*18.0°*	*335.5°*	*18.0°*	*335.5°*
TB-1 UC	10x	63.2°	221.2°	035.0°	30.8°	238.7°	26.8°	131.2°	1.147	*-0.310*	8.0	0.15	78.1°	215.5°	*10.3°*	*241.0°*	*10.3°*	*241.0°*
TB-1 UD	10x	29.4°	289.7°	044.4°	20.1°	330.3°	60.6°	199.7°	1.113	0.370	3.0	0.10	26.8°	248.0°			26.8°	338.0°
TB-1 UE	10x	63.8°	143.7°	151.4°	25.4°	310.2°	26.2°	053.7°	1.191	0.266	2.9	0.13	83.2°	146.4°			83.2°	236.4°
TB-1 UF	10x	54.8°	162.0°	098.7°	53.8°	266.9°	35.2°	072.0°	1.249	*-0.342*	4.1	0.13	76.5°	163.8°	*31.5°*	*265.0°*	*31.5°*	*265.0°*
TB-1 UG	10x	65.6°	188.4°	037.3°	33.5°	205.9°	24.4°	098.4°	1.785	*-0.579*	4.8	0.14	86.5°	187.2°	*19.6°*	*214.4°*	*19.6°*	*214.4°*
TB-1 UH	10x	38.8°	211.1°	095.1°	38.7°	307.6°	51.2°	121.1°	1.524	-0.276	10.1	0.17	57.9°	200.0°			57.9°	290.0°
TB-1 UI	10x	38.8°	235.3°	011.7°	07.3°	244.5°	51.2°	145.3°	1.803	*-0.800*	5.2	0.11	53.0°	216.4°	*14.0°*	*064.0°*	*14.0°*	*064.0°*
TB-1 UJ	10x	50.1°	070.5°	101.7°	48.6°	178.4°	39.9°	340.5°	2.026	*-0.317*	4.2	0.15	49.7°	089.3°	*41.5°*	*200.5°*	*41.5°*	*200.5°*
TB-1 UP	10x	35.9°	266.7°	164.0°	09.3°	073.7°	54.1°	176.7°	1.507	0.075	0.8	0.18	39.4°	238.2°			39.4	328.2°
TB-2 LA	10x	57.5°	306.4°	051.2°	41.1°	340.2°	32.5°	216.4°	1.153	0.252	0.4	0.07	64.5°	314.7°			64.5°	044.7°
TB-2 LC	2.5x	48.3°	178.3°	018.7°	13.9°	200.0°	41.7°	097.3°	1.388	0.372	4.3	0.63	29.2°	198.3°			29.2°	288.3°
TB-2 LD	10x	52.3°	201.8°	075.3°	50.0°	268.6°	37.7°	111.8°	2.773	0.011	3.4	0.31	37.0°	216.0°			37.0°	306.0°
TB-2 LE	2.5x	12.5°	267.0°	034.6°	07.1°	300.9°	77.5°	177.0°	1.543	0.128	3.5	0.73	26.0°	317.3°			26.0°	047.3°
TB-2 UA	10x	27.1°	151.9°	027.9°	12.3°	177.2°	62.9°	061.9°	1.075	0.087	5.8	0.11	08.7°	113.2°			08.7°	203.2°
TB-2 UB	10x	63.8°	203.4°	124.1°	48.0°	350.3°	26.2°	113.4°	1.314	*-0.847*	0.5	0.09	48.1°	212.3°	*45.5°*	*328.2°*	*45.5°*	*328.2°*
TB-2 UE	10x	36.8°	221.8°	123.7°	29.9°	351.6°	53.2°	131.8°	1.289	0.502	6.2	0.11	29.8°	252.5°			29.8°	342.5°
TB-2 UF	10x	75.5°	354.3°	050.8°	48.7°	011.3°	14.5°	264.3°	2.173	-0.224	3.2	0.16	83.3°	173.8°			83.3°	263.8°
TB-2 UG	10x	67.8°	349.9°	017.7°	16.4°	356.7°	22.2°	259.9°	1.156	*-0.681*	3.6	0.08	89.2°	349.2°	*18.6°*	*349.0°*	*18.6°*	*349.0°*
TB-2 UI	10x	74.8°	228.9°	119.8°	56.8°	024.3°	15.2°	138.9°	1.151	0.214	7.2	0.05	66.1°	235.9°			66.1°	325.9°
TB-2 UJ	10x	35.6°	302.3°	076.1°	34.4°	015.4°	54.4°	212.3°	1.148	-0.111	0.8	0.11	51.8°	315.7°			51.8°	045.7°
TB-2 UK	10x	53.5°	041.9°	122.1°	42.9°	178.4°	36.5°	311.9°	1.264	*-0.474*	3.5	0.10	67.0°	032.6°	*35.7°*	*194.3°*	*35.7°*	*194.3°*
TB-2 C(V)	10x	67.6°	230.0°	120.2°	53.1°	016.8°	22.4°	140.0°	4.128	*-0.790*	4.0	0.16	60.0°	239.9°	*58.5°*	*345.5°*	*58.5°*	*345.5°*
TB-2 D(V)	10x	27.1°	205.4°	144.9°	15.2°	353.4°	62.9°	115.4°	1.440	0.443	0.1	0.15	16.6°	252.4°			16.6°	342.4°
TB-2 H(V)	10x	38.6°	249.1°	104.6°	37.2°	357.5°	51.4°	159.1°	1.388	*-0.459*	3.2	0.12	40.1°	275.2°	*29.0°*	*341.0°*	*29.0°*	*341.0°*
TB-4 LA	10x	22.7°	147.1°	131.6°	16.8°	281.1°	67.3°	57.1°	1.565	0.443	8.9	0.16	10.2°	060.0°			10.2°	150.0°
TB-4 LB	10x	63.1°	185.0°	164.9°	13.4	358.1°	26.9°	095.0°	1.211	0.392	4.4	0.28	36.0°	192.0°			36.0°	282.0°
TB-4 LC	2.5x	57.1°	032.8°	055.3°	43.6°	070.9°	32.9°	302.8°	1.249	-0.262	5.7	0.39	77.0°	026.3°			77.0°	116.3°
TB-4 LE	2.5x	56.8°	016.2°	023.1°	19.2°	029.4°	33.2°	286.2°	1.577	-0.172	8.1	1.02	80.1°	012.0°			80.1°	102.0°
TB-4 UA	10x	67.4°	067.9°	166.5°	12.4°	242.7°	22.6°	337.9°	1.594	0.033	2.5	0.19	75.2°	060.0°			75.2°	150.0°
TB-4 UB	10x	52.8°	073.5°	082.4°	52.2	151.0°	37.2°	343.5°	1.454	-0.510	5.2	0.14	60.0°	057.5°	*53.0°*	*185.6°*	*53.0°*	*185.6°*
TB-4 UC	10x	72.5°	150.6°	125.0°	52.2°	307.4°	17.5°	060.6°	1.355	0.492	0.3	0.15	50.0°	145.7°			50.0°	235.7°
TB-4 UE	2.5x	72.0°	211.4°	124.7°	51.5°	007.4°	18.0°	121.4°	1.129	-0.362	0.4	0.68	53.6°	220.1°	*51.5°*	*335.0°*	*51.5°*	*335.0°*
TB-5 LA	10x	42.7°	295.3°	040.9°	26.4°	327.8°	47.3°	205.3°	1.311	-0.212	9.4	0.19	54.8°	304.0°			54.8°	034.0°
TB-5 LB	2.5x	35.6°	121.6°	039.3°	21.6°	155.2°	54.4°	031.6°	1.309	-0.551	4.3	0.31	25.5°	105.3°	*21.3°*	*161.0°*	*21.3°*	*161.0°*
TB-5 LC	2.5x	43.6°	338.0°	039.2°	25.9°	008.6°	46.4°	248.0°	1.146	0.060	7.7	0.25	60.0°	338.0°			60.0°	068.0°
TB-5 LD	2.5x	43.2°	005.4°	163.8°	11.0°	173.5°	46.8°	275.4°	1.298	0.183	7.7	0.37	58.0°	001.0°			58.0°	091.0°
TB-5 UA	10x	20.2°	201.2°	058.4°	17.1°	257.9°	69.8°	111.2°	1.370	0.660	7.3	0.17	12.5°	251.5°			12.5°	341.5°
TB-5 UB	10x	64.0°	112.1°	032.9°	29.2°	128.0°	26.0°	021.1°	1.286	-0.550	6.1	0.14	53.8°	104.6°	*36.0°*	*136.8°*	*36.0°*	*136.8°*
TB-5 UC	10x	50.3°	235.1°	070.3°	46.4°	295.9°	39.7°	145.1°	1.111	0.719	1.9	0.15	48.6°	249.0°			48.6°	339.0°
TB-5 UD	10x	46.6°	223.8°	059.1°	38.6°	272.7°	43.4°	133.8°	1.079	-0.306	2.9	0.15	41.0°	240.0°			41.0°	330.0°

a P' = degree of anisotropy

b T = shape parameter (oblate/prolate)

c vF = Global Incompatibility Index

Table 4.3. *SPO results from the Sheffield Beach sills including the petrofabric vector used to infer magma flow for each sample*

		Foliation			Maximum Axis		Minimum Axis					Grain size	Restored Foliation		Restored Lineation		Petrofabric Vector	
Sample	Mag.	Dip	Strike	Rake	Plunge	Trend	Plunge	Trend	[a]P'	[b]T	[c]vF (%)	proxy (mm)	Dip	Strike	Plunge	Trend	Plunge	Trend
SHF-2 LA	10x	53.9°	106.6°	053.4°	40.5°	145.1°	36.1°	016.6°	1.550	*-0.315*	8.6	0.27	61.0°	118.6°	*56.0°*	*145.0°*	*56.0°*	*145.0°*
SHF-2 LB	2.5x	86.9°	297.5°	046.6°	46.5°	300.8°	03.1°	207.5°	1.216	0.558	0.8	0.58	78.2°	295.3°			78.2°	025.3°
SHF-2 LC	10x	68.6°	056.0°	147.1°	30.4°	222.7°	21.4°	326.0°	1.124	0.436	5.2	0.17	58.5°	065.0°			58.5°	155.0°
SHF-2 LD	2.5x	63.9°	047.9°	048.6°	42.2°	074.5°	26.1°	317.9°	1.255	0.220	2.2	0.33	51.2°	057.3°			51.2°	147.3°
SHF-2 LE	2.5x	43.0°	036.1°	098.1°	42.5°	137.1°	47.0°	306.1°	2.599	*-0.664*	3.4	0.95	29.3°	055.2°	*27.0°*	*127.4°*	*27.0°*	*127.4°*
SHF-2 UA	10x	73.4°	142.5°	068.7°	63.2°	178.8°	16.6°	052.5°	1.351	*-0.501*	6.8	0.10	89.4°	144.2°	*27.8°*	*134.3°*	*27.8°*	*134.3°*
SHF-2 UB	10x	60.2°	220.5°	061.6°	49.7°	263.1°	29.8°	130.5°	1.272	0.153	2.6	0.14	75.9°	215.4°			75.9°	305.4°
SHF-2 UC	10x	89.6°	063.2°	131.9°	48.1°	242.7°	00.4°	333.2°	1.327	-0.001	5.4	0.13	80.2°	064.3°			80.2°	154.3°
SHF-2 UD	2.5x	79.8°	081.2°	057.0°	55.7°	096.4°	10.2°	351.2°	1.210	-0.189	0.1	0.49	77.4°	085.2°			77.4°	175.2°
SHF-3 LA	10x	76.8°	282.6°	018.3°	17.8°	286.9°	13.2°	192.6°	1.869	0.118	2.5	0.20	68.3°	278.0°			68.3°	008.0°
SHF-3 LB	10x	50.2°	232.8°	125.7°	38.6°	011.1°	39.8°	142.8°	1.387	-0.809	3.0	0.18	57.0°	221.0°	*29.0°*	*020.6°*	*29.0°*	*020.6°*
SHF-3 LC	10x	48.8°	165.9°	136.7°	31.0°	314.1°	41.2°	075.9°	1.121	-0.358	5.1	0.18	65.0°	164.7°	*37.0°*	*325.0°*	*37.0°*	*325.0°*
SHF-3 LD	10x	69.4°	013.5°	118.9°	55.1°	161.0°	20.6°	283.5°	1.413	-0.109	0.3	0.27	55.5°	018.5°			55.5°	108.5°
SHF-3 UA	10x	25.5°	003.5°	142.3°	15.2°	148.7°	64.5°	273.5°	1.566	-0.024	9.0	0.20	12.0°	034.0°			12.0°	124.0°
SHF-3 UB	10x	69.8°	287.2°	047.7°	43.9°	308.0°	20.2°	197.2°	1.133	0.234	4.7	0.17	60.6°	281.5°			60.6°	011.5°
SHF-3 UC	10x	53.6°	033.4°	083.9°	23.4°	116.7°	36.4°	303.4°	1.532	-0.581	0.3	0.18	44.4°	045.3°	*25.5°*	*085.0°*	*25.5°*	*085.0°*
SHF-3 UD	10x	70.9°	212.4°	096.8°	69.7°	322.4°	19.1°	122.4°	1.203	-0.313	1.3	0.13	80.7°	209.5°	*66.0°*	*008.0°*	*66.0°*	*008.0°*
SHF-4 LA	10x	74.6°	245.5°	019.2°	18.4°	250.8°	15.4°	155.5°	1.126	-0.453	3.5	0.11	78.0°	242.4°	*30.3°*	*250.0°*	*30.3°*	*250.0°*
SHF-4 LC	10x	86.3°	341.3°	140.6°	39.3°	158.2°	03.7°	251.3°	1.297	-0.640	4.5	0.12	74.3°	341.0°	*36.0°*	*150.0°*	*36.0°*	*150.0°*
SHF-4 UA	10x	66.9°	180.6°	149.1°	28.1°	347.7°	23.1°	090.6°	1.480	-0.659	4.7	0.15	78.2°	180.0°	*28.0°*	*354.0°*	*28.0°*	*354.0°*
SHF-4 UB	10x	44.2°	316.1°	068.9°	40.6°	017.9°	45.8°	226.1°	1.420	-0.081	2.7	0.10	34.0°	305.2°			34.0°	305.2°
SHF-4 UC	10x	54.2°	174.3°	047.8°	36.9°	207.0°	35.8°	084.3°	1.213	0.432	0.7	0.12	65.5°	173.9°			65.5°	263.9°
SHF-4 UD	10x	84.2°	294.9°	133.7°	46.0°	108.9°	05.8°	204.9°	1.341	-0.475	8.1	0.14	77.8°	293.0°	*35.5°*	*104.7°*	*35.5°*	*104.7°*
SHF-5 LE	10x	78.6°	289.8°	138.2°	40.8°	099.7°	11.4°	048.2°	1.172	-0.233	2.0	0.16	75.0°	288.0°			75.0°	018.0°
SHF-5 LF	10x	73.2°	069.3°	079.3°	70.1°	126.1°	16.8°	349.3°	1.394	-0.522	2.1	0.14	71.0°	072.0°	*51.0°*	*112.0°*	*52.0°*	*112.0°*
SHF-5 UA	10x	61.9°	169.4°	011.9°	10.5°	175.1°	28.1°	281.9°	1.098	0.188	4.1	0.08	71.6°	169.5°			71.6°	259.5°
SHF-5 UB	10x	28.0°	168.4°	106.3°	26.8°	276.7°	62.0°	016.3°	1.164	-0.182	8.7	0.16	38.0°	170.4°			38.0°	260.4°
SHF-5 UF	10x	71.3°	294.3°	046.3°	43.2°	312.9°	18.7°	316.3°	1.439	-0.128	1.7	0.21	66.4°	290.6°			66.4°	020.6°
SHF-6 LA	10x	65.4°	066.0°	053.4°	46.9°	095.3°	24.6°	323.4°	1.475	0.212	1.6	0.23	58.0°	072.0°			58.0°	162.0°
SHF-6 LB	2.5x	87.8°	243.3°	084.4°	83.9°	264.9°	02.2°	354.4°	1.213	0.236	4.6	0.46	79.0°	056.0°			79.0°	146.0°
SHF-6 LC	2.5x	61.5°	209.8°	167.8°	10.7°	023.9°	28.5°	077.8°	1.053	0.139	3.0	0.38	72.5°	208.0°			72.5°	298.0°
SHF-6 LD	2.5x	30.4°	043.7°	114.3°	27.4°	161.4°	59.6°	024.3°	1.072	-0.344	2.3	0.32	20.0°	061.8°	*19.7°*	*156.3°*	*19.7°*	*156.3°*
SHF-6 LF	2.5x	43.6°	037.1°	032.6°	21.8°	061.9°	46.4°	302.6°	1.195	-0.262	4.6	0.58	32.0°	045.5°			32.0°	135.5°
SHF-6 UA	10x	64.5°	079.9°	115.6°	54.4°	218.0°	25.5°	025.6°	1.353	0.116	8.2	0.20	60.0°	086.2°			60.0°	176.2°
SHF-6 UB	2.5x	84.8°	283.2°	039.2°	39.1°	287.5°	05.2°	309.2°	1.168	-0.421	0.8	0.51	85.3°	281.8°	*51.0°*	*288.0°*	*51.0°*	*288.0°*
SHF-6 UC	10x	13.5°	039.7°	066.6°	12.4°	105.7°	76.5°	336.6°	1.237	-0.049	1.7	0.12	06.0°	119.0°			06.0°	209.0°
SHF-6 UD	10x	76.6°	059.7°	079.1°	72.8°	109.9°	13.4°	349.1°	1.195	-0.352	3.2	0.18	68.4°	061.5°	*59.0°*	*105.0°*	*59.0°*	*105.0°*
SHF-6 UF	2.5x	08.2°	025.0°	021.1°	02.9°	045.9°	81.8°	291.1°	1.109	-0.222	2.0	0.34	03.5°	183.0°			03.5°	273.0°
SHF-6 UG	2.5x	34.6°	123.3°	111.5°	31.9°	238.8°	55.4°	021.5°	1.208	0.581	0.5	0.43	40.4°	138.2°			40.0°	228.2°

a P' = degree of anisotropy

b T = shape parameter (oblate/prolate)

c vF = Global Incompatibility Index

< 2% for the segmented images whereas 28% of the √*F* values for the results determined using unsegmented images are between 0 – 2% √*F*.

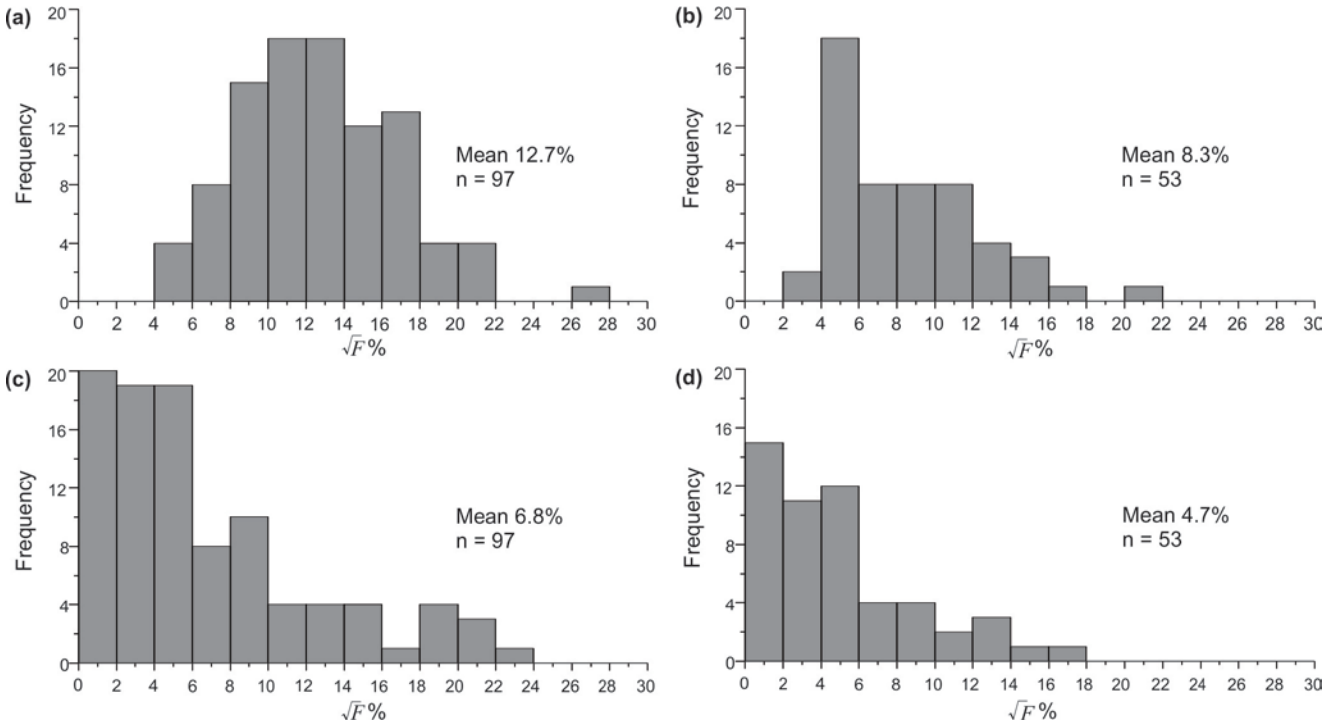

Fig. 4.4. Histograms depicting the frequency of √*F* values (% - Global Incompatibility Index) for (a) segmented images acquired at 10x magnification; (b) segmented images acquired at 2.5x magnification; (c) unsegmented images acquired at 10x magnification and (d) unsegmented images acquired at 2.5x magnification.

4.4.2. Relationship between plagioclase grain size and √F values

Fig. 4.5 illustrates the relationships between the maximum long axis length of the plagioclase grains and the √*F* values calculated for each sample when the images were segmented and unsegmented. Where the images were not segmented, the √*F* values increase as the maximum length of the plagioclase long axes increases, for all magnifications. For the lower magnification, the range of long axis lengths are from 0.20 mm to 0.64 mm, with 36 results yielding √*F* values of less than 10%. The 27 results that have √*F* values of less than 10% for the higher magnification do not exceed a long axis length of 0.204 mm. However 44% of the results have a grain size of < 0.20 mm with errors exceeding 10%. The r^2 values for the linear functions defining these proportional relationships are 0.62 for the 2.5x magnification images and 0.44 for the 10x magnification images. For the unsegmented images at both magnifications, the majority of the long axis data plot below the 10% √*F* boundary.

The minimum long axis length measured for the lower magnification images when the image is segmented or not segmented is the same length of 0.20 mm. This is also true of the higher magnification image where a minimum long axis length of ~0.05 mm was measured and the maximum long axis length with a $\sqrt{F}$ value of less than 10% is 0.32 mm.

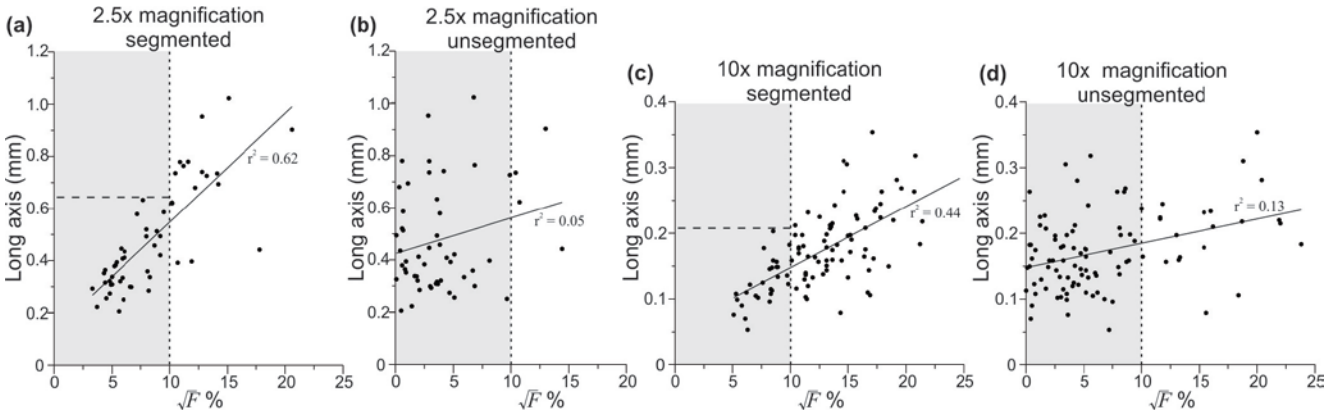

Fig. 4.5. Graphical representations of $\sqrt{F}$ values (%) against the grain size proxy for plagioclase of (a) segmented images at 2.5x magnification; (b) unsegmented images acquired at 2.5x magnification; (c) segmented images acquired at 10x magnification and (d) unsegmented images acquired at 10x magnification.

4.4.3. Strike differences between segmented and unsegmented images

Four results were determined for more than half of the samples because photomicrographs of the thin sections were taken at both higher and lower magnifications and analysed using segmented and unsegmented techniques. In order to resolve which result best defines the petrofabric, the resultant strikes of the foliations of the segmented and unsegmented images were plotted one against the other (Fig. 4.6). With an r^2 of 0.86, there is an acceptable fit between the resultant petrofabric strikes determined for the segmented and unsegmented images. Even though two methods were used, most of the samples showed similar direction values.

The outliers highlighted in dark grey (Fig. 4.6) have discrepancies of between 10º and 60º but do not plot near the bulk of the data as direction results from the segmented images exceed 360º, whereas the unsegmented directions do not. The data points highlighted in light grey represent results that dip in opposite directions (180° away) with respect to one another (Fig. 4.6).

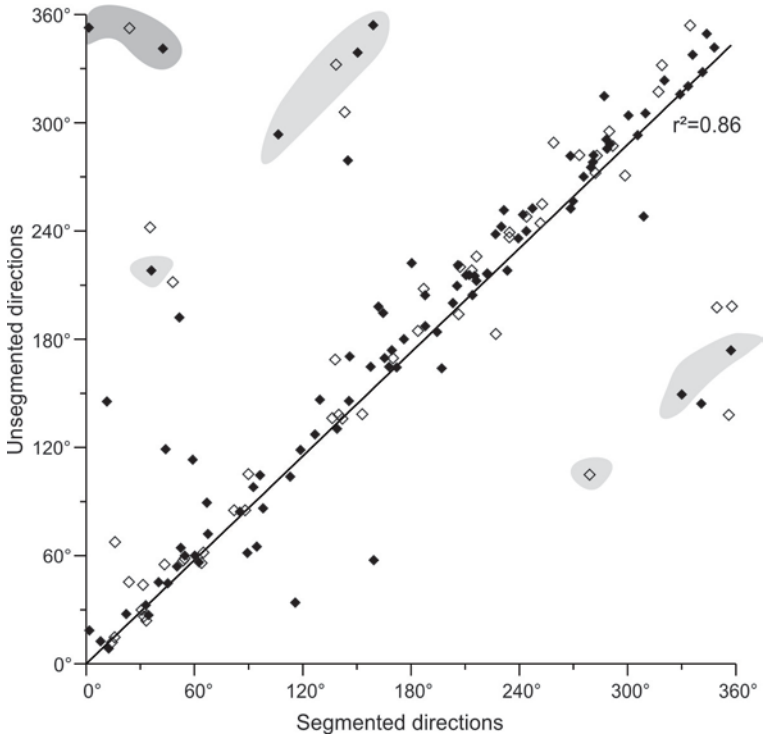

Fig. 4.6. Graphically represented direction values determined using the segmented and unsegmented images. The black diamonds are the results for the images at 10x magnification and the open diamonds are the results for the images at 2.5x magnification. Highlighted in dark grey are direction values with low discrepancies that do not plot on the trend line whereas the data points highlighted in light grey have values that are ~180º apart.

4.4.4. Ellipsoid shape and anisotropy

Results obtained using the SPO-2003 programme are defined in shape according to the shape parameter (T) and the corrected degree of anisotropy (P'). The shape parameter defines the ellipsoid as oblate when T > 0; triaxial when T = 0 and prolate when T < 0 (Jelinek, 1981; Tarling and Hrouda, 1993). Prolate fabrics are the dominant shape with 59.2% of the data having T values < 0 and an average value of -0.091 which is close to triaxial in shape (Fig. 4.7).

The average P' value (Jelinek, 1981) of the plagioclase fabric is 1.397, showing a strong degree of anisotropy. The highest P' values are found in the sills TB1, TB2, TB4 and SHF2 where sample TB 2C(V) has a degree of anisotropy of 4.128 (Table 4.2).

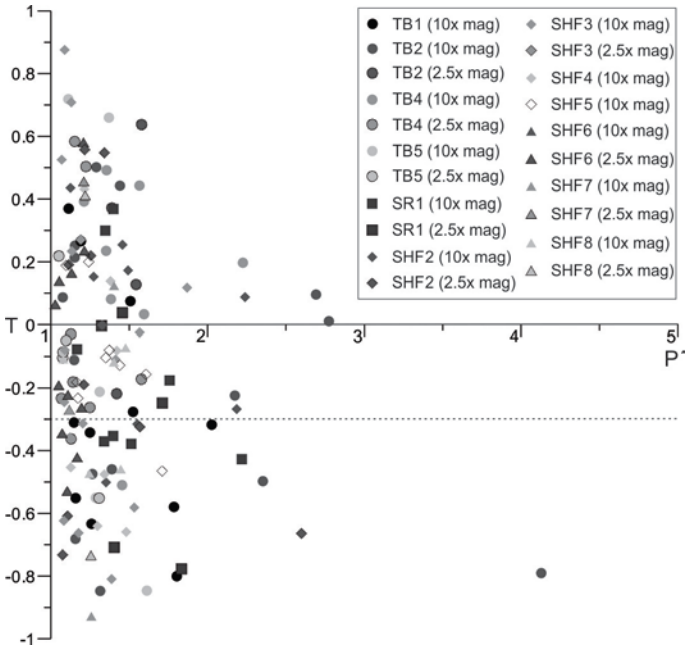

Fig. 4.7. Graphical illustration describing the plagioclase SPO fabric through the use of the degree of anisotropy (P') and the shape parameter (T); where the shape of the ellipsoid is oblate when T > 0 and prolate when the T < 0. The dashed line at T = -0.3 represents the value below which the samples are distinctly prolate.

4.4.5. Karoo dolerite sills

The above techniques have been applied to the samples from Thompson's Bay (Table 4.2) and Sheffield Beach (Table 4.3) with data from sills shown here in detail (Fig. 4.8 and 4.9 respectively). It should be noted that three sills, SR1, SHF7 and SHF8, have been used in the analytical portion of this study have been excluded in the following section because the data from the intrusions are limited and incomplete.

The petrofabrics determined for the sills from Thompson's Bay (Fig. 4.8) and Sheffield Beach (Fig. 4.9) are individually analysed. Arrows have been used to indicate the direction of the petrofabric derived from the SPO results at the sampling locality. Black arrows indicate the azimuth of the foliation and the red arrows represent the plunge direction of the lineations selected to represent the petrofabric. The length of the arrows indicates how steep the dip/plunge is for each petrofabric. Small grey stars have been drawn where there are morphological obstacles along the upper or lower contacts such as broken bridges or steps. The stars shown on TB1 and TB2 (Fig. 4.8b and c) represent magmatically formed ropy-flow structures (e.g. Liss et al., 2002).

The dip and azimuth of each foliation and plunge and plunge direction of each lineation have been stereographically displayed for the upper and lower contacts of each sill. The great circle on each stereogram is the dip and strike of the tilted country rock (Table 4.1). All the data have been plotted as lineations and then restored to the horizontal according to the country rocks dip and strike (Table 4.2 and 4.3).

4.4.5.1. Examples from Thompson's Bay

Four sills were analysed in detail from the Thompson's Bay area (Fig. 4.8), namely TB1, TB2, TB4 and TB5. TB1 contains small amygdales, xenoliths (partially disintegrated) and ropy-flow structures near the upper contact. TB2 is morphologically similar to TB1 and comprises all the same features. These features occur in discrete layers from (1) massive at the base to (2) finely and abundantly amygdaloidal in the centre to (3) a zone of elongated vesicles to (4) a massive unit comprising aligned xenoliths ~40 cm below the upper contact (Table 4.1). TB4 and TB5 are massive however TB4 has a central vesicle stringer and spherulitic plagioclase (Table 4.1).

Only the upper contact of TB1 was sampled as the lower contact was inaccessible. All the images were obtained at 10x magnification due to the fine grain size. Of the 11 samples analysed, eight of the resultant petrofabrics had prolate fabrics ($T < 0$) with seven of these samples having defined the petrofabric using lineation data. In Fig. 4.8b, the stereographically plotted petrofabrics show a spread of data; however two average directions may be interpreted as two petrofabrics with plunge and plunge directions of 31°/240° and 28°/334° respectively. The two average petrofabrics plunge ~90° away from each other.

Three zones were sampled for TB2, the upper and lower contacts and a 0.5 m thick vesicular zone which starts ~0.5 m below the upper contact of the intrusion and is laterally continuous. Four results were obtained for the lower zone, three results within the vesicular zone and eight results from the upper contact. A combination of 2.5x and 10x magnification images were selected to represent the petrofabrics for the lower zone as the plagioclase grain size was coarser at the base of the sill. Images obtained at 10x magnification were used for the upper contact and vesicular zone. All of the samples for the lower contact show oblate shapes with the shape of the fabrics for the upper contact and vesicular zones being both prolate and oblate.

The average petrofabrics obtained for the sampled zones of TB2 all showed moderate plunge angles that plunge towards the NNW. The data from the vesicular zone showing very little variation and constrain a well-defined fabric. The average plunge and plunge direction of the

lower contact, vesicular zone and upper contact are 54°/329°; 34°/343° and 46°/352° respectively (Fig. 4.8d). All of the results determined for the contacts and the vesicular zone plunge within a 25° directional range towards ~340°.

The upper and lower contacts of TB4 were sampled and four results were obtained from both of the contacts. Three of the results were determined using low magnification images. Four of the results showed prolate fabrics, with two of those results exhibiting strongly prolate fabrics and therefore resulting in the fabric being defined by the lineation. The data from each contact are wide-spread when stereographically represented yielding steeply inclined average fabrics (Fig.

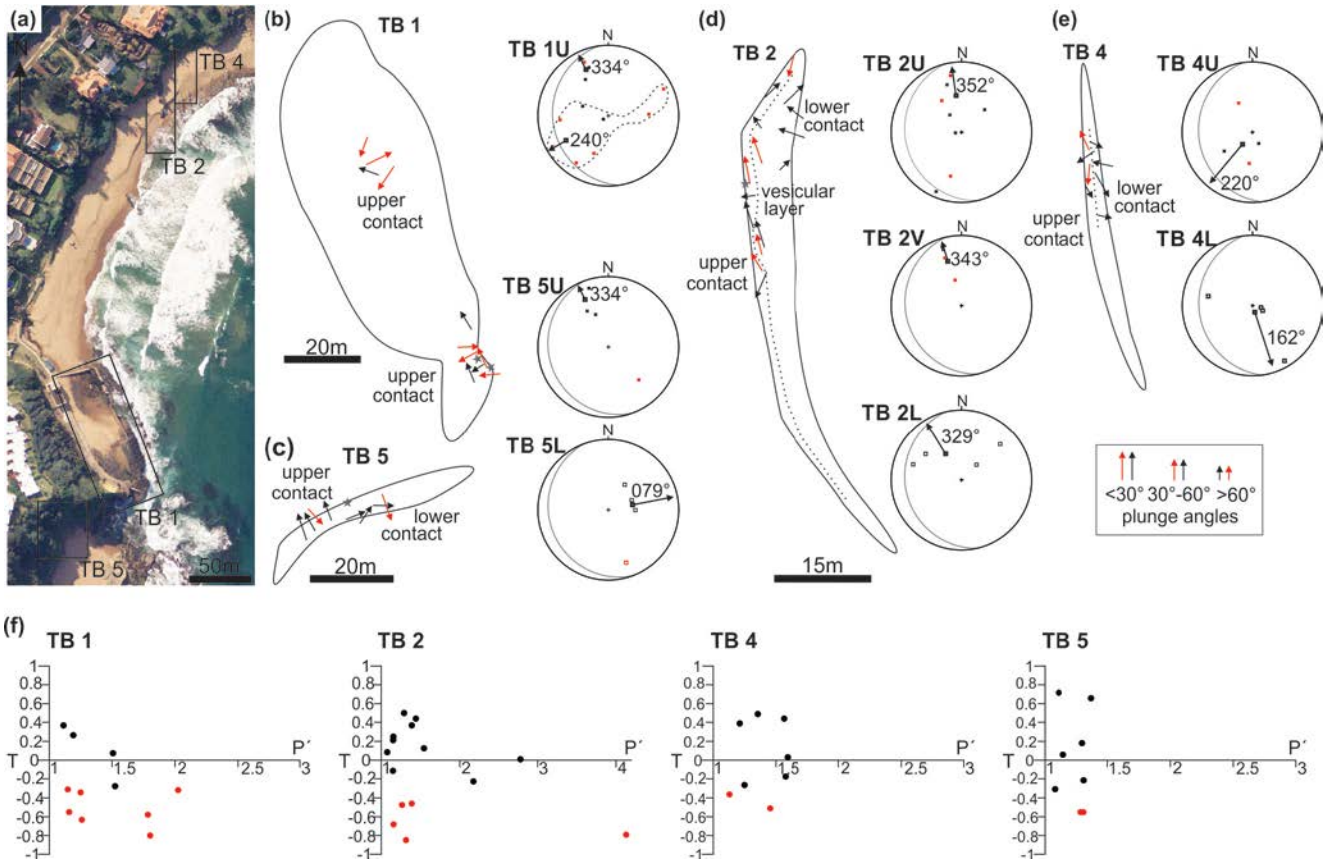

Fig. 4.8. (a) An aerial photograph of Thompson's Bay showing the layout and localities of the sills TB1, TB2, TB4 and TB5. (b) Samples from the upper contact of TB1 shown spatially along the exposed upper surface of the intrusion. The grey stars represent ropy-flow structures ~10 cm below the upper contact. The stereographic projection of TB1 shows the grouping of the results into two perpendicular averages. (c) Upper and lower contact results for TB5 and the stereographically projected fabrics, the grey star represents a small broken bridge along the upper contact (d) The results from TB2 are separated into the upper and lower contacts and the vesicular layer (right of the dashed line), the results for each layer/contact are stereographically presented and all plunge in the same general direction. The grey star represents an exposure of a layer of preferentially aligned elongated vesicles. (e) Schematically the upper and lower contacts of TB4 are separated by a dashed line with the data projected stereographically for each contact. Black arrows and red arrows represent fabrics in the schematics determined using the foliation and the lineation respectively. For the stereographic projections, the black points represent the foliation data, the red points represent the lineation data and the grey great circle is the dip and strike about which the data points have been restored to the horizontal. (f) P'/T plots for TB1, TB2, TB4 and TB5 with the black circles and red circles representing samples where the fabric was determined using the foliation and the lineation respectively.

4.8e). The plunge and plunge directions of the fabric in lower and upper contacts are 82°/162° and 72°/220° respectively, depicting an oblique relationship with ~60° separating the two averages.

Four results were obtained for both the upper and lower contacts of TB5 and are stereographically presented in Fig. 4.8c. Three of the eight results used low magnification images to determine the fabric. Two of the four prolate-shaped fabrics were classified as strongly prolate fabrics resulting in the lineation being used to determine the petrofabrics. The average fabric of the upper contact has a plunge and plunge direction of 26°/334°. The plunge and plunge direction of the lower contact fabric is 61°/079°, plunging at a steep angle ~90° away from the average petrofabric of the upper contact.

The sills TB1, TB2 and TB5 show a similar petrofabric average with respect to the results from the upper contacts. Overall the resultant petrofabrics of the upper contact of these three intrusions plunge at ~30° towards the NNW (Fig. 4.8). For the contacts TB1U and TB5U the average plunge directions are aligned and plunge towards 334°.

4.4.5.2. Examples from Sheffield Beach

Five sills at Sheffield Beach were analysed in this study including SHF2, SHF3, SHF4, SHF5 and SHF6 (Fig. 4.9). Compositionally the intrusions are all similar, with intrusions SHF4 and SHF5 showing a higher degree of alteration than the other sills. Only five results from SHF5 were conclusive in determining the petrofabric, as the other samples showed little to no fresh plagioclase. Morphologically the intrusions range in thickness from 1 m thick (SHF2) to 2.5 m thick (SHF6) and all the sills exhibit broken bridges and/or steps along the contacts with the country rocks. SHF4 and SHF6 are massive, SHF2 has a central vesicle stringer and SHF3 shows three parallel amygdaloidal stringers towards the upper contact of the intrusion.

Nine results were obtained from the samples from SHF2 (Fig. 4.9b), five from the lower contact and four from the upper contact. Four results were determined using samples photographed at 2.5x magnification. Four of the results showed prolate fabrics where $T < 0$ and of those four samples, three lineations were used to determine the petrofabric. The majority of the petrofabric data were steeply dipping with 78% of the results exhibiting angles of > 50°. Both of the contacts showed well-defined fabrics, with the average plunge and plunge directions being 77°/153° and 57°/139° for the upper and lower contacts respectively. The fabrics determined for the upper and lower contacts thus both plunge between the SE and SSE. Two results, one from

the upper contact and one from the lower contact, plunge in an opposite sense to the averages determined and appear to be in the same local position within the sill.

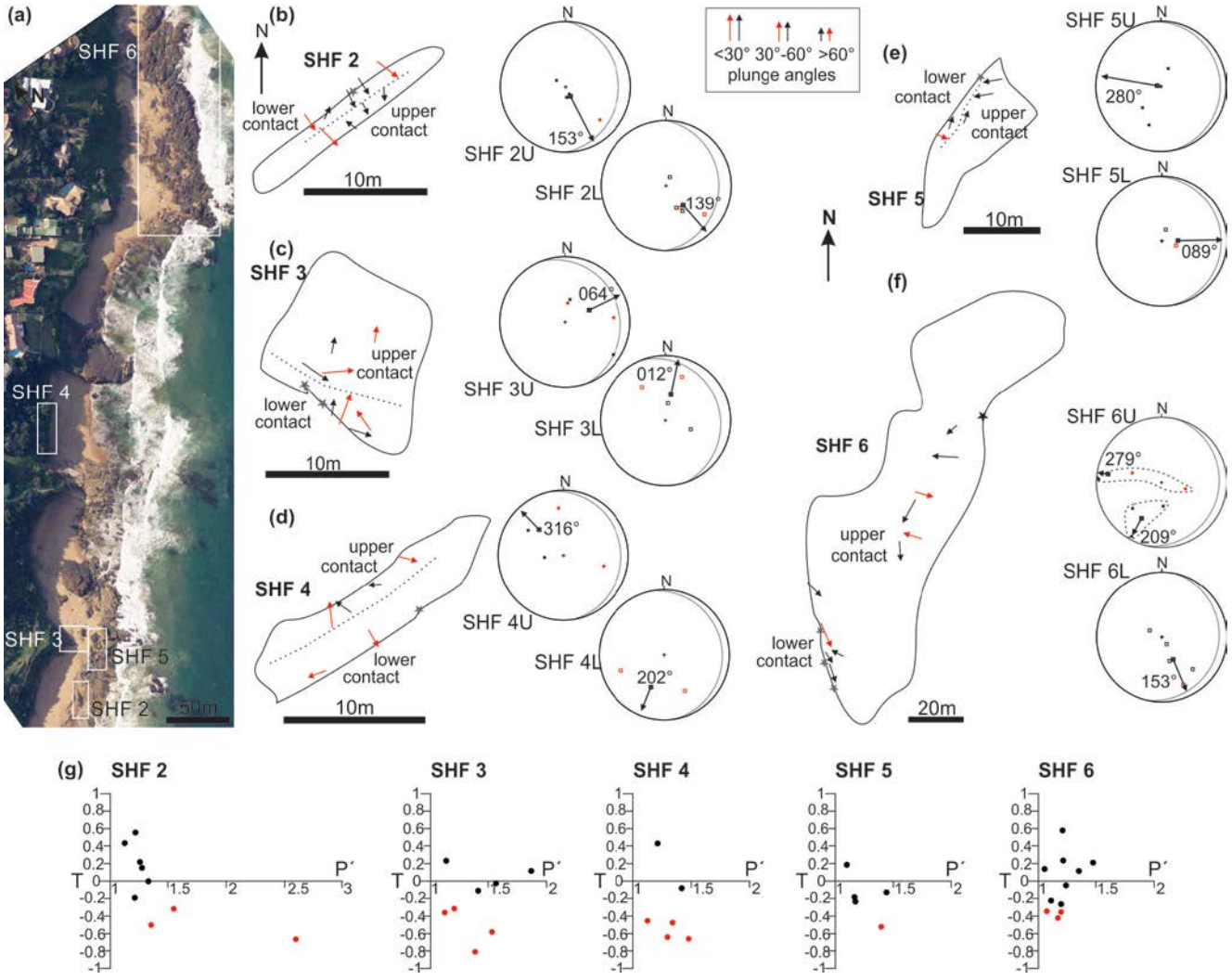

Fig. 4.9. (a) An aerial photograph of the southern portion of Sheffield Beach outlining the five sills sampled. (b) Schematic and stereograms showing the petrofabric directions determined for the upper and lower contacts of SHF2. The grey arrow represents a broken bridge remnant along the upper contact of the sill. (c) A schematic of SHF3 with the upper and lower contact results separated by a dashed line. Note the similarity of adjacent results along both the upper and lower contacts. The grey arrows indicate broken bridges preserved along the sill's lower contact. (d) The upper and lower contact results from SHF4 represented schematically and stereographically. The grey arrow indicates the position of a large step for the upper and lower contacts of the intrusion. (e) The upper and lower contact results of SHF5 are schematically separated by a dashed line. A few small steps are noted along the upper contact of the intrusion and indicated with a grey star. The stereographic projections of the sill data show that the petrofabrics from the upper contact dip in the opposite direction the lower contact data. (f) The largest sill sampled is SHF6 and the dolerite has intruded into a previous dolerite intrusion. The schematic and the stereograms show two distinct plunge directions along the upper contact and a consistent direction along the lower contact. The grey arrows represent small broken bridges of dolerite material whereas the black arrow indicates a large broken bridge structure of country rock material. (g) P'/T plots for SHF2, SHF3, SHF4, SHF5 and SHF6 with the black circles and red circles representing samples where the fabric was determined using the foliation and the lineation respectively.

For the sill SHF3 eight samples yielded results with four samples obtained from both the lower and the upper contacts; all the results were determined using 10x magnification images. Six of the eight samples showed prolate fabrics, with four of these results using lineations to determine the petrofabric direction. There is a large stereographic spread of the petrofabric data for both the upper and the lower contact (Fig. 4.9c). Schematically, there appears to be groupings of petrofabric directions along certain portions of both the upper and lower contacts for the intrusion (Fig. 4.9c). The average plunge and plunge directions of the upper and lower contact are 56°/064° and 57°/012° respectively; the errors associated with these averages are above average. Both averages for the contacts plunge in a general NE direction separated by ~40°.

The samples from SHF4 were petrographically poor in quality however when photographed at 10x magnification, all of the samples yielded adequate results. Six results were obtained, four of these from the upper contact and two from the lower contact (Fig. 4.9d). Only one sample showed an oblate shape and four samples, out of the five prolate samples, used the lineation to determine the petrofabric. The average plunge and plunge directions of the upper and lower contacts are 45°/316° and 45°/202°, therefore the averages were separated by ~110° between the two contacts. However, due to the low number of samples for the lower contact data, this result may not be statistically significant.

For the intrusion SHF5, only five results were obtained from the nine samples prepared due to a higher degree of alteration than that of the other sills. Of the five results, three were from the upper contact and two were from the lower contact. All five of these results were obtained using 10x magnification images. Four of the samples showed prolate fabrics with one result utilising the lineation to determine the petrofabric. As there is a wide spread of directional data, as seen when stereographically presented, the angles of the resultant fabric are steep (Fig. 4.9e). The average plunge and plunge directions of the upper and lower contact are 69°/280° and 70°/089° respectively and plunge in opposite directions with respect to one another.

Eleven samples from the upper and lower contacts of SHF6 yielded results, with the majority of the samples (64%) utilising the 2.5x magnification images. Six of the results exhibited prolate shapes with three of those samples determining the petrofabric through the use of the lineation. The petrofabric for the lower contact was well-defined with an average plunge and plunge direction of 58°/153°. For the upper contact, two population averages were inferred, showing a strong fabric plunging towards the SSW and a stronger correlation of results towards the W as seen in Fig. 4.9(f). The plunge and plunge directions for the two average petrofabrics for the

upper contact are 37°/209° and 18°/279°. Between the upper and lower contacts the relationships between the petrofabric averages are oblique.

For the intrusions sampled at Sheffield Beach there is very little similarity between the results from the separate sills. No two sills show the same average petrofabrics for either the upper or the lower contacts. The only directions that coincide are the upper contact averages of SHF5 and SHF6 which plunge in a westerly direction.

4.5. Discussion

4.5.1. Importance of √F, grain size and image segmentation

When images are segmented the grains are analysed in the set compartment they have been separated into. This causes grains (particularly when enlarged at higher magnifications) to be intersected and truncated by these segment boundaries or compartments. As the plagioclase crystals here are predominantly elongate, the segmented grains inaccurately represent the long and short grain axes. This can then affect the shape and therefore the ellipse from each image which then combined could alter the ellipsoid of the result in terms of the $\sqrt{F}$ values.

$\sqrt{F}$ values obtained through the use of the SPO-2003 programme calculate the incompabililty of the fit of the three 2-D ellipses into one 3-D ellipsoid. As the $\sqrt{F}$ increases, the compatibility of the final ellipsoid decreases. Results with $\sqrt{F}$ values of less than 10% are desirable therefore 10% $\sqrt{F}$ has been used as a threshold error above which the results are disregarded as being inaccurate in defining the sample petrofabric. The segmentation of the images has a pronounced effect on the $\sqrt{F}$ values when compared to the unsegmented images for images taken at both higher and lower magnifications. The images taken at 10x magnification showed a mean $\sqrt{F}$ value of 12.7% for the segmented images and 6.8% $\sqrt{F}$ for the unsegmented images. Only 27.8% of the segmented data is below 10% $\sqrt{F}$ whereas 78.4% of the unsegmented data are below the $\sqrt{F}$ 10% threshold. This is also the case with the lower magnification images but not to the same extent as the higher magnification data.

One way of reducing the $\sqrt{F}$ values for the results is to ensure the images are obtained at the ideal magnification for the size of the plagioclase grains. A threshold grain size can be determined using the segmented and unsegmented data from the lower and higher magnification data. At 10x magnification all of the results with $\sqrt{F}$ values < 10% have long axis lengths of < 0.2 mm. Therefore 0.2 mm has been designated as the grain size threshold for the grain size proxy to delineate the millimetre scale limit at which higher magnification images should be

obtained. If images are taken at the correct magnification, the error values for the results should be greatly reduced.

It thus appears that the problem with high $\sqrt{F}$ values is directly related to the image segmentation process. There is little difference between the actual direction results acquired when using the segmented versus the unsegmented technique as observed by the r^2 of 0.86 for the 150 results (Fig. 4.6). The errors ($\sqrt{F}$ values) observed from the results of the segmented images are almost always higher than with the results from the unsegmented images (Fig. 4.4). Therefore in order to reduce the error to a minimum, the segmented image data were disregarded and the unsegmented analysis process was relied upon instead. Using these parameters would allow for the most accurate results to be determined for the most compatible ellipsoids.

4.5.2. Shape constraints

The actual result that should be used for each sample site can be further constrained using the shape of the fabric as this affects the petrofabric result. For strongly prolate fabrics ($T < -0.3$) the minimum and intermediate axes of the shape ellipse become comparable in length, therefore the maximum axis defines the lineation that may be used to infer the plunge and plunge direction of the petrofabric. Where $T > -0.3$ the oblate fabric is defined using the dip and azimuth of the plane defined by the minimum axis.

This will determine a single result per sample site which would be the most theoretically and statistically robust. This is obtained by disregarding the segmented image data and thresholding the grain size in order to elucidate which images should be used for each analysis. Where there was an overlap of accurate results between the magnifications for one sample, the sample that exhibited the lower $\sqrt{F}$ value was manually selected; this was undertaken for 6% of the data.

4.5.3. Petrofabrics as magma flow indicators

The petrofabrics determined for the samples may have formed as a result of magma flow. In order to establish the origin of a fabric within an intrusion, certain criteria must be analysed such as the timing of fabric formation and the regional setting. It is apparent from the host rocks that there have been no regional ductile deformation or metamorphism associated with or post-dating the intrusion of these sills. The fabrics observed in the intrusions are therefore the result of internal processes and are a product of strain within the magma (Nicholas, 1992; Paterson et al., 1998). Such strain may be brought about by the original magma flow and may be affected

by internal processes such as magma convection or surges (Benn and Allard, 1989; Paterson et al., 1998).

A fabric pattern is typically formed during the last stages of magma injection and preserves the final increment of strain before the magma nears solidi and crystallises (Paterson et al., 1998). If there has not been any reorganisation of the particles in the magma before it crystallises, such as flattening due to overburden pressure, the preserved fabric may have formed in the direction of magma flow.

The dolerite sills studied here are typically thin (< 2m thick) and concordant with the stratigraphy. Therefore these intrusions will not have been affected by processes generally associated with large scale intrusions and magma chambers such as magma surges, convection and post-emplacement processes. Consequently it is likely that the preserved fabrics are related to the process of magma injection and flow assuming that there has been no post-intrusion flattening.

In order to infer magma flow in an intrusion, an imbrication of the crystal phases along the contacts of the intrusion (Fig. 4.8a) will typically dip in opposite directions along opposing margins therefore allowing a flow within the intrusion to be assumed (Gil-Imaz et al, 2006; Geoffroy et al, 2002). The dip of this crystal alignment is ideally between 15° and 20° degrees from the wall of the intrusion with the direction of dip inferring the magma flow (Blanchard et al., 1979). It has been shown that petrofabrics may preserve the primary magma flow patterns in igneous intrusions allowing these petrofabrics to infer magma flow directions (Archanjo et al., 1995; Launeau and Cruden, 1998; Horsman et al., 2005; Hastie et al., 2011b). The petrofabrics determined here for the upper and lower contacts of the intrusion will be used as a proxy for magma flow within these intrusions. The plunge and plunge directions of the fabrics for each sample site denote a petrofabric/flow vector about which the magma flow will be inferred.

4.5.4. The use of petrofabrics: examples from Thompson's Bay and Sheffield Beach

The sills from Thompson's Bay and Sheffield Beach were analysed at high and low magnification and analysed petrographically using the above parameters and techniques. The results that represent the determined petrofabrics for each contact were selected based on the Global Compatiblity Index ($\sqrt{F}$ values < 10%) and a grain size threshold of 0.2 mm. Therefore for each sample there was one result, which may be a foliation or a lineation dependant on the shape of the ellipsoid, and are stereographically represented as dip and azimuth or plunge and plunge direction respectively.

4.5.4.1. Thompson's Bay

For the sills at Thompson's Bay there is a correlation between the petrofabric data for the upper contacts of TB1, TB2 and TB5 whilst the results for TB4 show very little similarity to these sills. Using these petrofabric directions to imply magma flow would infer magma flow towards the NNW for these intrusions.

The upper contact of TB1 shows two strong petrofabric directions and possible magma flow towards 240° and 334°, however there appears to be overlap of these two directions when the data are plotted schematically at the sampling points (Fig. 4.8b). All of the petrofabric data for TB2 implies a direction of magma flow towards the NNW as all the average fabrics plunge in the same direction. Schematically there are minor discrepancies along the upper contact where there are flow vectors that differ in plunge direction, but overall the average fabrics are well defined. In order to predict magma flow using the data from the upper and lower contact, the average directions obtained from these contacts should dip in opposite directions. For TB2 however, the fabrics are coaxial.

For the sills TB4 and TB5 the average fabrics determined for the upper and lower contacts are oblique showing a weak relationship between the contacts. The fabric for the upper contact of TB5 is well defined; however the fabrics determined for both the contacts of TB4 and the lower contact of TB5 are not well defined as seen when the flow vectors are plotted schematically (Fig. 4.8c and e). Therefore the magma flow for TB4 may not be discernible from the results. For TB5 though, the upper contact data may be relied upon to infer magma flow. This indicates flow towards the NNW which coincides with the magma flow directions inferred for both TB1 and TB2. This would imply that the magma flow within these three sills was towards a NNW direction allowing a feeder point to the SSE to be inferred.

4.5.4.2. Sheffield Beach

For the sills at Sheffield Beach, the average petrofabric directions determined for the contacts of SHF2 are well defined and plunge in the same general direction. These show a coaxial relationship between the two contacts, implying magma flow towards the SE-SSE.

For SHF3 the average fabrics are not well defined. According to the schematic, there are certain areas along the upper and lower contacts where the fabrics may be grouped according to the plunge directions (Fig. 4.9c). This may have been the result of secondary fabrics unrelated to magma flow or could represent a complex flow pattern related to non-coaxial magmatic flow

(e.g. Nicholas, 1992). The broken bridge obstacles along the lower contact may also have contributed to the non-coaxial fabrics determined for these samples.

The samples from SHF4 (Fig. 4.9e) show a higher degree of alteration than the other sills and may explain why the average fabrics have been poorly defined. Although more detail might be attainable through the analysis of the individual data points, overall these fabrics may not accurately depict a magma flow direction.

SHF5 (Fig. 4.9c) is the only intrusion analysed to show an "ideal" fabric (Gil-Imaz et al., 2006) where the average petrofabric directions dip in opposite directions on the upper and lower contacts. Although there are few data points available according to the average petrofabric data, magma flow may be inferred towards the W.

The lower contact data for SHF6 (Fig. 4.9f) is well defined as plunging towards the SSE, whereas there are two distinct population directions present in the data from the upper contact. This is evident when these petrofabric vectors are plotted schematically. The data are spread out as such, no single average direction may be assigned to an area along the upper contact. In this scenario, magma flow is difficult to infer as the petrofabrics from the upper and lower contacts are oblique and the upper contact data shows two distinct directions. As the intrusion is within an older dolerite intrusion, it may be possible that the multiple flows occurred at this locality with no significant hiatus between magma pulses. If that is the case, then neither contact's data should be disregarded and more detailed analyses may need to be undertaken.

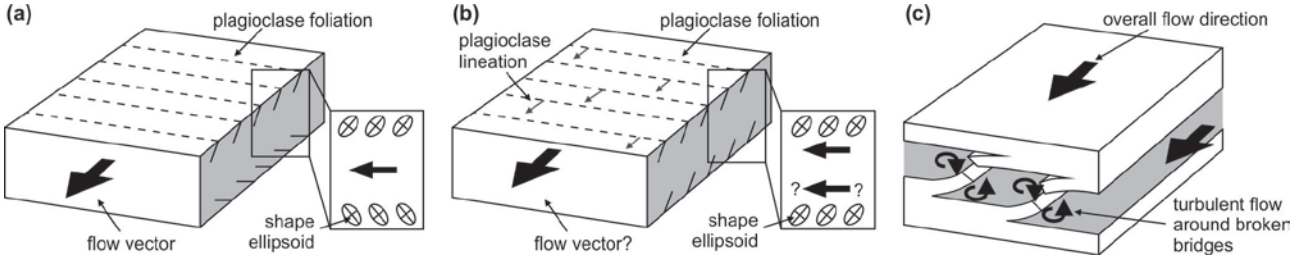

Fig. 4.10. (a) Illustration showing the expected imbrications of crystals along the upper and lower contact with the ellipsoids implying the direction of magma flow (after Gil-Imaz et al, 2006). (b) Imbrication pattern obtained for the sills TB2 and SHF2 where the upper and lower contact ellipsoids plunge towards the same direction; here implied flow along the bottom does not corroborate with that from the upper contact. Both the foliation and the lineation have been used to define the petrofabric. (c) Illustration representing the formation of broken bridges through the linkage of en echelon fractures; flow around the remnants of the broken bridges creates turbulent flow along these obstacles, after Nicholson and Pollard (1985).

Overall for Sheffield Beach, the sills show no clear link between the intrusion flow directions as with the sills studied at Thompson's Bay. Therefore no distinct regional pattern of magma flow

may be inferred. It is possible that the intrusions originate from separate magma sources but these fabric patterns need to be analysed in greater detail.

4.5.5. Summary

If these fabrics were preserved through the development of flow-related fabrics, the results indicate that the flow within sills is more complicated than flow within dykes. With regards to sills, the fabrics determined for the lower contacts may shed some light on the subject of preserved magma flow within planar intrusions.

For the intrusions analysed here, there is little to no relationship with the data obtained for the lower contacts of the sills. Assuming that the upper contact fabrics would imply a magma flow in the same direction as the fabrics were plunging (Fig. 4.10), it is possible the upper contact data could be relied upon to infer the direction of magma flow without the lower contact data. This would only be plausible in situations where no other fabrics (flow-related or not) may have been preserved along the lower contact zone.

An explanation for the unusual fabric pattern obtained between the lower and upper contacts may be related to magma flow around obstacles and features related to the lithological contacts with the country rocks, such as broken bridges. These features imply a magma flow oriented parallel to the strike of the bridge where magma segments have coalesced to form a larger intrusion (Pollard et al., 1975; Rickwood, 1990; Hansen and Cartwright, 2006; Hutton, 2009). These obstacles protrude into the area where the magma is injected and may locally deflect flow (e.g. Nicholson and Pollard, 1985). Such deflections may cause turbulent flow resulting in displacement gradients within the magma becoming highly variable. Consequently no relationship may be inferred between the overall magma flow and the local fabric that is preserved (Martin and Nokes, 1988). However, turbulent flow will normally not occur when magma is near solid and the final phase of strain will be preserved (Brandeis and Marsh, 1989), so any fabric abnormality near these obstacles may not necessarily be explained by this process.

It may be more fitting to use these petrofabrics to infer small-scale features within an intrusion, such as localised pockets of increased strain or subtle flow perturbations due to the shape of the intrusion chamber. The more numerous the samples from particular portions of the intrusion, the more detailed the strain analysis and inferred flow map. However this would be an incredibly time consuming process and may highlight even more small scale features rather than a large scale magma flow direction as desired.

Through the use of the grain size threshold, capturing photomicrographs has been simplified where one image may be obtained for analysis. Likewise, neglecting to segment the image will not significantly alter the result; however it can negatively affect the Global Incompatibility Index. Therefore through the careful selection of magnification when obtaining photomicrographs, by not segmenting the image during the SPO process and with the application of shape parameter data, good agreement of petrofabrics and inferred flow vectors between samples, from the same intrusion, may be produced.

References

Archanjo, C.J., Launeau, P., 2004. Magma flow inferred from preferred orientation of plagioclase of the Rio Ceará-Mirim dyke swarm (NE Brazil) and its AMS significance. In Martín-Hernández, F., Lüneberg, C.M., Aubourg, C., Jackson, M. (Eds) Magnetic Fabric: Methods and Applications, Special Publication of the Geological Society of London, 238, 285-298.

Archanjo, C.J., Launeau, P., Bouchez, J.L., 1995. Magnetic fabric vs. magnetite and biotite shape fabrics of the magnetite-bearing granite pluton of Gameleiras (Northeast Brazil). Physics of the Earth and Planetary Interiors, 86, 63-75.

Archanjo, C.J., Silva, M.G., Castro, J.C., Launeau, P., Trindade, R.I.F., Macedo, J.W.P., 2006. AMS and grain shape fabric of the Late Palaeozoic diamictites of the Southeastern Paraná Basin, Brazil. Journal of the Geological Society, 163, 95-106.

Archanjo, C.J., Campanha, G.A.C., Salazar, C.A., Launeau, P., 2012. Using AMS combined with mineral shape preferred orientation analysis to understand the emplacement fabrics of the Apiaí gabbro-norite (Ribeira Belt, SE Brazil). International Journal of Earth Science, 101, 731-745.

Benn, K. Allard, B., 1989. Preferred mineral orientations related to magmatic flow in ophiolite layered gabbros. Journal of Petrology, 30, 925-946.

Blanchard, J-P., Boyer, P., Gagny, C., 1979. Un nouveau critere de sens de mise en place dans une caisse filonienne: Le “pincement” des mineraux aux epontes: Orientation des minéraux dans un magma en écoulement. Tectonohysics, 53, 1-25.

Brandeis, G., Marsh, B.D., 1989. The convection liquidus in a solidifying magma chamber: a fluid dynamic investigation. Nature, 339, 613-616.

Geoffroy, L., Callot, J.P., Aubourg, C., Moreira, M., 2002. Is the common use of AMS in mafic dykes scientifically correct? Terra Nova 14, 183–190.

Gil-Imaz, A., Pocoví, A., Lago, M., Galé, C., Arranz, E., Rillo, C., Guerrero, E., 2006. Magma flow and thermal contraction fabric in tabular intrusions inferred from AMS analysis. A case study in a late-Variscan folded sill of the Albarracın Massif (southeastern Iberian Chain, Spain). Journal of Structural Geology 28, 641–653.

Hansen, D.M., Cartwright, J., 2006. The three-dimensional geometry and growth of forced folds above saucer-shaped igneous sills. Journal of Structural Geology, 28, 1520-1535.

Hastie, W.W., Aubourg, C., Watkeys, M.K., 2011a. When an inverse fabric is not inverse: an integrated AMS-SPO study in MORB-like dykes. Terra Nova, 23, 49-55.

Hastie, W.W., Aubourg, C., Watkeys, M.K., 2011b. Significance of magnetic and petrofabric in Karoo-feeder dykes, northern Lebombo. Tectonophysics, 513, 96-111.

Hastie, W.W., Watkeys, M.K., Aubourg, C., 2013. Characterisation of grain-size, shape and orientation of plagioclase in the Rooi Rand dyke swarm, South Africa. Tectonophysics, 583, 145-157.

Horsman, E., Tikoff, B., Morgan S., 2005. Emplacement-related fabric and multiple sheets in the Maiden Creek sill, Henry Mountains, Utah, USA. Journal of Structural Geology, 27, 1426-1444.

Hutton, D.H.W., 2009. Insights into magmatism in volcanic margins: bridge structures and a new mechanism of basic sill emplacement – Theron Mountains, Antartica. Petroleum Geoscience, 15, 269-278.

Jelinek, V. 1981. Characterisation of the magnetic fabric of rocks. Tectonophysics, 79, 63-67.

Jourdan, F., Féraud, G., Bertrand, H., Watkeys, M.K., Renne, P.R., 2008. $^{40}Ar/^{39}Ar$ ages of the sill complex of the Karoo large igneous province: implications for the Pliensbachian-Toarcian climate change. Geochemistry, Geophysics, Geosystems, 9, Q06009, dii:10.1029/2008GC001994.

Kattenhorn, S.A., 1994. Mechanisms of sill and dyke intrusion. Unpublished MSc dissertation, University of Natal, Durban.149 pp.

Launeau, P., 2004. Mise en évidence des écoulements magmatiques par analyse d'images 2-D des distributions 3-D d'Orientations Préferentielles de Formes. Bulletin of the Geological Society of France, 175, 331–350.

Launeau, P., Bouchez, J.-L., 1992. Mode et orientation préférentielle de forme des granites par analyse d'images numériques, Bulletin of the Geological Society of France, 163, 721-732.
Launeau, P., Cruden, A.R., 1998. Magmatic fabric acquisition mechanisms in a syenite: Results of a combined anisotropic of magnetic susceptibility and image analysis study. Journal of Geophysical Research, 103, 5067-5089.

Launeau, P., Robin, P.-F., 1996. Fabric analysis using the intercept method. Tectonophysics, 267, 91-119.

Launeau, P., Robin, P.-Y.F., 2005. Determination of fabric and strain ellipsoids from measured sectional ellipses—implementation and applications. Journal of Structural Geology, 27, 2223–2233.

Launeau, P., Archanjo, C.J., Picard, D., Arbaret, L., Robin, P.-Y.F., 2010. Two- and three-dimensional shape fabric analysis by the intercept methods in grey levels. Tectonophysics, 492, 230-239.

Liss, D., Hutton, D.H.W., Owens, W.H., 2002. Ropy flow structures: A neglected indicator of magma-flow direction in sills and dikes. Geology, 30, 715-718.

Marsh, B.D., 1989. Magma chambers. Annual Review of Earth and Planetary Science, 17, 439-474.

Martin, D., Nokes, R., 1988. Crystal settling in a vigorously convecting magma chamber. Nature, 332, 534-536.

Nicholson, R., Pollard, D.D., 1985. Dilation and linkage of echelon cracks. Journal of Structural Geology, 7, 583-590.

Nicholas, A., 1992. Kinematics in magmatic rocks with special reference to gabbros. Journal of Petrology, 33, 891-915.

Paterson, S.R., Fowler, T.K. Jr., Schmidt, K.L., Yoshinobu, A.S., Yuan, E.S., Miller, R.B., 1998. Interpreting magmatic fabric patterns in plutons. Lithos, 44, 53-82.

Pollard, D.D., Muller, O.H., Dockstader, D.R., 1975. The form and growth of fingered sheet intrusions. Geological Society of America Bulletin, 86, 351-363.

Rickwood, P.C., 1990. The anatomy of a dyke and the determination of propagation and magma-flow directions. In: Parker, A.J., Rickwood, P.C., Tucker, D.H. (Eds) Mafic dykes and Emplacement Mechanisms. *Proceedings of the Second international dyke conference, Adelaide, South Australia, 2,* 81-100.

Schofield, N., Stevenson, C., Reston, T., 2010. Magma fingers and host rock fluidization in the emplacement of sills. Geology, 38, 63-66.

Tait, S., Jaupart, C., 1990. Physical processes in the evolution of magmas. In: Nicholls, J., Russell, J.K. (Eds) Modern methods of igneous petrology: understanding magmatic processes. Reviews in Mineralogy and Geochemistry, 24, 125-152.

Tarling, D.H., Hrouda, F. 1993. The Magnetic Anisotropy of Rocks. Chapman and Hall, London, pp. 218.

Wylie, J.J., Helfrich, K.R., Dade, B., Lister, J.R., Salzig, J.F., 1999. Flow localization in fissure eruptions. Bulletin of Volcanology, 60, 432-440.

Yoshinobu, A.S., Okaya, D.A., Paterson, S.R., 1998. Modelling the thermal evolution of fault-controlled magma emplacement models: implications for the solidification of granitoid plutons. Journal of Structural Geology, 20, 1205-1218.

- CHAPTER 5 –

BRECCIA FORMATION DURING INTRUSION OF A DOLERITE SILL: AN EXAMPLE FROM SHEFFIELD BEACH

5.1. Introduction

This paper describes the occurrence and structure of a breccia associated with a 1.5 m thick dolerite sill of the Karoo Igneous Province (KIP) (Erlank, 1984) exposed on Sheffield Beach along the North Coast of KwaZulu-Natal, South Africa (Fig. 5.1a). Breccias have been previously described in the KIP; these developed close to the surface associated with vents and are common in the KIP's western portions (du Toit, 1904; Gevers, 1928; Svensen et al., 2006, 2007) or occur as invasive flows showing evidence of burrowing lava flows into wet sediments (Rawlings et al., 1999). This is the first recorded occurrence of a breccia formed by overlapping sill segments in a sub-volcanic environment in the KIP. The KIP volcanism and associated sub-volcanic dolerite sills range in age between 181 – 184 Ma (Jourdan et al., 2008). The dolerite sill described here intruded into the Permian Vryheid Formation of the Ecca Group, Karoo Supergroup. It is not possible to establish the exact depth of intrusion because it requires knowing the relative ages of overlying sills and volcanic flows and depends on the timing of the intrusion. If the injection of the sill segments occurred before the magmatism associated with the formation of the bulk of the KIP the sediment pile would be less than 1 km in thickness. If the sill segments formed towards the end of the KIP magmatic event, the overburden could have been in excess of 3 km.

This chapter describes the form and characteristics of this brecciated zone, quantifies the extent and characteristics of the breccia, and documents the relationship between the deformation in the host rocks and the brecciation process. These features are used to determine the environment and mode of formation of the breccia.

A breccia is a rock comprising angular polymict or monomict clasts (which are typically poorly sorted) within a finer-grained matrix. Breccias can form through numerous processes in various environments but coherent hosted breccias associated with thin sub-volcanic planar intrusions are uncommon and, therefore, requires explanation.

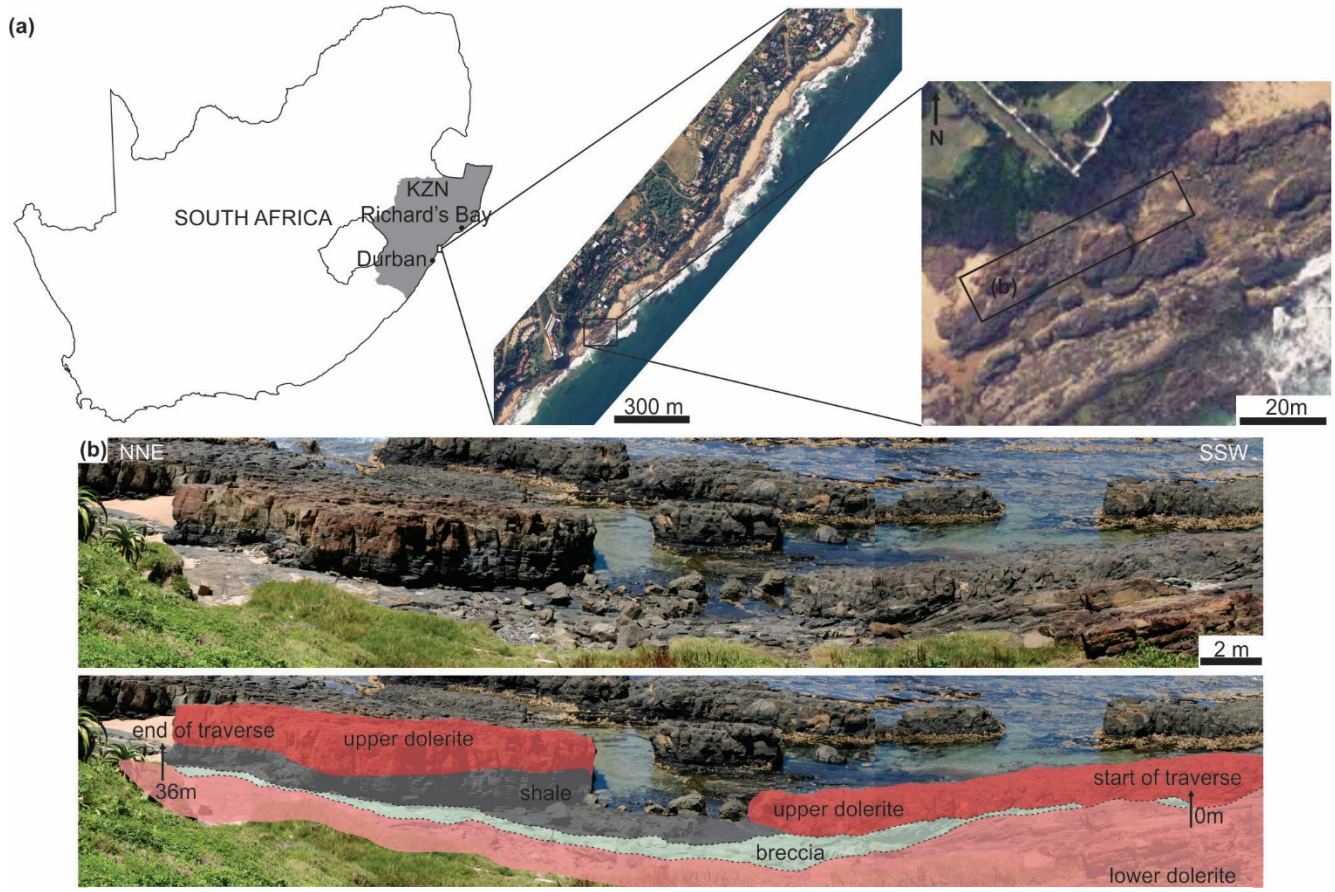

Fig. 5.1. (a) Location map of the dolerite sill studied at Sheffield Beach north of Durban along the Kwa-Zulu Natal North Coast. The area on the photograph is the section of the intrusion where the traverse was undertaken. (b) Photograph of the sill segments looking ENE. The saucer-shaped appearance of the sill is due to the perspective of the photograph. The lower photograph shows the outcrop of the lower and upper dolerites and the country rock wedge of shale where the breccia crops out. The traverse between 0 m and 36 m is marked on the photograph.

5.1.1. Breccias associated with magmatism

Numerous types of breccias are related to magmatism which may be broadly considered in terms of those associated with volcanism and those in sub-volcanic settings. Lavas fragment when coming into contact with air, water or sediments, while breccias in sub-volcanic settings can form in association with volcanic pipes and volatile-rich melts. Such environments include but are not limited to wet and dry sediments and lithified sedimentary rocks. In these settings the triggering events can be hot magma (or lava) encountering fluids that are rapidly vapourised, dynamic mixing of the magma/lava with the unconsolidated sediments and a combination of both, which can also often mobilise the sediment themselves.

One of the most studied breccias linked to sub-volcanic intrusions and extrusions of lavas are peperites. Peperites form in situ through the process of magma disintegration as the magma mixes with unconsolidated to poorly consolidated usually wet sediments (White et al., 2000).

Dynamic mixing can occur with dry unconsolidated sediments (e.g. Jerram and Stollhofen, 2002, Petry et al., 2007) in certain examples of lava flows and shallow intrusions in arid settings. The matrix of peperites consists of the formerly unconsolidated sedimentary components into which the magma intruded or lava flowed over, while the clasts consist of the fragmented parts of the magma/lava (e.g. Pichler, 1965; Honnorez and Kirst, 1975; Kokelaar, 1982; Jerram and Stollhofen, 2002). Such fragmentation can be attributed to numerous processes including quenching, autobrecciation, coherent-sediment density contrasts, explosive juvenile vesiculation, surface tension effects, instabilities associated with vapour films and pore-water steam explosions (Zimanowski et al., 1995, 1997; Skilling et al., 2002; Wohletz, 2002). The environment of formation can thus be diverse with peperite breccias forming in association with domes, dykes, sills, lava flows and welded pyroclastic flows (e.g. Busby-Spera and White, 1987; Hanson and Hargrove, 1999; Caroff et al., 2009). Not all peperite formation relies on the host sediments being unlithified, weak rocks such as coal may become abraded to sediment through the intrusion of a coherent resulting in a peperite forming (McClintock and White, 2002).

Sub-volcanic intrusions, comprising dry melts, that intrude lithified host rocks may create fluidised host rock surrounding the intrusion (e.g. Liss, 2004; Airoldi et al., 2011; Schofield et al., 2012a) or localised fractures infilled with coherent magmatic material (Schofield, 2009). The fluidisation of the country rocks typically occurs adjacent to these intrusions when sufficient overpressure results in fragmentation of the country rocks (Svensen et al., 2010). Through the intrusion and subsequent coalescence of magma fingers or lobes, the country rocks wedged between the adjacent magma fingers can be highly deformed through buckling and localised fragmentation (e.g. Pollard et al., 1975). The triggering event of fragmentation associated with dry melt is typically the fluid-rich environments into which, they intrude. Volatiles may also be produced as a result of the magma intrusion through the metamorphism of the country rocks particularly in shales and carbonaceous rocks (e.g. Svensen et al., 2007; Aarnes et al., 2011).

Breccias associated with volatile-rich melts (i.e. kimberlites) are triggered by the explosive behaviour of the melt and are common in the pipe-forming process of maar-diatreme volcanoes (e.g. Lorenz, 1986; Sparks et al., 2006; Svensen et al., 2006; Lorenz and Kurszlaukis, 2007; Valentine et al., 2014). These breccias typically surround the lower zone of volcanic vents. The high volatile component of the intrusion contributes to the explosion and causes fragmentation of the adjacent country rocks, resulting in a high percentage of xenoliths entrained into the

breccia (Sparks et al., 2006). These sub-volcanic breccias typically comprise clasts of fragmented country rocks in a matrix of either hydrothermal minerals that crystallised in the pore spaces (Svensen et al., 2006), or in a coherent matrix of the same composition as the intrusion that triggered fragmentation (Lorenz and Kurszlaukis, 2007; Barnett et al., 2011).

Small scale varieties of sub-volcanic breccias may form in response to the forceful intrusion of a planar magmatic body (e.g. dykes and sills). The fragmentation of the country rocks occurs contemporaneously with magma intrusion and through brittle emplacement mechanisms, and a significant increase in the pore fluid pressure (e.g. Delaney and Pollard, 1981; Lorenz and Kurszlaukis, 2007).

5.2. Methodology

The sedimentary country rocks into which the dolerite sills intruded were mapped in detail along a 42-m-long traverse aligned SSW to NNE (Fig. 5.2a). The thicknesses of the breccia and the host rocks were measured at one metre intervals along this traverse (Fig. 5.2b). The point where the sill segments become individual intrusions is the proximal area, with distal regions occurring away from this zone towards the NE. Distances measured along profile increase from the proximal to distal areas. Proximal the wedge of breccia is sandwiched between the two dolerite sill segments whereas distally the breccia occurs between the lower dolerite and overlying undeformed country rocks (Fig. 5.1b). The detailed observations, in the Section 5.3, describe the properties of the breccia and the relationship between the dolerite matrix, the breccia and the country rock.

Samples were collected for detailed petrographic analyses from the lower dolerite, upper dolerite and the breccia, in the form of thin sections. The petrographic analyses involved mineral determination of plagioclase composition estimation undertaken using the Michel-Levy technique (Nesse, 2000). Two petrographic samples were obtained from the upper contact of the lower dolerite, nine from the lower contact of the upper dolerite and one from the breccia. Where more than one phase of plagioclase occurred, all the plagioclase phases were analysed.

5.3. Results

Two 1.5 m thick sill segments are vertically partially-overlapping and are shallowly discordant with the sedimentary bedding, becoming concordant with the stratigraphy towards the NE. The sill segments predominantly comprise pyroxene and plagioclase and are defined as dolerites. A

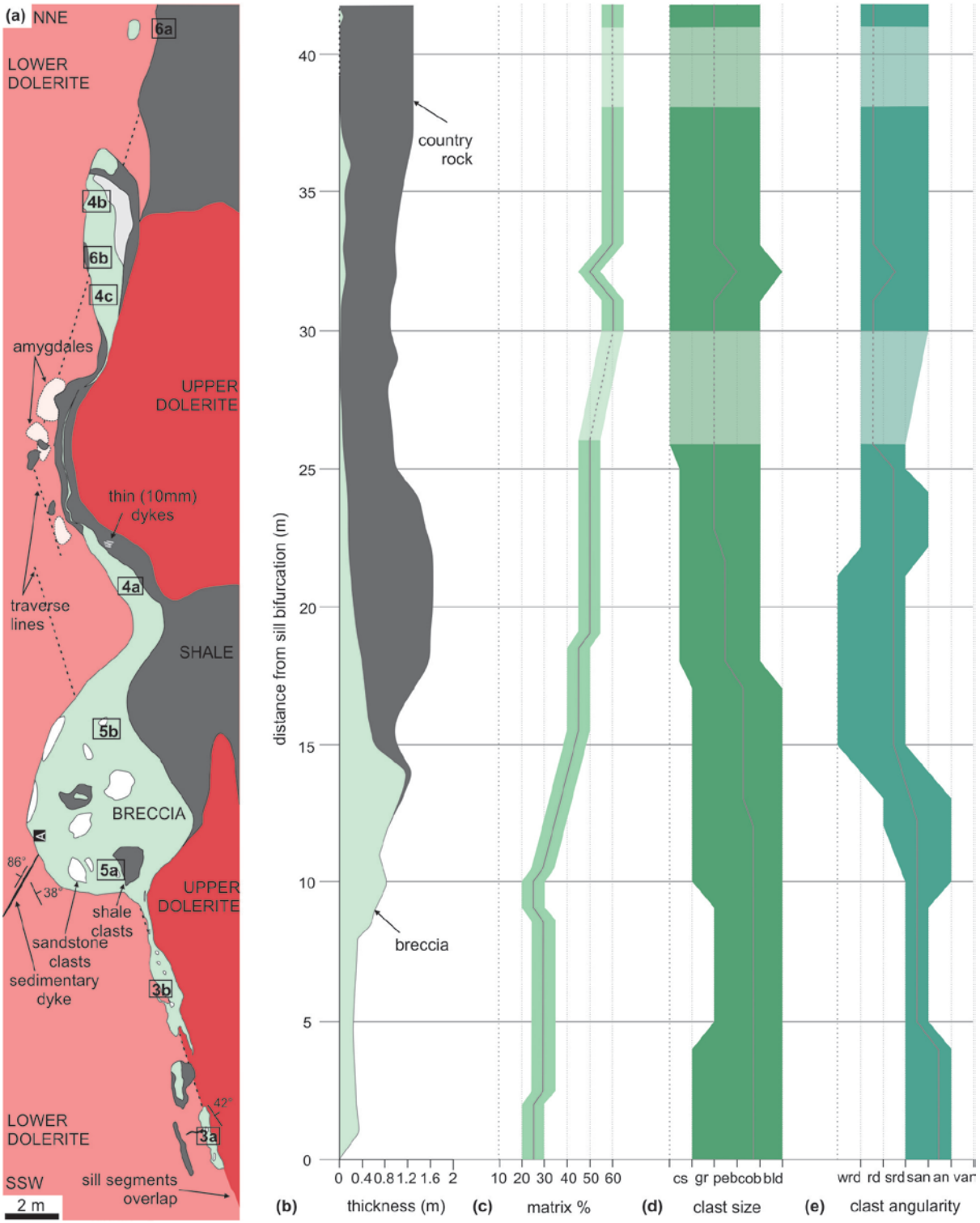

Fig. 5.2. (a) Geological map of the exposed dolerite sills, shale country rock and the breccia. The traverse is represented by the dashed lines. In the breccia pavement section there are numerous large clasts of comminuted shale and sandstone. Amygdales are common along the upper contact of the lower dolerite distally. The numbered rectangles represent the positions of the subsequent figures where photographs were taken (i.e. 3a refers to Fig. 6.3a). **A** represents the site where the petrographic breccia sample was obtained (Figs. 6.6b and c). Dip and strike symbols represent the contact between the sills and the breccia and the two thin sedimentary dykes in the lower dolerite. (b) The thickness of the breccia and the country rock wedge along profile from 0 m to 42 m. (c) Graphical representation of the matrix percentage in the breccia along profile. The light green area represents the range of matrix percentage, the grey line represent the estimated percentage. (d) Graphical representation of the range of clast sizes in the breccia (dark green area) and the modal grain size (grey line) along profile from coarse sand to boulder. (e) The degree of angularity of the clasts in the breccia from well-rounded to very angular. The blue-green area represents the range of angularity and the grey line represents the modal clast angularity.

wedge of deformed country rock has been sandwiched between these sill segments (Fig. 5.1b). This wedge contains the breccia zone, comprising fragmented country rock wedge, together with a dolerite matrix, that decreases in thickness distally.

The wedge of country rock between the sills increases in thickness distally, attaining a consistent thickness of 1.2 m once the sills become concordant with the stratigraphy. The country rocks consist of laminated shales with intermittent siltstone and sandstone lenses. In areas local to these sill segments, the shales can have high carbon contents and host thin coal seams. The sandstones are fine- to medium-grained and are quartz-rich. The frequency of the sandstone lenses increases towards the north where the sandstone becomes a ~0.15 m thick unit within the siltstone. Characteristically the breccia differs in thickness, matrix percentage, clast size, shape and angularity along the traverse profile. All of these have been quantified (Fig. 5.2b-e)

5.3.1. Breccia Zone Characteristics

Along profile the breccia gradually increases in thickness until it attains a maximum thickness of 1.2 m after which it abruptly thins to 0.6 m (at 14 – 15 m in Fig. 5.2b). The breccia then thins consistently along profile almost disappearing from the outcrop (between 26 – 30 m in Fig. 5.2b). A slight increase in the breccia thickness occurs at 32 m along profile.

The matrix surrounding the breccia country rock clasts is coherent dolerite. Generally the matrix percentage increases along profile from 25 % at the separation of the sill segments to 60% at the limit of the outcrop (Fig. 5.2c). Proximally, the matrix occurs as small pockets of dolerite in the breccia (Fig. 5.3a and b). The clasts have significant grain-to-grain boundaries whilst the smaller grains (granule to small pebble) are completely enveloped in the matrix. Distally, the matrix component of the breccia is greater than the clast component (~60%) so that the majority of the clasts are surrounded by matrix with little to no grain-to-grain boundaries present (Fig. 5.4a, b). A distinct decrease in the matrix percentage to 50% occurs briefly at 32 m along profile (Fig. 5.2c, 5.4c).

The breccia clast sizes range from sand sized clasts to boulders and the modal clast size decreases with increased distance from the sill segment separation (Fig. 5.2d). Proximally, there are several small boulders present in the breccia with 50% of the clasts being cobble (or larger) in size (Fig. 5.3a). The modal clast size decreases at 12 m along profile with no boulders present after 18 m along profile, except for at 32 m, where some of the clasts comprise small boulders

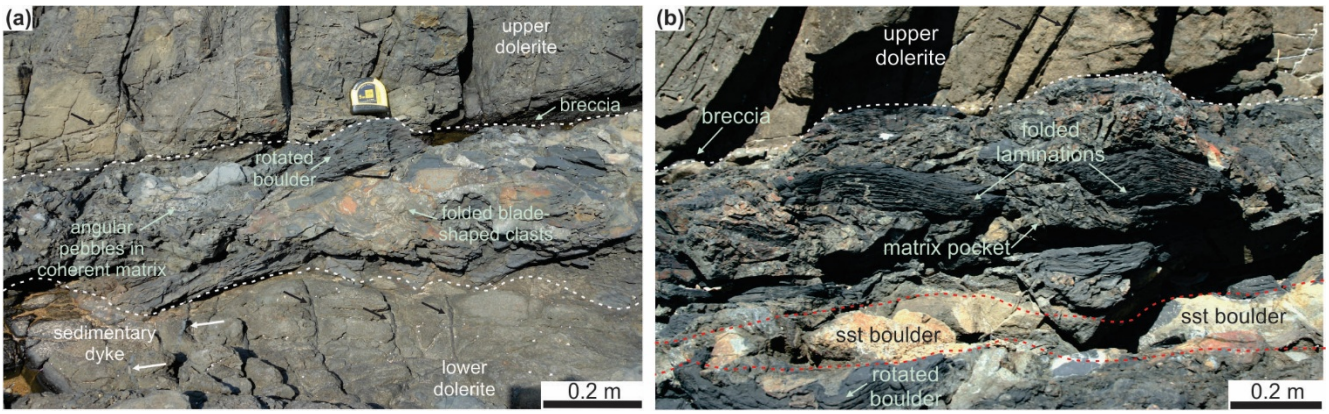

Fig. 5.3. Photographs of the breccia proximal to the separation of the sill segments. (a) The boundary of the breccia between the lower and upper dolerite is shown with a dashed line. Black arrows in the upper and lower dolerites indicate the positions of chlorite-filled veins, white arrows represent a sedimentary dykelet. Rotated boulders, and smaller clasts of shale, angular clasts and folded shale clasts occur in the breccia. (b) The boundary between the upper dolerite and the breccia is shown with a dashed white line. The dashed red lines represent a layer in the breccia where sandstone (sst) clasts are common. In the breccia are rotated boulders, some showing minor folding and pockets of matrix adjacent to the large clasts where smaller angular clasts occur.

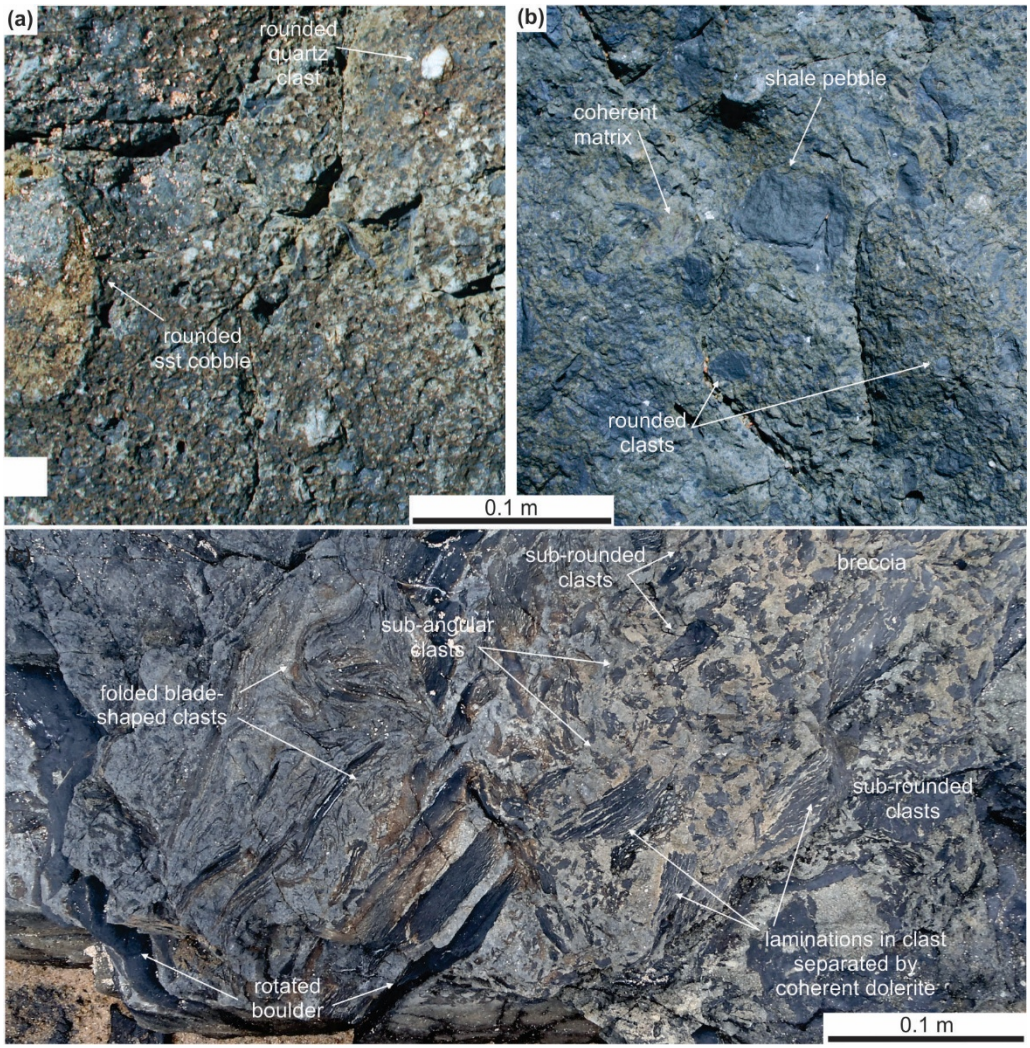

Fig. 5.4. Photographs from distal areas. (a) With a matrix percentage of ~50% the rounding of the larger clasts is increasing and the modal grain size, small pebble, of the clasts is decreasing distally. (b) Towards the most distal areas, the breccia comprises ~60% matrix with a significant amount of rounded clasts but still with a wide variation in clast sizes. (c) At 32 m along profile, the thickness of the breccia increases to 0.2 m and the characteristics of the clasts are different when compared to the adjacent breccia outcrops. Here the clasts are more angular with a higher component of thin blade-like clasts, some that are folded. The boulder-sized clasts are rotated to sub-vertical.

(Fig. 5.4c). Distally, the grain size range increases and includes coarse sand sized clasts (shale clasts) with small pebbles (sandstone clasts) as the modal clast size (Fig. 5.2d). A slight increase in the modal clast size occurs at 32 m along profile. The clast shapes in the proximal zones are typically either blade-shaped or disc-shaped with some of the smaller shale clasts rod-like in shape (Fig. 5.3a). The clast shapes in the distal zones are dominated by discs and spheres, with minor blade-shaped clasts occuring at 32 m along profile (Fig. 5.4c). Clast modal angularity decreases along profile from angular/sub-angular to sub-rounded/well-rounded and the range of the clast angularity increases distally (Fig. 5.2e). The clast angularity increase slightly at 32 m along profile.

5.3.2. Clast deformation and transport

Breccia clasts have been predominantly rotated and/or folded as observed in the blade-shaped clasts and several of the larger sandstone clasts have undergone minor melting. The amount of clast rotation decreases along profile; a large number of clasts in proximal areas have been rotated to vertical orientations (Fig. 5.3a). As with clast rotation, the clasts that show the highest degree of folding are the thin blade-shaped clasts. Proximally, folded blade-shaped clasts range in size and the amount of folding varies. The smaller blade-like clasts exhibit close to tight folds (e.g. Fig. 5.3a) while the larger clasts display gentle to open folds (e.g. Fig. 5.3b). The number of clasts that are folded and the intensity of folding decreases distally. In the distal zone the larger clasts have been fractured but have not been folded or rotated.

The boundaries of several sandstone clasts do not show sharp contacts and instead have diffuse boundaries that appear to be the result of partial melting. Large sandstone cobbles occasionally exhibit gradual contacts with the coherent matrix (Fig. 5.5a). Along the sandstone clast boundaries, small fingers of sandstone-material have migrated into the breccia forming veins or sandstone dykes (Fig. 5.5a and b). Shale granules have also been enveloped by the boundaries of the sandstone clasts (Fig. 5.5a and b).

Transport of the clasts within the breccia from their site of origin is easier to recognise in the proximal zones than the distal zones. Proximally there is a concentration of cobble to boulder-sized clasts within a horizontal layer surrounded by shale clasts (indicated by dashed red lines in Fig. 5.3b). However, between 10 – 20 m along profile, the larger sandstone and shale clasts occur randomly in the breccia with no preferred “layer” of the clasts. Distally there are very few sandstone clasts in contrast with the shale clasts therefore transport of the clasts is difficult to determine.

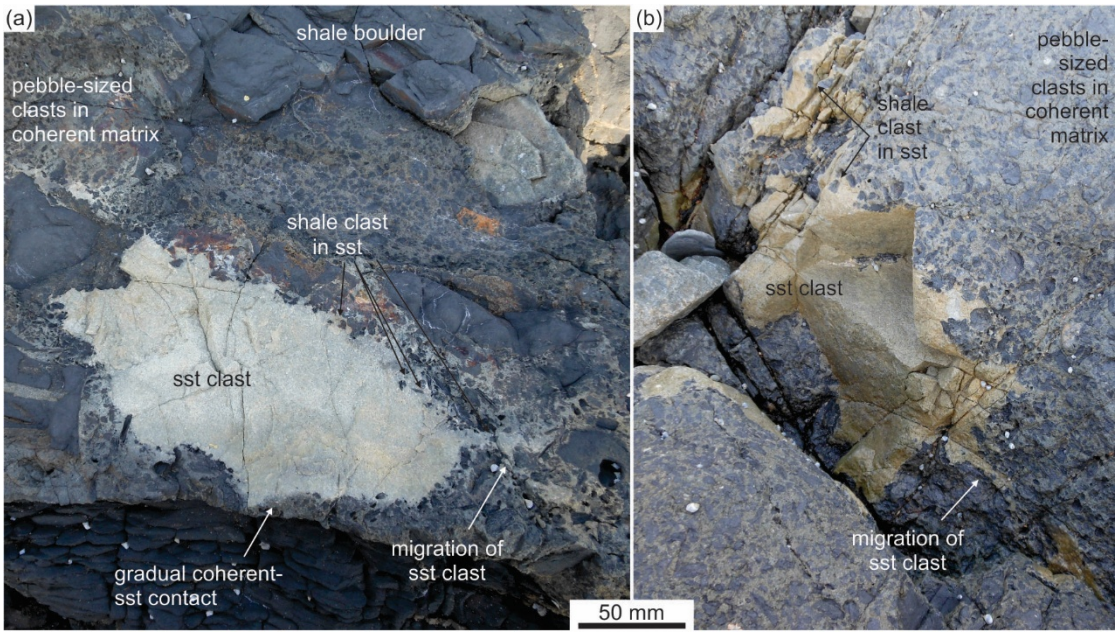

Fig. 5.5. Deformation of the sandstone clasts by partial melting of the clast boundaries (a) The large sandstone cobble shows gradual boundaries with the adjacent coherent. Small shale pebbles and granules have been entrained into the partially melted clasts exterior and some of the material has migrated into the surrounding breccia. (b) A second example of a partially melted sandstone clast with shale clasts entrained along the clast boundaries and the movement of partially melted material away from the clast.

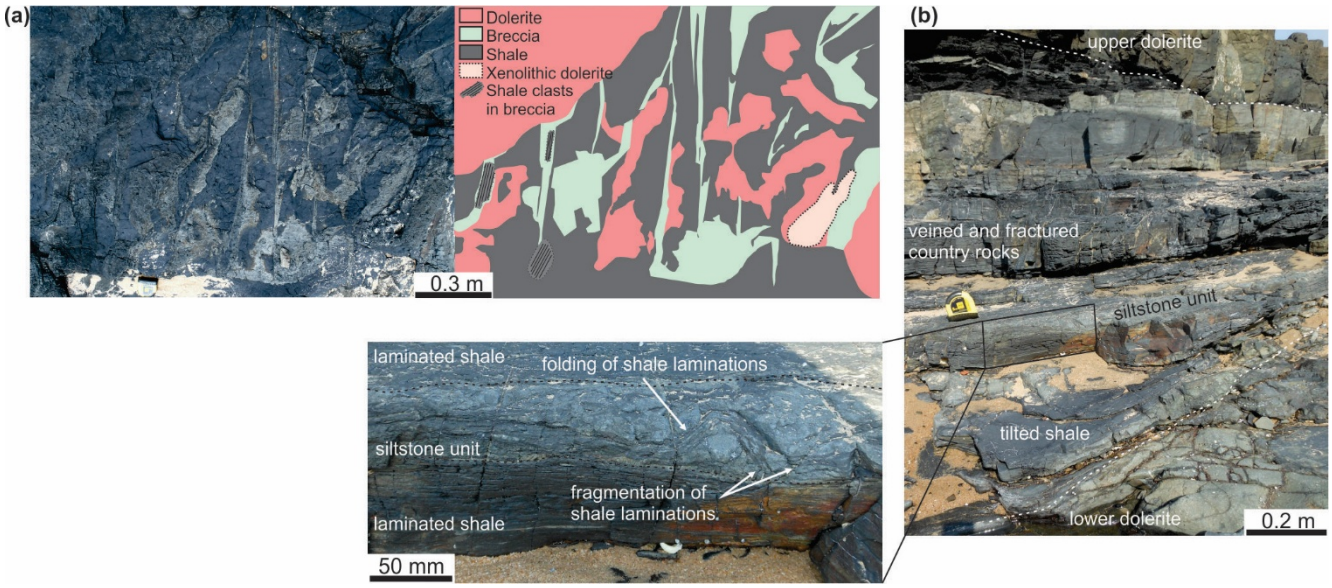

Fig. 5.6. Deformation in the country rocks above the breccia. (a) Photograph and sketch of a distal area of the breccia outcrop. The shale layers here have thin dolerite sills (millimetre to centimetre-scale) intruded along the lamination planes. There are signs of fragmentation in the breccia portions of the outcrop and thin breccia and coherent dykes that are intruded into the overlying country rocks. The xenolithic dolerite here hosts xenoliths of quartzofeldspathic composition and are most likely not derived locally. (b) Deformation in the country rocks, overlying the lower dolerite, in a ~10 cm thick unit of siltstone interbedded with shale laminations. The inset shows the fragmentation and folding of the shale layers within the siltstone unit.

5.3.3. Fragmentation of the surrounding rocks

The sill segments and country rocks adjacent to the breccia show deformation features such as fractures and veins on either side of the breccia in the lower and upper dolerites, which decrease distally. Two rheomorphic sedimentary dykelets (dark blue-grey in colour) extend into the lower dolerite (Fig. 5.2a) and several small chlorite veins occur in the upper and lower dolerite. Significant jointing parallel and perpendicular-to the breccia contacts occurs throughout the profile (Fig. 5.3a). At the uppermost extent of the distal breccia, small coherent dykelets, some hosting shale clasts, intrude upwards into the overlying country rocks (Fig. 5.6a).

Layers in a distal siltstone host-rock unit, 41 m along profile and 0.2 m above the lower dolerite-country rock contact, are folded and fragmented (Fig. 5.6b). The fragmentation is not extensive and does not occur adjacent to the breccia or the lower dolerite contact.

5.3.4. Microscopy

The lower dolerite is medium grained with a typical assemblage of a slightly altered dolerite comprising ~50% plagioclase, ~28% pyroxene, ~15% chlorite and opaques (7%) and is equigranular to sub-ophitic in texture with amygdales (~10% of the thin section) infilled with chlorite and subsequent quartz and/or calcite (Fig. 5.7a). Compositionally the upper dolerite is fine grained comprising 48% plagioclase, 20% pyroxene, 27% chlorite and 5% opaque minerals with very few (~1%) vesicles or amygdales present. The upper dolerite is glomeroporphyritic in texture with plagioclase glomerocrysts and the second plagioclase phase present as finer grains in the matrix.

Petrographically, the fine grained coherent breccia matrix is distinctly different from the lower and upper dolerites. There are no pyroxenes present and a significant component of the sample is made up of pale-yellow to pale-brown glass (Fig. 5.7b). The breccia sample consists of 32% plagioclase, 18% glass, 20% chlorite and 30% shale xenoliths. Where the shale xenoliths are laminated, the individual laminations have been separated with the opened gaps between the thin layers of shale filled with doleritic material (Fig. 5.7c).

Maximum %An in samples indicated that the plagioclase composition in the lower and upper dolerite was labradorite (65%An and ~57%An respectively). The plagioclase from the breccia sample was bytownite (73.5%An).

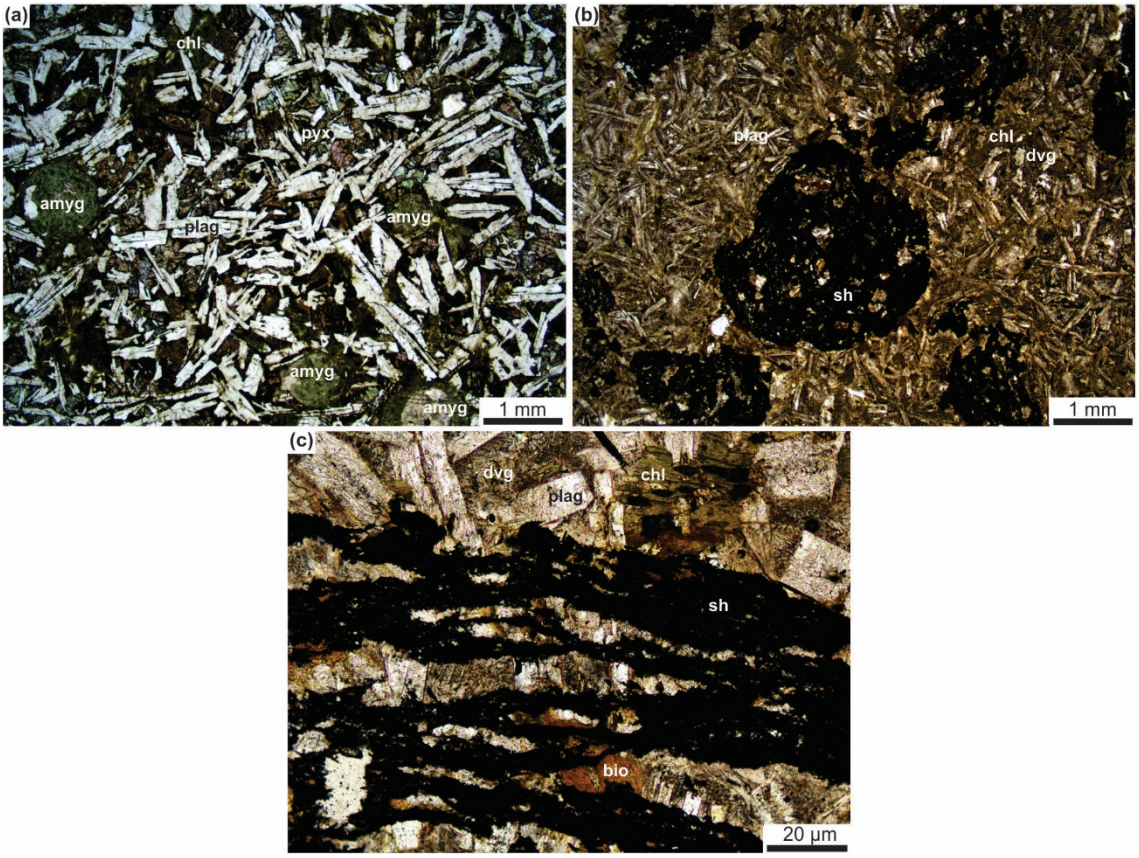

Fig. 5.7. Photomicrographs of the dolerite and breccia samples. (a) The upper dolerite is amygdaloidal and sub-ophitic in texture, at a higher magnification the texture of the sill is glomeroporphyritic. The amygdales have been infilled with chlorite and later calcite and quartz. (b) The breccia is characterised by opaque shale clasts that are sub-rounded to sub-angular. (c) At high magnifications, the composition of the coherent in the breccia is easily observed. Here the shale laminations are separated by the coherent comprising plagioclase and chlorite. Note the absence of pyroxene in (b) and (c). Plag = plagioclase, pyx = pyroxene, chl = chlorite, sh = shale, dvg = devitrified glass, amyg = amygdale.

5.4. Discussion

5.4.1. Fragmentation processes

When a coherent body comes into direct contact with groundwater, or near-surface water, the pore fluids in the rocks become vaporised. Heating a contained amount of water will increase the pressure on the rocks and once the water is flash-boiled to steam, the volume of the fluids drastically increases (Delaney, 1982). This pressure increase may lead to the brecciation of the rocks adjacent to the intrusion with the likelihood of country rock fragmentation increasing at higher stratigraphic levels (Delaney, 1982). In order for fragmentation to occur, the vapourised pore-fluid pressure would have to exceed the lithostatic pressure of the country rocks (Delaney, 1982; Jamtveit et al., 2004). If the heat source and the increased pressure in the rocks adjacent to the intrusion are sustained, a specific type of fragmentation may occur known as a phreatomagmatic explosion or a fuel-coolant-interaction type explosion (Lorenz, 1987; Kurszlaukis et al., 1998). In sub-volcanic settings, the explosive fragmentation and

hydrofracturing of the country rocks is induced by vapourisation and forced fluid flow of flash-boiled pore-water due to the heat of the sub-volcanic intrusion and results in the mixing of the intrusive melt with the fluid and the fragmented rocks (Zimanowski et al., 1997; Kurszlaukis et al., 1998; Wohletz, 1986, 2002; Savin et al., 2005, Lorenz and Kurszlaukis, 2007). The product of these explosions is a breccia that comprises components of country rock and/or the coherent itself where the intrusion has been overprinted by the fragmentation of the host rock and the original melt.

Breccias that typically form as a result of phreatomagmatic explosions are hydrothermal vent complexes which extend vertically from the heat source yielding a comminuted sedimentary-matrix breccia (Jamtveit et al., 2004; Svensen et al., 2006). Hydrothermal vents can also form in dry sedimentary rocks through the production of metamorphic fluids through devolitisation reactions triggered by the heat from the intrusion (Svensen et al., 2007; Aarnes et al., 2011). The subsequent build-up of pore pressure can be sufficient to fracture the overburden. Another common occurrence of sub-volcanic breccias occur in association with kimberlite volcanism or maar-diatreme formation where the volatile-rich melts create the fracturing in the adjacent country rocks (Sparks et al., 2006; Valentine et al., 2014). These breccias can have a sedimentary matrix or a coherent matrix depending on the proximity of the breccia to the intrusion.

5.4.2. Sheffield Beach breccia: characteristics and implications

In the case of the KZN North Coast sill, the country rock developed a breccia that attains a maximum thickness of 1.2 m and then drastically decreases in thickness until it occurs as a ~0.2 m thick unit along the upper contact of the lower dolerite. As with the thickness, all of the other characteristics of the breccia change with increasing distance distally (Fig. 5.2). The amount of matrix in the breccia increases almost three-fold along profile, with a significant reduction in the presence of grain-to-grain boundaries between the clasts in the distal regions. Clast sizes also decrease distally, both in the range of clast sizes and the modal clast size. The large range in clast sizes indicates that the brecciation of the rocks occurred rapidly. The absence of sandstone clasts in the distal regions is attributed to a lack of sandstone at the stratigraphic level where the fragmentation occurs.

Whilst there are sub-rounded and/or sub-angular clasts along the whole profile, there is a noticeable decrease in the angularity of the clasts from the proximal to distal zones. The shapes of the clasts are most likely attributed to the laminated nature of the country rocks, with the

blade-shaped clasts being derived from the separation of the shale clasts along lamination surfaces.

Deformation of the clasts in the breccia is more pronounced proximally when compared to the distal regions. The amount of clasts (and the size of the deformed clasts) that have been rotated and folded, decreases along profile. Distally, the energy available to deform the clasts in a ductile manner is therefore reduced as exhibited by the larger clasts in the distal regions that are fractured and not folded.

All of the characteristics of the breccia hint at a substantial decrease in energy towards the distal regions. There is also a distinct relationship between the thickness of the breccia and the properties of the clasts (i.e. clast number, size and angularity) as noticed along the profile length and at 32 m along profile where the breccia thickness increases briefly. Where the breccia is bound above and below by the coherent dolerite sills, the matrix percentage is at least 15% lower than when the wedge between the two sill segments is not comprised entirely of breccia. Once the breccia thins along profile, after the country rock wedge exceeds a thickness of 1.2 m, the amount of matrix and the amount of rounding of the clasts increases with an overall decrease in clast size. This gradual textural change is typically observed with water-magma interactions such as with peperitic terrains where the deformation decreases with distance from the intrusions (e.g. Orth and McPhie, 2003; Németh and White, 2009). Here the change is attributed to a decrease in both thermal and pore pressure with distance from the separation of the sill segments (Delaney, 1982). As the highly pressurised fluids were no longer confined to a narrow space between two impermeable sills, the fragmentation of the country rocks was considerably reduced. It follows that the confinement of the vaporised pore fluids between the dolerite sill segments created severe brecciation of the country rock wedge. The severity of the fragmentation decreased once the pressurised fluids were able to migrate through permeable and porous country rocks. The matrix component increased as the magma was able to migrate through the country rocks that were under less pore pressure. The thickness of the wedge of country rock between the overlapping sill segments is a limiting factor to the amount of pore pressure that can be produced through direct heating and therefore the extent of the rock fragmentation.

5.4.2.1. Matrix composition

The compositions of the upper and lower dolerites are significantly different when compared to the coherent matrix of the breccia. Pyroxene is not present in the breccia matrix as the pyroxene

crystals begin to crystallise after a particular level of crystallisation therefore lacking in the glomerocrysts and breccia sample where the presence of altered/devitrified is signification. In addition, the plagioclase grains are fine in the breccia sample and the composition of the plagioclase grains are more evolved in the upper and lower dolerites. These three factors imply that the dolerite matrix in the brecciated zone was quenched when compared to dolerite sills (Bowen, 1915; McDougall, 1962; Kushiro, 1973). The melt therefore intruded into the spaces between the brecciated clasts cooled more rapidly than the dolerite analysed in both the upper and lower dolerites, indicating that the breccia formed simultaneous with the intrusion of the sills.

5.4.3. Formation of the Sheffield Beach Breccia

The breccia preserved between the sills is clearly the result of severe fragmentation of the country rock wedge. In addition there is evidence of deformation in the surrounding rocks, both in the dolerites and the unfragmented country rocks. Thin sedimentary dykelets and chlorite-infilled veins extend down into the lower dolerite. These sedimentary dykelets form when the excessive pressurisation of volatile-rich country rocks (here the shale) by an intrusive body results in the fluidisation and subsequent mobilisation and injection of the fluidised material, typically into the intrusion (Svenson et al., 2010; Schofield et al., 2012a). This implies that the fluidisation of the country rocks was attributed to the presence of volatiles in the system. The origin of these volatiles could be attributed to pore fluids present in the country rocks or the production of volatiles through the metamorphism of the shales. However, as the breccia formed as the dolerite sills intruded into the host rocks, fluids formed by subsequent metamorphism could not have been present at this stage. The country rocks must have therefore consisted of an initially high component of pore fluids.

The heat of the coherent in the matrix of the breccia was sufficient to partially melt several sandstone clasts where the breccia is the thickest along profile. In the breccia, the boundaries of the sandstone clasts were partially melted by the intruding coherent, as evidenced by the migration of the melted sandstone material into the surrounding breccia. The fluidisation and partially melting of the sandstone clasts and the associated entrained shale clasts within the clasts adjacent to the coherent suggests that, even 15 m away from the point where the sill segments became separate, the heat within the zone of fragmentation was significant.

The formation of the Sheffield Beach breccia is best described by the sequence of events commencing with the intrusion of overlapping sill segments at slightly different stratigraphic

levels. These sill segments were most likely in the form of laterally propagating magma lobes (Fig. 5.8a). As magma flow is expected to flow towards the separation of the sill segments into isolated magma lobes, the direction here is inferred as being from SW to NE (Magee et al., 2012; Schofield et al., 2012b).

The country rock wedge between the sill segments was heated from above and below, thereby achieving a high temperature profile, greater than normally associated with a 1.5 m thick intrusion. Furthermore this wedge of water-saturated sedimentary rock was confined by the sills (Fig. 5.8a). The combination of high temperature and confinement rapidly heated the pore fluids in the country rocks until they flash boiled in the permeable and porous country rocks creating an intense spike in pressure. This pressure increase exceeded the yield strength of the country rocks causing significant fragmentation of the sandwiched sedimentary rocks (Fig. 5.8b). As this fragmentation commenced, the coherent dolerite from the surrounding intrusion was forced into the pore spaces that were created between the clasts of the fragmented country rocks (e.g. Wohletz, 2002; Jamtveit et al., 2004; Lorenz and Kurszlaukis, 2007). The coherent was thus

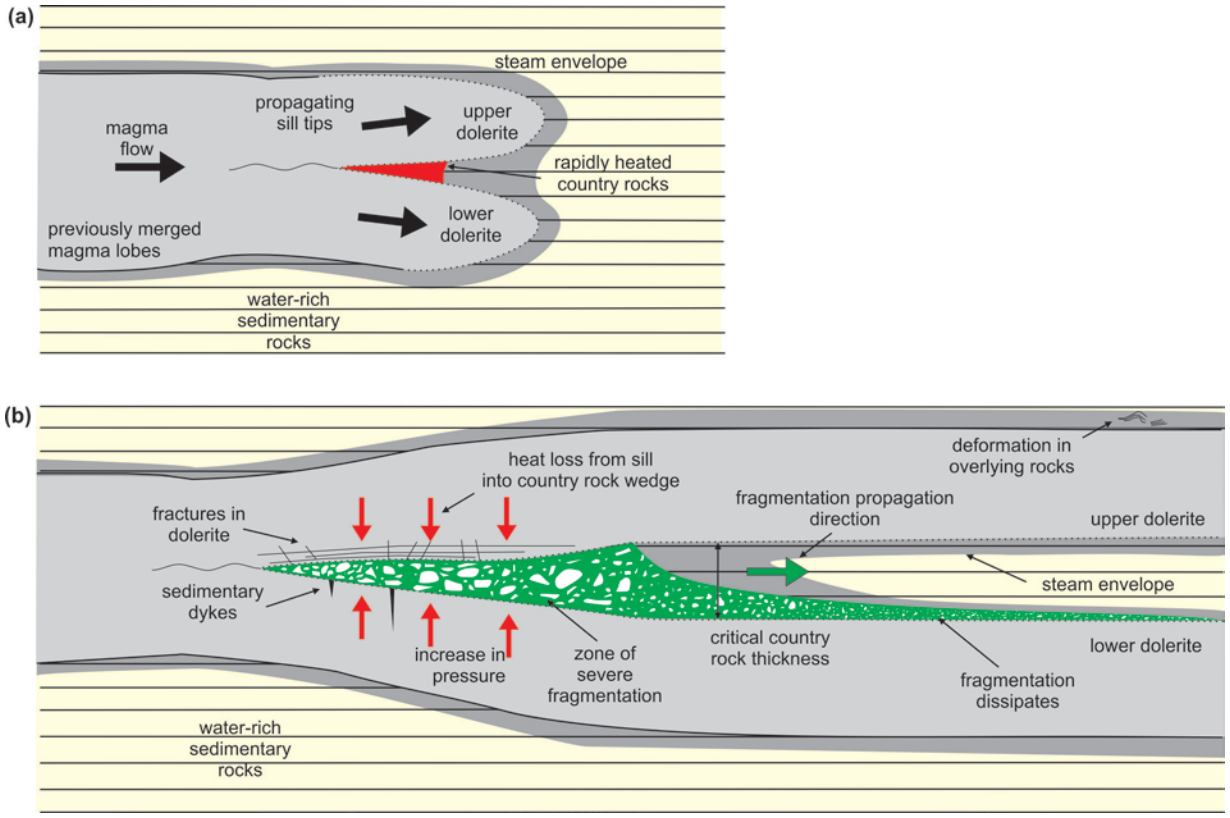

Fig. 5.8. Model showing the formation of the coherent dolerite matrix breccia. (a) The intrusion of magma lobes separating into two sill segments (the lower and upper dolerites) begins to heat up the pore fluids in the adjacent country rocks within the steam envelope. (c) Through the propagation of the coherent dolerite sill segments, the heat from the intrusion rapidly increases the pore-fluid pressure in the country rock wedge and fragmentation commences. The propagation of the fragmentation is outwards from the lobe separation. The fragmentation of the country rocks decreases in severity and vertical extent once a critical thickness of the country rock wedge is exceeded (~1.2 m thick).

quenched and comprises the matrix of the breccia. After the country rock wedge exceeded a critical thickness of 1.2 m, the zone where the fragmentation occurred drastically narrowed (Fig. 5.8b). As the distal regions were not exposed to the same pressures and temperatures as the proximal region, the distal country rocks were not fragmented to the same degree. Instead the breccia was confined to the upper contact of the lower dolerite zone where the temperature was the highest. The extent of the fragmentation in the country rocks is thus ultimately controlled by the thickness of the wedge confined between the two sill segments.

The contemporaneous nature of the country rock fragmentation and the sill injection signifies that the temperature and pressures were dramatically increased in a very short time frame. Along with the severe fragmentation of the country rock wedge to form the breccia, the deformation of the country rocks not adjacent to the dolerite sills suggests that the process of formation of the breccia was short-lived and violent. The intrusion of the dolerite may have occurred at a high stratigraphic level as the hydrostatic pressure required to overcome the lithostatic pressure and commence fragmentation is significantly reduced in near-surface environments (Delaney, 1982).

The fragmentation of the rocks confined between the dolerite sill segments occurred laterally and not vertically as is typical with fracturing associated with hydrothermal vent formation where there is no vertical limiting factor (e.g. Svensen et al., 2006, 2007). This lateral deformation is most likely attributed to the confinement of the country rocks between two coherent partially crystallised dolerite intrusions that have low porosity and permeability. This is a fortuitous situation where the breccia would most likely not have formed if the magma lobes did not overlap. If the sill had intruded as a single isolated intrusion, the surrounding country rocks may have been buckled (e.g. Pollard et al., 1975) or partially fluidised (e.g. Svensen et al., 2010) but would not have formed a coherent-matrix-hosted breccia as observed in this study. The overlapping magma lobes that formed the sill segments are thus, the key to the formation of this sub-volcanic dolerite breccia.

As the coherent breccia is not similar to breccias associated with kimberlite pipes or hydrothermal vents, the formation of this breccia is significant in the history of the volcanic system of the KIP. The dolerite sill segments here have intruded into water-saturated host rocks and the occurrence of this breccia occurring in confined zones in water-rich sedimentary rocks appears to be absent from the literature. The significance of this breccia pertains to the very particular environment in which it formed as the product of a basaltic magma intruding into

water-rich sedimentary rocks does not typically produce pervasive brecciation. It was the overlapping of the sill segments and the confinement of the vapourised pore fluids that created sufficient pore pressure to overcome the lithostatic pressure of the country rocks, an environment of formation that has not been previously documented in association with dolerite sills elsewhere.

The identification of these breccias in associated with small dolerite intrusions may provide key evidence in identifying intrusions that formed in high-level stratigraphic environments. The dolerites in this area were thought to have intruded into rocks with significant overburden, however with the identification of this breccia, the country rocks here were at a high crustal level when these dolerites intruded, an event that occurred prior to the breakup of Gondwana.

References

Aarnes, I., Svensen, H., Polteau, S., Planke, S., 2011. Contact metamorphism devolitization of shales in the Karoo Basin, South Africa, and the effects of multiple sill intrusions. Chemical Geology, 281, 181-194.

Airoldi, G., Muirhead, J.D., White, J.D.L., Rowland, J., 2011. Emplacement of magma at shallow depth: insights from field relationships at Allan Hills, south Victoria Land, East Antarctica. Antarctic Science, 23, 281-296.

Barnett, W.P., Kurszlaukis, S., Tait, M., Dirks, P., 2011. Kimberlite wall-rock fragmentation processes: Venetia K08 pipe development. Bulletin of Volcanology, 73, 941-958.

Bowen, N.L., 1915. The crystallisation of haplobasaltic, haplodioritic, and related magmas. American Journal of Science, 40, 161-185.

Busby-Spera, C.J., White, J.D.L., 1987. Variation in peperite textures associated with differing host-sediment properties. Bulletin of Volcanology, 49, 765-775.

Caroff, M., Vidal, M., Bénard, A., Darboux, J.-R., 2009. A late-Ordovician phreatomagmatic complex in marine soft-substrate environment: The Crozon volcanic system, Armorican Massif (France). Journal of Volcanology and Geothermal Research, 184, 351-366.

Delaney, P.T., 1982. Rapid intrusion of magma into wet rock: groundwater flow due to pore pressure increases. Journal of Geophysical Research, 87, 7739-7756.

Delaney, P.T., Pollard, D.D., 1981. Deformation of host rocks and flow of magma during growth of minette dikes and breccia-bearing intrusions near Ship Rock, New Mexico. Geological Survey Professional Paper, 1202.

Du Toit, A.L., 1904. Geological survey of the divisions of Aliwal North, Herschel, Barkly East and parts of Wodehouse. 9th Ann. Rep. Geol. Comm. Colonly of eh Cape of Good Hope, 1904, 71-181.

Erlank, A.J., 1984. Petrogenesis of the volcanic rocks of the Karoo Province. Special Publication of the Geological Society of South Africa, 13, 395 pp.

Gevers, T.W., 1928. The volcanic vents of the western Stormberg. Transactions of the Geological Society of South Africa., 31, 43-62.

Hanson, R.E. and Hargrove, U.S., 1999. Process of magma/ wet sediment interaction in a large-scale Jurassic andesitic peperite complex, northern Sierra Nevada, California. Bulletin of Volcanology, 60, 610-626.

Honnorez, J., Kirst, P., 1975. Submarine basaltic volcanism: morphometric parameters for discriminating hyaloclastites from hyalotuffs. Bulletin of Volcanology, 39, 1-25.

Jamtveit, B., Svensen, H., Podladchikov, Y.Y., Planke, S., 2004. Hydrothermal vent complexes associated with sill intrusions in sedimentary basins. In: Breitkreuz, C., Petford, N. (Eds) Physical Geology of High-Level Magmatic Systems. Geological Society of London, Special Publication, 234, 233-241.

Jerram, D.A., Stollhofen, H., (2002). Lava/sediment interaction in desert settings; are all peperite-like textures the result of magma-water interaction? Journal of Volcanology and Geothermal Research, 114, 231-249.

Jourdan, F., Féraud, G., Bertrand, H., Watkeys, M.K., Renne, P.R., 2008. $^{40}Ar/^{39}Ar$ ages of the sill complex of the Karoo large igneous province: implications for the Pliensbachian-Toarcian climate change. Geochemistry, Geophysics, Geosystems. 9, Q06009, doi:10.1029/2008GC001994.

Kokelaar, B.P., 1982. Fluidisation of wet sediments during the emplacement and cooling of various igneous bodies. Journal of the Geological Society of London, 139, 21-33.

Kurszlaukis, S., Franz, L. and Lorenz, V., 1998. On the first experimental phreatomagmatic explosion of a kimberlite melt. Journal of Volcanology and Geothermal Research, 80, 323-326.

Kushiro, I., 1973. The system diopside-anorthite-albite: determination of compositions of coexisting phases. Carnegie Institute, Washington Yearbook, 72, 502-507.

Liss, D., 2004. Emplacement processes and magma flow geometries of the Whin Sill complex. PhD thesis, University of Birmingham. 236 pp.

Lorenz, V., 1986. On the growth of maars and diatremes and its relevance to the formation of tuff rings. Bulletin of Volcanology, 48, 264-274.

Lorenz, V., 1987. Phreatomagmatism and its relevance. Chemical Geology, 62, 149-156.

Lorenz, V., Kurszlaukis, S., 2007. Root zone in the phreatomagmatic pipe emplacement model and consequences for the evolution of maar-diatreme volcanoes. Journal of Volcanology and Geothermal Research, 159, 4-32.

Magee, C., Stevenson, C.T.E., O'Driscoll, B., Petronis, M.S. 2012. Local and regional controls on the lateral emplacement of the Ben Hiant Dolerite intrusion, Ardnamurchan (NW Scotland). Journal of Structural Geology, 39, 66-82.

McClintock, M.K., White, J.D.L., 2002. Granulation of weak rock as a precursor to peperite formation: coal peperite: Coombs Hills, Antarctica. Journal of Volcanology and Geothermal Research, 114, 205-217.

McDougall, I., 1962. Differentiation of the Tasmanian Dolerites: Red Hill Dolerite-Granophyre Association. Geological Society of America Bulletin, 73, 279-316.

Németh, K., White, C.M., 2009. Intra-vent peperites related to the phreatomagmatic 71 Gulch Volcano, western Snake River Plain volcanic field, Idaho (USA). Journal of Volcanology and Geothermal Research, 183, 30-41.

Nesse, W.D., 2000. Introduction to Mineralogy. Oxford University Press, New York. Pp. 442.

Orth, K., McPhie, J., 2003. Textures formed during emplacement and cooling of a Palaeoproterozoic, small-volume rhyolitic sill. Journal of Volcanology and Geothermal Research, 128, 341-362.

Petry, K., Jerram, D.A., de Almeidal, D.P.M., Zerfass, H., 2007. Volcanic-sedimentary features in the Serra Geral Fm., Paraná Basin, southern Brazil: examples of dynamic lava-sediment interactions in an arid setting. Journal of Volcanology and Geothermal Research, 159, 313-325.

Pichler, H., 1965. Acid hyaloclastites. Bulletin of Volcanology, 28, 293-310.

Pollard, D.D., Muller, O.H., Dockstader, D.R., 1975. The form and growth of fingered sheet intrusions. Geological Society of America Bulletin, 86, 351-363.

Rawlings, D.J., Watkeys, M.K., Sweeney, R.J., 1999. Peperitic upper margin of an invasive flow, Karoo flood basalt province, northern Lebombo. South African Journal of Geology, 102, 377-383.

Savin, C., Grasso, J.-R., Bachelery, P., 2005. Seismic signature of a phreatic explosion: hydrofracturing damage at Karthala volcano, Grande Comore Island, Indian Ocean. Bulletin of Volcanology, 67, 717-731.

Schofield, N.J., 2009. Linking sill morphology to emplacement mechanisms. PhD Thesis, University of Birmingham. 210 pp.

Schofield, N.J., Brown, D.J., Magee, C., Stevensen, C.T., 2012a. Sill morphology and comparison of brittle and non-brittle emplacement mechanisms. Journal of the Geological Society of London, 169, 127-141.

Schofield, N., Heaton, L., Holford, S.P., Archer, S.G., Jackson, C.A.-L., Jolley, D.W., 2012b. Seismic imaging of 'broken bridges': linking seismic to outcrop-scale investigations of intrusive magma lobes. Journal of the Geological Society of London, 169, 421-426.

Skilling, I.P., White, J.D.L., McPhie, J. 2002. Peperite: a review of magma-sediment mingling. In: Skilling, I.P., White, J.D.L., McPhie, J. (Eds.), Peperite: Processes and Products of Magma-Sediment Mingling. Journal of Volcanology and Geothermal Research, 114, 1-17.

Sparks, R.S.J., Baker, L., Brown, R.J., Field, M., Schumacher, J., Stripp, G., Walters, A., 2006. Dynamical constraints on kimberlite volcanism. Journal of Volcanology and Geothermal Research, 155, 18-48.

Svensen, H., Jamtveit, B., Planke, S., Chevallier, L., 2006. Structure and evolution of hydrothermal vent complexes in the Karoo Basin, South Africa. Journal of the Geological Society of London, 163, 671-682.

Svensen, H., Planke, S., Chevallier, L., Malthe-Sørenssen, A., Corfy, F., Jamtveit, B., 2007. Hydrothermal venting of greenhouse gases triggering Early Jurassic global warming. Earth and Planetary Science Letters, 256, 554-566.

Svensen, H., Aarnes, I., Podladchikov, Y.Y., Jettestuen, E., Harstad, C.H., Planke, S., 2010. Sandstone dikes in dolerite sills: Evidence for high-pressure gradients and sediment mobilization during solidification of magmatic sheet intrusions in sedimentary basins. Geosphere, 6, 211-224.

Valentine, G.A., Graettinger, A.H., Sonder, I., 2014. Explosion depths for phreatomagmatic eruptions. Geophysical Research Letters, 41, 3045-3051.

White, J.D.L., McPhie, J., Skilling, I., 2000. Peperite: a useful genetic term. Bulletin of Volcanology, 62, 65-66.

Wohletz, K.H., 1986. Explosive magma-water interactions: Thermodynamics, explosion mechanisms, and field studies. Bulletin of Volcanology, 48, 245-264.

Wohletz, K.H., 2002. Water/magma interaction: some theory and experiments on peperite formation. Journal of Volcanology and Geothermal Research, 114, 19-35.

Zimanowski, B., Fröhlich, G., Lorenz, V., 1995. Experiments on steam explosion by interaction of water with silicate melts. Nuclear Engineering and Design, 155, 335-343.

Zimanowski, B., Büttner, R., Lorenz, V., Häfele, H.-G., 1997. Fragmentation of basaltic melt in the course of explosive volcanism. Journal of Geophysical Research, 102, 803-814.

- CHAPTER 6 –

A COMPARATIVE STUDY BETWEEN MAGMATIC AND MAGNETIC FABRICS WITH MAGMA FLOW INDICATORS TO INFER MAGMA FLOW

6.1. Introduction

Knowing the magma flow direction in a sill can provide information about the feeder system and the movement and migration of magma in the upper crust (Schofield et al., 2012a). By determining the magma flow directions in sills the plumbing systems attached to large igneous provinces can be better understood, as subvolcanic sills play an important role in supplying magma to overlying volcanic sequences (Cartwright and Hansen, 2006). The Karoo Igneous Province (KIP) of southern Africa involved not only the outpouring of voluminous continental flood basalts, but also the intrusion of an extensive sub-volcanic network of dykes and sills (Erlank, 1984). Magmatism that created the KIP occurred between ~183 Ma and ~174 Ma (Jourdan et al., 2005, 2007; Hastie et al., 2014) with the sills in the main Karoo Basin forming between 183.0 ± 0.5 – 182.3 ± 0.6 Ma (Svensen et al., 2012). Along the North Coast of KwaZulu-Natal (KZN), South Africa, numerous small planar sills, crop out along the coastline. Certain structures that occur in association with the sills, either through magma-host rock interactions or magmatic processes, can be used to indicate the direction of magma flow. These structures have previously been used to define magma flow regimes of both dykes (Pollard et al., 1975; Pollard, 1987; Rickwood, 1990; Liss et al., 2002) and sills (Nicholson and Pollard, 1985; Horsman et al., 2005).

Magma flow within small tabular intrusions has been inferred using magmatic fabrics. Techniques to procure a proxy for the magmatic fabric include Anisotropic Magnetic Susceptibility (AMS) and Shape Preferred Orientation (SPO) analyses. Magnetic fabrics are commonly used to infer the magma flow within igneous rocks, including lava flows, hypabyssal and plutonic rocks (Khan, 1962; Ellwood, 1978; Knight and Walker, 1988; Poland et al., 2004; Aubourg et al., 2008). This analytical technique is often supplemented with fabric data determined through petrographic analysis such as SPO studies (Launeau and Robin, 1996; Launeau and Cruden, 1998; Horsman et al., 2005; Hastie et al., 2014). This is necessary especially if the AMS fabric has been obtained from weakly anisotropic rocks, as the combination of independent fabric acquisition methods is the most accurate way to use

magmatic or magnetic fabrics to infer a sense of magma flow (Archanjo and Launeau 2004; Payacán et al., 2014).

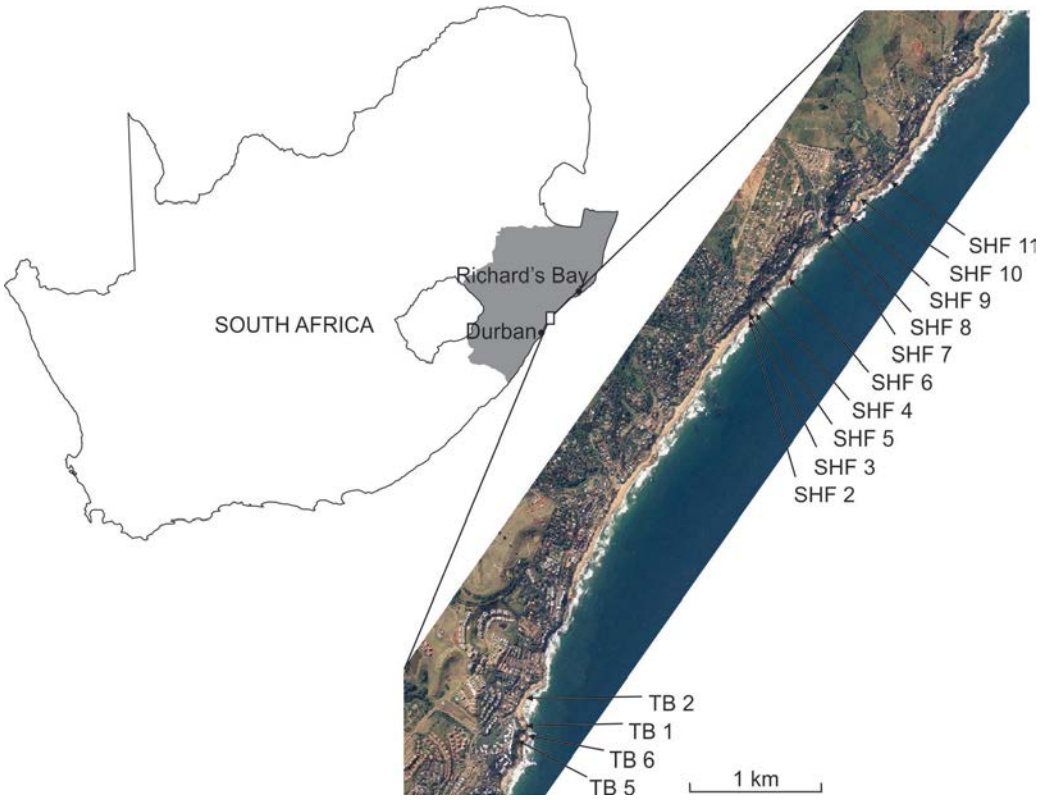

Fig. 6.1. Locality of the study area along the KwaZulu-Natal North Coast, South Africa. The 14 sills that have been analysed are named with reference to the areas Thompson's Bay (TB) in the south and Sheffield Beach (SHF) in the north.

The main aim of this chapter is to compare the field, SPO and AMS data obtained from sills in order to determine whether or not magma flow indicators can be used to adequately predict magma flow in sills. Similar studies have been undertaken on certain aspects of magma flow indicators with sills (e.g. Horsman et al., 2005) and other types of intrusions, such as dykes (e.g. Philpotts and Philpotts, 2007), and lava flows (e.g. Loock et al., 2008). Other studies have been undertaken comparing macroscopic magmatic textures (i.e. mineral lineation fabrics) with magnetic analyses to determine how well the magnetic fabric mimics the macroscopic magmatic fabric (e.g. O'Driscoll et al., 2008; Schopa et al., 2015). However, to the authors' knowledge no extensive studies on how capably different magma flow indicators predict magma flow in small tabular intrusions, based on comparisons of AMS and SPO techniques, have been published. Different morphological structures are incorporated into this study including magma lobes and broken bridge structures and the magma flow directions implied are scrutinised. This is achieved by (1) analysing the structures in the field area (2) analysing the fabrics along the sill contacts through AMS and SPO analyses; (3) inferring magma flow within the sills using the

SPO and AMS fabrics; (4) comparing the magma flow directions inferred from the fabric studies with the magma flow predicted by the magma flow indicators observed in the field.

Being able to use magma flow indicators as reliable predictors of magma flow would enable larger studies to be undertaken in the field without copious amounts of laboratory work required. Not all of the magma flow indicators analysed in this study may have the same degree of reliability in predicting a magma flow sense in these systems. Thus a hierarchy of structures could exist from accurate magma flow indicators to less accurate indicators. The results in this chapter are used to identify this hierarchy.

6.2. Geological Setting

The dolerite sills that are analysed in this study are constrained to an 8 km stretch of the littoral coastline of the KZN North Coast, South Africa (Fig. 6.1). The dolerites intruded Permian age sedimentary rocks of the Vryheid Formation of the Karoo Supergroup. The country rocks range from thinly laminated siltstones to shales and gritstones. The sills generally intrude into the finer grained sedimentary rocks. The study area is divided into three sections and named by beaches where the sills crop out. These areas from south to north are Thompson's Bay (TB), Shaka's Rock (SR) and Sheffield Beach (SHF), which has been divided into southern and northern Sheffield Beach. The sills range in thickness between 0.5 (SHF8) and > 6 m (SHF7) and are predominantly concordant with the stratigraphy. The intrusions were faulted and tilted by a series of brittle tectonic events related to the breakup of Gondwana (Watkeys, 2006). One of the sills (SHF6) is a composite sill where dolerite magma intruded into an older sill. Only the younger sill was sampled as the contacts of the older sill were not exposed.

6.3. Country Rock Deformation by Magma Intrusion

There are several types of structures found in the sills in the study area that have formed in response to the intrusion of the sills. The formation process typical of these structures allows the magma flow sense to be inferred from the preserved structures. The formation processes of these magma flow indicators are described below and the structures are divided into categories based on how they formed.

6.3.1. Brittle Propagation-related Structures

When magma in the form of lateral intrusions or sill segments intrude into rocks, and the fractures into which they are injected become dilated, the manner in which the country rock fractures can produce remnant structures. Examples of these are bridge structures and intrusive

steps that form when separate, propagating magmatic segments, that have exploited different stratigraphic horizons during emplacement become merged (Nicholson and Pollard, 1985; Nicholson and Ejiofor, 1987; Hutton, 2009; Schofield et al., 2012a, b). When the intruding magma segments are overlapping, bridge structures are produced. When the magma segments are adjacent but not overlapping, intrusive steps form (Fig. 6.2).

Bridge structures form when the country rock between two overlapping fractures is deformed (Fig. 6.2a). As the magma is injected and dilates the fractures, which may have straight or curved propagation paths, an intervening bridge structure is created. Post-fracture and magma injection, the excessive magma pressure can cross-fracture the country rock at inflection points

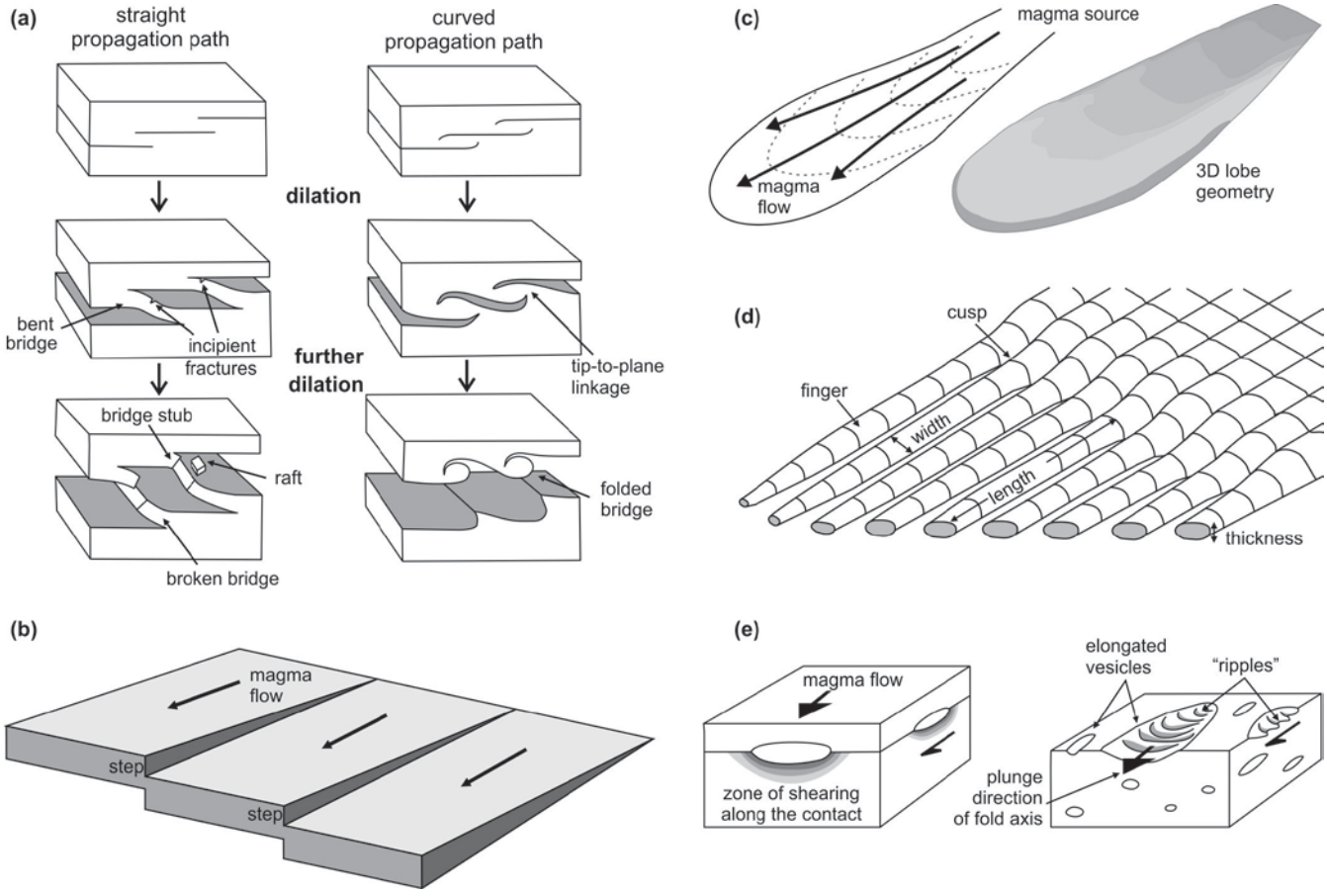

Fig. 6.2. The formation processes of magma flow indicators. (a) Bridge structures form through the propagation and dilation of overlapping fractures. Fracture propagation paths can be straight or curved. As the fractures are filled with the injecting magma, the magma tubes expand to form bent bridges of country rock which, when broken, form coalesced magma pods with remnant broken or rotated bridges and floating rafts. After Nicholson and Pollard (1985) and Kattenhorn and Watkeys (1995). (b) Steps are formed through the linkage of magma-filled fractures that are adjacent but do not overlap. Modified after Pollard et al. (1975) and Rickwood (1990). (c) An example of the shape of a magma lobe formed through dispersive magma flow away from the magma source. Redrawn after Stevenson et al., (2007). (d) The progressive formation of fingers shows how the finger thickness is related to the length of the finger. Redrawn after Pollard et al. (1975). (e) Deformation of vesicles along the upper surface of a sill where a skin of chilled magma around the vesicle becomes sheared resulting in the formation of ropy-flow structures. Magma flow is implied by the preserved "ripples".

forming a broken bridge (Nicholson and Ejiofor, 1987; Morris et al., 2008). The morphologies of these broken bridges may be either bent or rotated in shape this depends on whether the shape of the propagating fractures was straight or curved, with little deformation within the bridge beyond the zones of folding (Nicholson and Pollard, 1985). Where the bridge material breaks away from the country rock, the separated host rock segment, or "raft", is entrained into the intruding magma and the resultant host rock structure is termed a "bridge stub" (Fig. 6.2a).

Intruding magma segments that merge without lateral overlap join, by producing an intrusive step between the magma segments (Fig. 6.2b) (Pollard et al., 1975; Rickwood, 1990; Schofield et al., 2012a). Intrusive steps link sills at varying stratigraphic levels, with the vertical difference between the magma segments increasing with distance from the magma source (Rickwood, 1990; Schofield et al., 2012a). These intrusive steps are typically steeply inclined when compared to the sills with which they have become linked (Fig. 6.2b). As a result of fracture linkage and magma flow, the long axes of bridge structures and intrusive steps may be used to imply the orientation of primary flow within an intrusion.

6.3.2. Non-brittle Propagation-related Structures

Magma lobes (Fig. 6.2c) and fingers (Fig. 6.2d) form in separate fractures as magma initially intrudes into the host rock where host rock fluidisation, or disaggregation, may occur. These lobes later coalesce to form a continuous sheet-like intrusion (Pollard et al., 1975; Schofield et al., 2010, 2012a). The geometry of a magma lobe can be used to infer the magma flow direction. Here flow is towards the bulbous termination of the lobes, away from the lobe opening direction (Stevenson et al., 2007; Magee et al., 2012). Magma fingers form at the leading edge of an intruding sill. When preserved on the outskirts of sills, the magma flow may be inferred as being towards the direction in which the fingers diverge into separate intrusions (Pollard et al., 1975; Baer and Reches, 1987; Rickwood, 1990; Horsman et al., 2005; Schofield et al., 2012b).

6.3.3. Internal Magma Flow-related Structures

Magmas that have a relatively high volatile content may be subject to devolatilisation, with the exsolved vapours forming (micro- to macroscopic) vesicles as the magma/lava cools. Larger vesicles (>1 cm diameter) are the product of vesicle coalescence, which can rise vertically and create large, flattened vesicles near the upper contacts of an intrusion (Manga and Stone, 1994; Liss et al., 2002). Such vesicles may be deformed within the intrusion through continuous shearing as the magma flow moves. This causes the vesicles to become elongated parallel to magma flow. The long axes of elongated and flattened vesicles are therefore parallel to the direction of magma movement (Rickwood, 1990). The effect of magma movement in intrusions

that contain large vesicles is more pronounced and may form ropy-flow structures typically occurring in vesicles with long axis lengths of >6 cm (Fig. 6.2e) (e.g. Liss et al., 2002). These structures form when a rind of chilled magma on the outside of a large vesicle is plastically deformed, particularly when the underside of the vesicle is dragged into folds or "ripples" by the underlying flowing magma (Fig. 6.2e). The direction of flow is thus parallel to the plunge direction (trend) of the fold axis of the ripples (Fink and Fletcher, 1978; Liss et al., 2002).

The long axes of the structures are used in the Results Section below to infer magma flow directions or orientations. The long axes of linear structures are measured using plunge and plunge direction (e.g. magma lobes) and the long axes of planar structures were measured using dip and strike (e.g. intrusive steps).

6.4. Methods

6.4.1. Sample collection and preparation

The 14 sills analysed in this paper were sampled within 10-15 cm of the upper and lower sill contacts (where available). The samples were collected using a petroleum-powered handheld drill extracting 25 mm diameter cores. A minimum of four samples were collected from the upper and lower contacts of each intrusion. Where the sills showed discrete layers; these units were sampled and labelled separately from the margins (e.g. TB2). The cores obtained were orientated in the field using a core-orientator and a magnetic compass. These cores were divided, where one half was used for petrographic analyses (SPO) and the other half for magnetic analyses (AMS). The samples for SPO analyses were cut into three mutually perpendicular sections based on an XYZ coordinate system (Fig. 6.3a). The samples were prepared into thin sections for petrographic analyses and each thin section (three thin sections per sample) was photographed under crossed polarisers. The cores intended for AMS analyses were cut into cylinders not exceeding 25 mm in length. Samples were obtained both proximal and distal to the magma flow indicators, in order to compare results if localised discrepancies were found.

6.4.2. Shape-preferred Orientation Techniques

Defining the SPO is a process where the three-dimensional (3-D) shape ellipsoid of a mineral phase, plagioclase laths for this study, is determined. This fabric is representative of the magmatic fabric of the samples. The plagioclase grains were used to determine the magmatic fabric as the plagioclase grains are abundant and generally well-preserved with little to no alteration in most of the samples. The opaque minerals are predominantly parallel to the plagioclase laths petrographically therefore the plagioclase and opaque fabrics would most

likely be coaxial. A total number of 109 samples (327 photomicrographs) were analysed petrographically to obtain the fabrics of the plagioclase grains for 14 sills.

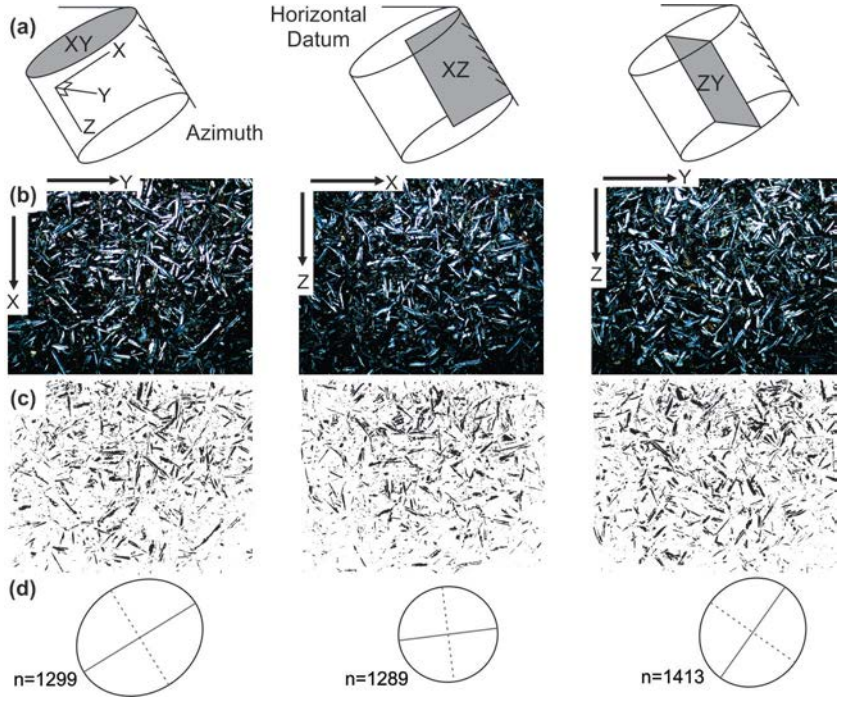

Fig. 6.3. Fabric acquisition by SPO techniques (a) Diagram of the mutually perpendicular sections (grey) cut from a standard drill core sample. Each sample comprises three orthogonal sections as defined by an XYZ coordinate system after Hastie et al. (2011a). (b) Photomicrographs from sample SHF 6 LF taken under cross-polarisers (5 mm in width) with the coordinate directions shown down dip in black arrows. (c) Filtered images which are to be analysed in the SPO-2003 programme where the plagioclase grains have been extracted using a threshold grey scale value. (d) The resultant ellipse determined for each section. From Hoyer and Watkeys (2015)

In order to measure the orientation and shape of the plagioclase crystals by means of measured ellipses, photomicrographs of the thin sections must be obtained and analysed at the suggested magnification, which depends on the sample grain size (Hoyer and Watkeys, 2015). These oriented photomicrographs (Fig. 6.3b) were then converted into negative black and white images and filtered using a threshold level so that the plagioclase grains could be extracted (Fig. 6.3c). Grains that were truncated by the image boundary were removed and any intersecting grains were manually separated. Each grain is therefore individually analysed to obtain an accurate result. The final digitised images were imported into the programme SPO-2003 (Launeau, 2004; Launeau and Robin, 1996, Launeau and Cruden, 1998) which creates a 2-D inertia tensor from all the stacked grain data and defines an ellipse (Launeau and Robin, 1996; 2005). The three mutually perpendicular 2-D tensors (Fig. 6.3d) are then combined in the programme Ellipsoid-2003 (Robin, 2002; Launeau, 2004; Launeau and Robin, 2005), where

each ellipse holds an equal weight regardless of the number of grains measured. This allows a 3-D ellipsoid to be created, the parameters of which define the fabric. The shape of the ellipsoid (T) and the degree of anisotropy (P'), which is the measure of how much the fabric differs from a spherical shape, are determined by the software and recorded for each ellipsoid. T is defined as prolate, triaxial or oblate when T is less than, equal to or greater than zero respectively (Jelinek, 1981). P′ is the measurement of the eccentricity of the ellipsoid (Tarling and Hrouda, 1993).

The ellipsoid is defined by a foliation and a lineation, representative of a planar and linear fabric respectively. The error in the fit of the ellipsoid is measured by the Global Incompatibility Index, $\sqrt{F}$, so that when $\sqrt{F}$ is zero the ellipses create a perfect fit (Launeau and Robin, 2005). Results with $\sqrt{F}$ of less than 10% are desirable and 10% $\sqrt{F}$ is the generally accepted value below which the results may be trusted for fit accuracy (Launeau and Robin, 2005; Hoyer and Watkeys, 2015).

6.4.3. Anisotropy of Magnetic Susceptibility Methodology

AMS is described using a second-rank tensor where the magnetic susceptibility κ has principal values κ_1 for the maximum axis, κ_2 for the intermediate axis and κ_3 for the minimum axis (Borradaile and Jackson, 2004). AMS was first used by Graham (1954) as a method to determine fabrics. The resultant fabrics were considered as directly related to aspects of the rock fabrics. Since then it has become a widely-used method in determining the magnetic fabrics in rocks and is still considered a powerful tool in rock fabric studies (Cañón-Tapia and Chávez-Álvarez, 2004). Mafic igneous rocks typically contain ferromagnetic Fe (and Ti) Oxides such as titanomagnetite, pyrrhotite and magnetite. These minerals may be in the state of single domain (SD), pseudo-single domain (PSD) and multiple domain (MD) (Rochette et al., 1999). The source of the AMS may be from three sources as recently defined by Cañón-Tapia (2004). The three sources are (1) normal fabrics where the κ_1 coincides with the long axis of the measured grain and κ_3 coincides with the short axis; (2) the SD effect (inverse fabrics), where the axes are inverted; κ_1 coincides with the short axis of the grain and κ_3 with the long axis (first proposed by Stephenson et al., 1986); (3) clustered magnetic grains where the AMS is a product of the cluster and not of the individual grains.

For igneous rocks, the interpretation of the AMS results relies on the development of a preferred orientation of the magnetic minerals in the rocks as a result of magma flow (Cañón-Tapia and Chávez-Álvarez, 2004). The orientation and distribution of these grains within a rock can be

determined by their response to an induced magnetic field producing a susceptibility ellipsoid that is anisotropic. The AMS of each sample was determined using the AGICO Kappabridge MFK1-FA susceptibility bridge at the Institute for Rock Magnetism at the University of Minnesota. The standard 15 position procedure was used during analyses (Jelinek, 1978). The results are illustrated using lower hemisphere stereograms with the principal axes, κ_1, κ_2 and κ_3, plotted stereographically as lineations. The parameters P' (degree of anisotropy) and T (shape parameter) are defined for each result (Jelinek, 1981; Tarling and Hrouda, 1993).

Fourteen sills were sampled for AMS analyses and 28 contacts or zones have been analysed; 14 were upper sill contacts, 12 were lower sill contacts and two were from demarcated zones of TB2. A total of 257 samples were analysed. Each sample individually represents a magnetic fabric result for that sample site; numerous samples have not been averaged in order to determine an average fabric for a localised area. The average orientations of the principal axes of the AMS ellipsoid is determined using Jelinek statistics (Jelinek, 1978), which are automatically calculated by the program Anisoft42 where five or more samples were analysed. For the results, there were five contacts where only four samples were analysed. The four data results the contacts TB6U, SHF2U, SHF4L, SHF9U and SHF10U were manually averaged (the average of the principal axes were individually statistically averaged), thus no error ellipses were calculated and are therefore absent from the related stereonets.

6.4.4. Fabric shapes

The shape of an ellipsoid, belonging to either a magmatic or magnetic fabric, is a critical factor when using the ellipsoid to define the fabric. Lineations have typically always been used to define petrofabrics however, it has been shown that the lineation is not always representative of

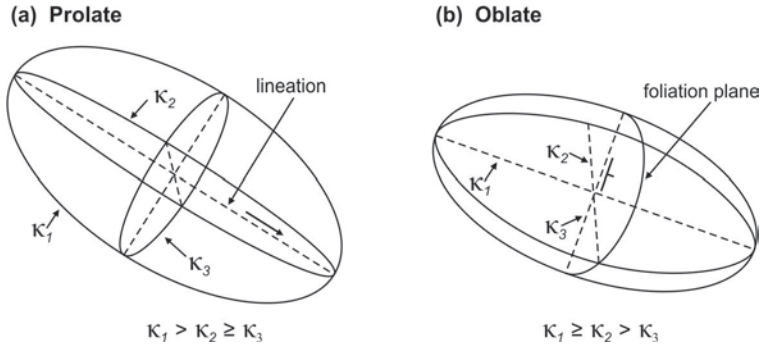

Fig. 6.4. AMS ellipsoids for (a) prolate-shaped ellipsoids where the long axis, κ_1, is the used to define the ellipsoid as a lineation as $\kappa_2 \approx \kappa_3$; (b) oblate-shaped ellipsoids where K3 is the pole to the foliation, the foliation is used to define the ellipsoid when the ellipsoid is oblate at $\kappa_1 \approx \kappa_2$..

the magma flow sense and should not be singularly relied upon to define the fabric (Geoffroy et al., 2002; Archanjo et al., 2012). Ellipsoids have three variable length axes and may be either prolate or oblate in shape. If an ellipsoid is prolate, the fabric will be best defined by the lineation, which for SPO is the plunge and plunge direction of the measured linear fabric determined using the SPO and for AMS is the lineation (i.e. parallel to the κ_1 axis). However with strongly oblate fabrics, the κ_1 and κ_2 axes may become inverted, thus the κ_1 axis would not reflect the lineation of the ellipsoid (Rochette et al., 1999; Borradaile and Lagroix, 2001). Therefore if the fabric is oblate, it is best defined by the foliation which for the SPO and AMS is the dip and azimuth of the foliation. Where the κ_3 axis (AMS) is the pole to the foliation (e.g. Archanjo et al., 2012).

6.5. Magnetic Mineralogy and its Significance

Analyses on small rock chips (measuring ~5x5x5 mm) and rock powders were undertaken in order to accurately constrain the properties of the magnetic phases present in the samples. These analyses were undertaken at the Institute for Rock Magnetism and the University of Minnesota.

6.5.1. Susceptibility-Temperature Curves

High temperature analyses were conducted on samples from each sill. These were undertaken in order to determine the Curie temperatures of the magnetic minerals present in the samples using the Kappabridge High-Temperature Suspectometer. With a Curie temperature between 575°C and 585°C, magnetite is the most common mineral identified in the sills studied and was present in all the samples (Table 6.1). Recorded transition temperatures of magnetite within the samples analysed ranged from 564°C (SHF7) to 595°C (SHF6). Pyrrhotite, with a Curie temperature of ~320°C, occurred in nine of the 14 samples analysed and is recognised by the less significant drop in magnetisation as seen for TB5 and SHF10 (Fig. 6.5a) suggesting that the magnetite contributes more significantly to the bulk susceptibility than pyrrhotite (Ferré et al., 2002). Goethite, with a transition temperature of 102°C, is only present in the sample from TB6, a sill that has been altered and largely silicified (Table 6.1).

A significant drop in remanence in the K-T curves between 564°C and 595°C indicated the presence of magnetite grains, the main magnetic component in the samples. Where the measured Curie temperature is higher than expected, above 585°C, maghemitisation may have occurred within the sills (Dunlop and Özdemir, 1997).

6.5.2. Low temperature transitions

The low temperature analyses were conducted using the Magnetic Properties Management System instrument (MPMS) where the remanence magnetisation of minerals at low temperatures (20 – 300 K) was measured. Stoichiometric magnetite (Fe_3O_4) has an unblocking temperature of between ~110 and 120 K called the Verwey Transition (T_v) where the grains transition from cubic to monoclinic in habit (Verwey, 1939; Zuo, 1990). Stoichiometric pyrrhotite (Fe_7S_8) transitions between 30 and 35 K exhibiting a distinct drop in remanence (Bensus and Meyer, 1964; Bensus, 1966; Rochette et al., 1990). This was recently named the Bensus Transition by Rochette et al. (2011).

The T_v of magnetite was evident in the majority of the samples analysed by low temperature suspectometry. Of the 14 sills analysed, only one sill (SHF2) exhibited no T_v (Fig. 6.5b). The other 13 samples yielded T_v results between 100 – 120 K showing the presence of magnetite. A marked "hump" is present in the RT cooling curve (i.e. SHF2 in Fig. 6.5b), which occurs in more than half of the samples.

A second transition is evident at low temperatures (20 – 35 K) for the majority of the samples (e.g. TB5 and SHF5 in Fig. 6.5b). The only sample to yield no drop in remanence other than at Tv is SHF10 (Table 6.1). Samples from TB1, TB2, TB5 and TB6 yielded a Bensus Transition of pyrrhotite 30 – 33 K. All of the other samples yielded a significant drop in remanence below 30K, possibly as a result of paramagnetic behaviour of magnetite (e.g. SHF11 in Fig. 6.5b) (Özdemir et al. 1993). For all of the samples, the FC curve yielded a higher remanence than the ZFC curves indicating a general SD grain size (Dunlop, 2002).

6.5.3. Magnetic Hysteresis

Analyses undertaken involving magnetic hysteresis properties were conducted using the MicroMag Vibrating Sample Magnetometer at room temperature. The domain state of magnetic minerals was inferred using the hysteresis properties of the samples (Rochette et al., 1999). Hysteresis curves were determined for the samples exposed to 1T magnetisation with magnetic moment determined at 5 mT increments. Three distinctly shaped hysteresis loops resulted from the 16 analyses undertaken on the samples, with examples of each presented in Fig. 6.5c. Narrow loops with strong ferromagnetic properties and low coercivities were the most common shapes recorded (e.g. TB5 in Fig. 6.5c). Three samples yielded constricted hysteresis loops (e.g. SHF2 in Fig. 6.5c) where the shape of the loop narrows and is typically attributed to magnetic overprinting by a secondary mineral. The hysteresis measurements from TB1 and TB2 yielded

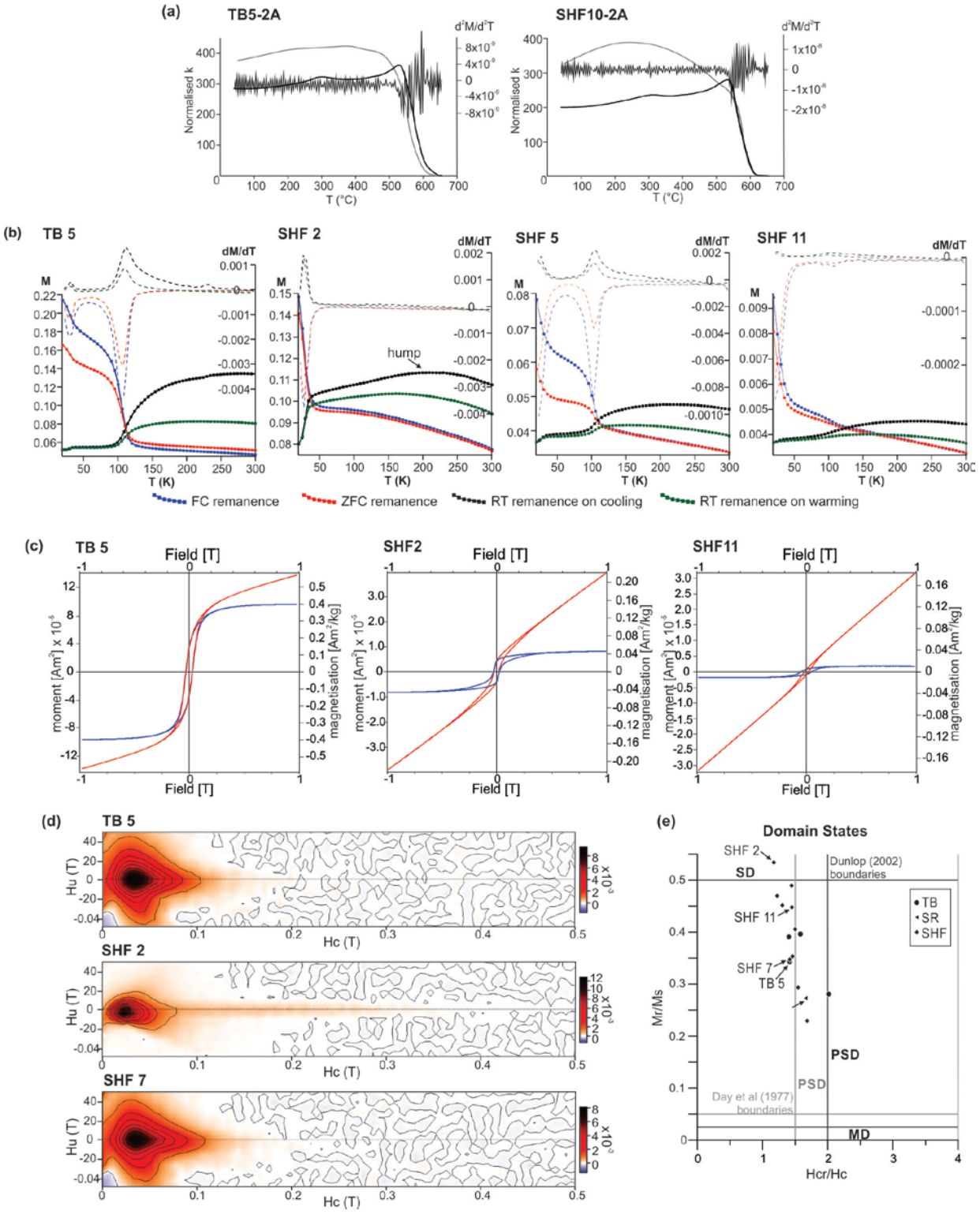

Fig. 6.5. (a) Graphical representation of susceptibility (K) against temperature (T) for samples from TB5 and SHF10. The bold black line is the heating curve, the grey line is the cooling curve and the thin black line is the derivative of the heating curve. (b) Low temperature results represented by Magnetisation (M) vs. Temperature (T) for the samples TB5, SHF2, SHF5 and SHF11 measuring the sample remanence recorded from the four cycles of cooling and warming under different field strengths. For TB5 and SHF5, the drop in remanence at ~30K is indicative of the presence of pyrrhotite. The drop in remanence at ~110K for represents the presence of magnetite. For SHF2 and SHF11, the drop in remanence at 27K could be attributed to superparagmagnetic magnetite or the presence of low temperature transitioning pyrrhotite. SHF2 shows no primary magnetite because of maghemitisation as indicated by the "hump" in the RT remanence cooling curve (Özdemir and Dunlop 2010). (c) Hysteresis results showing examples of three different shaped loops observed in the samples. TB 5: narrow loop with a strong ferromagnetic signature, SHF2: constricted or distorted ferromagnetic SD loop, SHF11: a small loop with a restricted magnetic moment attributed to the presence of a paramagnetic component (d) representation of FORC results plotted as H_u vs. H_c TB5 and SHF7 plots are dispersed between the Hu axis and the low values of H_c, SHF2 is restricted to low H_u values and extended along the H_c axis. (c) DCD plot with the Dunlop (2002) and Day et al (1977) parameters denoting the regions of SD, PSD and MD grain sizes. Majority of the samples plot in the PSD zone.

restricted loops which are attributed to pyrite, a paramagnetic mineral which is abundant in the two sills. The third hysteresis loop shape common to four of the samples analysed (e.g. SHF11 in Fig. 6.5c) is a loop with a restricted magnetic moment attributed to a strong presence of paramagnetic components. A significant component of maghemitisation also occurs in the three sills SHF2, SHF4 and SHF8, where the hysteresis loop is constricted as the presence of maghemite has distorted a classic ferromagnetic SD hysteresis loop (e.g. Dunlop and Özdemir, 1997).

Table 6.1. *Magnetic mineralogy results*

Sill	Low T transitions			Curie T		Grain size		
Name	T (K)	Mineral	Mgh?	T (°C)	Mineral	hysteresis	FORC (SF)	DCD plot
TB1	30	Po	minor	334°	Po	SP/SD	PSD (5)	PSD
	120	Mag		581°	Mag	Po dominant		
TB2	33	Po	minor	323°	Po	PSD	SD/PSD (6)	PSD
	116	Mag		580°	Mag	Po dominant		
TB5	31	Po	none	308°	Po	SP/SD	PSD (1)	PSD
	108	Mag		587°	Mag			
TB6	30	Po	minor	102°	Gt	SP/SD	PSD (1)	PSD
	121	Mag		572°	Mag			
SHF2	27	SP?	abundant	319°	Po	SD (constr.)	SD/PSD (1)	SD
				570°	Mag	Po dominant		
SHF3	28	SP?	none	585°	Mag	SP/SD	no data	PSD
	101	Mag						
SHF4	28	SP?	abundant	582°	Mag	SD (constr.)	PSD (1)	PSD
	111	Mag				Po dominant		
SHF5	22	SP?	minor	586°	Mag	SD	PSD (2)	PSD
	103	Mag						
SHF6	27	SP?	none	311°	Po	SP/SD	no data	PSD
	102	Mag		595°	Mag/Mgh			
SHF7	28	SP?	minor	564°	Mag	SP/SD	PSD (1)	PSD
	100	Mag						
SHF8	27	SP?	abundant	326°	Po	SD (constr.)	SD/PSD (2)	PSD
	108	Mag		588°	Mag/Mgh	Po dominant		
SHF9	22	SP?	minor	594°	Mag/Mgh	SD	PSD (4)	PSD
	103	Mag				Po dominant		
SHF10	110	Mag	none	319°	Po	SP/SD	no data	PSD
				576°	Mag			
SHF11	26	SP?	minor	342°	Po	SD	PSD (4)	PSD
	109	Mag		575°	Mag	Po dominant		

SF - shape factor
Mgh? - Degree of maghemitisation
(constr.) - constrained graph
SP - superparamagnetic signature

First-order reversal (FORC) curves were determined and plotted using FORCinel (Harrison & Feinberg 2008) in order to visually predict the grain size of the magnetic minerals present. FORC curves were produced for the majority of the samples; the bulk of the resultant graphs

showed typical PSD spreads where the FORC results exhibited a wide range from negative to positive H_u and partially distributed along the H_c axis (e.g. TB5 and SHF7 in Fig. 6.5d). Only one sample yielded a SD-type graph, SHF2 as seen in Fig. 6.5d, where the data are restricted along the H_u axis elongated along the H_c axis.

The coercivity, field strength and magnetisation of the samples were determined using DC Demagnetisation (DCD) analyses in order to plot the results in grain size/domain state graph using the Day et al. (1977) and Dunlop (2002) parameters. The DCD data, plotted from the hysteresis data, yielded an average PSD grain size (Fig. 6.5e). SHF2 is the only sample which plots above 0.5 on the M_r/M_s axis, yielding an SD grain size. Overall the majority of the hysteresis loops exhibit SD style curves (Dunlop and Özdemir, 1997). However, the DCD plot and projected FORC data show that all of the magnetic samples in the sills have a PSD grain size except for SHF2, which is SD in size (Smirnov, 2006).

6.6. Results

6.6.1. Petrography

The KZN North Coast Karoo sills comprise approximately 50% plagioclase, 45% clinopyroxene and 5% magnetite and/or pyrrhotite. Chlorite (replacing clinopyroxene) and biotite are present in some samples. Texturally the dolerites are most commonly sub-ophitic and variolitic, with some samples showing glomeroporphyritic textures. Minor interstitial devitrified glass is present in some of the samples (e.g. up to 25% in SHF8). The plagioclase grains are typically elongate in texture but can vary from acicular to lath-like. Clinopyroxene is typically stubby in texture but can also vary in texture and is plumose in some finer grained samples. The majority of the sills are amygdaloidal and/or vesicular with very few sills being massive throughout. The sills may have one or more of the following features: amygdales, large and small vesicles, xenoliths of basement and country rock material, variations in grain size and multiple layers.

6.6.2. Field Observations

The field structures that are considered representative of magma flow are here termed magma flow indicators and occur in a wide range of forms in the studied area. The original readings measured from the structures are recorded in Figs. 6.6 – 6.8 using arrows and directional readings. In Table 6.2 the readings have been restored to the horizontal using the respective sill's orientation. This restoration allows the similarities in magma flow directions to become evident prior to brittle deformation (e.g. coaxial bridge structures in SHF3 in Table 6.2). The

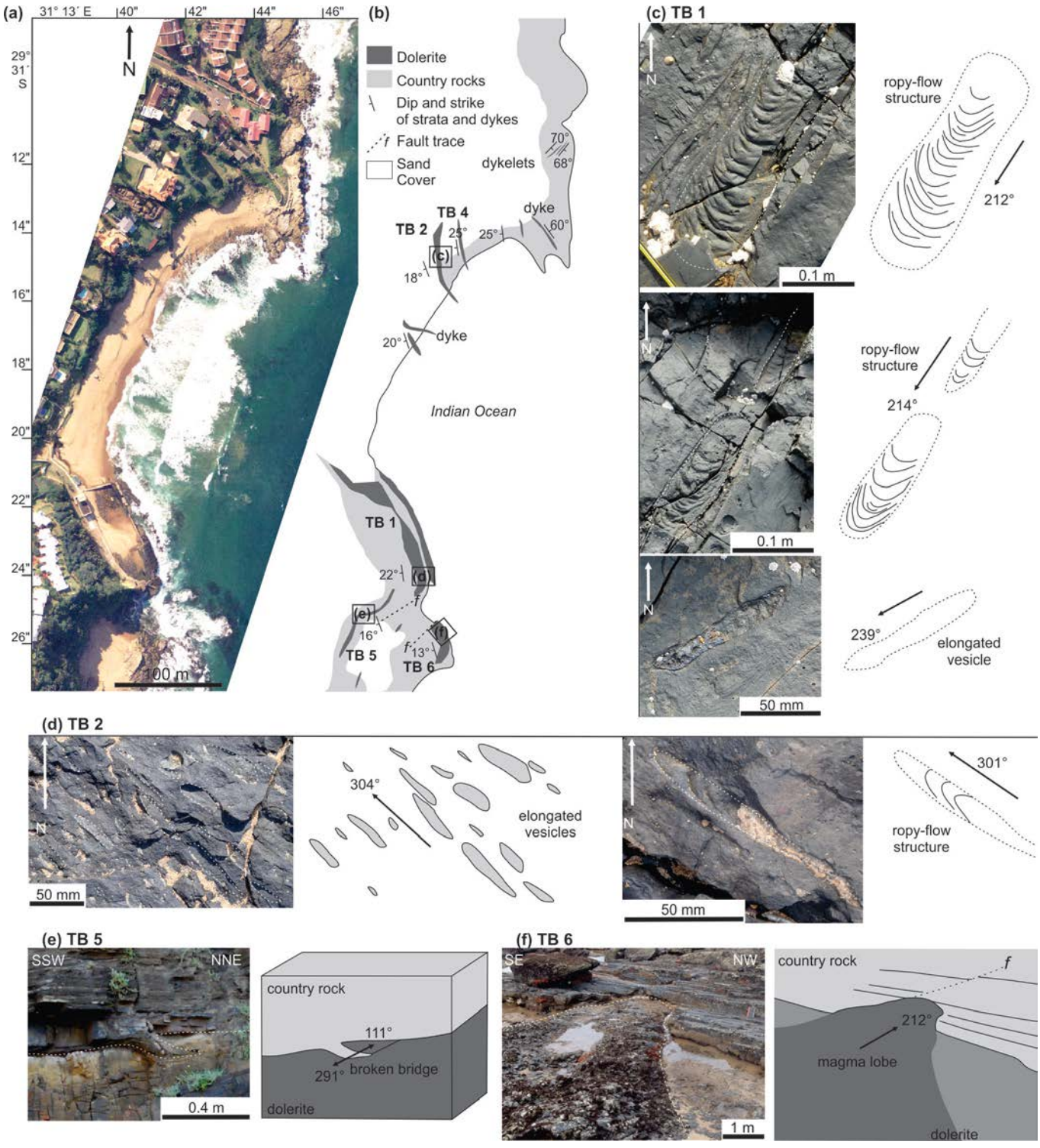

Fig. 6.6. Magma flow indicators from the sills at Thompson's Bay. (a) Aerial photograph of Thompson's Bay. (b) Geological map of the study area where the analysed sills are highlighted (c) Ropy-flow structures and elongated vesicles that occur ~10 cm below the upper contact of TB1 plunging towards the SW. (d) A ropy-flow structure and associated elongated vesicles occurring within the vesicular zone of TB2 plunging towards the WNW/NW. (e) A small broken bridge preserved along the upper contact of TB5 with a long axes oriented WNW-ESE. (f) A magma lobe is preserved along the upper contact of TB6 plunging towards the ~SSW – SW.

outcrops in the maps of the areas in Fig. 6.6 – 6.8 are only outcrop patterns and are not representative of the original shape in which the intrusions formed.

Several intrusions in the form of dykes and sills crop out along the Thompson's Bay section of coastline (Fig. 6.6a and b), dipping towards the SW and ranging in thickness from 1 m (TB4) to 3 m (TB1). The structures that have been preserved in the sills of Thompson's Bay include ropy-flow structures (TB1), elongated vesicles (TB2), broken bridge structures (TB5) and magma lobes (TB6). The elongated vesicles and ropy-flow structures that occur in TB1 and TB2 are not oriented similarly; the large vesicles along the upper contact of TB1 trend ~SSW (Fig. 6.6c) whereas the elongated vesicles in the vesicular layer of TB2 plunge towards ~WNW – NW (Fig. 6.6d). The lower contact of TB1 is not exposed. The vesicular layer in TB2 is 0.5 m thick and occurs ~0.5 m below the upper contact. Ropy-flow structures in both intrusions only appear to occur in vesicles with lengths greater than 6 cm.

Along the upper contact of TB5, a small (<20 cm in length) broken bridge structure with a long axis orientation trending WNW – ESE is apparent (Fig. 6.6e). Along the upper contact of TB6 two magma lobes were observed, trending SSW. The magma lobes have deformed the overlying stratigraphy so that it appears that the lobes intruded at a slightly higher stratigraphic level than the surrounding dolerite, where the lobe has coalesced with the main intrusion (Fig. 6.6f).

Several sills crop out in the southern Sheffield Beach area, five sills that were sampled; SHF2, SHF3, SHF4, SHF5 and SHF6 (Fig. 6.7a and b) ranging in thickness from 1 m (e.g. SHF2) to ~2.5 m (e.g. SHF6). Bridge structures and intrusive steps are the only magma flow indicators present in this area. The magma flow indicators in SHF2 comprise a broken bridge and bridge stub, on the upper and lower contacts respectively, with north-south oriented long axes (Fig. 6.7c). SHF3 is intruded into coarse sandstones, where two broken bridges have been preserved with WSW-ENE oriented long axes (once restored – see Table 6.2) (Fig. 6.7d).

SHF4 is characterised by an intrusive step along which parallel scours are preserved along the upper sill contact (Fig. 6.7e). These structures have NW-SE oriented long axes. SHF5 is a moderately dipping inclined sheet. Along its upper contact, a small broken bridge and a bridge stub are found, both of which have north-south oriented long axes (Fig. 6.7f). SHF6 is a sill intruded into an older dolerite sill. Along its southern lower contact there are three small magma flow indicators.

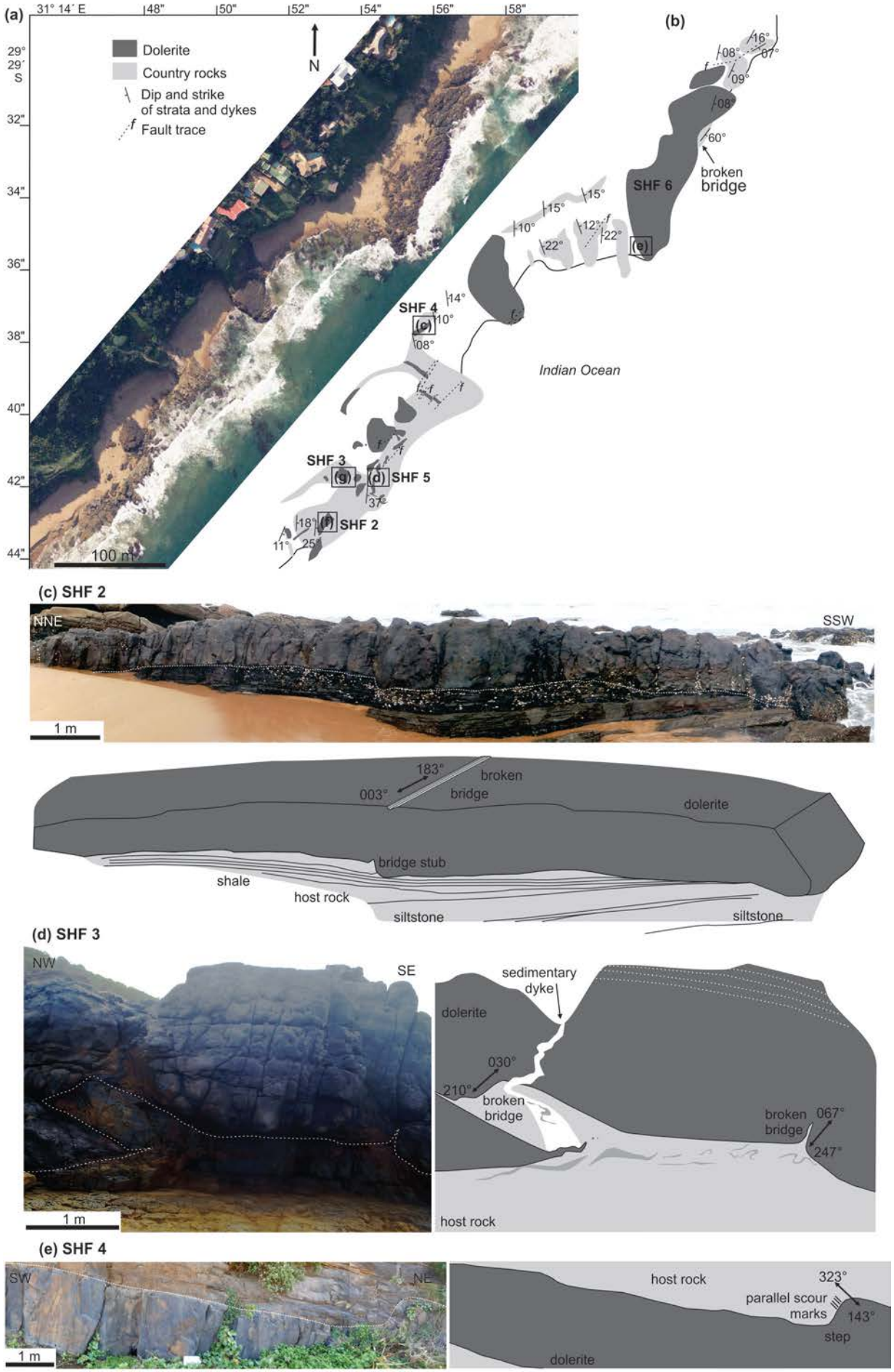
(a)
31° 14´ E
48"
50"
52"
54"
56"
58"
29° 29´ S
32"
34"
36"
38"
40"
42"
44"
Dolerite
Country rocks
Dip and strike of strata and dykes
Fault trace
N
100 m
(b)
SHF 6
broken bridge
SHF 4
SHF 3
SHF 5
SHF 2
Indian Ocean
(c) SHF 2
NNE
SSW
1 m
183°
003°
broken bridge
dolerite
bridge stub
shale
host rock
siltstone
siltstone
(d) SHF 3
NW
SE
1 m
sedimentary dyke
dolerite
030°
210°
broken bridge
broken bridge
067°
247°
host rock
(e) SHF 4
SW
NE
1 m
host rock
323°
parallel scour marks
143°
step
dolerite

Fig. 6.7.

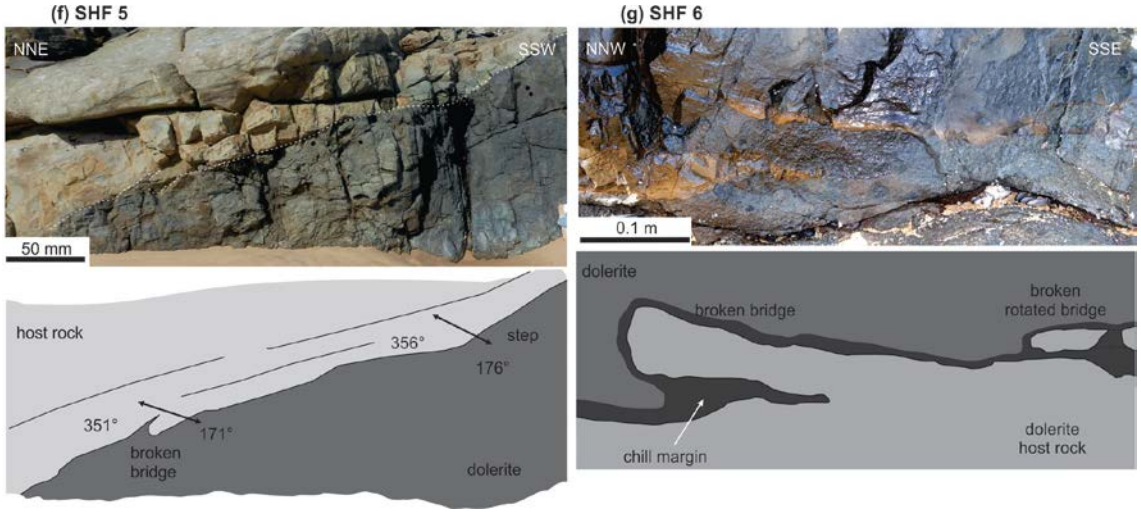

Fig. 6.7. continued. Magma flow indicators from the southern sills of Sheffield Beach. (a) Aerial photograph of southern Sheffield Beach. (b) Geological map of the study area where the analysed sills are highlighted. (c) SHF2 has a north-south oriented broken bridge structure along the upper contact and a bridge stub in the same position on the lower contact. (d) SHF3 has a broken bridge and an adjacent small bridge stub with parallel ENE-WSW orientated long axes preserved along the lower contact of the sill. The bridge material and underlying rock has partially melted and produced a rheomorphic sedimentary dyke that has intruded into the sill. Parallel vesicle stringers occur towards the upper contact of the intrusion. (e) An intrusive step occurs in SHF4, along the upper contact of the step, parallel scour marks plunge coaxial with the SE – SSE oriented long axis of the step. (f) SHF5 is a moderately inclined sheet that has a small broken bridge and step along the upper contact, both oriented ~north-south. (g) SHF6 is intruded into a dolerite sill and has deformed the material along the lower sill contact.

These comprise two broken bridges and a small bridge stub (e.g. Fig. 6.7g). Along the upper contact, a large NE-SW oriented broken bridge is apparent where a wedge of country rock has been tilted to an angle of 60°. Note the magma flow indicators along the lower contact are not all aligned parallel (Table 6.2).

Several sills crop out along the northern Sheffield Beach area; SHF7, SHF8, SHF9, SHF10 and SHF11 (Fig. 6.8a and b) and range in thickness from 0.5 m (i.e. SHF8) to greater than 6 m (i.e. SHF7). These are dominated by bridge structures. The exception is SHF7 where magma lobes crop out along the upper contact at the northern terminus of the sill. These lobes are separated by sub-parallel raised edges all plunging towards the NE (Fig. 6.8c). SHF8 is characterised by a stepped morphology of several NE-SW oriented broken bridges and bridge stubs (Fig. 6.8d). The broken bridge structure along the lower contact of SHF8 (Fig. 6.8e) has parabolic lines visible in the horn of dolerite preserved adjacent to the country rock segment that has been broken. SHF9 has a complicated morphology where the sill bifurcates into two (or more) sill segments; the lower segment is SHF9A and the upper segment is SHF9B. The wedge of brecciated material separating the two sill segments has a NE-SW oriented long axis. The lower sill segments (SHF9A) have three preserved magma flow indicators in the form of bridge stubs with NW-SE long axes (e.g. Fig. 6.8f). SHF9B is the upper magma segment and has two

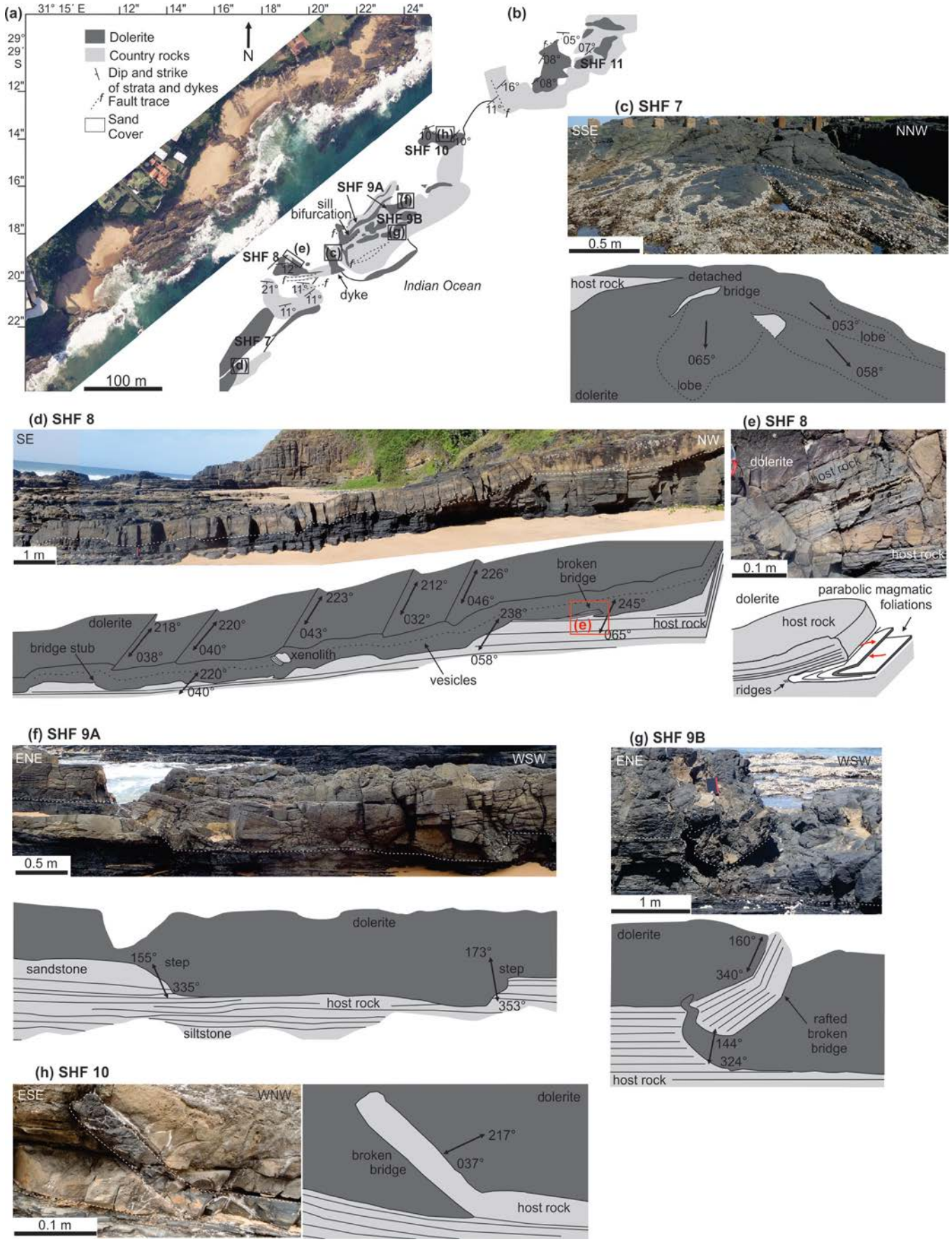
(a)
31° 15´ E
12"
14"
16"
18"
20"
22"
24"
29° 29´ S
12"
14"
16"
18"
20"
22"
Dolerite
Country rocks
Dip and strike of strata and dykes
Fault trace
Sand Cover
N
100 m
SHF 11
SHF 10
SHF 9A
SHF 9B
SHF 8
SHF 7
sill bifurcation
dyke
Indian Ocean
(b)
(c) SHF 7
SSE
NNW
0.5 m
host rock
detached bridge
053°
lobe
065°
058°
lobe
dolerite
(d) SHF 8
SE
NW
1 m
dolerite
bridge stub
218°
038°
220°
040°
223°
043°
212°
032°
226°
046°
broken bridge
238°
245°
065°
host rock
xenolith
058°
vesicles
220°
040°
(e) SHF 8
dolerite
host rock
0.1 m
dolerite
parabolic magmatic foliations
host rock
ridges
(f) SHF 9A
ENE
WSW
0.5 m
dolerite
sandstone
155°
step
335°
host rock
173°
step
353°
siltstone
(g) SHF 9B
ENE
WSW
1 m
dolerite
160°
340°
rafted broken bridge
144°
324°
host rock
(h) SHF 10
ESE
WNW
0.1 m
dolerite
broken bridge
217°
037°
host rock

Fig. 6.8.

preserved parallel broken bridges with NW-SE long axes (e.g. Fig. 6.8g). SHF10 has two parallel NE-SW oriented broken bridge structures preserved along the lower sill contact which are parallel (e.g. Fig. 6.8h). A small bridge stub occurs along the lower contact of SHF11 with a NW-SE oriented long axis. At the northern extent of SHF11, a broken bridge is preserved with a NE-SW oriented long axis.

6.6.3. Fabric analyses

6.6.3.1. Shape-preferred Orientation

The SPO data for the contacts of each sill are represented by lower hemisphere stereonets where the results have been restored to the horizontal using the measured dip and strike of the respective sill (Table 6.2). The average P' of the resultant ellipsoids was 1.364 and ranged from 1.053 to 2.773 with an outlier value of 4.128 (Fig. 6.9). The average T was -0.113, showing a weakly prolate shape (Fig. 6.9). The average angle between the foliation plane of the ellipsoid and the sill margin was moderately inclined at 45°. Where prolate fabrics occurred, the lineation has been used to define the fabric, represented by a plunging arrow whereas the foliations used to define the oblate fabrics, are represented by dip and strike symbols in Figs. 6.10 – 6.12.

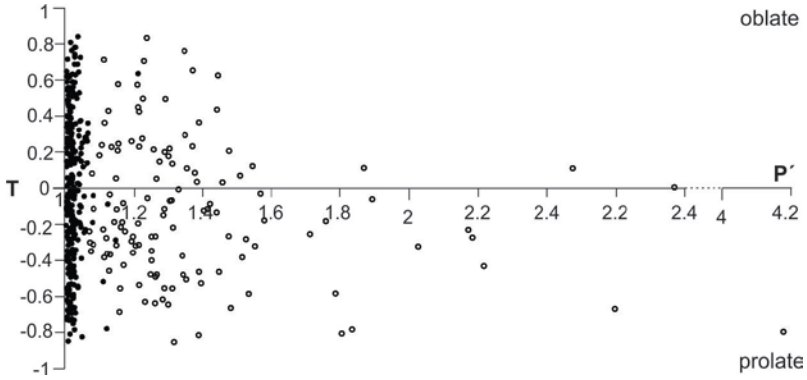

Fig. 6.9. The shape (T) of the AMS (filled circles) and SPO (open circles) ellipsoids where the AMS samples have significantly lower shape anisotropy (P′) when compared to the SPO samples. The AMS samples are evenly distributed from strongly oblate to strongly prolate. The SPO samples are more commonly prolate in shape with more prolate ellipsoids yielding higher shape anisotropies than for the oblate ellipsoids.

Fig. 6.8. Magma flow indicators from the northern sills of Sheffield Beach. (a) Aerial photograph of northern Sheffield Beach. (b) Geological map of the study area where the analysed sills are highlighted. (c) Magma lobes are preserved at the north-eastern extent of SHF7 plunging shallowly towards the ENE. (d) The sill SHF8 has numerous parallel bridge stubs and broken bridges along the lower and upper contacts of the sill oriented NE-SW. (e) A cross-sectional interpretation of the broken bridge structure along the lower contact of SHF8 showing the parabolic lineations visible in the horn of magma adjacent to the bridge (f) A section of SHF9A where two steps occur along the lower contact with sub-parallel long axes oriented ~NNW-SSE. (g) A broken bridge occurs along the lower contact of SHF9B where a horn of magma has rafted the country rock away from the underlying stratigraphy. (h) A small NE-SW oriented broken bridge along the lower contact of SHF10.

6.6.3.2. Anisotropy of Magnetic Susceptibility

The average for each contact is presented in Table 6.2. The average bulk susceptibility of the intrusions is 4150 x 10^{-6} SI ranging from 606 x 10^{-6} SI to 10100 x 10^{-6} SI. The degree of anisotropy ranges from near isotropic to weakly anisotropic with P' ranging from 1.003 and 1.057 and an average value of 1.021. The average T was -0.033 and with 54% of T values below 0, an almost neutral shape (Fig. 6.9). The fabrics are generally shallowly dipping where the average angle between fabric and the horizontal is 14° (disregarding data from three contacts with near vertical κ_1 axes). As with the SPO results the fabric were defined using the AMS lineation or foliation plane (where κ_3 is the foliation pole) which are represented in Figs. 6.10 – 6.12 with plunging arrows and dip and strike symbols respectively.

6.6.3.3. Results Format

The following results for the SPO and AMS fabrics, for Thompson's Bay and Sheffield Beach are represented individually at their respective sample locations and collectively through stereonet projections. This allows the proximal and collective fabrics to be compared separately with the orientation of the long axes of the magma flow indicators. The SPO and AMS results have been restored to the untilted orientation, using the orientation of each sill, resulting in SPO and AMS fabrics that are inclined with respect to the horizontal plane (the perimeter of the stereographic projections). Three contacts showed near vertical κ_1 axes, SHF9U, SHF9L and SHF11U. These average fabrics were defined by the foliation as the lineation was near vertical.

6.6.4. Fabrics of the Thompson's Bay Sills

The SPO and AMS fabrics of the upper contact of TB1 are locally parallel to sub-parallel with the SW plunge directions of the magma flow indicators (large white arrows in Fig. 6.10 – 6.12), defined predominantly by oblate fabrics (Fig. 6.10a). Distal to the magma flow indicators, half of the SPO and AMS results are coaxial with the ropy-flow structures. Collectively for the upper contact the AMS results are oblate and coaxial with the magma flow indicators where the collective SPO result for the upper contact differs by up to ~55°.

The collective SPO and AMS results for the vesicular layer (V) and the upper and lower contacts of TB2 plunge in opposite directions. The SPO results plunge coaxially across the three sampled zones towards the NNW, whereas the AMS results for all the zones plunge coaxially towards the SSE (Fig. 6.10b).

Table 6.2. *Sill orientations, magma flow indicators and petrofabric results*

Sill	Intrusion	Ropy-flow structures		Magma fingers		Steps		Broken Bridges		SPO flow vector(s) PD/P		AMS PD/P	
Name	S[a]/D[b]	PD[c]/P[d]	PD[e]	PD/P	PD[e]	S/D	S[e]	S/D	S[e]	Upper	Lower	Upper	Lower
TB1	172°/22°	212°/18°	215°							267°/44°		218°/14°	
		214°/18°	217°										
		239°/20°	240°										
TB2	167°/21°	306°/15°	304°							352°/46°	329°/54°	168°/01°	157°/39°
										334°/34°			163°/04°
		304°/18°	301°							(v)			(v)
TB5	160°/16°							291°/28°	307°	334°/26°	078°/61°	268°/07°	277°/03°
TB6	164°/13°			212°/10°	212°							306°/04°	
				204°/10°	205°								
SHF2	000°/20°							003°/34°	000°	153°/77°	139°/57°	172°/37°	200°/07°
SHF3	340°/17°					247°/76°	243°	030°/30°	064°	064°/56°	012°/57°	240°/33°	213°/30°
SHF4	350°/12°			143°/15°	144°	142°/65°	144°			316°/45°	202°/45°	323°/05°	155°/12°
				scours on step									
SHF5	353°/10°					356°/32°	359°	351°/39°	350°	280°/69°	089°/70°	163°/23°	187°/24°
SHF6	013°/13°					061°/85°	063°	330°/62°	324°	209°/37°	153°/58°	276°/04°	087°/01°
										279°/18°			
								203°/24°	201°				
								037°/60°	041°				
SHF7	056°/10°			053°/10°	055°	048°/16°	038°			289°/36°	317°/71°	294°/02°	132°/12°
				058°/12°	060°	038°/16°	019°						
				065°/06°	064°	048°/66°	048°						
SHF8	088°/09°					220°/40°	227°	065°/25°	057°	316°/56°	310°/72°	319°/01°	104°/12°
						226°/68°	228°						
						238°/48°	242°						
						218°/45°	224°						
						040°/46°	032°						
						043°/60°	037°						
						212°/66°	215°						
						046°/38°	038°						
SHF9A	065°/13°					353°/64°	346°	063°/35°	062°	281°/41°	062°/66°	144°/10°	026°/38°
						155°/59°	163°	058°/50°	056°				
SHF9B	065°/13°					151°/58°	160°	112°/27°	137°		061°/79°		105°/07°
						144°/55°	155°	340°/50°	329°				
								145°/38°	162°				
SHF10	059°/10°							217°/40°	220°	159°/82°	149°/22°	209°/10°	197°/04°
								207°/22°	211°				
SHF11	054°/10°					237°/37°	237°	124°/18°	145°	086°/26°	052°/45°	016°/00°	042°/26°

a strike
b dip
c plunge direction
d plunge
e restored orientation
v vesicular unit

Proximal to the magma flow indicators, the SPO and AMS fabrics differ from the trend of the elongated vesicles by ~30° in their respective directions. The majority of the SPO fabrics are oblate whereas the AMS results are predominantly prolate (Fig. 6.10b), mimicking the nature of the linear elongate vesicles.

Three of the four SPO results from the upper contact of TB5 plunge towards the NNW with the lower contact data plunging towards the east. Only the upper contact data have a similar trend to the bridge structure (Fig. 6.10c). The AMS data for the upper and lower contact plunge coaxially towards the west, differing by 20° - 30° to the strike of the magma flow indicator (Fig. 6.10c) (the upper contact individual samples are oblate, however collectively, the contact data are imbricated parallel to the lineation).

The thin sections for TB6 were unable to be analysed, thus only AMS results were available for the upper contact of TB6. These fabrics were not parallel; locally no samples exhibited fabrics that were coaxial to the plunge direction of the magma lobes. The average AMS plunge direction is oriented towards the WNW (Fig. 6.10d).

6.6.5. Fabrics of the Sheffield Beach Sills

The SPO vectors for the lower and upper contacts of SHF2 are steeply inclined towards the SE, differing by ~30° with respect to the magma flow indicator (Fig. 6.11a). Proximal to bridge structures along the upper and lower contacts, the fabrics are not coaxial to the majority of the results. The AMS results from the upper and lower contacts plunge coaxially towards the south, with the proximal samples along the upper contact plunging parallel to the trend of the bridge structure (Fig. 6.11a).

There are no individual SPO results that are parallel with the trend of the bridge structures of SHF3, however the overall upper contact fabric is coaxial with the magma flow indicators (Fig. 6.11b). The AMS data for the upper and lower contacts of SHF3 are coaxial and parallel with the trend of the bridge structures. Locally, the AMS results from the upper contact plunge parallel to the bridge structures whereas the lower contact data do not. All of the ellipsoids yielded prolate fabrics.

The upper and lower contact data from the SPO results of SHF4 show little to no correlation with the data spread over a wide range of plunge directions (Fig. 6.11c). Proximal to the intrusive step, one sample from the lower contact is parallel to the strike of the step. The AMS results from SHF4 from the upper and lower contacts are symmetrical and coaxial with the magma flow indicators. The proximal upper contact AMS results yielded the fabrics that were parallel with the intrusive step and scour marks.

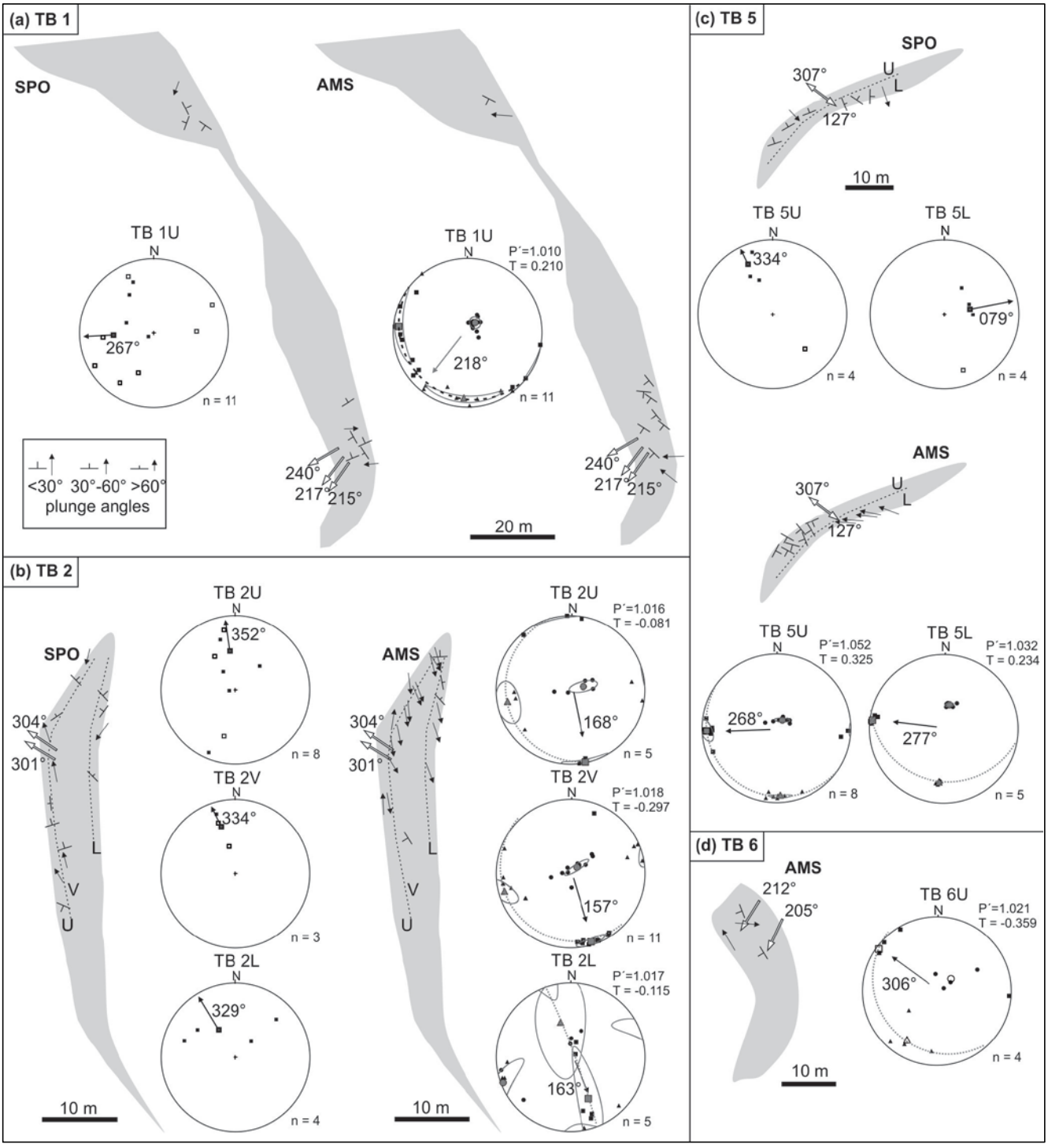

Fig. 6.10. Schematic representations of the SPO and AMS fabrics for the sills exposed at Thompson's Bay. The grey shapes are map-view outcrop outlines of the sills and do not reflect the original shape of the intrusions. The SPO and AMS fabrics are shown for (a) TB1, (b) TB2 and (c) TB5 and only the AMS fabrics for (d) TB6. The large (uni- and bi-directional) white arrows represent the direction/orientation of the magma flow indicators. The prolate fabrics are illustrated using dip and strike symbols with the dip direction of the ellipsoid showing the orientation of the foliation. The black arrows indicate samples with prolate fabrics. The length of the arrows and dip symbols represent the angle of the dip, the steeper the dip/plunge, the shorter the arrow/dip symbol. The stereonets illustrate the fabrics collectively across the upper (U) and lower (L) contacts. (V) is the vesicular layer that was sampled in TB2. For the SPO stereonets, the filled squares represent the foliation dip and azimuth of the oblate fabrics; the open squares represent the plunge and plunge direction of the lineations. For the AMS stereonets the squares represent the κ_1 axis, the triangle the κ_2 axis and the circle the κ_3 axis with the grey-filled and un-filled shapes representing the average across the contact. The grey ellipses are the error ellipses for the three average principal axes. The dashed grey great-circles are the foliation plane of the collective AMS fabric. The dashed black great-circles are representative of oblate fabrics where the foliation has been used to determine the fabric for the contact.

Few SPO results were obtained for SHF5 and therefore the collective fabrics are not well constrained; the fabrics are steeply dipping with only one result from each contact exhibiting plunge directions coaxial with the magma flow indicators (Fig. 6.11d). The lower and upper contact AMS data from SHF5 are coaxial towards the south. Proximally along the upper contact, the fabrics are parallel with the trend of the magma flow indicators.

The SPO data from the upper and lower contacts of SHF6 are not consistent or parallel (Fig. 6.11e). Proximal to the bridge structure along the upper contact, an oblate fabric is parallel to the magma flow indicators, however there is a separation in the results. Half plunge towards the west and the other half dip towards the SSW, hence there are two collective averages stereographically represented. The lower contact SPO data plunge coaxially towards the SSE parallel to one of the bridge structures. The AMS fabrics from SHF6 are shallowly plunging symmetrically (in opposite directions along the separate contacts) towards the west and east (Fig. 6.11e). Proximal to the magma flow indicators, the fabrics are not parallel to the trend of the bridge structures. This is mimicked in the overall AMS orientations for the contacts.

The SPO data from the upper and lower contact of SHF7 are coaxial and plunge towards the WNW – NW. These are however poorly constrained. The lower contact is spatially separated across the intrusion; all of the samples are distal to the magma lobes and show large variations in orientations (Fig. 6.12a). Only one result from the upper contact is parallel with the long axes of the magma lobes. The AMS results from the northern extent of the lower contact consistently plunge towards the south, however these results differ significantly from the AMS of the southern portion of the sill which plunges towards the north and the east (Fig. 6.12a). Although the upper and lower contact averages are symmetrical towards the WNW, the averages are poorly constrained. The upper contact AMS results are predominantly perpendicular to magma flow indicators.

Petrographically the samples obtained for SHF8 are of poor quality as the samples show fine varioles. The SPO data from the contacts are coaxial towards the NW and are proximally and collectively perpendicular to the numerous magma flow indicators (Fig. 6.12b).

Fig. 6.11. *continued.* For the SPO stereonets, the filled squares represent the foliation dip and azimuth of the oblate fabrics; the open squares represent the plunge and plunge direction of the lineations. For the AMS stereonets the squares represent the κ_1 axis, the triangle the κ_2 axis and the circle the κ_3 axis with the grey-filled and un-filled shapes representing the overall across the contact. The grey ellipses are the error ellipses for the three o principal axes. The dashed grey great-circles are the foliation plane of the collective AMS fabrics. The dashed black great-circles are representative of oblate fabrics where the foliation has been used to determine the fabric for the contact.

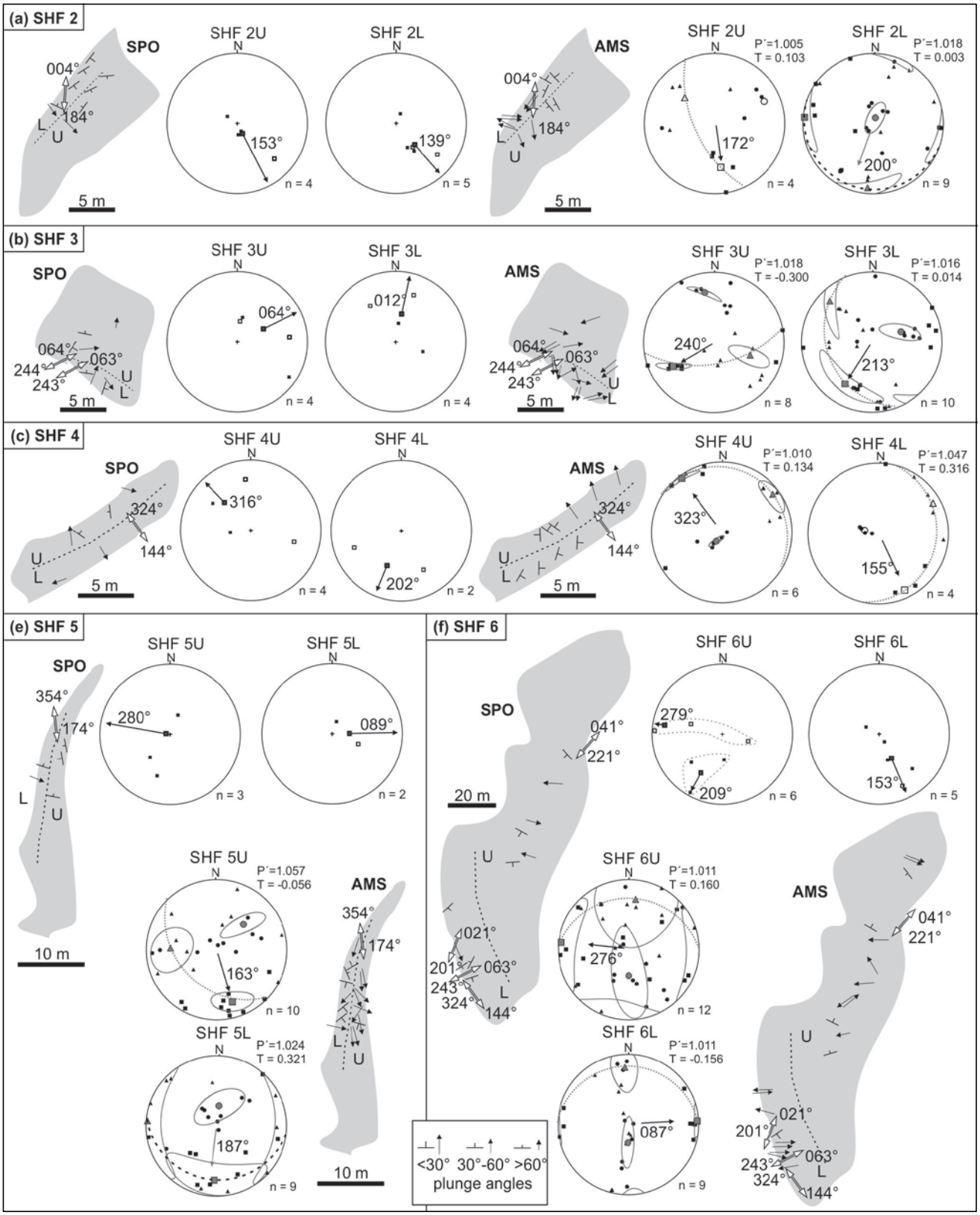

Fig. 6.11. Schematic representations of the SPO and AMS fabrics for the sills exposed along the southern Sheffield Beach area. The grey shapes are map-view outcrop outlines of the sills and do not reflect the original shape of the intrusions. The SPO and AMS fabrics are shown for (a) SHF2, (b) SHF3 and (c) SHF4, (d) SHF5 and (e) SHF6. The large (uni- and bi-directional) white arrows represent the direction/orientation of the magma flow indicators. The prolate fabrics are illustrated using dip and strike symbols with the dip direction of the ellipsoid showing the orientation of the foliation. The black arrows indicate samples with prolate fabrics. The length of the arrows and dip symbols represent the angle of the dip. The stereonets illustrate the fabrics collectively across the upper (U) and lower (L) contacts. *Continued on page 149.*

The numerous AMS samples from SHF8 show little correlation, with very few individual fabrics plunging/dipping parallel with the bridge structures. The average fabrics are poorly constrained however the fabrics are roughly symmetrical plunging towards the NW.

The number of samples obtained for the upper contact of the lower sill segment (SHF9A) of SHF9 were limited and the upper contact of SHF9B was not sampled due to a high degree of fracturing. The two SPO results from the upper contact of SHF9A are sub-parallel and plunge towards the west (Fig. 6.12c). For the lower contacts of the tubes SHF9A and SHF9B, very few samples were analysed petrographically in comparison with the outcrop volume. The lower contact results for SHF9A and SHF9B are coaxial and plunge towards the ENE, however the averages are poorly constrained. The SPO data are not parallel to the majority of the magma flow indicators; one result dips parallel to the bridge structure oriented 155° - 335° for SHF9B but is almost vertically inclined (Fig. 6.12c). The AMS results from the upper contact show inverse characteristics with the lineations plunging sub-vertically. The κ_3 axis plunges towards the SE and is used to define the average fabric. Proximal to the 155° - 335° oriented bridge structure, the fabrics are sub-parallel to the magma flow indicator orientation. However the average fabrics for the lower contacts of SHF9A and SHF9B are poorly defined and plunge towards the NNE and ESE respectively (Fig. 6.12c).

The SPO results from the upper and lower contacts of SHF10 are coaxial and plunge towards the SE however, the upper contact is almost vertical and the fabrics are not parallel with the bridge structure orientations (Fig. 6.12d). The AMS data from the lower and upper contacts of SHF10 plunge coaxially towards the SSW and are proximally and collectively parallel with the long axes of the magma flow indicators (Fig. 6.12d).

Fig. 6.12. Schematic representations of the SPO and AMS fabrics for the sills exposed along the northern Sheffield Beach area. The SPO and AMS fabrics are shown for (a) SHF7, (b) SHF8, (c) SHF9, (d) SHF10 and (e) SHF11. The large (uni- and bi-directional) white arrows represent the direction/orientation of the magma flow indicators. The prolate fabrics are illustrated using dip and strike symbols with the dip direction of the ellipsoid showing the orientation of the foliation. The length of the arrows and dip symbols represent the angle of the dip. The black arrows indicate samples with prolate fabrics. The stereonets illustrate the fabrics collectively across the upper (U) and lower (L) contacts. For the SPO stereonets, the filled squares represent the foliation dip and azimuth of the oblate fabrics; the open squares represent the plunge and plunge direction of the lineations. For the AMS stereonets the squares represent the κ_1 axis, the triangle the κ_2 axis and the circle the κ_3 axis with the grey-filled and un-filled shapes representing the average across the contact. The grey ellipses are the error ellipses for the three average principal axes. The dashed grey great circles are the foliation plane of the collective AMS fabrics. The dashed black great circles are representative of oblate fabrics where the foliation has been used to determine the fabric for the contact.

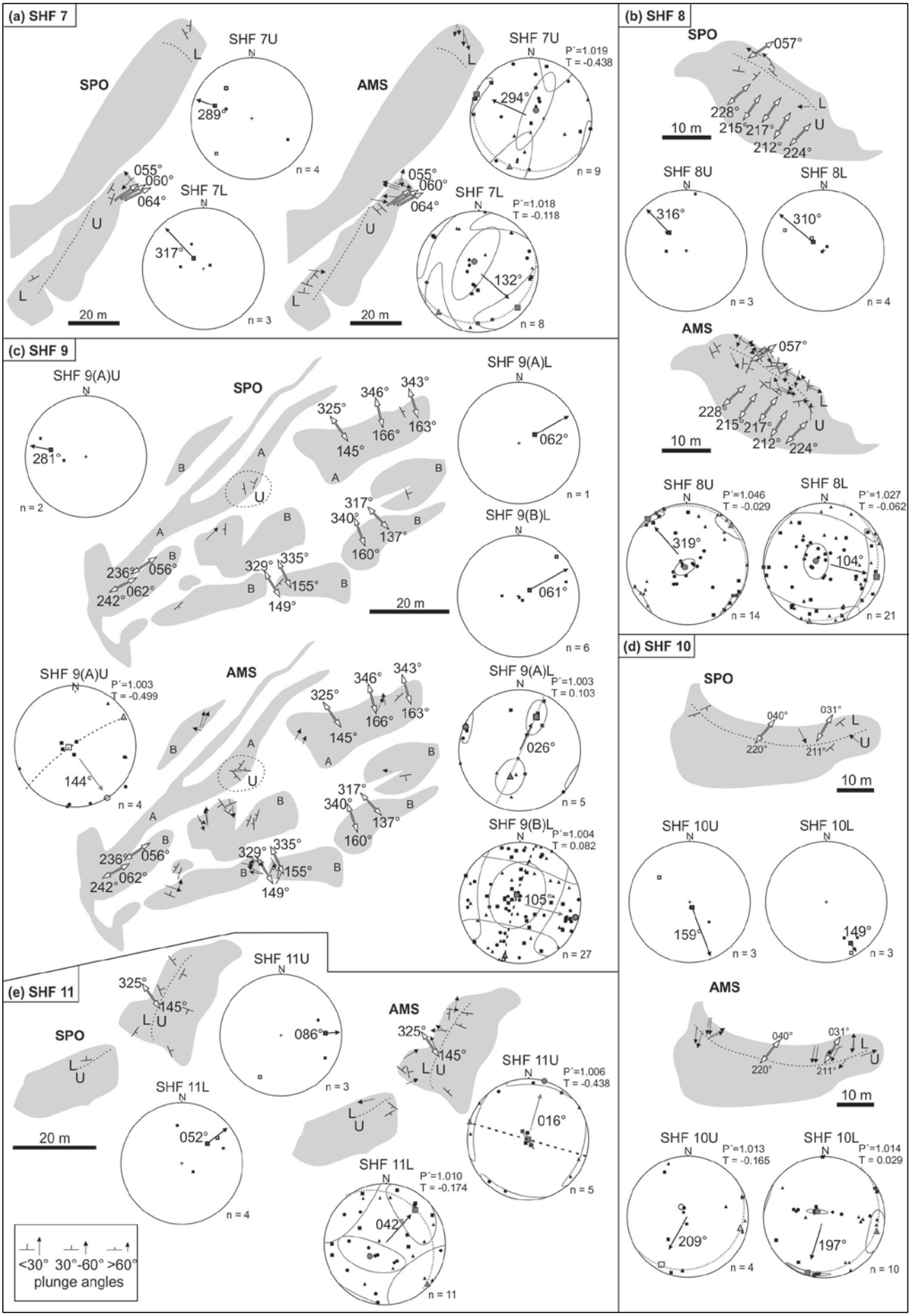
(a) SHF 7
SPO
SHF 7U
289°
n = 4
055°
060°
064°
SHF 7L
317°
n = 3
20 m
AMS
SHF 7U
P′=1.019
T = -0.438
294°
n = 9
SHF 7L
P′=1.018
T = -0.118
132°
n = 8
(b) SHF 8
SPO
057°
228°
215°
217°
212°
224°
10 m
SHF 8U
316°
n = 3
SHF 8L
310°
n = 4
AMS
SHF 8U
P′=1.046
T = -0.029
319°
n = 14
SHF 8L
P′=1.027
T = -0.062
104°
n = 21
(c) SHF 9
SHF 9(A)U
281°
n = 2
SPO
SHF 9(A)L
062°
n = 1
SHF 9(B)L
061°
n = 6
20 m
AMS
SHF 9(A)U
P′=1.003
T = -0.499
144°
n = 4
SHF 9(A)L
P′=1.003
T = 0.103
026°
n = 5
SHF 9(B)L
P′=1.004
T = 0.082
105°
n = 27
(d) SHF 10
SPO
040°
031°
220°
211°
10 m
SHF 10U
159°
n = 3
SHF 10L
149°
n = 3
AMS
SHF 10U
P′=1.013
T = -0.165
209°
n = 4
SHF 10L
P′=1.014
T = 0.029
197°
n = 10
(e) SHF 11
SPO
SHF 11U
086°
n = 3
SHF 11L
052°
n = 4
20 m
AMS
SHF 11U
P′=1.006
T = -0.438
016°
n = 5
SHF 11L
P′=1.010
T = -0.174
042°
n = 11
<30° 30°-60° >60°
plunge angles

Fig. 6.12.

For both the upper and lower contacts of SHF11 the collective fabrics are poorly defined. Only one result from the lower contact is parallel with the trend of the bridge structure, but has a steep plunge. The lower and upper contact SPO data for SHF11 both the shows little to no correlation with the magma flow indicators (Fig. 6.12e). The AMS data from SHF11 are similarly poorly constrained. The lower contact AMS results yielded two samples which plunge coaxially with the magma flow indicator, however in general the data plunge towards the NE, perpendicular to the strike of the broken bridge. The lineation data from the upper contact are vertical, therefore the average fabric vector was determined using the foliation, and thus plunges towards the NNE (Fig. 6.12e).

6.7. Discussion

6.7.1. Fabrics as magma flow indicators

Understanding how fabrics form requires knowledge of the timing of fabric formation and the regional setting (Paterson et al., 1998). A fabric forming in the last stages of magma intrusion preserves the final increment of strain before the magma nears solidification and crystallises (Paterson et al., 1998). If there has been no reorganisation of the particles in the magma before it crystallises (e.g. such as flattening due to overburden pressure), the preserved fabric may be used to obtain the direction of magma flow. No regional ductile deformation or metamorphism associated with or post-dating the intrusion of these sills has been observed in the study area. The sills analysed in this study have not been affected by post-emplacement processes or large scale magma chamber processes (such as crystal settling) as the majority of the sills are less than 2 m thick. All the textures observed also appear to be magmatic in origin. It follows that the fabrics that are preserved are related to the original process of sill intrusion and magma flow providing no post-intrusion flattening has occurred. The fabrics determined for the samples are thus likely to have formed as a result of internal processes (such as primary magma flow)and a product of magma strain (Nicholas, 1992; Paterson et al., 1998). Such strain may be brought about by the original magma flow but may be affected by internal processes such as magma convection or surges/pulses of magma (Benn and Allard, 1989; Paterson et al., 1998). Strain in an inhomogeneous fluid, where the viscosities differ between the particles and the matrix, results in a preferred orientation of the crystals parallel to the direction in which they were sheared or deformed (Gay, 1966, 1967).

6.7.1.1. Shape-preferred Orientation

Plagioclase fabrics may preserve the primary magma flow patterns in igneous intrusions allowing these fabrics to infer magma flow directions (Launeau and Cruden, 1998; Horsman et

al., 2005; Hastie et al., 2011a). Melt viscosities play a crucial role in the formation and preservation of crystal fabrics in intrusive igneous rocks (Paterson et al., 1998). In a Binghamian liquid, where the melt comprises more than 30% crystals, crystal fabrics will develop as a result of crystal movement in rigid-body rotation as a result of magma flow (Fernández and Gasquet, 1994; Hrouda et al., 1999). Magma flow in an intrusion may be inferred in a sill if a crystal imbrication and development of a preferred orientation occurs along the intrusion contacts. This imbrication typically dips in opposite directions along opposing margins with the direction of convergence indicating the direction of magma flow (Blanchard et al., 1979; Geoffroy et al., 2002; Gil-Imaz et al., 2006). The dip of this crystal alignment is ideally between 15° and 20° from the wall of the intrusion with the direction of dip inferring the magma flow (Blanchard et al., 1979). In this study, there are a significant number of samples that have steep dip angles; only ~16% of the individual SPO results yielded fabrics with dip angles of less than 20° (Table 7.3). The SPO fabrics may have originally been imbricated along the upper and lower contacts of the intrusions with a late stage process overprinting the fabric creating steeply dipping fabrics. Thus the fabrics may not necessarily represent the initial direction of magma flow.

6.7.1.2. Anisotropy of Magnetic Susceptibility

The magnetic mineralogy of the samples is dominated by magnetite as evidenced by the Curie temperature and low temperature analyses where magnetite occurred in almost every sample (Table 6.1). Where there was no magnetite signature this was as a result of maghemitisation of the magnetite (e.g. SHF2). Pyrrhotite occurs in more than half of the sills, however the magnetite signature is dominant in the K-T curves and low-temperature analyses. The degree of anisotropy of the samples is low, averaging 1.021, which considering the presence of pyrrhotite in the majority of the samples is unusual as pyrrhotite may yield a platy or tabular habit when compared to the typical granular habit of magnetite. One reason for this may be that the pyrrhotite minerals are granular in habit and have not greatly affected the overall shape of the magnetic fabrics. This is evident in the samples that do not have any pyrrhotite present as they do not show any significant difference with the degree of anisotropy in samples that do exhibit pyrrhotite. The shape (T) of the ellipsoids obtained from samples that yielded pyrrhotite range from strongly prolate (e.g. T = -0.727) to strongly oblate (e.g. T = 0.694) (see Section 8 in Appendix B). This is unlike examples from Ferré et al. (2002) where the occurrence of pyrrhotite greatly affects the shape and degree of anisotropy of the fabrics from these samples, producing strongly oblate ellipsoids, compared to the samples with only magnetite present. The AMS signature is thus most likely a product of the magnetite grains as the presence of

pyrrhotite does not have a noticeable effect of the fabric characteristics. Where maghemitisation has occurred, the bulk susceptibility and the shape anisotropy may be affected but the orientation of the AMS ellipsoid will be unaffected as the maghemitised zones on the magnetite grains will mimic the pre-existing magnetite fabric (Krása and Herrero-Bervera, 2005).

The source of the AMS can be attributed to "normal" fabrics due to the PSD nature of the grains and the shallowly plunging κ_1 axes that are parallel with the long axis of the ellipsoid, thus minimising the SD-effect that may lead to "inverse" fabrics (SHF2 was the only sample that showed a SD grain size). PSD grains mimic the form and behaviour of MD grains; the grains that most commonly yield AMS ellipsoids that may be attributed to "normal" magnetic fabrics (Rochette et al., 1999). The exceptions include three contacts that yielded vertical to sub-vertical κ_1 axes; the upper and lower contacts of SHF9A and SHF9B respectively and the upper contact of SHF11. The most likely origin of these "inverse" fabrics forming is the growth of magnetite grains late in the sequence of mineral crystallisation as suggested by Ferré et al. (2002). This magnetite crystal growth phase occurs after the majority of the magma has crystallised and the magnetite grains grow along the plagioclase crystal faces (Ferré et al., 2002). Two processes occur to produce these fabrics; plagioclase crystals become linked in a chain network during early stages of magma flow (Philpotts et al., 1999) and later compaction extracts pockets of melt trapped between these crystals (Ferré et al., 2002). At this stage, magnetite and biotite crystallise along the plagioclase crystal faces. This trend is observed in the samples from the sills SHF9 and SHF11 (see Table 4b in Appendix B) where the magnetite grains are elongate in shape and occur along the long axis of the plagioclase laths, the steep foliations may therefore be a product of late stage magnetite crystallisation as described above.

In small tabular intrusions, the AMS is a product of flow where solid and gas particles are in suspension within a continuously liquid phase (Cañón-Tapia, 2004). As magma channels are typically small for dykes and sills, the boundaries are often sheared and the flow laminar. The mineral fabric thus has a high probability of being preserved (Martín-Hernández et al., 2004). As the bulk of the fabrics in this study are normal, the orientation and imbrication of the fabrics along the contacts may be used as a proxy for magma flow. Where inverse fabrics occur in AMS results, the imbrication of the foliation (κ_3) is used to retrieve the sense of magma flow (Geoffroy et al., 2002). The angle between the average AMS fabric and the horizontal is ~29° (including the near vertical fabrics), with 51% of the fabrics yielding dip/plunge angles of less than 20°. The AMS fabrics have much shallower dip/plunge angles than the fabrics obtained for

the SPO ellipsoids, thus the AMS may be a more reliable indicator of the magma flow direction as the fabrics are more likely a product of imbrication by magma flow.

6.7.2. Fabric Discrepancies

The relationship between the SPO and AMS results can be categorised into sills where the results from the two methods are (1) coaxial, (2) plunging in opposite directions and (3) show little to no correlation. The sill contacts where the SPO and AMS results are coaxial are SHF2U, SHF4U, SHF6U, SHF7U, SHF8U and SHF11L (Fig. 6.13). Fabrics that plunge in opposite directions occur along the contacts TB5L, SHF3U, SHF3L, SHF7L, SHF8L and TB2; the fabrics for the upper and lower contacts and the vesicular zone plunge in almost exact opposite directions for the SPO and AMS results. All of the remaining contacts from all the other intrusions exhibit little to no relationship between the AMS and SPO results (Fig. 6.13).

Most studies that use both SPO and AMS to determine magmatic fabrics use a small amount of petrographic data and compare these few results with the AMS results in order to confirm a correlation between the two methods (e.g. Poland et al., 2004). Therefore the petrographic results are typically used in conjunction with the AMS results (e.g. Horsman et al., 2005; Aubourg et al., 2008; Hastie et al., 2011a, b). Results vary widely between the two techniques as evidenced here. Similar situations are observed by Archanjo and Launeau (2004), where the SPO and AMS results significantly differed. The discrepancies were attributed primarily to the timing of the fabric formation, as the plagioclase grains recorded the final stage of magma flow whereas the AMS results could have been affected by a later sub-solidus reaction (Archanjo and Launeau, 2004). In the samples analysed here, the SPO fabrics were obtained using strongly anisotropic plagioclase crystals and the AMS fabrics were obtained using weakly anisotropic magnetite crystals. Hence, the fabrics represent two different fabrics, the magmatic and magnetic fabrics, which do not always coincide in this study. This could be the result of a higher degree of rigid-body rotation as a result of magma flow in the larger elongate plagioclase crystals when compared to the fine grained, granular magnetite crystals. Both techniques are therefore important when attempting to understand overall magmatic processes that resulted in the different fabrics.

From the parabolic lineations observed along the lower contact of SHF8 in the horn of magma between the broken bridge and undeformed country rock (Fig. 6.8e), it appears that these are the linear representations of magmatic foliation planes. It can thus be inferred that the magma flow processes around these protruding structures may not be laminar and could affect a portion of

the crystals around these disrupted areas within the sill. As the field magma flow indicators may have been preserved through both localised and large scale magmatic processes, all of the fabric results will be compared to the multitude of directions obtained from the field magma flow indicators.

6.7.3. Asymmetrical Fabrics across Contacts

The fabrics between the contacts are asymmetrical for a large portion of the AMS results and some of the SPO results. In order to infer magma flow, symmetrical fabrics along each contact should dip 180° away from one another. Instead the fabrics here are coaxial and asymmetrical across the upper and lower contacts. Asymmetrical contacts resulting from the SPO analyses include TB2, SHF2, SHF8 and SHF10 and may also include SHF7 and SHF11 which are both separated by <30° (grey arrows in Fig. 6.13).

For the AMS results, two thirds of the results show asymmetrical fabrics. This includes TB2, TB5, SHF2, SHF3, SHF5, SHF10 and SHF11 (black arrows in Fig. 6.13). The sills that showed ideal symmetrical fabrics between the contacts were SHF5 for the SPO results (although these averages were poorly constrained) and SHF4, SHF6 and SHF7 for the AMS results (Fig. 6.13). Sills where the fabrics are oblique across the contacts include TB5, SHF3, SHF4, SHF6 and SHF9 for the SPO results and SHF8 and SHF9A for the AMS results.

When analysing fabrics along dyke contacts, Correa-Gomes et al. (2001) found that as the amount of simple shear along the dyke contacts increased, the contact fabrics became increasingly asymmetrical. The introduction of simple shear into an intrusion could be attributed to movement along the intrusion plane. As a result of shear within an intrusion, the apparent fabric may not be able to accurately infer magma flow (Correa-Gomes et al., 2001). However, when an intruding magma body is sheared and the contact fabrics become asymmetrical within the dyke/sill walls, the dip/plunge direction of the fabrics still indicate a sense of magma flow (Correa-Gomes et al., 2001; Clemente et al., 2007). Therefore the results obtained here, even though they are asymmetrical, could indicate the direction in which magma flowed. This is especially true when a well constrained upper contact fabric is determined, as the trend of the sheared fabric along the upper contact will be parallel to the direction of magma flow under all the strain conditions as discussed by Correa-Gomes et al. (2001).

From field evidence it is clear that the dolerite sills did not intrude into an actively shearing fault zone as the sills preferentially intrude into planar, finer-grained sedimentary rocks. Any brittle

deformation in the area occurred post-intrusion where the deformation is largely taken up by steeply inclined normal or transform faults. It follows therefore that the fabrics from the upper and lower contacts of the sills should correlate with the magma flow indicators measured in the field. This relationship is documented below.

6.7.4. Fabric Correlations with Magma Flow Indicators

For many of the intrusions, there were similarities between the fabric results and the inferences made from the magma flow indicator orientations measured in the study area (Fig. 6.13). Where the SPO data are coaxial with the trend of the magma flow indicators, the stereographic fit of the average principal axes are generally poor with a high error margin. These poorly defined average fabrics are not reliable indicators as the SPO ellipsoids proximal to these structures are not parallel with the magma flow indicators (e.g. SHF3 and SHF4 in Fig. 6.11). The lower contact of SHF6 is the only contact where both the individual and average SPO data are coaxial with one of the bridge structures in the immediate area. The AMS fabrics show a much stronger correlation with the long axes of the magma flow indicators. The contacts where the AMS and magma flow indicator data are coaxial are TB1U, SHF2U and L, SHF3U and L, SHF4U and L, SHF5U and L, SHF10U and L. The upper and lower contacts of these sills are generally both coaxial as the contact AMS data are asymmetrical. Where the magma flow indicator orientations and AMS plunge directions are coaxial, the data are consistent with well constrained average fabrics for the contacts.

When comparing the correlation of the field magma flow indicators with the data from the AMS and SPO analyses, it was clear that the AMS results coincide more regularly with the field data than the SPO results do. In this study it appears that the AMS fabrics are the most reliable fabrics to compare with the magma flow directions inferred from the field magma flow indicators. Even though the AMS data coincides more regularly with the field data, there are sills where only the SPO data are coaxial with the direction of magma flow inferred by the field observations (e.g. SHF6L and SHF9AL). Therefore the fabric results from the SPO data cannot be ignored but when interpreting the actual magma flow direction, the AMS results should be more heavily relied upon (e.g. Horsman et al., 2005).

For all of the contacts where the fabric data (AMS and/or SPO) are coaxial with the magma flow indicators, the upper contact fabric data almost always coincides with the directions/orientations of the magma flow indicators. Thus the upper contact data may be more

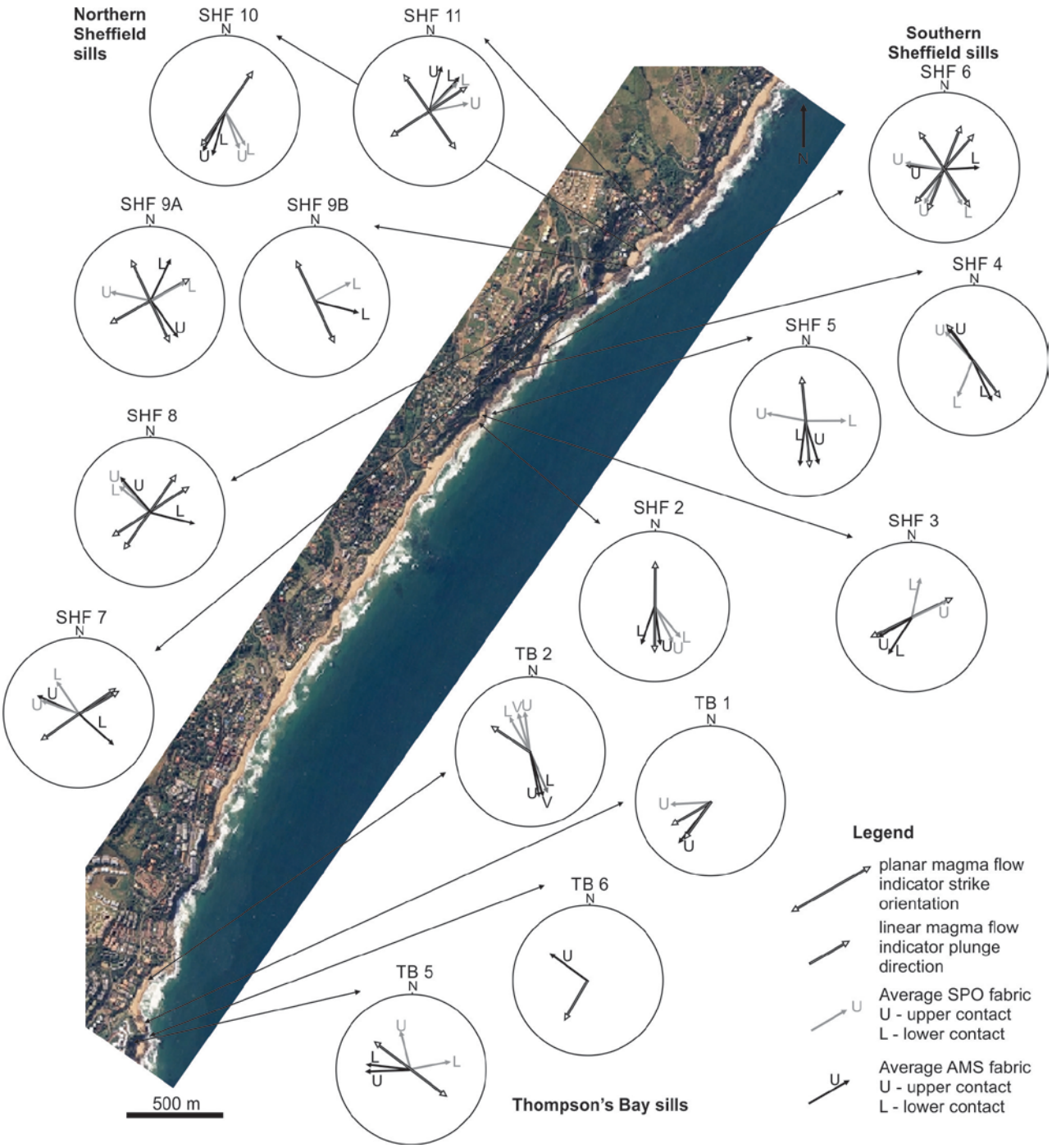

Fig. 6.13. The results from the analyses and field observations for the sills analysed in this study. For each sill, the orientation data are represented by two dimensional plots where only the directions or orientations of the results are represented by arrows. The bi-directional white arrows illustrate the orientation of the long axes of planar magma flow indicators (these include bridge structures and intrusive steps). The uni-directional white arrows illustrate the direction of the long axes of linear magma flow indicators (these include ropy-flow structures, elongated vesicles and magma lobes). The grey arrows are representative of the directions of the SPO fabrics collectively across the upper (U) and lower (L) contacts. The black arrows are representative of the directions of the AMS fabrics collectively across the upper (U) and lower (L) contacts. (V) is the vesicular layer in TB2 where the elongated vesicles are abundant.

significant in determining the magma flow directions in sills where the imbricated fabrics would imply magma flow parallel to the fabric orientation. If the upper contact data are generally coaxial with the magma flow indicators, perhaps the lower contact data are not a product of magma flow and may have resulted instead from a late-stage process such as shearing within the magma along slightly inclined surfaces (e.g. with the inclined sheet SHF5) or from pure shear related to flattening (Gay, 1967).

6.7.5. How well do Magma Flow Indicators Indicate Magma Flow?

For six out of the nine sills sampled where broken bridges occur along the contacts, the fabric vectors determined were parallel to the long axes of the bridge structures. This direction or orientation is therefore consistent with the fabric analyses and a magma flow direction may be implied. Thus bridge structures may indeed be used as tools to infer magma flow directions in sills. SHF4 exhibits the only large intrusive step in the field area; the SPO and AMS fabrics are coaxial both locally and collectively with the orientations of the steps and the parallel magma injection scour marks. Although only one example was present in the field area, the accurate match between the fabrics would imply that intrusive steps are good indicators of a magma flow sense.

The elongated vesicles in the vesicular zone of TB2 and the fabric data did not plunge in the same direction. The average fabrics for the AMS and SPO were well constrained and were asymmetrical across the different layers of the sill. The plunge directions of the fabrics differed from the magma flow indicators by ~30°. Thus these elongated vesicles did not accurately imply a magma flow direction. This may be due to the vesicles occurring within a discrete layer within the sill and not along the top contact, as with TB1. The sheared vesicles may also have been pushed upwards against a more viscous material (more crystallised) with this secondary flow causing the vesicles to become deformed and thus preferentially preserving the second flow.

The fabric results from the sills where magma lobes were preserved along the upper contacts (TB6 and SHF7) showed little to no correlation with the indicators either proximal to the lobes and collectively across the contacts. The fabrics indicate that the magma flow was actually perpendicular to these structures rather than parallel to them. It is thus more likely that the long axes of the magma lobes are indicative of the initial magma intrusion direction (Schofield et al., 2012b). Here it appears that once the lobes coalesce and are incorporated into the main body of the intrusion, the flow of magma may be momentarily localised between the now merged sill

segments. This would be the last stage of magma flow and is therefore the event that is preserved. If magma fingers/lobes are preserved ahead of an intrusion and have not coalesced with the main magma body, the magmatic fabrics within these structures may still accurately imply the direction of magma flow (e.g. Pollard et al., 1975; Horsman et al., 2005).

This trend of late stage flow appears to be mimicked in SHF8 where several small sill segments have merged, resulting in the formation of numerous bridge structures. The fabrics for SHF8 imply that magma flow in the sill was perpendicular to the well-defined magma flow indicators, as with the magma lobes. This flow direction could explain the parabolic foliations present in the horn of magma adjacent to the host rock bridge, which could not have formed parallel to the long axis of the bridge structure due to magma flow. It is thus possible that through the coalescence of numerous sill segments, a late stage magma flow occurred perpendicular to the original flow direction of the magma – the initial magma propagation direction. The plethora of magma flow indicators in SHF8 clearly indicates that the initial direction of magma injection and thus the true direction of magma flow from the source.

In conclusion therefore it is clear that fabrics obtained from thin sills can be misleading in inferring magma flow directions, where even well-defined fabrics may not be indicative of the magma flow in intrusions. These fabrics may instead preserve the last movement of magma between previously separate sill segments that have subsequently merged. In further studies it should be noted that not only SPO and AMS fabrics should be relied upon to infer the magma flow regime in sills. The structural remnants of the magma injection phase, such as broken bridge structures, may be a key factor in determining the sense of magma flow in sills.

References

Archanjo, C.J., Launeau, P., 2004. Magma flow inferred from preferred orientations of plagioclase of the Rio Ceará-Mirim dyke swarm (NE Brazil) and its AMS significance. In: Martín-Hernández, F., Luneberg, C.M., Aubourg, C., Jackson, M., (Eds) Magnetic Fabric: Methods and Applications. Geological Society of London Special Publication, 238, 285-298.

Archanjo, C.J., Campanha, G.A.C., Salazar, C.A., Launeau, P., 2012. Using AMS combined with mineral shape preferred orientation to understand the emplacement fabrics of the Apiaí gabbro-norite (Ribeira Belt, SE Brazil). International Journal of Science, 101, 731-745.

Aubourg, C., Tshoso, G., Le Gall, B., Bertrand, H., Tiercelin, J.-J., Kampunzu, A.B., Dyment, J., Modisi, M., 2008. Magma flow revealed by magnetic fabric in the Okavango giant dyke swarm, Karoo igneous province, northern Botswana. Journal of Volcanology and Geothermal Research, 170, 247-261.

Baer, G., Reches, Z., 1987. Flow patterns of magma in dikes, Makhtesh Ramon, Israel. Geology, 15, 569-572.

Benn, K., Allard, B. 1989. Preferred mineral orientations related to magmatic flow in ophiolite layered gabbros. Journal of Petrology, 30, 925-946.

Bensus, M.J. 1966. Propriétés magnétiques de la pyrrhotine naturelle. Unpublished PhD Thesis, University of Strasbourg, 78 pp.

Bensus, M.J. & Meyer, A.J. 1964. Nouvelles données expérimentales sue le magnétisme de la pyrrhotine naturelle. Proceedings of the International Conference on Magnetism, Nottingham, 507-511.

Blanchard, J.-P., Boyer, P., Gagny, C., 1979. Un nouveau critere de sens de mise en place dans une caisse filonienne: Le “pincement” des mineraux aux epontes: Orientation des minéraux dans un magma en écoulement. Tectonohysics, 53, 1-25.

Borradaile, G.J., Jackson, M., 2004. Anisotropy of magnetic susceptibility (AMS): magnetic fabric of deformed rocks. In: Martín-Hernández, F., Luneberg, C.M., Aubourg, C., Jackson, M., (Eds) Magnetic Fabric: Methods and Applications. Geological Society of London Special Publication, 238, 1-7.

Borradaile, G.J., Lagroix, F., 2001. Magnetic fabrics reveal upper mantle flow fabrics in the Troodos Ophiolite Complex. Cyprus Journal of Structural Geology, 23, 1299-1317.

Bouchez, J.L., 1997. Granite is Never Isotropic: An Introduction to AMS Studies of Granitic Rocks. In: Bouchez, J.L., (Eds) Granite: From Segregation of Melt to Emplacement Fabrics. Petrology and Structural Geology, 8, 95-112

Cañón-Tapia, E., 2004. Anisotropy of magnetic susceptibility of lava flows and dykes: a historical account. In: Martín-Hernández, F., Luneberg, C.M., Aubourg, C., Jackson, M., (Eds) Magnetic Fabric: Methods and Applications. Geological Society of London Special Publication, 238, 1-7.

Cañón-Tapia, E., Chávez-Álvarez, M.J., 2004. Theoretical aspects of particle movement in flowing magma: implications for the anisotropy of magnetic susceptibility in dykes. In: Martín-Hernández, F., Luneberg, C.M., Aubourg, C., Jackson, M., (Eds) Magnetic Fabric: Methods and Applications. Geological Society of London Special Publication, 238, 227-249.

Cartwright, J., Hansen, D.M., 2006. Magma transport through the crust via interconnected sill complexes. Geology, 19, 929-932.

Correa-Gomes, L.C., Souza Filho, C.R., Martins, C.J.F.N., Oliviera, E.P., 2001. Development of symmetrical and asymmetrical fabrics in sheet-like igneous bodies: the role of magma flow and wall-rock displacements in theoretical and natural cases. Journal of Structural Geology, 23, 1415-1428.

Clemente, C.S., Amorós, E.B., Crespo, M.G., 2007. Dike intrusion under shear stress: Effects on magnetic and vesicle fabrics in dikes from rift zones of Tenerife (Canary Islands). Journal of Structural Geology, 29, 1931-1941.

Day, R.M., Fuller, M. & Schmidt, V.A. 1977. Hysteresis properties of titanomagnetites: grain size and composition dependence. Physics of the Earth and Planetary Interiors, 13, 260-267.

Dunlop, D.J., 2002. Theory and application of the Day plot (M_{rs}/M_s versus H_{cr}/H_c): 2. Application to data for rocks, sediments and soils. Journal of Geophysical Research, 107(B3), 2057, doi:10.1029/2001JB000487.

Dunlop, D.J., Özdemir, Ö., 1997. Rock Magnetism: Fundamentals and frontiers. Cambridge Univeristy Press, United Kingdom, 573 pp.

Ellwood, B.B., 1978. Flow and emplacement direction determined for selected basaltic bodies using magnetic susceptibility anisotropy measurements. Earth and Planetary Science Letters3, 41, 1270-1273.

Erlank, A.J., 1984. Petrogenesis of the Volcanic Rocks of the Karoo Province. Geological Society of South Africa Special Publication, 13, 395 pp.

Ernst, R.E., Baragar, W.R.A., 1992. Evidence from magnetic fabric for the flow pattern of magma in the Mackenzie giant radiating dyke swarm. Nature, 356, 511-513.

Fernández, A.N., Gasquet, D.R., 1994. Relative reheological evolution of chemical contrasted coeval magmas: example of the Tichka plutonic complex (Morocco). Contribution in Mineralogy and Petrology, 116, 316-326.

Ferré, E.C., Bordarier, C., Marsh, J.S., 2002. Magma flow inferred from AMS fabrics in a layered mafic sill, Insizwa, South Africa. Tectonophysics, 354, 1-23.

Fink, J.H., Fletcher, R.C., 1978. Ropy pahoehoe: Surface folding of a viscous fluid. Journal of Volcanology and Geothermal Research, 4, 151-170.

Gay, N.C., 1966. Orientation of mineral lineation along the flow direction in rocks: A discussion. Tectonophysics, 3, 559-564.

Gay, N.C., 1967. Pure shear and simple shear deformation of inhomogeneous viscous fluids. 1. Theory. Tectonophysics, 5, 211-234.

Geoffroy, L., Callot, J.P., Aubourg, C., Moreira, M., 2002. Is the common use of AMS in mafic dykes scientifically correct? Terra Nova, 14, 183–190.

Gil-Imaz, A., Pocoví, A., Lago, M., Galé, C., Arranz, E., Rillo, C., Guerrero, E., 2006. Magma flow and thermal contraction fabric in tabular intrusions inferred from AMS analysis. A case study in a late-Variscan folded sill of the Albarracı'n Massif (southeastern Iberian Chain, Spain). Journal of Structural Geology, 28, 641–653.

Graham, J.W., 1954. Magnetic susceptibility anisotropy, an unexploited fabric element. Bulletin of the Geological Society of America, 65, 1257-1258.

Harrison, R.J. & Feinberg, J.M., 2008. FORCinel: An improved algorithm for calculating first-order reversal curve distributions using locally weighted regression smoothing. Geochemistry, Geophysics, Geosystems, 9, Q05016, doi: 10/1029/2008GC001987.

Hastie, W.W., Aubourg, C., Watkeys, M.K., 2011a. Significance of magnetic and fabric in Karoo-feeder dykes, northern Lebombo. Tectonophysics, 513, 96-111.

Hastie, W.W., Aubourg, C., Watkeys, M.K., 2011b. When an inverse fabric is not inverse: an integrated AMS-SPO study in MORB-like dykes. Terra Nova, 23, 49-55.

Hastie, W.W., Watkeys, M.K., Aubourg, C., 2014. Magma flow in dyke swarms of the Karoo LIP: Implications for the mantle plume hypothesis. Gondwana Research, 25, 736-755.

Horsman, E., Tikoff, B., Morgan S., 2005. Emplacement-related fabric and multiple sheets in the Maiden Creek sill, Henry Mountains, Utah, USA. Journal of Structural Geology, 27, 1426-1444.

Hoyer, L., Watkeys, M.K., 2015. Assessing SPO techniques to constrain magma flow: examples from sills of the Karoo Igneous Province, South Africa. Tectonophysics, 656, 61-73.

Hrouda, F., Táborská, S., Schulmann, K., Ježek, J., Dolejš, D., 1999. Magnetic fabric an rheology of co-mingled magmas in the Nasavrky Plutonic Complex (E. Bohemia): implications for intrusive strain regime and emplacement mechanism. Tectonophysics, 307, 93-111.

Hutton, D.H.W., 2009. Insights into magmatism in volcanic margins: bridge structures and a new mechanism of basic sill emplacement – Theron Mountains, Antarctica. Petroleum Geoscience, 15, 269-278.

Jelinek, V., 1978. Statistical processing of anisotropy of magnetic susceptibility measured on a group of specimens and its applications. Studies in Geophysics and Geodynamics, 22, 50-62.

Jelinek, V. 1981. Characterisation of the magnetic fabric of rocks. Tectonophysics, 79, 63-67.

Jourdan, F., Féraud, G., Bertrand, H., Kampunzu, A. B., Tshoso, G., Watkeys, M.K., and Le Gall, B., 2005. Karoo large igneous province: Brevity, origin and relation to mass extinction question by new $^{40}Ar/^{39}Ar$ age data. Geology, 33, 745-748.

Jourdan, F., Féraud, G., Bertrand, H., Watkeys, M.K., and Renne, P.R., 2007. Distinct brief major events in the Karoo large igneous province clarified by new $^{40}Ar/^{39}Ar$ ages on the Lesotho basalts. Lithos, 98, 195-209.

Kattenhorn, S.A., Watkeys, M.K., 1995. Blunt-ended dyke segments. Journal of Structural Geology, 17, 1535-1542.

Khan, M.A., 1962. Anisotropy of magnetic susceptibility of some igneous and metamorphic rocks. Journal of Geophysical Research, 67, 2873-2885.

Knight, M.D., Walker, G.P.L., 1988. Magma flow directions in dikes of the Koolau Complex, Oahu, determined from magnetic fabric studies. Journal of Geophysical Research, 93, 4301-4319.

Krása, D., Herrero-Bervera, E., 2005. Alteration induced changes of magnetic fabric as exemplified by dykes of the Koolau volcanic range. Earth and Planetary Science Letters, 240, 445-453.

Launeau, P., 2004. Mise en évidence des écoulements magmatiques par analyse d'images 2-D des distributions 3-D d'Orientations Préferentielles de Formes. Bulletin of the Geological Society of France, 175, 331–350.

Launeau, P., Cruden, A.R., 1998. Magmatic fabric acquisition mechanisms in a syentire: Results of a combined anisotropy of magnetic susceptibility and image analysis study. Journal of Geophysical Research, 103, 5067-5089.

Launeau, P., Robin, P.-Y.F., 1996. Fabric analysis using the intercept method. Tectonophysics, 267, 91-119.

Launeau, P., Robin, P.-Y.F., 2005. Determination of fabric and strain ellipsoids from measured sectional ellipses—implementation and applications. Journal of Structural Geology, 27, 2223–2233.

Liss, D., Hutton, D.H.W., Owens, W.H., 2002. Ropy flow structures: A neglected indicator of magma-flow direction in sills and dikes. Geology, 30, 715-718.

Loock S., Diot, H., Van Wyk de Vries, B., Launeau, P., Merle, O., Vedboin, F., Petronis, M.S., 2008. Lava flow internal structure found from AMS and textural data: An example in methodology form the Chaîne des Puys, France. Journal of Volcanology and Geothermal Research, 177, 1092-1104.

Magee, C., Stevenson, C.T.E., O'Driscoll, B., Petronis, M.S. 2012. Local and regional controls on the lateral emplacement of the Ben Hiant Dolerite intrusion, Ardnamurchan (NW Scotland). Journal of Structural Geology, 39, 66-82.

Manga, M., Stone, H.A., 1994. Interactions between bubbles in magmas and laves: effects of bubble deformation. Journal of Volcanology and Geothermal Research, 63, 267-279.

Martín-Hernández, F., Luneberg, C.M., Aubourg, C., Jackson, M., 2004. Magnetic fabric: methods and applications – an introduction. In: Martín-Hernández, F., Luneberg, C.M., Aubourg, C., Jackson, M., (Eds) Magnetic Fabric: Methods and Applications. Geological Society of London Special Publication, 238, 1-7.

Morris, G.A., Kamada, M., Martinez, V., 2008. Emplacement of the Etive Dyke Swarm, Scotland: implacations of dyke morphology and AMS data. In: Thomson, K., Petford, N., (Eds) Structure and emplacement of High-Level Magmatic Systems. Geological Society, London Special Publication, 302, 149-158.

Nicholas, A., 1992. Kinematics in magmatic rocks with special reference to gabbros. Journal of Petrology, 33, 891-915.

Nicholson, R., Ejiofor, I.B., 1987. The three-dimensional morphology of arrays of echelon and sigmoidal, mineral-filled fractures: data from north Cornwall. Journal of the Geological Society of London, 144, 79-83.

Nicholson, R., Pollard, D.D., 1985. Dilation and linkage of echelon cracks. Journal of Structural Geology, 7, 583-590.

O'Driscoll, B., Stevenson, C.T.E., Troll, V.R., 2008. Mineral Lamination Development in Layered Gabbros of the British Palaeogene Igneous Province: A Combined Anisotropy of Magnetic Susceptibility, Quantitative Textural and Mineral Chemistry Study. Journal of Petrology, 49, 1187-1221.

Özdemir, Ö., Dunlop, D.J. & Moskowitz, B.M. 1993. The effect of oxidation on the Verwey transition in magnetite. Geophysical Research Letters, 20, 1671-1674.

Paterson, S.R., Fowler, T.K. Jr., Schmidt, K.L., Yoshinobu, A.S., Yuan, E.S., Miller, R.B., 1998. Interpreting magmatic fabric patterns in plutons. Lithos, 44, 53-82.

Payacán, I., Gutiérrez, F., Gelman, S.E., Bachmann, O., Parada, M.Á., 2014. Comparing magnetic and magmatic fabrics to constrain the magma flow record in La Gloria pluton, central Chile. Journal of Structural Geology, 32-46.

Philpotts, A.R., Philpotts, D.E. 2007. Upward and downward flow in a camptonite dike as recorded by deformed vesicles and the anisotropy of magnetic susceptibility (AMS). Journal of Volcanology and Geothermal Research, 161, 81-94.

Philpotts, A.R., Brustman, C.M., Shi, J., Carlson, W.D., Denison, C., 1999. Plagioclase-chain networks in slowly cooled basaltic magmas. American Mineralogist, 84, 1819-1829.

Poland, M.P., Fink, J.H., Tauxe, L. 2004. Patterns of magma flow in segmented silicic dikes at Summer Coon volcano, Colorado: AMS and thin sections analysis. Earth and Planetary Science Letters, 219, 155-169.

Pollard, D.D., 1987. Elementary fracture mechanics applied to the structural interpretation of dykes. In: Halls, H.C., Fahrig, W.F., (Eds) Mafic Dyke Swarms. Geological Association of Canada Special Paper, 34, 5-24.

Pollard, D.D., Muller, O.H., Dockstader, D.R., 1975. The form and growth of fingered sheet intrusions. Geological Society of America Bulletin, 86, 351-363.

Rickwood, P.C., 1990. The anatomy of a dyke and the determination of propagation and magma-flow directions. In: Parker, A.J., Rickwood, P.C., Tucker, D.H., (Eds) Mafic dykes and Emplacement Mechanisms. Proceedings of the Second international dyke conference, Adelaide, South Australia, 2, 81-100.

Robin, P.-Y.F., 2002. Determination of fabric and strain ellipsoids from measured sectional ellipses – Theory. Journal of Structural Geology, 24, 531-544.

Rochette, P., Fillion, G., Mattéi, J.-L., Dekkers, M.J. 1990. Magnetic transition at 30 – 34 K in pyrrhotite: insight into a widespread occurrence of this mineral in rocks. Earth and Planetary Science Letters, 98, 319-328.

Rochette, P., Jackson, M., Aubourg, C., 1992. Rock magnetism and the interpretation of anisotropy of magnetic susceptibility. Reviews in Geophysics, 30, 209-226.

Rochette, P., Aubourg, C., Perrin, M., 1999. Is this magnetic fabric normal? A review and case studies in volcanic formations. Tectonophysics, 307, 219-234.

Rochette, P., Fillion, G., Dekkers., 2011. The Low-Temperature Magnetic Transition of Monoclinic Pyrrhotite. IRM Quarterly, 21 (1).

Tarling, D.H., Hrouda, F. 1993. The Magnetic Anisotropy of Rocks. Chapman and Hall, London, pp. 218.

Schofield, N., Heaton, L., Holford, S.P., Archer, S.G., Jackson, C.A.-L., Jolley, D.W., 2012a. Seismis imaging of 'broken bridges': linking seismic to outcrop-scale investigations of intrusive magma lobes. Journal of the Geological Society of London, 169, 421-426.

Schofield, N., Brown, D.J., Magee, C., Stevenson, C.T., 2012b. Sill morphology and comparison of brittle and non-brittle emplacement mechanisms. Journal of the Geological Society of London, 169, 127-141.

Schopa, A., Floess, D., de Saint Blanquat, M., Annen, C., Launeau, P., 2015. The relation between magnetite and silicate fabric in granitoids of the Adamello Batholith. Tectonophysics, 642, 1-15.

Smirnov, A.V. 2006. Low-temperature magnetic properties of magnetite using first-order reversal curve analysis: Implications for the pseudo-single-domain state. Geophysics, Geochemistry, Geosystems, 7, 11, Q11011, doi: 10.1029/2006GC001397.

Stephenson, A., Sadikun, S., Potter, D.K., 1986. A theoretical and experimental comparison of the anisotropies of magnetic susceptibility and remanence in rocks and minerals, Geophysical Journal International, 84, 185-200.

Stevenson, C.T.E., Owens, W.H., Hutton, D.H.W., 2007. Flow lobes in granite: The determination of magma flow direction in the Trawenagh Bay Granite, northwestern Ireland, using anisotropy of magnetic susceptibility. Geological Society of America Bulletin, 119, 1368-1386.

Svensen, H., Corfu, F., Polteau, S., Hammer, Ø., Planke, S., 2012. Rapid magma emplacement in the Karoo Large Igneous Province. Earth and Planetary Science Letters, 325-326, 1-9.

Verwey, E.J. 1939. Electron conduction of magnetite (Fe_3O_4) and its transition point at low temperature. Nature, 144, 327-328.

Watkeys, M.K., 2006. The break-up of Gondwana: a South African perspective. In: Johnson, M.R., Anhaeusser, C.R., Thomas, R.J., (Eds.). The Geology of South Africa. Geological Society of South Africa, Council for Geoscience, 531–539.

Zuo, J.M., 1990. Charge ordering in magnetite at low temperatures. Physical Review, 42, 8451-8464

- CHAPTER 7 -

MAGMA FLOW DIRECTIONS IN KAROO SILLS, KWAZULU-NATAL IMPLICATIONS FOR INTRUSIVE MECHANISMS AND MAGMA SOURCE

Note: This discussion, combined with the methodologies and techniques described in *Chapter 2* and the geological background presented in *Chapter 3*, is currently being combined in a manuscript in preparation for peer review. In order to reduce repetition, this chapter has been edited and does not include a detailed introduction or methods section.

7.1. Introduction

The vast sub-volcanic network of dykes and sills of the Karoo Igneous Province (KIP) is associated with extensive continental flood basalts (Fig. 7.1) (Erlank, 1984). Magmatism of the KIP commenced at ~183 Ma and ceased at ~174 Ma (Jourdan et al., 2005, 2007; Hastie et al., 2014). This magmatic event is usually ascribed to a mantle plume impacting the lithosphere beneath or just east of the Nuanetsi Igneous Province (now known as Mwenezi) which had previously been recognised as a triple junction; a pattern supposedly imposed on the lithosphere by the mantle plume (Fig. 7.1) (Burke and Dewey, 1973). In this model, igneous activity commenced above that site, and then spread outwards before narrowing and concentrating above the zone of impact (White and McKenzie, 1989; Campbell and Griffiths, 1990; Cox, 1992; Ernst and Buchan, 1997; Storey and Kyle, 1997). An alternate point of view is that the preserved geochemical and geological patterns are artefacts of lithospheric architecture (Sweeney and Watkeys, 1990; Watkeys, 2002; Jourdan et al., 2006, 2009). Geochronological studies also show that igneous activity did not spread out from the proposed plume site, thus indicating that a plume alone cannot account for the distribution of lithologies and associated structures (Jourdan et al., 2005, 2007, 2008; Hastie et al., 2014).

One test of these opposing views is to establish the magma flow direction in the dykes and sills forming the sub-volcanic network of the KIP. Such work has recently been undertaken on the sills in the main Karoo Basin, where the magma flow was shown to be from the NW (Ferré et al., 2015). Similar studies have also been conducted on the Okavango Dyke Swarm (ODS) (Aubourg et al., 2008), the Northern Lebombo Dyke Swarm (NLDS) and the Rooi Rand Dyke

Swarm (RRDS) (Hastie et al., 2011, 2014), which show that these dykes injected laterally away from the proposed plume head site (Fig. 7.1). The Underberg Dyke Swarm (UDS) has also been studied to determine the dyke geochemistry and intrusion direction, showing that the dykes were not fed from a source associated with the Karoo triple junction (Fig. 7.1) (Riley et al., 2006).

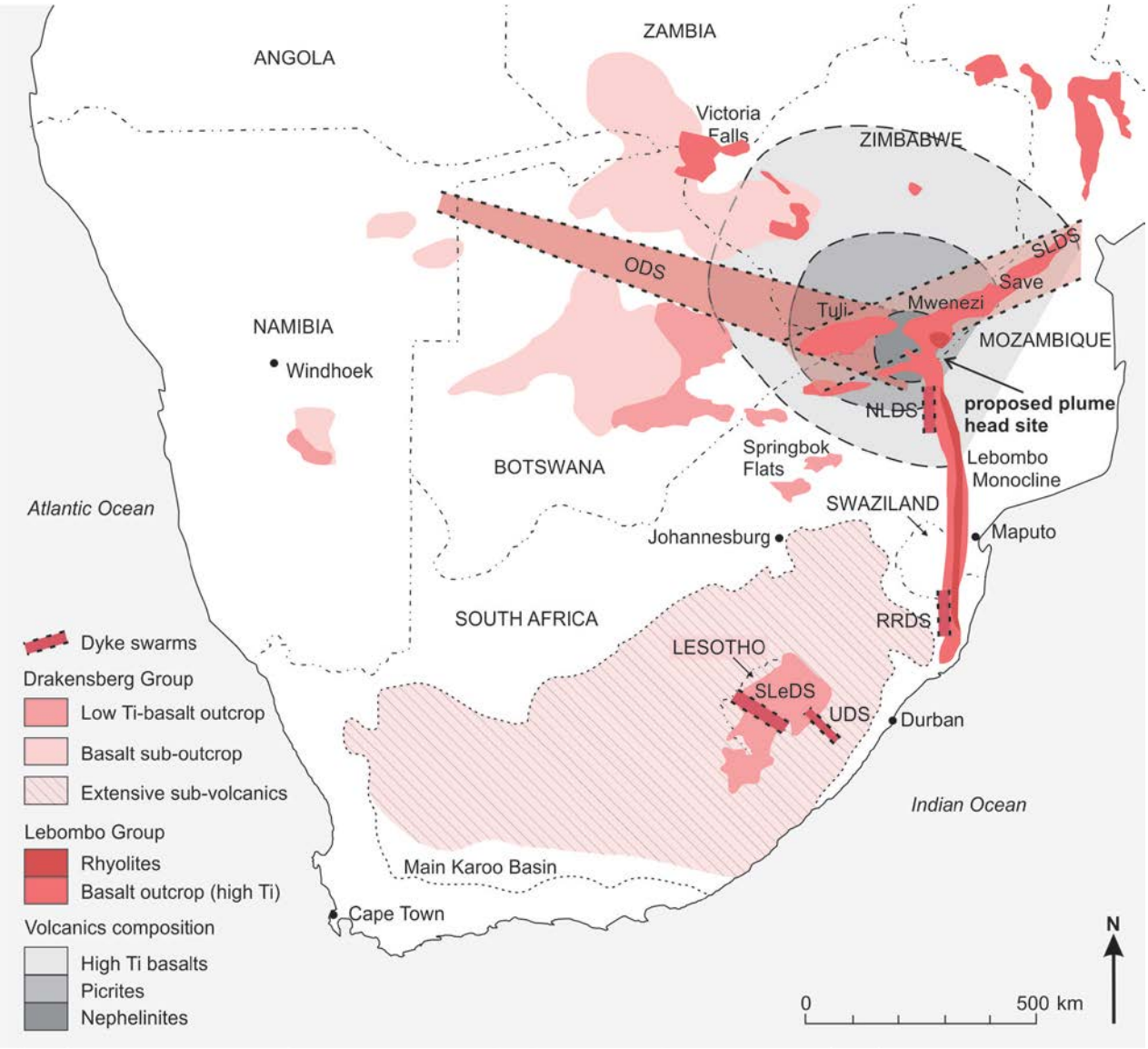

Fig. 7.1. The geographical extent of the rocks associated with the KIP including flood basalt sequences and dyke swarms. The proposed plume head site is where a mantle plume is thought to have impacted the lithosphere at Mwenezi. RRDS = Rooi Rand Dyke Swarm, NLDS = Northern Lebombo Dyke Swarm, ODS = Okavango Dyke Swarm. After Duncan and Marsh (2006); Jourdan et al. (2009); Klausen (2009).

Analysing sills should help to constrain the magma source and whether magma was transported significant distances away from the magma source. This will provide information about where the melts originated and the migration of magma in the upper crust, allowing the plumbing system of the KIP to be better understood (Schofield et al., 2012a; Cartwright and Hansen, 2006).

The magma flow directions of numerous small Karoo sills that crop out along the North Coast of KwaZulu-Natal (KZN), South Africa, are here analysed. These intrusions contain structures that have long been used to define magma flow regimes of both dykes (Pollard et al., 1975; Pollard, 1987; Rickwood, 1990; Liss et al., 2002) and sills (Nicholson and Pollard, 1985; Horsman et al., 2005). Therefore they afford the opportunity to compare the directions of magma flow as inferred from a number of different indicators. This chapter reports on the results from field work observations, the Shape-preferred Orientation (SPO) of microscopic minerals and the Anisotropy of Magnetic Susceptibility (AMS) analyses of sub-microscopic magnetic minerals. A sense of magma flow will be established for the sills, as well as the mechanism by which the sills were intruded. By using these magma flow directions and intrusive mechanisms, the source of the magma may be inferred.

7.1.1. Effingham-type Dolerites

Frankel (1969) analysed numerous dolerite intrusions along the KwaZulu-Natal North Coast and showed that the sills were more silicic in composition than typical dolerites, ranging in composition from andesites to dacites with SiO_2 wt% of ~66%. These rocks were characterised by the features observed in the intrusions: variolitic margin textures, abundant amygdales and xenoliths of basement and country rock (Frankel, 1969). This dolerite type was assumed to have formed through the assimilation of felsic basement rocks with a volatile-enriched magma (Frankel, 1969).

7.2. Results

7.2.1. Magma Flow Indicators

There are several different types of magma flow structures, related to the formation of the sills in the field area, as described in *Chapter 6*. These structures range from broken bridge structures, bridge stubs, intrusive steps, ropy-flow structures, elongated vesicles and magma lobes. The long axes of these structures are here used to imply the sense of magma flow in the intrusions as the processes that formed these structures are directly related to the mechanisms of magma intrusion. The long axes of the magma flow indicators in the study area are not all

identical however; there are a few distinct directions/orientations that are common amongst these structures (Fig. 7.2). As evidenced by both uni-directional and bi-directional magma flow indicators, the long axes of the structures are dominated by a NE – SW orientation (Fig. 7.2).
A second distinct orientation, representative of the magma flow indicator long axes, is NW – SE, which is perpendicular to the most common direction. A north-south orientation is also clearly observed in Fig. 7.2, representative of the orientations measured from the sills SHF2 and SHF5. There is a significant lack of east-west oriented long axes of the magma flow indicators.

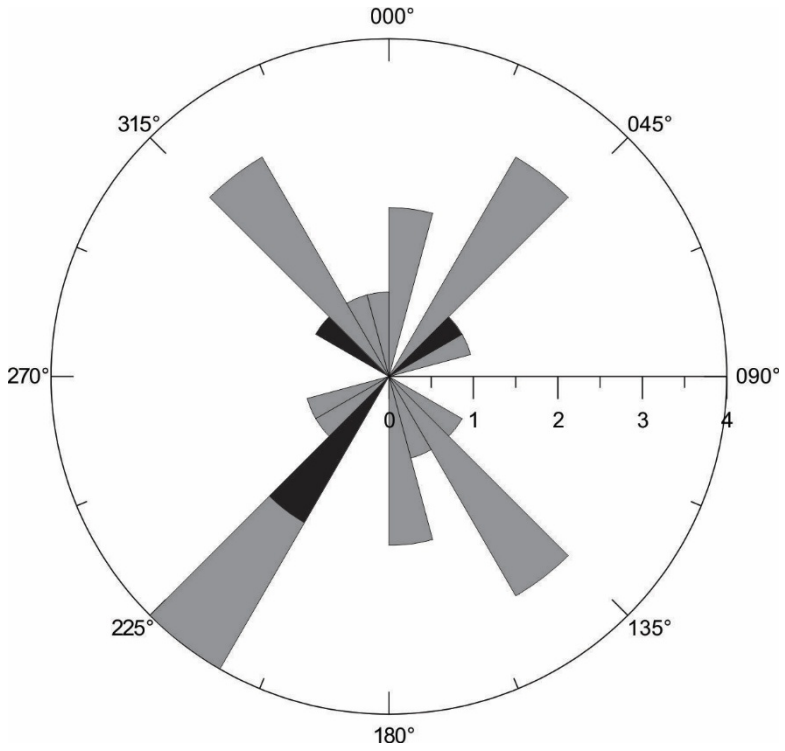

Fig. 7.2. Rose diagram, with 15° bin sizes, showing the primary long axis directions of the magma flow indicators of the sills from Thompson's Bay and Sheffield Beach. The black segments are representative of uni-directional data, ie. linear structures. The grey segments are representative of bi-directional data, ie. planar structures.

7.2.2. Dykes

Although the number of dykes observed in the field area is limited, the trend directions of these sub-vertical dykes are significant. Towards the northern extent of the Thompson's Bay area, two ~10 cm wide 040° striking dykelets crop out (yielding dips of 84° once restored to the horizontal) (Fig. 7.3a and b). Just north of TB4, the remnants of a 1 m wide dyke crops out, with a dip and strike of 60°/324° (restored dip and strike of 80°/326°) (Fig. 7.3c). South of TB2 is a second ~1 m thick dyke with a NW-SE trend. A 0.5 m wide dyke crops out 220 m south of TB6 with a dip and strike of 80°/329° (restored dip and strike of 85°/150°).

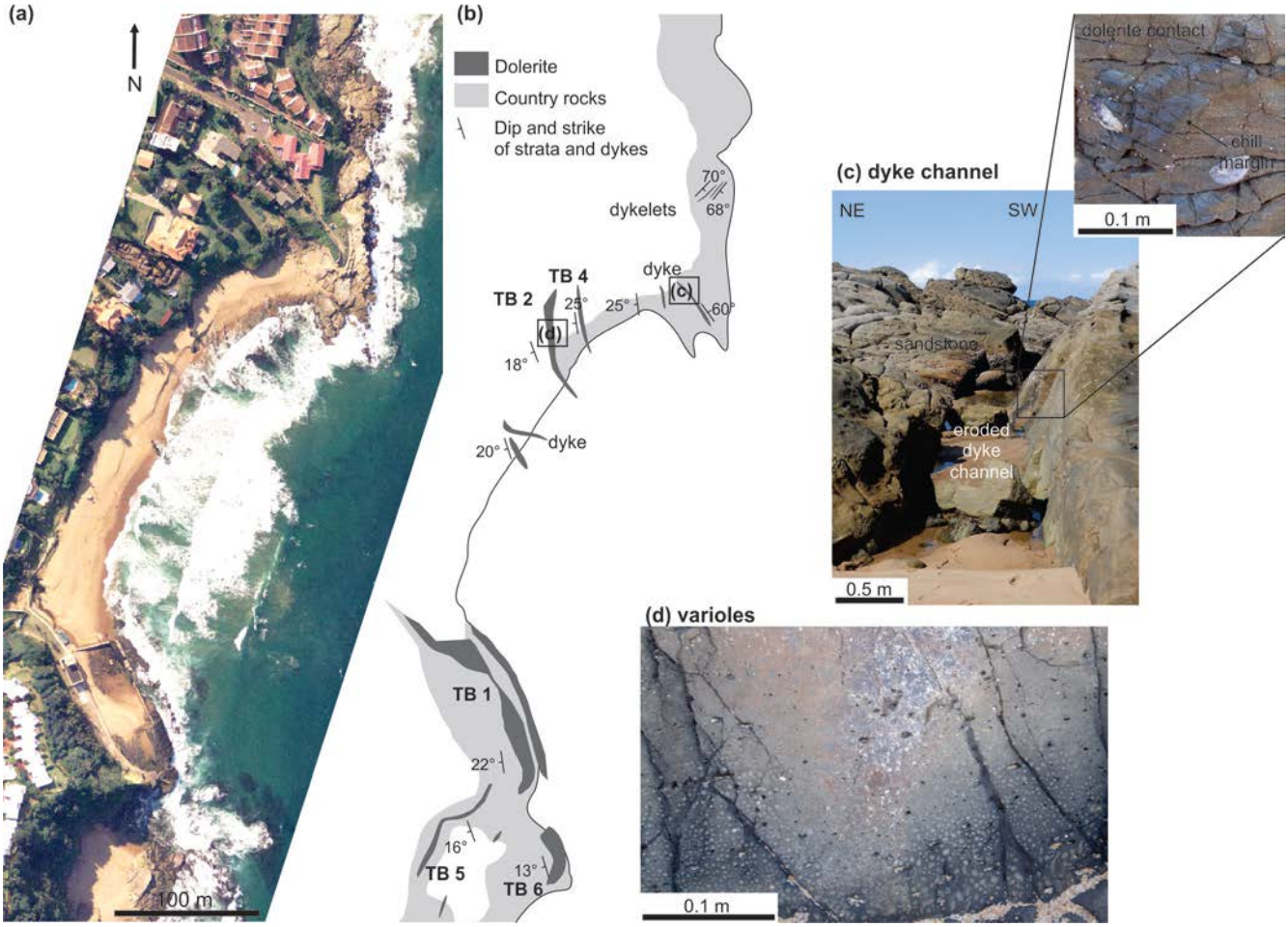

Fig. 7.3. (a) Aerial photograph of the Thompson's Bay area with (b) showing the outcrop pattern of the sills and dykes along the coastline. (c) A sub-vertically dipping dyke (once restored to the horizontal) has been eroded with only remnants of the chill margin preserved on the dyke wall (enlarged area). (d) Varioles collecting and coalescing at the base of a discrete magma layer in the sill TB2.

There are no dykes cropping out along the southern Sheffield Beach area. However, an ~8 m wide, NW-SE striking dyke crops out in the northern Sheffield Beach area, to the south of SHF9 (Fig. 7.4a and b). Thinner dykelets extend from this dyke with dips and strikes of ~75°/332° (restored dip and strike 75°/328°). A small vertical broken bridge is preserved along the north-western contact (Fig. 7.4c).

7.2.3. Sill Mineralogy and Geochemistry

Within the study area, the chemistry of the sills changes microscopically as a result of the degree of alteration of the minerals and the inclusion of additional components, such as xenocrysts, amygdales and infilled fractures. Cryptocrystalline material is present in all of the intrusions and can reach volumes of up to 25% (in SHF8). The groundmass textures range from sub-ophitic to variolitic, with four of the sills showing glomeroporphyritic textures (SHF7,

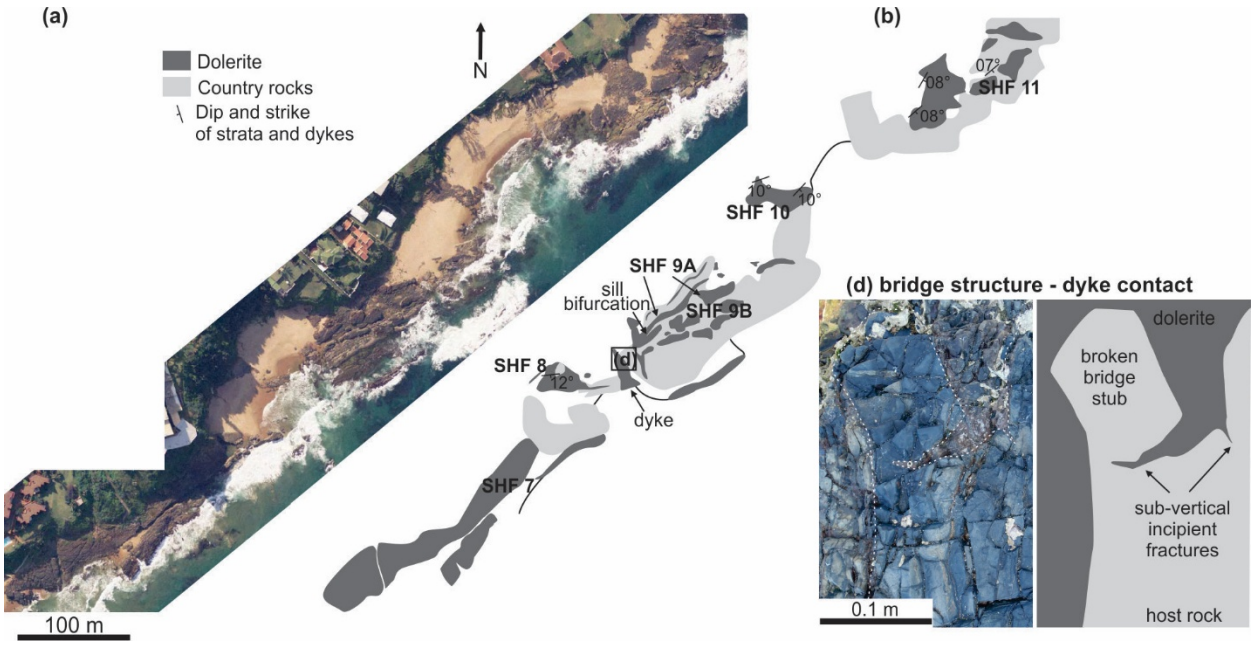

Fig. 7.4. (a) Aerial photograph of the northern Sheffield Beach area with (b) showing the outcrop pattern of the sills and dykes along this section of coastline. (c) A sub-vertically dipping broken bridge structure occurs along the NW contact of the dyke between SHF8 and SHF9.

SHF9, SHF10 and SHF11). In one discrete layer in the sill TB2, varioles occur in abundance, appearing to collect at the base of a magma layer where they coalesce (Fig. 7.3d). Vesicles and amygdales are present in most of the sills with the vesicles being infilled with quartz and/or calcite and/or chlorite. In thin section, there are areas of chlorite and quartz crystallisation common in the samples however these appear to be a product with later infilling or the product of disaggregated xenolithic material.

The sill SHF6 was sampled for geochemical analyses; this sill has an overall similar appearance to the majority of the sills in the study area. Two samples (G1 and G2) were analysed using standard whole rock X-ray Fluorescence (XRF) techniques in order to obtain the major and selected trace element compositions. Samples were taken from the centre of the intrusion. Care was taken when obtaining the samples, so that only the dolerite material was sampled, ensuring that any geochemical influence, from amygdales or xenoliths, would be excluded. The results from the two sills are generally similar (Table. 7.1). The loss on ignition for the two samples is 6.96% and 2.32% showing the presence of volatiles in the system. The SiO_2 wt% is 51.84% and 49.37% for G1 and G2 respectively (Table 7.1). The sample with the lower SiO_2 wt% shows slight differences in the other major elements with respect to G1; lower TiO_2 and Fe_2O_3 wt% and higher MgO, Mn_3O_4, CaO and Na_2O wt% (Table 7.1). The trace element compositions of

the two samples are similar, except for the Mn content, which is significantly higher in the G2 sample when compared to the G1 sample.

Table 7.1. Geochemical Results for Samples from SHF6

	Sample name			Sample name	
Oxides (%)	SHF6-G1	SHF6-G2	Trace elements (ppm)	SHF6-G1	SHF6-G2
SiO_2	51.84	49.38	Sc	41	34
TiO_2	1.14	0.87	V	330	236
Al_2O_3	16.72	15.72	Cr	376	337
Fe_2O_3	13.73	11.65	Mn	812	1310
Mn_3O_4	0.12	0.18	Co	50	52
MgO	6.57	8.25	Ni	113	127
CaO	6.53	10.37	Cu	89	78
Na_2O	1.82	2.05	Zn	101	85
K_2O	0.73	0.50	Ga	19	20
P_2O_5	0.14	0.10	Ge	1	1
SO_3	0.61	0.23	Rb	20.1	14.6
V_2O_5	0.06	0.05	Sr	195	165.5
Cr_2O_3	0.05	0.05	Y	15.7	20.7
SrO	0.03	0.01	Zr	93.2	71.7
ZrO_2	0.02	0.01	Nb	2.2	2.5
BaO	0.03	0.01	Ba	266	139
NiO	0.02	0.02	La	10	4
CuO	0.01	0.01	Ce	9	13
ZnO	0.01	0.01	Nd	10	4
Loss On Ignition	6.96	2.32	Hf	5	7
Sum	100.16	99.49	Hg	10	2
			Pb	4	2.9
			U	1	1.3

The MgO wt% is 6.57% and 8.25% for G1 and G2 respectively. Where the MgO content of the sills increases, the amount of Fe_2O_3, TiO_2 and Y decreases. The TiO_2 wt% is low being less than 1.5% as is the Zr component, which is less than 150 ppm.

7.2.4. Volatiles Present in the System

Eleven of the 16 sills sampled in the study area exhibit features other than magma flow indicators, ranging from vesicles (and subsequent amygdales), entrained country rock and basement xenoliths, rheomorphic sedimentary dykes and confined (fluid-assisted brecciation) (*Chapter 5*). The sills that are massive, and do not show any of these features are TB5, SHF4 and SHF5 (Table 7.2). SHF10 and SHF11 are massive however, the abundance of chlorite after phenocrystic pyroxene is noted.

Table 7.2. *Sill Properties and Characteristics*

Sill	Geographical co-ordinates				Approximate Thickness	
Name	Latitude	Longitude	Dip	Strike	(m)	Characteristics
TB1	29° 31' 39.05"	31° 13' 41.17"	22°	172°	3.0	Large vesicles, basement xenolithic, minor amygdales
TB2	29° 31' 14.69"	31° 13' 42.05"	21°	167°	2.5	Numerous vesicles, amygdaloidal layer, basement xenolith layer
TB4	29° 31' 13.87"	31° 13' 42.87"	25°	172°	1.0	Central vesicle stringer
TB5	29° 31' 25.17"	31° 13' 39.03"	16°	160°	2.0	Massive
TB6	29° 31' 25.71"	31° 13' 41.21"	13°	164°	unknown	Fine vesicles
SR1	29° 30' 50.76"	31° 13' 54.48"	20°	206°	2.0	Small xenoliths along upper contact, vesicles
SHF2	29° 29' 43.44"	31° 14' 46.68"	20°	000°	1.0	Central vesicle stringer
SHF3	29° 29' 41.64"	31° 14' 46.93"	17°	340°	2.2	Isolated sections of fluidised host rock material, sedimentary dykes, amygdales upper contact
SHF4	29° 29' 37.32"	31° 14' 49.56"	12°	350°	1.5	Massive
SHF5	29° 29' 41.28"	31° 14.48.48"	10°	353°	1.2	Massive
SHF6	29° 29' 32.64"	31° 14' 57.48"	13°	013°	2.5	Basement and country rock xenoliths, sedimentary dykes
SHF7	29° 29' 23.64"	31° 15' 07.56"	10°	056°	>6	Vesicles, pods of previously crystallised doleritic xenoliths
SHF8	29° 29' 19.32"	31° 15' 10.44"	09°	088°	0.5	Central vesicle stringer
SHF9A	29° 29' 17.02"	31° 15' 14.83"	13°	065°	1.5	Dolerite-matrix country rock breccia, small
SHF9B	29° 29' 18.20"	31° 15' 14.10"	13°	065°	1.5	basement xenoliths, abundant vesicles and amygdales, significant chlorite component
SHF10	29° 29' 14.23"	31° 15' 17.26"	10°	059°	1	Significant chlorite component
SHF11	29° 29' 10.55"	31° 15' 24.85"	10°	054°	1.5	Significant chlorite component

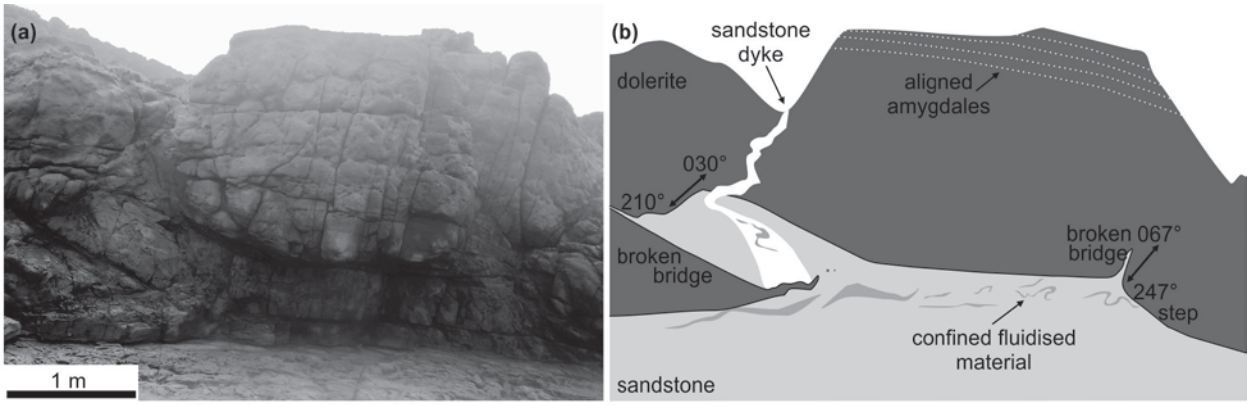

Fig. 7.5. An example of the production of fluidised material through magma intrusion from SHF3. (a) Photograph of the sill, (b) sketch showing the relationship between the underlying sandstone and the fluidised sandstone material. Some of the material is confined beneath the sill and some intrudes upwards, in the broke bridge structure, and then cross-cuts the dolerite.

The sills generally intrude above a discontinuity. These discontinuities typically comprise the contact between an underlying sandstone and overlying shale. The sills do not intrude along the lithological contact however; there is almost always a thin layer of shale between the lower contact of the sill and the more competent layer. The only sill that has intruded into a sandstone unit is SHF3, where small amounts of fluidisation of the underlying sandstone and a broken bridge structure was recognised (Fig. 7.5). Some of this fluidised material was confined beneath the sill however, the migration of the majority of this material resulted in a sedimentary dyke that subsequently penetrated the sill (Fig. 7.5).

7.2.5. SPO results

A total number of 126 samples (378 photomicrographs) were analysed petrographically to obtain the fabrics of the plagioclase grains for 16 sills for Thompson's Bay (TB), Shaka's Rock (SR) and Sheffield Beach (SHF). The opaque grains were not petrographically examined. However, as the opaque grains are commonly parallel to the plagioclase laths, the fabrics should be coaxial. The SPO data for the contacts of each sill are represented by lower hemisphere stereonets and presented in Fig. 7.6. The resultant average fabric for each sill contact was typically only moderately constrained, even when several samples were analysed.

7.2.5.1. Thompson's Bay and Shaka's Rock

The SPO results for the upper contact of TB1 are poorly constrained and have a wide spread of data. The average fabric across this upper contact plunges towards 267° (Fig. 7.6). The vesicular unit within TB2 was analysed as well as the upper and lower contacts. The upper contact data are moderately constrained and plunge towards 352°. The SPO data for the vesicular zone are well constrained and plunge shallowly towards 343°. The lower contact SPO data are wide spread and have an average plunge direction of 329°. The upper and lower contact data from TB4 are steeply inclined and moderately constrained, plunging towards 220° and 162° respectively (Fig. 7.6). Three of the four SPO results from the upper contact data of TB5 plunge towards the NNW with an average plunge direction of 334°. The lower contact data are less consistent with an average fabric plunging towards 079°. Due to the silicification and alteration of the dolerite, petrographic studies were not undertaken on the samples from TB6. The centre of SR1 was sampled in conjunction with the upper and lower contacts. The data from the upper contact of SR1 appear to be spurious, the poorly constrained average fabric plunges towards 050° (Fig. 7.6). Two data points from the lower contact are steeply inclined and plunge on

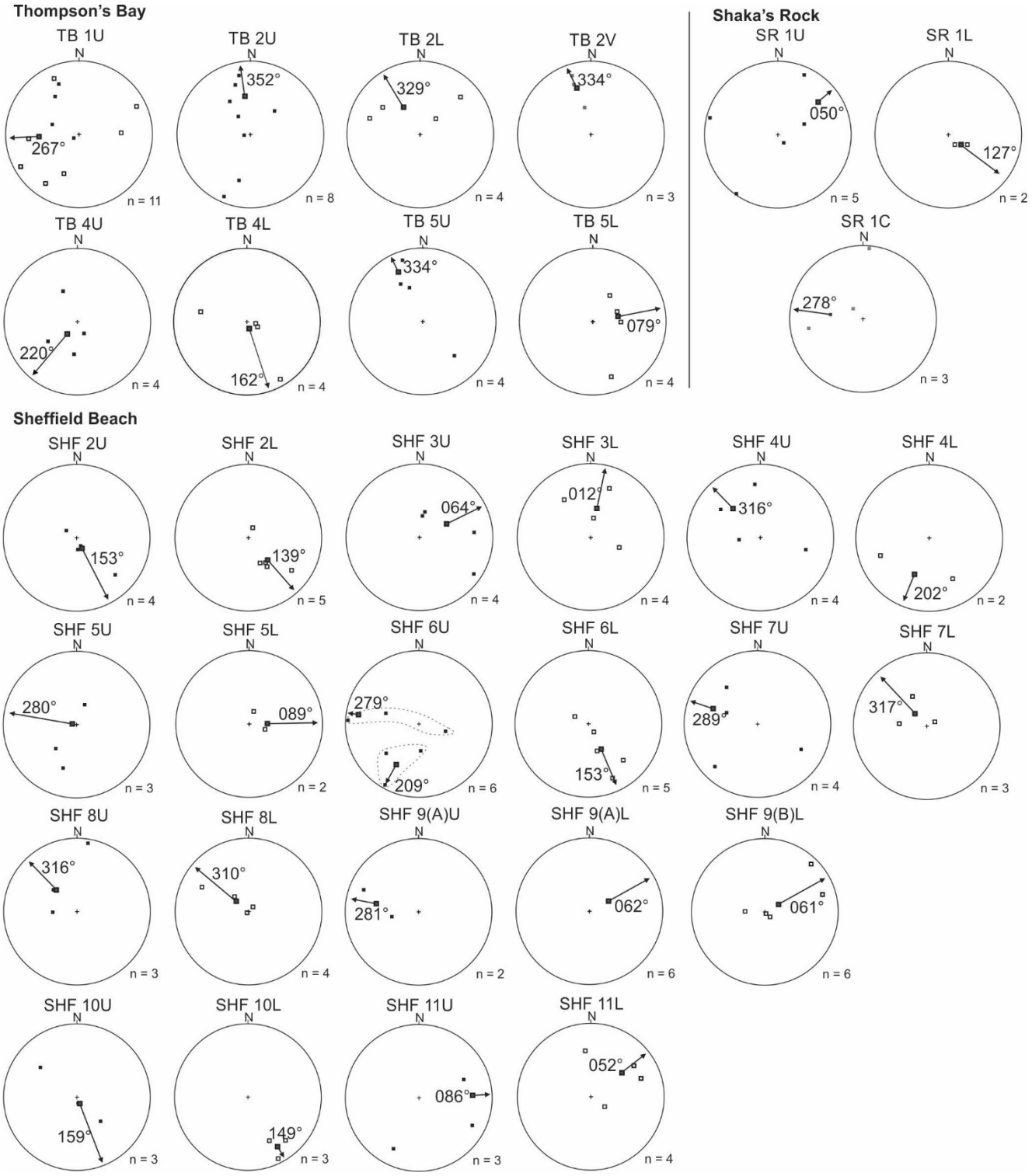

Fig. 7.6. The SPO results from the contacts of the sills sampled from Thompson's Bay, Shaka's Rock and Sheffield Beach. The filled squares are the SPO results defined by the foliation and the open squares are the results defined by the lineation. The grey-filled squares mark the plunge and plunge direction of the average fabric across the contact. The degree angle is the plunge direction of the resultant average fabric. n = number of samples.

average towards 127°. The results from the centre of the intrusion are sparse and poorly constrained with the average fabric plunging towards 278° (Fig. 7.6).

7.2.5.2. Sheffield Beach sills

The SPO fabrics for the lower and upper contacts of SHF2 are moderately constrained with both contact data plunging steeply, the upper contact data towards 153° and the lower contact data towards 139° (Fig. 7.6). The SPO data from the upper and lower contacts of SHF3 are scattered and thus yielded a poorly defined average fabric plunging towards 064° and 012° respectively. For the SHF4 SPO data, the average fabrics are shallowly plunging towards 316°, for the upper contact and 202°, for the lower contact. These data are however, poorly constrained. The average fabric results for the upper and lower contacts of SHF5 are symmetrical about the sill contacts, plunging towards 280° and 089° respectively, with a steeply dipping (to almost vertical) average fabric along the upper contact (Fig. 7.6). Although the results are symmetrical, the data are poorly constrained. The results from the upper contact of SHF6 plunge in two different directions, either towards 279° or towards 209° This is due to the perpendicular fabric distribution noted locally (*Chapter 6*). The lower contact data are well defined with the average fabric plunging moderately towards 153° (Fig. 7.6).

The SPO data from the upper and lower contacts of SHF7 are very poorly constrained with large variations in plunge directions and plunge angles. This is particularly the case with the lower contact, which plunges steeply towards 317° (Fig. 7.6). The average fabric from the upper contact of SHF7 plunges shallowly towards 289°. The samples obtained for SHF8 comprise fine varioles resulting in only a few samples yielding satisfactory ellipsoids. The upper and lower contact average fabric data are both steeply plunging towards 316° and 310° respectively. For SHF9 the number of samples obtained for the upper contact of SHF9A was limited, and the upper contact of SHF9B was not sampled due to a high degree of fracturing. The two SPO results from the upper contact of SHF9A are sub-parallel and plunge shallowly towards 281°. The average SPO fabrics from the lower contacts of SHF9A and SHF9B plunge towards 062° and 061° respectively (Fig. 7.6). The SPO results from the upper contact of SHF10 are wide spread stereographically with the average fabric plunging almost vertically towards 159°. The lower contact data yielded a well constrained average fabric, plunging shallowly towards 149°. For both the upper and lower contacts of SHF11, the average fabrics are poorly defined. The average fabrics for the upper and lower contacts plunge towards 086° and 052° respectively (Fig. 7.6).

7.2.6. AMS Results

For the 16 sills that were sampled, 283 AMS samples were analysed (Fig. 7.7). The majority of the contacts are shallowly plunging and are well constrained. Three contacts showed near vertical K_1 axes (SHF9U, SHF9L and SHF11U), hence the average fabrics were defined using the K_3 axes. The average angle between the resultant magnetic fabric (lineation) and the sill margin is 29° (including data from three contacts with near vertical K_1 axes).

Magnetic analyses conducted on samples from each sill (*Chapter 6*) show that the dominant magnetic phase is magnetite. Maghemitisation has occurred in half of the samples and minor pyrrhotite is present in the majority of the samples. The magnetite in the samples yielded predominantly PSD grain sizes.

7.2.6.1. Thompson's Bay and Shaka's Rock

The AMS foliation from the upper contact of TB1 dips towards 218°, with a well-defined average fabric that is oblate in shape. Four zones/contacts were analysed from TB2 (Fig. 7.7). The AMS results from the upper contact of TB2 plunge towards 168° coaxially with the results from the vesicular zone and the lower contact which plunge towards 157° and 163° respectively. A discrete layer (TB2A), characterised by fine (<1 mm) amygdales was also sampled and analysed. This layer yielded an average AMS fabric plunging towards 234°. The AMS results from TB4 plunge coaxially with the upper and lower contact averages which plunge towards 298° and 285° respectively (Fig. 7.7). The TB5 upper contact AMS data plunges towards 268°, parallel with the average fabric of the lower contact, which plunges towards 277°. The average AMS fabric from the upper contact of TB6 plunges towards 306°, and is moderately constrained. The overall AMS fabric from the upper contact of SR1 (at Shaka's Rock) plunges towards 238°. This differs from the central zone and the lower contact data which plunge coaxially towards 288° and 305° respectively (Fig. 7.7).

7.2.6.2. Sheffield Beach sills

The AMS data from the upper contact of SHF2 plunges towards 172°, coaxial with the lower contact fabric, which plunges towards 200° with an oblate fabric (Fig. 7.7). The results from the AMS analyses from the upper contact of SHF3 plunge on average towards 240°, and are better constrained that the lower contact data, which plunges towards 213°. The AMS results from SHF4 yielded well constrained average fabric directions for the upper and lower contacts, which plunge symmetrically towards 323° and 155° respectively (Fig. 7.7). The lower and upper contact AMS data from SHF5 plunge towards 163° and 187° respectively. These fabrics are

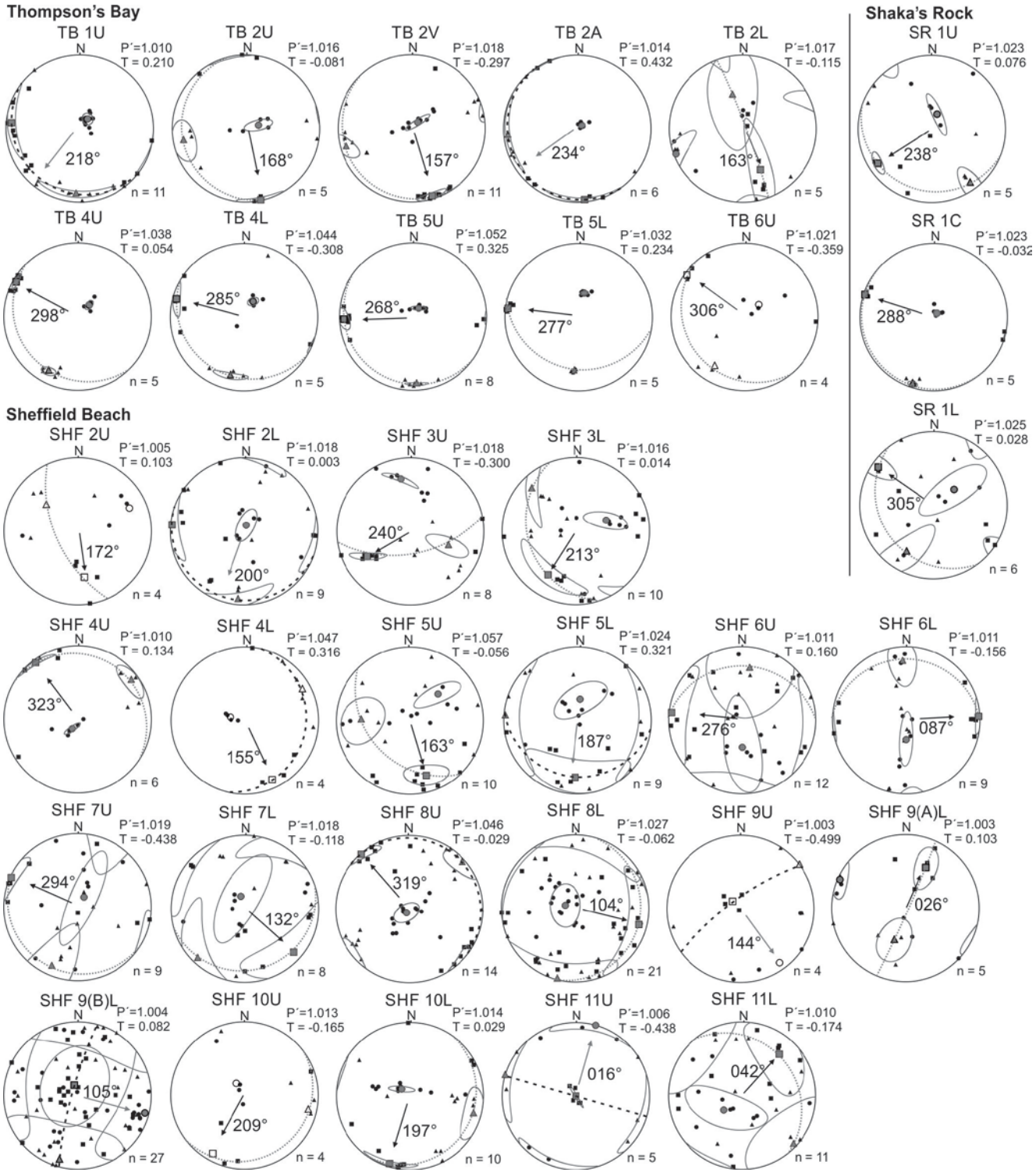

Fig. 7.7. The AMS results from the contacts of the sills sampled from Thompson's Bay and Sheffield Beach. The black squares = κ_1 axis, the black triangles = κ_2 axis and the black circles = κ_3 axis. The larger grey-filled (and unfilled) shapes are the averages of the respective κ axes. The grey ellipses are the 95% confidence ellipses determined for the average κ axes and the grey dashed lines are the planes of the foliations. Where the foliation defines the fabric for the contact, this line is a dashed black line. The arrows and degree values indicate the plunge direction of the average fabric; the black arrows are used when the overall fabric is linear, the grey arrows are used when the overall fabric is planar. n = the number of samples, P′ is the shape anisotropy and T is the shape parameter.

moderately defined and the lower contact average is defined by an oblate fabric. The AMS results from SHF6 are sub-horizontal, plunging shallowly towards 276° and 087° for the upper and lower contact respectively; the upper contact average fabric is moderately to poorly constrained (Fig. 7.7).

Table 7.3: *Magma flow direction implied by results from field observations, SPO and AMS analyses*

		Magma flow indicators			SPO flow vector(s) PD/P		AMS PD/P		Magma
Sill Name	Intrusion Strike/Dip*	Plunge Direction	Strike Direction	Magma flow indicator type	Upper	Lower	Upper	Lower	Flow Direction
TB1	172°/22°	216°/240°		ropy-flow structure	267°/44°		218°/14°		SW
TB2	167°/21°	304°		elongated vesicles	352°/46°	329°/54°	168°/01°	157°/39°	NNW/SSE
		301°		ropy-flow structure	343°/34° (v)		234°/07° (a)	163°/04° (v)	
TB4	172°/25°			N/A	220°/72°	162°/82°	298°/06°	285°/06°	WNW
TB5	160°/16°		307°	broken bridge structure	334°/26°	079°/61°	268°/07°	277°/03°	W
TB6	164°/13°	212°/205°		magma lobe			306°/04°		NW
SR1	206°/20°			N/A	050°/31°	127°/72°	238°/14°	305°/10	NW
					278°/53° (centre)		288°/02° (centre)		
SHF2	000°/20°		000°	broken bridge structure	153°/77°	139°/57°	172°/37°	200°/07°	S
SHF3	340°/17°		064°/243°	broken bridge structure	064°/56°	012°/57°	240°/33°	213°/30°	SW
SHF4	350°/12°	144°	144°	Scour marks/ intrusive step	316°/45°	202°/45°	323°/05°	155°/12°	NW
SHF5	353°/10°		359°/350°	broken bridge structure	280°/69°	089°/70°	163°/23°	187°/24°	S
SHF6	013°/13°		324°/031°	broken bridge structure	209°/37°; 279°/18°	153°/58°	276°/04°	087°/01°	W
SHF7	056°/10°	055°/060°/064°		magma lobe	289°/36°	317°/71°	294°/02°	132°/12°	NE-ENE
SHF8	088°/09°		226°/036°	bridge stub	316°/56°	310°/72°	319°/01°	104°/12°	NE
			060°	broken bridge structure					
SHF9A	065°/13°		043°/345°	broken bridge/bridge stub	281°/41°	062°/66°	144°/10°	026°/38°	NE
SHF9B	065°/13°		155°	broken bridge structure		061°/79°		105°/07°	SE
SHF10	059°/10°		220°	broken bridge structure	159°/82°	149°/22°	209°/16°	197°/04°	SW
SHF11	054°/10°		237°/145°	broken bridge structure	078°/20°	044°/46°	016°/00°	042°/26°	NE

*strike/dip of the stratigraphy adjacent to the sill. SHF5 is still inclined once restored to the horizontal with a strike and dip of 27°/007°

a amygdaloidal unit

v vesicular unit

The AMS results from SHF7 are only moderately constrained. However, the average fabrics for the upper and lower contacts, which plunge shallowly towards 294° and 132° respectively, are near symmetrical. The AMS results from the upper contact of SHF8 are well constrained with the average fabric plunging towards 319°, symmetrical with the lower contact, which plunges towards104° (Fig. 7.7). The AMS results from the upper contact of SHF9 are fairly well constrained with the average fabric plunging towards 144°, defined by the short axis of the ellipsoid. For the lower contact of SHF9A, the average fabric is fairly well-defined and plunges towards 026°. The lower contact data for SHF9B is poorly constrained, yielding a triaxial-shaped average fabric, plunging towards 105°, defined using the short axis of the ellipsoid. The AMS average fabrics from the upper and lower contacts of SHF10 are well constrained and

plunge towards 209° and 197° respectively (Fig. 7.7). The AMS data from the upper contact of SHF11 yielded an almost vertical κ_1 axis therefore the fabric was defined using the short axis of the ellipsoid. This yielded an average fabric that plunges towards 016°. The data from the lower contact are moderately constrained with the average fabric plunging towards 042° (Fig. 7.7).

7.3. Discussion

7.3.1. Magma flow indicators

The structures analysed here (and in detail in *Chapter 6*) have all been used previously to infer magma flow in sills and dykes and imply either a magma flow direction or orientation depending on the long axes of the structures (e.g. Nicholson and Pollard, 1985; Rickwood, 1990; Kattenhorn, 1994; Liss et al., 2002; Schofield et al., 2012b). All the field data collected from magma flow indicators from the sills at Thompson's Bay and Sheffield Beach show common magma flow directions implied by the features across all the intrusions. Two main groupings are apparent from the structures at Thompson's Bay and Sheffield Beach, which are predominantly oriented NE-SW or NW-SE. The sills that imply a NE-SW intrusion orientation are TB1, TB6, SHF3, SHF6, SHF7, SHF8, SHF9, SHF10 and SHF11. The NW-SE orientations were derived from the following sills; TB2, TB5, SHF4, SHF6, SHF9 and SHF11. A third grouping occurs in the results; a north-south orientation obtained from SHF2 and SHF5 in the southern Sheffield Beach area (Fig. 7.2).

7.3.2. Fabrics indicating magma flow

The regional setting of an intrusion, and the timing of the fabric formation, are factors that have an effect on the preservation potential of a magmatic fabric formed by magma flow (Paterson et al., 1998). In order to infer magma flow using a magmatic (or magnetic) fabric, the preferred orientation of the crystals should be parallel across the intrusion and imbricated shallowly in the direction of magma flow; the direction in which the crystals were sheared (Gay, 1966, 1967). In narrow magma channels, like with the sills analysed in this study, the boundaries are often sheared, and the flow laminar, thus the mineral fabric along the sill contacts has a high probability of being preserved (Martín-Hernández et al., 2004). As the sills here have most likely not been affected by post-intrusion events that would alter the primary magmatic fabrics, it follows that the fabrics that are likely preserved are related to the original internal processes of sill intrusion and magma flow related strain (Nicholas, 1992; Paterson et al., 1998).

The orientations implied by the magma flow indicators and the fabric results are represented by the average direction determined for each intrusion using the three methods in Table 7.3. For the

majority of the sills, the SPO and/or AMS data coincided with the magma flow directions/orientations implied by the magma flow indicators.

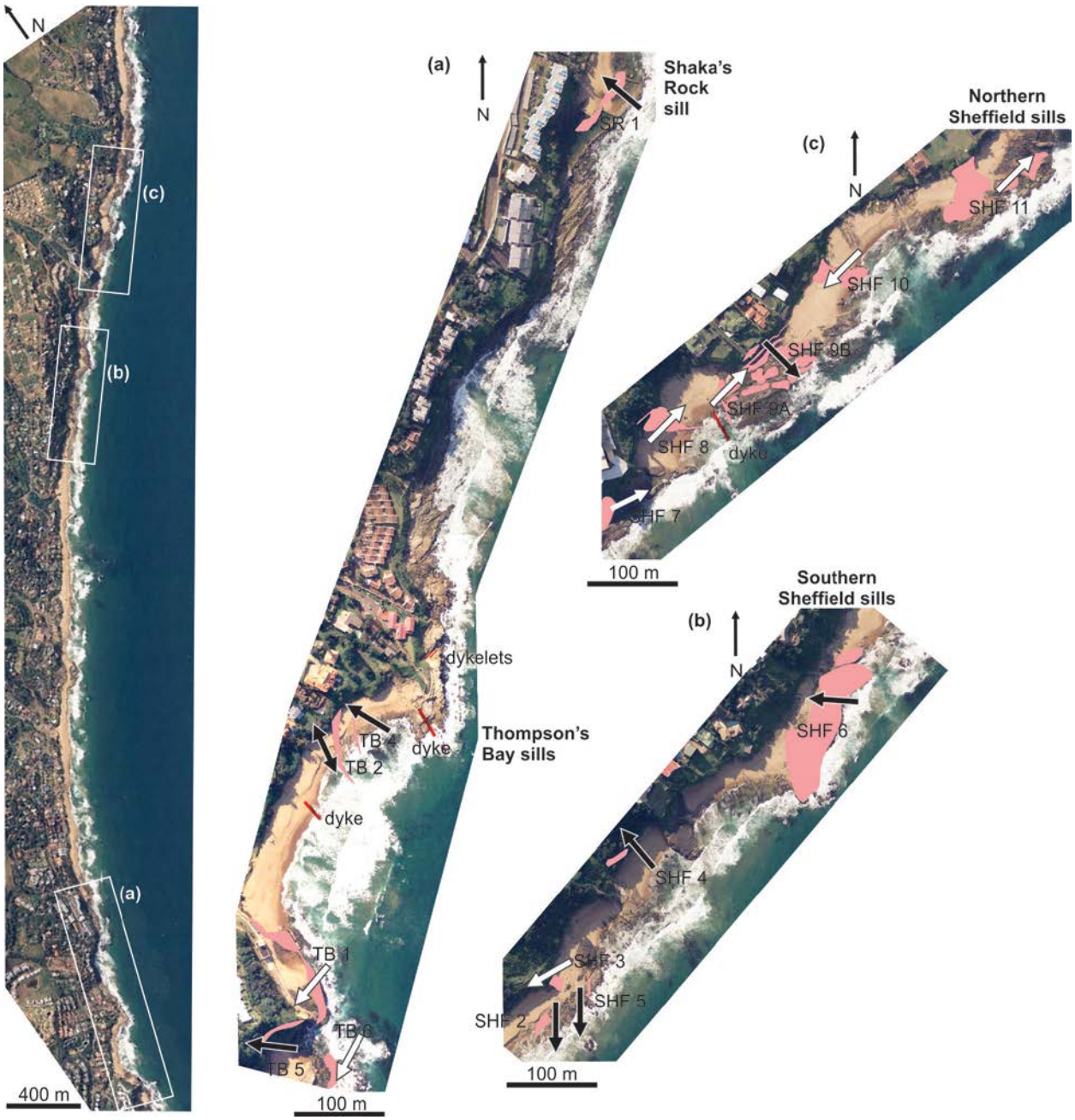

Fig. 7.8. Magma flow directions of the sills from (a) Thompson's Bay, (b) southern Sheffield Beach and (c) northern Sheffield Beach. The white arrows (with grey outlines) indicate the magma flow directions oriented NE-SW. The black arrows (with grey outlines) indicate the magma flow directions that are predominantly NW-SE. The red/pink shapes are the outline of the sills that were analysed in this study.

The SPO results from the contacts TB2V, TB5U, SHF2L, SHF6L and SHF10L are well constrained with shallowly to moderately inclined average plunge directions (Fig. 7.6). However, the majority of the results from the sill contacts are not well constrained, with a large

number of the overall fabrics being steeply inclined with respect to the sill contacts. In *Chapter 6*, it has been shown the SPO and AMS fabrics can be used to infer magma flow as the fabrics can be directly related to the preserved magmatic fabric along the contacts. Thus, if the SPO and/or AMS data are well constrained, and show parallel individual fabrics, then the imbrication direction of the fabrics can be used to imply a magma flow direction. However, from the individual SPO results (described in *Chapter 6*), it is evident that the SPO fabrics are not very consistent in terms of their direction or imbrication along the sill contacts. The fabrics are not distinctly parallel and therefore the imbrication of the fabrics is weak. Even though locally the fabrics match the magma flow direction implied by the long axes of the magma flow indicators (*Chapter 6*), it appears that the collective contact data are not representative of an overall magma flow direction, as the average fabrics are too poorly constrained.

The main magnetic component in the samples is magnetite, and minor pyrrhotite, with a PSD domain state (*Chapter 6*). The fabrics that have been measured using AMS have thus been extracted from the magnetite and/or pyrrhotite grains. These minerals are successful carriers of magmatic fabrics and can therefore be used as adequate indicators of the magma flow (Arbaret et al., 2013).

For the AMS results, not all of the average fabric vectors coincide with the SPO results. The AMS and SPO data from the contacts TB1U, SR1C, SHF2U, SHF4U, SHF6U, SHF7U and SHF11L are coaxial indicating a link between the magmatic and magnetic fabrics (Fig. 7.7). For a significant number of contacts, the SPO and AMS results plunge in opposite directions (e.g. TB2U, SR1 and SHF3) and two thirds of the sills yielded AMS results that plunge coaxially with the magma flow indicators (e.g. TB1, SHF2, SHF3) (Fig. 7.7). The fabrics obtained collectively for the sill contacts are generally shallowly plunging and parallel across the intrusions. Thus, unlike the SPO fabrics, the AMS appear to be well imbricated along the sill contacts, and are most likely the more accurate indicators of the magma flow directions, as evidenced by the higher number of coincidental orientations with the magma flow indicators. The majority of the magma flow directions within the sills are therefore defined by the upper contact AMS fabrics. However, the magma flow in the sills TB6, SHF7 and SHF8 have been defined solely on the long axes of the magma flow indicators. As shown in *Chapter 6*, these intrusions have recorded a late-stage magma flow between coalescing sill segments, resulting in the fabrics being oriented perpendicular to the magma flow indicators. The actual magma flow direction that is important in this study, is the initial propagation direction of the sills, as this is the direction that may be used to imply a mechanism of intrusion and a probable magma source.

Where there are no data from magma flow indicators, for example with TB4 and SR1, the average magma flow direction was extracted from the upper contact (for TB4) and centre (for SR1) AMS data. These results are well constrained and, as shown from the results from the other sills, most regularly correspond with the direction of magma flow implied by the magma flow indicators.

7.3.3. Magma flow directions

The magma flow directions determined for the 16 sills along the KZN North Coast can generally be grouped into two orientation categories. The first orientation category includes seven of the intrusions that yielded magma flow in either a NE or SW direction; TB1, TB6, SHF3, SHF7, SHF8, SHF9, SHF10 and SHF11 (white arrows in Fig. 7.8). Of the other nine sills analysed, the magma flow directions were varied (black arrows in Fig. 7.8); five sills yielded NW-SE oriented magma flow directions/orientations; TB2, TB4, SR1, SHF4 and possibly the upper sill segment of SHF9 (SFH9B). Also included in this second category are TB5 and SHF6 that yielded flow approximately towards the west, however the magma flow indicators implied initial intrusion directions oriented ~NW-SE. SHF2 and SHF5 do not seem to fit in with the above directions as these sills show magma flow towards the south, but have been included in the second category, represented by black arrows in Fig. 7.8.

As described in *Chapter 2* (*Section 2.2*), the most common formation process of a sill is through the deflection of a dyke along a discontinuity, where the dyke becomes the magma conduit that feeds magma to the sills. When the magma flow in a dyke is vertical, the orientation of the magma flow within the sill is expected to be perpendicular to the orientation of the feeder dyke, thus flowing perpendicular to the orientation of the dyke (Fig. 7.9a) (Ferré et al., 2002). If the sills were fed by a pipe feeder system, the sills would be radially fed and the flow directions may not be predictable (Fig. 7.9b).

The few dykes observed in the study area are typically sub-vertical and strike NW-SE (Fig. 7.3 and 7.4). Once restored according to the surrounding tilted stratigraphy, the dykes in the Thompson's Bay area all yielded original dips of greater than 80°. The 8m-wide NW-SE oriented dyke, intruded adjacent to SHF9, exhibited a broken bridge structure (Fig. 7.4d). This structure has been shown to be an adequate predictor of magma flow (*Chapter 6*) and therefore indicates vertical flow within this dyke (Nicholson and Pollard 1985; Kattenhorn and Watkeys 1995).

If the NW-SE oriented dykes are related to the sills that yielded NE and SW magma flow directions (i.e. SHF8 and SHF10), then perhaps there is a difference between these sills and the sills that yielded perpendicular magma flow directions (black arrows in Fig. 7.8). This second set of sills do not appear to be associated with any feeder dykes, as the desired dyking orientation is only represented by two thin, laterally discontinuous dykelets less than 2 m in length. These different category sills could have thus formed by different mechanisms.

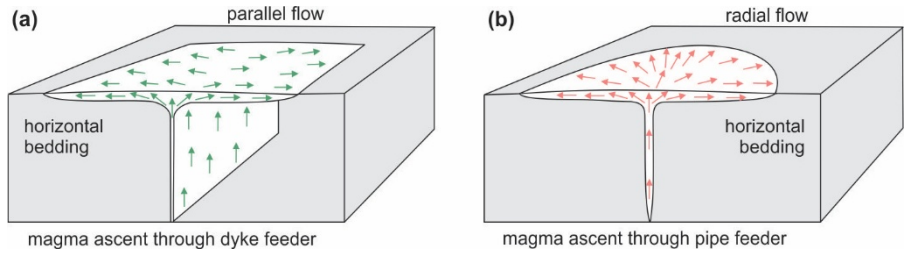

Fig. 7.9. Illustration showing (a) parallel flow originated from vertical flow in a dyke where the magma flow in the sill is perpendicular to the trend of the dyke and (b) radial magma flow produced from a pipe feeder. After Ferré et al. (2002).

7.3.4. Geochemistry of the sills

The geochemistry of the basalts in the KIP is generally more evolved than typical basalts, with SiO_2 wt% of more than 52%, and should actually be termed basaltic andesites (Duncan and Marsh, 2006). Previous analyses undertaken on sills along the KZN North Coast yielded evolved compositions; with the sills ranging from andesites to dacites (Frankel, 1969). The samples analysed here have lower SiO_2 wt% than expected for the sills along the coastline, ranging from ~49% to ~51.5% SiO_2 wt%. The Zr component is less than 150 ppm and the TiO_2 wt% is less than 1.5%. When the MgO wt% increases the Fe_2O_3, TiO_2 and Y components decrease. These trends are typical of tholeiites (Riley et al., 2006). When these data are plotted on an AFM diagram, the sills are defined as tholeiitic basalts. Thus the sills analysed in this study are low-Ti-Zr tholeiitic basalts, the same composition as the bulk of the magmatism associated with the southern extent of the KIP (Duncan and Marsh, 2006) and consistent with the typical Karoo low-Ti magma type as defined by Cox et al. (1967) and Sweeney et al. (1994). The composition may be close to andesitic (>52% SiO_2) for one of the samples; however the samples do not have high felsic components and thus are distinctly different in composition to the samples analysed by Frankel (1969). As the features present in the majority of the sills are however similar to the sills sampled by Frankel (1969), the geochemical differences may be a factor of sampling sizes and localities; this study excluded the geochemical analysis of any

inclusions that were amygdaloidal or xenolithic in nature. The loss on ignition is up to ~7% for one of the geochemistry samples, indicating a significant volatile component in the system, either from an initially wet melt or from fluids in the adjacent country rocks.

In comparison to the UDS sampled by Riley et al. (2006), the SiO_2 wt% are similar, where the Al_2O_3, Fe_2O_3 and MgO components of the Sheffield sill are higher than the UDS and the CaO and Na_2O components are lower. There is also a significantly higher loss on ignition from the Sheffield sill indicating a volatile-rich melt. As discussed in *Chapter 5*, there was a significant volatile component present in the rocks that enabled them to be fractured to the degree of the Sheffield Beach breccia (e.g. Svensen et al., 2006). This indicates that the intrusions occurred at relatively shallow depths, as the large volume change required to trigger fragmentation will only occur at pressures below the critical point of water (~221 bars), which is exceeded below depths of ~700 m (Duncan and Marsh, 2006).

Most of the sills in the area have been affected by the presence of fluids in the system. Fluid interactions with country rock resulting from the intrusion have produced rheomorphic sedimentary dykes, a confined breccia and abundant vesicles and amygdales. The sills that exhibit these features have previously been classed as Effingham-type dolerites (Frankel, 1969). The fluids may have been part of the melt, as the magma entrained numerous basement and country rock xenoliths, however it is likely that the sills intruded into volatile-rich country rocks, or that volatiles were produced upon intrusion of the sills through devolitisation of the shales (e.g. Aarnes et al., 2011). The xenolithic components of the sills in this study may not have led to significant crustal contamination in the geochemical samples, but may indicate that the source is a typical Karoo magma with a higher volatile composition or a magma atypical of a Karoo signature.

7.3.5. Intrusive mechanisms

The first category sills all yielded well-defined NE-SW magma flow and could have been fed by the NW-SE dykes by parallel flow from the feeder (Fig. 7.9a). Parallel magma flow would be the intrusive mechanism, with magma injected with consistent parallel flow directions in these seven sills (white arrows in Fig. 7.8). The strike of the NW-SE dykes indicates that the minimum stress direction in the crust was perpendicular to the strike at the time of formation. It is highly likely that the sills TB1 and TB6 are segments of the same intrusion, this is also possible for the intrusions SHF7, SHF9, SHF10 and SHF11 based on very similar textures and

magma flow directions. These sills may have formed at different levels or may have become faulted into repetitive sequences.

The ~320 - 330° strike of the NW-SE dykes is the same as the UDS dykes, that have an approximate Ar^{40}/Ar^{39} age of ~176 Ma (Riley et al., 2006). The dykes of the UDS occur in Lesotho, intrusive into the Drakensberg basalts, and extend towards the coast (Riley et al., 2006). Magma flow within these dykes was shown to be lateral within the sills from the SW to the NE. This magma flow direction, and the similarity of the dolerite compositions led Riley et al. (2006) to conclude that the UDS may be a Ferrar magmatic product that has overlapped with Karoo magmatism. The orientation of the UDS and the lateral magma flow direction in the NW extent of the dykes that may be a product of localised lateral flow at high stratigraphic levels, could be the same event that formed the sills in the study area. Magma flow in the dykes along the KZN coastline was vertical, the dykes of the same orientation may have been fed by lateral flow in the distal regions. This trend occurs in other dykes distal to the magma source including the dykes of the ODS (Aubourg et al., 2008) and the NLDS (Hastie et al., 2011). This would indicate that the sills along the coastline are proximal to the magma source.

Vertically intruding dykes exhibiting vertical flow would suggest that the magmas originated from a broad rather than narrow melt zone (e.g. Ernst and Baragar, 1992), implying that the magmas could have been transported from a large area below which melt was produced. This may be linked to the thinning of the lithosphere related to the initial break up of Gondwana, and the rifting of the Lebombo “monocline” (Cox, 1992; Klausen, 2009).

The magma flow directions/orientations within the second category sills (with varied but predominantly NW-SE magma flow directions), cannot be linked to a significant dyking event. Therefore they are unlikely to have been fed by locally significant dykes through parallel flow, as with the first category sills. Instead, these intrusions could be part of a sill-fed system where the main magma transport occurs through the linking of sills through thin dykes (not observed), intrusive steps (e.g. SHF4) and inclined sheets (i.e. SHF5), termed a “crack-lid” model by Muirhead et al. (2014). In this model, sills are the primary magma conduits, transporting magma laterally and into overlying intrusions. Dykes are uncommon in this model and where they do occur, intrude in no particular orientation. This would create a different dyke pattern to the parallel NW-SE oriented dykes and would thus not indicate a minimum compressive stress orientation. In these systems, magma may have been transported from a more distal source as the formation process of these high-level systems (<4 km depth) allow for long transport

distances within the sills (e.g. Cartwright and Hansen, 2006; Muirhead et al., 2014). Interconnected sill complexes such as these are able to transport magma great horizontal and vertical distances, and can ultimately erupt as lava flows (Cartwright and Hansen, 2006; Muirhead et al., 2012).

7.3.6. Implications for the magma source

The formation of the KIP as a whole has generally been ascribed to the impact of a mantle plume at the base of the lithosphere (e.g. Burke and Dewey, 1973; White and McKenzie, 1989; Campbell and Griffiths, 1990; Cox, 1992; Ernst and Buchan, 1997; Storey and Kyle, 1997). The location of such a plume has been widely conjectured, with the most common position beneath or just east of the Nuanetsi Igneous Province, which had previously been recognised as a triple junction (Burke and Dewey, 1973). For a plume to be responsible for the formation of the magmatism of the KIP, igneous activity would have begun above the plume head site, and then spread outwards before narrowing and concentrating above the impact site (White and McKenzie, 1989; Campbell and Griffiths, 1990; Cox, 1992; Ernst and Buchan, 1997; Storey and Kyle, 1997). The shape of the Karoo triple junction tectonic pattern was originally considered to be the result of the strain imposed on the lithosphere by the plume. However geological and geochronological data have recently shown that the triple junction pattern is an artefact of Archaean lithospheric architecture providing a crustal weakness for melts to utilise as magma pathways (Sweeney and Watkeys, 1990; Watkeys, 2002; Jourdan et al., 2006, 2009). Geochronology also indicates that igneous activity did not spread out from the proposed plume site as there are significant age differences between the lavas and the dyke swarms geographically across the KIP (Jourdan et al., 2005, 2007, 2008; Hastie et al., 2014).

Elliot and Fleming (2000) showed an overlap of magmatism of the Ferrar and Karoo provinces, evidenced by the geochemical similarities between the Golden Gate basalts in northern Lesotho and the Ferrar low-Ti magmas of Antarctica. More evidence was presented by Riley et al. (2006), showing that the UDS in KwaZulu-Natal and Lesotho were formed from magmas with Ferrar signatures with a possible magma source to the SE. This magma source corroborates with Elliot and Fleming's (2000) inference that the Ferrar magmatism formed by the impact of a mantle plume beneath Gondwana at the Weddell Sea triple junction and overlaps with the KIP rocks. The magmatism became separated in localised zones of magmatism, one at the Karoo triple junction, producing the high-Ti basalts of the KIP, and a second magmatic centre at the Weddell Sea triple junction that formed the Ferrar dolerites in Antarctica. Karoo and Ferrar magmatic overlap is also evident in the dolerite dykes that occur in the Falkland Islands

(Mitchell et al., 1999). Upon reconstruction of Gondwana, it appears that a centralised magma source in the Weddell Sea could have easily produced melts that formed intrusions in the Falkland Islands, Antarctica and South Africa (Fig. 7.10). However, the anomalously hot material in the mantle that produced the melts may not necessarily be ascribed to a mantle plume source, as described by Elliot and Fleming (2000).

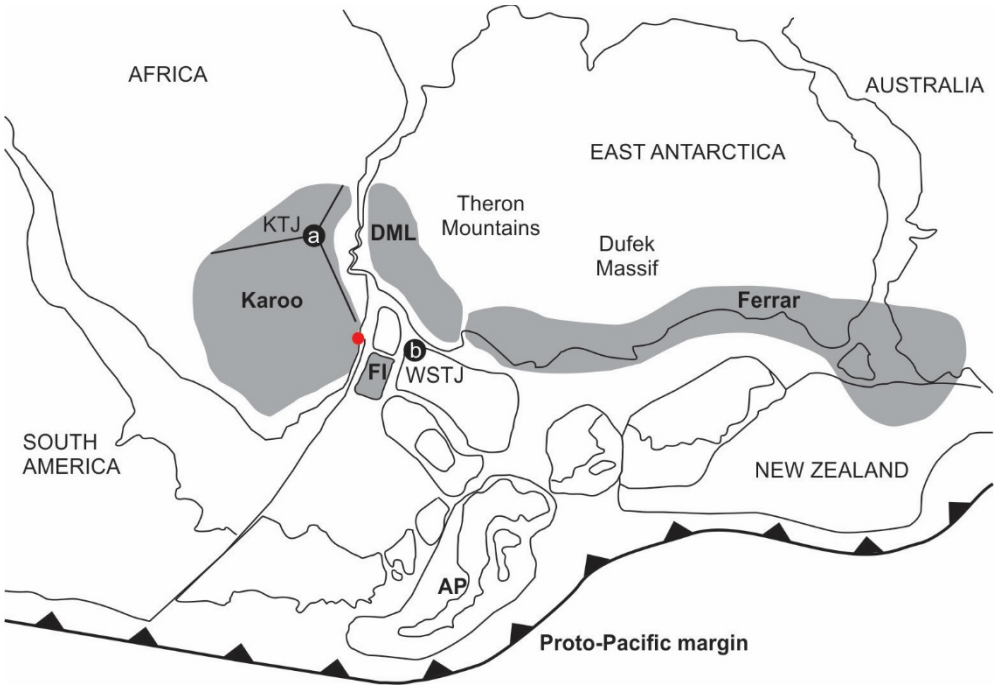

Fig. 7.10. Illustration showing the assembly of the continents prior to Gondwana breakup. The red circle shows the approximate location of the study area. (a) The Karoo Triple Junction (KTJ) at Mwenezi, the position of impact of a mantle plume as proposed Burke and Dewey (1973). (b) Elliot and Fleming (2000) proposed that the Weddell Sea Triple Junction (WSTJ) may have been one of the centres of magmatism, as well as at the KTJ. The result of a mantle plume impacting the lithosphere beneath Gondwana. After Riley et al. (2006) and Hastie (2012).

Rather than rely upon the impact of a plume at the base of the lithosphere to trigger a large scale magmatic event, mantle melting could have been triggered by global warming of the mantle underneath the supercontinent of Gondwana (Coltice et al., 2009). This model of melt production was first proposed by Anderson (1994) after thermal anomalies were observed in the mantle underneath supercontinents (Anderson, 1982). These supercontinents are insulated from processes that could cool the mantle, such as subduction (Anderson, 1982). This model shows that large amounts of magmatism can result from the tectonic plate reorganisation without the need to introduce a mantle plume (Anderson, 1994). These magmas are produced in the mantle beneath supercontinents and transported upwards through weakened portions of the lithosphere, such as extensional zones occurring principally in relation to the initial stages of continental

extension or breakup (Anderson, 1994). Using the theory behind this model, Hawkesworth et al. (1999) suggested that the Karoo magmatic event could be as a result of mantle insulation beneath Gondwana. The melts then took advantage of crustal weaknesses hence, a large portion of magmatism became focused in the Limpopo Belt and along the boundaries of the Kaapvaal Craton (Hawkesworth et al., 1999). Coltice et al. (2007) modelled the process of supercontinent incubation and showed that mantle material beneath aggregated continents could increase in temperature by up to 100°C, an increase sufficient to trigger partial melting in the subcontinental lithospheric mantle (Anderson, 1982) particularly if aided by the presence of volatiles (Gallagher and Hawkesworth, 1992). This "global mantle warming" model explains the slower rate of eruption and the large expanse of the magmatism, when compared to a typical mantle plume model where magmatism is radially occurring and spatially limited. Coltice et al. (2009), and later Hastie et al. (2014), interpreted the formation of the KIP as a result of global mantle warming, corroborating the proposal set forth by Hawkesworth et al. (1999), and therefore showing that the Karoo triple junction should no longer be used as evidence for a mantle plume at Mwenezi.

From the sills studied here, it is apparent that there was a lack of involvement of magmatism originating from the supposed Karoo triple junction. If the dykes and sills belonging to the dyke-fed system were formed from magma that originated from a mantle plume beneath the Karoo triple junction, the dykes should be oriented north-south, parallel to the Lebombo monocline and the flow direction of regional dyke swarms and sills east-west. This is clearly not the case, and it can be shown that the sills in the study area were not related to magmatism centred at Mwenezi.

The sills analysed here are categorised into a dyke-fed system and a sill-fed system that have NE-SW and NW-SE intrusion orientations respectively. The dyke-fed sills are more likely to be linked to the UDS, which have intruded laterally from a magma source towards the SE (Riley et al., 2006). The dykes and sills in the study area were most likely produced from a relatively proximal source, interpreted from the vertical flow in the dykes. If they form part of the UDS event, they may have originated from melts produced from the mantle beneath a region southeast of the present KZN coastline, possibly in the region of the Wedddell Sea prior to Gondwana breakup. This would agree with the theory that the Weddell Sea Triple Junction was one of the main foci of magmatism that produced magmas across southern Africa, the Falkland Islands and Antarctica (Elliot and Fleming, 2000).

The sill-fed sills, with NW-SE intrusion directions, may have formed from a separate magmatic episode. The different magma intrusion directions of the two categories of the sills cannot be differentiated by their geochemistry or inclusions, such that sills from both categories exhibit associated volatiles and xenoliths. The contaminated Ferrar magmas are typically more siliceous than the Karoo magmas (Riley et al., 2006). Therefore it is possible that the sills in this study are a remnant of overlap of Ferrar magmas in South Africa, along with the Golden Gate lavas (Elliot and Fleming, 2000) and the UDS (Riley et al., 2006). The nature of these sills would appear to be of a high-level system that formed from the same magma chamber as the magmas that formed the first category sills. However, these sills were intruded in a different manner and therefore perhaps intruded at a different time through magmatism at small igneous centres such as with the RRDS (Hastie et al., 2014). Thinning of the continental lithosphere, along what is now the coastline, may have promoted melt migration, post-dating the main Karoo volcanic event. This thinning could be attributed to early stages of Gondwana break-up (Cox, 1992) and may be contemporaneous with the bulk of magmatism that formed the Ferrar dolerites, which could be slightly younger than the Karoo basalts, or at least the same age at 182.8 Ma (Burgess et al., 2015).

It is proposed that the sills here are the product of magmatism that originated from a Weddell Sea location, and that the melts that formed these intrusions originated from a global mantle melting event beneath the supercontinent Gondwana. The variations in the melts that are produced across Gondwana could be attributed to variations in the mantle composition due to the proximity of the Ferrar source to subducting material. It could also be possible that the composition of the mantle beneath the supercontinent may have relict architectures, such as Archaean and post-Archaean lithospheric mantle types. This difference in composition could allow fractionation of slightly different magmas due to the expanse of the melt producing zones. There is no need to have only one direct magma chamber source in the mantle for the magmatism of the KIP, it would seem necessary to have more than one source of material to produce the multitude of magmas in the diverse localities across Gondwana. With the results from this study it would appear that there may be more overlap of the Karoo and Ferrar magmatism than is currently recognised.

References

Aarnes, I., Svensen, H., Polteau, S., Planke, S., 2011. Contact metamorphism devolitization of shales in the Karoo Basin, South Africa, and the effects of multiple sill intrusions. Chemical Geology, 281, 181-194.

Anderson, D.L., 1982. Hotspots, polar wander, Mesozoic convection, and the geoid. Nature, 297, 391-393.

Anderson, D.L., 1994. Superplumes or supercontinents? Geology, 22, 39-42.

Arbaret, L., Launeau, P., Diot, H., Sizaret, S., 2013. Magnetic and shape fabrics of magnetite in simple shear flows. Journal of Volcanology and Geothermal Research, 249, 25-38.

Aubourg, C., Tshoso, G., Le Gall, B., Bertrand, H., Tiercelin, J.-J., Kampunzu, A.B., Dyment, J., Modisi, M., 2008. Magma flow revealed by magnetic fabric in the Okavango giant dyke swarm, Karoo igneous province, northern Botswana. Journal of Volcanology and Geothermal Research, 170, 247-261.

Burgess, S.D., Bowring, S.A., Fleming, T.H., Elliot, D.H., 2015. High-precision geochronology links the Ferrar large igneous province with early-Jurassic ocean anoxia and biotic crisis. Earth and Planetary Science Letters, 415, 90-99.

Burke, K., Dewey, J.F. 1973. Plume-generated triple junctions: key indicators in applying plate tectonics to old rocks. Journal of Geology, 81, 406-433.

Campbell, I.H., Griffiths, R.W. 1990. Implications of mantle plume structure for the evolution of flood basalts. Earth and Planetary Science Letters, 99, 79-93.

Cartwright, J., Hansen, D.M., 2006. Magma transport through the crust via interconnected sill complexes. Geology, 19, 929-932.

Coltice, N., Phillips, B.R., Bertrand, H., Ricard, Y., Rey, P., 2007. Global warming of the mantle at the origin of flood basalts over supercontinents. Geology, 35, 391-394.

Coltice, N., Bertrand, H., Rey, P., Jourdan, F., Phillips. B.R. and Ricard, Y. 2009. Global warming of the mantle beneath continents back to the Archaean. Gondwana Research, 15, 254-266.

Cox, K.G. 1992. Karoo igneous activity, and the early stages of the break-up of Gondwanaland. In: Storey, B.C., Alabaster, T., and Pankhurst, R.J., (Eds.), Magmatism and the Causes of Continental Break-up. Geological Society of London Special Publication, 68, 37-148.

Cox, K.G., MacDonald, R., Hornung, G., 1967. Geochemical and petrographic provinces in the Karroo basalts of southern Africa. American Mineralogist, 52, 1451-1474.

Duncan, A.R., Marsh, J.S., 2006. The Karoo Igneous Province. In: Johnson, M.R., Anhaeusser, C.R., Thomas, R.J., (Eds.) The Geology of South Africa. Geological Society of South Africa, 501-520.

Elliot, D.H., Fleming, T.H., 2000. Weddell triple junction: The principal focus of Ferrar and Karoo magmatism during initial

Erlank, A.J., 1984. Petrogenesis of the volcanic rocks of the Karoo province. Geological Society of South Africa Special Publication, 13, 395 pp.

Ernst, R.E., Baragar, W.R.A., 1992. Evidence from magnetic fabric for the flow pattern of magma in the Mackenzie giant radiating dyke swarm. Nature, 356, 511-513.

Ernst, R.E., Buchan, K.L., 1997. Giant Radiating Swarms: Their Use in Identifying Pre-Mesozoic Large Igneous Provinces and Mantle Plumes. Geophysical Monographs, 100, 297-333.

Ferré, E.C., Bordarier, C., Marsh, J.S., 2002. Magma flow inferred from AMS fabrics in a layered mafic sill, Insizwa, South Africa. Tectonophysics, 354, 1-23.

Ferré, E., Geissman, J., Maes, S., Gillim, A., Marsh, J., 2015. Magma dynamics above the Karoo Plume, South Africa. Geophysical Research Abstracts, 17, EGU General Assembly, EGU2015-7077.

Frankel, J.J. 1969. The distribution and origin of the Effingham rock type, a dolerite derivative of intermediate composition, in Natal and Zululand, South Africa. Geological Society of America Memoir, 115, 149-173.

Gallagher, K., Hawkesworth, K., 1992. Dehydration melting and the generation of continental flood basalts. Nature, 358, 57-59.

Gay, N.C. 1966. Orientation of mineral lineation along the flow direction in rocks: A discussion. Tectonophysics, 3, 559-564.

Gay, N.C. 1967. Pure shear and simple shear deformation of inhomogeneous viscous fluids. 1. Theory. Tectonophysics, 5, 211-234.

Hastie, WW., 2012. Rock Farbic Study of the Northern Lebombo and Rooi Rand Dyke Swarms – Regional and Local Implications. Unpublished PhD thesis, University of KwaZulu-Natal, 370 pp.

Hastie, W.W., Aubourg, C., Watkeys, M.K., 2011. Significance of magnetic and petrofabric in Karoo-feeder dykes, northern Lebombo. Tectonophysics, 513, 96-111.

Hastie, W.W., Watkeys, M.K., Aubourg, C., 2014. Magma flow in dyke swarms of the Karoo LIP: Implications for the mantle plume hypothesis. Gondwana Research, 25, 736-755.

Hawkesworth, C.J., Kelley, S., Turner, S., Le Roex, A., Storey B.C., 1999. Mantle processes during Gondwana break-up and dispersal. Journal of African Earth Sciences, 28, 239-261.

Horsman, E., Tikoff, B., Morgan S., 2005. Emplacement-related fabric and multiple sheets in the Maiden Creek sill, Henry Mountains, Utah, USA. Journal of Structural Geology, 27, 1426-1444.

Jourdan, F., Féraud, G., Bertrand, H., Kampunzu, A.B., Tshoso, G., Watkeys, M.K., Le Gall., B., 2005. Karoo large igneous province: Brevity, origin and relation to mass extinction question by new $^{40}Ar/^{39}Ar$ age data. Geology, 33, 745-748.

Jourdan, F., Féraud, G., Bertrand, H., Watkeys, M.K., Kampunzu, A.B., Le Gall, B. 2006. Basement control on dyke distribution in Large Igneous Provinces: Case study of the Karoo triple junction. Earth and Planetary Science Letters, 241, 307-322.

Jourdan, F., Féraud, G., Bertrand, H., Watkeys, M.K., Renne, P.R. 2007. Distinct brief major events in the Karoo large igneous province clarified by new $^{40}Ar/^{39}Ar$ ages on the Lesotho basalts. Lithos, 98, 195-209.

Jourdan, F., Féraud, G., Bertrand, H., Watkeys, M.K., Renne, P.R., 2008. $^{40}Ar/^{39}Ar$ ages of the sill complex of the Karoo large igneous province: implications for the Pliensbachian-Toarcian climate change. Geochem. Geophys. Geosys. 9, Q06009, doi:10.1029/2008GC001994.

Jourdan, F., Bertrand, H., Féraud, G., Le Gall, B., Watkeys, M.K. 2009. Lithospheric mantle evolution monitored by overlapping large igneous provinces: Case study in southern Africa. Lithos, 107, 257-268.

Kattenhorn, S.A. 1994. Mechanisms of sill and dyke intrusion. MSc thesis, University of Natal (Durban), South Africa.

Kattenhorn, S.A., Watkeys, M.K., 1995. Blunt-ended dyke segments. Journal of Structural Geology, 17, 1535-1542.

Klausen, M.B. 2009. The Lebombo monocline and associated feeder dyke swarm: diagnostic of a successful and highly volcanic rifted margin? Tectonophysics, 468, 42-62.

Liss, D., Hutton, D.H.W., Owens, W.H., 2002. Ropy flow structures: A neglected indicator of magma-flow direction in sills and dikes. Geology, 30, 715-718.

Martín-Hernández, F., Luneberg, C.M., Aubourg, C., Jackson, M., 2004. Magnetic fabric: methods and applications – an introduction. In: Martín-Hernández, F., Luneberg, C.M., Aubourg, C., Jackson, M. (Eds.) Magnetic Fabric: Methods and Applications. Geological Society, London, Spec. Publ., 238, pp. 1-7.

Mitchell, C., Ellam, R.M., Cox, K.G., 1999. Mesozoic dolerite dikes of the Falkland Islands: Petrology, petrogenesis and implications for geochemical provinciality in Gondwanaland low-Ti basaltic rocks. Journal of the Geological Society of London, 156, 901-916.

Muirhead, J.D., Airlodi, G., Rowland, J.V., White, J.D.L., 2012. Interconnected sills and inclined sheet intrusions control shallow magma transport in the Ferrar large igneous province, Antarctica. Geological Society of America Bulletin, 124, 162-180.

Muirhead, J.D., Airlodi, G., White, J.D.L., Rowland, J.V., 2014. Cracking the lid: Sill-fed dikes are the likely feeders of flood basalt eruptions. Earth and Planetary Science Letters, 406, 187-197.

Nicholas, A., 1992. Kinematics in magmatic rocks with special reference to gabbros. Journal of Petrology, 33, 891-915.

Nicholson, R., Pollard, D.D., 1985. Dilation and linkage of echelon cracks. Journal of Structural Geology, 7, 583-590.

Paterson, S.R., Fowler, T.K. Jr., Schmidt, K.L., Yoshinobu, A.S., Yuan, E.S., Miller, R.B., 1998. Interpreting magmatic fabric patterns in plutons. Lithos, 44, 53-82.

Pollard, D.D., 1987. Elementary fracture mechanics applied to the structural interpretation of dykes. In: Halls, H.C. and Fahrig, W.F. (Eds.) Mafic Dyke Swarms. Geological Association of Canada Special Paper, 34, 5-24.

Pollard, D.D., Muller, O.H., Dockstader, D.R., 1975. The form and growth of fingered sheet intrusions. Geological Society of America Bulletin, 86, 351-363.

Rickwood, P.C., 1990. The anatomy of a dyke and the determination of propagation and magma-flow directions. In: Parker, A.J., Rickwood, P.C. and Tucker, D.H. (Eds.) Mafic dykes and Emplacement Mechanisms. Proceedings of the Second international dyke conference, Adelaide, South Australia, 2, 81-100.

Riley, T.R., Curtis, M.L., Leat, P.T., Watkeys, M.K., Duncan, R.A., Millar, I.L., Owens, W.H. 2006. Overlap of Karoo and Ferrar Magma Types in KwaZulu-Natal, South Africa. Journal of Petrology, 47, 541-566.

Schofield, N., Heaton, L., Holford, S.P., Archer, S.G., Jackson, C.A.-L., Jolley, D.W., 2012a. Seismic imaging of 'broken bridges': linking seismic to outcrop-scale investigations of intrusive magma lobes. Journal of the Geological Society of London, 169, 421-426.

Schofield, N., Brown, D.J., Magee, C., Stevenson, C.T., 2012b. Sill morphology and comparison of brittle and non-brittle emplacement mechanisms. Journal of the Geological Society of London, 169, 127-141.

Storey, B.C., Kyle, P.R., 1997. An active mantle mechanism for Gondwana break-up. South African Journal of Geology, 10, 283-290.

Svensen, H., Jamtveit, B., Planke, S., Chevallier, L., 2006. Structure and evolution of hydrothermal vent complexes in the Karoo Basin, South Africa. Journal of the Geological Society of London, 163, 671-682.

Sweeney, R.J., Watkeys, M.K., 1990. A possible link between Mesozoic lithosphere architecture and Gondwana flood basalts. Journal of African Earth Sciences, 10, 707-716.

Sweeney, R.J., Duncan, A.R., Erlank, A.J., 1994. Geochemistry and petrogenesis of central Lebombo basalts from the Karoo Igneous Province. Journal of Petrology, 35, 95-125.

Watkeys, M.K. 2002. Development of the Lebombo rifted volcanic margin of southeast Africa. In: Menzies, M.A., Klemperer, S.L., Ebinger, C.J. & Baker, J. (Eds), Volcanic Rifted Margins. Geological Society of America Special Paper, 362, 27-46.

White, R.S., McKenzie, D., 1989. Magmatism at rift zones: The generation of volcanic continental margins and flood basalts. Journal of Geophysical Research, 94, 7685-7729.

- CHAPTER 8 –

CONCLUSIONS

The main aim of this thesis was to determine the magma flow directions in 16 sills along the KZN North Coast of South Africa. This was undertaken through field work and fabric analyses. These processes entailed making observations of magma flow indicators, mapping of the sills, sampling on the sill contacts and undertaking petrographic and magnetic analyses on the samples. The conclusions stated in this chapter are separated into conclusions pertaining to the chapters of this thesis. The conclusions resulting from the discussion in *Chapter 6* and *7* comprise the final conclusions for the thesis based on the principal aims.

Chapter 4

When conducting Shape-preferred Orientation (SPO) analyses on the sill samples, the variation in the grain sizes of the samples requires the technical parameters to be set in order to obtain systematically accurate fabrics. As dolerite sills vary in grain size and texture, it is important to incorporate the variance in plagioclase grain size into the petrographic analyses. This increases the reliability of the results and allows for more accurate petrofabrics to be determined. For the sills studied here the plagioclase crystal long axis length was used to define a threshold grain size of 0.2 mm. When this maximum grain size was exceeded, this required that photomicrographs should be obtained at a lower magnification (i.e. 2.5x) and not at a higher magnification (i.e. 10x).

When the images analysed were segmented, here into 9 segments, the resultant ellipsoids yielded larger incompatibility indices ($\sqrt{F}$ values) between ellipses than when the images were not segmented. As the final fabric orientations did not significantly differ when the images were not segmented, it was concluded that the images analysed should not be segmented during the SPO process. Through the use of a shape parameter, the petrofabrics were further constrained, as the long axis of the ellipsoid (the lineation) showed that it provides an accurate fabric when the fabrics were strongly prolate.

Chapter 5

The mechanism of emplacement of the dolerite sills appears to be strongly associated with the presence of volatiles in the adjacent country rocks, and possibly also associated with the magma. One prime example of a volatile-rich system is the SHF9 sill where a sub-volcanic coherent dolerite matrix breccia occurs between two dolerite sill segments intruding as separating magma lobes. The breccia comprises fragmented shales and sandstones in a quenched dolerite matrix. The matrix component increases distally whilst the clast sizes and angularity decrease distally relative to the thickness of the breccia. It was concluded that a high volatile component was present in the country rocks when the dolerite intruded. Coupled with a narrow confined space (~1 m thick), the pressure increase from the rapidly vapourised fluids led to severe fragmentation of the country rock wedge which, propagated laterally from the separation of the sill segments. As the distance increased distally, and a larger volume of country rock was confined between the two sill segments, the heat and pressure decreased. This decrease halted the fragmentation driving force, which caused the fragmentation to decrease distally.

The evidence of how the breccia formed, from the field observations, indicates that (1) there was enough heat associated with the intrusion that the pore fluids of the country rocks were vapourised; (2) the pore fluid pressure in the country rock wedge, that was sandwiched between the lower and upper dolerite, increased rapidly proximal to the point of separation of the magma lobes; (3) the increased pressure on the country rock wedge caused severe fragmentation of the country rocks; (4) there was very little mixing of the fragmented country rock and the coherent in the upper and lower dolerites signifying that the vapourised pore fluids did not act in an explosive manner. The trigger for the fragmentation of the country rock wedge was the separation of the magma lobes into two sub-vertically adjacent sill segments, and the subsequent spike in pore fluid pressure that the intrusions created. The brecciation of the country rock likely occurred at high crustal levels, signifying that the formation of the sills in this part of the KIP was in an upper crustal environment.

Chapter 6

The magma flow indicators studied in the sills have provided vital information on the intrusion directions as well as the relationships between the structural features and the preserved fabrics. Magma flow indicators come in many shapes and forms and have been previously assumed as inferring magma flow in small tabular intrusions. The data from the AMS and SPO analyses were not always consistently coaxial with the magma flow indicators, this may be a result of

different shape anisotropies of the different minerals analysed; SPO analyses strongly anisotropic elongate plagioclase crystals whilst AMS analyses weakly anisotropic fine grained granular magnetite crystals. However, the upper contact SPO and AMS data were parallel with the long axes of the magma flow indicators more regularly than the fabric data obtained from the lower contacts of the sills. Since the fabrics across the upper and lower contacts were commonly asymmetrical, the fabric results from the upper contact were concluded as being more representative of the sense of magma flow. This was particularly true of the AMS fabrics, which were more commonly parallel with the trend of the magma flow indicators. Therefore the magnetic fabric of the magnetite grains appears to be the more reliable result to use when inferring magma flow directions within the sills studied here, as compared to the magmatic fabrics obtained from the plagioclase grains. These AMS fabrics should thus be preferentially used to infer the direction of magma flow.

A hierarchy of structures that can be used to predict a sense of magma flow was proposed, from least to most effective. This included magma lobes, ropy-flow structures and elongated vesicles, bridge structures and intrusive steps. Magma lobes that were preserved along the upper contact of the sills where the lobes had coalesced with the main magma body were concluded as being poor indicators of the final stages of magma flow. However, it would appear that once the magma lobes had coalesced with the main body of the intrusion, the magma flow determined by the fabric analyses was actually perpendicular to these structures. These fabrics are concluded to have recorded the final magma movements after the lobes formed, as the lobes merged. Ropy-flow structures may adequately infer magma flow however these were more accurate when they occurred close to the upper contact of the sill. Bridge structures, including broken bridges and bridge stubs, accurately predicted magma flow within sills and could be reliable features to infer a magma flow orientation. However, as with magma lobes, the bridge structure orientation preserved the initial intrusion direction. Late stage magma flow overprinted the magma flow sense implied by bridge structures as evidenced by the SPO and AMS fabrics. This scenario is probable if numerous overlapping segments merge and the already intruded magma is able to flow between the sills segments, perpendicular to the long axes of the bridge structures. Magma flow orientations derived from intrusive steps, and magma-injection-related scour marks, are considered to be the successful indicators of magma flow.

Chapter 7

The magma flow directions for 16 sills along the KZN North Coast were determined using the combined results obtained from the field magma flow indicators, the plagioclase SPO fabrics

and AMS fabrics. Based on the magma flow direction determined within the sills, it can be concluded that the sills can be separated into two different orientation categories based on the directions in which the magma flowed in the sills (see Fig. 7.8, page 182). These directions were perpendicular; the first category sills yielded NE-SW magma flow whereas the second category yielded predominantly NW-SE magma flow.

The variation in the direction of intrusion of the dolerite sills was attributed to different intrusive mechanisms for the two sill groupings. The mechanism of intrusion for the NE-SW magma flow sills was fed by dykes of the NW-SE oriented Underberg Dyke Swarm. The mechanism of intrusion for the NW-SE magma flow sills was a sill-fed system that formed due to crustal thinning of the lithosphere along the present coastline during the early stages of Gondwana breakup.

The magma flow directions were used to infer a magma source for these sills. It was concluded that this source is most likely in the region of the Weddell Sea in the pre-Gondwana breakup continental configuration. The melts are concluded as having been produced by global mantle warming beneath the supercontinent Gondwana that created large scale partial melting of the upper mantle. Due to the extent of the melt production, this may have yielded magmas with varied compositions and volatile components. This could be one explanation for the differences in the Karoo and Ferrar magmas, as these localised magmatic centres may have extracted varied melt compositions from the mantle as the mantle source for the Ferrar magmas was more proximal to subducting lithospheric material. Another explanation could be that the magmas were derived from the Archaean lithospheric mantle and the post-Archaean lithospheric mantle respectively for the Karoo and Ferrar provinces. It is concluded that a mantle plume is not required to produce the magmas that formed the KZN North Coast sills and conclusively that these magmas did not originate from a source proximal to the Mwenezi triple junction.

- APPENDIX A -

PAPER 1 – Tectonophysics, Volume 656, pages 61-73

Assessing SPO techniques to constrain magma flow: Examples from sills of the Karoo Igneous Province, South Africa.

Tectonophysics 656 (2015) 61–73

Contents lists available at ScienceDirect

Tectonophysics

journal homepage: www.elsevier.com/locate/tecto

Assessing SPO techniques to constrain magma flow: Examples from sills of the Karoo Igneous Province, South Africa

Lauren Hoyer *, Michael K. Watkeys

Geological Sciences, School of Agricultural, Earth and Environmental Sciences, University of KwaZulu-Natal, Westville Campus, Private Bag X54001 Durban 4000, South Africa

ARTICLE INFO

Article history:
Received 12 November 2014
Received in revised form 25 May 2015
Accepted 2 June 2015
Available online 18 June 2015

Keywords:
Petrofabric
Shape Preferred Orientation (SPO)
Magma flow
Sills

ABSTRACT

Shape ellipsoids that define the petrofabrics of plagioclase in Jurassic Karoo dolerite sills in KwaZulu-Natal, South Africa are rigorously constrained using the long axis lengths of plagioclase crystals and ellipse incompatibility. This has been undertaken in order to determine the most effective technique to determine petrofabrics when using the SPO-2003 programme (Launeau and Robin, 2005). The technique of segmenting an image for analysis is scrutinised and as a process is found redundant. A grain size threshold is defined to assist with the varying grain sizes observed within and between sills. Where grains exceed the 0.2 mm size threshold, images should be acquired at a high magnification (i.e., 10× magnification). Petrofabrics are determined using the foliation and the lineation of the ellipsoid as defined by the maximum and minimum principal axes (respectively) of the resultant ellipsoid. Samples with strongly prolate fabrics are isolated allowing further constraint on the petrofabric to be made. Once the efficacy of the petrofabric determination process has been determined, the resultant foliations (and lineations) then elucidate the most accurate petrofabric attainable. The most accurate petrofabrics will be determined by using the correct magnification when the images are obtained and to run the analyses without segmenting the image. The fabrics of the upper and lower contacts of the Karoo dolerite sills are analysed in detail using these techniques and the fabrics are used as a proxy for magma flow.

1. Introduction

The Shape Preferred Orientations (SPO) analysis of minerals has been widely used in a number of studies in order to define a shape ellipsoid for the minerals under analysis. This is often done in order to determine the magma flow within dykes (Archanjo and Launeau, 2004; Hastie et al., 2011a,b, 2013; Launeau and Robin, 2005) and sills (Horsman et al., 2005; Kattenhorn, 1994). With the introduction of the SPO-2003 and Ellipsoid-2003 software packages (Launeau, 2004; Launeau and Robin, 2005) the determination of the SPO of mineral phases has become a tool in describing the petrofabric associated with intrusions and intrusion mechanisms. Petrographic analyses are often integrated with Anisotropic Magnetic Susceptibility (AMS) analyses in order to determine not only the petrofabric but also the magnetic fabrics of the intrusions (e.g., Archanjo et al., 2006, 2012; Geoffroy et al., 2002; Hastie et al., 2011b; Horsman et al., 2005).

This study investigates dolerite sills that crop out along the KwaZulu-Natal North Coast (Fig. 1), South Africa, and which are part of the extensive ca. 184–181 Ma sills of the Karoo Igneous Province (Jourdan et al., 2008). They were sampled to obtain the petrofabric in order to infer the principal magma flow directions. Fabrics form from numerous flow-related and regional scale processes, but in order for a fabric to be preserved, the process of formation must occur at a particular point in the intrusion history. For plutonic rocks, a "crystal-mush zone" occurs at the margins of the intrusion whilst the magma is cooling and crystallising. As the pluton cools, this zone migrates inwards (Marsh, 1989; Tait and Jaupart, 1990). Once the viscosity of the melt changes from a low viscosity Newtonian melt to a higher viscosity, crystal-dense Bingham melt, the magma is near solidi; it is at this point that the fabrics become preserved (Paterson et al., 1998; Yoshinobu et al., 1998).

In order to successfully analyse the magma flow within an intrusion, it is necessary to analyse the fabric within the sill and determine whether or not these fabrics imply magma flow mechanisms and directions. Whilst using the SPO programmes it became evident that in order to obtain the most accurate petrofabric results, certain parameters needed to be analysed to elucidate which analytical technique should be used. The aim of this study is to ascertain the most accurate petrofabric data through the use of the SPO-2003 programme. The results need to be well-defined by using the correct analytical techniques so that the petrofabric data may be used to infer the magma flow direction in the sills sampled. In order to determine the most accurate results, the techniques used to acquire the petrofabric data must be constrained. The techniques that are scrutinised include (1) the error in the fit of the resultant ellipsoids as indicated by the Global Incompatibility Index ($\sqrt{F}$); (2) whether or not an image should be segmented upon analysis to improve the quality of the result and (3) in particular the variation in the

* Corresponding author.
E-mail address: lauren_hoyer@hotmail.com (L. Hoyer).

http://dx.doi.org/10.1016/j.tecto.2015.06.006
0040-1951/

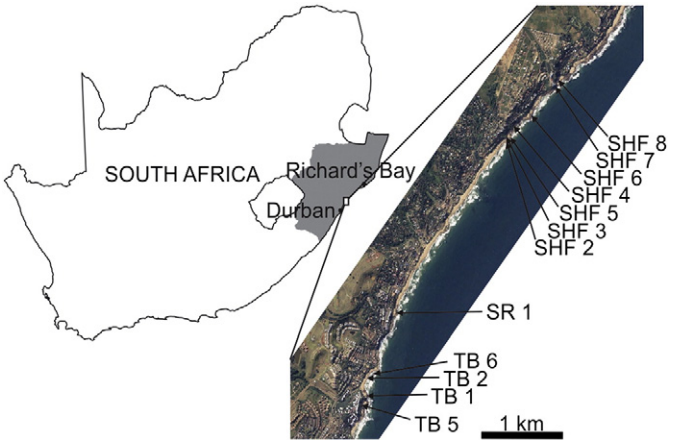

Fig. 1. The geographical position of the study area ~40 km north of Durban in KwaZulu-Natal, South Africa. The sills that were sampled and incorporated into this study are indicated and labelled on the aerial photograph.

grain size of the plagioclase crystals that are to be analysed. Grain size has been previously discussed when defining how petrofabrics within intrusions may differ due to the presence of different crystal generations (e.g., Hastie et al., 2013). However prior to determining the shape ellipsoid for a sample, the grain size is generally not taken into consideration when selecting the magnification at which photomicrographs are taken. The issues of $\sqrt{F}$ are highlighted using the results from twelve sills sampled from the KwaZulu-Natal North Coast at Thompson's Bay (TB), Shaka's Rock (SR) and Sheffield Beach (SHF).

Due to tectonic activity related to the break-up of Gondwana, the rocks have been tilted and rotated so that there is no distinct link between the intrusions sampled here and the main Karoo Basin dolerites. This study should enable significant petrofabric results to be ascertained and possible magma flow directions to be inferred. This could greatly further the understanding of not only dolerite sill emplacement but also the extent and origin of the Karoo dolerites.

2. Geological settings

The study area spans an 8 km stretch of coastline where numerous dolerite sills crop out. The beaches are narrow and only small portions of the intrusions may be observed at any one locality. The dolerite suite is predominantly composed of sills with minor dykes that are poorly exposed. The sills are intruded into the Permian aged Vryheid Formation, of the Karoo Supergroup supracrustals. The country rocks comprise thinly laminated siltstones, shales and gritstones with minor interbedded coal seams and Iron-rich shales. The dolerites are Jurassic in age, ranging between 184 Ma and 181 Ma (Jourdan et al., 2008) and typically intrude into the laminated finer grained country rocks, although occasionally into the gritstones (e.g., SHF5).

Post-dating the intrusion of the dolerite suite was a series of brittle tectonic events related to the break-up of Gondwana. The faulting events that created the coastline have been preserved in both the country rocks and the dolerite intrusions, manifested as locally tilted and rotated stratigraphy.

2.1. Dolerite petrography and petrology

The sills investigated typically comprise ~50% plagioclase and ~45% augite, with the remaining fraction (5%) taken up by magnetite and minor pyrrhotite. Chlorite and biotite may also be present where alteration has taken place. For some of the sills, the original minerals are no longer discernible from alteration minerals and were therefore disregarded for this study.

Macroscopically the intrusions may contain one or all of the following features: amygdales, large and small vesicles, xenoliths of quartzofeldspathic material or local country rock and multiple layers indicating numerous magma pulses (Table 1). Microscopically, the grain size varies widely between the sills, and occasionally also between the upper and lower contacts (Fig. 2).

The texture of the dolerites may also vary between and within the sills. This becomes an important consideration when the petrofabric is being analysed in terms of magma flow fabrics. The majority of the samples that were photomicrographed exhibited intergranular textures, although some samples show interesting plagioclase and/or pyroxene textures. A range of textures from acicular to spherulitic to variolitic plagioclase were observed with some sections showing fine grained plumose textured augite (Fig. 2). All of the textures appear to be magmatic in origin, although some samples have textural overprinting caused by alteration phases such as chlorite. Such samples were either disregarded or only photomicrographed at the fresh portions of the thin section.

Magma flow indicators occur within the sills and comprise magmatic features such as ropy-flow structures and magma lobes (Table 1). The morphological features such as broken bridges and steps along the contacts of the sills may have been obstacles that had a local effect on the magma flow (Schofield et al., 2010; Wylie et al., 1999).

3. Methods

3.1. Sampling and sample preparation

Twenty five millimetre diameter cores were collected using a petroleum-powered handheld drill and were typically sited within 10–15 cm of the sill contacts. All cores obtained were orientated in the field using a core-orientator and a magnetic compass. Ideally between 4 and 8 samples were collected from opposing sill margins (where available) within a single intrusion. The majority of the intrusions were thin (<2 m thick) and therefore cross-sectional sampling throughout such sills was not possible. However, for some of the thicker intrusions, certain layers or portions of the sill were sampled. The intrusion TB2 yielded samples not only from the margins but from a vesicular zone where ~4 cm long elongated vesicles were observed plunging towards the NW. The centre of the sills TB4 and SR1 were also sampled due to a distinct difference in grain size between the centre and the margins of the sills.

The cores were cut into mutually perpendicular sections based on a randomly assigned XYZ coordinate system (Fig. 3). The samples were prepared into thin sections for petrographic analyses and each thin section (3 per sample) was photographed under crossed polarisers. To account for the large variations in grain sizes within and between the intrusions, the thin sections were photographed at both lower and higher magnifications (2.5× and 10× magnification respectively) in order to image the greatest range of grain sizes. A total of 102 samples were photographed (306 thin sections); this resulted in 97 samples (291 thin sections) photographed at 10× magnification and 53 samples (159 thin sections) photographed at 2.5× magnification.

3.2. Shape Preferred Orientation (SPO) of plagioclase

The photomicrographs of orientated thin sections were digitised in order to measure the orientation and shape of the plagioclase crystals by means of measured ellipses. The images obtained were changed into negative black and white images and filtered using a threshold level of 128 in the image manipulation software ArcSoft Photostudio. This allowed only the plagioclase grains from each section to be extracted. Any grains that were truncated by the image boundary were removed. The thresholding process allows for only the lightest coloured portions of the image to remain. Where twinning of the plagioclase occurs, the twin in or close to extinction may not be preserved through the thresholding technique. If the entire grain is not preserved, this may affect subsequent results such as the average shape of the grains in the

Table 1
Geographical positions and characteristics of the sills from Thompson's Bay and Sheffield Beach.

Sill	Geographical co-ordinates				Approximate	
Name	Latitude	Longitude	Dip	Strike	Thickness (m)	Characteristics
TB1	29° 31′ 39.05″	31° 13′ 41.17″	22°	172°	3.0	Xenolithic, minor amygdales
TB2	29° 31′ 14.69″	31° 13′ 42.05″	21°	167°	2.5	Elongated vesicle layer (highest degree of alteration), amygdaloidal layer, xenolithic zone
TB4	29° 31′ 13.87″	31° 13′ 42.87″	25°	172°	1.0	Central vesicle stringer, spherulitic plagioclase and pyroxene
TB5	29° 31′ 25.17″	31° 13′ 39.03″	16°	160°	2.0	Massive, small broken bridge along upper contact
SR1	29° 30′ 50.76″	31° 13′ 54.48″	20°	206°	2.0	Xenolithic at upper contact, spherulitic increase in grain size from margins to centre
SHF2	29° 29′ 43.44″	31° 14′ 46.68″	20°	000°	1.0	Fine grained with spherulitic plagioclase
SHF3	29° 29′ 41.64″	31° 14′ 46.93″	17°	340°	2.2	Large broken bridge and associated rheomorphic dyke intruding sill, amygdaloidal layers
SHF4	29° 29′ 37.32″	31° 14′ 49.56″	12°	350°	1.5	Above average degree of alteration
SHF5	29° 29′ 41.28″	31° 14′ 48.48″	10°	353°	1.2	High degree of alteration
SHF6	29° 29′ 32.64″	31° 14′ 57.48″	13°	013°	2.5	Occasional spherulitic pyroxene, large xenoliths (some wholly melted)
SHF7	29° 29′ 23.64″	31° 15′ 07.56″	10°	056°	>10	Phenocrystic plagioclase at the lower contact, xenolithic
SHF8	29° 29′ 19.32″	31° 15′ 10.44″	09°	088°	0.5	High degree of alteration, central vesicle stringer, xenolithic

section and the degree of anisotropy of the grains. Once the threshold has been applied, any intersecting grains are manually separated. This allows each grain to be analysed individually in order to obtain an accurate fabric. The final digitised images were then imported into the programme SPO-2003 (Launeau, 2004; Launeau and Bouchez, 1992; Launeau and Robin, 2005) which creates a 2-D inertia tensor from all the grain data and defines an ellipse (Launeau and Robin, 1996; 2005). The 2-D inertia tensor is formed by the stacking of every grain in the image into a column which determines the average shape within the image. The three mutually perpendicular 2-D tensors are then combined in the programme Ellipsoid-2003, where each ellipse holds an equal weight regardless of the number of grains measured. This allows a 3-D ellipsoid to be created, the parameters of which define the petrofabric. The shape of the ellipsoid (T) and the degree of anisotropy (P′) are determined by the software and recorded for each ellipsoid (Jelinek, 1981). T, as defined by Jelinek (1981), is the best descriptive formula used to define ellipsoidal shapes (Tarling and Hrouda, 1993).

According to Launeau and Robin (2005) the images should be segmented before the grains are analysed in order to obtain the maximum number of combinations of the three 2-D ellipses. For the segmentation of each image, nine overlapping rectangles (each rectangle is one quarter of the size of the image) are used as separate images, therefore allowing for the formation of 9 ellipses per thin section. Three perpendicular images are used in one sample, therefore nine segments from each image allow for 279 combinations of these ellipses. In unsegmented images, where one image is the equivalent of one segment, only three combinations are possible. Hence, the more combinations that are utilised in the analysis of each image, the more accurately the final ellipsoid is constrained. Once analyses had been undertaken on the samples in this study, it was clear that the segmentation process may not be statistically favourable in determining the petrofabric. Where each image was segmented into nine portions; many grains were truncated at the segment to segment boundary and therefore misrepresented the fabrics each segment could produce. Therefore, for each sample the SPO results were obtained using segmented and unsegmented images.

When the ellipses are combined an error in the fit of the ellipsoid may occur and is measured by the Global Incompatibility Index ($\sqrt{F}$) (Launeau and Robin, 2005). A perfect fit of the three ellipses would result in a $\sqrt{F}$ value of 0. However the $\sqrt{F}$ value can be in excess of 26%, as in this study, where the compatibility of the ellipses in forming the final ellipsoid is low and therefore the ellipsoids may not be a reliable

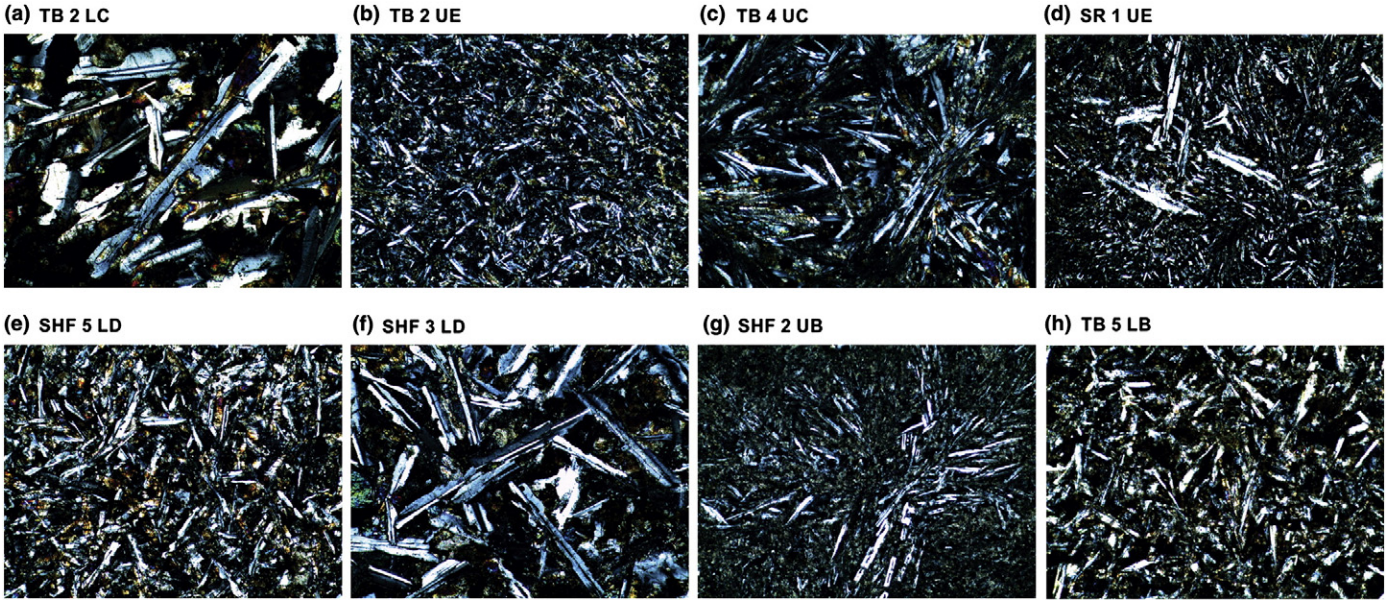

Fig. 2. Examples of photomicrographs with all images obtained at the same magnification (1.2 mm in width). (a) and (f) show a larger overall grain size than the finer grained sections of (b), (e), (g) and (h). (c) and (g) display textures between plumose augite crystals and variolitic to spherulitic plagioclase. (d) Elongate plagioclase phenocrysts within a finer grained matrix. (a), (c), and (f) show intergranular textures; (b), (d), (e), (g) and (h) are hemicrystalline.

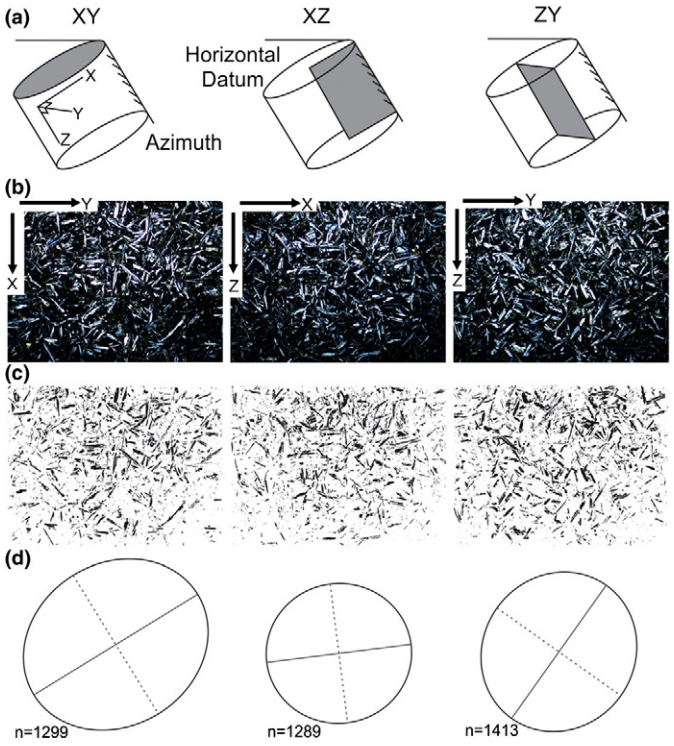

Fig. 3. (a) Diagram of the mutually perpendicular sections (grey) cut from a standard drill core sample. Each sample comprises three orthogonal sections as defined by an XYZ coordinate system after Hastie et al. (2011a). (b) Photomicrographs from sample SHF 6 LF taken under cross-polarisers (5 mm in width) with the coordinate directions shown down dip in black arrows. (c) Filtered images which are to be analysed in the SPO-2003 programme where the plagioclase grains have been extracted using a threshold grey scale value. (d) The resultant ellipse determined for each section.

result. Results with $\sqrt{F}$ values <10% are desirable (Launeau and Robin, 2005; Launeau et al., 2010) and are the generally accepted value below which the results may be trusted for accuracy.

3.3. Grain size

The long and short axes of the plagioclase grains were obtained using 2-D ellipse data from each sample set. For each image analysed, a table of data is acquired detailing the information obtained for every grain. The scale of the photomicrograph is used to change the scale of the images and therefore grains from pixels to millimetres. As the maximum size of the plagioclase grains in each thin section was the priority, an average long axis was determined for each sample. This was done by averaging the mean of the 10 largest grains from each section. This averaged maximum grain length is then used as a proxy for grain size for each sample. This does not accurately represent the mean grain size of each sample but is used as a tool for differentiating between samples at the same photomicrograph magnifications.

4. Results

Twelve dolerite sills were petrographically analysed to infer a magma flow regime. Here the processes and techniques used in order to determine the petrofabrics are described. The individual sample data for the sills from Thompson's Bay and Sheffield Beach are tabulated in Tables 2 and 3 respectively. Examples of the petrofabric results are discussed in Section 4.5. below, where these techniques have been applied to the fabric determination process.

4.1. Analyses errors

As the data were analysed, the results revealed that there were clear discrepancies in not only the final ellipsoid orientations but the $\sqrt{F}$ values for the same images at different magnifications (Fig. 4). For the samples photographed at 10× magnification there is a significant difference in the number of samples that have $\sqrt{F}$ values <10% (Fig. 4). For the images obtained at the higher magnification (10× magnification) and segmented, there are no $\sqrt{F}$ values less than 4%. The mean $\sqrt{F}$ value is 12.7% and 27.8% of the data plot below 10% $\sqrt{F}$. For the unsegmented images at higher magnification the $\sqrt{F}$ values are much lower with a mean value of 6.8%; 76 results (78.4%) show $\sqrt{F}$ values lower than 10%. There is also a large fraction of data (21.3%) that show errors of between 0 and 2% $\sqrt{F}$, the closest fit that may be obtained for any ellipsoid.

This trend is mimicked in the lower magnification images; the mean $\sqrt{F}$ values for the segmented and unsegmented images are 8.3% and 4.7% respectively. At 2.5× magnification the $\sqrt{F}$ values that occur below the 10% $\sqrt{F}$ mark comprise 67.9% and 86.8% of the population of 53 samples for the segmented and unsegmented images respectively. No results have $\sqrt{F}$ values <2% for the segmented images whereas 28% of the $\sqrt{F}$ values for the results determined using unsegmented images are between 0 and 2% $\sqrt{F}$.

4.2. Relationship between plagioclase grain size and $\sqrt{F}$ values

Fig. 5 illustrates the relationships between the maximum long axis length of the plagioclase grains and the $\sqrt{F}$ values calculated for each sample when the images were segmented and unsegmented. Where the images were not segmented, the $\sqrt{F}$ values increase as the maximum length of the plagioclase long axes increases, for all magnifications. For the lower magnification, the range of long axis lengths are from 0.20 mm to 0.64 mm, with 36 results yielding $\sqrt{F}$ values of less than 10%. The 27 results that have $\sqrt{F}$ values of less than 10% for the higher magnification do not exceed a long axis length of 0.204 mm. However 44% of the results have a grain size of <0.20 mm with errors exceeding 10%. The r^2 values for the linear functions defining these proportional relationships are 0.62 for the 2.5× magnification images and 0.44 for the 10× magnification images. For the unsegmented images at both magnifications, the majority of the long axis data plot below the 10% $\sqrt{F}$ boundary.

The minimum long axis length measured for the lower magnification images when the image is segmented or not segmented is the same length of 0.20 mm. This is also true of the higher magnification image where a minimum long axis length of ~0.05 mm was measured and the maximum long axis length with a $\sqrt{F}$ value of less than 10% is 0.32 mm.

4.3. Strike differences between segmented and unsegmented images

Four results were determined for more than half of the samples because photomicrographs of the thin sections were taken at both higher and lower magnifications and analysed using segmented and unsegmented techniques. In order to resolve which result best defines the petrofabric, the resultant strikes of the foliations of the segmented and unsegmented images were plotted one against the other (Fig. 6). With an r^2 of 0.86, there is an acceptable fit between the resultant petrofabric strikes determined for the segmented and unsegmented images. Even though two methods were used, most of the samples showed similar direction values.

The outliers highlighted in dark grey (Fig. 6) have discrepancies of between 10° and 60° but do not plot near the bulk of the data as direction results from the segmented images exceed 360°, whereas the unsegmented directions do not. The data points highlighted in light grey represent results that dip in opposite directions (180° away) with respect to one another (Fig. 6).

4.4. Ellipsoid shape and anisotropy

Results obtained using the SPO-2003 programme are defined in shape according to the shape parameter (T) and the corrected degree of anisotropy (P′). The shape parameter defines the ellipsoid as oblate when T > 0; triaxial when T = 0 and prolate when T < 0 (Jelinek, 1981; Tarling and Hrouda, 1993). Prolate fabrics are the dominant shape with 59.2% of the data having T values <0 and an average value of −0.091 which is close to triaxial in shape (Fig. 7).

The average P′ value (Jelinek, 1981) of the plagioclase fabric is 1.397, showing a strong degree of anisotropy. The highest P′ values are found in the sills TB1, TB2, TB4 and SHF2 where sample TB 2C(V) has a degree of anisotropy of 4.128 (Table 2).

4.5. Karoo dolerite sills

The above techniques have been applied to the samples from Thompson's Bay (Table 2) and Sheffield Beach (Table 3) with data from sills shown here in detail (Fig. 8 and 9 respectively). It should be noted that three sills, SR1, SHF7 and SHF8, have been used in the analytical portion of this study have been excluded in the following section because the data from the intrusions are limited and incomplete.

The petrofabrics determined for the sills from Thompson's Bay (Fig. 8) and Sheffield Beach (Fig. 9) are individually analysed. Arrows have been used to indicate the direction of the petrofabric derived from the SPO results at the sampling locality. Black arrows indicate the azimuth of the foliation and the red arrows represent the plunge direction of the lineations selected to represent the petrofabric. The length of the arrows indicates how steep the dip/plunge is for each petrofabric. Small grey stars have been drawn where there are morphological obstacles along the upper or lower contacts such as broken bridges or steps. The stars shown on TB1 and TB2 (Fig. 8b and c) represent magmatically formed ropy-flow structures (e.g., Liss et al., 2002).

The dip and azimuth of each foliation and plunge and plunge direction of each lineation have been stereographically displayed for the upper and lower contacts of each sill. The great circle on each stereogram is the dip and strike of the tilted country rock (Table 1). All the data have been plotted as lineations and then restored to the horizontal according to the country rocks dip and strike (Tables 2 and 3).

4.5.1. Examples from Thompson's Bay

Four sills were analysed in detail from the Thompson's Bay area (Fig. 8), namely TB1, TB2, TB4 and TB5. TB1 contains small amygdales, xenoliths (partially disintegrated) and ropy-flow structures near the

Table 2
SPO results from the Thompson's Bay sills including the petrofabric vector used to infer magma flow for each sample.

		Foliation			Maximum axis		Minimum axis					Grain size	Restored foliation		Restored lineation		Petrofabric vector	
Sample	Mag.	Dip	Strike	Rake	Plunge	Trend	Plunge	Trend	[a]P′	[b]T	[c]√F (%)	Proxy (mm)	Dip	Strike	Plunge	Trend	Plunge	Trend
TB-1 UA	10×	69.0°	265.0°	158.3°	20.2°	086.8°	21.0°	175.0°	1.158	*−0.551*	4.0	0.12	69.7°	256.5°	*41.5°*	*088.0°*	*41.5°*	*088.0°*
TB-1 UB	10×	61.4°	328.1°	037.2°	32.1°	348.1°	28.6°	238.1°	1.259	*−0.633*	6.0	0.14	41.8°	320.2°	*18.0°*	*335.5°*	*18.0°*	*335.5°*
TB-1 UC	10×	63.2°	221.2°	035.0°	30.8°	238.7°	26.8°	131.2°	1.147	*−0.310*	8.0	0.15	78.1°	215.5°	*10.3°*	*241.0°*	*10.3°*	*241.0°*
TB-1 UD	10×	29.4°	289.7°	044.4°	20.1°	330.3°	60.6°	199.7°	1.113	0.370	3.0	0.10	26.8°	248.0°			26.8°	338.0°
TB-1 UE	10×	63.8°	143.7°	151.4°	25.4°	310.2°	26.2°	053.7°	1.191	0.266	2.9	0.13	83.2°	146.4°			83.2°	236.4°
TB-1 UF	10×	54.8°	162.0°	098.7°	53.8°	266.9°	35.2°	072.0°	1.249	*−0.342*	4.1	0.13	76.5°	163.8°	*31.5°*	*265.0°*	*31.5°*	*265.0°*
TB-1 UG	10×	65.6°	188.4°	037.3°	33.5°	205.9°	24.4°	098.4°	1.785	*−0.579*	4.8	0.14	86.5°	187.2°	*19.6°*	*214.4°*	*19.6°*	*214.4°*
TB-1 UH	10×	38.8°	211.1°	095.1°	38.7°	307.6°	51.2°	121.1°	1.524	−0.276	10.1	0.17	57.9°	200.0°			57.9°	290.0°
TB-1 UI	10×	38.8°	235.3°	011.7°	07.3°	244.5°	51.2°	145.3°	1.803	*−0.800*	5.2	0.11	53.0°	216.4°	*14.0°*	*064.0°*	*14.0°*	*064.0°*
TB-1 UJ	10×	50.1°	070.5°	101.7°	48.6°	178.4°	39.9°	340.5°	2.026	*−0.317*	4.2	0.15	49.7°	089.3°	*41.5°*	*200.5°*	*41.5°*	*200.5°*
TB-1 UP	10×	35.9°	266.7°	164.0°	09.3°	073.7°	54.1°	176.7°	1.507	0.075	0.8	0.18	39.4°	238.2°			39.4	328.2°
TB-2 LA	10×	57.5°	306.4°	051.2°	41.1°	340.2°	32.5°	216.4°	1.153	0.252	0.4	0.07	64.5°	314.7°			64.5°	044.7°
TB-2 LC	2.5×	48.3°	178.3°	018.7°	13.9°	200.0°	41.7°	097.3°	1.388	0.372	4.3	0.63	29.2°	198.3°			29.2°	288.3°
TB-2 LD	10×	52.3°	201.8°	075.3°	50.0°	268.6°	37.7°	111.8°	2.773	0.011	3.4	0.31	37.0°	216.0°			37.0°	306.0°
TB-2 LE	2.5×	12.5°	267.0°	034.6°	07.1°	300.9°	77.5°	177.0°	1.543	0.128	3.5	0.73	26.0°	317.3°			26.0°	047.3°
TB-2 UA	10×	27.1°	151.9°	027.9°	12.3°	177.2°	62.9°	061.9°	1.075	0.087	5.8	0.11	08.7°	113.2°			08.7°	203.2°
TB-2 UB	10×	63.8°	203.4°	124.1°	48.0°	350.3°	26.2°	113.4°	1.314	*−0.847*	0.5	0.09	48.1°	212.3°	*45.5°*	*328.2°*	*45.5°*	*328.2°*
TB-2 UE	10×	36.8°	221.8°	123.7°	29.9°	351.6°	53.2°	131.8°	1.289	0.502	6.2	0.11	29.8°	252.5°			29.8°	342.5°
TB-2 UF	10×	75.5°	354.3°	050.8°	48.7°	011.3°	14.5°	264.3°	2.173	−0.224	3.2	0.16	83.3°	173.8°			83.3°	263.8°
TB-2 UG	10×	67.8°	349.9°	017.7°	16.4°	356.7°	22.2°	259.9°	1.156	*−0.681*	3.6	0.08	89.2°	349.2°	*18.6°*	*349.0°*	*18.6°*	*349.0°*
TB-2 UI	10×	74.8°	228.9°	119.8°	56.8°	024.3°	15.2°	138.9°	1.151	0.214	7.2	0.05	66.1°	235.9°			66.1°	325.9°
TB-2 UJ	10×	35.6°	302.3°	076.1°	34.4°	015.4°	54.4°	212.3°	1.148	−0.111	0.8	0.11	51.8°	315.7°			51.8°	045.7°
TB-2 UK	10×	53.5°	041.9°	122.1°	42.9°	178.4°	36.5°	311.9°	1.264	*−0.474*	3.5	0.10	67.0°	032.6°	*35.7°*	*194.3°*	*35.7°*	*194.3°*
TB-2 C(V)	10×	67.6°	230.0°	120.2°	53.1°	016.8°	22.4°	140.0°	4.128	*−0.790*	4.0	0.16	60.0°	239.9°	*58.5°*	*345.5°*	*58.5°*	*345.5°*
TB-2 D(V)	10×	27.1°	205.4°	144.9°	15.2°	353.4°	62.9°	115.4°	1.440	0.443	0.1	0.15	16.6°	252.4°			16.6°	342.4°
TB-2 H(V)	10×	38.6°	249.1°	104.6°	37.2°	357.5°	51.4°	159.1°	1.388	*−0.459*	3.2	0.12	40.1°	275.2°	*29.0°*	*341.0°*	*29.0°*	*341.0°*
TB-4 LA	10×	22.7°	147.1°	131.6°	16.8°	281.1°	67.3°	57.1°	1.565	0.443	8.9	0.16	10.2°	060.0°			10.2°	150.0°
TB-4 LB	10×	63.1°	185.0°	164.9°	13.4	358.1°	26.9°	095.0°	1.211	0.392	4.4	0.28	36.0°	192.0°			36.0°	282.0°
TB-4 LC	2.5×	57.1°	032.8°	055.3°	43.6°	070.9°	32.9°	302.8°	1.249	−0.262	5.7	0.39	77.0°	026.3°			77.0°	116.3°
TB-4 LE	2.5×	56.8°	016.2°	023.1°	19.2°	029.4°	33.2°	286.2°	1.577	−0.172	8.1	1.02	80.1°	012.0°			80.1°	102.0°
TB-4 UA	10×	67.4°	067.9°	166.5°	12.4°	242.7°	22.6°	337.9°	1.594	0.033	2.5	0.19	75.2°	060.0°			75.2°	150.0°
TB-4 UB	10×	52.8°	073.5°	082.4°	52.2	151.0°	37.2°	343.5°	1.454	−0.510	5.2	0.14	60.0°	057.5°	*53.0°*	*185.6°*	*53.0°*	*185.6°*
TB-4 UC	10×	72.5°	150.6°	125.0°	52.2°	307.4°	17.5°	060.6°	1.355	0.492	0.3	0.15	50.0°	145.7°			50.0°	235.7°
TB-4 UE	2.5×	72.0°	211.4°	124.7°	51.5°	007.4°	18.0°	121.4°	1.129	−0.362	0.4	0.68	53.6°	220.1°	*51.5°*	*335.0°*	*51.5°*	*335.0°*
TB-5 LA	10×	42.7°	295.3°	040.9°	26.4°	327.8°	47.3°	205.3°	1.311	−0.212	9.4	0.19	54.8°	304.0°			54.8°	034.0°
TB-5 LB	2.5×	35.6°	121.6°	039.3°	21.6°	155.2°	54.4°	031.6°	1.309	−0.551	4.3	0.31	25.5°	105.3°	*21.3°*	*161.0°*	*21.3°*	*161.0°*
TB-5 LC	2.5×	43.6°	338.0°	039.2°	25.9°	008.6°	46.4°	248.0°	1.146	0.060	7.7	0.25	60.0°	338.0°			60.0°	068.0°
TB-5 LD	2.5×	43.2°	005.4°	163.8°	11.0°	173.5°	46.8°	275.4°	1.298	0.183	7.7	0.37	58.0°	001.0°			58.0°	091.0°
TB-5 UA	10×	20.2°	201.2°	058.4°	17.1°	257.9°	69.8°	111.2°	1.370	0.660	7.3	0.17	12.5°	251.5°			12.5°	341.5°
TB-5 UB	10×	64.0°	112.1°	032.9°	29.2°	128.0°	26.0°	021.1°	1.286	−0.550	6.1	0.14	53.8°	104.6°	*36.0°*	*136.8°*	*36.0°*	*136.8°*
TB-5 UC	10×	50.3°	235.1°	070.3°	46.4°	295.9°	39.7°	145.1°	1.111	0.719	1.9	0.15	48.6°	249.0°			48.6°	339.0°
TB-5 UD	10×	46.6°	223.8°	059.1°	38.6°	272.7°	43.4°	133.8°	1.079	−0.306	2.9	0.15	41.0°	240.0°			41.0°	330.0°

[a] P′ = Degree of anisotropy.
[b] T = Shape parameter (oblate/prolate).
[c] √F = Global Incompatibility Index.

Table 3
SPO results from the Sheffield Beach sills including the petrofabric vector used to infer magma flow for each sample.

		Foliation			Maximum axis		Minimum axis					Grain size	Restored foliation		Restored lineation		Petrofabric vector	
Sample	Mag.	Dip	Strike	Rake	Plunge	Trend	Plunge	Trend	[a]P′	[b]T	[c]√F (%)	Proxy (mm)	Dip	Strike	Plunge	Trend	Plunge	Trend
SHF-2 LA	10×	53.9°	106.6°	053.4°	40.5°	145.1°	36.1°	016.6°	1.550	*−0.315*	8.6	0.27	61.0°	118.6°	*56.0°*	*145.0°*	*56.0°*	*145.0°*
SHF-2 LB	2.5×	86.9°	297.5°	046.6°	46.5°	300.8°	03.1°	207.5°	1.216	0.558	0.8	0.58	78.2°	295.3°			78.2°	025.3°
SHF-2 LC	10×	68.6°	056.0°	147.1°	30.4°	222.7°	21.4°	326.0°	1.124	0.436	5.2	0.17	58.5°	065.0°			58.5°	155.0°
SHF-2 LD	2.5×	63.9°	047.9°	048.6°	42.2°	074.5°	26.1°	317.9°	1.255	0.220	2.2	0.33	51.2°	057.3°			51.2°	147.3°
SHF-2 LE	2.5×	43.0°	036.1°	098.1°	42.5°	137.1°	47.0°	306.1°	2.599	*−0.664*	3.4	0.95	29.3°	055.2°	*27.0°*	*127.4°*	*27.0°*	*127.4°*
SHF-2 UA	10×	73.4°	142.5°	068.7°	63.2°	178.8°	16.6°	052.5°	1.351	*−0.501*	6.8	0.10	89.4°	144.2°	*27.8°*	*134.3°*	*27.8°*	*134.3°*
SHF-2 UB	10×	60.2°	220.5°	061.6°	49.7°	263.1°	29.8°	130.5°	1.272	0.153	2.6	0.14	75.9°	215.4°			75.9°	305.4°
SHF-2 UC	10×	89.6°	063.2°	131.9°	48.1°	242.7°	00.4°	333.2°	1.327	−0.001	5.4	0.13	80.2°	064.3°			80.2°	154.3°
SHF-2 UD	2.5×	79.8°	081.2°	057.0°	55.7°	096.4°	10.2°	351.2°	1.210	−0.189	0.1	0.49	77.4°	085.2°			77.4°	175.2°
SHF-3 LA	10×	76.8°	282.6°	018.3°	17.8°	286.9°	13.2°	192.6°	1.869	0.118	2.5	0.20	68.3°	278.0°			68.3°	008.0°
SHF-3 LB	10×	50.2°	232.8°	125.7°	38.6°	011.1°	39.8°	142.8°	1.387	−0.809	3.0	0.18	57.0°	221.0°	*29.0°*	*020.6°*	*29.0°*	*020.6°*
SHF-3 LC	10×	48.8°	165.9°	136.7°	31.0°	314.1°	41.2°	075.9°	1.121	−0.358	5.1	0.18	65.0°	164.7°	*37.0°*	*325.0°*	*37.0°*	*325.0°*
SHF-3 LD	10×	69.4°	013.5°	118.9°	55.1°	161.0°	20.6°	283.5°	1.413	−0.109	0.3	0.27	55.5°	018.5°			55.5°	108.5°
SHF-3 UA	10×	25.5°	003.5°	142.3°	15.2°	148.7°	64.5°	273.5°	1.566	−0.024	9.0	0.20	12.0°	034.0°			12.0°	124.0°
SHF-3 UB	10×	69.8°	287.2°	047.7°	43.9°	308.0°	20.2°	197.2°	1.133	0.234	4.7	0.17	60.6°	281.5°			60.6°	011.5°
SHF-3 UC	10×	53.6°	033.4°	083.9°	23.4°	116.7°	36.4°	303.4°	1.532	−0.581	0.3	0.18	44.4°	045.3°	*25.5°*	*085.0°*	*25.5°*	*085.0°*
SHF-3 UD	10×	70.9°	212.4°	096.8°	69.7°	322.4°	19.1°	122.4°	1.203	−0.313	1.3	0.13	80.7°	209.5°	*66.0°*	*008.0°*	*66.0°*	*008.0°*
SHF-4 LA	10×	74.6°	245.5°	019.2°	18.4°	250.8°	15.4°	155.5°	1.126	−0.453	3.5	0.11	78.0°	242.4°	*30.3°*	*250.0°*	*30.3°*	*250.0°*
SHF-4 LC	10×	86.3°	341.3°	140.6°	39.3°	158.2°	03.7°	251.3°	1.297	−0.640	4.5	0.12	74.3°	341.0°	*36.0°*	*150.0°*	*36.0°*	*150.0°*
SHF-4 UA	10×	66.9°	180.6°	149.1°	28.1°	347.7°	23.1°	090.6°	1.480	−0.659	4.7	0.15	78.2°	180.0°	*28.0°*	*354.0°*	*28.0°*	*354.0°*
SHF-4 UB	10×	44.2°	316.1°	068.9°	40.6°	017.9°	45.8°	226.1°	1.420	−0.081	2.7	0.10	34.0°	305.2°			34.0°	305.2°
SHF-4 UC	10×	54.2°	174.3°	047.8°	36.9°	207.0°	35.8°	084.3°	1.213	0.432	0.7	0.12	65.5°	173.9°			65.5°	263.9°
SHF-4 UD	10×	84.2°	294.9°	133.7°	46.0°	108.9°	05.8°	204.9°	1.341	−0.475	8.1	0.14	77.8°	293.0°	*35.5°*	*104.7°*	*35.5°*	*104.7°*
SHF-5 LE	10×	78.6°	289.8°	138.2°	40.8°	099.7°	11.4°	048.2°	1.172	−0.233	2.0	0.16	75.0°	288.0°			75.0°	018.0°
SHF-5 LF	10×	73.2°	069.3°	079.3°	70.1°	126.1°	16.8°	349.3°	1.394	−0.522	2.1	0.14	71.0°	072.0°	*51.0°*	*112.0°*	*52.0°*	*112.0°*
SHF-5 UA	10×	61.9°	169.4°	011.9°	10.5°	175.1°	28.1°	281.9°	1.098	0.188	4.1	0.08	71.6°	169.5°			71.6°	259.5°
SHF-5 UB	10×	28.0°	168.4°	106.3°	26.8°	276.7°	62.0°	016.3°	1.164	−0.182	8.7	0.16	38.0°	170.4°			38.0°	260.4°
SHF-5 UF	10×	71.3°	294.3°	046.3°	43.2°	312.9°	18.7°	316.3°	1.439	−0.128	1.7	0.21	66.4°	290.6°			66.4°	020.6°
SHF-6 LA	10×	65.4°	066.0°	053.4°	46.9°	095.3°	24.6°	323.4°	1.475	0.212	1.6	0.23	58.0°	072.0°			58.0°	162.0°
SHF-6 LB	2.5×	87.8°	243.3°	084.4°	83.9°	264.9°	02.2°	354.4°	1.213	0.236	4.6	0.46	79.0°	056.0°			79.0°	146.0°
SHF-6 LC	2.5×	61.5°	209.8°	167.8°	10.7°	023.9°	28.5°	077.8°	1.053	0.139	3.0	0.38	72.5°	208.0°			72.5°	298.0°
SHF-6 LD	2.5×	30.4°	043.7°	114.3°	27.4°	161.4°	59.6°	024.3°	1.072	−0.344	2.3	0.32	20.0°	061.8°	*19.7°*	*156.3°*	*19.7°*	*156.3°*
SHF-6 LF	2.5×	43.6°	037.1°	032.6°	21.8°	061.9°	46.4°	302.6°	1.195	−0.262	4.6	0.58	32.0°	045.5°			32.0°	135.5°
SHF-6 UA	10×	64.5°	079.9°	115.6°	54.4°	218.0°	25.5°	025.6°	1.353	0.116	8.2	0.20	60.0°	086.2°			60.0°	176.2°
SHF-6 UB	2.5×	84.8°	283.2°	039.2°	39.1°	287.5°	05.2°	309.2°	1.168	−0.421	0.8	0.51	85.3°	281.8°	*51.0°*	*288.0°*	*51.0°*	*288.0°*
SHF-6 UC	10×	13.5°	039.7°	066.6°	12.4°	105.7°	76.5°	336.6°	1.237	−0.049	1.7	0.12	06.0°	119.0°			06.0°	209.0°
SHF-6 UD	10×	76.6°	059.7°	079.1°	72.8°	109.9°	13.4°	349.1°	1.195	−0.352	3.2	0.18	68.4°	061.5°	*59.0°*	*105.0°*	*59.0°*	*105.0°*
SHF-6 UF	2.5×	08.2°	025.0°	021.1°	02.9°	045.9°	81.8°	291.1°	1.109	−0.222	2.0	0.34	03.5°	183.0°			03.5°	273.0°
SHF-6 UG	2.5×	34.6°	123.3°	111.5°	31.9°	238.8°	55.4°	021.5°	1.208	0.581	0.5	0.43	40.4°	138.2°			40.0°	228.2°

[a] P′ = Degree of anisotropy.
[b] T = Shape parameter (oblate/prolate).
[c] √F = Global Incompatibility Index.

upper contact. TB2 is morphologically similar to TB1 and comprises all the same features. These features occur in discrete layers from (1) massive at the base to (2) finely and abundantly amygdaloidal in the centre to (3) a zone of elongated vesicles to (4) a massive unit comprising aligned xenoliths ~40 cm below the upper contact (Table 1). TB4 and TB5 are massive however TB4 has a central vesicle stringer and spherulitic plagioclase (Table 1).

Only the upper contact of TB1 was sampled as the lower contact was inaccessible. All the images were obtained at 10× magnification due to the fine grain size. Of the 11 samples analysed, eight of the resultant petrofabrics had prolate fabrics (T < 0) with seven of these samples having defined the petrofabric using lineation data. In Fig. 8b, the stereographically plotted petrofabrics show a spread of data; however two average directions may be interpreted as two petrofabrics with plunge and plunge directions of 31°/240° and 28°/334° respectively. The two average petrofabrics plunge ~90° away from each other.

Three zones were sampled for TB2, the upper and lower contacts and a 0.5 m thick vesicular zone which starts ~0.5 m below the upper contact of the intrusion and is laterally continuous. Four results were obtained for the lower zone, three results within the vesicular zone and eight results from the upper contact. A combination of 2.5× and 10× magnification images were selected to represent the petrofabrics for the lower zone as the plagioclase grain size was coarser at the base of the sill. Images obtained at 10× magnification were used for the upper contact and vesicular zone. All of the samples for the lower contact show oblate shapes with the shape of the fabrics for the upper contact and vesicular zones being both prolate and oblate.

The average petrofabrics obtained for the sampled zones of TB2 all showed moderate plunge angles that plunge towards the NNW. The data from the vesicular zone showing very little variation and constrain a well-defined fabric. The average plunge and plunge direction of the lower contact, vesicular zone and upper contact are 54°/329°; 34°/343° and 46°/352° respectively (Fig. 8d). All of the results determined for the contacts and the vesicular zone plunge within a 25° directional range towards ~340°.

The upper and lower contacts of TB4 were sampled and four results were obtained from both of the contacts. Three of the results were determined using low magnification images. Four of the results showed prolate fabrics, with two of those results exhibiting strongly prolate fabrics and therefore resulting in the fabric being defined by the lineation. The data from each contact are wide-spread when stereographically represented yielding steeply inclined average fabrics (Fig. 8e). The plunge and plunge directions of the fabric in lower and upper contacts are 82°/162° and 72°/220° respectively, depicting an oblique relationship with ~60° separating the two averages.

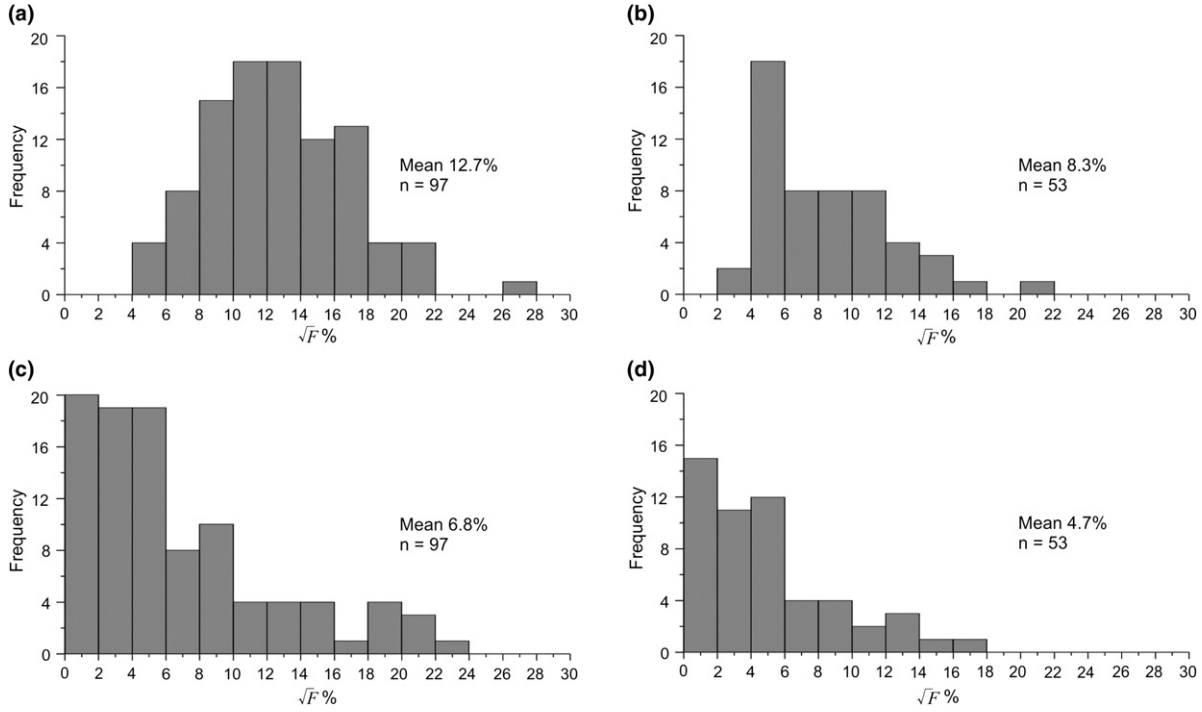

Fig. 4. Histograms depicting the frequency of √F values (% — Global Incompatibility Index) for (a) segmented images acquired at 10× magnification; (b) segmented images acquired at 2.5× magnification; (c) unsegmented images acquired at 10× magnification and (d) unsegmented images acquired at 2.5× magnification.

Four results were obtained for both the upper and lower contacts of TB5 and are stereographically presented in Fig. 8c. Three of the eight results used low magnification images to determine the fabric. Two of the four prolate-shaped fabrics were classified as strongly prolate fabrics resulting in the lineation being used to determine the petrofabrics. The average fabric of the upper contact has a plunge and plunge direction of 26°/334°. The plunge and plunge direction of the lower contact fabric is 61°/079°, plunging at a steep angle ~90° away from the average petrofabric of the upper contact.

The sills TB1, TB2 and TB5 show a similar petrofabric average with respect to the results from the upper contacts. Overall the resultant petrofabrics of the upper contact of these three intrusions plunge at ~30° towards the NNW (Fig. 8). For the contacts TB1U and TB5U the average plunge directions are aligned and plunge towards 334°.

4.5.2. Examples from Sheffield Beach

Five sills at Sheffield Beach were analyzed in this study including SHF2, SHF3, SHF4, SHF5 and SHF6 (Fig. 9). Compositionally the intrusions are all similar, with intrusions SHF4 and SHF5 showing a higher degree of alteration than the other sills. Only five results from SHF5 were conclusive in determining the petrofabric, as the other samples showed little to no fresh plagioclase. Morphologically the intrusions range in thickness from 1 m thick (SHF2) to 2.5 m thick (SHF6) and all the sills exhibit broken bridges and/or steps along the contacts with the country rocks. SHF4 and SHF6 are massive, SHF2 has a central vesicle stringer and SHF3 shows three parallel amygdaloidal stringers towards the upper contact of the intrusion.

Nine results were obtained from the samples from SHF2 (Fig. 9b), five from the lower contact and four from the upper contact. Four results were determined using samples photographed at 2.5× magnification. Four of the results showed prolate fabrics where T < 0 and of those

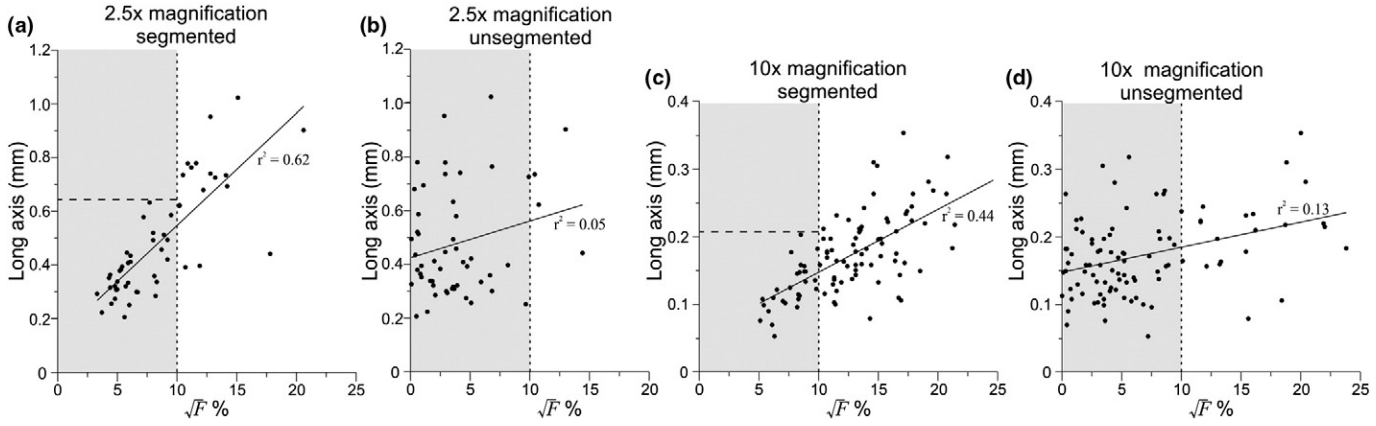

Fig. 5. Graphical representations of √F values (%) against the grain size proxy for plagioclase of (a) segmented images at 2.5× magnification; (b) unsegmented images acquired at 2.5× magnification; (c) segmented images acquired at 10× magnification and (d) unsegmented images acquired at 10× magnification.

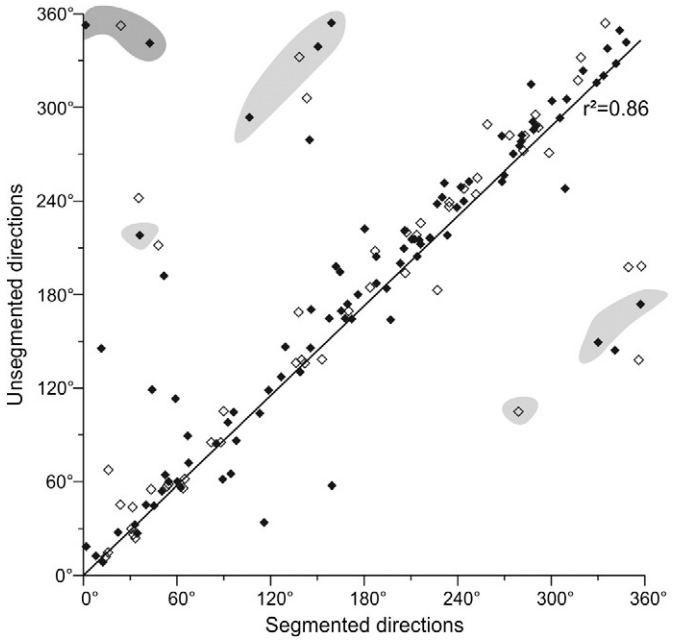

Fig. 6. Graphically represented direction values determined using the segmented and unsegmented images. The black diamonds are the results for the images at 10× magnification and the open diamonds are the results for the images at 2.5× magnification. Highlighted in dark grey are direction values with low discrepancies that do not plot on the trend line whereas the data points highlighted in light grey have values that are ~180° apart.

four samples, three lineations were used to determine the petrofabric. The majority of the petrofabric data were steeply dipping with 78% of the results exhibiting angles of >50°. Both of the contacts showed well-defined fabrics, with the average plunge and plunge directions being 77°/153° and 57°/139° for the upper and lower contacts respectively. The fabrics determined for the upper and lower contacts thus both plunge between the SE and SSE. Two results, one from the upper contact and one from the lower contact, plunge in an opposite sense

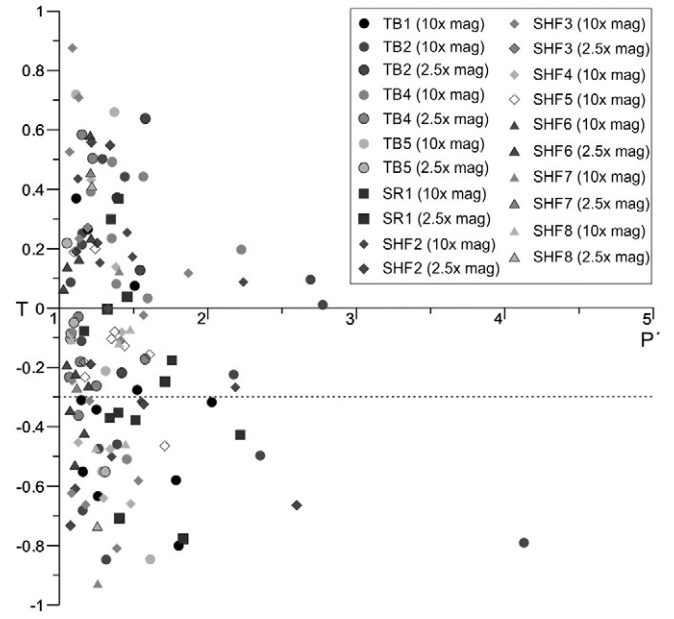

Fig. 7. Graphical illustration describing the plagioclase SPO fabric through the use of the degree of anisotropy (P′) and the shape parameter (T); where the shape of the ellipsoid is oblate when T > 0 and prolate when the T < 0. The dashed line at T = −0.3 represents the value below which the samples are distinctly prolate.

to the averages determined and appear to be in the same local position within the sill.

For the sill SHF3 eight samples yielded results with four samples obtained from both the lower and the upper contacts; all the results were determined using 10× magnification images. Six of the eight samples showed prolate fabrics, with four of these results using lineations to determine the petrofabric direction. There is a large stereographic spread of the petrofabric data for both the upper and the lower contact (Fig. 9c). Schematically, there appears to be groupings of petrofabric directions along certain portions of both the upper and lower contacts for the intrusion (Fig. 9c). The average plunge and plunge directions of the upper and lower contact are 56°/064° and 57°/012° respectively; the errors associated with these averages are above average. Both averages for the contacts plunge in a general NE direction separated by ~40°.

The samples from SHF4 were petrographically poor in quality however when photographed at 10× magnification, all of the samples yielded adequate results. Six results were obtained, four of these from the upper contact and two from the lower contact (Fig. 9d). Only one sample showed an oblate shape and four samples, out of the five prolate samples, used the lineation to determine the petrofabric. The average plunge and plunge directions of the upper and lower contacts are 45°/316° and 45°/202°, therefore the averages were separated by ~110° between the two contacts. However, due to the low number of samples for the lower contact data, this result may not be statistically significant.

For the intrusion SHF5, only five results were obtained from the nine samples prepared due to a higher degree of alteration than that of the other sills. Of the five results, three were from the upper contact and two were from the lower contact. All five of these results were obtained using 10× magnification images. Four of the samples showed prolate fabrics with one result utilising the lineation to determine the petrofabric. As there is a wide spread of directional data, as seen when stereographically presented, the angles of the resultant fabric are steep (Fig. 9e). The average plunge and plunge directions of the upper and lower contact are 69°/280° and 70°/089° respectively and plunge in opposite directions with respect to one another.

Eleven samples from the upper and lower contacts of SHF6 yielded results, with the majority of the samples (64%) utilising the 2.5× magnification images. Six of the results exhibited prolate shapes with three of those samples determining the petrofabric through the use of the lineation. The petrofabric for the lower contact was well-defined with an average plunge and plunge direction of 58°/153°. For the upper contact, two population averages were inferred, showing a strong fabric plunging towards the SSW and a stronger correlation of results towards the W as seen in Fig. 9(f). The plunge and plunge directions for the two average petrofabrics for the upper contact are 37°/209° and 18°/279°. Between the upper and lower contacts the relationships between the petrofabric averages are oblique.

For the intrusions sampled at Sheffield Beach there is very little similarity between the results from the separate sills. No two sills show the same average petrofabrics for either the upper or the lower contacts. The only directions that coincide are the upper contact averages of SHF5 and SHF6 which plunge in a westerly direction.

5. Discussion

5.1. Importance of √F, grain size and image segmentation

When images are segmented the grains are analysed in the set compartment they have been separated into. This causes grains (particularly when enlarged at higher magnifications) to be intersected and truncated by these segment boundaries or compartments. As the plagioclase crystals here are predominantly elongate, the segmented grains inaccurately represent the long and short grain axes. This can then affect the shape and therefore the ellipse from each image which then combined could alter the ellipsoid of the result in terms of the √F values.

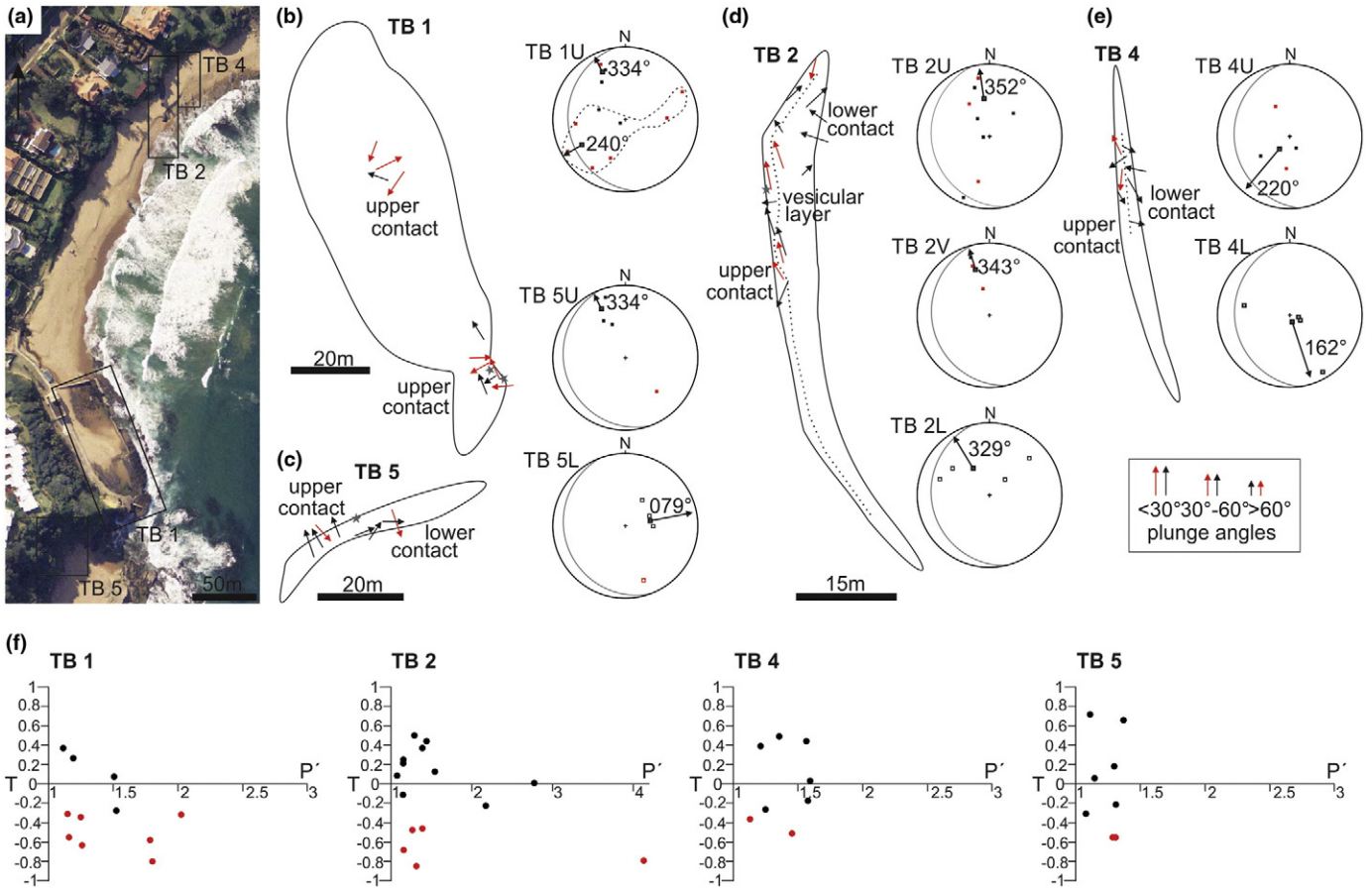

Fig. 8. (a) An aerial photograph of Thompson's Bay showing the layout and localities of the sills TB1, TB2, TB4 and TB5. (b) Samples from the upper contact of TB1 shown spatially along the exposed upper surface of the intrusion. The grey stars represent ropy-flow structures ~10 cm below the upper contact. The stereographic projection of TB1 shows the grouping of the results into two perpendicular averages. (c) Upper and lower contact results for TB5 and the stereographically projected fabrics, the grey star represents a small broken bridge along the upper contact. (d) The results from TB2 are separated into the upper and lower contacts and the vesicular layer (right of the dashed line), the results for each layer/contact are stereographically presented and all plunge in the same general direction. The grey star represents an exposure of a layer of preferentially aligned elongated vesicles. (e) Schematically the upper and lower contacts of TB4 are separated by a dashed line with the data projected stereographically for each contact. Black arrows and red arrows represent fabrics in the schematics determined using the foliation and the lineation respectively. For the stereographic projections, the black points represent the foliation data, the red points represent the lineation data and the grey great circle is the dip and strike about which the data points have been restored to the horizontal. (f) P′/T plots for TB1, TB2, TB4 and TB5 with the black circles and red circles representing samples where the fabric was determined using the foliation and the lineation respectively.

$\sqrt{F}$ values obtained through the use of the SPO-2003 programme calculate the incompatibility of the fit of the three 2-D ellipses into one 3-D ellipsoid. As the $\sqrt{F}$ increases, the compatibility of the final ellipsoid decreases. Results with $\sqrt{F}$ values of less than 10% are desirable therefore 10% $\sqrt{F}$ has been used as a threshold error above which the results are disregarded as being inaccurate in defining the sample petrofabric. The segmentation of the images has a pronounced effect on the $\sqrt{F}$ values when compared to the unsegmented images for images taken at both higher and lower magnifications. The images taken at 10× magnification showed a mean $\sqrt{F}$ value of 12.7% for the segmented images and 6.8% $\sqrt{F}$ for the unsegmented images. Only 27.8% of the segmented data is below 10% $\sqrt{F}$ whereas 78.4% of the unsegmented data are below the $\sqrt{F}$ 10% threshold. This is also the case with the lower magnification images but not to the same extent as the higher magnification data.

One way of reducing the $\sqrt{F}$ values for the results is to ensure the images are obtained at the ideal magnification for the size of the plagioclase grains. A threshold grain size can be determined using the segmented and unsegmented data from the lower and higher magnification data. At 10× magnification all of the results with $\sqrt{F}$ values <10% have long axis lengths of <0.2 mm. Therefore 0.2 mm has been designated as the grain size threshold for the grain size proxy to delineate the millimetre scale limit at which higher magnification images should be obtained. If images are taken at the correct magnification, the error values for the results should be greatly reduced.

It thus appears that the problem with high $\sqrt{F}$ values is directly related to the image segmentation process. There is little difference between the actual direction results acquired when using the segmented versus the unsegmented technique as observed by the r^2 of 0.86 for the 150 results (Fig. 6). The errors ($\sqrt{F}$ values) observed from the results of the segmented images are almost always higher than with the results from the unsegmented images (Fig. 4). Therefore in order to reduce the error to a minimum, the segmented image data were disregarded and the unsegmented analysis process was relied upon instead. Using these parameters would allow for the most accurate results to be determined for the most compatible ellipsoids.

5.2. Shape constraints

The actual result that should be used for each sample site can be further constrained using the shape of the fabric as this affects the petrofabric result. For strongly prolate fabrics ($T < -0.3$) the minimum and intermediate axes of the shape ellipse become comparable in length, therefore the maximum axis defines the lineation that may be used to infer the plunge and plunge direction of the petrofabric.

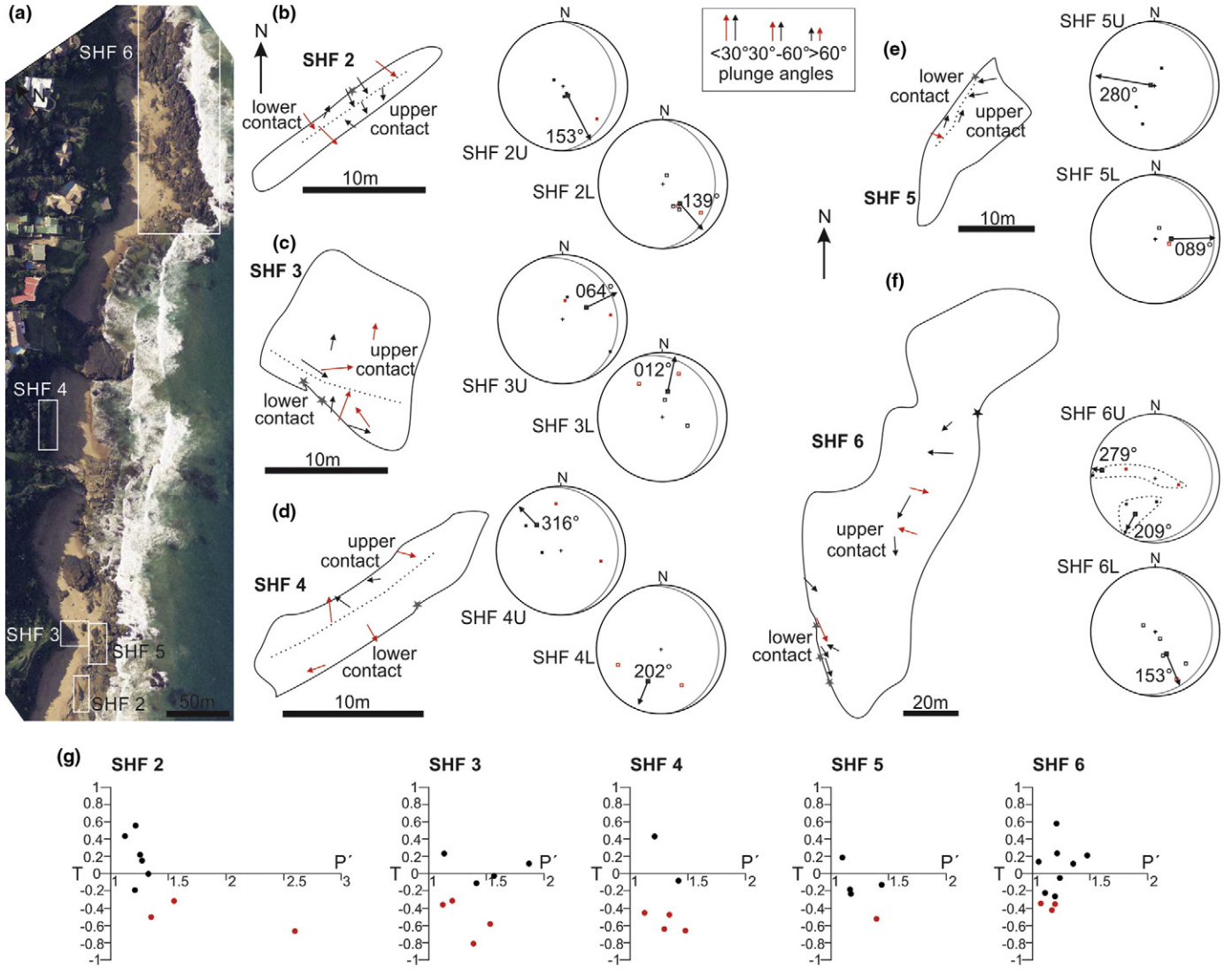

Fig. 9. (a) An aerial photograph of the southern portion of Sheffield Beach outlining the five sills sampled. (b) Schematic and stereograms showing the petrofabric directions determined for the upper and lower contacts of SHF2. The grey arrow represents a broken bridge remnant along the upper contact of the sill. (c) A schematic of SHF3 with the upper and lower contact results separated by a dashed line. Note the similarity of adjacent results along both the upper and lower contacts. The grey arrows indicate broken bridges preserved along the sill's lower contact. (d) The upper and lower contact results from SHF4 represented schematically and stereographically. The grey arrow indicates the position of a large step for the upper and lower contacts of the intrusion. (e) The upper and lower contact results of SHF5 are schematically separated by a dashed line. A few small steps are noted along the upper contact of the intrusion and indicated with a grey star. The stereographic projections of the sill data show that the petrofabrics from the upper contact dip in the opposite direction the lower contact data. (f) The largest sill sampled is SHF6 and the dolerite has intruded into a previous dolerite intrusion. The schematic and the stereograms show two distinct plunge directions along the upper contact and a consistent direction along the lower contact. The grey arrows represent small broken bridges of dolerite material whereas the black arrow indicates a large broken bridge structure of country rock material. (g) P′/T plots for SHF2, SHF3, SHF4, SHF5 and SHF6 with the black circles and red circles representing samples where the fabric was determined using the foliation and the lineation respectively.

Where $T > -0.3$ the oblate fabric is defined using the dip and azimuth of the plane defined by the minimum axis.

This will determine a single result per sample site which would be the most theoretically and statistically robust. This is obtained by disregarding the segmented image data and thresholding the grain size in order to elucidate which images should be used for each analysis. Where there was an overlap of accurate results between the magnifications for one sample, the sample that exhibited the lower $\sqrt{F}$ value was manually selected; this was undertaken for 6% of the data.

5.3. Petrofabrics as magma flow indicators

The petrofabrics determined for the samples may have formed as a result of magma flow. In order to establish the origin of a fabric within an intrusion, certain criteria must be analysed such as the timing of fabric formation and the regional setting. It is apparent from the host rocks that there have been no regional ductile deformations or metamorphism associated with or post-dating the intrusion of these sills. The fabrics observed in the intrusions are therefore the result of internal processes and are a product of strain within the magma (Nicholas, 1992; Paterson et al., 1998). Such strain may be brought about by the original magma flow and may be affected by internal processes such as magma convection or surges (Benn and Allard, 1989; Paterson et al., 1998).

A fabric pattern is typically formed during the last stages of magma injection and preserves the final increment of strain before the magma nears solidi and crystallises (Paterson et al., 1998). If there has not been any reorganisation of the particles in the magma before it crystallises, such as flattening due to overburden pressure, the preserved fabric may have formed in the direction of magma flow.

The dolerite sills studied here are typically thin (<2 m thick) and concordant with the stratigraphy. Therefore these intrusions will not have been affected by processes generally associated with large scale

intrusions and magma chambers such as magma surges, convection and post-emplacement processes. Consequently it is likely that the preserved fabrics are related to the process of magma injection and flow assuming that there has been no post-intrusion flattening.

In order to infer magma flow in an intrusion, an imbrication of the crystal phases along the contacts of the intrusion (Fig. 8a) will typically dip in opposite directions along opposing margins therefore allowing a flow within the intrusion to be assumed (Geoffroy et al., 2002; Gil-Imaz et al., 2006). The dip of this crystal alignment is ideally between 15° and 20° degrees from the wall of the intrusion with the direction of dip inferring the magma flow (Blanchard et al., 1979). It has been shown that petrofabrics may preserve the primary magma flow patterns in igneous intrusions allowing these petrofabrics to infer magma flow directions (Archanjo et al., 1995; Hastie et al., 2011b; Horsman et al., 2005; Launeau and Cruden, 1998). The petrofabrics determined here for the upper and lower contacts of the intrusion will be used as a proxy for magma flow within these intrusions. The plunge and plunge directions of the fabrics for each sample site denote a petrofabric/flow vector about which the magma flow will be inferred.

5.4. The use of petrofabrics: examples from Thompson's Bay and Sheffield Beach

The sills from Thompson's Bay and Sheffield Beach were analysed at high and low magnification and analysed petrographically using the above parameters and techniques. The results that represent the determined petrofabrics for each contact were selected based on the Global Compatibility Index ($\sqrt{F}$ values $<10\%$) and a grain size threshold of 0.2 mm. Therefore for each sample there was one result, which may be a foliation or a lineation dependant on the shape of the ellipsoid, and are stereographically represented as dip and azimuth or plunge and plunge direction respectively.

5.4.1. Thompson's Bay

For the sills at Thompson's Bay there is a correlation between the petrofabric data for the upper contacts of TB1, TB2 and TB5 whilst the results for TB4 show very little similarity to these sills. Using these petrofabric directions to imply magma flow would infer magma flow towards the NNW for these intrusions.

The upper contact of TB1 shows two strong petrofabric directions and possible magma flow towards 240° and 334°, however there appears to be overlap of these two directions when the data are plotted schematically at the sampling points (Fig. 8b). All of the petrofabric data for TB2 implies a direction of magma flow towards the NNW as all the average fabrics plunge in the same direction. Schematically there are minor discrepancies along the upper contact where there are flow vectors that differ in plunge direction, but overall the average fabrics are well defined. In order to predict magma flow using the data from the upper and lower contact, the average directions obtained from these contacts should dip in opposite directions. For TB2 however, the fabrics are coaxial.

For the sills TB4 and TB5 the average fabrics determined for the upper and lower contacts are oblique showing a weak relationship between the contacts. The fabric for the upper contact of TB5 is well defined; however the fabrics determined for both the contacts of TB4 and the lower contact of TB5 are not well defined as seen when the flow vectors are plotted schematically (Fig. 8c and e). Therefore the magma flow for TB4 may not be discernible from the results. For TB5 though, the upper contact data may be relied upon to infer magma flow. This indicates flow towards the NNW which coincides with the magma flow directions inferred for both TB1 and TB2. This would imply that the magma flow within these three sills was towards a NNW direction allowing a feeder point to the SSE to be inferred.

5.4.2. Sheffield Beach

For the sills at Sheffield Beach, the average petrofabric directions determined for the contacts of SHF2 are well defined and plunge in the same general direction. These show a coaxial relationship between the two contacts, implying magma flow towards the SE-SSE.

For SHF3 the average fabrics are not well defined. According to the schematic, there are certain areas along the upper and lower contacts where the fabrics may be grouped according to the plunge directions (Fig. 9c). This may have been the result of secondary fabrics unrelated to magma flow or could represent a complex flow pattern related to non-coaxial magmatic flow (e.g., Nicholas, 1992). The broken bridge obstacles along the lower contact may also have contributed to the non-coaxial fabrics determined for these samples.

The samples from SHF4 (Fig. 9e) show a higher degree of alteration than the other sills and may explain why the average fabrics have been poorly defined. Although more detail might be attainable through the analysis of the individual data points, overall these fabrics may not accurately depict a magma flow direction.

SHF5 (Fig. 9c) is the only intrusion analysed to show an "ideal" fabric (Gil-Imaz et al., 2006) where the average petrofabric directions dip in opposite directions on the upper and lower contacts. Although there are few data points available according to the average petrofabric data, magma flow may be inferred towards the W.

The lower contact data for SHF6 (Fig. 9f) is well defined as plunging towards the SSE, whereas there are two distinct population directions present in the data from the upper contact. This is evident when these petrofabric vectors are plotted schematically. The data are spread out as such, no single average direction may be assigned to an area along the upper contact. In this scenario, magma flow is difficult to infer as the petrofabrics from the upper and lower contacts are oblique and the upper contact data shows two distinct directions. As the intrusion is within an older dolerite intrusion, it may be possible that the multiple flows occurred at this locality with no significant hiatus between magma pulses. If that is the case, then both contact's data should be considered however more detailed analyses may need to be undertaken in order to fully constrain magma flow.

Overall for Sheffield Beach, the sills show no clear link between the intrusion flow directions as with the sills studied at Thompson's Bay. Therefore no distinct regional pattern of magma flow may be inferred. It is possible that the intrusions originate from separate magma sources but these fabric patterns need to be analyzed in greater detail.

5.5. Summary

If these fabrics were preserved through the development of flow-related fabrics, the results indicate that the flow within sills is more complicated than flow within dykes. With regards to sills, the fabrics determined for the lower contacts may shed some light on the subject of preserved magma flow within planar intrusions.

For the intrusions analyzed here, there is little to no relationship with the data obtained for the lower contacts of the sills. Assuming that the upper contact fabrics would imply a magma flow in the same direction as the fabrics were plunging (Fig. 10), it is possible the upper contact data could be relied upon to infer the direction of magma flow without the lower contact data. This would only be plausible in situations where no other fabrics (flow-related or not) may have been preserved along the lower contact zone.

An explanation for the unusual fabric pattern obtained between the lower and upper contacts may be related to magma flow around obstacles and features related to the lithological contacts with the country rocks, such as broken bridges. These features imply a magma flow oriented parallel to the strike of the bridge where magma segments have coalesced to form a larger intrusion (Hansen and Cartwright, 2006; Hutton, 2009; Pollard et al., 1975; Rickwood, 1990). These obstacles protrude into the area where the magma is injected and may locally deflect flow (e.g., Nicholson and Pollard, 1985). Such deflections may

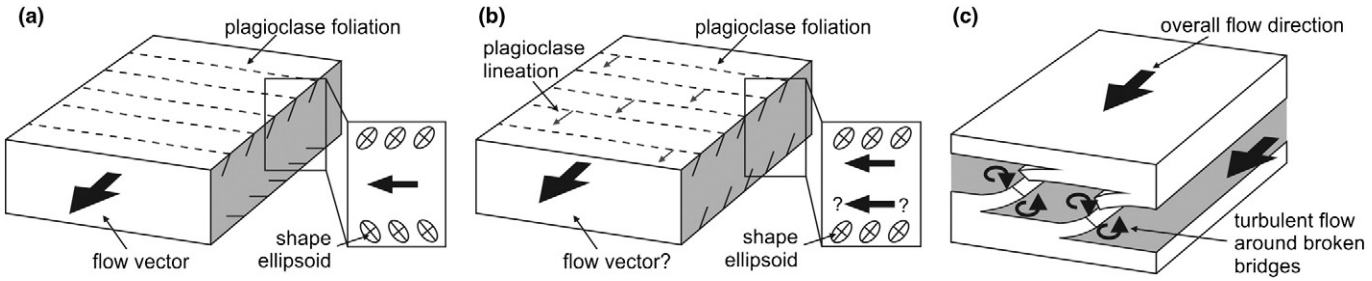

Fig. 10. (a) Illustration showing the expected imbrications of crystals along the upper and lower contact with the ellipsoids implying the direction of magma flow (after Gil-Imaz et al., 2006). (b) Imbrication pattern obtained for the sills TB2 and SHF2 where the upper and lower contact ellipsoids plunge towards the same direction; here implied flow along the bottom does not corroborate with that from the upper contact. Both the foliation and the lineation have been used to define the petrofabric. (c) Illustration representing the formation of broken bridges through the linkage of en echelon fractures; flow around the remnants of the broken bridges creates turbulent flow along these obstacles, after Nicholson and Pollard (1985).

cause turbulent flow resulting in displacement gradients within the magma becoming highly variable. Consequently no relationship may be inferred between the overall magma flow and the local fabric that is preserved (Martin and Nokes, 1988). However, turbulent flow will normally not occur when magma is near solid and the final phase of strain will be preserved (Brandeis and Marsh, 1989), so any fabric abnormality near these obstacles may not necessarily be explained by this process.

It may be more fitting to use these petrofabrics to infer small-scale features within an intrusion, such as localised pockets of increased strain or subtle flow perturbations due to the shape of the intrusion chamber. The more numerous the samples from particular portions of the intrusion, the more detailed the strain analysis and inferred flow map. However this would be an incredibly time consuming process and may highlight even more small scale features rather than a large scale magma flow direction as desired.

Through the use of the grain size threshold, capturing photomicrographs has been simplified where one image may be obtained for analysis. Likewise neglecting to segment the image will not significantly alter the result; however it can negatively affect the Global Incompatibility Index. Therefore through the careful selection of magnification when obtaining photomicrographs, by not segmenting the image during the SPO process and with the application of shape parameter data, good agreement of petrofabrics and inferred flow vectors between samples, from the same intrusion, may be produced.

6. Conclusions

Dolerite sills vary in grain size and texture so it is important to incorporate this variance in plagioclase grain size into petrographic analyses. This increases the reliability of the results and allows for more accurate petrofabrics to be determined. For the sills studied here, a standardised value of 0.2 mm long axis length has defined the threshold grain size which, when exceeded, indicates that photomicrographs should be obtained at a lower magnification (i.e., 2.5×) and not at a higher magnification (i.e., 10×).

When the images analyzed are segmented, here into 9 segments, the resultant ellipsoids have larger incompatibility indices ($\sqrt{F}$ values) between ellipses than when not segmented. As the results do not significantly vary from the finite ellipsoids obtained by not segmenting the images, it can be concluded that the images analyzed should not be segmented during the SPO process. Using a shape parameter allows the petrofabric to be further constrained by taking into account the maximum axis of the ellipsoid (the lineation) where the fabrics are strongly prolate.

It was concluded that the most reliable technique that produces the most accurate petrofabric results is not to segment the image but to photograph the sample at the appropriate magnification. This technique was successfully applied to twelve sills from the KwaZulu-Natal North Coast between Thompson's Bay and Sheffield Beach and the derived petrofabrics were used to infer magma flow within these intrusions.

Acknowledgements

The authors would like to thank Laurent Arbaret and an anonymous reviewer for their constructive reviews of a previous version of this paper and Patrick Launeau for assistance with the SPO-2003 programme. L. Hoyer would like to thank S. Aberdeen, K. Benallack, D. Cousins, A. Krebs, K. Ridgeway, L. Salazmann, J. Weitz and E. Wiles for their assistance during drilling. The authors also acknowledge Mukesh Seyambu of the University of KwaZulu-Natal for assistance with thin section preparation. L. Hoyer acknowledges a free-standing NRF Scarce Skills Scholarship.

References

Archanjo, C.J., Launeau, P., 2004. Magma flow inferred from preferred orientation of plagioclase of the Rio Ceará-Mirim dyke swarm (NE Brazil) and its AMS significance. In: Martín-Hernández, F., Lüneberg, C.M., Aubourg, C., Jackson, M. (Eds.), Magnetic Fabric: Methods and Applications. Special Publication of the Geological Society of London 238, pp. 285–298.

Archanjo, C.J., Launeau, P., Bouchez, J.L., 1995. Magnetic fabric vs. magnetite and biotite shape fabrics of the magnetite-bearing granite pluton of Gameleiras (Northeast Brazil). Phys. Earth Planet. Inter. 86, 63–75.

Archanjo, C.J., Silva, M.G., Castro, J.C., Launeau, P., Trindade, R.I.F., Macedo, J.W.P., 2006. AMS and grain shape fabric of the Late Palaeozoic diamictites of the Southeastern Paraná Basin, Brazil. J. Geol. Soc. 163, 95–106.

Archanjo, C.J., Campanha, G.A.C., Salazar, C.A., Launeau, P., 2012. Using AMS combined with mineral shape preferred orientation analysis to understand the emplacement fabrics of the Apiaí gabbro-norite (Ribeira Belt, SE Brazil). Int. J. Earth Sci. 101, 731–745.

Benn, K., Allard, B., 1989. Preferred mineral orientations related to magmatic flow in ophiolite layered gabbros. J. Petrol. 30, 925–946.

Blanchard, J.-P., Boyer, P., Gagny, C., 1979. Un nouveau critere de sens de mise en place dans une caisse filonienne: Le "pincement" des mineraux aux epontes: Orientation des minéraux dans un magma en écoulement. Tectonophysics 53, 1–25.

Brandeis, G., Marsh, B.D., 1989. The convection liquidus in a solidifying magma chamber: a fluid dynamic investigation. Nature 339, 613–616.

Geoffroy, L., Callot, J.P., Aubourg, C., Moreira, M., 2002. Is the common use of AMS in mafic dykes scientifically correct? Terra Nova 14, 183–190.

Gil-Imaz, A., Pocoví, A., Lago, M., Galé, C., Arranz, E., Rillo, C., Guerrero, E., 2006. Magma flow and thermal contraction fabric in tabular intrusions inferred from AMS analysis. A case study in a late-Variscan folded sill of the Albarracı'n Massif (southeastern Iberian Chain, Spain). J. Struct. Geol. 28, 641–653.

Hansen, D.M., Cartwright, J., 2006. The three-dimensional geometry and growth of forced folds above saucer-shaped igneous sills. J. Struct. Geol. 28, 1520–1535.

Hastie, W.W., Aubourg, C., Watkeys, M.K., 2011a. When an inverse fabric is not inverse: an integrated AMS-SPO study in MORB-like dykes. Terra Nova 23, 49–55.

Hastie, W.W., Aubourg, C., Watkeys, M.K., 2011b. Significance of magnetic and petrofabric in Karoo-feeder dykes, northern Lebombo. Tectonophysics 513, 96–111.

Hastie, W.W., Watkeys, M.K., Aubourg, C., 2013. Characterisation of grain-size, shape and orientation of plagioclase in the Rooi Rand dyke swarm, South Africa. Tectonophysics 583, 145–157.

Horsman, E., Tikoff, B., Morgan, S., 2005. Emplacement-related fabric and multiple sheets in the Maiden Creek sill, Henry Mountains, Utah, USA. J. Struct. Geol. 27, 1426–1444.

Hutton, D.H.W., 2009. Insights into magmatism in volcanic margins: bridge structures and a new mechanism of basic sill emplacement — Theron Mountains, Antarctica. Pet. Geosci. 15, 269–278.

Jelinek, V., 1981. Characterisation of the magnetic fabric of rocks. Tectonophysics 79, 63–67.

Jourdan, F., Féraud, G., Bertrand, H., Watkeys, M.K., Renne, P.R., 2008. $^{40}Ar/^{39}Ar$ ages of the sill complex of the Karoo large igneous province: implications for the Pliensbachian–Toarcian climate change. Geochem. Geophys. Geosyst. 9, Q06009. http://dx.doi.org/10.1029/2008GC001994.

Kattenhorn, S.A., 1994. Mechanisms of sill and dyke intrusion. Unpublished MSc dissertation, University of Natal, Durban.149 pp.

Launeau, P., 2004. Mise en évidence des écoulements magmatiques par analyse d'images 2-D des distributions 3-D d'Orientations Préferentielles de Formes. Bull. Soc. Geol. Fr. 175, 331–350.

Launeau, P., Bouchez, J.-L., 1992. Mode et orientation préférentielle de forme des granites par analyse d'images numériques. Bull. Soc. Geol. Fr. 163, 721–732.

Launeau, P., Cruden, A.R., 1998. Magmatic fabric acquisition mechanisms in a syenite: results of a combined anisotropic of magnetic susceptibility and image analysis study. J. Geophys. Res. 103, 5067–5089.

Launeau, P., Robin, P.-F., 1996. Fabric analysis using the intercept method. Tectonophysics 267, 91–119.

Launeau, P., Robin, P.-Y.F., 2005. Determination of fabric and strain ellipsoids from measured sectional ellipses—implementation and applications. J. Struct. Geol. 27, 2223–2233.

Launeau, P., Archanjo, C.J., Picard, D., Arbaret, L., Robin, P.-Y.F., 2010. Two- and three-dimensional shape fabric analysis by the intercept methods in grey levels. Tectonophysics 492, 230–239.

Liss, D., Hutton, D.H.W., Owens, W.H., 2002. Ropy flow structures: a neglected indicator of magma-flow direction in sills and dikes. Geology 30, 715–718.

Marsh, B.D., 1989. Magma chambers. Ann. Rev. Earth Planet. Sci. 17, 439–474.

Martin, D., Nokes, R., 1988. Crystal settling in a vigorously convecting magma chamber. Nature 332, 534–536.

Nicholas, A., 1992. Kinematics in magmatic rocks with special reference to gabbros. J. Petrol. 33, 891–915.

Nicholson, R., Pollard, D.D., 1985. Dilation and linkage of echelon cracks. J. Struct. Geol. 7, 583–590.

Paterson, S.R., Fowler Jr., T.K., Schmidt, K.L., Yoshinobu, A.S., Yuan, E.S., Miller, R.B., 1998. Interpreting magmatic fabric patterns in plutons. Lithos 44, 53–82.

Pollard, D.D., Muller, O.H., Dockstader, D.R., 1975. The form and growth of fingered sheet intrusions. Geol. Soc. Am. Bull. 86, 351–363.

Rickwood, P.C., 1990. The anatomy of a dyke and the determination of propagation and magma-flow directions. In: Parker, A.J., Rickwood, P.C., Tucker, D.H. (Eds.), Mafic Dykes and Emplacement Mechanisms. Proceedings of the Second International Dyke Conference, Adelaide, South Australia. 2, pp. 81–100.

Schofield, N., Stevenson, C., Reston, T., 2010. Magma fingers and host rock fluidization in the emplacement of sills. Geology 38, 63–66.

Tait, S., Jaupart, C., 1990. Physical processes in the evolution of magmas. In: Nicholls, J., Russell, J.K. (Eds.), Modern methods of igneous petrology: understanding magmatic processes. Reviews in Mineralogy and Geochemistry 24, pp. 125–152.

Tarling, D.H., Hrouda, F., 1993. The Magnetic Anisotropy of Rocks. Chapman and Hall, London, p. 218.

Wylie, J.J., Helfrich, K.R., Dade, B., Lister, J.R., Salzig, J.F., 1999. Flow localization in fissure eruptions. Bull. Volcanol. 60, 432–440.

Yoshinobu, A.S., Okaya, D.A., Paterson, S.R., 1998. Modelling the thermal evolution of fault-controlled magma emplacement models: implications for the solidification of granitoid plutons. J. Struct. Geol. 20, 1205–1218.

- APPENDIX B –

SUPPLEMENTARY INFORMATION

1. **Locality map of the study area**

2. **Sketch maps of the structural data from the study area**
   (a) Southern Thompson's Bay
   (b) Northern Thompson's Bay and Shaka's Rock
   (c) Southernmost Sheffield Beach
   (d) Central Sheffield Beach
   (e) Northern Sheffield Beach

3. **Sketch maps showing the sample localities for**
   (a) Thompson's Bay and Shaka's Rock
   (b) Southern Sheffield Beach
   (c) Northern Sheffield Beach

4. **Tabulated sill and sample data**
   (a) Sill Properties
   (b) Sill Characteristics
   (c) Representative photomicrographs from the sampled contacts

5. **Ellipsoid tensor diagrams**
   (a) Raw data for sample TB-3C(V) acquired at 10 x magnification
   (b) Raw data for sample SHF-3UA acquired at 10 x magnification
   (c) Raw data for sample SHF-11LA acquired at 10 x magnification

6. **Tabulated SPO data**
   (a) 2-D ellipse data for samples obtained at 2.5 x magnification
   (b) 2-D ellipse data for samples obtained at 10 x magnification
   (c) 3-D ellipse data for samples from Thompson's Bay and Shaka's Rock
   (d) 3-D ellipse data for samples from Sheffield Beach

7. **Magnetic mineralogy data**
   (a) Susceptibility-Temperature (K-T) Curves
   (b) Low Temperature Demagnetisation Curves
   (c) Hysteresis Curves
   (d) First Order Reversal Curve plots (H_u-H_c plots)

8. **Tabulated AMS data**
   (a) Results from Thompson's Bay and Shaka's Rock
   (b) Results from Sheffield Beach

1. Locality map of the study area

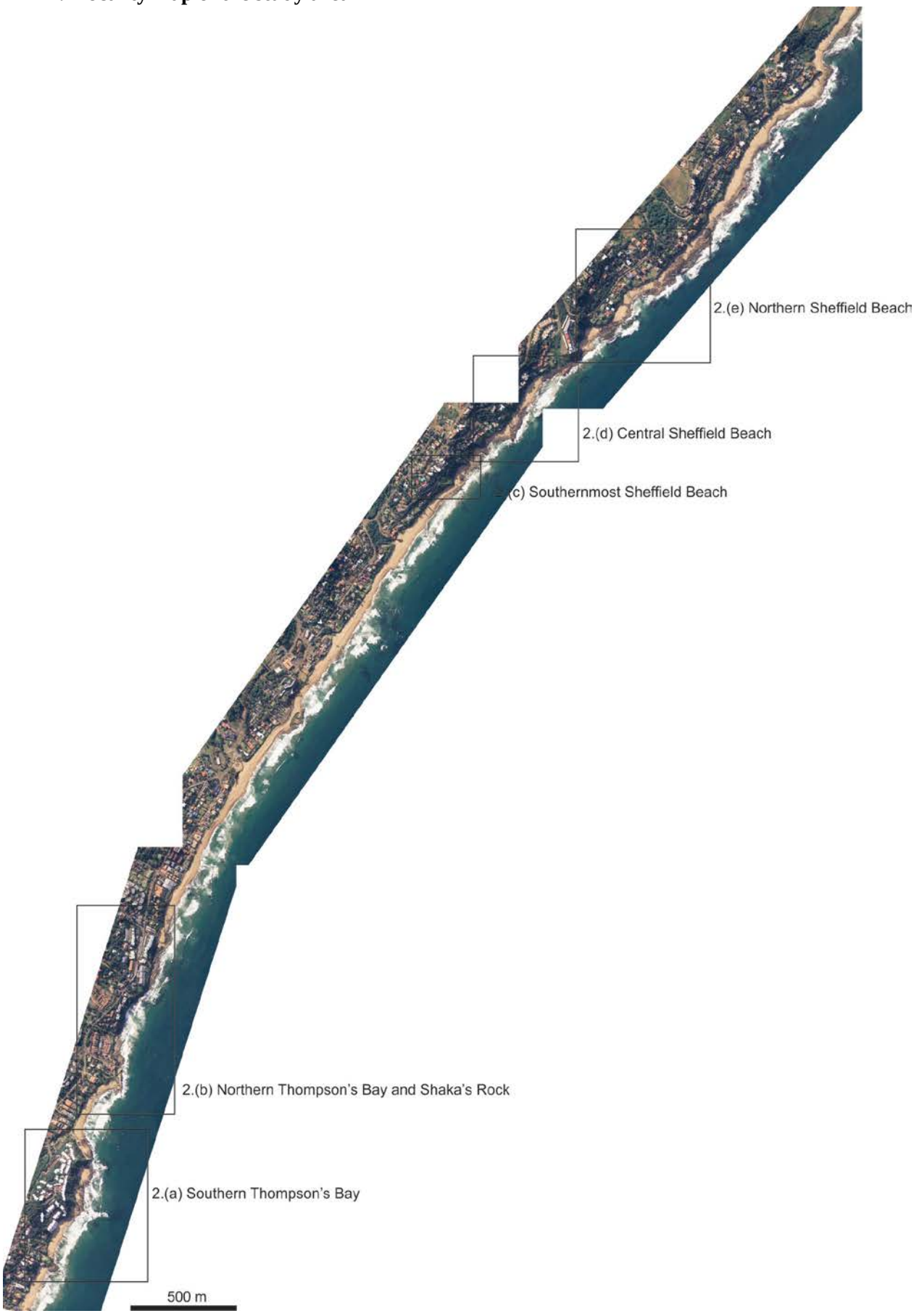

2. Sketch maps of the structural data from the study area

(a) Sketch map of the structural data from Southern Thompson's Bay

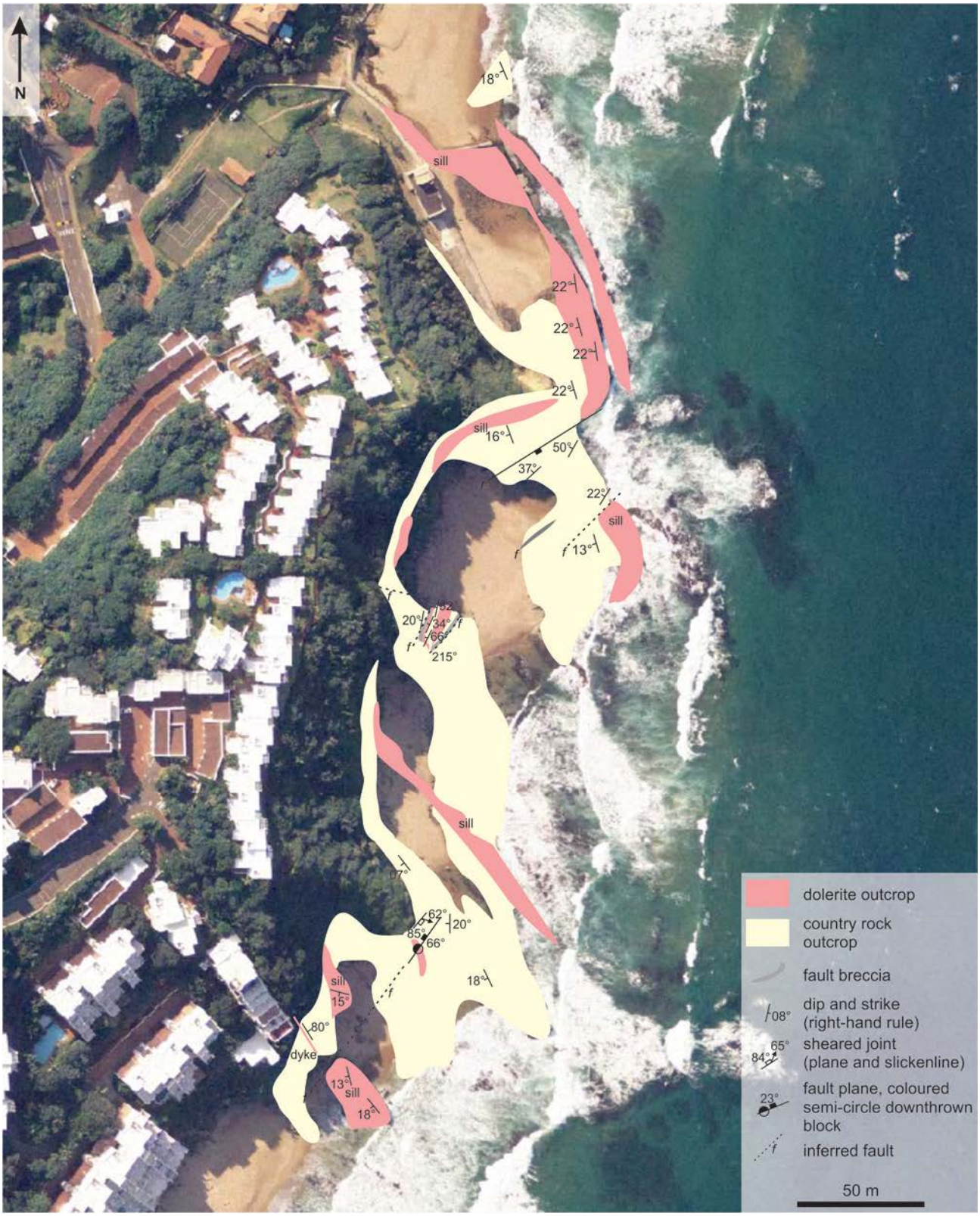

(b) Sketch map of the structural data from Northern Thompson's Bay and Shaka's Rock

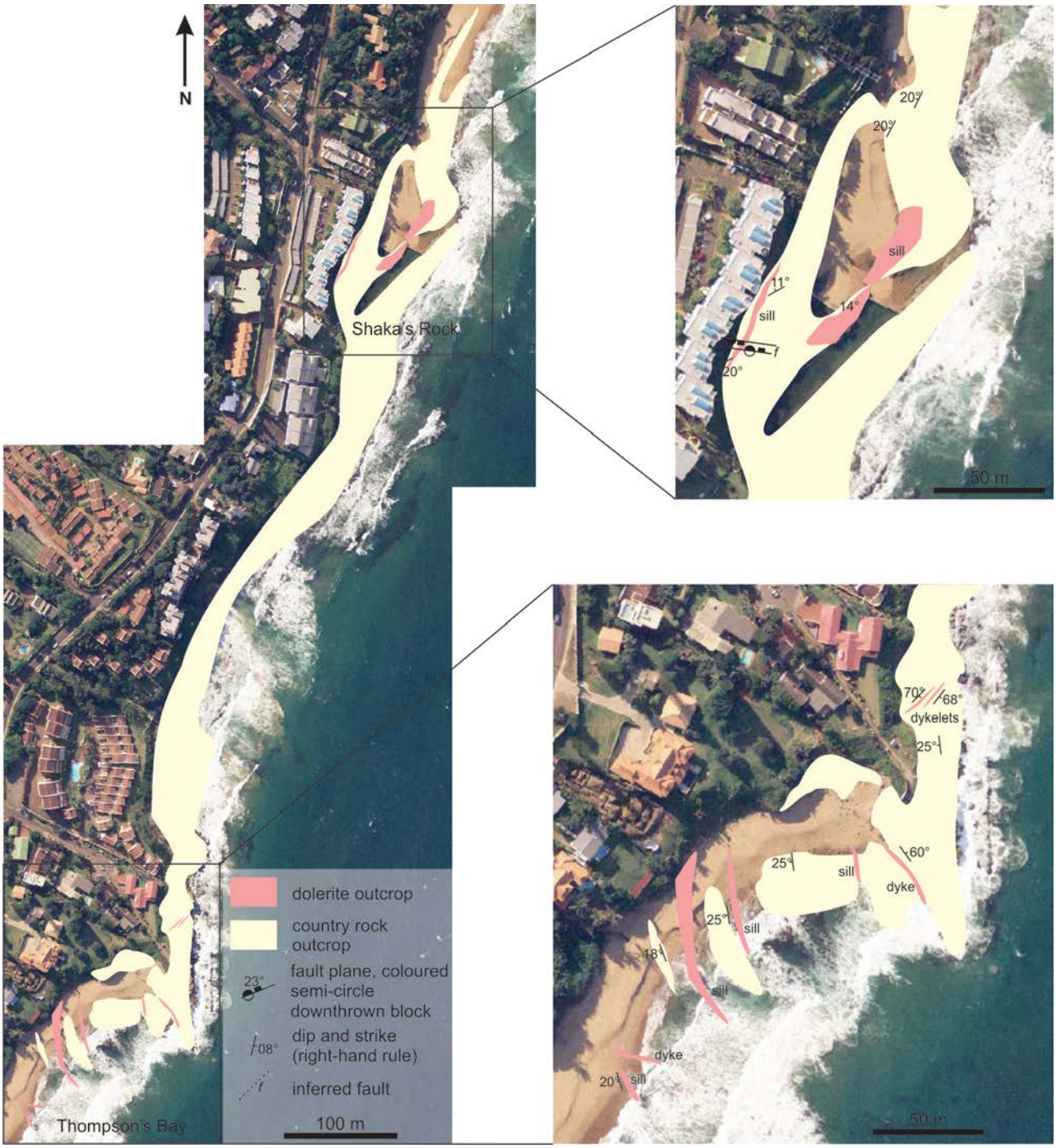

(c) Sketch map of the structural data from Southern Sheffield Beach

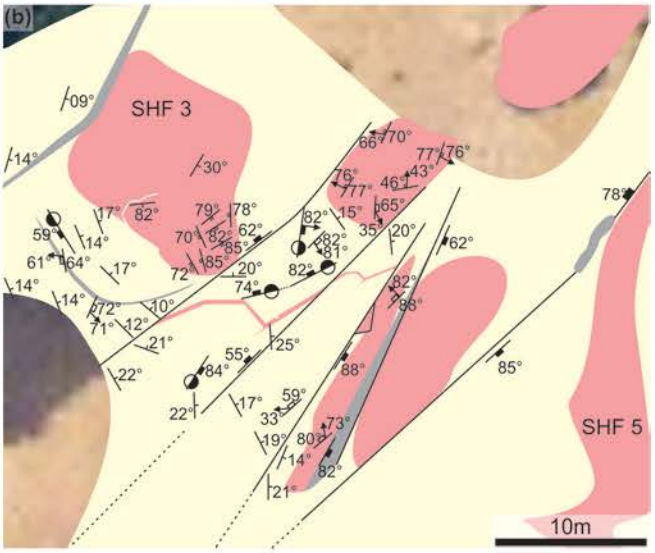

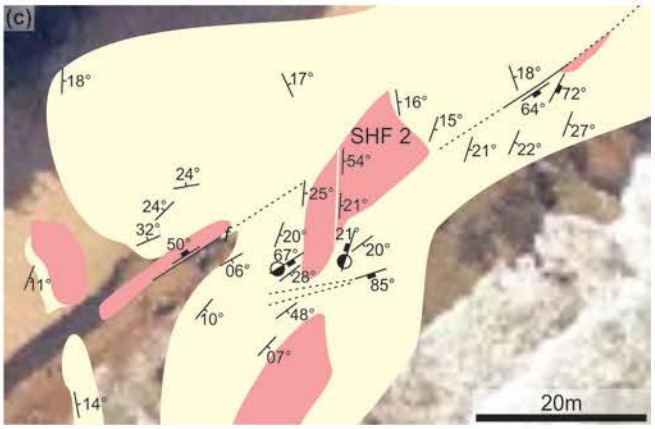

(d) Sketch map of the structural data from Central Sheffield Beach

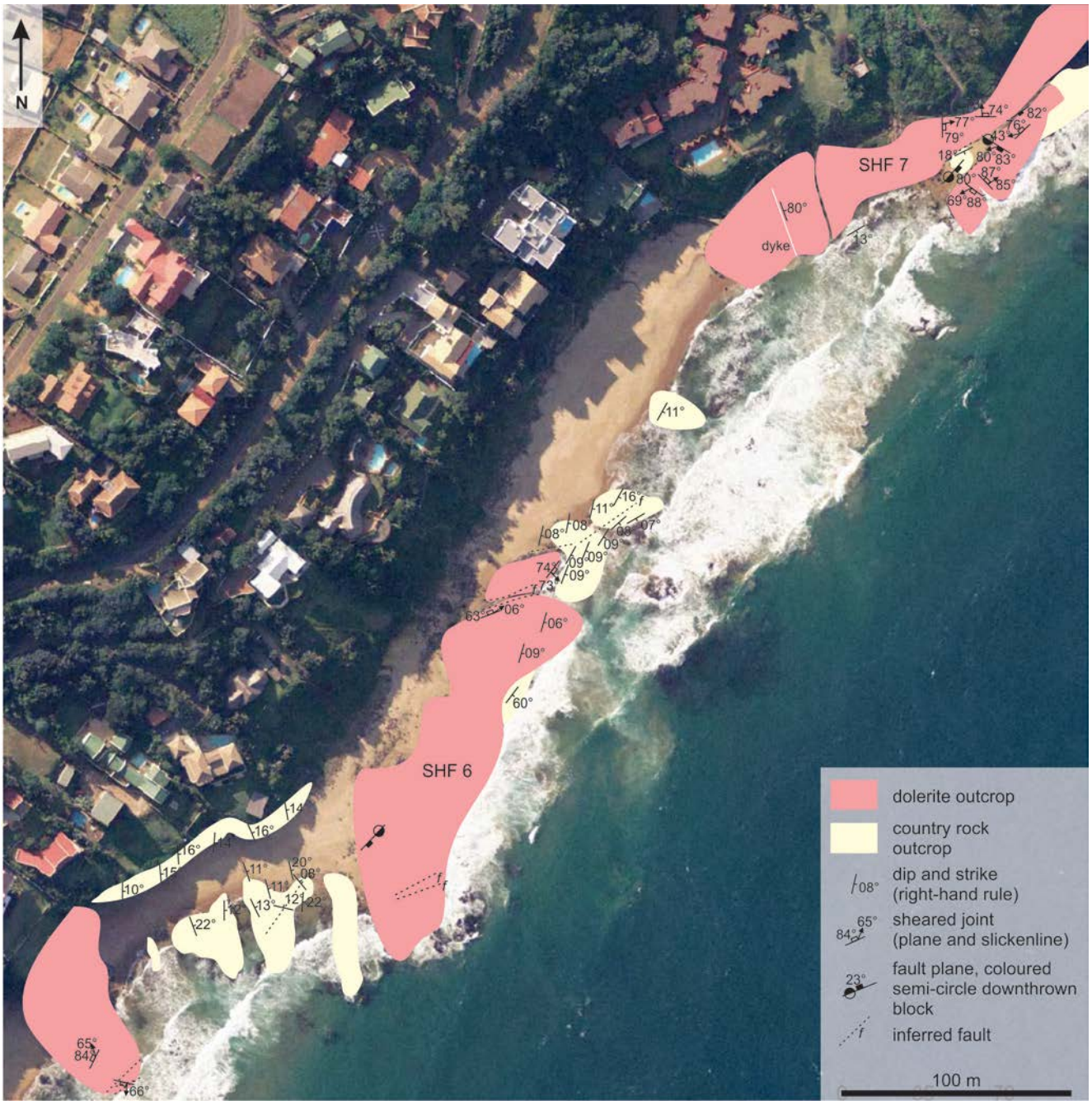

(e) Sketch map of the structural data from Northern Sheffield Beach

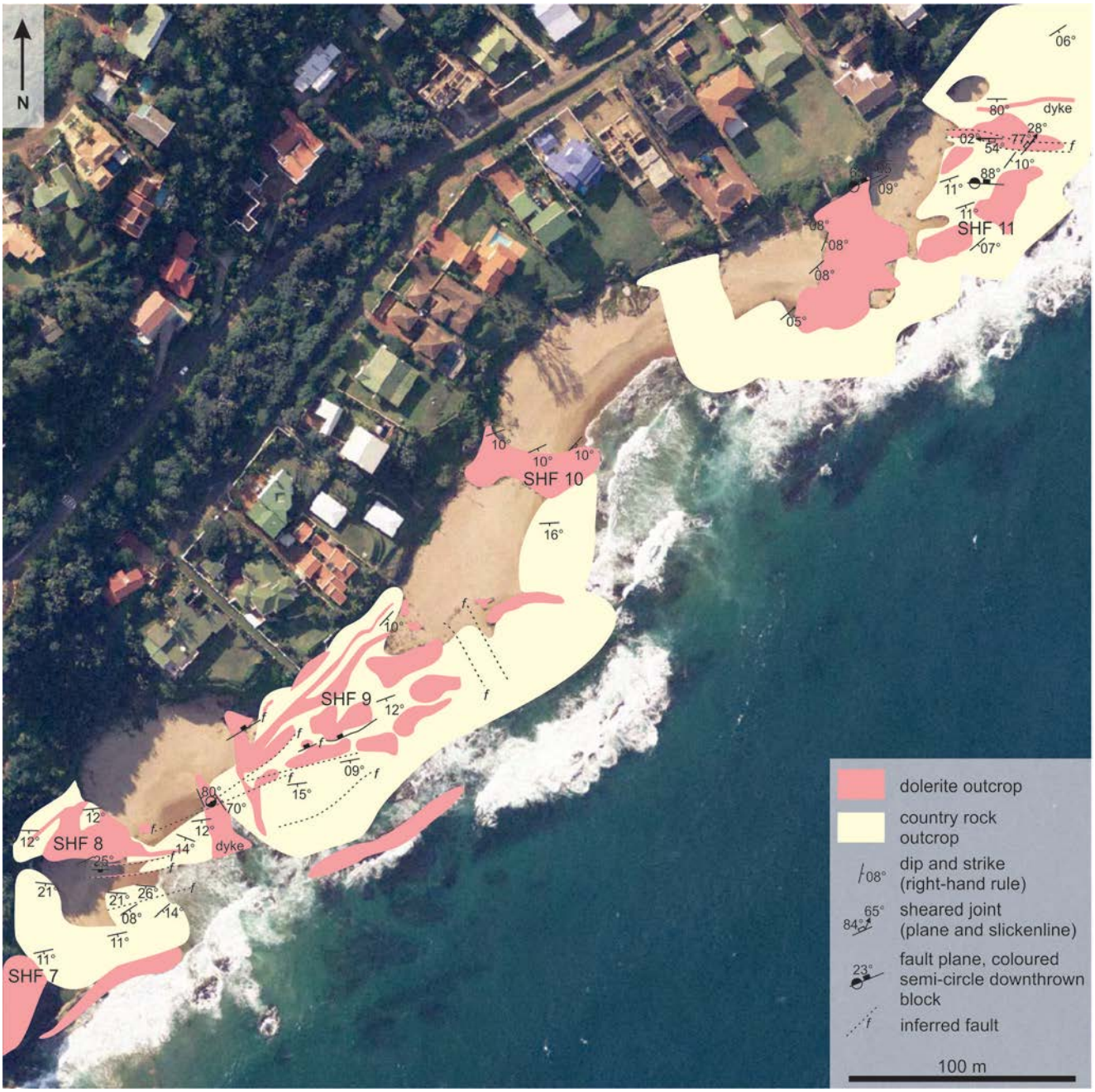

3. Sketch maps showing sample localities

(a) Sketch map showing the sample localities for Thompson's Bay and Shaka's Rock

(b) Sketch map showing the sample localities for Southern Sheffield Beach

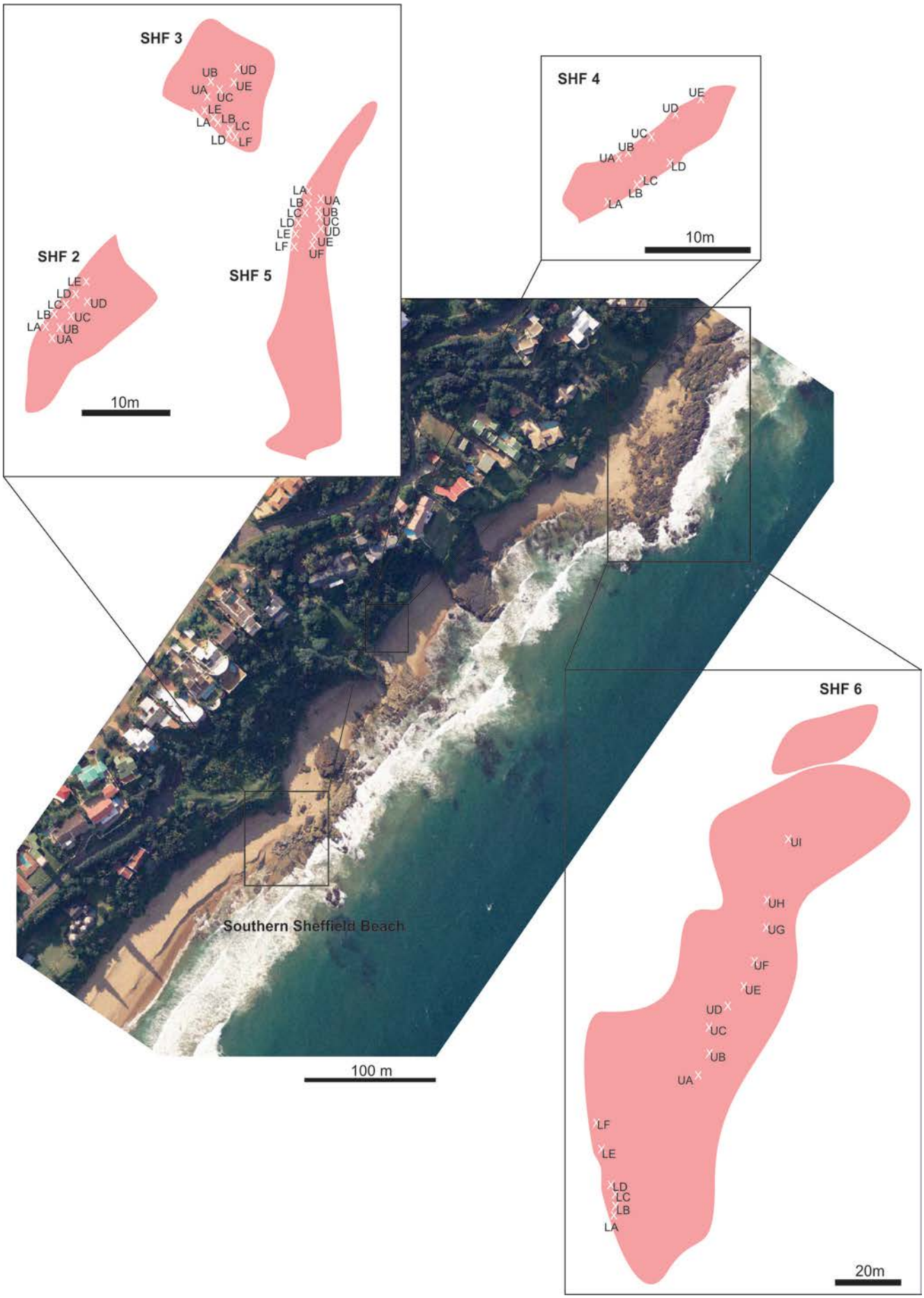

(c) Sketch map showing the sample localities for Northern Sheffield Beach

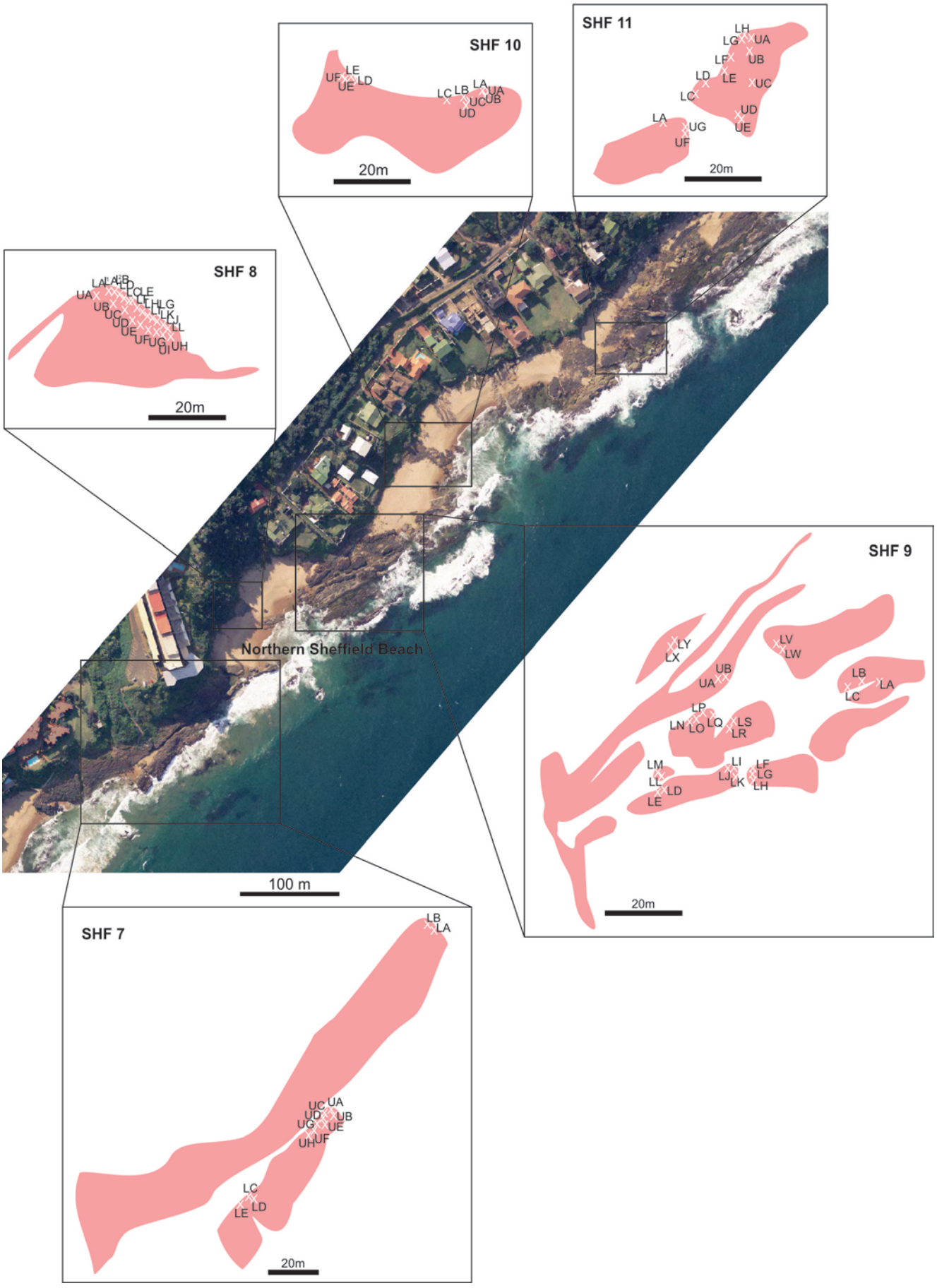

4. Tabulated sill and sample data

(a) Sill properties

Sill Name	Geographical co-ordinates		Sill Orientation		Approximate	Number of
	Latitude	Longitude	Dip	Strike	Thickness (m)	samples
TB1	29° 31' 39.05"	31° 13' 41.17"	22°	172°	3	16
TB2	29° 31' 14.69"	31° 13' 42.05"	21°	167°	2.5	27
TB4	29° 31' 13.87"	31° 13' 42.87"	25°	172°	1	14
TB5	29° 31' 25.17"	31° 13' 39.03"	16°	160°	2	9
TB6	29° 31' 26.04"	31° 13' 41.80"	13°	164°	unknown	4
SR1	29° 30' 50.76"	31° 13' 54.48"	20°	206°	2	16
SHF2	29° 29' 43.44"	31° 14' 46.68"	20°	000°	1	9
SHF3	29° 29' 41.64"	31° 14' 46.93"	17°	340°	2.2	12
SHF4	29° 29' 37.32"	31° 14' 49.56"	12°	350°	1.5	9
SHF5	29° 29' 41.28"	31° 14.48.48"	37°	005°	1.2	12
SHF6	29° 29' 32.64"	31° 14' 57.48"	13°	013°	2.5	16
SHF7	29° 29' 23.64"	31° 15' 07.56"	10°	056°	>10	13
SHF8	29° 29' 19.32"	31° 15' 10.44"	09°	088°	0.5	21
SHF9	29° 29' 17.88"	31° 15' 14.04"	13°	065°	1.5	28
SHF10	29° 29' 13.92"	31° 15' 17.28"	10°	065°	1	11
SHF11	29° 29' 10.68"	31° 15' 24.48"	10°	054°	1.5	15

(b) Sill Characteristics

Sill Name	Contact	Degree of alteration	Sill Texture	Glass %
TB1	U	moderate	Variolitic and amygdaloidal, minor perthitic Or phenocrysts	10 - 15
TB2	U	moderate	Subophitic with interstitial glass	10 - 20
	V	high	Subophitic with interstitial glass	10 - 20
	L	none	Subophitic to ophitic	5 - 10
TB4	U	none	Variolitic and amygdaloidal	< 5
	L	none	Variolitic with plagioclase laths	5 - 10
TB5	U	minor	Subophitic (fine grained)	< 5
	L	minor	Subophitic	5 - 10
TB6	U	unknown	Variolitic and glassy	unknown
SR1	U	none	Variolitic and amygdaloidal	10 - 15
	C	none	Coarse varioles, plagioclase laths	~5
	L	unknown	Glassy to variolitic and amygdaloidal, minor phenocrysts	10 - 15
SHF2	U	minor	Variolitic with plagioclase laths	10 - 15
	L	minor	Variolitic to subophitic	~10
SHF3	U	minor	Subophitic, minor plagioclase phenocrysts	10 - 15
	L	minor	Subophitic	< 5
SHF4	U	high	Variolitic with minor plagioclase	~10
	L	high	and pyroxene phenocrysts	~10
SHF5	U	minor	Subophitic with minor amygdales	5 - 10
	L	minor	Subophitic, minor amygdales and varioles	< 5
SHF6	U	minor	Variolitic with plagioclase laths, minor amygdales	5 - 10
	L	minor	Predominantly variolitic, subophitic	5 - 10
SHF7	U	moderate	Subophitic with large plagioclase laths	< 5
	L	minor	Glomeroporphyritic with subophitic groundmass	< 5
SHF8	U	minor	Glassy to variolitic, minor plagioclase phenocrysts	> 25
	L	minor	Variolitic and amygdaloidal, minor plagioclase phenocrysts	> 50
SHF9	U	minor	Subophitic and amygdaloidal	< 1
	L	moderate	Glomeroporphyritic with subophitic groundmass	~5
SHF10	U	minor	Glomeroporphyritic with subophitic groundmass	5 - 10
	L	moderate	and chlorite phenocrysts (after pyroxene)	~10
SHF11	U	minor	Glomeroporphyritic with subophitic groundmass	~10
	L	moderate	and chlorite phenocrysts (after pyroxene)	5 - 10

(b) continued

Sill Name	Contact	Opaque grains and the relationship to plagioclase grains	Other characteristics
TB1	U	Blebby opaques associated with glass	Xenolithic, sulphide sphericules.
TB2	U	No distinct relationship	Xenolithic zone below vesicular layer
	V	Elongate and parallel	Elongated vesicles < 5 cm in length, some infilled
	L	Elongate and parallel	Amygdales (~ 2 mm) pervasive above lower contact
TB4	U	Elongate and parallel to blebby	Vesicle stringer occurs in the centre of the sill
	L	Opaques associated with glass	
TB5	U	Blebby, surrounds plagioclase	Massive
	L	Blebby, surrounds plagioclase	
TB6	U	indistinguishable	Silicification abundant, contamination from country rocks
SR1	U	Elongate and parallel	Xenolithic at upper contact
	C	Abundant, elongate and parallel	
	L	Very fine blebs surrounding plagioclase	
SHF2	U	Abundant, elongate and parallel	Vesicle stringer occurs in the centre of the sill
	L	Abundant, elongate and parallel	
SHF3	U	Abundant, elongate and surrounding plagioclase	Rheomorphic sedimentary dyke intrusive into sill
	L	Abundant, elongate and parallel	Parallel vesicle stringers near the upper contact
SHF4	U	Abundant, elongate and parallel	Massive
	L	Abundant, elongate and parallel	
SHF5	U	Abundant, elongate and parallel	Massive
	L	Blebby, surrounds plagioclase	
SHF6	U	Absent in varioles, weak relationship	Large country rock xenoliths sandwiched between two dolerite
	L	Blebby, surrounds plagioclase	generations. Numerous rheomorphic sedimentary dykes
SHF7	U	Blebby, surrounds plagioclase	Xenolithic, large patches of coarser material occurring
	L	Blebby, weak relationship	throughout the sill
SHF8	U	Abundant and clustered in glass	Central vesicle stringer, xenoliths of adjacent country rock
	L	Abundant and clustered in glass	
SHF9	U	Abundant, elongate and parallel	Main sill branches into two sill segments, the lower segment
	L	Abundant and parallel to plagioclase	bifurcates into two subsequent sill segments. Sedimentary dykes.
SHF10	U	Blebby, weak relationship	Massive
	L	Blebby, weak relationship	
SHF11	U	Abundant and parallel to plagioclase	Massive
	L	Abundant, elongate and parallel	

(c) Representative photomicrographs from the sampled contacts

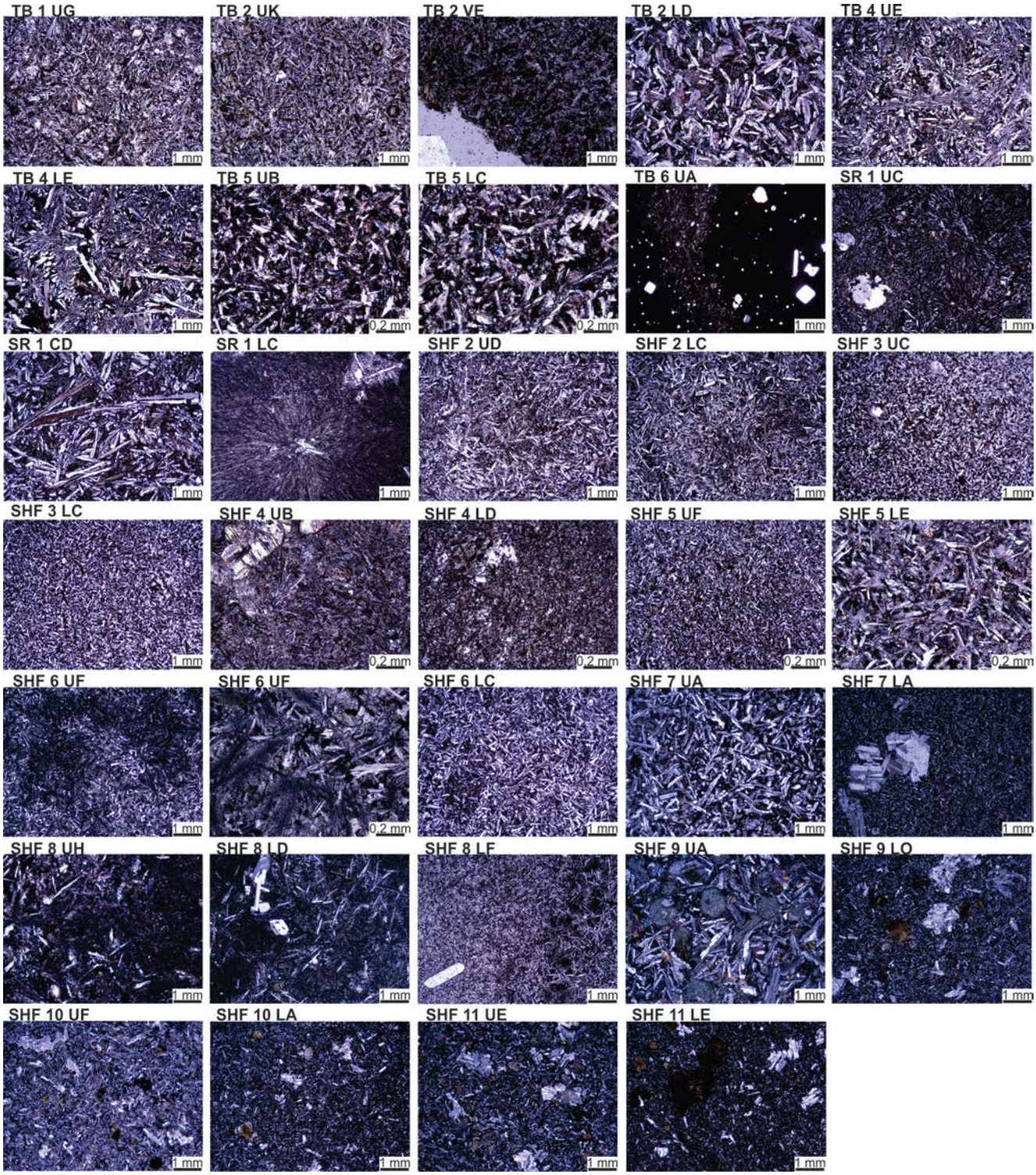

5. Ellipsoid tensor diagrams showing raw data extracted from the Ellipsoid-2003 before fabric restoration

(a) TB-2C(V) 10x

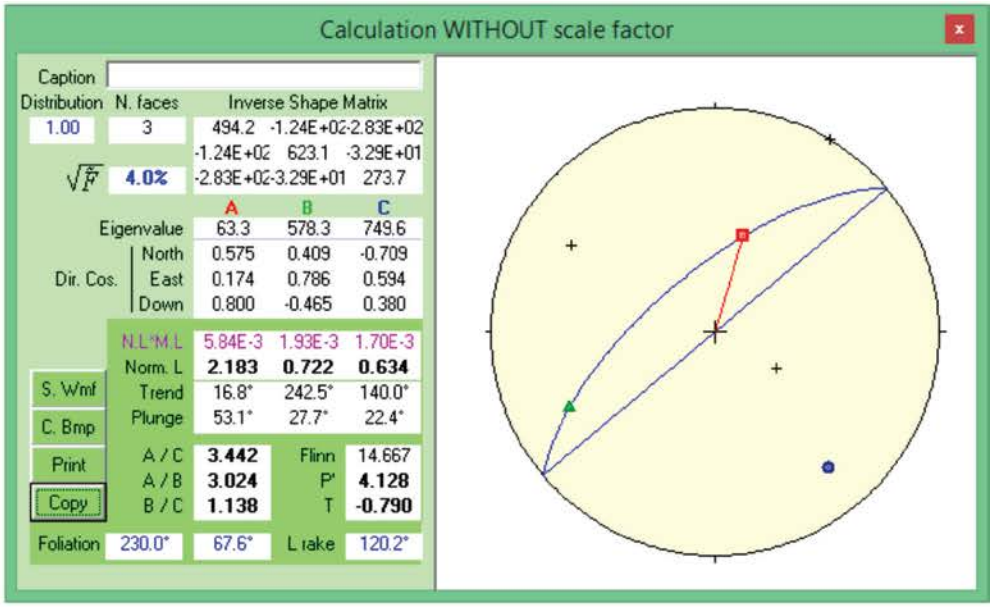

T = -0.79 strongly prolate sample defined by lineation "A" = 53.1°/016.8° (plunge/direction)

(b) SHF-3UA 10x

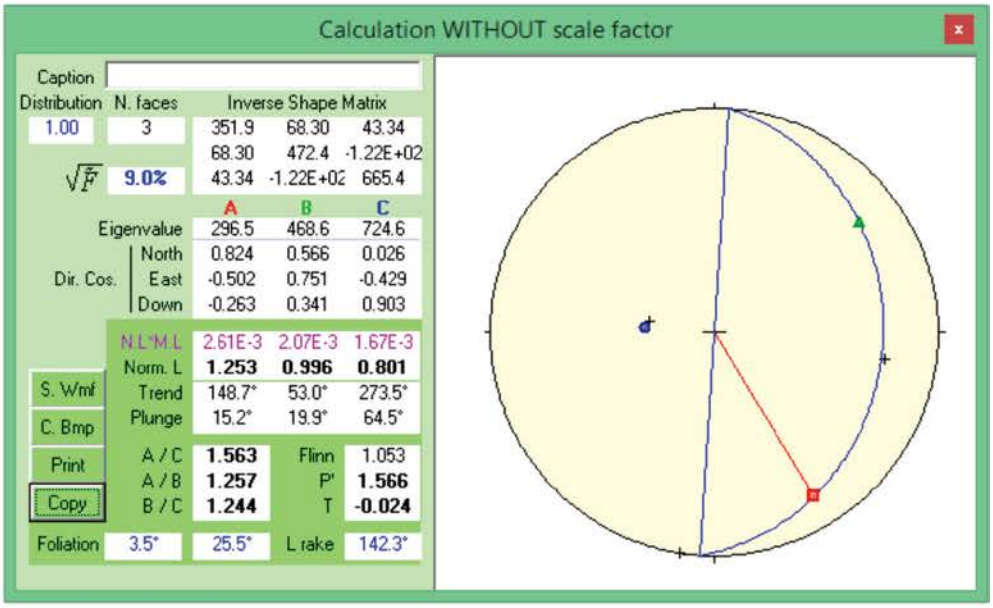

T = -0.024 nearly triaxial sample defined by foliation = 25.5°/003.5° (dip/strike)

(c) SHF-11LA 10x

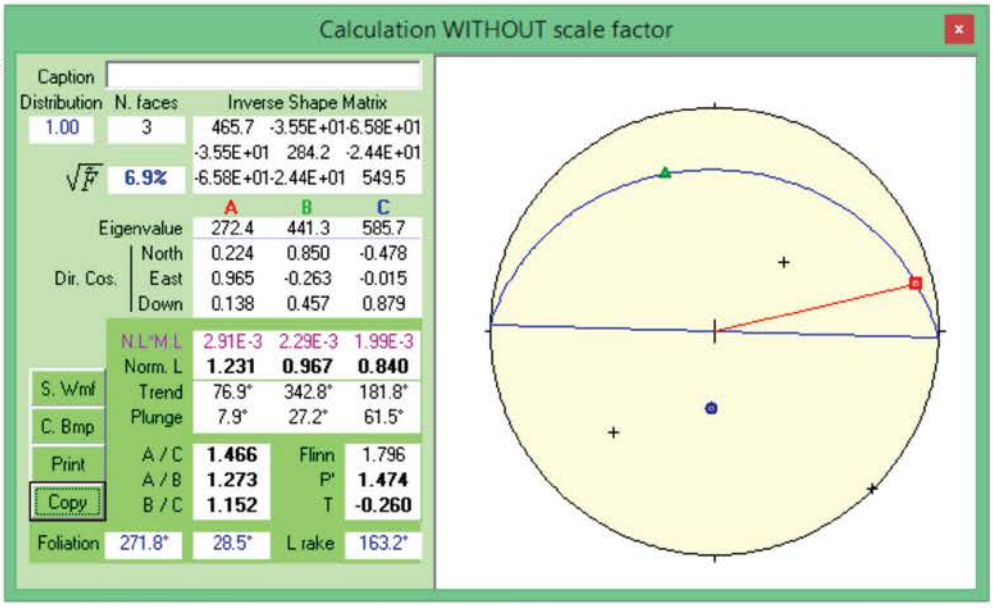

T = -0.26 weakly prolate sample defined by foliation = 28.5°/271.8° (dip/strike)

6. Tabulated SPO data

(a) 2-D ellipse data for samples obtained at 2.5 x magnification

Sample	Original Strike	Thin Section	Strike + Mag Dec	Dip	Mag 2.5x	Strike	Dip	Rake	Long axis	Short axis	Weight	Grains
TB-4 UA		XY	207°	39°	1_XY	207°	39°	067.6°	0.00507	0.00490	1	1458
	103°	XZ	127°	90°	1_XZ	127°	90°	059.6°	0.00347	0.00325	1	2345
		ZY	037°	51°	1_YZ	037°	51°	005.7°	0.00358	0.00324	1	2525
TB-4 UB		XY	201°	37°	1_XY	201°	37°	033.7°	0.00463	0.00418	1	2248
	087°	XZ	111°	90°	1_XZ	111°	90°	026.6°	0.00451	0.00419	1	2114
		ZY	021°	53°	1_YZ	021°	53°	108.2°	0.00453	0.00409	1	2168
TB-4 UC		XY	209°	37°	1_XY	209°	37°	040.7°	0.00439	0.00401	1	1860
	105°	XZ	129°	90°	1_XZ	129°	90°	092.5°	0.00519	0.00486	1	1678
		ZY	039°	53°	1_YZ	039°	53°	001.0°	0.00414	0.00383	1	1960
TB-4 UE		XY	217°	20°	1_XY	217°	20°	148.3°	0.00728	0.00687	1	2006
	103°	XZ	127°	90°	1_XZ	127°	90°	110.8°	0.00805	0.00733	1	1501
		ZY	037°	70°	1_YZ	037°	70°	042.6°	0.00743	0.00707	1	1727
TB-4 LA		XY	052°	72°	1_XY	052°	72°	109.5°	0.00514	0.00473	1	2385
	298°	XZ	322°	90°	1_XZ	322°	90°	020.4°	0.00544	0.00463	1	2179
		ZY	232°	18°	1_YZ	232°	18°	095.0°	0.00428	0.00406	1	2742
TB-4 LB		XY	039°	66°	1_XY	039°	66°	125.0°	0.00791	0.00748	1	1754
	285°	XZ	309°	90°	1_XZ	309°	90°	103.4°	0.00895	0.00776	1	1217
		ZY	219°	24°	1_YZ	219°	24°	175.8°	0.01077	0.00889	1	1279
TB-4 LC		XY	104°	80°	1_XY	104°	80°	044.3°	0.00627	0.00534	1	1418
	350°	XZ	014°	90°	1_XZ	014°	90°	077.6°	0.00586	0.00548	1	1860
		ZY	284°	10°	1_YZ	284°	10°	120.3°	0.00627	0.00541	1	1966
TB-4 LE		XY	009°	54°	1_XY	009°	54°	021.3°	0.01180	0.00847	1	1383
	255°	XZ	279°	90°	1_XZ	279°	90°	125.5°	0.00953	0.00724	1	1631
		ZY	189°	36°	1_YZ	189°	36°	006.5°	0.01247	0.00911	1	1408
TB-5 UA		XY	078°	80°	1_XY	078°	80°	152.7°	0.00518	0.00501	1	2541
	324°	XZ	348°	90°	1_XZ	348°	90°	108.3°	0.00511	0.00475	1	2413
		ZY	258°	10°	1_YZ	258°	10°	081.0°	0.00488	0.00457	1	2340
TB-5 UB		XY	075°	78°	1_XY	075°	78°	164.5°	0.00466	0.00410	1	2845
	321°	XZ	345°	90°	1_XZ	345°	90°	096.4°	0.00452	0.00420	1	3145
		ZY	255°	12°	1_YZ	255°	12°	095.1°	0.00425	0.00398	1	2792
TB-5 UC		XY	093°	77°	1_XY	093°	77°	121.2°	0.00487	0.00481	1	2407
	339°	XZ	003°	90°	1_XZ	003°	90°	085.1°	0.00449	0.00409	1	2901
		ZY	273°	13°	1_YZ	273°	13°	064.7°	0.00425	0.00394	1	2954
TB-5 UD		XY	072°	78°	1_XY	072°	78°	162.4°	0.00553	0.00525	1	2275
	318°	XZ	342°	90°	1_XZ	342°	90°	103.8°	0.00461	0.00445	1	2858
		ZY	252°	12°	1_YZ	252°	12°	064.4°	0.00564	0.00513	1	2332
TB-5 LA		XY	109°	82°	1_XY	109°	82°	027.4°	0.00537	0.00506	1	2540
	355°	XZ	019°	90°	1_XZ	019°	90°	038.8°	0.00530	0.00506	1	2303
		ZY	289°	08°	1_YZ	289°	08°	130.3°	0.00521	0.00510	1	2383

(a) continued

Sample	Original Strike	Thin Section	Strike + Mag Dec	Dip	Mag 2.5x	Strike	Dip	Rake	Long axis	Short axis	Weight	Grains
TB-5 LB		XY	185°	80°	1_XY	185°	80°	020.5°	0.00547	0.00446	1	2296
	071°	XZ	095°	90°	1_XZ	095°	90°	020.6°	0.00470	0.00456	1	2570
		ZY	005°	10°	1_YZ	005°	10°	139.3°	0.00507	0.00420	1	2256
TB-5 LC		XY	114°	74°	1_XY	114°	74°	052.1°	0.00504	0.00477	1	2151
	000°	XZ	024°	90°	1_XZ	024°	90°	026.0°	0.00562	0.00475	1	2289
		ZY	294°	16°	1_YZ	294°	16°	048.3°	0.00476	0.00452	1	2393
TB-5 LD		XY	199°	76°	1_XY	199°	76°	176.1°	0.00589	0.00455	1	2088
	085°	XZ	109°	90°	1_XZ	109°	90°	047.8°	0.00491	0.00425	1	2925
		ZY	019°	14°	1_YZ	019°	14°	142.0°	0.00510	0.00456	1	2005
SR-1 UA		XY	243°	39°	1_XY	243°	39°	051.4°	0.00149	0.00114	1	3022
	129°	XZ	153°	90°	1_XZ	153°	90°	123.9°	0.00120	0.00111	1	2892
		ZY	063°	51°	1_YZ	063°	51°	021.9°	0.00131	0.00116	1	2909
SR-1 UB		XY	261°	33°	1_XY	261°	33°	123.4°	0.00157	0.00114	1	2798
	147°	XZ	171°	90°	1_XZ	171°	90°	151.8°	0.00147	0.00124	1	2359
		ZY	081°	57°	1_YZ	081°	57°	143.0°	0.00181	0.00149	1	2150
SR-1 UC		XY	174°	11°	1_XY	174°	11°	044.5°	0.00241	0.00138	1	1710
	060°	XZ	084°	90°	1_XZ	084°	90°	160.5°	0.00195	0.00141	1	1979
		ZY	354°	79°	1_YZ	354°	79°	007.8°	0.00251	0.00153	1	1448
SR-1 UD		XY	271°	23°	1_XY	271°	23°	154.7°	0.00144	0.00124	1	2578
	157°	XZ	181°	90°	1_XZ	181°	90°	032.6°	0.00125	0.00117	1	2604
		ZY	091°	67°	1_YZ	091°	67°	115.0°	0.00146	0.00137	1	2301
SR-1 UE		XY	282°	11°	1_XY	282°	11°	064.2°	0.00126	0.00121	1	2711
	168°	XZ	192°	90°	1_XZ	192°	90°	134.3°	0.00162	0.00135	1	2117
		ZY	102°	79°	1_YZ	102°	79°	034.1°	0.00142	0.00111	1	3018
SR-1 CA		XY	034°	78°	1_XY	034°	78°	166.0°	0.01023	0.00861	1	1304
	280°	XZ	304°	90°	1_XZ	304°	90°	031.5°	0.01190	0.00790	1	1233
		ZY	214°	12°	1_YZ	214°	12°	131.9°	0.01096	0.00768	1	1407
SR-1 CB		XY	023°	83°	1_XY	023°	83°	068.4°	0.01044	0.00929	1	1017
	269°	XZ	293°	90°	1_XZ	293°	90°	174.4°	0.01300	0.00981	1	982
		ZY	203°	07°	1_YZ	203°	07°	052.0°	0.00996	0.00790	1	1429
SR-1 CC		XY	062°	22°	1_XY	062°	22°	126.0°	0.01171	0.00751	1	1212
	308°	XZ	332°	90°	1_XZ	332°	90°	176.2°	0.01177	0.00833	1	1253
		ZY	242°	68°	1_YZ	242°	68°	167.6°	0.01045	0.00908	1	1450
SR-1 CD		XY	123°	04°	1_XY	123°	04°	062.4°	0.01019	0.00914	1	1404
	009°	XZ	033°	90°	1_XZ	033°	90°	017.0°	0.01175	0.00896	1	1363
		ZY	303°	86°	1_YZ	303°	86°	102.8°	0.01193	0.00937	1	1224
SR-1 CE		XY	076°	78°	1_XY	076°	78°	120.0°	0.00975	0.00790	1	1478
	322°	XZ	346°	90°	1_XZ	346°	90°	102.5°	0.01061	0.00824	1	1484
		ZY	256°	12°	1_YZ	256°	12°	149.5°	0.01036	0.00811	1	1335

(a) continued

Sample	Original Strike	Thin Section	Strike + Mag Dec	Dip	Mag 2.5x	Strike	Dip	Rake	Long axis	Short axis	Weight	Grains
SR-1 LA		XY	012°	77°	1_XY	012°	77°	125.7°	0.00174	0.00136	1	2466
	258°	XZ	282°	90°	1_XZ	282°	90°	133.6°	0.00182	0.00112	1	2208
		ZY	192°	13°	1_YZ	192°	13°	003.1°	0.00169	0.00145	1	2521
SR-1 LB		XY	014°	71°	1_XY	014°	71°	124.6°	0.00204	0.00193	1	1801
	260°	XZ	284°	90°	1_XZ	284°	90°	133.1°	0.00219	0.00163	1	1631
		ZY	194°	19°	1_YZ	194°	19°	112.8°	0.00169	0.00129	1	2463
SR-1 LC		XY	039°	82°	1_XY	039°	82°	136.3°	0.00122	0.00101	1	1916
	285°	XZ	309°	90°	1_XZ	309°	90°	159.5°	0.00166	0.00125	1	2329
		ZY	219°	08°	1_YZ	219°	08°	005.2°	0.00214	0.00161	1	1277
SR-1 LD		XY	039°	65°	1_XY	039°	65°	144.1°	0.00128	0.00091	1	2255
	285°	XZ	309°	90°	1_XZ	309°	90°	119.1°	0.00191	0.00115	1	1897
		ZY	219°	25°	1_YZ	219°	25°	018.2°	0.00233	0.00107	1	1495
SR-1 LF		XY	174°	16°	1_XY	174°	16°	148.9°	0.00214	0.00193	1	1315
	060°	XZ	084°	90°	1_XZ	084°	90°	033.8°	0.00145	0.00120	1	1346
		ZY	354°	74°	1_YZ	354°	74°	003.0°	0.00167	0.00124	1	2166
SHF-2 LA		XY	285°	63°	1_XY	285°	63°	153.7°	0.00636	0.00505	1	2556
	171°	XZ	195°	90°	1_XZ	195°	90°	083.8°	0.00672	0.00527	1	2188
		ZY	105°	27°	1_YZ	105°	27°	127.3°	0.00699	0.00626	1	1772
SHF-2 LB		XY	258°	55°	1_XY	258°	55°	059.6°	0.00708	0.00621	1	2240
	144°	XZ	168°	90°	1_XZ	168°	90°	098.8°	0.00702	0.00630	1	1295
		ZY	078°	35°	1_YZ	078°	35°	040.6°	0.00684	0.00603	1	2133
SHF-2 LC		XY	251°	72°	1_XY	251°	72°	167.9°	0.00622	0.00598	1	2257
	137°	XZ	161°	90°	1_XZ	161°	90°	143.7°	0.00706	0.00670	1	1923
		ZY	071°	18°	1_YZ	071°	18°	106.5°	0.00601	0.00558	1	2523
SHF-2 LD		XY	226°	65°	1_XY	226°	65°	171.2°	0.00424	0.00372	1	3041
	112°	XZ	136°	90°	1_XZ	136°	90°	065.7°	0.00460	0.00383	1	3008
		ZY	046°	25°	1_YZ	046°	25°	027.3°	0.00388	0.00356	1	2960
SHF-2 LE		XY	283°	76°	1_XY	283°	76°	140.4°	0.00830	0.00493	1	1807
	169°	XZ	193°	90°	1_XZ	193°	90°	050.3°	0.00481	0.00346	1	2019
		ZY	103°	14°	1_YZ	103°	14°	053.0°	0.00501	0.00359	1	2498
SHF-2 UA		XY	050°	33°	1_XY	050°	33°	083.6°	0.00361	0.00356	1	2521
	296°	XZ	320°	90°	1_XZ	320°	90°	141.1°	0.00416	0.00366	1	2977
		ZY	230°	57°	1_YZ	230°	57°	141.5°	0.00400	0.00381	1	2740
SHF-2 UB		XY	093°	35°	1_XY	093°	35°	017.6°	0.00643	0.00438	1	960
	339°	XZ	003°	90°	1_XZ	003°	90°	118.0°	0.00363	0.00333	1	2174
		ZY	273°	55°	1_YZ	273°	55°	048.8°	0.00458	0.00322	1	2317
SHF-2 UC		XY	048°	25°	1_XY	048°	25°	105.6°	0.00405	0.00379	1	2085
	294°	XZ	318°	90°	1_XZ	318°	90°	081.9°	0.00401	0.00359	1	2391
		ZY	228°	65°	1_YZ	228°	65°	061.4°	0.00420	0.00406	1	2610

(a) continued

Sample	Original Strike	Thin Section	Strike + Mag Dec	Dip	Mag 2.5x	Strike	Dip	Rake	Long axis	Short axis	Weight	Grains
SHF-2 UD		XY	051°	46°	1_XY	051°	46°	060.4°	0.00632	0.00553	1	2312
	297°	XZ	321°	90°	1_XZ	321°	90°	109.8°	0.00781	0.00674	1	1776
		ZY	231°	44°	1_YZ	231°	44°	024.5°	0.00716	0.00682	1	2036
SHF-3 LA		XY	159°	71°	1_XY	159°	71°	167.8°	0.00649	0.00624	1	1760
	045°	XZ	069°	90°	1_XZ	069°	90°	143.5°	0.00542	0.00515	1	1978
		ZY	339°	19°	1_YZ	339°	19°	007.3°	0.00606	0.00582	1	1841
SHF-3 LB		XY	151°	70°	1_XY	154°	70°	096.0°	0.00553	0.00512	1	2071
	037°	XZ	061°	90°	1_XZ	061°	90°	096.3°	0.00504	0.00485	1	2456
		ZY	331°	20°	1_YZ	331°	20°	092.5°	0.00625	0.00547	1	2143
SHF-3 LC		XY	180°	74°	1_XY	180°	74°	161.0°	0.00572	0.00536	1	2463
	066°	XZ	090°	90°	1_XZ	090°	90°	057.9°	0.00599	0.00572	1	2154
		ZY	000°	16°	1_YZ	000°	16°	025.4°	0.00579	0.00558	1	2331
SHF-3 LD		XY	182°	65°	1_XY	182°	65°	153.3°	0.00765	0.00725	1	1734
	068°	XZ	092°	90°	1_XZ	092°	90°	088.4°	0.00681	0.00656	1	2091
		ZY	002°	25°	1_YZ	002°	25°	061.6°	0.00733	0.00685	1	1858
SHF-3 UA		XY	009°	24°	1_XY	009°	24°	018.8°	0.00652	0.00551	1	1900
	255°	XZ	279°	90°	1_XZ	279°	90°	134.9°	0.00732	0.00646	1	1912
		ZY	189°	66°	1_YZ	189°	66°	041.2°	0.00535	0.00489	1	2144
SHF-3 UB		XY	252°	17°	1_XY	252°	17°	047.1°	0.00524	0.00491	1	2630
	138°	XZ	162°	90°	1_XZ	162°	90°	081.7°	0.00541	0.00502	1	2599
		ZY	072°	73°	1_YZ	072°	73°	040.7°	0.00491	0.00481	1	2768
SHF-3 UC		XY	232°	17°	1_XY	232°	17°	035.2°	0.00609	0.00573	1	2486
	120°	XZ	142°	90°	1_XZ	142°	90°	063.7°	0.00631	0.00573	1	2208
		ZY	052°	73°	1_YZ	052°	73°	049.3°	0.00509	0.00449	1	2357
SHF-3 UD		XY	031°	28°	1_XY	031°	28°	104.7°	0.00341	0.00331	1	3674
	277°	XZ	301°	90°	1_XZ	301°	90°	111.0°	0.00389	0.00359	1	2919
		ZY	211°	62°	1_YZ	211°	62°	176.6°	0.00367	0.00359	1	2424
SHF-6 LA		XY	191°	59°	1_XY	191°	59°	125.1°	0.00710	0.00665	1	1888
	077°	XZ	101°	90°	1_XZ	101°	90°	098.0°	0.00656	0.00610	1	2116
		YZ	011°	31°	1_YZ	011°	31°	075.7°	0.00696	0.00661	1	2185
SHF-6 LB		XY	209°	69°	1_XY	209°	69°	071.0°	0.00652	0.00604	1	2059
	095°	XZ	119°	90°	1_XZ	119°	90°	096.7°	0.00657	0.00544	1	2214
		YZ	029°	21°	1_YZ	029°	21°	044.1°	0.00669	0.00603	1	2137
SHF-6 LC		XY	199°	67°	1_XY	199°	67°	125.8°	0.00639	0.00635	1	2116
	085°	XZ	109°	90°	1_XZ	109°	90°	130.7°	0.00656	0.00650	1	1963
		YZ	019°	23°	1_YZ	019°	23°	006.6°	0.00696	0.00648	1	1906
SHF-6 LD		XY	302°	56°	1_XY	302°	56°	167.1°	0.00562	0.00535	1	2229
	188°	XZ	212°	90°	1_XZ	212°	90°	018.7°	0.00571	0.00560	1	2161
		YZ	122°	34°	1_YZ	122°	34°	055.9°	0.00519	0.00489	1	2495
SHF-6 LF		XY	280°	71°	1_XY	280°	71°	148.4°	0.00815	0.00690	1	1771
	166°	XZ	190°	90°	1_XZ	190°	90°	153.9°	0.00732	0.00704	1	1761
		YZ	100°	19°	1_YZ	100°	19°	125.4°	0.00789	0.00733	1	1752

(a) continued

Sample	Original Strike	Thin Section	Strike + Mag Dec	Dip	Mag 2.5x	Strike	Dip	Rake	Long axis	Short axis	Weight	Grains
SHF-6 UA		XY	267°	65°	1_XY	267°	65°	033.2°	0.00492	0.00450	1	2801
	153°	XZ	177°	90°	1_XZ	177°	90°	049.7°	0.00527	0.00483	1	2736
		YZ	087°	25°	1_YZ	087°	25°	097.9°	0.00488	0.00466	1	2814
SHF-6 UB		XY	269°	45°	1_XY	269°	45°	035.4°	0.00637	0.00567	1	2151
	155°	XZ	179°	90°	1_XZ	179°	90°	105.0°	0.00561	0.00515	1	2443
		YZ	089°	45°	1_YZ	089°	45°	170.4°	0.00637	0.00594	1	2173
SHF-6 UC		XY	131°	24°	1_XY	131°	24°	150.6°	0.00364	0.00355	1	2860
	017°	XZ	041°	90°	1_XZ	041°	90°	118.0°	0.00412	0.00407	1	2623
		YZ	311°	66°	1_YZ	311°	66°	156.8°	0.00367	0.00366	1	2956
SHF-6 UD		XY	325°	75°	1_XY	325°	75°	074.3°	0.00535	0.00521	1	2481
	211°	XZ	235°	90°	1_XZ	235°	90°	027.9°	0.00608	0.00590	1	1981
		YZ	145°	15°	1_YZ	145°	15°	115.2°	0.00510	0.00491	1	2594
SHF-6 UF		XY	276°	68°	1_XY	276°	68°	166.0°	0.00476	0.00441	1	2740
	162°	XZ	186°	90°	1_XZ	186°	90°	175.4°	0.00572	0.00536	1	2369
		YZ	096°	22°	1_YZ	096°	22°	126.5°	0.00520	0.00493	1	2475
SHF-6 UG		XY	250°	68°	1_XY	250°	68°	027.5°	0.00738	0.00621	1	1767
	136°	XZ	160°	90°	1_XZ	160°	90°	024.8°	0.00709	0.00630	1	2082
		YZ	070°	22°	1_YZ	070°	22°	122.6°	0.00637	0.00623	1	1925
SHF-7 LA		XY	337°	79°	1_XY	337°	79°	154.6°	0.00508	0.00465	1	2946
	223°	XZ	247°	90°	1_XZ	247°	90°	096.0°	0.00517	0.00472	1	3164
		YZ	157°	11°	1_YZ	157°	11°	178.5°	0.00490	0.00465	1	2652
SHF-7 LB		XY	015°	83°	1_XY	015°	83°	161.5°	0.00439	0.00390	1	3015
	261°	XZ	285°	90°	1_XZ	285°	92°	059.8°	0.00425	0.00356	1	3513
		YZ	195°	07°	1_XZ	195°	07°	142.5°	0.00455	0.00443	1	3359
SHF-7 LC		XY	210°	76°	1_XY	210°	76°	014.8°	0.01122	0.00878	1	1058
	096°	XZ	120°	90°	1_XZ	120°	90°	072.1°	0.01218	0.00847	1	924
		ZY	030°	14°	1_YZ	030°	14°	029.7°	0.01017	0.00924	1	972
SHF-7 LE		XY	287°	64°	1_XY	287°	64°	167.0°	0.00920	0.00889	1	1183
	173°	XZ	197°	90°	1_XZ	197°	90°	153.4°	0.00833	0.00704	1	1235
		ZY	107°	26°	1_YZ	107°	26°	141.4°	0.00997	0.00817	1	1187
SHF-7 UA		XY	359°	40°	1_XY	359°	40°	159.7°	0.00792	0.00752	1	1423
	245°	XZ	269°	90°	1_XZ	269°	90°	028.2°	0.00759	0.00725	1	1284
		ZY	179°	50°	1_YZ	179°	50°	136.1°	0.00928	0.00746	1	1379
SHF-7 UB		XY	079°	38°	1_XY	079°	38°	151.2°	0.00955	0.00813	1	1120
	325°	XZ	349°	90°	1_XZ	349°	90°	140.2°	0.00868	0.00772	1	1246
		ZY	259°	52°	1_YZ	259°	52°	176.6°	0.00832	0.00755	1	1337
SHF-7 UE		XY	045°	23°	1_XY	045°	23°	039.2°	0.00733	0.00672	1	1503
	291°	XZ	315°	90°	1_XZ	315°	90°	141.7°	0.00863	0.00724	1	1435
		ZY	225°	67°	1_YZ	225°	67°	152.4°	0.00827	0.00782	1	1236
SHF-7 UG		XY	341°	52°	1_XY	341°	52°	016.3°	0.01060	0.00882	1	984
	227°	XZ	251°	90°	1_XZ	251°	90°	045.3°	0.00901	0.00794	1	1232
		ZY	161°	38°	1_YZ	161°	38°	098.1°	0.00975	0.00788	1	1028

(a) continued

Sample	Original Strike	Thin Section	Strike + Mag Dec	Dip	Mag 2.5x	Strike	Dip	Rake	Long axis	Short axis	Weight	Grains
SHF-8 LC		XY	292°	70°	1_XY	292°	70°	027.8°	0.00059	0.00051	1	2599
	178°	XZ	202°	90°	1_XZ	202°	90°	073.7°	0.00061	0.00058	1	2360
		ZY	112°	20°	1_YZ	112°	20°	150.7°	0.00060	0.00051	1	2866
SHF-8 LD		XY	288°	65°	1_XY	288°	65°	178.8°	0.00616	0.00490	1	2288
	174°	XZ	198°	90°	1_XZ	198°	90°	143.2°	0.00645	0.00547	1	1279
		ZY	108°	25°	1_YZ	108°	25°	168.9°	0.00556	0.00536	1	1614
SHF-8 UH		XY	107°	32°	1_XY	107°	32°	061.0°	0.00370	0.00349	1	2699
	353°	XZ	017°	90°	1_XZ	017°	90°	156.2°	0.00406	0.00343	1	1571
		ZY	287°	58°	1_YZ	287°	58°	070.9°	0.00432	0.00386	1	2565
SHF-10 UB		XY	105°	20°	1_XY	105°	20°	021.0°	0.00532	0.00497	1	2245
	351°	XZ	015°	90°	1_XZ	015°	90°	072.8°	0.00538	0.00513	1	2313
		YZ	285°	70°	1_YZ	285°	70°	032.5°	0.00520	0.00480	1	2301
SHF-10 UD		XY	107°	29°	1_XY	107°	29°	052.5°	0.00633	0.00547	1	2209
	353°	XZ	017°	90°	1_XZ	017°	90°	155.1°	0.00532	0.00509	1	2185
		YZ	287°	61°	1_YZ	287°	61°	000.6°	0.00547	0.00532	1	1919
SHF-11 UE		XY	269°	17°	1_XY	269°	17°	163.7°	0.00588	0.00552	1	2027
	155°	XZ	179°	90°	1_XZ	179°	90°	157.3°	0.00590	0.00556	1	2239
		YZ	089°	73°	1_YZ	089°	73°	058.3°	0.00529	0.00499	1	2316

(b) 2-D ellipse data for samples obtained at 10 x magnification

Sample	Original Strike	Thin Section	Strike + Mag Dec	Dip	Mag 10x	Strike	Dip	Rake	Long axis	Short axis	Weight	Grains
TB-1A		XY	205°	33°	1_XY	205°	33°	035.0°	0.00094	0.00088	1	1643
	091°	XZ	115°	90°	1_XZ	115°	90°	007.6°	0.00197	0.00187	1	1154
		ZY	025°	57°	1_YZ	025°	57°	058.1°	0.00188	0.00166	1	1007
TB-1B		XY	195°	27°	1_XY	195°	27°	147.7°	0.00197	0.00160	1	1572
	081°	XZ	105°	90°	1_XZ	105°	90°	133.9°	0.00163	0.00152	1	1584
		ZY	015°	63°	1_YZ	015°	63°	039.3°	0.00193	0.00178	1	1277
TB-1C		XY	197°	31°	1_XY	197°	31°	031.4°	0.00190	0.00169	1	1465
	083°	XZ	107°	90°	1_XZ	107°	90°	136.7°	0.00169	0.00148	1	1490
		ZY	017°	59°	1_YZ	017°	59°	039.1°	0.00165	0.00163	1	1392
TB-1D		XY	218°	35°	1_XY	218°	35°	111.6°	0.00153	0.00143	1	1636
	104°	XZ	128°	90°	1_XZ	128°	90°	172.2°	0.00174	0.00162	1	1437
		ZY	038°	55°	1_YZ	038°	55°	021.5°	0.00190	0.00177	1	1401
TB-1E		XY	193°	24°	1_XY	193°	24°	120.5°	0.00179	0.00159	1	1533
	079°	XZ	103°	90°	1_XZ	103°	90°	140.5°	0.00190	0.00168	1	1584
		ZY	013°	66°	1_YZ	013°	66°	130.5°	0.00180	0.00163	1	1497
TB-1F		XY	192°	26°	1_XY	192°	26°	087.8°	0.00180	0.00158	1	1589
	078°	XZ	102°	90°	1_XZ	102°	90°	122.5°	0.00202	0.00168	1	1477
		ZY	012°	64°	1_YZ	012°	64°	150.0°	0.00180	0.00166	1	1514
TB-1G		XY	231°	29°	1_XY	231°	29°	161.0°	0.00215	0.00186	1	901
	117°	XZ	141°	90°	1_XZ	141°	90°	073.6°	0.00184	0.00161	1	1513
		ZY	051°	61°	1_YZ	051°	61°	141.2°	0.00218	0.00127	1	1375
TB-1H		XY	205°	24°	1_XY	205°	24°	107.5°	0.00194	0.00170	1	1344
	091°	XZ	115°	90°	1_XZ	115°	90°	143.3°	0.00222	0.00134	1	1409
		ZY	025°	66°	1_YZ	025°	66°	011.4°	0.00201	0.00184	1	1298
TB-1I		XY	209°	39°	1_XY	209°	39°	030.4°	0.00165	0.00106	1	1475
	095°	XZ	119°	90°	1_XZ	119°	90°	157.3°	0.00158	0.00132	1	1475
		ZY	029°	51°	1_YZ	029°	51°	019.9°	0.00182	0.00134	1	1399
TB-1J		XY	181°	32°	1_XY	181°	32°	040.5°	0.00166	0.00113	1	2147
	067°	XZ	091°	90°	1_XZ	091°	90°	060.1°	0.00151	0.00136	1	1767
		ZY	001°	58°	1_YZ	001°	58°	126.1°	0.00202	0.00120	1	1642
TB-1 P		XY	223°	26°	1_XY	223°	26°	035.3°	0.00189	0.00166	1	1286
	109°	XZ	133°	90°	1_XZ	133°	90°	157.9°	0.00182	0.00150	1	1562
		ZY	043°	64°	1_YZ	043°	64°	023.4°	0.00241	0.00165	1	1317
TB-2 UA		XY	189°	20°	1_XY	189°	20°	102.4°	0.00148	0.00145	1	1800
	075°	XZ	099°	90°	1_XZ	099°	90°	075.8°	0.00130	0.00129	1	2384
		ZY	009°	70°	1_YZ	009°	70°	169.8°	0.00143	0.00129	1	2295
TB-2 UB		XY	186°	24°	1_XY	186°	24°	145.1°	0.00138	0.00122	1	1893
	072°	XZ	096°	90°	1_XZ	096°	90°	104.7°	0.00138	0.00121	1	1918
		ZY	006°	66°	1_YZ	006°	66°	040.8°	0.00190	0.00160	1	1609
TB-2 C(V)		XY	211°	26°	1_XY	211°	26°	144.2°	0.00201	0.00155	1	1359
	097°	XZ	121°	90°	1_XZ	121°	90°	102.8°	0.00288	0.00165	1	898
		ZY	031°	64°	1_YZ	031°	64°	041.3°	0.00314	0.00171	1	930

(b) continued

Sample	Original Strike	Thin Section	Strike + Mag Dec	Dip	Mag 10x	Strike	Dip	Rake	Long axis	Short axis	Weight	Grains
TB-2 D(V)		XY	186°	33°	1_XY	186°	33°	158.0°	0.00198	0.00178	1	1393
	072°	XZ	096°	90°	1_XZ	096°	90°	153.5°	0.00199	0.00153	1	1460
		ZY	006°	57°	1_YZ	006°	57°	008.3°	0.00224	0.00160	1	1444
TB-2 UE		XY	165°	31°	1_XY	165°	31°	155.9°	0.00133	0.00125	1	2166
	051°	XZ	075°	90°	1_XZ	075°	90°	154.9°	0.00151	0.00127	1	2020
		ZY	345°	59°	1_YZ	345°	59°	034.8°	0.00144	0.00115	1	2251
TB-2 UF		XY	207°	42°	1_XY	207°	42°	142.7°	0.00287	0.00158	1	950
	093°	XZ	117°	90°	1_XZ	117°	90°	086.0°	0.00206	0.00141	1	1137
		ZY	027°	48°	1_YZ	027°	48°	071.6°	0.00192	0.00187	1	1074
TB-2 UG		XY	283°	31°	1_XY	283°	31°	071.2°	0.00122	0.00111	1	2165
	169°	XZ	193°	90°	1_XZ	193°	90°	159.0°	0.00120	0.00105	1	2141
		ZY	103°	59°	1_YZ	103°	59°	067.2°	0.00134	0.00128	1	2409
TB-2 H(V)		XY	189°	30°	1_XY	189°	30°	140.7°	0.00168	0.00143	1	1538
	075°	XZ	099°	90°	1_XZ	099°	90°	124.3°	0.00150	0.00140	1	1913
		ZY	009°	60°	1_YZ	009°	60°	028.8°	0.00148	0.00113	1	1851
TB-2 UI		XY	232°	22°	1_XY	232°	22°	136.4°	0.00086	0.00083	1	2859
	118°	XZ	142°	90°	1_XZ	142°	90°	096.3°	0.00120	0.00104	1	1604
		ZY	052°	68°	1_YZ	052°	68°	010.3°	0.00097	0.00089	1	2545
TB-2 UJ		XY	237°	29°	1_XY	237°	29°	126.7°	0.00147	0.00135	1	2084
	123°	XZ	147°	90°	1_XZ	147°	90°	149.4°	0.00146	0.00134	1	1568
		ZY	057°	61°	1_YZ	057°	61°	030.1°	0.00131	0.00120	1	2341
TB-2 UK		XY	170°	29°	1_XY	170°	29°	038.5°	0.00136	0.00116	1	2453
	056°	XZ	080°	90°	1_XZ	080°	90°	076.3°	0.00135	0.00124	1	2181
		ZY	350°	61°	1_YZ	350°	61°	142.6°	0.00148	0.00127	1	1679
TB-2 LA		XY	030°	62°	1_XY	030°	62°	059.3°	0.00104	0.00095	1	1620
	276°	XZ	300°	90°	1_XZ	300°	90°	024.7°	0.00076	0.00073	1	1861
		ZY	210°	28°	1_YZ	300°	28°	040.6°	0.00083	0.00078	1	1992
TB-2 LC		XY	038°	70°	1_XY	038°	70°	145.5°	0.00438	0.00228	1	780
	284°	XZ	308°	90°	1_XZ	308°	90°	079.1°	0.00308	0.00241	1	889
		ZY	218°	20°	1_YZ	218°	20°	173.8°	0.00349	0.00212	1	1184
TB-2 LD		XY	049°	57°	1_XY	049°	57°	156.2°	0.00436	0.00230	1	1184
	295°	XZ	319°	90°	1_XZ	319°	90°	052.8°	0.00448	0.00219	1	848
		ZY	229°	33°	1_YZ	229°	33°	080.3°	0.00361	0.00282	1	701
TB-2 LE		XY	059°	56°	1_XY	059°	56°	159.8°	0.00576	0.00209	1	611
	305°	XZ	329°	90°	1_XZ	329°	90°	021.9°	0.00397	0.00276	1	951
		ZY	239°	34°	1_YZ	239°	34°	063.6°	0.00425	0.00203	1	1112
TB-4 UA		XY	207°	39°	1_XY	207°	39°	038.1°	0.00271	0.00175	1	921
	103°	XZ	127°	90°	1_XZ	127°	90°	063.2°	0.00208	0.00173	1	1113
		ZY	037°	51°	1_YZ	037°	51°	020.0°	0.00156	0.00135	1	1069
TB-4 UB		XY	201°	37°	1_XY	201°	37°	027.5°	0.00179	0.00158	1	1506
	087°	XZ	111°	90°	1_XZ	111°	90°	054.7°	0.00232	0.00188	1	1174
		ZY	021°	53°	1_YZ	021°	53°	109.5°	0.00243	0.00172	1	960

(b) continued

Sample	Original Strike	Thin Section	Strike + Mag Dec	Dip	Mag 10x	Strike	Dip	Rake	Long axis	Short axis	Weight	Grains
TB-4 UC		XY	209°	37°	1_XY	209°	37°	102.7°	0.00218	0.00173	1	890
	105°	XZ	129°	90°	1_XZ	129°	90°	129.8°	0.00197	0.00173	1	1161
		ZY	039°	53°	1_YZ	039°	53°	116.5°	0.00222	0.00178	1	1086
TB-4 UE		XY	217°	20°	1_XY	217°	20°	082.8°	0.00295	0.00183	1	937
	103°	XZ	127°	90°	1_XZ	127°	90°	103.8°	0.00230	0.00215	1	1107
		ZY	037°	70°	1_YZ	037°	70°	052.9°	0.00251	0.00226	1	925
TB-4 LA		XY	052°	72°	1_XY	052°	72°	154.7°	0.00258	0.00192	1	899
	298°	XZ	322°	90°	1_XZ	322°	90°	006.8°	0.00290	0.00194	1	834
		ZY	232°	18°	1_YZ	232°	18°	040.0°	0.00221	0.00182	1	991
TB-4 LB		XY	039°	66°	1_XY	039°	66°	156.3°	0.00358	0.00312	1	671
	285°	XZ	309°	90°	1_XZ	309°	90°	060.4°	0.00331	0.00300	1	596
		ZY	219°	24°	1_YZ	219°	24°	128.0°	0.00580	0.00510	1	271
TB-4 LC		XY	104°	80°	1_XY	104°	80°	038.9°	0.00467	0.00235	1	515
	350°	XZ	014°	90°	1_XZ	014°	90°	155.3°	0.00301	0.00228	1	716
		ZY	284°	10°	1_YZ	284°	10°	090.4°	0.00413	0.00232	1	524
TB-4 LE		XY	009°	54°	1_XY	009°	54°	081.0°	0.00265	0.00220	1	1130
	255°	XZ	279°	90°	1_XZ	279°	90°	023.0°	0.00302	0.00224	1	1347
		ZY	189°	36°	1_YZ	189°	36°	097.6°	0.00218	0.00183	1	1511
TB-5 UA		XY	078°	80°	1_XY	078°	80°	165.4°	0.00225	0.00160	1	987
	324°	XZ	348°	90°	1_XZ	348°	90°	012.0°	0.00231	0.00193	1	938
		ZY	258°	10°	1_YZ	258°	10°	089.8°	0.00223	0.00212	1	927
TB-5 UB		XY	075°	78°	1_XY	075°	78°	040.8°	0.00236	0.00215	1	820
	321°	XZ	345°	90°	1_XZ	345°	90°	131.8°	0.00240	0.00202	1	828
		ZY	255°	12°	1_YZ	255°	12°	050.9°	0.00238	0.00204	1	786
TB-5 UC		XY	093°	77°	1_XY	093°	77°	150.5°	0.00205	0.00189	1	1120
	339°	XZ	003°	90°	1_XZ	003°	90°	051.2°	0.00199	0.00186	1	1168
		ZY	273°	13°	1_YZ	273°	13°	123.2°	0.00195	0.00188	1	1076
TB-5 UD		XY	072°	78°	1_XY	075°	78°	166.8°	0.00243	0.00212	1	872
	318°	XZ	342°	90°	1_XZ	342°	90°	088.9°	0.00228	0.00207	1	1135
		ZY	252°	12°	1_YZ	252°	12°	084.8°	0.00269	0.00250	1	862
TB-5 LA		XY	109°	82°	1_XY	109°	82°	172.0°	0.00263	0.00213	1	967
	355°	XZ	019°	90°	1_XZ	019°	90°	050.6°	0.00243	0.00206	1	1026
		ZY	289°	08°	1_YZ	289°	08°	049.2°	0.00262	0.00227	1	731
TB-5 LB		XY	185°	80°	1_XY	185°	80°	028.6°	0.00372	0.00271	1	490
	071°	XZ	095°	90°	1_XZ	095°	90°	068.7°	0.00263	0.00215	1	798
		ZY	005°	10°	1_YZ	005°	10°	143.9°	0.00207	0.00163	1	1108
SHF-2 LA		XY	285°	63°	1_XY	285°	63°	163.1°	0.00222	0.00193	1	1814
	171°	XZ	195°	90°	1_XZ	195°	90°	049.7°	0.00214	0.00150	1	1793
		ZY	105°	27°	1_YZ	105°	27°	036.0°	0.00227	0.00179	1	2153
SHF-2 LB		XY	258°	55°	1_XY	258°	55°	036.4°	0.00337	0.00148	1	1610
	144°	XZ	168°	90°	1_XZ	168°	90°	099.8°	0.00217	0.00172	1	1684
		ZY	078°	35°	1_YZ	078°	35°	065.0°	0.00256	0.00215	1	1482

(b) continued

Sample	Original Strike	Thin Section	Strike + Mag Dec	Dip	Mag 10x	Strike	Dip	Rake	Long axis	Short axis	Weight	Grains
SHF-2 LC		XY	251°	72°	1_XY	251°	72°	176.5°	0.00020	0.00018	1	1746
	137°	XZ	161°	90°	1_XZ	161°	90°	076.1°	0.00023	0.00021	1	1379
		ZY	071°	18°	1_YZ	071°	18°	141.5°	0.00021	0.00020	1	1634
SHF-2 LD		XY	226°	65°	1_XY	226°	65°	002.3°	0.00184	0.00151	1	2251
	112°	XZ	136°	90°	1_XZ	136°	90°	121.3°	0.00176	0.00130	1	2315
		ZY	046°	25°	1_YZ	046°	25°	130.0°	0.00180	0.00122	1	2664
SHF-2 LE		XY	283°	76°	1_XY	283°	76°	146.9°	0.00205	0.00109	1	2163
	169°	XZ	193°	90°	1_XZ	193°	90°	032.1°	0.00139	0.00090	1	3337
		ZY	103°	14°	1_YZ	103°	14°	158.7°	0.00199	0.00123	1	1993
SHF-2 UA		XY	050°	33°	1_XY	050°	33°	111.2°	0.00127	0.00108	1	2376
	296°	XZ	320°	90°	1_XZ	320°	90°	119.5°	0.00152	0.00123	1	1929
		ZY	230°	57°	1_YZ	230°	57°	074.8°	0.00188	0.00158	1	1891
SHF-2 UB		XY	093°	35°	1_XY	093°	35°	139.7°	0.00158	0.00128	1	1783
	339°	XZ	003°	90°	1_XZ	003°	90°	067.9°	0.00118	0.00110	1	2426
		ZY	273°	55°	1_YZ	273°	55°	067.0°	0.00155	0.00137	1	1745
SHF-2 UC		XY	048°	25°	1_XY	048°	25°	006.9°	0.00138	0.00114	1	1850
	294°	XZ	318°	90°	1_XZ	318°	90°	090.0°	0.00178	0.00149	1	1044
		ZY	228°	65°	1_YZ	228°	65°	052.9°	0.00187	0.00157	1	1152
SHF-2 UD		XY	051°	46°	1_XY	051°	46°	173.4°	0.00251	0.00175	1	1386
	297°	XZ	321°	90°	1_XZ	321°	90°	101.4°	0.00268	0.00209	1	1495
		ZY	231°	44°	1_YZ	231°	44°	165.2°	0.00272	0.00224	1	1113
SHF-3 LA		XY	159°	71°	1_XY	159°	71°	122.1°	0.00220	0.00146	1	1572
	045°	XZ	069°	90°	1_XZ	069°	90°	082.4°	0.00197	0.00189	1	1568
		ZY	339°	19°	1_YZ	339°	19°	121.3°	0.00241	0.00149	1	1608
SHF-3 LB		XY	151°	70°	1_XY	151°	70°	145.6°	0.00214	0.00184	1	1460
	037°	XZ	061°	90°	1_XZ	061°	90°	052.8°	0.00219	0.00192	1	1327
		ZY	331°	20°	1_YZ	331°	20°	053.7°	0.00219	0.00174	1	1372
SHF-3 LC		XY	180°	74°	1_XY	180°	74°	152.9°	0.00201	0.00189	1	1532
	066°	XZ	090°	90°	1_XZ	090°	90°	128.0°	0.00218	0.00197	1	1253
		ZY	000°	16°	1_YZ	000°	16°	136.7°	0.00227	0.00216	1	1053
SHF-3 LD		XY	182°	65°	1_XY	182°	65°	035.0°	0.00305	0.00257	1	1275
	068°	XZ	092°	90°	1_XZ	092°	90°	071.6°	0.00284	0.00216	1	1309
		ZY	002°	25°	1_YZ	002°	25°	165.5°	0.00251	0.00229	1	1223
SHF-3 UA		XY	009°	24°	1_XY	009°	24°	148.9°	0.00221	0.00170	1	1690
	255°	XZ	279°	90°	1_XZ	279°	90°	155.4°	0.00277	0.00191	1	1020
		ZY	189°	66°	1_YZ	189°	66°	177.6°	0.00197	0.00152	1	1683
SHF-3 UB		XY	252°	17°	1_XY	252°	17°	059.2°	0.00216	0.00196	1	1181
	138°	XZ	162°	90°	1_XZ	162°	90°	110.2°	0.00217	0.00198	1	1262
		ZY	072°	73°	1_YZ	072°	73°	022.5°	0.00195	0.00187	1	1499
SHF-3 UC		XY	232°	17°	1_XY	232°	17°	054.7°	0.00259	0.00227	1	897
	120°	XZ	142°	90°	1_XZ	142°	90°	024.8°	0.00235	0.00168	1	1629
		ZY	052°	73°	1_YZ	052°	73°	045.2°	0.00191	0.00165	1	1758

(b) continued

Sample	Original Strike	Thin Section	Strike + Mag Dec	Dip	Mag 10x	Strike	Dip	Rake	Long axis	Short axis	Weight	Grains
SHF-3 UD		XY	031°	28°	1_XY	031°	28°	003.6°	0.00136	0.00129	1	2402
	277°	XZ	301°	90°	1_XZ	301°	90°	070.5°	0.00143	0.00118	1	2506
		ZY	211°	62°	1_YZ	211°	62°	098.1°	0.00144	0.00130	1	2484
SHF-4 LA		XY	093°	84°	1_XY	093°	84°	160.7°	0.00120	0.00109	1	2760
	339°	XZ	003°	90°	1_XZ	003°	90°	095.1°	0.00121	0.00116	1	2893
		ZY	273°	06°	1_YZ	273°	06°	151.2°	0.00130	0.00120	1	2834
SHF-4 LC		XY	115°	85°	1_XY	115°	85°	048.3°	0.00145	0.00125	1	2647
	001°	XZ	025°	90°	1_XZ	025°	90°	118.7°	0.00127	0.00110	1	2619
		ZY	295°	05°	1_YZ	295°	05°	048.5°	0.00142	0.00123	1	2450
SHF-4 LD		XY	113°	87°	1_XY	113°	87°	053.9°	0.00175	0.00130	1	2056
	359°	XZ	023°	90°	1_XZ	023°	90°	019.3°	0.00161	0.00121	1	2036
		ZY	293°	03°	1_YZ	293°	03°	001.9°	0.00173	0.00146	1	1977
SHF-4 UA		XY	038°	85°	1_XY	038°	85°	025.9°	0.00169	0.00154	1	2341
	284°	XZ	308°	90°	1_XZ	308°	90°	045.1°	0.00147	0.00120	1	2670
		ZY	218°	05°	1_YZ	218°	05°	127.0°	0.00157	0.00117	1	2722
SHF-4 UB		XY	046°	81°	1_XY	046°	81°	045.0°	0.00133	0.00098	1	2594
	292°	XZ	316°	90°	1_XZ	316°	90°	024.2°	0.00137	0.00124	1	2944
		ZY	226°	09°	1_YZ	226°	09°	128.1°	0.00139	0.00122	1	2728
SHF-4 UC		XY	066°	90°	1_XY	066°	90°	128.1°	0.00138	0.00117	1	2459
	312°	XZ	336°	90°	1_XZ	336°	90°	009.8°	0.00142	0.00135	1	2459
		ZY	246°	00°	1_YZ	246°	00°	116.5°	0.00140	0.00125	1	2255
SHF-4 UD		XY	050°	80°	1_XY	050°	80°	064.0°	0.00162	0.00136	1	2218
	296°	XZ	320°	90°	1_XZ	320°	90°	119.5°	0.00140	0.00112	1	2715
		ZY	230°	10°	1_YZ	230°	10°	067.7°	0.00140	0.00119	1	2706
SHF-5 LB		XY	278°	69°	1_XY	278°	69°	104.6°	0.00180	0.00151	1	1853
	164°	XZ	188°	90°	1_XZ	188°	90°	031.0°	0.00196	0.00188	1	1738
		ZY	098°	21°	1_YZ	098°	21°	033.9°	0.00207	0.00169	1	1994
SHF-5 LC		XY	279°	66°	1_XY	279°	66°	111.1°	0.00197	0.00176	1	1564
	165°	XZ	189°	90°	1_XZ	189°	90°	006.0°	0.00200	0.00160	1	2013
		ZY	099°	24°	1_YZ	099°	24°	042.0°	0.00201	0.00153	1	2062
SHF-5 LD		XY	199°	72°	1_XY	199°	72°	058.7°	0.00204	0.00168	1	1799
	085°	XZ	109°	90°	1_XZ	109°	90°	108.1°	0.00186	0.00139	1	1907
		ZY	019°	18°	1_YZ	019°	18°	107.8°	0.00177	0.00146	1	2254
SHF-5 LE		XY	296°	80°	1_XY	296°	80°	141.4°	0.00182	0.00165	1	1905
	182°	XZ	206°	90°	1_XZ	206°	90°	103.6°	0.00183	0.00163	1	1843
		ZY	116°	10°	1_YZ	116°	10°	172.4°	0.00175	0.00159	1	1999
SHF-5 LF		XY	288°	60°	1_XY	288°	60°	118.3°	0.00194	0.00159	1	1608
	174°.	XZ	198°	90°	1_XZ	198°	90°	078.3°	0.00244	0.00190	1	1144
		ZY	108°	30°	1_YZ	108°	30°	075.2°	0.00200	0.00192	1	1408
SHF-5 UA		XY	309°	84°	1_XY	309°	84°	017.4°	0.00107	0.00102	1	2933
	195°	XZ	219°	90°	1_XZ	219°	90°	061.0°	0.00121	0.00116	1	2850
		ZY	129°	06°	1_YZ	129°	06°	055.2°	0.00147	0.00136	1	1645

(b) continued

Sample	Original Strike	Thin Section	Strike + Mag Dec	Dip	Mag 10x	Strike	Dip	Rake	Long axis	Short axis	Weight	Grains
SHF-5 UB		XY	299°	84°	1_XY	299°	84°	016.8°	0.00203	0.00169	1	1797
	185°	XZ	209°	90°	1_XZ	209°	90°	055.8°	0.00179	0.00170	1	1976
		ZY	119°	06°	1_YZ	119°	06°	119.5°	0.00146	0.00138	1	2170
SHF-5 UE		XY	269°	82°	1_XY	269°	82°	057.6°	0.00256	0.00198	1	1432
	154°	XZ	179°	90°	1_XZ	179°	90°	081.1°	0.00247	0.00164	1	1619
		ZY	089°	08°	1_YZ	089°	08°	117.2°	0.00254	0.00188	1	1476
SHF-5 UF		XY	282°	86°	1_XY	282°	86°	177.3°	0.00266	0.00133	1	1929
XY 1	168°	XZ	192°	90°	1_XZ	192°	90°	111.9°	0.00212	0.00162	1	1760
		ZY	102°	04°	1_YZ	102°	04°	017.8°	0.00215	0.00172	1	1606
SHF-5 UF		XY	282°	86°	1_XY	282°	86°	045.0°	0.00242	0.00208	1	1573
XY 2	168°	XZ	192°	90°	1_XZ	192°	90°	111.9°	0.00212	0.00162	1	1760
		ZY	102°	04°	1_YZ	102°	04°	017.8°	0.00215	0.00172	1	1606
SHF-6 LA		XY	191°	59°	1_XY	191°	59°	052.0°	0.00237	0.00190	1	1543
	077°	XZ	101°	90°	1_XZ	101°	90°	048.4°	0.00230	0.00174	1	1665
		YZ	011°	31°	1_YZ	011°	31°	077.4°	0.00237	0.00181	1	1461
SHF-6 LB		XY	209°	69°	1_XY	209°	69°	119.6°	0.00265	0.00208	1	1107
	095°	XZ	119°	90°	1_XZ	119°	90°	143.4°	0.00261	0.00191	1	1519
		YZ	029°	21°	1_YZ	029°	21°	065.8°	0.00262	0.00169	1	1433
SHF-6 LC		XY	199°	67°	1_XY	199°	67°	167.5°	0.00227	0.00189	1	1764
	085°	XZ	109°	90°	1_XZ	109°	90°	058.5°	0.00256	0.00185	1	1589
		YZ	019°	23°	1_YZ	019°	23°	002.9°	0.00233	0.00198	1	1514
SHF-6 LD		XY	302°	56°	1_XY	302°	56°	052.2°	0.00217	0.00177	1	1516
	188°	XZ	212°	90°	1_XZ	212°	90°	172.5°	0.00196	0.00188	1	1695
		YZ	122°	34°	1_YZ	122°	34°	125.0°	0.00207	0.00191	1	1999
SHF-6 LF		XY	280°	71°	1_XY	280°	71°	056.8°	0.00265	0.00242	1	1299
	166°	XZ	190°	90°	1_XZ	190°	90°	155.0°	0.00350	0.00205	1	1289
		YZ	100°	19°	1_YZ	100°	19°	106.5°	0.00272	0.00203	1	1413
SHF-6 UA		XY	267°	65°	1_XY	267°	65°	011.8°	0.00179	0.00173	1	1880
	153°	XZ	177°	90°	1_XZ	177°	90°	058.1°	0.00183	0.00136	1	2225
		YZ	087°	25°	1_YZ	087°	25°	157.6°	0.00180	0.00157	1	1861
SHF-6 UB		XY	269°	45°	1_XY	269°	45°	022.7°	0.00256	0.00184	1	1751
	155°	XZ	179°	90°	1_XZ	179°	90°	085.1°	0.00271	0.00197	1	1621
		YZ	089°	45°	1_YZ	089°	45°	130.2°	0.00205	0.00175	1	1673
SHF-6 UC		XY	131°	24°	1_XY	131°	24°	167.8°	0.00135	0.00124	1	2337
	017°	XZ	041°	90°	1_XZ	041°	90°	006.8°	0.00135	0.00121	1	2442
		YZ	311°	66°	1_YZ	311°	66°	162.5°	0.00161	0.00133	1	2357
SHF-6 UD		XY	325°	75°	1_XY	325°	75°	106.2°	0.00184	0.00158	1	1978
	211°	XZ	235°	90°	1_XZ	235°	90°	100.8°	0.00196	0.00172	1	1725
		YZ	145°	15°	1_YZ	145°	15°	089.1°	0.00178	0.00167	1	2036
SHF-6 UF		XY	276°	68°	1_XY	276°	68°	136.6°	0.00186	0.00135	1	1660
	162°	XZ	186°	90°	1_XZ	186°	90°	106.2°	0.00228	0.00203	1	1290
		YZ	096°	22°	1_YZ	096°	22°	092.0°	0.00202	0.00163	1	1552

(b) continued

Sample	Original Strike	Thin Section	Strike + Mag Dec	Dip	Mag 10x	Strike	Dip	Rake	Long axis	Short axis	Weight	Grains
SHF-6 UG		XY	250°	68°	1_XY	250°	68°	041.0°	0.00198	0.00188	1	1546
	136°	XZ	160°	90°	1_XZ	160°	90°	038.5°	0.00228	0.00185	1	1473
		YZ	070°	22°	1_YZ	070°	22°	172.4°	0.00239	0.00212	1	1179
SHF-7 LA		XY	337°	79°	1_XY	337°	79°	146.2°	0.00227	0.00191	1	1731
	223°	XZ	247°	90°	1_XZ	247°	90°	129.9°	0.00211	0.00194	1	1371
		YZ	157°	11°	1_YZ	157°	11°	156.7°	0.00209	0.00185	1	1326
SHF-7 LB		XY	015°	83°	1_XY	015°	83°	140.1°	0.00193	0.00143	1	1762
	261°	XZ	285°	90°	1_XZ	285°	90°	084.0°	0.00172	0.00149	1	2220
		YZ	195°	07°	1_YZ	195°	07°	118.4°	0.00198	0.00160	1	1765
SHF-8 LC		XY	292°	70°	1_XY	292°	70°	023.5°	0.00233	0.00185	1	1549
	178°	XZ	202°	90°	1_XZ	202°	90°	151.9°	0.00203	0.00200	1	1601
		ZY	112°	20°	1_YZ	112°	20°	178.1°	0.00185	0.00170	1	1829
SHF-8 LD		XY	288°	65°	1_XY	288°	65°	060.5°	0.00194	0.00147	1	1669
	174°	XZ	198°	90°	1_XZ	198°	90°	107.7°	0.00209	0.00153	1	1718
		ZY	108°	25°	1_YZ	108°	25°	069.0°	0.00214	0.00194	1	1260
SHF-8 LE		XY	283°	61°	1_XY	283°	61°	047.4°	0.00164	0.00142	1	2082
	169°	XZ	193°	90°	1_XZ	193°	90°	050.9°	0.00161	0.00160	1	1844
		ZY	103°	29°	1_YZ	103°	29°	046.7°	0.00167	0.00123	1	2858
SHF-8 LF		XY	010°	79°	1_XY	010°	79°	078.2°	0.00215	0.00193	1	1366
	256°	XZ	280°	90°	1_XZ	280°	90°	114.3°	0.00222	0.00185	1	1468
		ZY	190°	21°	1_YZ	190°	21°	120.1°	0.00198	0.00149	1	1499
SHF-8 LK		XY	358°	76°	1_XY	358°	76°	148.2°	0.00179	0.00154	1	1763
	244°	XZ	268°	90°	1_XZ	268°	90°	021.9°	0.00156	0.00147	1	1945
		ZY	178°	14°	1_YZ	178°	14°	008.9°	0.00172	0.00129	1	1858
SHF-8 UA		XY	098°	25°	1_XY	098°	25°	066.8°	0.00212	0.00179	1	2043
	344°	XZ	008°	90°	1_XZ	008°	90°	143.2°	0.00269	0.00164	1	1951
		ZY	278°	65°	1_YZ	278°	65°	074.1°	0.00198	0.00152	1	1986
SHF-8 UB		XY	126°	35°	1_XY	126°	35°	007.4°	0.00119	0.00108	1	2724
	012°	XZ	036°	90°	1_XZ	036°	90°	159.5°	0.00134	0.00124	1	2782
		ZY	306°	55°	1_YZ	306°	55°	033.3°	0.00128	0.00126	1	2324
SHF-8 UC		XY	111°	41°	1_XY	111°	41°	140.5°	0.00134	0.00127	1	2003
	357°	XZ	021°	90°	1_XZ	021°	90°	006.0°	0.00145	0.00136	1	2109
		ZY	291°	49°	1_YZ	291°	49°	077.9°	0.00138	0.00126	1	1988
SHF-8 UH		XY	107°	32°	1_XY	107°	32°	000.9°	0.00189	0.00167	1	1607
	353°	XZ	017°	90°	1_XZ	017°	90°	147.1°	0.00181	0.00153	1	1780
		ZY	287°	58°	1_YZ	287°	58°	054.9°	0.00208	0.00185	1	1144
SHF-9 LA		XY	003°	84°	1_XY	003°	84°	002.1°	0.00228	0.00219	1	938
	249°	XZ	273°	90°	1_XZ	273°	90°	160.5°	0.00266	0.00199	1	1089
		ZY	183°	06°	1_YZ	183°	06°	050.8°	0.00267	0.00254	1	916
SHF-9 LE		XY	013°	57°	1_XY	013°	57°	052.1°	0.00227	0.00175	1	1300
	259°	XZ	283°	90°	1_XZ	283°	90°	075.5°	0.00249	0.00212	1	1008
		ZY	193°	33°	1_YZ	193°	33°	025.1°	0.00247	0.00209	1	1073

(b) continued

Sample	Original Strike	Thin Section	Strike + Mag Dec	Dip	Mag 10x	Strike	Dip	Rake	Long axis	Short axis	Weight	Grains
SHF-9 LG		XY	202°	37°	1_XY	202°	37°	004.3°	0.00214	0.00195	1	1145
	088°	XZ	112°	90°	1_XZ	112°	90°	091.9°	0.00203	0.00170	1	1090
		ZY	022°	53°	1_YZ	022°	53°	049.9°	0.00263	0.00222	1	1028
SHF-9 LN		XY	359°	78°	1_XY	359°	78°	005.5°	0.00216	0.00184	1	1137
	245°	XZ	269°	90°	1_XZ	269°	90°	148.2°	0.00180	0.00167	1	1268
		ZY	179°	12°	1_YZ	179°	12°	053.0°	0.00182	0.00154	1	1363
SHF-9 LO		XY	275°	77°	1_XY	275°	77°	054.3°	0.00227	0.00186	1	1115
	161°	XZ	185°	90°	1_XZ	185°	90°	075.6°	0.00178	0.00158	1	1722
		ZY	095°	13°	1_YZ	095°	13°	094.5°	0.00212	0.00171	1	1233
SHF-9 LU		XY	141°	75°	1_XY	141°	75°	031.0°	0.00195	0.00166	1	1576
	027°	XZ	051°	90°	1_XZ	051°	90°	069.6°	0.00203	0.00165	1	1410
		ZY	321°	15°	1_YZ	321°	15°	008.3°	0.00180	0.00163	1	1563
SHF-9 UA		XY	310°	60°	1_XY	310°	60°	023.9°	0.01239	0.00951	1	850
	196°	XZ	220°	90°	1_XZ	220°	90°	046.6°	0.01109	0.00963	1	961
		ZY	130°	30°	1_YZ	130°	30°	033.1°	0.01074	0.00891	1	938
SHF-9 UB		XY	304°	52°	1_XY	304°	52°	029.3°	0.01269	0.00783	1	1028
	190°	XZ	214°	90°	1_XZ	214°	90°	004.9°	0.01226	0.00855	1	1048
		ZY	124°	38°	1_YZ	124°	38°	179.5°	0.01072	0.00851	1	1097
SHF-10 LA		XY	272°	68°	1_XY	272°	68°	154.1°	0.00174	0.00145	1	1758
	158°	XZ	182°	90°	1_XZ	182°	90°	020.4°	0.00211	0.00156	1	1290
		YZ	092°	22°	1_YZ	092°	22°	118.3°	0.00194	0.00170	1	1371
SHF-10 LC		XY	014°	75°	1_XY	014°	75°	146.3°	0.00188	0.00166	1	1455
	260°	XZ	284°	90°	1_XZ	284°	90°	142.2°	0.00200	0.00186	1	1366
		YZ	194°	15°	1_YZ	194°	15°	145.5°	0.00241	0.00198	1	1105
SHF-10 LE		XY	359°	88°	1_XY	359°	88°	147.7°	0.00259	0.00233	1	788
	245°	XZ	269°	90°	1_XZ	269°	90°	142.7°	0.00259	0.00221	1	861
		YZ	179°	02°	1_YZ	179°	02°	089.4°	0.00302	0.00245	1	788
SHF-10 UB		XY	105°	20°	1_XY	105°	20°	132.6°	0.00287	0.00266	1	816
	351°	XZ	015°	90°	1_XZ	015°	90°	155.7°	0.00350	0.00261	1	775
		YZ	285°	70°	1_YZ	285°	70°	136.2°	0.00305	0.00219	1	765
SHF-10 UD		XY	107°	29°	1XY	107°	29°	119.3°	0.00372	0.00342	1	463
	353°	XZ	017°	90°	1_XZ	017°	90°	154.1°	0.00259	0.00246	1	697
		YZ	287°	61°	1_YZ	287°	61°	125.4°	0.00342	0.00268	1	779
SHF-10 UF		XY	029°	77°	1_XY	029°	77°	072.3°	0.00261	0.00232	1	1042
	275°	XZ	299°	90°	1_XZ	299°	90°	088.6°	0.00257	0.00231	1	937
		YZ	209°	13°	1_YZ	209°	13°	047.5°	0.00231	0.00195	1	960
SHF-11 LA		XY	315°	54°	1_XY	315°	54°	118.0°	0.00260	0.00238	1	923
	201°	XZ	225°	90°	1_XZ	225°	90°	169.4°	0.00230	0.00174	1	1260
		YZ	135°	36°	1_YZ	135°	36°	150.1°	0.00271	0.00213	1	804

(b) continued

Sample	Original Strike	Thin Section	Strike + Mag Dec	Dip	Mag 10x	Strike	Dip	Rake	Long axis	Short axis	Weight	Grains
SHF-11 LB		XY	203°	51°	1_XY	203°	51°	009.6°	0.00211	0.00200	1	1080
	089°	XZ	113°	90°	1_XZ	113°	90°	083.8°	0.00289	0.00227	1	923
		YZ	023°	39°	1_YZ	023°	39°	069.5°	0.00238	0.00217	1	997
SHF-11 LE		XY	202°	62°	1_XY	202°	62°	167.3°	0.00177	0.00148	1	1606
	188°	XZ	112°	90°	1_XZ	112°	90°	028.1°	0.00218	0.00185	1	1401
		YZ	022°	28°	1_YZ	022°	28°	107.1°	0.00165	0.00158	1	1724
SHF-11 LH		XY	234°	68°	1_XY	234°	68°	147.4°	0.00216	0.00183	1	1592
	120°	XZ	144°	90°	1_XZ	144°	90°	005.6°	0.00190	0.00181	1	1354
		YZ	054°	22°	1_YZ	054°	22°	009.8°	0.00221	0.00196	1	1305
SHF-11 UB		XY	077°	16°	1_XY	077°	16°	118.7°	0.00234	0.00219	1	1053
	323°	XZ	347°	90°	1_XZ	347°	90°	159.4°	0.00248	0.00231	1	713
		YZ	257°	74°	1_YZ	257°	74°	166.2°	0.00240	0.00190	1	1156
SHF-11 UC		XY	174°	11°	1_XY	174°	11°	045.9°	0.00231	0.00204	1	1019
	060°	XZ	084°	90°	1_XZ	084°	90°	148.9°	0.00215	0.00201	1	1182
		YZ	354°	79°	1_YZ	354°	79°	159.1°	0.00250	0.00207	1	1152
SHF-11 UE		XY	269°	17°	1_XY	269°	17°	086.1°	0.00244	0.00235	1	884
	155°	XZ	179°	90°	1_XZ	179°	90°	085.8°	0.00308	0.00235	1	866
		YZ	089°	73°	1_YZ	089°	73°	030.0°	0.00244	0.00230	1	1032

(c) 3-D ellipse data for samples from Thompson's Bay and Shaka's Rock

		Foliation			Lineation		Minimum Axis			
Sample	Mag.	Dip	Strike	Rake	Plunge	Trend	Plunge	Trend	[a]P'	[b]T
TB-1 UA	10x	69.0°	265.0°	158.3°	20.2°	086.8°	21.0°	175.0°	1.158	*-0.551*
TB-1 UB	10x	61.4°	328.1°	037.2°	32.1°	348.1°	28.6°	238.1°	1.259	*-0.633*
TB-1 UC	10x	63.2°	221.2°	035.0°	30.8°	238.7°	26.8°	131.2°	1.147	*-0.310*
TB-1 UD	10x	29.4°	289.7°	044.4°	20.1°	330.3°	60.6°	199.7°	1.113	0.370
TB-1 UE	10x	63.8°	143.7°	151.4°	25.4°	310.2°	26.2°	053.7°	1.191	0.266
TB-1 UF	10x	54.8°	162.0°	098.7°	53.8°	266.9°	35.2°	072.0°	1.249	*-0.342*
TB-1 UG	10x	65.6°	188.4°	037.3°	33.5°	205.9°	24.4°	098.4°	1.785	*-0.579*
TB-1 UH	10x	38.8°	211.1°	095.1°	38.7°	307.6°	51.2°	121.1°	1.524	-0.276
TB-1 UI	10x	38.8°	235.3°	011.7°	07.3°	244.5°	51.2°	145.3°	1.803	*-0.800*
TB-1 UJ	10x	50.1°	070.5°	101.7°	48.6°	178.4°	39.9°	340.5°	2.026	*-0.317*
TB-1 UP	10x	35.9°	266.7°	164.0°	09.3°	073.7°	54.1°	176.7°	1.507	0.075
TB-2 LA	10x	57.5°	306.4°	051.2°	41.1°	340.2°	32.5°	216.4°	1.153	0.252
TB-2 LC	2.5x	48.3°	178.3°	018.7°	13.9°	200.0°	41.7°	097.3°	1.388	0.372
TB-2 LD	10x	52.3°	201.8°	075.3°	50.0°	268.6°	37.7°	111.8°	2.773	0.011
TB-2 LE	2.5x	12.5°	267.0°	034.6°	07.1°	300.9°	77.5°	177.0°	1.543	0.128
TB-2 UA	10x	27.1°	151.9°	027.9°	12.3°	177.2°	62.9°	061.9°	1.075	0.087
TB-2 UB	10x	63.8°	203.4°	124.1°	48.0°	350.3°	26.2°	113.4°	1.314	*-0.847*
TB-2 UE	10x	36.8°	221.8°	123.7°	29.9°	351.6°	53.2°	131.8°	1.289	0.502
TB-2 UF	10x	75.5°	354.3°	050.8°	48.7°	011.3°	14.5°	264.3°	2.173	-0.224
TB-2 UG	10x	67.8°	349.9°	017.7°	16.4°	356.7°	22.2°	259.9°	1.156	*-0.681*
TB-2 UI	10x	74.8°	228.9°	119.8°	56.8°	024.3°	15.2°	138.9°	1.151	0.214
TB-2 UJ	10x	35.6°	302.3°	076.1°	34.4°	015.4°	54.4°	212.3°	1.148	-0.111
TB-2 UK	10x	53.5°	041.9°	122.1°	42.9°	178.4°	36.5°	311.9°	1.264	*-0.474*
TB-2 C(V)	10x	67.6°	230.0°	120.2°	53.1°	016.8°	22.4°	140.0°	4.128	*-0.790*
TB-2 D(V)	10x	27.1°	205.4°	144.9°	15.2°	353.4°	62.9°	115.4°	1.440	0.443
TB-2 H(V)	10x	38.6°	249.1°	104.6°	37.2°	357.5°	51.4°	159.1°	1.388	*-0.459*
TB-4 LA	10x	22.7°	147.1°	131.6°	16.8°	281.1°	67.3°	57.1°	1.565	0.443
TB-4 LB	10x	63.1°	185.0°	164.9°	13.4	358.1°	26.9°	095.0°	1.211	0.392
TB-4 LC	2.5x	57.1°	032.8°	055.3°	43.6°	070.9°	32.9°	302.8°	1.249	-0.262
TB-4 LE	2.5x	56.8°	016.2°	023.1°	19.2°	029.4°	33.2°	286.2°	1.577	-0.172
TB-4 UA	10x	67.4°	067.9°	166.5°	12.4°	242.7°	22.6°	337.9°	1.594	0.033
TB-4 UB	10x	52.8°	073.5°	082.4°	52.2	151.0°	37.2°	343.5°	1.454	*-0.510*
TB-4 UC	10x	72.5°	150.6°	125.0°	52.2°	307.4°	17.5°	060.6°	1.355	0.492
TB-4 UE	2.5x	72.0°	211.4°	124.7°	51.5°	007.4°	18.0°	121.4°	1.129	-0.362
TB-5 LA	10x	42.7°	295.3°	040.9°	26.4°	327.8°	47.3°	205.3°	1.311	-0.212
TB-5 LB	2.5x	35.6°	121.6°	039.3°	21.6°	155.2°	54.4°	031.6°	1.309	*-0.551*
TB-5 LC	2.5x	43.6°	338.0°	039.2°	25.9°	008.6°	46.4°	248.0°	1.146	0.060
TB-5 LD	2.5x	43.2°	005.4°	163.8°	11.0°	173.5°	46.8°	275.4°	1.298	0.183
TB-5 UA	10x	20.2°	201.2°	058.4°	17.1°	257.9°	69.8°	111.2°	1.370	0.660
TB-5 UB	10x	64.0°	112.1°	032.9°	29.2°	128.0°	26.0°	021.1°	1.286	*-0.550*
TB-5 UC	10x	50.3°	235.1°	070.3°	46.4°	295.9°	39.7°	145.1°	1.111	0.719
TB-5 UD	10x	46.6°	223.8°	059.1°	38.6°	272.7°	43.4°	133.8°	1.079	*-0.306*
SR-1 CA	2.5x	43.5°	183.7°	148.3°	21.2°	339.6°	46.5°	093.7°	1.711	-0.248
SR-1 CC	2.5x	13.7°	166.4°	019.5°	04.5°	185.4°	76.3°	076.4°	1.833	-0.777
SR-1 CE	2.5x	86.9°	044.8°	133.1°	46.8°	221.4°	03.1°	314.8°	1.456	0.038
SR-1 UA	10x	85.0°	282.9°	024.5°	24.4°	285.2°	05.0°	192.9°	1.339	*-0.370*
SR-1 UB	10x	67.4°	212.8°	167.4°	11.6°	027.9°	22.6°	122.8°	1.513	*-0.378*
SR-1 UC	10x	67.2°	203.2°	012.1°	05.5°	213.9°	62.8°	113.2°	2.218	*-0.427*
SR-1 UD	10x	62.0°	057.6°	160.3°	17.4°	228.0°	28.0°	327.6°	1.167	-0.077
SR-1 UE	10x	46.2°	325.5°	102.7°	44.8°	073.5°	43.8°	235.5°	1.347	0.300
SR-1 LA	10x	45.8°	027.9°	100.3°	44.9°	132.4°	44.2°	297.9°	1.757	-0.176
SR-1 LD	10x	60.4°	145.4°	145.4°	29.6°	221.7°	29.6°	330.5°	2.477	0.116

a P' = degree of anisotropy

b T = shape parameter (oblate/prolate)

(c) continued

Sample	$^{c}\sqrt{F}$ (%)	Grain size proxy (mm)	Restored Foliation			Restored Lineation	
			Dip	Strike	Azimuth	Plunge	Trend
TB-1 UA	4.0	0.12	69.7°	256.5°	346.5°	*41.5°*	*088.0°*
TB-1 UB	6.0	0.14	41.8°	320.2°	050.2°	*18.0°*	*335.5°*
TB-1 UC	8.0	0.15	78.1°	215.5°	305.5°	*10.3°*	*241.0°*
TB-1 UD	3.0	0.10	26.8°	248.0°	338.0°		
TB-1 UE	2.9	0.13	83.2°	146.4°	236.4°		
TB-1 UF	4.1	0.13	76.5°	163.8°	355.0°	*31.5°*	*265.0°*
TB-1 UG	4.8	0.14	86.5°	187.2°	277.2°	*19.6°*	*214.4°*
TB-1 UH	10.1	0.17	57.9°	200.0°	290.0°		
TB-1 UI	5.2	0.11	53.0°	216.4°	306.4°	*14.0°*	*064.0°*
TB-1 UJ	4.2	0.15	49.7°	089.3°	179.3°	*41.5°*	*200.5°*
TB-1 UP	0.8	0.18	39.4°	238.2°	328.2°		
TB-2 LA	0.4	0.07	64.5°	314.7°	044.7°		
TB-2 LC	4.3	0.63	29.2°	198.3°	288.3°		
TB-2 LD	3.4	0.31	37.0°	216.0°	306.0°		
TB-2 LE	3.5	0.73	26.0°	317.3°	047.3°		
TB-2 UA	5.8	0.11	08.7°	113.2°	203.2°		
TB-2 UB	0.5	0.09	48.1°	212.3°	302.3°	*45.5°*	*328.2°*
TB-2 UE	6.2	0.11	29.8°	252.5°	342.5°		
TB-2 UF	3.2	0.16	83.3°	173.8°	263.8°		
TB-2 UG	3.6	0.08	89.2°	349.2°	079.2°	*18.6°*	*349.0°*
TB-2 UI	7.2	0.05	66.1°	235.9°	325.9°		
TB-2 UJ	0.8	0.11	51.8°	315.7°	045.7°		
TB-2 UK	3.5	0.10	67.0°	032.6°	122.6°	*35.7°*	*194.3°*
TB-2 C(V)	4.0	0.16	60.0°	239.9°	329.9°	*58.5°*	*345.5°*
TB-2 D(V)	0.1	0.15	16.6°	252.4°	342.4°		
TB-2 H(V)	3.2	0.12	40.1°	275.2°	005.2°	*29.0°*	*341.0°*
TB-4 LA	8.9	0.16	10.2°	060.0°	150.0°		
TB-4 LB	4.4	0.28	36.0°	192.0°	282.0°		
TB-4 LC	5.7	0.39	77.0°	026.3°	116.3°		
TB-4 LE	8.1	1.02	80.1°	012.0°	102.0°		
TB-4 UA	2.5	0.19	75.2°	060.0°	150.0°		
TB-4 UB	5.2	0.14	60.0°	057.5°	147.5°	*53.0°*	*185.6°*
TB-4 UC	0.3	0.15	50.0°	145.7°	235.7°		
TB-4 UE	0.4	0.68	53.6°	220.1°	310.1°	*51.5°*	*335.0°*
TB-5 LA	9.4	0.19	54.8°	304.0°	034.0°		
TB-5 LB	4.3	0.31	25.5°	105.3°	185.3°	*21.3°*	*161.0°*
TB-5 LC	7.7	0.25	60.0°	338.0°	068.0°		
TB-5 LD	7.7	0.37	58.0°	001.0°	091.0°		
TB-5 UA	7.3	0.17	12.5°	251.5°	341.5°		
TB-5 UB	6.1	0.14	53.8°	104.6°	194.6°	*36.0°*	*136.8°*
TB-5 UC	1.9	0.15	48.6°	249.0°	339.0°		
TB-5 UD	2.9	0.15	41.0°	240.0°	330.0°		
SR-1 CA	5.0	0.74	26.0°	169.6°	259.6°		
SR-1 CC	0.7	0.78	12.5°	067.6°	157.6°	*04.3°*	*005.0°*
SR-1 CE	1.3	0.69	74.0°	225.9°	315.9°		
SR-1 UA	3.6	0.13	81.0°	285.5°	015.5°	*05.0°*	*284.0°*
SR-1 UB	0.4	0.18	48.0°	215.0°	305.0°	*11.6°*	*024.0°*
SR-1 UC	5.4	0.24	07.3°	198.0°	288.0°	*02.0°*	*215.0°*
SR-1 UD	5.2	0.18	78.7°	054.0°	144.0°		
SR-1 UE	2.3	0.16	58.2°	337.6°	067.6°		
SR-1 LA	0.5	0.16	65.8°	027.0°	117.0°		
SR-1 LD	0.6	0.11	77.0°	056.0°	146.0°		

c √F = Global Incompatibility Index

(d) 3-D ellipse data for samples from Sheffield Beach

		Foliation			Lineation		Minimum Axis			
Sample	Mag.	Dip	Strike	Rake	Plunge	Trend	Plunge	Trend	[a]P'	[b]T
SHF-2 LA	10x	53.9°	106.6°	053.4°	40.5°	145.1°	36.1°	016.6°	1.550	*-0.315*
SHF-2 LB	2.5x	86.9°	297.5°	046.6°	46.5°	300.8°	03.1°	207.5°	1.216	0.558
SHF-2 LC	10x	68.6°	056.0°	147.1°	30.4°	222.7°	21.4°	326.0°	1.124	0.436
SHF-2 LD	2.5x	63.9°	047.9°	048.6°	42.2°	074.5°	26.1°	317.9°	1.255	0.220
SHF-2 LE	2.5x	43.0°	036.1°	098.1°	42.5°	137.1°	47.0°	306.1°	2.599	*-0.664*
SHF-2 UA	10x	73.4°	142.5°	068.7°	63.2°	178.8°	16.6°	052.5°	1.351	*-0.501*
SHF-2 UB	10x	60.2°	220.5°	061.6°	49.7°	263.1°	29.8°	130.5°	1.272	0.153
SHF-2 UC	10x	89.6°	063.2°	131.9°	48.1°	242.7°	00.4°	333.2°	1.327	-0.001
SHF-2 UD	2.5x	79.8°	081.2°	057.0°	55.7°	096.4°	10.2°	351.2°	1.210	-0.189
SHF-3 LA	10x	76.8°	282.6°	018.3°	17.8°	286.9°	13.2°	192.6°	1.869	0.118
SHF-3 LB	10x	50.2°	232.8°	125.7°	38.6°	011.1°	39.8°	142.8°	1.387	-0.809
SHF-3 LC	10x	48.8°	165.9°	136.7°	31.0°	314.1°	41.2°	075.9°	1.121	-0.358
SHF-3 LD	10x	69.4°	013.5°	118.9°	55.1°	161.0°	20.6°	283.5°	1.413	-0.109
SHF-3 UA	10x	25.5°	003.5°	142.3°	15.2°	148.7°	64.5°	273.5°	1.566	-0.024
SHF-3 UB	10x	69.8°	287.2°	047.7°	43.9°	308.0°	20.2°	197.2°	1.133	0.234
SHF-3 UC	10x	53.6°	033.4°	083.9°	23.4°	116.7°	36.4°	303.4°	1.532	-0.581
SHF-3 UD	10x	70.9°	212.4°	096.8°	69.7°	322.4°	19.1°	122.4°	1.203	-0.313
SHF-4 LA	10x	74.6°	245.5°	019.2°	18.4°	250.8°	15.4°	155.5°	1.126	-0.453
SHF-4 LC	10x	86.3°	341.3°	140.6°	39.3°	158.2°	03.7°	251.3°	1.297	-0.640
SHF-4 UA	10x	66.9°	180.6°	149.1°	28.1°	347.7°	23.1°	090.6°	1.480	-0.659
SHF-4 UB	10x	44.2°	316.1°	068.9°	40.6°	017.9°	45.8°	226.1°	1.420	-0.081
SHF-4 UC	10x	54.2°	174.3°	047.8°	36.9°	207.0°	35.8°	084.3°	1.213	0.432
SHF-4 UD	10x	84.2°	294.9°	133.7°	46.0°	108.9°	05.8°	204.9°	1.341	-0.475
SHF-5 LE	10x	78.6°	289.8°	138.2°	40.8°	099.7°	11.4°	048.2°	1.172	-0.233
SHF-5 LF	10x	73.2°	069.3°	079.3°	70.1°	126.1°	16.8°	349.3°	1.394	-0.522
SHF-5 UA	10x	61.9°	169.4°	011.9°	10.5°	175.1°	28.1°	281.9°	1.098	0.188
SHF-5 UB	10x	28.0°	168.4°	106.3°	26.8°	276.7°	62.0°	016.3°	1.164	-0.182
SHF-5 UF	10x	71.3°	294.3°	046.3°	43.2°	312.9°	18.7°	316.3°	1.439	-0.128
SHF-6 LA	10x	65.4°	066.0°	053.4°	46.9°	095.3°	24.6°	323.4°	1.475	0.212
SHF-6 LB	2.5x	87.8°	243.3°	084.4°	83.9°	264.9°	02.2°	354.4°	1.213	0.236
SHF-6 LC	2.5x	61.5°	209.8°	167.8°	10.7°	023.9°	28.5°	077.8°	1.053	0.139
SHF-6 LD	2.5x	30.4°	043.7°	114.3°	27.4°	161.4°	59.6°	024.3°	1.072	-0.344
SHF-6 LF	2.5x	43.6°	037.1°	032.6°	21.8°	061.9°	46.4°	302.6°	1.195	-0.262
SHF-6 UA	10x	64.5°	079.9°	115.6°	54.4°	218.0°	25.5°	025.6°	1.353	0.116
SHF-6 UB	2.5x	84.8°	283.2°	039.2°	39.1°	287.5°	05.2°	309.2°	1.168	-0.421
SHF-6 UC	10x	13.5°	039.7°	066.6°	12.4°	105.7°	76.5°	336.6°	1.237	-0.049
SHF-6 UD	10x	76.6°	059.7°	079.1°	72.8°	109.9°	13.4°	349.1°	1.195	-0.352
SHF-6 UF	2.5x	08.2°	025.0°	021.1°	02.9°	045.9°	81.8°	291.1°	1.109	-0.222
SHF-6 UG	2.5x	34.6°	123.3°	111.5°	31.9°	238.8°	55.4°	021.5°	1.208	0.581
SHF-7 LA	2.5x	88.4°	332.5°	143.8°	36.2°	151.3°	01.6°	242.5°	1.118	-0.270
SHF-7 LB	2.5x	52.5°	178.3°	076.6°	50.5°	246.8°	37.5°	088.3°	1.210	0.456
SHF-7 LE	2.5x	42.8°	244.9°	168.0°	08.1°	056.1°	47.2°	154.9°	1.302	-0.064
SHF-7 UA	2.5x	56.8°	302.8°	030.5°	25.1°	320.6°	33.2°	212.8°	1.260	*-0.486*
SHF-7 UB	2.5x	44.2°	071.5°	150.1°	20.1°	229.0°	45.8°	341.5°	1.213	*-0.532*
SHF-7 UE	2.5x	41.2°	035.0°	065.9°	37.0°	094.2°	48.8°	305.0°	1.191	-0.288
SHF-7 UG	2.5x	44.6°	194.7°	083.3°	44.2°	275.4°	45.4°	104.7°	1.263	0.058
SHF-8 LC	10x	28.2°	179.3°	119.5°	24.3°	302.0°	61.8°	089.3°	1.246	*-0.473*
SHF-8 LD	10x	81.9°	162.4°	118.8°	60.2°	328.0°	08.1°	072.4°	1.446	*-0.459*
SHF-8 LE	10x	88.6°	329.3°	176.5°	03.5°	149.2°	01.4°	239.3°	1.402	-0.118
SHF-8 LF	10x	76.0°	313.3°	152.1°	27.1°	126.1°	14.0°	223.3°	1.345	0.767
SHF-8 UB	10x	02.1°	079.6°	067.8°	02.0°	147.4°	87.9°	349.6°	1.080	-0.108
SHF-8 UC	10x	47.7°	217.9°	153.1°	19.6°	019.0°	42.3°	127.9°	1.105	0.245
SHF-8 UH	2.5x	63.7°	174.5°	012.9°	11.6°	180.3°	26.3°	084.5°	1.160	-0.209
SHF-9 LA	10x	23.8°	012.7°	071.2°	22.4°	082.3°	66.2°	282.7°	1.307	-0.061
SHF-9 LE	10x	79.4°	227.9°	138.6°	40.6°	038.7°	10.6°	137.9°	1.369	0.238
SHF-9 LG	10x	85.9°	223.5°	125.2°	54.6°	037.7°	04.1°	133.5°	1.286	-0.109

(d) continued

		Foliation			Lineation		Minimum Axis			
Sample	Mag.	Dip	Strike	Rake	Plunge	Trend	Plunge	Trend	[a]P'	[b]T
SHF-9 LN	10x	27.9°	033.0°	010.2°	04.8°	042.0°	62.1°	303.0°	1.230	*-0.625*
SHF-9 LO	10x	63.0°	176.6°	071.0°	57.3°	229.4°	27.0°	086.6°	1.309	0.141
SHF-9 LU	10x	65.6°	337.4°	125.0°	48.3°	126.8°	24.4°	247.4°	1.301	0.225
SHF-9 UA	2.5x	57.1°	160.8°	178.6°	01.2°	340.1°	32.9°	070.8°	1.382	0.041
SHF-9 UB	2.5x	21.3°	193.4°	145.5°	11.9°	340.8°	68.7°	103.4°	1.893	-0.055
SHF-10 LA	10x	33.3°	046.0°	158.4°	11.7°	207.7°	56.7°	346.0°	1.376	0.091
SHF-10 LC	10x	80.6°	337.9°	163.6°	16.2°	155.2°	09.4°	247.9°	1.281	*-0.612*
SHF-10 LE	10x	43.4°	065.5°	041.5°	27.1°	098.2°	46.6°	039.9°	1.260	-0.261
SHF-10 UB	2.5x	88.8°	129.9°	153.1°	26.9°	309.3°	01.2°	316.4°	1.112	*-0.378*
SHF-10 UD	10x	63.2°	045.7°	033.5°	29.5°	062.4°	26.8°	315.7°	1.287	0.206
SHF-10 UF	10x	86.8°	254.8°	117.6°	68.8°	068.8°	03.2°	164.8°	1.235	0.839
SHF-11 LA	10x	28.5°	271.8°	163.2°	07.9°	076.9°	61.5°	181.8°	1.474	-0.260
SHF-11 LB	10x	80.2°	035.5°	080.3°	76.2°	080.0°	09.8°	305.5°	1.283	-0.143
SHF-11 LE	10x	31.6°	355.7°	143.8°	18.0°	143.8°	58.4°	265.7°	1.227	0.712
SHF-11 LH	10x	27.7°	325.6°	083.2°	27.5°	047.9°	62.3°	235.6°	1.212	*-0.308*
SHF-11 UB	10x	28.1°	035.5°	015.9°	07.4°	049.5°	61.9°	305.5°	1.222	0.281
SHF-11 UC	10x	26.3°	104.7°	099.4°	26.0°	205.2°	63.7°	014.7°	1.249	*-0.395*
SHF-11 UE	2.5x	37.1°	352.5°	077.2°	36.1°	066.6°	52.9°	262.5°	1.069	-0.295

a P' = degree of anisotropy

b T = shape parameter (oblate/prolate)

(d) continued

Sample	$^{c}\sqrt{F}$ (%)	Grain size proxy (mm)	Restored Foliation			Restored Lineation	
			Dip	Strike	Azimuth	Plunge	Trend
SHF-2 LA	8.6	0.27	61.0°	118.6°	208.6°	*56.0°*	*145.0°*
SHF-2 LB	0.8	0.58	78.2°	295.3°	025.3°		
SHF-2 LC	5.2	0.17	58.5°	065.0°	155.0°		
SHF-2 LD	2.2	0.33	51.2°	057.3°	147.3°		
SHF-2 LE	3.4	0.95	29.3°	055.2°	145.2°	*27.0°*	*127.4°*
SHF-2 UA	6.8	0.10	89.4°	144.2°	234.2°	*27.8°*	*134.3°*
SHF-2 UB	2.6	0.14	75.9°	215.4°	305.4°		
SHF-2 UC	5.4	0.13	80.2°	064.3°	154.3°		
SHF-2 UD	0.1	0.49	77.4°	085.2°	175.2°		
SHF-3 LA	2.5	0.20	68.3°	278.0°	008.0°		
SHF-3 LB	3.0	0.18	57.0°	221.0°	311.0°	*29.0°*	*020.6°*
SHF-3 LC	5.1	0.18	65.0°	164.7°	254.7°	*37.0°*	*325.0°*
SHF-3 LD	0.3	0.27	55.5°	018.5°	108.5°		
SHF-3 UA	9.0	0.20	12.0°	034.0°	124.0°		
SHF-3 UB	4.7	0.17	60.6°	281.5°	011.5°		
SHF-3 UC	0.3	0.18	44.4°	045.3°	135.3°	*25.5°*	*085.0°*
SHF-3 UD	1.3	0.13	80.7°	209.5°	299.5°	*66.0°*	*008.0°*
SHF-4 LA	3.5	0.11	78.0°	242.4°	332.4°	*30.3°*	*250.0°*
SHF-4 LC	4.5	0.12	74.3°	341.0°	071.0°	*36.0°*	*150.0°*
SHF-4 UA	4.7	0.15	78.2°	180.0°	270.0°	*28.0°*	*354.0°*
SHF-4 UB	2.7	0.10	34.0°	305.2°	305.2°		
SHF-4 UC	0.7	0.12	65.5°	173.9°	263.9°		
SHF-4 UD	8.1	0.14	77.8°	293.0°	023.0°	*35.5°*	*104.7°*
SHF-5 LE	2.0	0.16	75.0°	288.0°	018.0°		
SHF-5 LF	2.1	0.14	71.0°	072.0°	162.0°	*51.0°*	*112.0°*
SHF-5 UA	4.1	0.08	71.6°	169.5°	259.5°		
SHF-5 UB	8.7	0.16	38.0°	170.4°	260.4°		
SHF-5 UF	1.7	0.21	66.4°	290.6°	020.6°		
SHF-6 LA	1.6	0.23	58.0°	072.0°	162.0°		
SHF-6 LB	4.6	0.46	79.0°	056.0°	146.0°		
SHF-6 LC	3.0	0.38	72.5°	208.0°	298.0°		
SHF-6 LD	2.3	0.32	20.0°	061.8°	151.8°	*19.7°*	*156.3°*
SHF-6 LF	4.6	0.58	32.0°	045.5°	135.5°		
SHF-6 UA	8.2	0.20	60.0°	086.2°	176.2°		
SHF-6 UB	0.8	0.51	85.3°	281.8°	011.8°	*51.0°*	*288.0°*
SHF-6 UC	1.7	0.12	06.0°	119.0°	209.0°		
SHF-6 UD	3.2	0.18	68.4°	061.5°	151.5°	*59.0°*	*105.0°*
SHF-6 UF	2.0	0.34	03.5°	183.0°	273.0°		
SHF-6 UG	0.5	0.43	40.4°	138.2°	228.2°		
SHF-7 LA	4.4	-	79.8°	332.3°	062.3°		
SHF-7 LB	6.1	-	58.5°	184.7°	274.7°		
SHF-7 LE	1.5	-	53.0°	244.0°	334.0°		
SHF-7 UA	0.1	-	62.0°	298.0°	028.0°	*35.0°*	*320.0°*
SHF-7 UB	4.9	-	35.0°	075.0°	165.0°	*19.0°*	*225.0°*
SHF-7 UE	6.3	-	32.0°	030.0°	120.0°		
SHF-7 UG	10.4	-	53.0°	200.0°	290.0°		
SHF-8 LC	3.5	-	29.5°	194.5°	284.5°	*29.4°*	*298.3°*
SHF-8 LD	10.0	-	79.5°	164.3°	254.3°	*67.2°*	*317°*
SHF-8 LE	0.0	-	88.2°	149.3°	239.3°		
SHF-8 LF	9.3	-	83.0°	312.0°	042.0°		
SHF-8 UB	7.5	-	06.0°	164.7°	009.0°		
SHF-8 UC	4.0	-	53.7°	279.0°	313.0°		
SHF-8 UH	10.1	-	63.0°	179.0°	269.0°		
SHF-9 LA	5.9	-	19.0°	343.0°	073.0°		
SHF-9 LE	8.3	-	88.0°	047.0°	137.0°		
SHF-9 LG	3.8	-	81.5°	043.0°	133.0°		

(d) continued

Sample	$^{c}\sqrt{F}$ (%)	Grain size proxy (mm)	Restored Foliation			Restored Lineation	
			Dip	Strike	Azimuth	Plunge	Trend
SHF-9 LN	9.2	-	18.0°	010.0°	100.0°	*10.0°*	*043.6°*
SHF-9 LO	9.8	-	68.3°	182.2°	272.2°		
SHF-9 LU	2.2	-	66.0°	332.0°	062.0°		
SHF-9 UA	0.8	-	60.0°	170.0°	260.0°		
SHF-9 UB	5.1	-	20.6°	212.0°	292.0°		
SHF-10 LA	5.0	-	23.0°	049.2°	139.2°		
SHF-10 LC	0.1	-	77.0°	336.5°	066.5°	*07.0°*	*154.0°*
SHF-10 LE	10.0	-	34.0°	064.2°	154.2°		
SHF-10 UB	1.5	-	88.0°	130.0°	220.0°	*36.0°*	*309.0°*
SHF-10 UD	4.0	-	52.0°	046.0°	136.0°		
SHF-10 UF	0.7	-	82.5°	074.8°	164.8°		
SHF-11 LA	6.9	-	37.0°	263.0°	353.0°		
SHF-11 LB	5.2	-	71.0°	035.0°	125.0°		
SHF-11 LE	1.4	-	28.0°	339.5°	069.5°		
SHF-11 LH	4.0	-	30.0°	308.0°	038.0°	*28.0°*	*053.0°*
SHF-11 UB	7.8	-	19.0°	026.5°	116.5°		
SHF-11 UC	4.1	-	21.0°	124.0°	214.0°	*21.5°*	*202.0°*
SHF-11 UE	6.5	-	34.0°	338.0°	068.0°		

c $\sqrt{F}$ = Global Incompatibility Index

7. Magnetic mineralogy data

(a) Susceptibility-Temperature (K-T) Curves

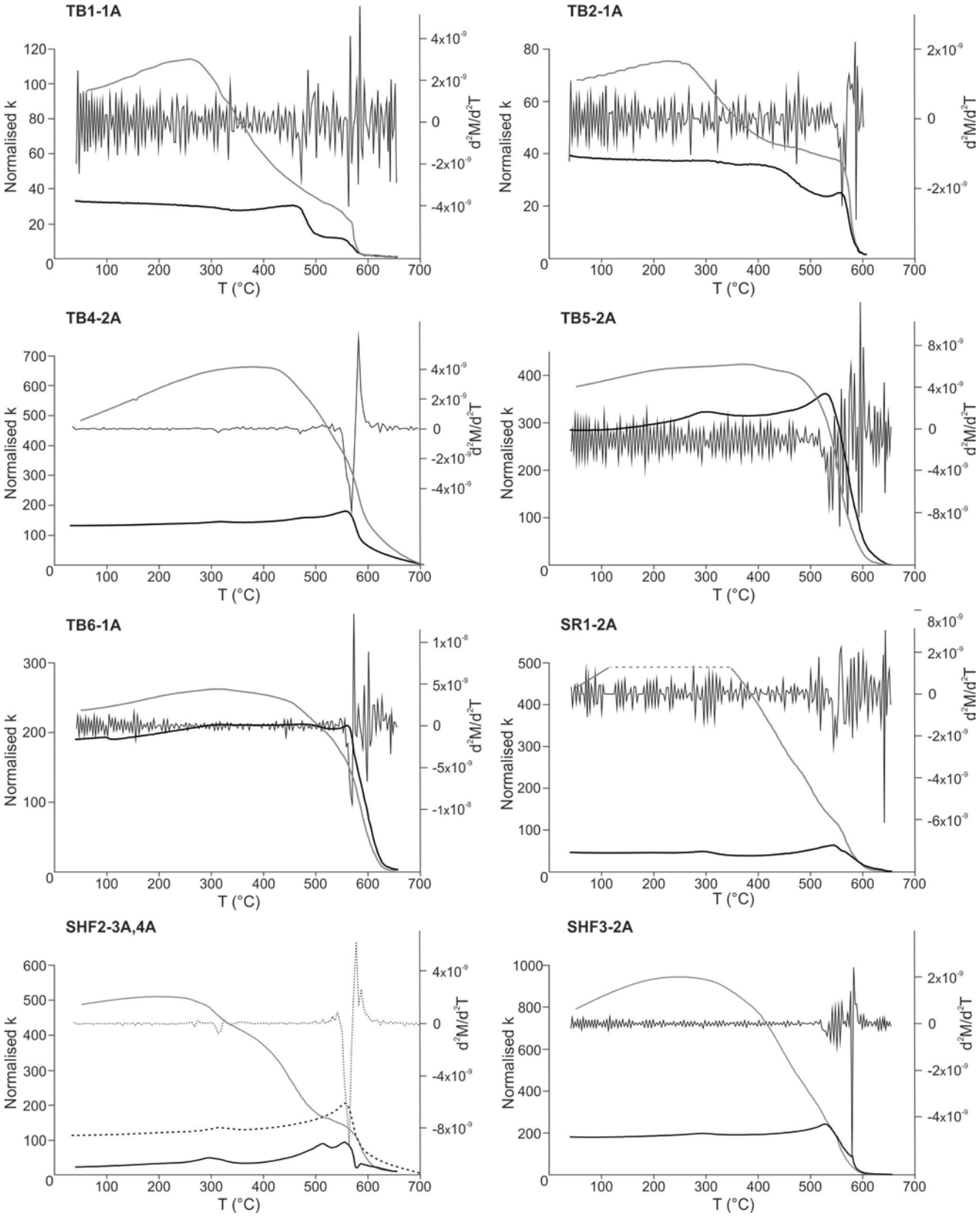

(a) continued

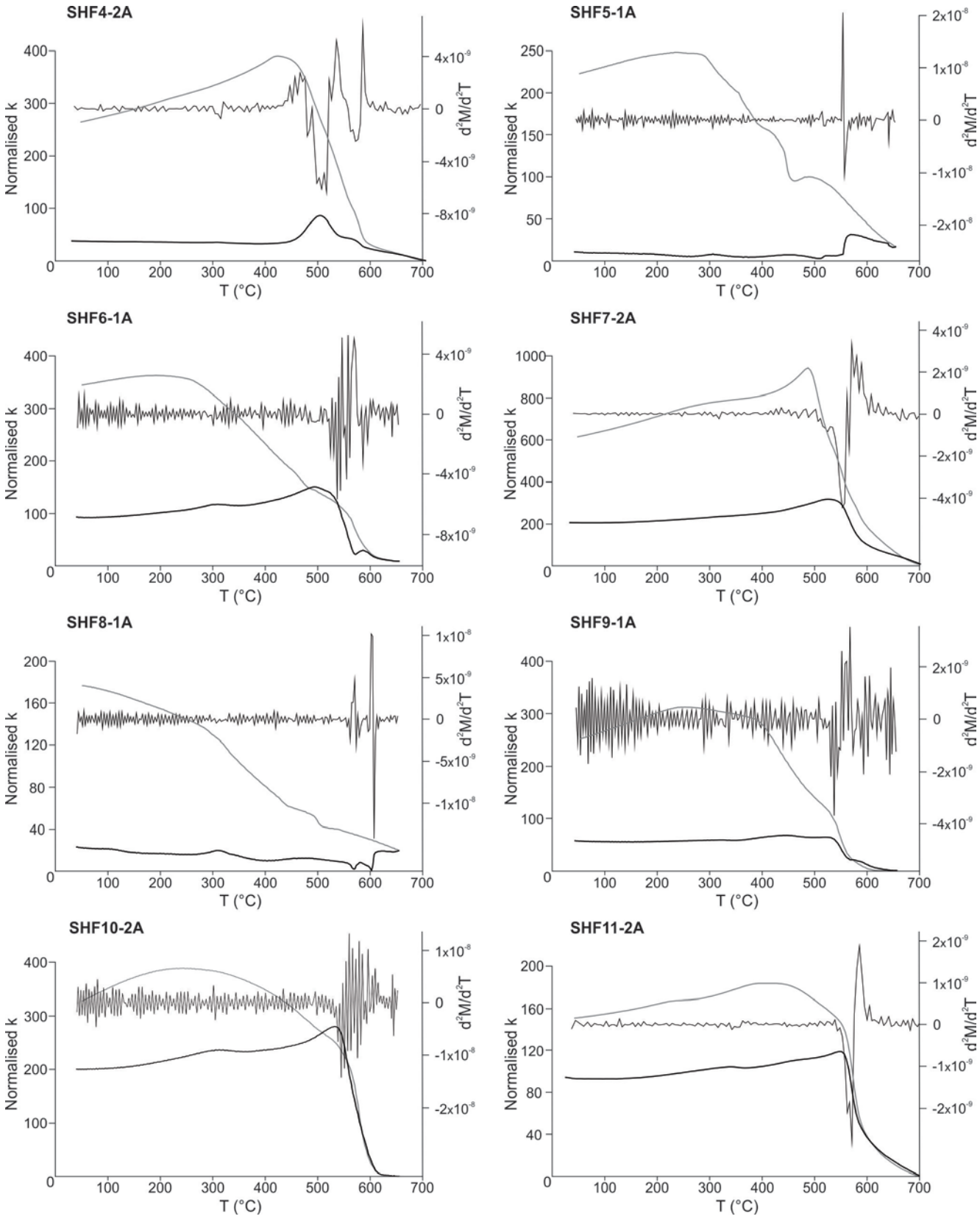
SHF4-2A
SHF5-1A
SHF6-1A
SHF7-2A
SHF8-1A
SHF9-1A
SHF10-2A
SHF11-2A
Normalised k
T (°C)
d²M/d²T

(b) Low Temperature Demagnetisation Curves

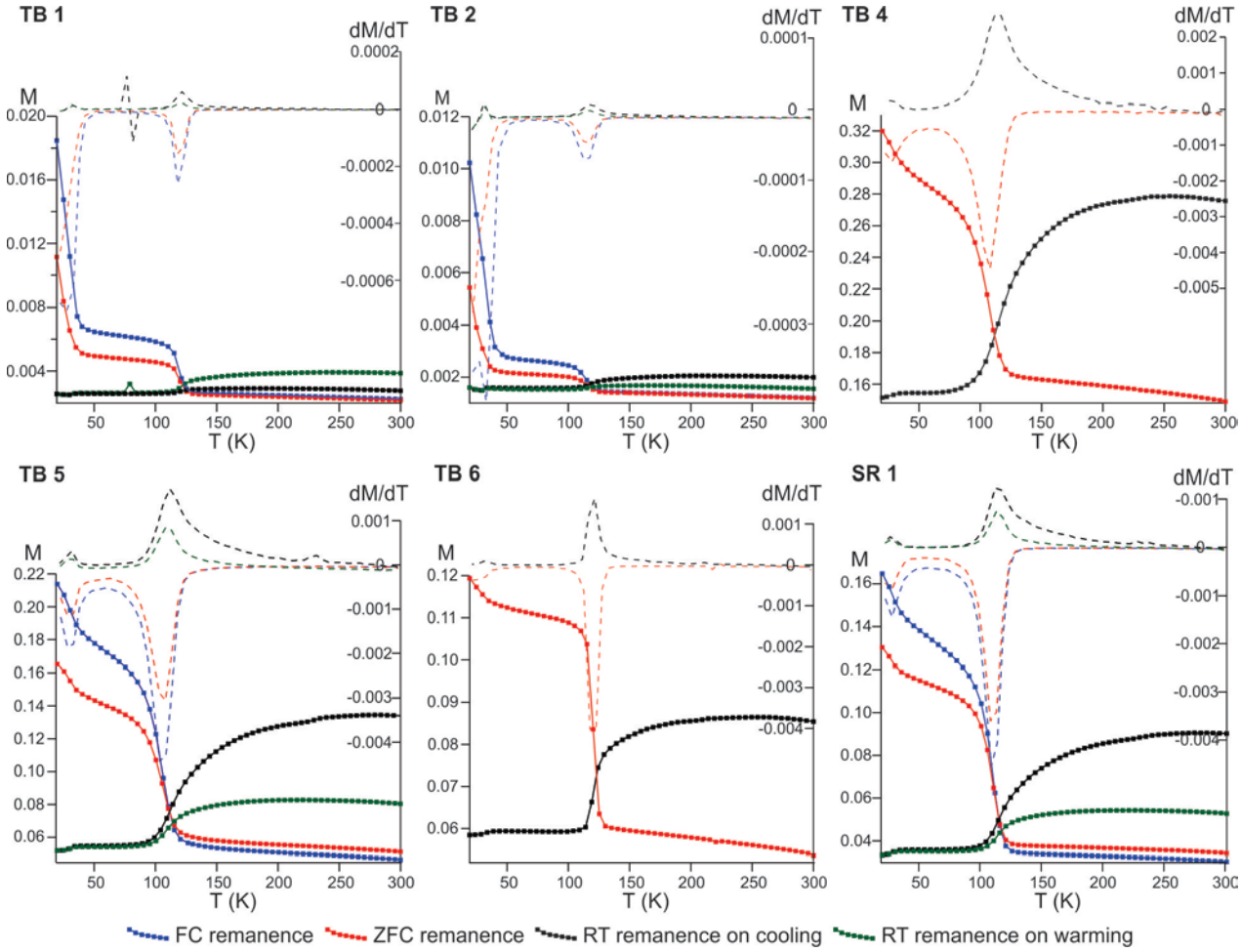

(b) continued

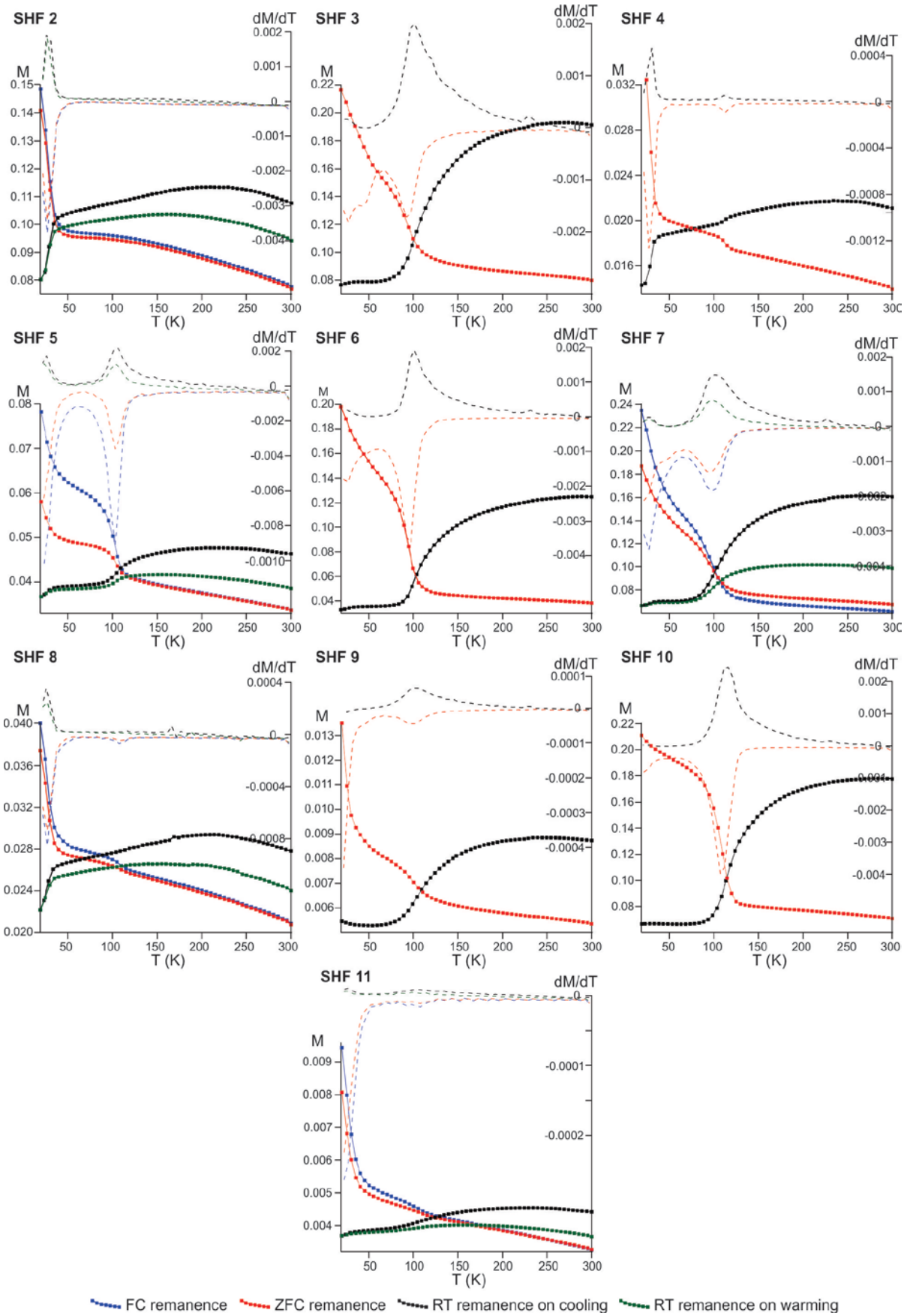
SHF 2
SHF 3
SHF 4
SHF 5
SHF 6
SHF 7
SHF 8
SHF 9
SHF 10
SHF 11
M
dM/dT
T (K)
FC remanence
ZFC remanence
RT remanence on cooling
RT remanence on warming

(c) Hysteresis Curves

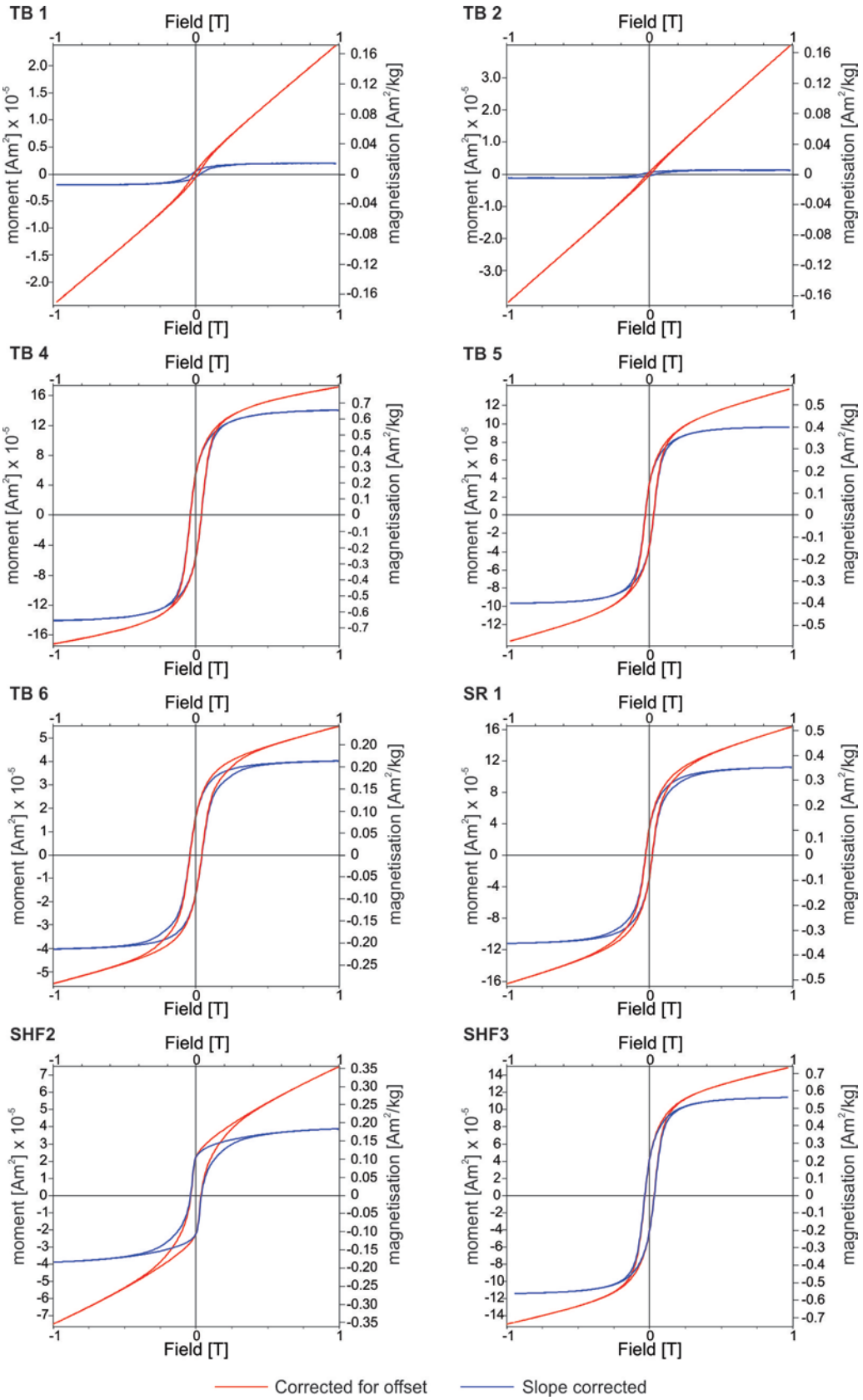

(c) continued

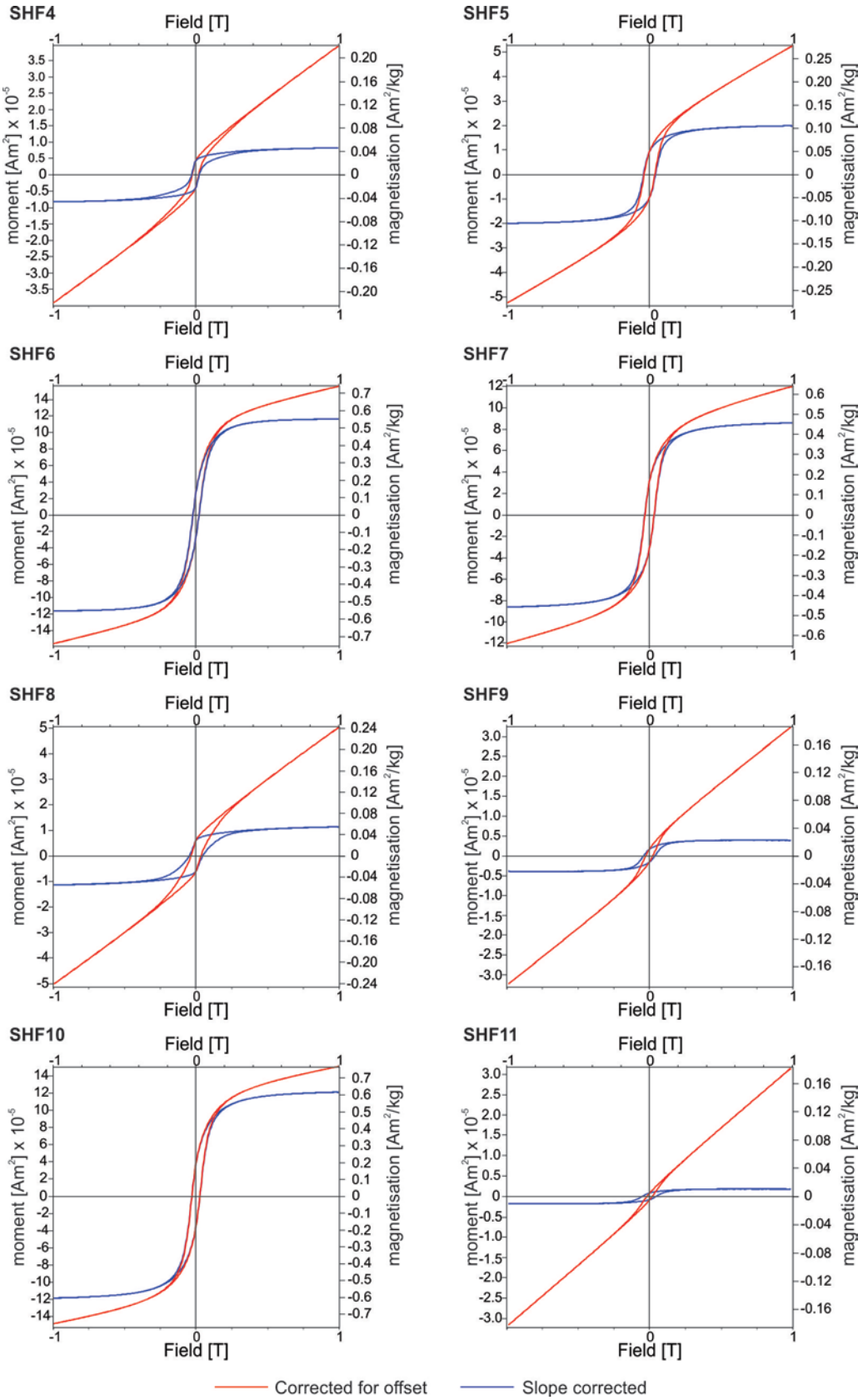
SHF4
SHF5
SHF6
SHF7
SHF8
SHF9
SHF10
SHF11
Field [T]
moment [Am²] x 10⁻⁵
magnetisation [Am²/kg]
Corrected for offset
Slope corrected

(d) First Order Reversal Curve plots

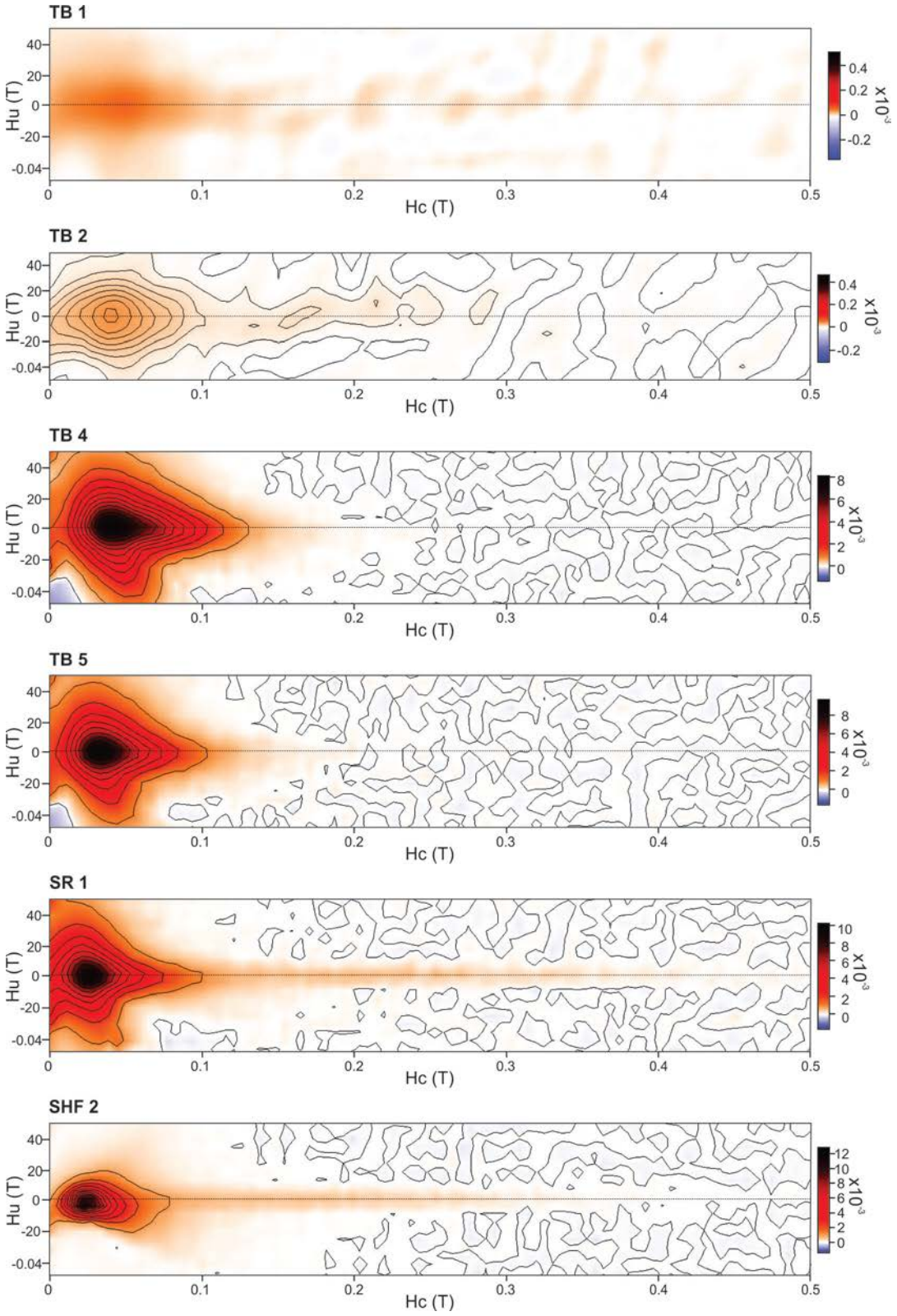

(d) continued

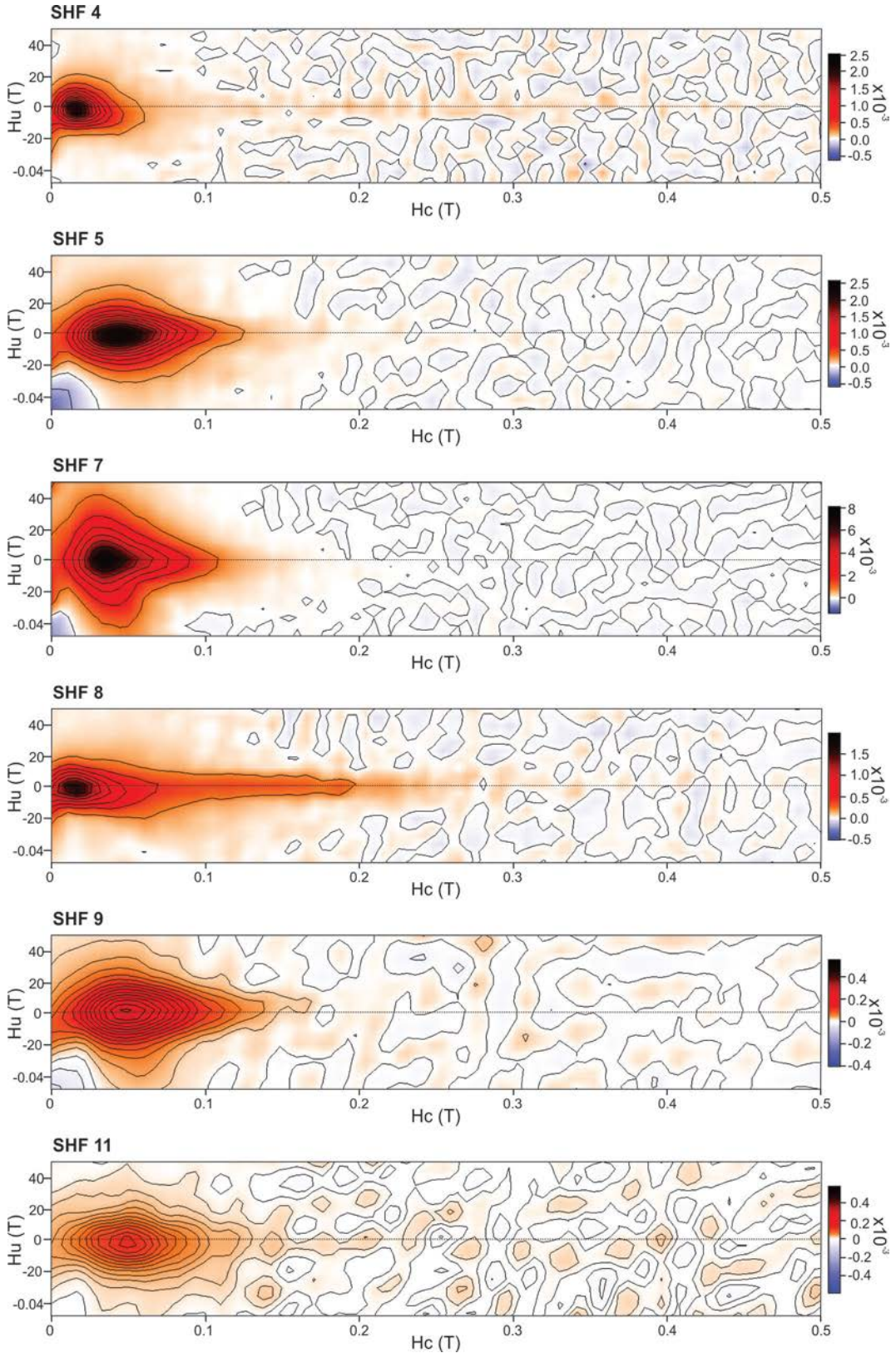

8. Tabulated AMS data

(a) Results from Thompson's Bay and Shaka's Rock

				Principal axes plunge direction				Axis Length		
Name	Km	Pj	T	K1dec	K1inc	K3dec	K3inc	K1	K2	K3
TB-1A	696.8	1.005	0.476	051.2°	03.7°	151.7°	70.7°	1.0009	1.0013	0.9978
TB-1B	631.0	1.007	0.402	288.7°	13.2°	097.1°	76.6°	1.0011	1.0023	0.9966
TB-1F	690.0	1.005	-0.027	264.1°	11.9°	146.3°	65.6°	0.9997	1.0022	0.9981
TB-1G	815.6	1.014	-0.276	272.9°	06.5°	150.9°	77.9°	0.9986	1.0075	0.9940
TB-1H	791.5	1.013	0.814	319.6°	13.2°	135.6°	76.7°	1.0036	1.0034	0.9930
TB-1L	606.2	1.010	-0.349	302.2°	28.2°	149.6°	58.9°	0.9997	1.0022	0.9981
TB-1M	687.5	1.007	0.462	258.9°	11.9°	126.2°	72.7°	1.0009	1.0023	0.9969
TB-1N	907.0	1.013	0.135	238.4°	10.1°	105.5°	75.3°	1.0021	1.0042	0.9938
TB-1P	763.9	1.013	0.175	228.5°	06.7°	119.8°	70.0°	1.0029	1.0031	0.9941
TB-1O-2	929.2	1.012	0.347	278.7°	05.8°	159.4°	78.2°	1.0011	1.0050	0.9939
TB-10-1	935.3	1.011	0.152	306.0°	15.2°	150.1°	73.5°	1.0016	1.0032	0.9952
TB-2AA	590.4	1.012	0.281	349.6°	14.0°	144.8°	74.6°	1.0048	1.0011	0.9942
TB-2AB-1	643.9	1.012	0.429	037.9°	08.6°	159.1°	73.6°	1.0030	1.0027	0.9943
TB-2AB-2	592.6	1.011	0.317	044.9°	06.1°	151.8°	69.9°	1.0023	1.0028	0.9949
TB-2AC-1	603.6	1.019	0.543	339.0°	20.7°	146.0°	68.8°	1.0050	1.0031	0.9919
TB-2AC-2	589.7	1.019	0.457	337.0°	21.1°	157.1°	68.9°	1.0049	1.0031	0.9921
TB-2AD	616.9	1.009	0.565	325.2°	20.8°	124.4°	67.9°	1.0024	1.0015	0.9961
TB-2LA	544.5	1.010	-0.136	339.7°	01.7°	089.1°	84.9°	1.0044	1.0002	0.9955
TB-2LB	934.2	1.018	0.265	341.5°	07.0°	145.2°	82.8°	1.0073	1.0021	0.9906
TB-2LC	2401.6	1.016	0.310	166.9°	05.4°	060.1°	71.9°	1.0064	1.0011	0.9925
TB-2LD	1934.9	1.021	-0.585	111.7°	78.8°	224.5°	04.4°	0.9943	0.9948	1.0110
TB-2LE	1855.1	1.022	-0.427	150.5°	70.1°	257.2°	05.9°	0.9980	0.9918	1.0102
TB-UF-1117	654.1	1.024	0.144	357.9°	20.8°	120.7°	55.0°	1.0087	0.9979	0.9935
TB-2UI	620.4	1.011	-0.440	010.8°	22.7°	176.1°	66.6°	1.0042	0.9987	0.9971
TB-2UJ	792.5	1.010	0.191	353.6°	20.7°	212.2°	64.2°	1.0033	1.0004	0.9963
TB-2D	553.6	1.018	-0.143	317.2°	21.5°	115.0°	67.0°	1.0036	1.0022	0.9942
TB-2UF-2	571.0	1.019	-0.155	347.7°	15.2°	105.6°	59.8°	1.0084	0.9976	0.9939
TB-2VA	727.4	1.021	-0.226	327.7°	16.4°	090.0°	61.2°	1.0067	0.9999	0.9934
TB-2VB-1	786.8	1.018	-0.333	351.0°	14.3°	175.4°	75.6°	1.0084	0.9983	0.9933
TB-2VC-1	675.9	1.018	-0.047	350.3°	16.0°	137.4°	71.2°	1.0078	0.9995	0.9927
TB-2VC-2	525.3	1.021	-0.220	354.6°	12.9°	128.1°	71.6°	1.0098	0.9981	0.9921
TB-2VD-1	829.3	1.014	-0.525	336.9°	18.5°	175.5°	70.5°	1.0049	0.9991	0.9960
TB-2VD-2	792.1	1.013	-0.489	337.7°	17.0°	193.3°	69.4°	1.0048	0.9992	0.9961
TB-2VE-1	654.4	1.014	-0.447	345.3°	19.7°	216.2°	60.5°	1.0054	0.9983	0.9963
TB-2VE-2	593.0	1.022	-0.381	326.3°	14.4°	085.4°	62.2°	1.0068	1.0001	0.9931
TB-2VF-1	577.0	1.022	-0.272	343.9°	16.3°	115.5°	66.2°	1.0094	0.9980	0.9927
TB-2VF-2	566.7	1.014	-0.088	026.9°	30.9°	171.4°	53.7°	1.0018	1.0007	0.9976
TB-2VB-2	700.2	1.018	-0.238	349.1°	11.8°	128.5°	74.6°	1.0083	0.9987	0.9930
TB-3LB	2609.2	1.017	-0.455	200.9°	02.8°	290.9°	01.6°	1.0074	0.9951	0.9975
TB-3LD	8479.9	1.043	-0.098	252.7°	02.1°	137.0°	85.2°	1.0005	1.0197	0.9799
TB-4LG	8613.7	1.040	-0.089	301.1°	18.3°	129.1°	71.5°	1.0032	1.0118	0.9851
TB-4UH-1	5654.2	1.028	0.166	287.3°	21.0°	094.7°	68.5°	1.0023	1.0085	0.9892
TB-4UH-2	8660.7	1.036	0.170	286.4°	18.9°	115.4°	70.9°	1.0025	1.0122	0.9852
TB-4LE-1	10972.1	1.034	-0.539	268.1°	24.1°	098.6°	65.5°	0.9942	1.0136	0.9922
TB-4LE-2	7153.8	1.046	-0.818	291.1°	09.3°	187.5°	55.1°	0.9924	1.0202	0.9874
TB-4LF	10074.3	1.055	0.288	251.9°	09.0°	120.7°	76.5°	1.0061	1.0202	0.9737
TB-4LC	11209.1	1.044	-0.384	279.3°	13.1°	091.5°	76.8°	0.9952	1.0208	0.9840
TB-4UA	10155.4	1.041	-0.194	298.2°	24.2°	136.3°	64.6°	1.0002	1.0114	0.9883
TB-4UD	10203.7	1.038	-0.127	300.9°	20.8°	129.2°	69.1°	1.0024	1.0106	0.9870
TB-4UE	6917.3	1.047	0.256	287.6°	14.2°	142.3°	72.9°	1.0037	1.0176	0.9787
TB-5LA	11192.7	1.038	0.026	275.1°	07.1°	041.3°	78.0°	0.9999	1.0176	0.9826
TB-5LB	3370.3	1.025	0.593	276.6°	17.9°	054.4°	66.4°	1.0037	1.0069	0.9894
TB-5LC-2	8607.0	1.033	0.033	274.0°	07.4°	033.5°	75.2°	0.9996	1.0156	0.9848
TB-5LD	3536.4	1.029	0.527	278.5°	13.7°	058.0°	72.2°	1.0044	1.0095	0.9862

(a) continued

				Principal axes plunge direction				Axis Length		
Name	Km	Pj	T	K1dec	K1inc	K3dec	K3inc	K1	K2	K3
TB-5LC-1	8126.7	1.034	-0.008	272.7°	09.0°	035.0°	73.6°	0.9990	1.0161	0.9849
TB-5UA	8557.3	1.037	0.329	099.8°	05.5°	219.7°	79.1°	1.0036	1.0150	0.9813
TB-5UB	11748.8	1.063	0.368	246.9°	09.4°	108.0°	77.7°	1.0097	1.0212	0.9691
TB-5UC	10263.7	1.055	0.280	272.2°	02.2°	165.0°	82.7°	1.0043	1.0240	0.9717
TB-5UD-1	10065.7	1.040	0.379	276.1°	12.5°	098.3°	77.5°	1.0049	1.0149	0.9802
TB-5UD-2	9410.3	1.042	0.382	267.9°	07.8°	125.4°	80.2°	1.0048	1.0169	0.9783
TB-5UE-1	11148.3	1.063	0.310	261.2°	16.3°	106.6°	72.1°	1.0061	1.0216	0.9723
TB-5UE-2	8063.5	1.058	0.286	263.5°	19.2°	105.3°	69.5°	1.0050	1.0188	0.9763
TB-5UE-3	11767.8	1.061	0.266	266.1°	19.5°	114.1°	68.1°	1.0042	1.0200	0.9759
TB-6UA	7956.7	1.016	0.191	301.3°	17.6°	098.1°	71.0°	1.0025	1.0042	0.9933
TB-6UB	5000.6	1.024	-0.779	311.6°	14.8°	129.4°	75.2°	1.0022	1.0043	0.9935
TB-6UC	7393.6	1.026	-0.196	274.0°	02.0°	021.8°	83.5°	0.9982	1.0136	0.9882
TB-6UD	7786.2	1.017	-0.652	328.7°	16.5°	072.9°	39.6°	1.0053	0.9983	0.9964
SR-1CA	2819.3	1.043	0.197	106.8°	00.9°	199.6°	71.9°	1.0019	1.0178	0.9803
SR-1CB	1169.3	1.024	-0.034	109.3°	03.7°	213.3°	75.0°	1.0005	1.0102	0.9893
SR-1CC	1009.8	1.015	0.297	285.0°	03.9°	178.7°	76.2°	1.0013	1.0064	0.9923
SR-1CD	2818.6	1.015	-0.462	103.6°	06.8°	242.2°	81.0°	0.9983	1.0076	0.9941
SR-1CE	2551.7	1.016	-0.157	292.5°	06.3°	175.0°	76.6°	1.0001	1.0067	0.9932
SR-1LA	6244.6	1.033	0.694	061.8°	02.7°	162.4°	75.6°	1.0066	1.0105	0.9829
SR-1LB	6966.8	1.043	0.155	272.6°	42.8°	081.6°	46.6°	1.0018	1.0006	0.9977
SR-1LC	5899.6	1.026	0.210	302.7°	01.8°	200.3°	81.7°	1.0045	1.0089	0.9866
SR-1LD	5646.7	1.012	-0.349	297.0°	14.2°	035.7°	31.1°	0.9984	1.0035	0.9982
SR-1LE	4150.2	1.023	-0.531	127.1°	10.1°	224.4°	35.5°	1.0003	1.0048	0.9949
SR-1LF	5628.0	1.011	-0.009	119.5°	25.7°	210.5°	01.9°	0.9969	1.0021	1.0010
SR-1UB	2920.0	1.041	0.732	020.6°	12.4°	175.2°	76.3°	1.0114	1.0096	0.9790
SR-1UC-1	5183.3	1.028	-0.489	059.1°	04.6°	302.8°	79.6°	1.0008	1.0100	0.9893
SR-1UC-2	4718.5	1.028	-0.337	059.6°	05.1°	306.3°	77.2°	1.0014	1.0102	0.9884
SR-1UD	3535.2	1.010	0.437	201.8°	62.5°	038.0°	26.6°	0.9985	0.9994	1.0021
SR-1UE	2627.6	1.009	0.038	218.0°	13.9°	321.8°	43.9°	1.0012	1.0008	0.9980

*Highlighted values were used as the proxy for magma flow

(b) Results from Sheffield Beach

				Principal axes plunge direction				Axis Length		
Name	Km	Pj	T	K1dec	K1inc	K3dec	K3inc	K1	K2	K3
SHF-2LA-1	1759.4	1.010	-0.727	283.1°	13.2°	146.8°	72.0°	0.9981	1.0049	0.9970
SHF-2LA-2	1800.4	1.012	-0.628	289.9°	04.9°	198.9°	11.6°	0.9970	1.0054	0.9977
SHF-2LB-1	7247.0	1.021	-0.002	092.3°	04.7°	357.4°	46.2°	0.9950	1.0103	0.9946
SHF-2LB-2	8892.9	1.021	0.001	091.1°	07.2°	352.5°	49.8°	0.9958	1.0099	0.9942
SHF-2LC-1	10524.6	1.021	0.154	220.7°	34.1°	018.7°	53.8°	1.0008	1.0031	0.9961
SHF-2LD	719.3	1.002	-0.374	296.5°	66.6°	107.9°	23.2°	0.9998	0.9995	1.0007
SHF-2LC-2	9478.1	1.020	0.255	220.8°	36.6°	028.1°	52.8°	1.0009	1.0027	0.9965
SHF-2LE-1	1445.9	1.036	0.651	159.7°	16.8°	331.8°	73.0°	1.0099	1.0071	0.9830
SHF-2LE-2	1376.1	1.024	0.694	122.8°	10.6°	335.8°	77.4°	1.0052	1.0071	0.9877
SHF-2UA	649.6	1.002	0.016	149.3°	50.6°	274.8°	25.5°	1.0002	0.9994	1.0003
SHF-2UB	3683.3	1.011	0.373	170.0°	20.3°	056.7°	46.9°	1.0031	0.9990	0.9978
SHF-2UC-1	599.5	1.003	-0.042	186.1°	75.5°	046.0°	11.2°	0.9993	0.9992	1.0015
SHF-2UC-2	554.2	1.003	0.063	187.9°	70.7°	054.7°	13.5°	0.9997	0.9991	1.0012
SHF-3LA	7936.2	1.020	0.568	205.5°	49.4°	060.7°	35.0°	1.0026	0.9963	1.0011
SHF-3LB	807.1	1.006	-0.310	240.5°	01.7°	332.0°	43.0°	0.9995	1.0022	0.9984
SHF-3LC-1	898.1	1.008	-0.687	085.3°	02.6°	350.9°	59.0°	0.9980	1.0047	0.9973
SHF-2LC-2	706.2	1.011	0.031	089.3°	23.1°	183.2°	09.1°	0.9946	1.0046	1.0008
SHF-2LD-1	7491.5	1.021	0.162	205.0°	43.2°	074.2°	34.9°	1.0044	0.9943	1.0013
SHF-3LD-2	7467.2	1.022	0.012	210.1°	42.0°	067.8°	41.3°	1.0037	0.9962	1.0001
SHF-3LE-1	9663.1	1.025	0.748	176.3°	21.7°	057.6°	50.3°	1.0058	0.9999	0.9944
SHF-3LE-2	9771.1	1.025	0.734	169.4°	21.1°	052.9°	49.2°	1.0050	1.0003	0.9947
SHF-3LF-1	798.7	1.006	-0.469	068.7°	16.6°	304.7°	62.0°	0.9995	1.0023	0.9982
SHF-3LF-2	723.8	1.010	-0.648	077.2°	10.4°	173.6°	31.2°	0.9972	1.0050	0.9978
SHF-3UA-1	915.0	1.004	-0.580	248.7°	28.0°	151.3°	13.7°	0.9990	1.0012	0.9999
SHF-3UA-2	979.5	1.005	-0.392	253.6°	31.5°	013.0°	38.6°	0.9988	1.0015	0.9997
SHF-3UB	681.7	1.006	-0.630	104.3°	17.5°	194.7°	01.2°	0.9981	1.0027	0.9992
SHF-3UC	706.7	1.005	0.565	079.4°	03.1°	348.8°	10.9°	0.9973	1.0019	1.0008
SHF-3UD	6222.4	1.043	0.229	251.0°	00.0°	341.0°	05.6°	0.9824	1.0148	1.0028
SHF-3UE	6131.1	1.023	-0.359	251.5°	39.9°	346.2°	05.6°	0.9915	1.0050	1.0035
SHF-3UF-1	6867.3	1.034	-0.546	246.2°	43.8°	009.4°	29.7°	0.9909	1.0048	1.0043
SHF-3UF-2	3915.5	1.027	-0.686	251.5°	45.2°	016.2°	29.4°	0.9928	1.0034	1.0039
SHF-4LA	703.8	1.006	0.523	163.6°	25.6°	308.5°	59.6°	1.0016	1.0004	0.9980
SHF-4LB	700.5	1.016	0.080	186.2°	10.9°	321.3°	74.8°	1.0071	1.0003	0.9926
SHF-4LC	723.1	1.011	0.265	120.9°	27.8°	308.2°	62.0°	1.0012	1.0024	0.9964
SHF-4LD	1145.4	1.014	0.396	143.0°	20.5°	305.1°	68.6°	1.0038	1.0023	0.9940
SHF-4UA	859.9	1.007	0.403	239.1°	09.6°	018.3°	77.4°	1.0013	1.0024	0.9964
SHF-4UB-1	827.4	1.012	0.254	132.9°	07.6°	265.5°	78.8°	1.0029	1.0029	0.9942
SHF-4UB-2	902.3	1.018	0.216	132.4°	07.2°	261.4°	78.6°	1.0043	1.0045	0.9911
SHF-4UC	769.7	1.010	0.057	144.4°	05.5°	338.0°	84.3°	1.0032	1.0018	0.9950
SHF-4UD	712.2	1.007	-0.395	342.1°	01.9°	244.8°	75.8°	1.0032	0.9995	0.9973
SHF-4UE	649.1	1.005	0.271	165.1°	08.5°	269.4°	59.1°	1.0019	0.9998	0.9984
SHF-5LA-2	603.6	1.002	0.200	199.5°	21.5°	010.2°	68.2°	1.0007	1.0002	0.9991
SHF-5LB-1	1317.0	1.024	0.787	222.0°	04.9°	013.6°	84.5°	1.0067	1.0066	0.9867
SHF-5LB-2	1249.2	1.016	-0.300	125.2°	50.4°	249.5°	25.0°	0.9993	0.9974	1.0034
SHF-5LC	1115.4	1.027	0.787	260.9°	02.5°	000.1°	74.9°	1.0050	1.0090	0.9860
SHF-5LD-1	3051.7	1.031	-0.008	225.9°	54.9°	046.1°	35.1°	0.9975	0.9973	1.0053
SHF-5LD-2	8648.0	1.038	0.084	233.5°	50.5°	035.7°	38.2°	0.9953	1.0012	1.0035
SHF-5LE-1	6330.1	1.034	0.846	154.7°	35.1°	328.0°	54.7°	1.0031	1.0062	0.9907
SHF-5LE-2	4698.6	1.027	0.635	187.7°	26.7°	330.5°	57.7°	1.0045	1.0039	0.9916
SHF-5LF	2794.7	1.013	-0.141	100.0°	15.0°	330.7°	67.0°	0.9990	1.0058	0.9953
SHF-5UA-1	559.0	1.005	-0.363	168.7°	14.7°	068.9°	32.9°	1.0022	0.9986	0.9992
SHF-5UA-2	559.4	1.004	-0.671	175.6°	28.8°	058.1°	40.1°	1.0014	0.9989	0.9996
SHF-5UB	1375.7	1.210	0.642	135.2°	10.3°	039.3°	29.8°	0.9885	1.0095	1.0020
SHF-5UC-1	5972.9	1.024	0.205	156.5°	13.7°	020.7°	71.3°	1.0077	1.0028	0.9896

(b) continued

				Principal axes plunge direction				Axis Length		
Name	Km	Pj	T	K1dec	K1inc	K3dec	K3inc	K1	K2	K3
SHF-5UC-2	5888.8	1.027	0.365	109.1°	24.8°	285.4°	65.1°	1.0036	1.0063	0.9900
SHF-5UD	5094.3	1.037	0.295	215.8°	18.5°	071.6°	67.6°	1.0108	1.0044	0.9849
SHF-5UE-1	1431.7	1.020	-0.179	168.6°	22.3°	335.6°	67.1°	1.0076	0.9990	0.9935
SHF-5UE-2	1130.8	1.012	0.434	209.3°	13.6°	001.2°	74.7°	1.0034	1.0024	0.9943
SHF-5UF-1	2813.6	1.109	-0.513	172.4°	37.6°	268.6°	07.9°	1.0295	0.9602	1.0103
SHF-5UF-2	2349.5	1.119	-0.773	163.6°	44.8°	273.3°	18.8°	1.0158	0.9665	1.0177
SHF-6LA	6179.7	1.010	-0.465	260.4°	05.9°	350.6°	01.4°	0.9961	1.0053	0.9986
SHF-6LB-1	10908.2	1.006	-0.842	089.0°	02.6°	180.1°	25.1°	0.9980	1.0037	0.9983
SHF-6LB-2	11126.2	1.011	-0.413	102.2°	04.9°	356.4°	72.7°	0.9986	1.0055	0.9958
SHF-6LC-1	9155.8	1.006	-0.074	087.2°	06.6°	187.9°	58.2°	0.9991	1.0030	0.9979
SHF-6LC-2	2684.9	1.004	0.198	086.6°	09.0°	187.4°	49.7°	0.9992	1.0020	0.9988
SHF-6LD	7893.4	1.031	0.505	237.3°	03.7°	122.8°	81.1°	1.0068	1.0096	0.9836
SHF-6LE	6328.6	1.008	-0.539	285.7°	05.5°	034.5°	73.4°	0.9989	1.0040	0.9970
SHF-6LF-1	12497.5	1.011	0.441	269.1°	03.6°	179.0°	01.8°	0.9941	1.0044	1.0015
SHF-6LF-2	12519.7	1.010	-0.216	085.9°	00.2°	355.8°	10.6°	0.9957	1.0051	0.9992
SHF-6UA	1540.8	1.015	-0.175	351.3°	63.0°	160.1°	26.6°	0.9965	0.9986	1.0049
SHF-6UB	11966.3	1.012	0.402	268.2°	38.9°	177.2°	01.3°	0.9932	1.0038	1.0030
SHF-6UC	7569.1	1.005	-0.046	045.6°	27.7°	211.8°	61.6°	1.0005	1.0008	0.9987
SHF-6UD-1	5365.7	1.007	-0.239	238.3°	22.9°	133.3°	31.5°	0.9996	1.0011	0.9994
SHF-6UD-2	10253.6	1.008	0.032	049.3°	01.0°	139.7°	19.0°	0.9996	1.0007	0.9997
SHF-6UE	9745.5	1.017	-0.122	266.6°	06.7°	161.8°	65.4°	0.9982	1.0086	0.9933
SHF-6UF	6414.1	1.007	0.495	332.1°	15.2°	100.7°	66.4°	1.0022	1.0006	0.9972
SHF-6UG	5070.0	1.004	0.722	273.3°	14.5°	157.1°	59.7°	1.0002	1.0011	0.9987
SHF-6UH	8621.1	1.020	-0.606	311.0°	00.6°	219.4°	68.4°	1.0024	1.0046	0.9930
SHF-6UI-1	7846.0	1.007	0.632	131.3°	54.7°	232.0°	07.5°	0.9996	0.9984	1.0020
SHF-6UJ-1	4703.9	1.012	0.464	111.1°	10.4°	349.3°	70.9°	1.0013	1.0045	0.9942
SHF-6UJ-2	10870.0	1.019	0.360	116.1°	13.5°	336.9°	72.4°	1.0023	1.0065	0.9912
SHF-7LA-1	992.6	1.003	-0.143	176.9°	21.5°	351.6°	68.5°	1.0011	0.9999	0.9990
SHF-7LA-2	897.6	1.003	-0.723	159.2°	21.1°	259.5°	24.8°	1.0011	0.9993	0.9996
SHF-7LB-1	3414.7	1.022	-0.260	179.8°	66.1°	074.1°	06.9°	0.9997	0.9908	1.0094
SHF-7LB-2	4650.6	1.026	-0.250	156.5°	69.1°	248.1°	00.6°	0.9982	0.9901	1.0117
SHF-7LC	7449.7	1.026	0.163	094.6°	04.0°	349.4°	75.3°	1.0005	1.0121	0.9874
SHF-7LE-1	13038.0	1.017	0.038	311.0°	12.8°	159.5°	75.5°	1.0031	1.0047	0.9922
SHF-7LE-2	11080.1	1.018	0.230	310.5°	09.4°	167.9°	78.2°	1.0037	1.0052	0.9911
SHF-7LD	9486.0	1.029	-0.002	096.7°	06.0°	316.4°	82.2°	1.0000	1.0137	0.9863
SHF-7UC-1	8149.5	1.021	-0.387	290.5°	09.0°	033.8°	55.4°	0.9976	1.0090	0.9934
SHF-7UC-2	8700.2	1.022	-0.468	289.5°	06.9°	028.5°	52.4°	0.9968	1.0098	0.9934
SHF-7UE	8869.1	1.016	-0.689	275.3°	13.3°	179.8°	22.2°	0.9947	1.0083	0.9969
SHF-7UG	5952.6	1.021	-0.449	280.2°	06.1°	015.3°	40.1°	0.9945	1.0106	0.9949
SHF-7UH-1	5743.1	1.023	-0.459	314.1°	14.9°	045.3°	04.7°	1.0010	1.0014	0.9976
SHF-7UA	8567.0	1.019	-0.474	017.5°	03.6°	282.1°	56.6°	1.0091	0.9970	0.9939
SHF-7UB-1	652.2	1.004	0.362	094.5°	81.9°	342.5°	03.1°	0.9981	1.0003	1.0016
SHF-7UB-2	7334.7	1.016	-0.719	103.2°	10.7°	009.0°	21.0°	0.9952	1.0082	0.9965
SHF-7UH-2	7180.9	1.024	-0.657	314.4°	15.0°	218.7°	20.3°	1.0015	1.0027	0.9958
SHF-8LG-2	873.0	1.056	-0.223	070.0°	08.8°	247.6°	81.2°	0.9995	1.0240	0.9765
SHF-8LH-1	4489.2	1.023	-0.726	185.5°	23.4°	330.6°	62.2°	1.0098	0.9948	0.9954
SHF-8LH-2	1290.3	1.014	0.455	153.9°	18.4°	001.6°	69.4°	1.0034	1.0026	0.9940
SHF-8LI-1	1318.8	1.061	0.145	301.7°	01.8°	037.6°	72.8°	1.0079	1.0202	0.9720
SHF-8LJ	4451.4	1.017	-0.088	193.6°	17.4°	307.8°	52.7°	1.0062	0.9982	0.9956
SHF-8LK	1680.0	1.052	-0.239	332.7°	26.5°	140.2°	63.0°	1.0134	0.9995	0.9871
SHF-8LL-1	1766.0	1.016	-0.357	120.9°	18.6°	290.1°	71.1°	1.0006	1.0046	0.9949
SHF-8LL-2	1649.2	1.019	-0.198	110.0°	19.0°	308.2°	70.1°	0.9996	1.0072	0.9932
SHF-8LA-1	1156.1	1.005	-0.237	195.3°	43.8°	102.3°	03.1°	1.0011	0.9978	1.0011
SHF-8LA-2	1040.3	1.006	-0.589	307.4°	15.5°	055.4°	48.1°	1.0002	1.0011	0.9987
SHF-8LB-1	1279.9	1.007	0.550	105.6°	37.1°	216.1°	24.8°	0.9985	1.0006	1.0008

(b) continued

				Principal axes plunge direction				Axis Length		
Name	Km	Pj	T	K1dec	K1inc	K3dec	K3inc	K1	K2	K3
SHF-8LB-2	1459.3	1.021	-0.032	042.3°	34.4°	269.4°	44.9°	1.0038	0.9980	0.9982
SHF-8LC-1	1236.0	1.025	-0.170	259.1°	11.5°	044.3°	76.1°	0.9988	1.0116	0.9897
SHF-8LC-2	1137.2	1.017	0.340	267.6°	17.3°	039.0°	64.8°	1.0007	1.0060	0.9933
SHF-8LD-1	4141.1	1.022	-0.265	215.5°	19.7°	328.0°	46.9°	1.0035	1.0011	0.9953
SHF-8LD-2	2406.9	1.026	0.161	216.6°	21.6°	340.8°	54.8°	1.0030	1.0042	0.9928
SHF-8LE-1	1172.6	1.019	-0.601	131.9°	11.8°	233.5°	43.8°	1.0019	1.0028	0.9953
SHF-8LE-2	650.4	1.023	-0.053	159.2°	12.5°	359.0°	76.7°	1.0090	1.0010	0.9900
SHF-8LF-1	1235.7	1.018	0.515	267.3°	07.9°	142.2°	76.3°	1.0024	1.0066	0.9910
SHF-8LF-2	590.8	1.006	0.400	054.2°	03.0°	155.5°	74.8°	1.0012	1.0020	0.9968
SHF-8LG-1	1716.9	1.122	-0.082	097.6°	07.8°	269.2°	82.1°	0.9968	1.0565	0.9467
SHF-8UA	1388.3	1.038	0.536	321.0°	01.7°	224.3°	75.7°	1.0105	1.0088	0.9807
SHF-8UB-1	1641.3	1.027	0.171	302.3°	03.1°	137.8°	86.8°	1.0046	1.0093	0.9861
SHF-8UB-2	709.7	1.008	-0.029	152.2°	02.3°	059.0°	53.8°	1.0027	0.9998	0.9975
SHF-8UC-1	1694.2	1.145	-0.281	312.4°	00.9°	067.0°	87.7°	1.0260	1.0340	0.9400
SHF-8UC-2	1723.2	1.079	-0.035	124.2°	02.4°	358.7°	85.8°	1.0110	1.0259	0.9631
SHF-8UD-1	1951.6	1.077	-0.184	329.1°	06.1°	070.8°	62.0°	1.0266	1.0008	0.9726
SHF-8UD-2	1909.9	1.049	0.124	315.0°	13.0°	091.5°	72.4°	1.0118	1.0094	0.9789
SHF-8UE-1	1833.9	1.043	-0.210	337.4°	05.0°	085.5°	74.1°	1.0185	0.9995	0.9821
SHF-8UE-2	1789.5	1.031	-0.179	322.2°	17.9°	193.2°	62.8°	1.0059	1.0041	0.9900
SHF-8UF	1492.3	1.010	-0.583	107.6°	03.5°	208.3°	71.8°	0.9987	1.0050	0.9963
SHF-8UG-1	1548.8	1.038	-0.183	298.0°	04.0°	200.8°	61.4°	0.9995	1.0143	0.9862
SHF-8UG-2	1780.6	1.016	0.770	347.9°	46.5°	127.6°	35.9°	1.0014	0.9984	1.0002
SHF-8UH-1	1592.5	1.034	-0.280	003.2°	14.9°	155.1°	73.2°	1.0160	0.9967	0.9873
SHF-8UH-2	1473.5	1.052	-0.039	331.1°	13.4°	096.4°	67.6°	1.0186	1.0016	0.9799
SHF-9LA	8394.8	1.010	0.541	228.9°	14.5°	050.4°	75.5°	1.0025	1.0027	0.9948
SHF-9LB	1412.9	1.003	0.275	318.4°	77.0°	109.3°	11.4°	1.0001	0.9985	1.0014
SHF-9LD	5953.6	1.005	-0.124	021.8°	39.0°	267.2°	27.2°	1.0013	0.9982	1.0005
SHF-9LE-2	5588.9	1.005	0.316	106.3°	11.9°	204.1°	32.8°	0.9989	1.0015	0.9997
SHF-9LF	868.1	1.005	-0.619	141.4°	53.5°	275.3°	27.2°	0.9999	0.9989	1.0012
SHF-9LG-2	1101.2	1.005	-0.240	251.0°	83.0°	097.3°	06.3°	0.9996	0.9979	1.0025
SHF-9LH	930.0	1.002	0.201	039.9°	71.0°	298.6°	03.9°	0.9999	0.9991	1.0010
SHF-9LI-1	686.1	1.001	0.228	271.7°	71.7°	026.2°	07.8°	0.9995	1.0000	1.0005
SHF-9LI-2	704.3	1.002	-0.069	119.6°	10.6°	343.4°	75.4°	1.0002	1.0008	0.9990
SHF-9LJ	634.0	1.003	0.367	085.2°	35.4°	350.2°	06.9°	0.9985	1.0009	1.0006
SHF-9LK-2	633.2	1.003	-0.559	297.3°	08.7°	195.6°	53.3°	0.9998	1.0010	0.9992
SHF-9LL	773.8	1.003	-0.234	017.1°	50.3°	109.1°	01.7°	1.0004	0.9987	1.0010
SHF-9LM	750.5	1.003	0.496	001.5°	65.9°	118.6°	11.5°	1.0001	0.9990	1.0009
SHF-9LN-2	645.6	1.003	0.253	358.6°	10.3°	267.1°	08.0°	1.0013	0.9985	1.0002
SHF-9LO-2	692.9	1.002	0.552	109.2°	56.6°	006.8°	08.1°	0.9990	1.0004	1.0006
SHF-9LP	572.3	1.002	0.125	342.8°	03.9°	206.6°	84.6°	1.0007	1.0001	0.9992
SHF-9LQ-1	726.7	1.001	0.345	011.7°	37.1°	205.4°	52.1°	1.0001	1.0001	0.9999
SHF-9LQ-2	783.2	1.001	0.154	026.0°	03.8°	124.8°	66.6°	1.0004	1.0001	0.9996
SHF-9LQ-3	596.0	1.000	-0.200	164.9°	37.3°	314.5°	48.5°	1.0001	1.0000	1.0000
SHF-9LR-1	888.0	1.006	-0.441	007.1°	80.4°	108.6°	01.9°	0.9992	0.9979	1.0030
SHF-9LR-2	953.0	1.008	-0.435	324.6°	75.4°	104.4°	11.3°	0.9990	0.9971	1.0038
SHF-9LT-2	636.1	1.001	-0.110	355.1°	28.8°	146.5°	57.9°	1.0004	0.9999	0.9997
SHF-9LV	725.1	1.003	0.597	029.7°	22.1°	292.7°	16.8°	1.0007	0.9988	1.0005
SHF-9LW	779.9	1.003	-0.120	037.9°	55.8°	283.8°	15.5°	1.0001	0.9989	1.0009
SHF-9LY-1	733.4	1.004	-0.067	195.5°	05.4°	097.3°	56.3°	1.0017	0.9996	0.9988
SHF-9LY-2	689.6	1.004	0.278	204.3°	02.1°	109.5°	66.1°	1.0016	1.0003	0.9982
SHF-9LE-1	5877.8	1.006	0.324	089.0°	18.2°	195.7°	41.3°	0.9985	1.0024	0.9991
SHF-9LG-1	912.2	1.006	0.339	133.1°	62.5°	299.8°	26.8°	1.0001	0.9986	1.0014
SHF-9LK-1	665.3	1.001	0.655	291.6°	53.9°	177.7°	16.5°	0.9995	1.0003	1.0002
SHF-9LN-1	614.8	1.001	-0.101	152.8°	14.3°	269.5°	60.3°	1.0003	1.0000	0.9997
SHF-9LO-1	641.2	1.001	0.626	354.9°	20.6°	106.3°	44.2°	1.0005	0.9998	0.9998

(b) continued

				Principal axes plunge direction				Axis Length		
Name	Km	Pj	T	K1dec	K1inc	K3dec	K3inc	K1	K2	K3
SHF-9LS	1110.5	1.009	-0.559	328.0°	83.7°	105.6°	04.7°	0.9983	0.9967	1.0049
SHF-9LU	1129.1	1.003	-0.261	045.6°	31.9°	313.5°	03.3°	0.9999	0.9998	1.0003
SHF-9LT-1	776.5	1.002	0.409	026.9°	00.3°	118.6°	79.2°	1.0008	1.0004	0.9989
SHF-9LX	607.0	1.003	0.282	326.0°	75.7°	156.2°	14.1°	0.9989	1.0000	1.0011
SHF-9UA-2	692.0	1.002	-0.398	334.6°	77.8°	184.2°	10.7°	0.9991	0.9997	1.0012
SHF-9UB-1	675.2	1.002	-0.549	339.9°	69.3°	092.5°	08.3°	0.9998	0.9991	1.0011
SHF-9UA-1	680.8	1.003	-0.709	068.1°	79.0°	304.1°	06.2°	0.9993	0.9992	1.0015
SHF-9UB-2	645.5	1.003	-0.341	031.0°	64.9°	159.5°	16.3°	0.9993	0.9997	1.0011
SHF-10LA-1	5292.6	1.007	-0.404	178.1°	04.3°	086.8°	16.7°	1.0039	0.9972	0.9989
SHF-10L-2	3727.4	1.009	-0.300	185.5°	12.8°	293.0°	53.0°	1.0044	0.9982	0.9974
SHF-10LB-1	7951.6	1.010	0.338	244.5°	22.8°	059.2°	67.1°	1.0013	1.0025	0.9962
SHF-10LB-2	8180.0	1.009	0.623	207.9°	23.7°	075.0°	57.2°	1.0027	1.0002	0.9972
SHF-10LC-1	9599.7	1.021	-0.598	188.6°	08.0°	291.5°	57.7°	1.0108	0.9955	0.9937
SHF-10LC-2	8857.9	1.022	-0.661	187.0°	12.0°	297.9°	59.1°	1.0112	0.9951	0.9937
SHF-10LD-1	5952.6	1.014	0.001	244.1°	05.9°	351.3°	70.6°	1.0006	1.0055	0.9940
SHF-10LD-2	7049.2	1.018	0.057	240.3°	05.9°	351.5°	74.2°	1.0016	1.0065	0.9919
SHF-10-LE-1	8050.3	1.018	0.596	189.2°	09.6°	335.5°	78.6°	1.0061	1.0033	0.9906
SHF-10LE-2	8182.2	1.018	0.639	183.7°	13.1°	339.9°	75.7°	1.0056	1.0034	0.9910
SHF-10UA	8623.8	1.007	-0.539	250.4°	05.1°	123.4°	81.5°	0.9993	1.0035	0.9972
SHF-10UC	5782.9	1.008	-0.366	215.6°	58.3°	335.7°	17.2°	0.9981	0.9991	1.0028
SHF-10UE	6755.5	1.019	0.072	195.7°	11.3°	014.7°	78.7°	1.0078	1.0010	0.9912
SHF-10UF	7027.2	1.018	0.173	183.6°	17.2°	012.0°	72.7°	1.0067	1.0010	0.9924
SHF-11LA	8864.4	1.012	-0.110	259.4°	21.5°	126.1°	60.1°	0.9993	1.0041	0.9966
SHF-11LB	13183.0	1.020	-0.745	064.8°	46.9°	309.8°	21.6°	0.9959	1.0004	1.0037
SHF-11LC-1	9487.7	1.012	-0.670	038.2°	10.7°	206.1°	79.1°	1.0029	1.0009	0.9962
SHF-11LC-2	8057.4	1.011	-0.222	037.5°	07.5°	274.2°	76.5°	1.0035	1.0014	0.9951
SHF-11LD	7384.4	1.004	-0.089	238.8°	01.1°	329.5°	33.5°	0.9995	1.0011	0.9994
SHF-11LF-2	8464.2	1.008	-0.530	272.2°	21.9°	134.2°	61.6°	0.9984	1.0036	0.9980
SHF-11LG-1	2850.6	1.006	-0.276	087.7°	49.6°	235.2°	35.6°	0.9990	1.0001	1.0010
SHF-11LH	5986.0	1.008	0.357	013.7°	02.0°	281.4°	47.8°	1.0034	0.9987	0.9979
SHF-11LE	10067.6	1.020	-0.023	337.7°	07.4°	191.4°	81.1°	1.0082	1.0013	0.9905
SHF-11LF-1	985.2	1.002	0.153	314.3°	52.2°	187.6°	24.9°	0.9994	1.0002	1.0004
SHF-11LG-2	4580.2	1.005	0.235	186.2°	09.5°	096.1°	00.4°	1.0020	0.9976	1.0004
SHF-11UB	6656.8	1.011	-0.675	002.3°	73.5°	202.4°	15.5°	0.9972	0.9976	1.0052
SHF-11UD	866.9	1.002	-0.615	026.7°	73.8°	222.0°	15.6°	0.9996	0.9996	1.0009
SHF-11UG	913.4	1.002	0.018	081.0°	84.9°	216.0°	03.6°	0.9993	0.9997	1.0010
SHF-11UA	1871.6	1.011	-0.803	099.4°	76.8°	006.0°	00.8°	0.9965	0.9978	1.0057
SHF-11UF	1334.5	1.004	-0.114	100.1°	78.3°	329.8°	07.7°	0.9986	0.9995	1.0019

*Highlighted values were used as the proxy for magma flow